



**Luís Miguel Monteiro
Maфра**

**RMN de Materiais Híbridos Inorgânicos-Orgânicos
Cristalinos: Métodos e Aplicações**

**NMR of Crystalline Inorganic-Organic Hybrid
Materials: Methods and Applications**



**Luís Miguel Monteiro
Mafrá**

**RMN de Materiais Híbridos Inorgânicos-Orgânicos
Cristalinos: Métodos e Aplicações**

**NMR of Crystalline Inorganic-Organic Hybrid
Materials: Methods and Applications**

Tese apresentada à Universidade de Aveiro para cumprimento dos requisitos necessários à obtenção do grau de Doutor em Química, realizada sob a orientação científica do Dr. João Rocha, Professor Catedrático do Departamento de Química da Universidade de Aveiro e de Dr. Christian Fernandez, Professor Catedrático da Universidade de Caen (França).

Apoio financeiro do POCTI no âmbito
do III Quadro Comunitário de Apoio.

Apoio financeiro da FCT e do FSE no
âmbito do III Quadro Comunitário de
Apoio.

Dedico este trabalho à minha esposa, **Ana** pelo seu grande apoio e paciência durante os meus estudos de doutoramento. Esta tese é também dedicada aos meus pais, **Rosário** e **Luís** que sempre me apoiaram.

o júri / the jury

Presidente / President

Reitora da Universidade de Aveiro

Prof. Dr. João Carlos Matias Celestino Gomes da Rocha

professor catedrático do Departamento de Química da Universidade de Aveiro

Prof. Dr. Christian Fernandez

professor catedrático da Universidade de Caen-Basse Normandie

Prof. Dr. Artur Manuel Soares Silva

professor catedrático do Departamento de Química da Universidade de Aveiro

Prof. Dr. Jean-Paul Amoureux

professor Catedrático da Universidade de Lille

Prof. Dr. Ana Maria Pissarra Coelho Gil

professora associada do Departamento de Química da Universidade de Aveiro

Prof. Dr. Florence Babonneau

directeur de Recherche CNRS da Universidade de Paris VI

Agradecimentos

No decorrer dos meus estudos de doutoramento várias pessoas contribuíram, directa ou indirectamente para o sucesso do trabalho apresentado nesta tese.

Em primeiro, gostaria de agradecer às pessoas da Universidade de Aveiro com as quais mantive uma relação de trabalho maior proximidade.

Para começar, Gostaria de agradecer, especialmente, ao Prof. João Rocha por me ter aceite no seu grupo de investigação para 3 anos de estudos de doutoramento. Desejo expressar-lhe o meu agradecimento por me ter dado toda a liberdade para desenvolver as minhas próprias ideias e por ter-me dado a conhecer muitos outros grupos de investigação com os quais mantenho colaborações presentes e futuras podendo eu contribuir com estudos de RMN. Agradeço-lhe também pelas longas e frutíferas conversas e ensinamentos que me deu acerca da técnica RMN e acima de tudo por ter partilhado comigo a sua fantástica experiência neste campo de estudos e o seu ponto de vista acerca da carreira científica, em certos encontros no seu gabinete. Por fim, gostaria de enfatizar o seu entusiasmo contagioso e encorajamento durante o decorrer da minha tese. Agradeço, também, ao Dr. Fa-Nian Shi pela sua contribuição na síntese de materiais híbridos e ao Dr. Filipe Paz com quem eu colaborei em diversos trabalhos no decorrer da minha tese e partilhei ideias interessantes acerca da conjugação RMN/raios-X. Muitas das nossas discussões resultaram e resultarão em interessantes trabalhos científicos. Gostaria também de demonstrar a minha gratidão ao Prof. Luís Carlos e Dr. Rute Ferreira pelas suas colaborações em alguns dos meus trabalhos no que diz respeito a estudos de luminescência.

Gostaria de agradecer ao Prof. Christian Fernandez por me ter ensinado e partilhado comigo o seu ponto de vista acerca de diversos conceitos da técnica RMN, tais como ciclagem de fases e processamento de sinal, quando ainda era um aprendiz no campo da RMN. Foi um prazer participar com ele em diversos eventos científicos onde, muitas vezes, momentos menos convencionais mas de certa forma inspiradores aconteceram. Tenho também de lhe agradecer por me ter transferido entusiasmo e energia quando discutíamos novas ideias para a utilização da RMN. Guardo excelentes recordações das muitas discussões científicas, jantares, bebidas alcoólicas, etc. Agradeço ainda o facto de me ter apresentado diversas referências internacionais da comunidade RMN durante as conferências em que participamos juntos. Agradeço ao Nicolas Malicki pela sua contribuição no método de ciclagem de fases do tipo multiplex e também desejo expressar a minha gratidão aos meus colegas do laboratório LCS pelo convívio, hospitalidade e ajuda que me proporcionaram, tendo estes elementos sido importantes para a minha integração no grupo.

Gostaria de agradecer ao Prof. Artur Silva e Prof. Ana Gil por terem aceite o convite para participarem como membros do júri na defesa da minha tese. Estou igualmente grato ao Prof. Jean-Paul Amoureux e Prof. Florence Babonneau por também participarem como membros do júri. Tive o prazer de falar e viver uma semana no mesmo apartamento, numa conferência no Colorado, com o Prof. Jean-Paul Amoureux onde falamos de ciência (não muito, mas o suficiente) e onde pude divertir-me com o seu sentido de humor muito característico.

Estou muito grato ao Dr. Hans Foerster pelas suas respostas e opiniões bastante profissionais aos meus inúmeros “emails” onde o questionava sobre diversos pormenores técnicos acerca de sequências de pulsos e hardware. Sem a sua ajuda preciosa a minha vida seria mais complicada. De igual modo, gostaria de agradecer ao Dr. Stefan Steuernagel pelas suas importantes sugestões.

Gostaria de agradecer ao Prof. José García, por me ter convidado a conhecer o seu grupo científico em Oviedo, me ter guiado através de magníficas paisagens e dado a conhecer a culinária da região asturiana. Agradeço-lhe também por ter financiado a minha estadia e a da minha mulher durante a minha visita científica à Universidade de Oviedo. Gostaria de agradecer à Dr. Aránzazu Espina e especialmente ao Dr. Sergei Khainakov pelas nossas discussões científicas muito interessantes acerca de colaborações presentes e futuras.

Desejo expressar ainda o meu agradecimento à fundação para a ciência e tecnologia (FCT) pelo suporte financeiro através da bolsa de doutoramento (SFRH/BD/13858/2003) e ao POCTI, FEDER e Région Basse-Normandie pelo financiamento no decorrer dos meus estudos. Agradeço ainda ao Departamento de Química de Aveiro, CICECO e ao LCS pela disponibilidade dos meios necessários à execução deste trabalho.

Para finalizar gostaria de demonstrar a minha gratidão ao meu gato preto (Eros) que me acompanhou durante todo o período em que estive a escrever a tese. Sem ele as noites seriam mais fatídicas e rotineiras e a tese levaria, provavelmente, mais tempo a ser escrita.

palavras-chave

RMN do Estado Sólido, Desacoplamento de Protão, Desacoplamento Homonuclear, CRAMPS, FS-LG, 2D HETCOR, 2D HOMICOR, Híbridos Inorgânicos-Orgânicos, Núcleos Quadrupolares, MQMAS, STMAS, Ciclagem de Fases Multiplex, CTP, SPAM, Processamento de Sinal.

Resumo

Na primeira das três partes em que esta tese está organizada apresentam-se algumas ideias e conceitos fundamentais em Ressonância Magnética Nuclear (RMN). Em particular, dá-se uma panorâmica dos métodos disponíveis para realizar o desacoplamento homonuclear ^1H - ^1H por impulsos, baseados no desacoplamento dito Frequency-Switched Lee-Goldburg (FS-LG). Discute-se, também, como otimizar as condições experimentais que permitem registar espectros de alta resolução de RMN bidimensional (2D).

A segunda parte desta tese apresenta casos de estudo de RMN dos seguintes materiais híbridos inorgânicos-orgânicos: complexos (i) binuclear e (ii) hexanuclear de germânio, ambos contendo ácidos fosfônicos como ligandos (respectivamente, pmida^{4-} e hedp^{4-}); (iii) um aluminofosfato microporoso, e (iv) um γ -titanofosfato lamelar tendo como hóspedes, respectivamente, metilamina e hexilamina. Estes sólidos são ricos em núcleos ^1H e, por esta razão, as linhas espectrais de RMN de ^1H sofrem alargamento homogêneo devido ao forte acoplamento dipolar homonuclear. Assim, não é de estranhar que os materiais híbridos tenham, até a data, sido objecto de poucos estudos de RMN de ^1H . Nesta tese mostra-se que o desacoplamento FS-LG é uma técnica muito poderosa e robusta para estudar estes materiais, permitindo a aquisição, sob condições de alta resolução de ^1H , de espectros 2D com correlação homo e heteronuclear ^1H -X (X = ^1H , ^{13}C , ^{31}P , ^{27}Al). Ilustra-se, também, o uso de técnicas de reacoplamento dipolar, nomeadamente BABA, POSTC7 e RFDR. Usada em combinação com dados de difracção de raios-X, a informação RMN permite construir um modelo claro da estrutura dos materiais híbridos.

Na terceira parte desta tese propõe-se uma nova técnica de RMN para estudo de núcleos quadrupolares, de spin 3/2 e 5/2, em sólidos. Concretamente, relata-se um método para a obtenção de espectros de núcleos quadrupolares de spin semi-inteiro, que permite o registo simultâneo dos chamados "multiple coherence transfer pathways (CTP)", reduzindo consideravelmente o tempo de experiência. Usa-se uma ciclagem de fases do tipo "multiplex", com registo separado de cada CTP na memória do computador, tendo em vista a selecção e o processamento de sinal após a aquisição. A aplicação, a estes conjuntos de dados, de uma mudança discreta da fase numérica permite gerar os CTPs alvo e combiná-los de forma a obter espectros 2D sem componentes dispersivas. Mostra-se, ainda, que é possível realizar experiências múltiplas com diferentes CTPs, durante o tempo de uma única experiência, por exemplo a aquisição de espectros 3QMAS/5QMAS, MQMAS/STMAS e MQMAS/DQF-STMAS. Finalmente, demonstra-se que acoplando o chamado soft-pulse added mixing (SPAM) e uma ciclagem de fases do tipo "multiplex duplo" permite adicionar construtivamente os CTPs, mesmo se estes tiverem sinal oposto. Encurta-se, desta forma, consideravelmente o tempo experimental, relativamente ao método multiplex simples.

keywords

Solid-State NMR, Proton Decoupling, Homonuclear Decoupling, CRAMPS, FS-LG, 2D HETCOR, 2D HOMCOR, Inorganic-Organic Hybrid, Quadrupolar Nuclei, MQMAS, STMAS, Multiplex Phase Cycling, CTP, SPAM, Signal Processing.

Abstract

This thesis is organised in three parts, and the first one presents some basic NMR concepts and ideas. In particular, an overview of the ^1H - ^1H homonuclear decoupling pulse methods, based on Frequency-Switched Lee-Goldburg (FS-LG) decoupling, is given. The optimisation of the experimental conditions which afford high-resolution two-dimensional (2D) NMR spectra is also discussed.

In its second part, this thesis presents a number of NMR case studies centred on the following inorganic-organic hybrid materials: (i) a germanium binuclear and (ii) a germanium hexanuclear complex, both containing phosphonic acid ligands (pmida^{4-} and hedp^{4-} , respectively); (iii) a microporous aluminophosphate, and (iv) a layered γ -titanium phosphate containing, respectively, methylamine and hexylamine guests. These solids are rich in ^1H nuclei and, because of this, their ^1H NMR spectral lines are usually broadened homogeneously by the strong homonuclear dipolar couplings. It is, thus, no wonder that hybrid materials have not been much studied by ^1H NMR. Here, I show that FS-LG decoupling is a very powerful and robust technique to study these materials, allowing the acquisition, under ^1H high-resolution, of 2D homo- and hetero-nuclear correlation ^1H -X (X = ^1H , ^{13}C , ^{31}P , ^{27}Al) NMR spectra. Dipolar recoupling techniques such as BABA, POSTC7 and RFDR were also employed. When used in tandem with X-ray diffraction data, the information forthcoming from these NMR studies provides a clear structural picture of the hybrid materials.

In the third part of this thesis I introduce a new NMR method to study $I = 3/2$ and $5/2$ quadrupole nuclei in powdered solids. More specifically, a new processing method to obtain 2D NMR spectra of half-integer quadrupole nuclei is described. This scheme allows the simultaneous acquisition of multiple-coherence transfer pathways (CTP), thus shortening considerably the experimental time. A "multiplex" phase cycling procedure is employed, which allows recording separately in the computer memory each CTP, for post-acquisition signal selection and processing. By applying a numerical phase shift to these data sets it is possible to generate the targeted CTPs and combine them to obtain pure-absorption 2D spectra. I also demonstrate the feasibility of performing multiple experiments with distinct CTPs, during the timespan of a single experiment, for example the simultaneous acquisition of 3QMAS/5QMAS, MQMAS/STMAS and MQMAS/DQF-STMAS. Finally, I demonstrate that coupling the so-called "soft-pulse added mixing" (SPAM) and "double-multiplex" phase cycling allows the constructive addition of CTPs, even if they have opposite signs. The result is a considerable reduction in the experimental time as compared to the simple multiplex method.

Contents

0.1	Acronyms	iv
0.2	Accounts of some of the work reported here have been given in:	vii
I	Theoretical Background of Solid-State NMR	1
1	NMR Theoretical Background	2
1.1	State Vectors and Superposition in Hilbert Space	2
1.2	The Density Operator	4
1.2.1	Definition	4
1.2.2	The Density Operator at Equilibrium	6
1.2.3	Equation of Motion	7
1.2.4	The Expectation Value	7
2	The Nuclear Spin Hamiltonian	9
2.1	Cartesian Representation	9
2.2	Tensors and Spherical Tensor Representation of Hamiltonians	12
2.2.1	Secular Approximation	13
2.3	Tools for Describing Rotations in the Solid-State NMR	14
2.3.1	Reference Frame Transformations	14
2.3.2	Euler Angles and Wigner Matrix	16
2.3.3	Internal Hamiltonian Under the Effect of MAS Spatial Averaging	18
2.4	NMR Interactions in Terms of Irreducible Spherical Tensors	21
2.4.1	Zeeman Interaction	21
2.4.2	Zeeman Interaction and Interaction With <i>rf</i> Field	23
2.4.3	Chemical Shift Interaction	24
2.4.4	Direct Dipole-Dipole Interaction	25
2.4.5	Indirect Dipole-Dipole Interaction	27
2.4.6	Electric Quadrupole Interaction	28
2.4.7	Second-Order Interactions Involving Cross-Terms	31
3	Two-Dimensional NMR Concepts: Selection and Detection of the NMR Signal	34
3.1	Basic Principle	34
3.2	Phase Sensitive Detection in t_2	35
3.3	Phase Sensitive Detection in t_1 : States vs TPPI	37
3.3.1	Hypercomplex Acquisition (States)	38
3.3.2	TPPI Acquisition	39
3.4	Aliasing in NMR	41
3.4.1	Aliasing in the Frequency Domain	41

3.5	CTP and Phase Cycling Concepts	41
3.5.1	CTP	41
3.5.2	Phase Cycling Principle	43
4	^1H-^1H Homonuclear Dipolar Decoupling	48
4.1	Introduction	48
4.2	Overview of Homonuclear Decoupling Schemes	50
4.3	Theoretical Tools	55
4.3.1	The Average Hamiltonian Theory and the “Toogling Frame”	55
4.3.2	Alternatives to AHT: Other Effective Hamiltonian Theories	58
4.4	FS-LG Principle	58
4.5	The FS-LG Hamiltonian	61
4.5.1	The radiofrequency (<i>rf</i>) Time Evolution Propagator for FS-LG	61
4.5.2	The FS-LG Interaction frame Hamiltonian	62
4.6	Insertion of FS-LG Blocks in 2D Nuclear Magnetic Resonance (NMR) Experiments: Experimental Hints	64
4.7	Pulse Scheme Explanation	64
4.8	Phase Cycling Schemes	67
4.9	Calibration of the FS-LG Homonuclear Dipolar Decoupling	68
4.9.1	Typical FS-LG Set-Up	68
4.9.2	FS-LG Optimisation Through 2D Homonuclear Correlation Spectra	71
4.9.3	Difficulties Related With ^1H - ^1H Decoupling Schemes	74
4.10	Some Examples of 2D $^1\text{H}\{\text{FS-LG}\}\text{-X}$ HETCOR Spectra	74
4.10.1	^1H - ^{89}Y FS-LG CP HETCOR	74
4.10.2	^1H - ^{13}C FS-LG HMQC	75
5	2D Homonuclear Dipolar Recoupling Experiments: Spectral Interpretation	77
5.1	Homonuclear Recoupling Sequences	77
5.1.1	BABA	79
5.1.2	C7 and POSTC7	81
5.1.3	2D DQ-SQ Homonuclear Correlation Spectra: Interpretation and Examples	81
II	Solid-State NMR Applications to Crystalline Inorganic-Organic Hybrid Materials	86
6	General Introduction	87
7	Instrumentation	89
8	Studies of Phosphonic Acid Based Metal-Organic Hybrid Discrete Units	91
8.1	A Germanium Binuclear Complex	91
8.1.1	Experimental Section	92
8.1.2	Results and Discussion	95
8.1.3	Conclusion	109
8.2	A $\text{Ge}^{4+}/\text{HEDP}^{4-}$ Hexanuclear Complex Containing Heteroaromatic Residues	109
8.2.1	Experimental Section	109

8.2.2	Results and Discussion	116
8.2.3	Conclusion	131
9	Studies of Amine Guests in Hybrid Materials	132
9.1	NMR Characterisation of Microporous Aluminophosphate, IST-1	132
9.1.1	Experimental Section	132
9.1.2	Results and Discussion	133
9.1.3	Conclusion	142
9.2	NMR characterisation Characterization of Layered γ-Titanium Phosphate ($C_6H_{13}NH_3$)[Ti(HPO₄)(PO₄)]·H₂O	142
9.2.1	Experimental Section	143
9.2.2	Results and Discussion	145
9.2.3	Conclusion	154
III	New Methods for Observation of Quadrupolar Nuclei	155
10	Application of Multiplex Phase Cycling to MQMAS and STMAS Experiments	156
10.1	High-Resolution Spectra of Half-Integer Quadrupolar Nuclei	156
10.2	The MQMAS Experiment	160
10.2.1	The Principle	160
10.2.2	Detection of Pure Absorption 2D Spectra	162
10.3	The STMAS Experiment	167
10.3.1	The Principle	167
10.3.2	Suppression of Unwanted CTPs	168
10.4	Signal Selection by Multiplex Phase Cycling	170
10.4.1	The Principle	170
10.4.2	CTP Selection in MQMAS Experiments: Nested vs Multiplex Phase Cyclings	174
10.4.3	Experimental Demonstration of the Multiplex Approach	180
10.4.4	Sensitivity Enhancement Through Multiple CTP Selection: The Multiplex-SHR-SPAM Acquisition Scheme	183
10.4.5	Experimental Demonstrations of the Multiplex-SPAM Approach	190
10.4.6	Simultaneous Acquisition of Multiple Experiments	192
10.4.7	Concluding Remarks: Advantages and Disadvantages of Multiplex Phase Cycling	197
10.4.8	Instrumentation and Processing Program	199
11	Conclusions and Outlook	200
11.1	Main Conclusions	200
11.2	Future NMR Studies on Hybrid Materials	202
11.3	Future Methodology Developments in Quadrupolar Nuclei	204
	Appendices	206
A	Nuclear Spin Operators	206
B	Wigner Matrices	208
C	Interpretation of MQMAS Spectra	210

D Spin Coefficients $C^k(\hat{I}_z, m)$ for MQMAS and STMAS	214
E Math Reminder	217
E.1 Complex Numbers	218
E.2 Series Expansions of e^x , $\sin x$, $\cos x$ and e^{ix}	219
E.3 Elementary Rotation Operator	219
E.4 Some Trigonometric Relations	221
F Additional Data for the Study of Hybrid Materials	223
F.1 Ge Binuclear Complex	224
F.1.1 Additional Spectra and Figures: ^1H MAS NMR, Powder XRD	224
F.1.2 Table of Hydrogen Bond Lengths	225
F.1.3 Histogram of the $\text{P}\cdots\text{H}$ and $\text{C}\cdots\text{H}$ Distances	226
F.2 A Germanium/HEDP $^{4-}$ Hexanuclear Complex Containing Heteroaromatic Residues	230
F.2.1 Additional Spectra and Tables: NMR Spectra, powder XRD, Hydrogen Bond Lengths for Structures I and II	230
F.3 Layered γ -Titanium Phosphate ($\text{C}_6\text{H}_{13}\text{NH}_3$)[Ti(HPO $_4$)(PO $_4$)] $\cdot\text{H}_2\text{O}$	236
F.3.1 Additional Tables: Atomic Coordinates, Bond Lengths and Angles	236
F.3.2 Thermogravimetric Data	238
F.3.3 X-ray Data	238
F.3.4 SEM Images	239
Bibliography	240

0.1 Acronyms

1D	One-Dimensional
2D	Two-Dimensional
3D	Three-Dimensional
AHT	Averaged Hamiltonian Theory
BABA	Back-to-Back
CP	Cross-Polarisation
CP-MAS	Cross-Polarisation
CQ	Quadrupole Coupling Constant
CRAMPS	Combined Rotation and Multiple-Pulse Sequences
CS	Chemical Shift
CSA	Chemical Shift Anisotropy
CT	Central Transition
CTP	Coherence Transfer Pathway
DAS	Dynamical Angle Spinning

DQ	Double-Quantum
DQF	Double-Quantum-Filtered
DFT	Discrete Fourier Transform
DOR	Double Rotation
DSC	Differential Scanning Calorimetry
DTG	Differential Thermogravimetry
EA	Elemental Analysis
EFG	Electric Field Gradient
FS-LG	Frequency-Switched Lee-Goldburg
FT	Fourier Transform
FTIR	Fourier Transform Infrared
HETCOR	Heteronuclear Correlation
HH	Hartmann-Hahn
HMQC	Heteronuclear Multiple-Quantum Coherence
HOMCOR	Homonuclear Correlation
LG	Lee-Goldburg
LG-CP	Lee-Goldburg Cross-Polarisation
LAB	Laboratory
MAS	Magic-Angle Spinning
NMR	Nuclear Magnetic Resonance
MQ	Multiple-Quantum
MQMAS	Multiple-Quantum Magic-Angle Spinning
PAS	Principal Axis System
PM-LG	Phase-Modulated Lee-Goldburg
POSTC7	Permutationally Offset Stabilised C7
RAMP-CP	Ramped-Amplitude Cross-Polarization
RAS	Rotor Axis System
RF	Rotating Frame
rf	radiofrequency
RFDR	radiofrequency-Driven Recoupling

SHR	States-Haberkorn-Ruben
SPAM	Soft-Pulse-Added-Mixing
SQ	Single-Quantum
SSNMR	Solid-State Nuclear Magnetic Resonance
ST	Satelite Transition
STMAS	Satelite-Transition Magic-Angle Spinning
TG	thermogravimetry
TPPI	Time-Proportional Phase Incrementation
XRD	X-ray Diffraction

0.2 Accounts of some of the work reported here have been given in:

- Mafra, L., Paz, F. A. A., Shi, F. N., Rocha, J., Trindade, T., Fernandez, C., Makal, A., Wozniak, K., and Klinowski, J., *Chemistry: A European journal*, X-Ray Diffraction and Solid-State NMR Studies of a Germanium Binuclear Complex, 12 (**2006**) 363-375.
- Mafra, L., Rocha, J., Fernandez, C., Paz, F. A. A., *Journal of Magnetic Resonance*, Characterization of Microporous Aluminophosphate IST-1 using ^1H Lee-Goldburg Techniques, 180 (**2006**) 236-244.
- Mafra, L., Paz, F. A. A., Shi, F. N., Ferreira, R. A., Carlos, L. D., Trindade, T., Fernandez, C., Klinowski, J., and Rocha, J., Crystal structure, Solid-State NMR and Photoluminescence studies of Organic-Inorganic Hybrid Materials $(\text{HL})_6[\text{Ge}_6(\text{OH})_6(\text{hedp})_6]\cdot 2(\text{L})\cdot n\text{H}_2\text{O}$, L=hqn or phen., (**2006**). Accepted in *European Journal of Inorganic Chemistry*.
- Mafra, L., Paz, F. A. A., Rocha, J., Espina, A., Khainakov, S. A., Garca, J. R., Fernandez, C., *Chemistry of Materials*, Structural Characterization of Layered γ -Titanium Phosphate $(\text{C}_6\text{H}_{13}\text{NH}_3)[\text{Ti}(\text{HPO}_4)(\text{PO}_4)]\cdot\text{H}_2\text{O}$, 17 (**2005**) 6287-6294.
- Paz, F. A. A., Rocha, J., Klinowski, J., Trindade, T., Shi, F. N., and Mafra, L., *Progress in Solid State Chemistry*, Optimized Hydrothermal Synthesis of Multi-Dimensional Hybrid Coordination Polymers Containing Flexible Organic Ligands, 33 (**2005**) 113-125.
- Karmaoui, M., Mafra, L., Ferreira, R. A. S. Rocha, J., Carlos, L. D., Pinna, N., *Journal of Physical Chemistry C*, Photoluminescent Rare-Earth Based Biphenolate Lamellar Nanostructures, (**2006**), submitted.
- Malicki, N., Mafra, L., Quoineaud, A.-A., Rocha, J., Thibault-Starzyk, F., and Fernandez, C., *Solid State NMR*, Multiplex MQMAS NMR of Quadrupolar Nuclei, 28 (**2005**) 13-21.

Part I

Theoretical Background of Solid-State NMR

Chapter 1

NMR Theoretical Background

1.1 State Vectors and Superposition in Hilbert Space

Consider a simple case of a spin-1/2 two-level system in quantum mechanics. When one spin-1/2 is placed in a magnetic field, the two possible states are: $|\alpha\rangle$ and $|\beta\rangle$, the former represents the spin aligned with the magnetic field and has lower energy (on the assumption of $\gamma > 0$, $E = \langle\alpha| -\gamma B_0 \hat{I}_z |\alpha\rangle$), the latter represents the spin aligned against the magnetic field and has a higher energy. The value of ΔE (i.e., the energy difference between these two states) is dependent on the strength of the magnetic field: $\Delta E = \hbar\gamma B_0$. If a *rf* field, B_1 , with frequency ω_1 is applied perpendicularly to the main magnetic field, B_0 , so that $\hbar\omega_0$ equals ΔE , a transition between the two states can occur. In this case one can say that a coherence has been established between the two states. For a 90° *rf* pulse, the spin state evolves into the following state under the *rf* field (See Appendices A and E.3) [1]:

$$|\psi\rangle = \frac{1}{\sqrt{2}} |\alpha\rangle + \frac{1}{\sqrt{2}} |\beta\rangle \quad (1.1a)$$

or

$$|\psi\rangle = \frac{1}{\sqrt{2}} |\alpha\rangle - \frac{1}{\sqrt{2}} |\beta\rangle \quad (1.1b)$$

depending on the phase of the B_1 -field, the spin is then in the superposition state of the “Zeeman eigenbasis” $|\alpha\rangle$ and $|\beta\rangle$ (using the Dirac “ket” vector and “bra” vector representation). In the case of a single spin-1/2, an arbitrary state $|\psi\rangle$ or $\langle\psi|$ can be constructed as a linear superposition of the two basis states $|\alpha\rangle$ and $|\beta\rangle$:

$$|\psi\rangle = c_\alpha(t) |\alpha\rangle + c_\beta(t) |\beta\rangle \quad (1.2)$$

$$\langle\psi| = c_\alpha^*(t) \langle\alpha| + c_\beta^*(t) \langle\beta| \quad (1.3)$$

where $c_\alpha(t)$ and $c_\beta(t)$ are complex numbers, and the basis kets $|\alpha\rangle$ and $|\beta\rangle$ eigenstates of the Zeeman Hamiltonian, and the states $|\alpha\rangle$ and $|\beta\rangle$ are orthogonal, i.e., $\langle\alpha|\beta\rangle = 0$. [2] Therefore, just like the description of a vector in real space, the spin state $|\psi\rangle$ or $\langle\psi|$ can be described as a vector in Hilbert space, as shown in Fig. 1.1. The norm of the vector is interpreted as the statistical probability of finding the system in the particular state.

As mentioned above, once chosen a basis set of wave functions, one can describe any state vector as a linear combination of these wave functions. All the information about the state

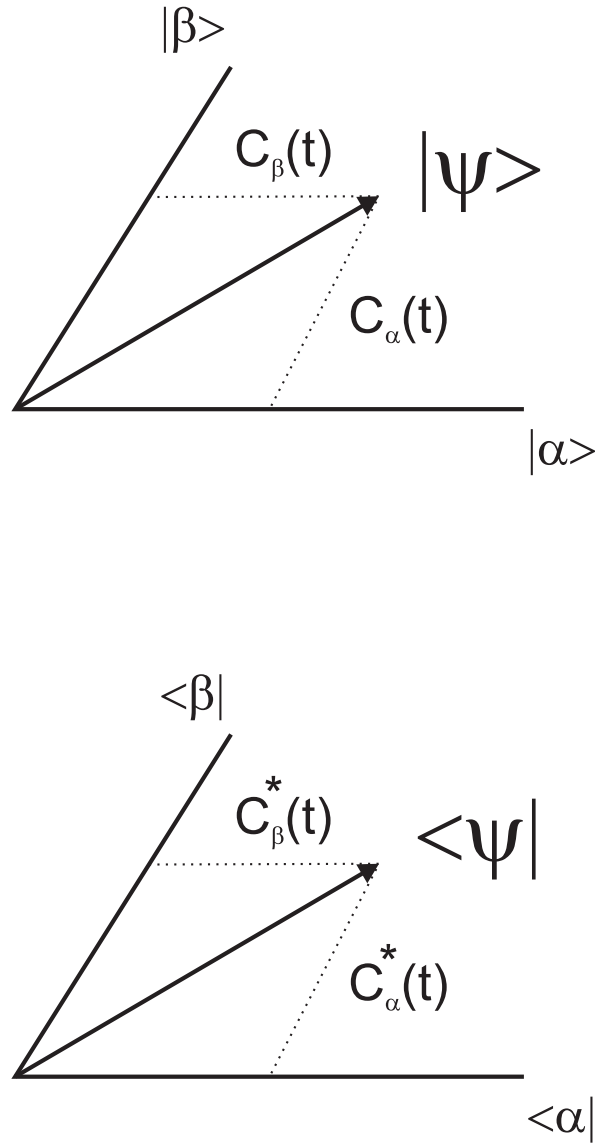


Fig. 1.1: Schematic representation of states $|\psi\rangle$ and $\langle\psi|$ in Hilbert space as a function of the Zeeman eigenbasis.

vector is in the coefficients of this linear combination. In general, any state vector $|\psi(t)\rangle$ containing N_s spins-1/2 may be described by the following equation:

$$|\psi(t)\rangle = \sum_{i=1}^{N_s} c_i(t) |i\rangle, \quad c_i \in \mathbb{C} \quad (1.4)$$

where each coefficient c_i is the contribution of the eigenstate $|i\rangle$ to the overall state vector $|\psi\rangle$ and can be obtained through the scalar product of $\langle i | \psi \rangle$. N_s is the number of states $N_s = \{|1\rangle, |2\rangle, \dots, |N_s\rangle\}$. In summary, a spin state vector can be described by linear combinations of a set of orthonormal eigenstates (or “eigenbasis”) in Hilbert space. Its length can not be changed, i.e., the sum of the squares of the coefficients in Eq. 1.4 must be equal to 1,

$$\sum_{i=1}^{N_s} |c_i(t)|^2 = 1 \quad (1.5)$$

The complex coefficients $c_i(t)$ may be written

$$c_i(t) = |c_i(t)| \exp[i\phi_i(t)] \quad (1.6)$$

By applying pulses to the spins one can change the orientation of vectors in Hilbert space by operating on the present state and causing it to rotate to another state.

1.2 The Density Operator

1.2.1 Definition

The density operator is a standard quantum mechanical tool for dealing with coherence and mixed states. A macroscopic sample is made up of a enormous number of interacting spins but its description is simplified if the system can be considered as a multitude of independent systems. Properties can be studied over individual spin systems and then statistical arguments can be invoked to describe the overall spin system. [3] Further information about the density operator formalism may be found in Refs. [4–10].

Using the Dirac formalism, the density operator, $\hat{\rho}(t)$, can be defined as:

$$\hat{\rho}(t) = \overline{|\psi_k(t)\rangle \langle \psi_k(t)|} = \sum_k P^k |\psi_k(t)\rangle \langle \psi_k(t)| \quad (1.7)$$

where P^k is the probability that a spin system of the ensemble is in one of several possible states $|\psi_k(t)\rangle$, $\sum_k P^k = 1$, and the bar denotes the ensemble average. According to Eq. 1.4, $|\psi_k(t)\rangle$ can be written as:

$$|\psi_k(t)\rangle = \sum_{i=1}^{N_s} c_i^k(t) |i\rangle, \quad c_i \in \mathbb{C} \quad (1.8)$$

In the general case of an ensemble consisting of multiple-spin systems, the density operator can be expressed as a Zeeman product basis as follows,

$$\hat{\rho}(t) = \sum_{i,j=1}^{N_s} \rho_{ij}(t) |i\rangle \langle j| \quad (1.9)$$

where $\rho_{ij}(t) = \langle i | \hat{\rho}(t) | j \rangle$, are the density matrix elements.

$$\rho_{ii}(t) = \overline{c_i^k(t) c_i^k(t)^*} = \overline{|c_i^k(t)|^2}, \quad (\text{diagonal elements}) \quad (1.10)$$

$$(1.11)$$

$$\begin{aligned} \rho_{ij}(t) &= \overline{c_i^k(t) c_j^k(t)^*} = \\ &= \overline{|c_i^k(t)| |c_j^k(t)| \exp\{i[\phi_i(t) - \phi_j(t)]\}}, \quad (\text{off-diagonal elements}) \end{aligned} \quad (1.12)$$

where $\rho_{ii}(t)$ are called the *populations* of the states $|i\rangle$, and $\rho_{ij}(t)$ expresses a “coherence superposition” (or simply *coherences*) between states $|i\rangle$ and $|j\rangle$. $\rho_{ij}(t)$ represents an n -quantum coherence ($n = M_i - M_j$), is defined as the difference in the Zeeman quantum

number between two states $|i\rangle$ and $|j\rangle$ in coherent superposition. For $n = \pm 1$, it is related to the transverse magnetisation components and can be directly observed, but for $n \neq \pm 1$, it does not lead to observable magnetisation and can only be detected indirectly. This indirect detection of non-observable coherences is of great importance in most of the NMR experiments. Table 1.1, shows a summary of some types of coherence orders.

Table 1.1: Coherence orders and their corresponding spin operators

$\hat{\rho}$ (spin operators)	ρ_{ij}	
\hat{I}_i^+	+1	Single-quantum (SQ) coherence
\hat{I}_i^-	-1	
$\hat{I}_i^+ \hat{I}_j^-$	0	Zero-quantum (ZQ) coherence
$\hat{I}_i^- \hat{I}_j^+$	0	
$\hat{I}_i^+ \hat{I}_j^+$	+2	Double-quantum (DQ) coherence
$\hat{I}_i^- \hat{I}_j^-$	-2	

For the existence of coherence between states $|i\rangle$ and $|j\rangle$, some conditions must be fulfilled for Eq. 1.9:

- The spin states of the individual spin-systems must be superposition states, involving $|i\rangle$ and $|j\rangle$;
- The phases $\phi_i(t)$ and $\phi_j(t)$ must be correlated over the ensemble.

Example

In NMR *rf* pulses usually induce the existence of coherence in a spin ensemble is equivalent to the existence of correlated spin states.

As an example, for an ensemble of isolated spins-1/2, the density matrix in the Zeeman basis may be written as:

$$\hat{\rho}(t) = \begin{pmatrix} \langle \alpha | \hat{\rho}(t) | \alpha \rangle & \langle \alpha | \hat{\rho}(t) | \beta \rangle \\ \langle \beta | \hat{\rho}(t) | \alpha \rangle & \langle \beta | \hat{\rho}(t) | \beta \rangle \end{pmatrix} = \begin{pmatrix} \overline{c_\alpha^k(t) c_\alpha^k(t)^*} & \overline{c_\alpha^k(t) c_\beta^k(t)^*} \\ \overline{c_\beta^k(t) c_\alpha^k(t)^*} & \overline{c_\beta^k(t) c_\beta^k(t)^*} \end{pmatrix} \quad (1.13)$$

the elements $\langle \alpha | \hat{\rho}(t) | \alpha \rangle$ and $\langle \beta | \hat{\rho}(t) | \beta \rangle$ give the fractional populations of the states $|\alpha\rangle$ and $|\beta\rangle$, respectively. If the magnitudes of these elements are different there is a net *longitudinal* spin polarisation (and magnetisation) along the static field direction. The two off-diagonal elements $\langle \beta | \hat{\rho}(t) | \alpha \rangle$ and $\langle \alpha | \hat{\rho}(t) | \beta \rangle$ correspond to -1 and +1 quantum coherences (-1QC and +1QC), respectively. The presence of Single-Quantum (SQ) coherences in the ensemble is equivalent to a net spin polarization (and magnetization) in the *transverse* plane of the rotating frame. The spin density operator may be expressed as a linear combination of spin operators of the system. Net longitudinal magnetization corresponds to a density operator proportional to \hat{I}_z , whereas transverse magnetization corresponds to $\hat{\rho}(t)$ being proportional to a combination of \hat{I}_x and \hat{I}_y , or equivalently, a linear combination of \hat{I}^+ and \hat{I}^- . (See Appendix A for the relationship between the various operators.)

According to Eq. 1.9, the density operator of an ensemble of isolated spins-1/2 may be written,

$$\begin{aligned}
\hat{\rho}(t) &= \sum_{i,j=\alpha,\beta}^{N_s} \langle i | \hat{\rho}(t) | j \rangle \cdot | i \rangle \langle j | = \\
&= \langle \alpha | \hat{\rho}(t) | \alpha \rangle \cdot | \alpha \rangle \langle \alpha | + \langle \alpha | \hat{\rho}(t) | \beta \rangle \cdot \underbrace{| \alpha \rangle \langle \beta |}_{\hat{I}^+} + \\
&+ \langle \beta | \hat{\rho}(t) | \alpha \rangle \cdot \underbrace{| \beta \rangle \langle \alpha |}_{\hat{I}^-} + \langle \beta | \hat{\rho}(t) | \beta \rangle \cdot | \beta \rangle \langle \beta |
\end{aligned} \tag{1.14}$$

Eq. 1.14 corresponds to the matrix representation in Eq. 1.13.

The operators $| \alpha \rangle \langle \beta |$ and $| \beta \rangle \langle \alpha |$ correspond to -1QC and +1QC, respectively. For example, it may be verified that the operator $| \alpha \rangle \langle \beta |$ converts state $| \alpha \rangle$ into state $| \beta \rangle$, by letting it operate on each of them.

$$(| \beta \rangle \langle \alpha |) \cdot | \alpha \rangle = | \beta \rangle \cdot \langle \alpha | \alpha \rangle = | \beta \rangle \tag{1.15}$$

and

$$(| \beta \rangle \langle \alpha |) \cdot | \beta \rangle = | \beta \rangle \cdot \langle \alpha | \beta \rangle = 0 \tag{1.16}$$

Likewise, it may be demonstrated that $| \alpha \rangle \langle \beta | = \hat{I}^+$.

1.2.2 The Density Operator at Equilibrium

The starting point for any NMR experiment is the spin ensemble at thermal equilibrium in a strong magnetic field \vec{B} . Over the ensemble, there is a net polarization pointing along the static magnetic field (i.e., a net longitudinal polarization). This corresponds to a density operator being proportional to \hat{I}_z . [3] In the limit of high temperatures ($k_B T \gg |\hbar \gamma_I B_0|$, which is easily fulfilled at room temperature), the simplified density operator in an external magnetic field in thermal equilibrium can be described as,

$$\hat{\rho}_{eq} \propto \left(\hat{1} + \beta_I \hat{I}_z \right) \tag{1.17}$$

where the Boltzmann factor (β_I), is given by

$$\beta_I = \frac{-\hbar \gamma_I B_0}{k_B T} \tag{1.18}$$

where $k_B = 1.381 \times 10^{-23} JK^{-1}$ is the Boltzmann constant and T is the temperature (K). The unity operator $\hat{1}$, commutes with all the operators and consequently can not influence the time development of $\hat{\rho}(t)$, then it can be dropped for the sake of simplicity. β_I will not affect any of the results as well, and thus can be dropped. Thus, the thermal equilibrium density operator used for NMR experiments may be approximately expressed as follows:

$$\hat{\rho}_{eq} \approx \hat{I}_z = \sum_{i=0}^{N_s} \hat{I}_{iz} \tag{1.19}$$

Note that in the case of weak B_0 and high Quadrupole Coupling Constant (CQ) values the the thermal equilibrium density operator is no longer a pure Zeeman operator, i.e., the eigenstates are no longer pure Zeeman states.

1.2.3 Equation of Motion

In quantum mechanics, the density operator, $\hat{\rho}(t)$, describes the state of the spin system, while the Hamiltonian ($\hat{\mathcal{H}}(t)$) represents the time-dependent Hamiltonian describing the relevant nuclear spin interactions and the external operations that try to change the state of the system. The motion of $\hat{\rho}(t)$ may be derived from the Schrödinger equation which describes the evolution of the spin system.

$$\frac{d}{dt} |\psi(t)\rangle = -i\hat{\mathcal{H}}(t) |\psi(t)\rangle, \quad (\text{Schrödinger equation}) \quad (1.20)$$

where $\psi(t)$ is the nuclear spin wavefunction describing the spin system and $\hat{\mathcal{H}}(t)$ (having angular frequency units) is the time dependent hermitian operator, so-called the *Hamiltonian*. Derived from Eq. 1.20, one obtains the well-known Liouville-von Neumann equation (“equation of motion”), which is of central importance for calculating dynamical systems.

$$\frac{d}{dt} \hat{\rho}(t) = -i [\hat{\mathcal{H}}(t), \hat{\rho}(t)] \quad (1.21)$$

The simulation of a NMR experiment essentially amounts to a numerical evaluation of Eq. 1.21. [11] The commutator $[\hat{\mathcal{H}}(t), \hat{\rho}(t)]$ in Eq. 1.21 means that the outcome of two consecutive operators depends on the order in which the operator act. Only when the operator is zero can the two corresponding observables be measured simultaneously, or consecutively but in any order, in this case. The two operators are said to commute with each other. So the presence of the commutator in Eq. 1.21 shows that there must exist some fundamental incompatibility between the density operator and the Hamiltonian if the system is to change with time. The formal solution of Eq. 1.21 may be written as,

$$\hat{\rho}(t) = U(t, 0) \hat{\rho}(0) U^{-1}(t, 0) \quad (1.22)$$

where $\hat{\rho}(0)$ is the density operator at thermal equilibrium described before in Eq. 1.19 (or a density operator resulting from a given preparation sequence) and $\hat{U}(t, 0)$ is the unitary propagator (i.e., the exponential operator) responsible for the spin dynamics in the period from 0 to t . $\hat{U}(t, 0)$ is related to the Hamiltonian according to the following expression:

$$U(t, 0) = \hat{T} \exp \left\{ -i \int_0^t H(t') dt' \right\} \quad (1.23)$$

with \hat{T} being the Dyson time-ordering operator relevant for Hamiltonians containing non-commuting components. Although a large number of advanced numerical integration methods [11, 12] may in principle, be applied to derive $\hat{U}(t, 0)$, it typically proves most efficient to approximate the integral by a simple time-ordered product

$$\hat{U}(t, 0) = \prod_{j=0}^{n-1} \exp \{-iH(j\Delta t) \Delta t\} \quad (1.24)$$

where n is the number of infinitesimal time intervals Δt over each of which the Hamiltonian may be considered time-independent and which overall span the full period from 0 to $t = n\Delta t$.

1.2.4 The Expectation Value

The knowledge of $\hat{\rho}(t)$ permits calculation of the expectation value, $\langle O(t) \rangle$ of any operator according to the relationship, [11]

$$\langle O(t) \rangle = \text{Tr} \left\{ \hat{O} \hat{\rho}(t) \right\} \quad (1.25)$$

For example, the acquired NMR time-domain signal $s(t)$ corresponds to the expectation value $\langle O \rangle$ of an “observable operator” \hat{O} . In principle, \hat{O} may be any Hermitian spin operator, because one may only directly detect quantized systems through Hermitian operators. [10] The time-domain signal $s(t) = \langle O(t) \rangle$ may be calculated from the trace of the product between the density operator and the observable operator \hat{O} .

Chapter 2

The Nuclear Spin Hamiltonian

The total Hamiltonian for a nucleus subjected to a static external magnetic field and exposed to *rf* pulses may be written as:

$$\hat{\mathcal{H}}_{Total} = \underbrace{\hat{\mathcal{H}}^Z + \hat{\mathcal{H}}_1(t)}_{\hat{H}_{ext}(t)} + \underbrace{\hat{\mathcal{H}}^{CS} + \hat{\mathcal{H}}^D + \hat{\mathcal{H}}^J + \hat{\mathcal{H}}^Q + \dots}_{\hat{H}_{int}} \quad (2.1)$$

where \hat{H}_{ext} and \hat{H}_{int} are the external and internal Hamiltonian, respectively. The various Hamiltonian elements in Eq. 2.1 are labeled as follows:

- \hat{H}^Z : Zeeman Hamiltonian (external static magnetic field)
- $\hat{H}_1(t)$: *rf* Hamiltonian (external oscillating *rf* magnetic field)
- \hat{H}^{CS} : Chemical Shift Hamiltonian (induced magnetic fields originating from orbital motions of electrons)
- \hat{H}^D : Dipolar Hamiltonian (through space dipole-dipole interaction between nuclear spins)
- \hat{H}^J : J-coupling Hamiltonian (through bond dipole-dipole interaction between nuclear spins)
- \hat{H}^Q : Electric Quadrupole Hamiltonian

Each of these interactions will be briefly discussed later in section 2.4.

2.1 Cartesian Representation

The general representation of an Hamiltonian operator in NMR interaction can be expressed as a product between vectors and matrix operators,

$$\hat{\mathcal{H}}^\Lambda = C^\Lambda \left(\hat{\mathbf{X}}_i \right)^{Local} \cdot \mathbf{A}^{\Lambda, i\zeta} \cdot \hat{\mathbf{Y}}_\zeta^\Lambda = \quad (2.2)$$

$$= C^\Lambda \left(\hat{X}_x, \hat{X}_y, \hat{X}_z \right)^{Local} \cdot \begin{bmatrix} \mathcal{A}_{xx}^\Lambda & \mathcal{A}_{xy}^\Lambda & \mathcal{A}_{xz}^\Lambda \\ \mathcal{A}_{yx}^\Lambda & \mathcal{A}_{yy}^\Lambda & \mathcal{A}_{yz}^\Lambda \\ \mathcal{A}_{zx}^\Lambda & \mathcal{A}_{zy}^\Lambda & \mathcal{A}_{zz}^\Lambda \end{bmatrix} \cdot \begin{pmatrix} \hat{Y}_x^\Lambda \\ \hat{Y}_y^\Lambda \\ \hat{Y}_z^\Lambda \end{pmatrix} = \quad (2.3)$$

$$= C^\Lambda \sum_{u=x,y,z} \sum_{v=x,y,z} \left(\hat{X}_u \right)^{Local} \cdot \mathcal{A}_{uv}^{\Lambda, i\zeta} \cdot \hat{Y}_v^\Lambda \quad (2.4)$$

where $\mathbf{A}^{\Lambda, i\varsigma}$ is a second-rank *Cartesian coupling tensor* describing the coupling between two nuclear spins i and j , represented by the nuclear spin vector operators $\hat{\mathbf{X}}_i^{Local}$ and $\hat{\mathbf{Y}}_j^\Lambda$ ($\varsigma = j$), respectively. Additionally, $\mathbf{A}^{\Lambda, i\varsigma}$ may also be the coupling between $\hat{\mathbf{X}}_i^{Local}$ and the magnetic field operator $\hat{\mathbf{Y}}_{j'}^\Lambda$ ($\varsigma = j'$). $\hat{\mathbf{Y}}_\varsigma^\Lambda$ is a vector operator interacting with $\hat{\mathbf{X}}_i^{Local}$, whose exact nature depends on the particular spin interaction Λ . $\hat{\mathbf{Y}}_\varsigma^\Lambda$ can be either a field vector or a nuclear spin vector operator, here labeled as $\hat{\mathbf{Y}}_{j'}^\Lambda$ and $\hat{\mathbf{Y}}_j^\Lambda$, respectively. For each interaction Λ there is a constant C^Λ . The interactions are summarized in Table 2.1 along with the interactions with external fields.

Table 2.1: Summary of NMR interactions in the Cartesian representations

\hat{H}^A	C^A	$\hat{\mathbf{X}}_i^{Local}$	$\mathbf{A}^{\Lambda, is}$	$\hat{\mathbf{Y}}_s^A$	Typical Size (Hz)	Comments
$\hat{\mathcal{H}}^Z$	$-\gamma_i$		$\hat{\mathbf{1}}$	B_0	$10^7 - 10^9$	Interaction with main magnetic field
$\hat{\mathcal{H}}_1$	$-\gamma_i$		$\hat{\mathbf{1}}$	$B_1(t)$	$10^3 - 10^5$	Interaction with rf field
$\hat{\mathcal{H}}^{CS}$	$-\gamma_i$		δ^i	B_0	$10^2 - 10^5$	Alteration of the magnetic field by the electrons
$\hat{\mathcal{H}}^D$	b_{ij}	$\hat{\mathbf{I}}^i$	D_{ij}	$\hat{\mathbf{I}}^j$ or $\hat{\mathbf{S}}^j$	$10^3 - 10^4$	Through-space spin-spin interaction, axially symmetric traceless tensor
$\hat{\mathcal{H}}^J$	2π		J_{ij}	$\hat{\mathbf{I}}^j$ or $\hat{\mathbf{S}}^j$	$1 - 10^3$	spin-spin interaction mediated via the bonding electrons
$\hat{\mathcal{H}}^Q$	$\frac{eQ}{I(2I-1)}$		eq	$\hat{\mathbf{I}}^i$	$10^3 - 10^7$	Interaction of nuclear quadrupolar moment with the electric field gradient (q), effectively an \hat{I}^2 interaction

2.2 Tensors and Spherical Tensor Representation of Hamiltonians

In mathematics, a tensor is (in an informal sense) a generalized linear quantity or geometrical entity that can be expressed as a multi-dimensional array relative to a choice of basis of the particular space on which it is defined. A tensor belongs to the study of geometry. A tensor is *independent* of any chosen frame of reference.

The *rank* of a particular tensor is the number of array indices required to describe such a quantity. For example, (i) mass, temperature, and other scalar quantities are tensors of **rank-0**; (ii) force, momentum and other vector-like quantities are tensors of **rank-1**; (iii) a linear transformation such as an anisotropic relationship (relativistic mass) between force and acceleration vectors is a tensor of **rank-2**. Specifically, a 2^{nd} rank tensor quantifying stress in a Three-Dimensional (3D)/solid object has components which can be conveniently represented as 3×3 array.

In the description of NMR interactions, the Cartesian representation of the Hamiltonians may, sometimes, be unsuitable, since the Cartesian representation is reducible. [13] As rotational transformations are abundantly used in NMR it becomes more straightforward to express the Hamiltonian of an interaction in the spherical tensor representation. Spherical tensor operators have specific symmetry properties with respect to rotations in 3D space, which facilitates the representation of a given Hamiltonian in several different axis frames as it will be discussed in section 2.3.

A Cartesian tensor \mathbf{A}^Λ (Eq. 2.2) is a reducible rank-2 tensor containing nine real components (3×3 matrix) and it can be reduced into three irreducible tensors: a rank-0 (\mathbf{A}_0^Λ), rank-1 (\mathbf{A}_1^Λ) and rank-2 (\mathbf{A}_2^Λ) tensors. Then, the Cartesian matrix in Eq. 2.2 may be reduced as follows [14]:

$$\mathbf{A}^{\Lambda, is} = \begin{pmatrix} \mathcal{A}_{xx}^\Lambda & \mathcal{A}_{xy}^\Lambda & \mathcal{A}_{xz}^\Lambda \\ \mathcal{A}_{yx}^\Lambda & \mathcal{A}_{yy}^\Lambda & \mathcal{A}_{yz}^\Lambda \\ \mathcal{A}_{zx}^\Lambda & \mathcal{A}_{zy}^\Lambda & \mathcal{A}_{zz}^\Lambda \end{pmatrix} \rightarrow \mathbf{A}_0^\Lambda + \mathbf{A}_1^\Lambda + \mathbf{A}_2^\Lambda \quad (2.5)$$

The irreducible tensors \mathbf{A}_k^Λ of rank- k have $2k + 1$ elements or irreducible tensor operators $\mathcal{A}_{k,q}^\Lambda$, each with different order, q ; with $q = \{-k, k - 1, \dots, -k\}$.

$$\mathbf{A}_0^\Lambda = (\mathcal{A}_{0,0}^\Lambda) \quad (2.6)$$

$$\mathbf{A}_1^\Lambda = (\mathcal{A}_{1,-1}^\Lambda; \mathcal{A}_{1,0}^\Lambda; \mathcal{A}_{1,1}^\Lambda) \quad (2.7)$$

$$\mathbf{A}_2^\Lambda = (\mathcal{A}_{2,-2}^\Lambda; \mathcal{A}_{2,-1}^\Lambda; \mathcal{A}_{2,0}^\Lambda; \mathcal{A}_{2,1}^\Lambda; \mathcal{A}_{2,2}^\Lambda) \quad (2.8)$$

where each rank- k tensor defines: (i) a scalar ($k = 0$), proportional to the trace of \mathbf{A} (Eq. 2.6), (ii) an antisymmetric ($k = 1$, Eq. 2.7) and (iii) a symmetric ($k = 2$, Eq. 2.8) part of the Cartesian tensor. The elements, $\mathcal{A}_{k,q}^\Lambda$ can be described in terms of the Cartesian elements \mathcal{A}_{uv}^Λ , with $u, v = \{x, y, z\}$. This relation between $\mathcal{A}_{k,q}^\Lambda$ and \mathcal{A}_{uv}^Λ can be found elsewhere. [15]

Eq. 2.4 can be expressed as the scalar product between two tensors, \mathbf{A}_k^Λ and $\hat{\mathbf{T}}_k^\Lambda$. Thus, the Hamiltonian for a given interaction Λ with rank- k can be written as follows:

$$\hat{\mathcal{H}}^\Lambda = C^\Lambda \sum_{k=0}^2 [\mathbf{A}_k^\Lambda]^F \cdot [\hat{\mathbf{T}}_k^\Lambda]^F = \quad (2.9)$$

$$= C^\Lambda \sum_{k=0}^2 \sum_{q=-k}^k (-1)^q \underbrace{[\mathcal{A}_{k,q}^\Lambda]^F}_{\text{Spatial part}} \cdot \underbrace{[\hat{\mathcal{T}}_{k,q}^\Lambda]^F}_{\text{Spin/Spin-field part}} \quad (2.10)$$

where $\sum_{k=0}^2 \mathbf{A}_k^\Lambda$ corresponds to a reduction of the Cartesian matrix \mathbf{A}^Λ , and $\sum_{k=0}^2 \hat{\mathbf{T}}_k^\Lambda$ corresponds to a reduction of the Cartesian matrix $\hat{\mathbf{T}}^\Lambda = \hat{\mathbf{X}}_i^{Local} \hat{\mathbf{Y}}_\zeta^\Lambda$ with elements \hat{T}_{uv}^Λ with $u, v = \{x, y, z\}$. \mathbf{A}_k^Λ is called a spatial tensor. It is worth mentioning that if $\hat{\mathbf{Y}}_\zeta^\Lambda$ is a spin operators ($\zeta = j$), $\hat{\mathbf{T}}_k^\Lambda$ is called a *spin* tensor. On the other hand, if $\hat{\mathbf{Y}}_\zeta^\Lambda$ is an external magnetic field ($\zeta = j'$), then $\hat{\mathbf{T}}_k^\Lambda$ is called a *spin-field* tensor. [3] $\hat{\mathcal{T}}_{k,q}^\Lambda$ is the element q of the irreducible spherical tensor of rank- k , built from the condensation of the two vector operators $\hat{\mathbf{X}}_i^{Local}$ and $\hat{\mathbf{Y}}_\zeta^\Lambda$ in Eq. 2.2. [15]

The classification of spatial and spin parts of the Hamiltonian is usually straightforward but may in some cases be obscure. Indeed, and to be more exact, Eq. 2.10 is composed by *three* terms. A first term corresponding to the spatial part, $\mathcal{A}_{k,q}^\Lambda$ and a second term, $\hat{\mathcal{T}}_{k,q}^\Lambda$, composed by two spin tensor terms (e.g. dipolar interaction and J-coupling interactions) or involving a spin/external magnetic field terms (e.g. Chemical Shift (CS)). Both cases depend whether the $\hat{\mathcal{T}}_{k,q}^\Lambda$ term is a component of a spin tensor ($\hat{\mathcal{T}}_k^{\Lambda,j}$) or a spin-field tensor ($\hat{\mathcal{T}}_k^{\Lambda,j'}$).

Thus, from Eq. 2.10, one can see that the rotations in real and spin/spin-field space are separated. The superscript letter “ F ” indicates the reference frame where the Hamiltonian is defined. The exact form of the tensor elements depend upon the axis frame of choice. The various frame transformations to express the Hamiltonian in a desired coordinate system will be discussed later in section 2.3.1. But before discussing frame transformations one should arrive to a simplified Hamiltonian equation employing the “secular approximation” to perform frame transformation calculus in a easier way.

2.2.1 Secular Approximation

In NMR, an approximation so-called “high field” (or secular) approximation is applied when the “size” of the Zeeman Hamiltonian, $\hat{\mathcal{H}}^Z$ is much larger than the “size” of $\hat{\mathcal{H}}_{int}$ (i.e. $|\hat{\mathcal{H}}^Z| \gg |\hat{\mathcal{H}}_{int}|$, with the exclusion of $\hat{\mathcal{H}}^Q$, in some cases). Under this regime, it is possible to treat the spin interactions as a perturbation of $\hat{\mathcal{H}}^Z$ and calculate the new energy levels considering only the first-order time-independent perturbation theory correction. In this regime it is possible to use the Zeeman eigenstates $|I, m\rangle$ as eigenbasis to define the average Hamiltonian. For more details the reader is referred to the original monographs. [15, 16]

The usual internal Hamiltonian can be decomposed in two parts:

$$\hat{\mathcal{H}}_{int} = \hat{\mathcal{H}}_{int}^{sec} + \hat{\mathcal{H}}_{int}^{n,sec} \quad (2.11)$$

where $\hat{\mathcal{H}}_{int}^{sec}$ and $\hat{\mathcal{H}}_{int}^{n,sec}$ are the secular and nonsecular terms of the internal Hamiltonian, respectively. However, in high-field approximation, only the secular terms commute with the Zeeman Hamiltonian, and therefore only these terms need to be retained. Then the following commutators are obtained

$$\left[\hat{\mathcal{H}}_{int}^{sec}, \hat{\mathcal{H}}^Z \right] = 0 \quad (2.12)$$

or

$$\left[\hat{\mathcal{H}}_{int}^{nsec}, \hat{\mathcal{H}}^Z \right] \neq 0 \quad (2.13)$$

if $\hat{\mathcal{H}}_{int}$ commutes or not with $\hat{\mathcal{H}}^Z$, respectively. Only the portion that commutes with the Zeeman Hamiltonian (Eq. 2.12) is needed to calculate the perturbed energy levels and therefore determine the positions of the resonance lines in the spectrum.

In the spherical tensor notation, one has:

$$\left[\hat{\mathcal{T}}_{k,q}^\Lambda, \hat{I}_Z \right] = q \hat{\mathcal{T}}_{k,q}^\Lambda \quad (2.14)$$

Comparing Eqs. 2.12 and 2.14, shows that only tensor elements with $q = 0$ contribute to the secular part of the internal Hamiltonian in a strong external magnetic field, if the system is described in the Laboratory (LAB) frame. In addition, due to the fact that the spin interactions in NMR are expressed by rank-2 tensors the summation in Eq. 2.10 goes only until $k = 2$. However, the antisymmetric part with $k = 1$ of spin interactions does not contribute to the spectrum in the first order, and can be neglected. [15] To summarize, only the tensor elements with $k = 0, 2$ and $q = 0$ will be retained in a high-field approximation and the expression in Eq. 2.10 can be simplified to:

$$\hat{\mathcal{H}}^\Lambda = C^\Lambda \sum_{k=0,2} [\mathcal{A}_{k,0}^\Lambda]^{LAB} [\hat{\mathcal{T}}_{k,0}^\Lambda]^{LAB} = \quad (2.15a)$$

$$= C^\Lambda \left([\mathcal{A}_{0,0}^\Lambda]^{LAB} [\hat{\mathcal{T}}_{0,0}^\Lambda]^{LAB} + [\mathcal{A}_{2,0}^\Lambda]^{LAB} [\hat{\mathcal{T}}_{2,0}^\Lambda]^{LAB} \right) \quad (2.15b)$$

The expression of Eq. 2.15 is the one that will be used to derive the nuclear spin interaction expression in the following sections. It is worth mentioning that such approximation is not valid for most of the quadrupolar nuclei. The quadrupole interaction gives rise to a breakdown of the secular approximation Eq. 2.15 is no longer valid. This happens because the second-order quadrupolar effects arise from a quadrupolar cross-term which give rise to a rank-4 tensor as it may be seen later (Eq. 2.92).

2.3 Tools for Describing Rotations in the Solid-State NMR

2.3.1 Reference Frame Transformations

In general, a given NMR Hamiltonian can always be expressed using Eq. 2.15 as long as both spatial and spin tensors are referred to the same coordinate system or reference frame. One of the reasons, given above, for the use of an irreducible spherical tensor representation to express the Hamiltonians, resides on the ease to employ 3D rotations to the spin and/or spatial part in a separate way. The discussion of many properties in NMR spectroscopy relies on transforming the overall Hamiltonian, or only a part of it, between different reference frames. Typically, the relevant frame transformations involved in Solid-State Nuclear Magnetic Resonance (SSNMR), depending on the nature of the experiment, are:

LAB or L: Denotes the laboratory axis system, where the z-axis is along the static magnetic field. In the high field approximation, all spin Hamiltonians involve components of spatial tensors written in the LAB frame, **L**.

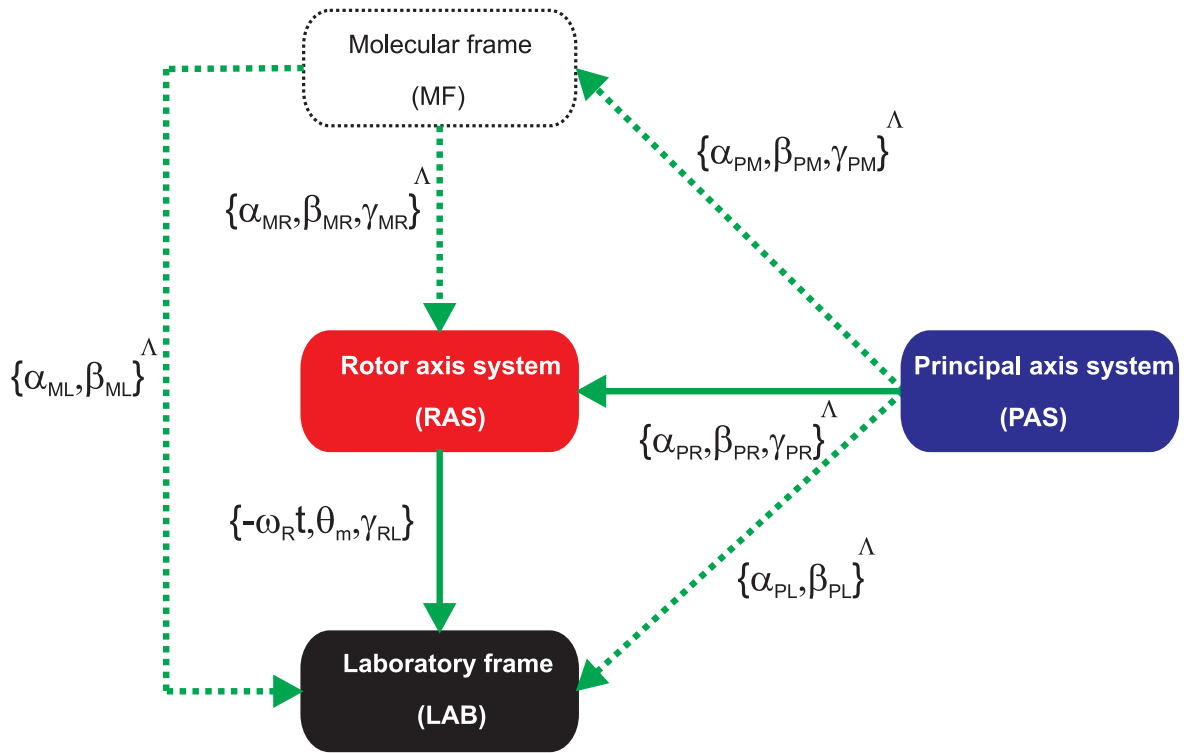


Fig. 2.1: Coordinate system applicable in SSNMR. The transformation between coordinate frames described in terms of Euler angles, e.g. $\Omega_{PR}^\Lambda = \{\alpha_{PR}, \beta_{PR}, \gamma_{PR}\}^\Lambda$ is the transformation from the PAS of an interaction Λ to the RAS of reference. γ_{RL} is not necessary as the Hamiltonian is invariant to rotation about the LAB z – axis at high field. The coordinates systems used in this thesis are indicated by the continuous arrows, i.e. $PAS \xrightarrow{\Omega_{PR}^\Lambda} RAS \xrightarrow{\Omega_{RL}} LAB$ (See Fig. 2.3 in section 2.3.3).

PAS or P: Denotes the principal axis system where a given interaction tensor of a spin i or a spin pair ij , is diagonal. The PAS depends on the molecular structure. It is fixed to the molecule, and so varies with molecular orientation, then different PAS orientations with respect to the LAB frame reflect different strengths of a certain interaction Λ . It is worth mentioning that anisotropic tensors have their simplest form in their own PAS;

MF or M: Denotes a molecular reference frame (which can be chosen arbitrarily);

CF or C: Denotes the crystal frame. This frame is only important in single crystal studies and might be a system of crystallographic axes fixed with respect to the unit cell (For the sake of simplicity, this frame is not present in Fig. 2.1);

RAS or R: Denotes the rotor axis system in which the z -axis coincides with the rotor axis. The sample is spun at the magic angle at a fixed angular frequency ω_R , associated with a rotational period

$$\tau_R = \frac{2\pi}{\omega_R} \quad (2.16)$$

corresponding to the time interval for the rotor to make a complete revolution. The sample rotation gives rise to time-dependent Euler transformation angles $\Omega_{RL}(t)$ relat-

ing the rotor frame \mathbf{R} to the LAB frame \mathbf{L} . the expression for $\Omega_{RL}(t)$ can be viewed in Fig. 2.1. This frame is important in Magic-Angle Spinning (MAS) experiments and will be abundantly used in other sections of this thesis. Further details about frame transformations involving the RAS are given in section 2.3.3.

In this thesis only the reference frames, LAB, PAS and RAS, are relevant to determine the final Hamiltonian expression. Some of the reference frames discussed above are related to each other through rotations using the Euler angles (Fig. 2.1).

2.3.2 Euler Angles and Wigner Matrix

Generically, a rotation $\hat{R}_{\mathbf{n}}(\theta)$ about an arbitrary axis \mathbf{n} by θ to transform an initial frame $A = (X^A, Y^A, Z^A)$ into a frame $D = (X^D, Y^D, Z^D)$ can be described by three Euler angles $\Omega_{AD}^\Lambda = \{\alpha_{AD}, \beta_{AD}, \gamma_{AD}\}^\Lambda$, where Λ depict the NMR interaction suffering such transformation (Fig. 2.2). There are three different recipes for realizing this rotational transformation according to ref. [17] However in this thesis I prefer to explain rotation between reference frames by means of two “intermediate” axis frames $B = (X^B, Y^B, Z^B)$ and $C = (X^C, Y^C, Z^C)$ as depicted in Fig. 2.2. Then, to rotate the “old” axis frame A to the “new” frame D , the following path is followed:

$$A^{old} \xrightarrow{\hat{R}_{z^A}(\alpha_{AB}^\Lambda)} B \xrightarrow{\hat{R}_{y^B}(\beta_{BC}^\Lambda)} C \xrightarrow{\hat{R}_{z^C}(\gamma_{CD}^\Lambda)} D^{new} \quad (2.17)$$

The rotations expressed in Eq. 2.17 can be decomposed in three parts, where each enumeration below, corresponds to the circled numbers depicted in Fig. 2.2:

1. Rotate about the z^A -axis through an angle α_{AB}^Λ , transforming the old axis frame A into the intermediate axis frame B ;
2. Rotate about the new intermediate y^B -axis through an angle β_{BC}^Λ , transforming the intermediate axis frame B into a second intermediate axis frame C ;
3. Rotate about the intermediate z^C -axis through an angle γ_{CD}^Λ , transforming the axis frame C into the final axis frame D .

A rotation operator $\hat{R}_{\mathbf{n}}(\theta)$ to transform frame A in D can thus be written as (see Appendix E.3):

$$\hat{R}_{\mathbf{n}}(\Omega_{AD}^\Lambda) = \exp(-i\alpha_{AD}\hat{I}_{Z^A}) \exp(-i\beta_{AD}\hat{I}_{Y^B}) \exp(-i\alpha_{AD}\hat{I}_{Z^C}) = \quad (2.18)$$

$$= \hat{R}_{z^A}(\alpha_{AD}^\Lambda) \hat{R}_{y^B}(\beta_{AD}^\Lambda) \hat{R}_{z^C}(\gamma_{AD}^\Lambda) \quad (2.19)$$

To apply rotation in rank-2 tensors present in NMR interactions one needs a matrix representation of such rotation operators. This matrix representation of rotations can be expressed in the spherical basis of the angular momentum, and is known as the *Wigner matrix*. Then, a Wigner matrix applied to a rank- k tensor, to rotate an axis frame A to D by a set of Euler angles Ω_{AD}^Λ , may be expressed as:

$$\hat{D}_{q',q}^{(k)}(\Omega_{AD}^\Lambda) = \exp(-iq'\alpha) d_{q',q}^{(k)}(\beta) \exp(-iq\gamma) \quad (2.20)$$

where $d_{q',q}^{(k)}$ is the *reduced Wigner rotation matrix elements*, and have the general expression [17]:

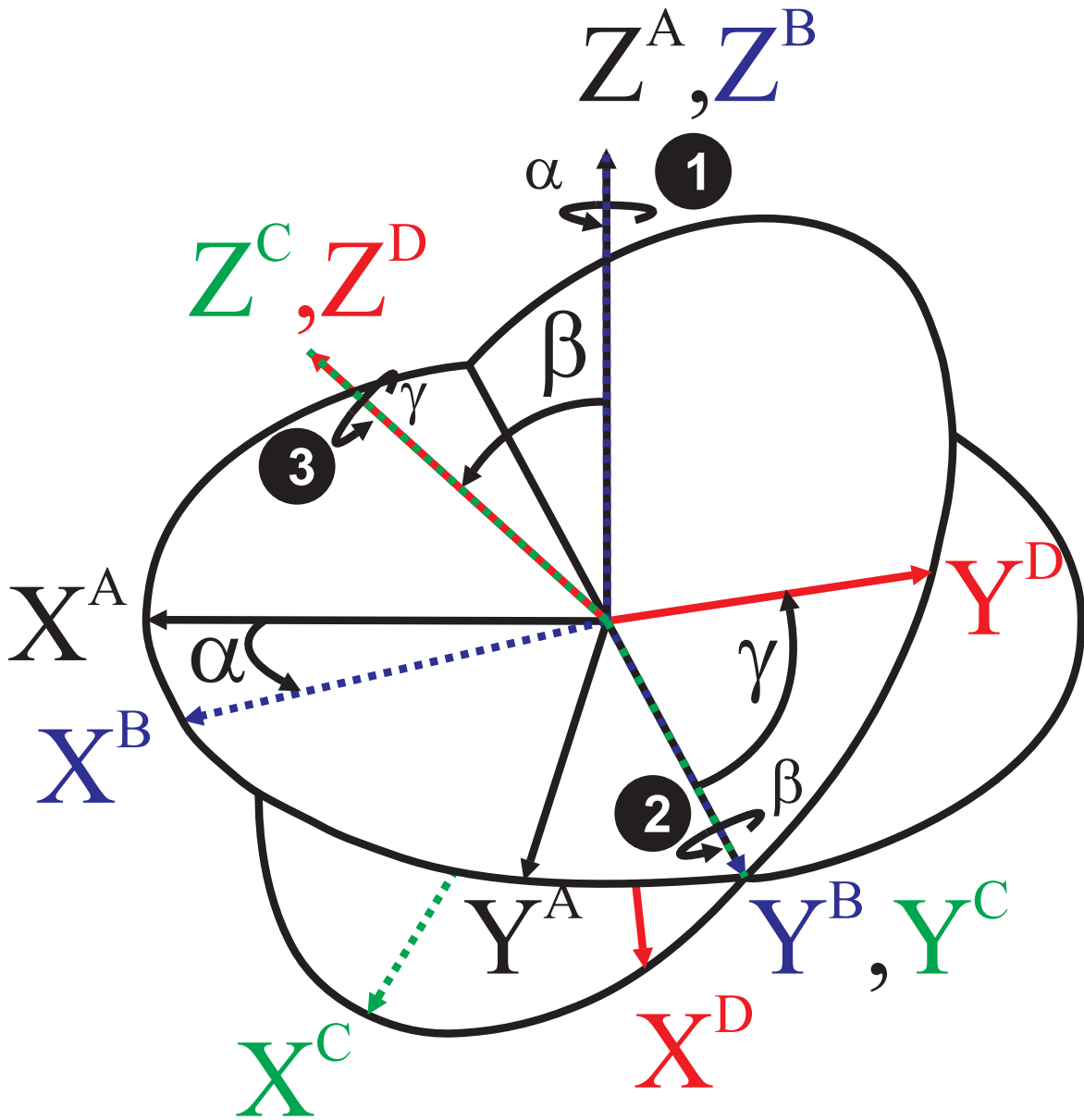


Fig. 2.2: Euler angles $\{\alpha, \beta, \gamma\}$ in the rotational transformation from a frame A to D. Frames B and C are intermediate axis frames. The circled numbers depict the chronological order of the rotations (see text for description).

$$\begin{aligned}
 d_{q',q}^{(k)}(\beta) &= \sum_p \frac{(-1)^p \sqrt{(k+q')!(k-q')!(k+q)!(k-q)!}}{p!(k+q'-p)!(k-q-p)!(p+q-q')!} \times \\
 &\times \left(\cos \frac{\beta}{2}\right)^{2k-2p-q+q'} \left(-\sin \frac{\beta}{2}\right)^{2p+q-q'} \quad (2.21)
 \end{aligned}$$

with $p = \{-k, -k+1, \dots, +k\}$. The values of $d_{q',q}^{(k)}$ for $k = 1, 2, 4$ can be found in Appendix B.

The main transformational property of Wigner matrices under the rotation from the A axis system to B and then from B to D is the following:

$$\hat{\mathcal{D}}_{q',q}^{(k)}(\Omega_{AD}^\Lambda) = \sum_{q''=-k}^k \hat{\mathcal{D}}_{q',q''}^{(k)}(\Omega_{AB}^\Lambda) \hat{\mathcal{D}}_{q'',q}^{(k)}(\Omega_{BD}^\Lambda) \quad (2.22)$$

Various useful symmetries of Wigner matrices can be found in the monograph of Varshalovich *et al.* [18]

The transformation of an axis frame A into a axis frame D (rotation, $\hat{R}_n(\Omega_{AD}^\Lambda)$) of a spherical tensor $\hat{A}_{k,q}^\Lambda$, may be expressed as:

$$[A_{k,q}^\Lambda]^D = \hat{R}_n(\Omega_{AD}^\Lambda) [A_{k,q}^\Lambda]^A \hat{R}_n^{-1}(\Omega_{AD}^\Lambda) = \quad (2.23)$$

$$= \sum_{q'=-k}^k [A_{k,q'}^\Lambda]^A \hat{\mathcal{D}}_{q',q}^{(k)}(\Omega_{AD}^\Lambda) \quad (2.24)$$

Now lets describe how the anisotropic parts of the Hamiltonian, (the $[\hat{A}_{2,0}^\Lambda]^L$ term of Eq. 2.15a), in the LAB axis frame, \mathbf{L} , can be expressed in terms of the elements of these tensor interactions in their principal axis systems, \mathbf{P} . Then, employing Eq. 2.24, the spatial part of Eq. 2.15 may be written as:

$$[A_{2,0}^\Lambda]^L = \sum_{q'=-2}^2 [A_{2,q'}^\Lambda]^P \hat{\mathcal{D}}_{q',0}^{(2)}(\Omega_{PL}^\Lambda) \quad (2.25)$$

Eq. 2.25 is only applicable for static samples. An additional reference frame, \mathbf{R} , is needed to expressed an internal interaction under rotating samples. This will be discussed in the next section.

2.3.3 Internal Hamiltonian Under the Effect of MAS Spatial Averaging

In isotropic liquids all anisotropic interactions are averaged out by fast isotropic molecular motion. This can also be done for second-rank interactions in solids provided that the macroscopic sample is rotated rapidly about the proper axis. This axis must be tilted by the so called magic-angle, $\arccos\left(\frac{1}{\sqrt{3}}\right) \approx 54.74^\circ$, with respect to the static magnetic field. MAS averages out all anisotropic rank-2 interactions. In a rotating solid the rotating-frame Hamiltonian is time-dependent. (The rotating-frame transformation of the Hamiltonian must not be confused with the rotor axis frame.)

The anisotropic part of a given internal interaction is time-dependent under MAS, since the orientation of the tensor with respect to the LAB frame is time-dependent. It is natural to consider additional transformations from frames \mathbf{P} to \mathbf{R} and then from frames \mathbf{R} to \mathbf{L} , since the orientation of a rank-2 tensor is fixed in the rotor frame and the transformation $\mathbf{R} \rightarrow \mathbf{L}$ has a simple form. Thus, combining Eqs. 2.22 and 2.24, Eq. 2.25 can be rewritten as follows (Fig. 2.3):

$$[A_{2,0}^\Lambda]^L = \sum_{q'=-2}^2 [A_{2,q'}^\Lambda]^R \hat{\mathcal{D}}_{q',0}^{(2)}(\Omega_{RL}(t)) = \quad (2.26)$$

$$= \sum_{q'=-2}^2 \sum_{q''=-2}^2 [A_{2,q''}^\Lambda]^P \hat{\mathcal{D}}_{q'',q'}^{(2)}(\Omega_{PR}^\Lambda) \hat{\mathcal{D}}_{q',0}^{(2)}(\Omega_{RL}(t)) \quad (2.27)$$

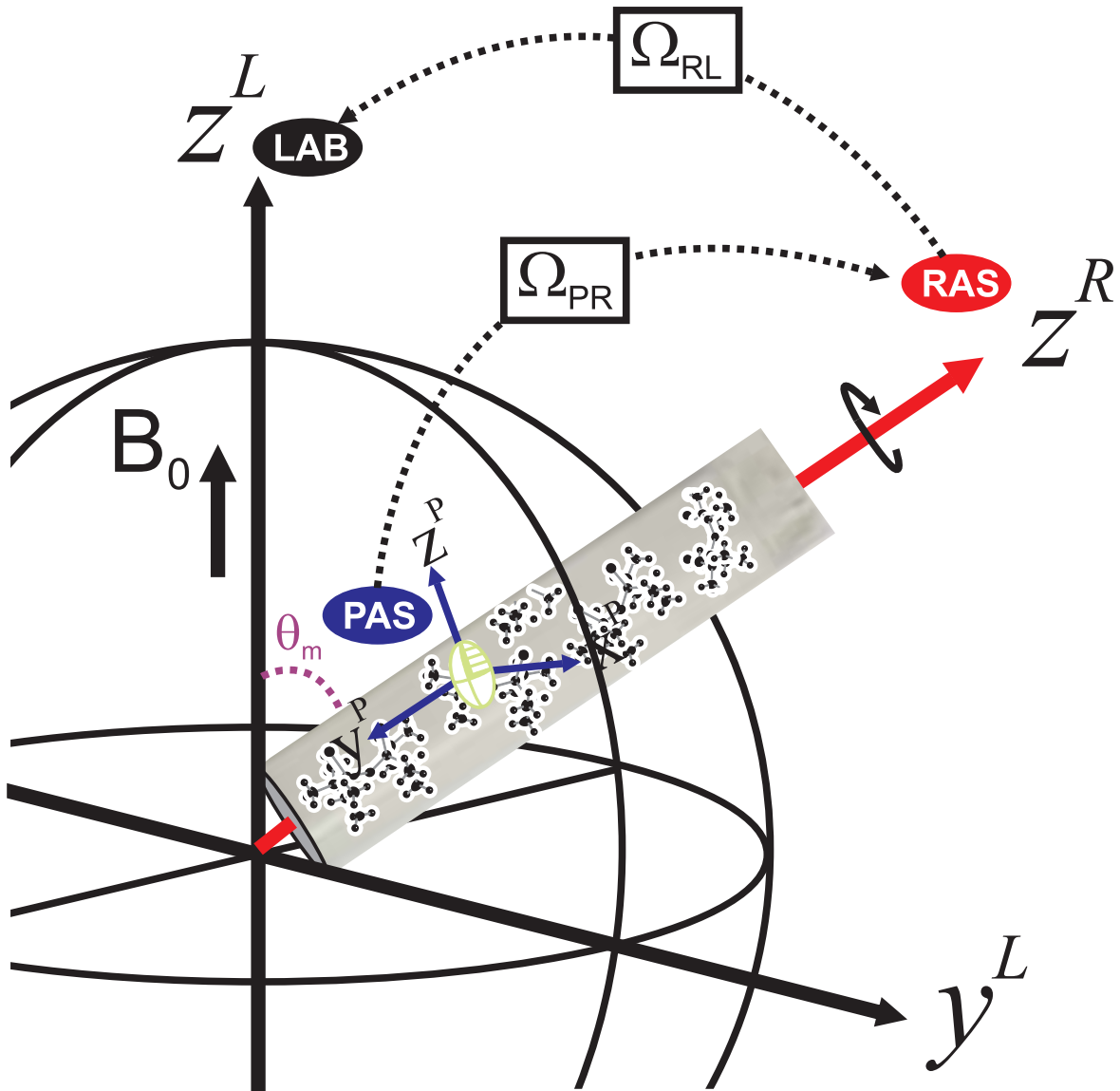


Fig. 2.3: Relevant coordinate system applicable in SSNMR for rotating solids.

Replacing $\hat{D}_{q',0}^{(2)}(\Omega_{RL}^\Lambda(t))$ by the expression of Eq. 2.20, one will obtain the spatial tensor correspondent to an Hamiltonian which describes an interaction Λ for a single crystal under MAS.

$$[\mathcal{A}_{2,0}^\Lambda]^L = \sum_{q'=-2}^2 \sum_{q''=-2}^2 [\mathcal{A}_{2,q''}^\Lambda]^P \hat{D}_{q'',q'}^{(2)}(\Omega_{PR}^\Lambda) d_{q',0}^{(2)}(\theta_m) \exp(iq'\omega_R t) \quad (2.28)$$

Eq. 2.28 can be identified with a time-dependent frequency $\omega_\Lambda(t) = [\mathcal{A}_{2,0}^\Lambda]^L$. Furthermore, the inspection of this expression reveals that it is a Fourier series, i.e. a periodic function modulated by ω_R ,

$$\omega_\Lambda(t) = \sum_{q'=-2}^2 \underbrace{\sum_{q''=-2}^2 [\mathcal{A}_{2,q''}^\Lambda]^P \hat{D}_{q'',q'}^{(2)}(\Omega_{PR}^\Lambda) d_{q',0}^{(2)}(\theta_m)}_{\omega_\Lambda^{(q')}} \exp(iq'\omega_R t) = \quad (2.29)$$

$$= \sum_{q'=-2}^2 \omega_\Lambda^{(q')} \exp(iq'\omega_R t) \quad (2.30)$$

where $\omega_\Lambda^{(q')}$ have five Fourier components related to the tensor components $[\mathcal{A}_{2,q''}^\Lambda]^P$. The frequency $\omega_\Lambda(t)$ is a real number, and the Fourier components $\omega_\Lambda^{(q')}$ and $\omega_\Lambda^{(-q')}$ are related by:

$$\omega_\Lambda^{(q')} = \left\{ \omega_\Lambda^{(-q')} \right\}^* \quad (2.31)$$

This relationship is useful, for example, to speed up numerical calculations, because it follows that only $\omega_\Lambda^{(q')}$ for $q' \geq 0$ needs to be calculated explicitly. [3]

Clearly, Eq. 2.30 shows how MAS induces a time-periodic modulation of the rank-2 spatial tensors. The value of $\omega_\Lambda(t_0)$ is equal to that following completion of a full rotational period: $\omega_\Lambda(t_0) = \omega_\Lambda(t_0 + \tau_R)$. This may be verified by inserting the two different time points into Eq. 2.30. Using $\omega_R \tau_R = 2\pi$, the exponential factor may be expressed as:

$$\exp[iq'\omega_R(t_0 + \tau_R)] = \exp(iq'\omega_R t_0) \exp(2iq'\pi) = \exp(iq'\omega_R t_0) \quad (2.32)$$

This demonstrates that the spatial part of the Hamiltonian is periodic in time. Thus, if the spinning frequency ω_R is sufficiently fast in comparison with a given rank-2 internal interaction frequency then, this interaction will be averaged out and no spinning sidebands manifold appear in the spectrum.

In short, the secular Hamiltonian, $\hat{\mathcal{H}}^\Lambda$ of Eq. 2.15b under the effect of MAS can be rewritten in a convenient way, using the addition theorem of Eq. 2.27 in order to include the frame transformations $PAS \rightarrow RAS \rightarrow LAB$:

$$\begin{aligned} \hat{\mathcal{H}}^\Lambda &= C^\Lambda \times \left(\underbrace{\mathcal{A}_{0,0}^\Lambda \hat{\mathcal{T}}_{0,0}^\Lambda}_{\omega_\Lambda^{(0)}} + [\mathcal{A}_{2,0}^\Lambda]^L \left[\hat{\mathcal{T}}_{2,0}^\Lambda \right]^L \right) = \quad (2.33) \\ &= C^\Lambda \times \left(\omega_\Lambda^{(0)} + \underbrace{\left[\sum_{q'=-2}^2 \sum_{q''=-2}^2 [\mathcal{A}_{2,q''}^\Lambda]^P \hat{D}_{q'',q'}^{(2)}(\Omega_{PR}^\Lambda) d_{q',0}^{(2)}(\theta_m) \exp(iq'\omega_R t) \right]}_{[\mathcal{A}_{2,0}^\Lambda]^L} \left[\hat{\mathcal{T}}_{2,0}^\Lambda \right]^L \right) = \\ &= C^\Lambda \times \left(\omega_\Lambda^{(0)} + \sum_{q'=-2}^2 \omega_\Lambda^{(q')} \exp(iq'\omega_R t) \left[\hat{\mathcal{T}}_{2,0}^\Lambda \right]^L \right) \quad (2.34) \end{aligned}$$

where $\omega_\Lambda^{(0)}$ and $\omega_\Lambda^{(q')}$ are the isotropic and anisotropic components of the interactions. The values of the reduced Wigner matrix elements $d_{q',0}^{(2)}(\theta_m)$ and $d_{q'',q'}^{(2)}(\Omega_{PR}^\Lambda)$ can be found in

Table B.2 in Appendix B. The spatial tensors defined in the PAS, $[\mathcal{A}_{2,q''}^\Lambda]^P$ and the spin tensors $[\hat{\mathcal{T}}_{2,0}^\Lambda]^L$ are given in terms of the Cartesian angular momentum operators in Table 2.2.

2.4 NMR Interactions in Terms of Irreducible Spherical Tensors

The general Cartesian representation of the relevant NMR interaction can be found in Table 2.1. In this section the NMR interactions will be briefly described in their spherical tensor representation with the help of Table 2.2, which allows the construction of a given Hamiltonian. For a full description of the external and internal Hamiltonian it is advisable to consult some important reviews. [3, 15, 17, 19, 20]

2.4.1 Zeeman Interaction

In the absence of an external static magnetic field all spin energy levels are degenerate and the nuclear spin are randomly oriented in space without a net magnetisation. The simplest spin system is that consisting of an isolated spin in a static, uniform magnetic field of the NMR experiment, with no other interactions interfering. In this case, the degeneracy is lost and various energy levels are created depending on the nuclear spin number. Then the nuclear spin acquires a preferential orientation, with respect to the strong magnetic field. In quantum mechanics language this corresponds to unequally populated energy Zeeman levels. In a strong and static magnetic field \mathbf{B}_0 ($B_0 \gg 1\text{T}$) the dominant Zeeman Hamiltonian, $\hat{\mathcal{H}}^Z$ of a nucleus i can be expressed as

$$\hat{\mathcal{H}}_i^Z = -\hat{\boldsymbol{\mu}}_i \cdot \mathbf{B}_0 = \quad (2.38)$$

$$= -\gamma_i \hat{\mathbf{I}}^i \cdot \hat{\mathbf{1}} \cdot \mathbf{B}_0 \quad (\text{Cartesian representation}) \quad (2.39)$$

where $\hat{\boldsymbol{\mu}}_i = \gamma_i \hat{\mathbf{I}}^i$ is the nuclear magnetic moment operator and γ_i is the magnetogyric ratio (in units of $rad \cdot s^{-1}$) of spin i . The nuclear magnetic moment is parallel to the spin angular momentum pointing either in the same ($\gamma > 0$) or in the opposite ($\gamma < 0$) direction. [21, 22]

Usually the orientation of the external magnetic field is taken along the z -axis $\mathbf{B}_0 = B_0 \mathbf{e}_{z,L}$ (with $\mathbf{e}_{z,L}$ being a unit vector along z^L) of the LAB frame, and then Eq. 2.39 can be written as:

$$\hat{\mathcal{H}}_i^Z = -\gamma_i \begin{pmatrix} 0 \\ 0 \\ B_0 \end{pmatrix} \cdot \begin{pmatrix} \hat{I}_x^i \\ \hat{I}_y^i \\ \hat{I}_z^i \end{pmatrix} = \quad (2.40)$$

$$= -\gamma_i B_0 \hat{I}_Z^i = \quad (2.41)$$

$$= \omega_0^i \hat{I}_Z^i = \quad (2.42)$$

$$= [\mathcal{A}_{0,0}^Z]^{LAB} \cdot [\hat{\mathcal{T}}_{0,0}^{Z,ij'}]^{LAB} \quad (\text{spherical tensor representation}) \quad (2.43)$$

where ω_0^i is the Larmor frequency of a particular spin i . $\hat{\mathcal{T}}_{0,0}^{Z,ij'}$ is a spin-field tensor expressing the interaction between a spin i and a magnetic field vector j' . The spatial and spin-field tensor values of Eq. 2.43 can be found in Table 2.2.

Table 2.2: The spatial and spin components of various NMR interactions

Interaction (Λ)	C^Λ	$A_{0,0}^\Lambda$	$\hat{T}_{0,0}^\Lambda$	$[A_{2,0}^\Lambda]^{LAB}$	$[A_{2,0}^\Lambda]^{PAS}$	$[A_{2,\pm 1}^\Lambda]^{PAS}$	$[A_{2,\pm 2}^\Lambda]^{PAS}$	$[\hat{T}_{2,0}^\Lambda]^{LAB}$
Zeeman (Z)	$-\gamma_i$	$-\sqrt{3}$	$-\frac{1}{\sqrt{3}}B_0\hat{I}_z^i$	-	-	-	-	-
Chemical Shift (CS)	$-\gamma_i$	$-\sqrt{3}\delta_{iso}^i$	$-\frac{1}{\sqrt{3}}B_0\hat{I}_z^i$	ω_{CSA}^i	$\sqrt{\frac{3}{2}}\delta_{aniso}^i$	0	$-\frac{1}{2}\eta^J CS \delta_{aniso}^i$	$\sqrt{\frac{3}{2}}B_0\hat{I}_z^i$
Homonuclear Dipolar (D_{ij})	1	-	-	ω_D^{ij}	$\sqrt{6}b^{ij}$	0	0	$\frac{1}{\sqrt{6}}(3\hat{I}_z^i\hat{I}_z^j - \hat{I}^i \cdot \hat{I}^j)$
Heteronuclear Dipolar (D_{JS})	1	-	-	ω_D^{IS}	$\sqrt{\frac{3}{2}}\hat{I}_z^i\hat{S}_z^j$	0	0	$\frac{1}{\sqrt{6}}(3\hat{I}_z^i\hat{I}_z^j - \hat{I}^i \cdot \hat{I}^j)$
Homonuclear J-coupling (J_{ij})	1	$-2\pi\sqrt{3}J_{iso}^{ij}$	$-\frac{1}{\sqrt{3}}\hat{I}^i \cdot \hat{I}^j$	$\omega_{J,aniso}^{ij}$	$-2\pi\sqrt{\frac{3}{2}}J_{aniso}^{ij}$	0	$-\frac{1}{2}\eta^J J_{aniso}^i$	$\frac{1}{\sqrt{6}}(3\hat{I}_z^i\hat{I}_z^j - \hat{I}^i \cdot \hat{I}^j)$
Heteronuclear J-coupling (J_{IS})	1	$-2\pi\sqrt{3}J_{iso}^{IS}$	$-\frac{1}{\sqrt{3}}\hat{I}_z^i\hat{S}_z^j$	$\omega_{J,aniso}^{IS}$	$-2\pi\sqrt{\frac{3}{2}}J_{aniso}^{IS}$	0	$-\frac{1}{2}\eta^J J_{aniso}^i$	$\omega_{J,aniso}^{IS}\sqrt{\frac{3}{2}}\hat{I}_z^i\hat{S}_z^j$
1 st -order Quadrupolar (Q)	$\frac{C_Q}{2I(2I-1)}$	-	-	$\omega_{Q,i}^i$	$\sqrt{\frac{3}{2}}$	0	$\frac{1}{2}\eta^Q$	$\frac{1}{\sqrt{6}}[3\hat{I}_{z,i}^2 - \hat{I}_i^2]$

The Nuclear spin interaction Hamiltonians shown in the first column may be constructed from Eq. 2.15b (under secular approximation) as the product of a constant C^Λ , the spatial $A_{2,q}^\Lambda$ and spin $\hat{T}_{2,q}^\Lambda$ parts both in the LAB frame. The isotropic components A_{iso} depicted in Table 2.2 [e.g. δ_{iso}^i (in ppm) and J_{iso}^{ij} (in Hz)], The anisotropies A_{aniso} of the spatial tensors [e.g. δ_{aniso}^i (in ppm) and J_{aniso}^{ij} (in Hz)] and the *asymmetry parameter* (η^Λ) for each interaction are defined as, respectively:

$$A_{iso} = \frac{1}{3}Tr(A_{uv}^{PAS}) = \frac{1}{3}([A_{xx}]^{PAS} + [A_{yy}]^{PAS} + [A_{zz}]^{PAS}); \quad A_{aniso} = [A_{zz}]^{PAS} - A_{iso}; \quad \text{and} \quad \eta^\Lambda = \frac{[A_{yy}]^{PAS} - [A_{xx}]^{PAS}}{[A_{zz}]^{PAS} - A_{iso}}, \quad \text{only for } \Lambda = CS, J \quad (2.35)$$

The expression of η^Q is defined later in the text. The dipolar coupling constants b_{ij} and b_{JS} (in rad.s⁻¹) are defined as:

$$b^{ij} = \gamma_i^2 \frac{\mu_0 \hbar}{4\pi r_{ij}^3}; \quad b^{JS} = \gamma_I \gamma_S \frac{\mu_0 \hbar}{4\pi r_{IS}^3} \quad (2.36)$$

where r_{ij} and r_{JS} are the internuclear distances between two spins in the homonuclear and heteronuclear spin pair, respectively. $\mu_0 = 4\pi \cdot 10^7 N \cdot C^{-2} \cdot s^2$ is the permeability of vacuum and \hbar is Planck's constant ($\hbar = 6.62608 \times 10^{-34}$ J.s) divided by 2π . For the 1st order quadrupolar interaction, the *quadrupolar coupling constant* (C_Q) (in angular frequency) is given by:

$$C_Q = \frac{e^2 q Q}{\hbar} \quad (2.37)$$

2.4.2 Zeeman Interaction and Interaction With *rf* Field

During some time intervals of NMR experiments, the sample is irradiated with linearly polarized *rf* field $\mathbf{B}_1(t)$ of strength $2B_1$, frequency ω_c (carrier frequency) and phase ϕ^c (pulse phase) has the form:

$$\mathbf{B}_1(t) = 2B_1 \cos(\omega_c t + \phi^c) \quad (2.44)$$

When the Hamiltonian for a *rf* field, \hat{H}_1 applied along the x-axis, has the same form as the Zeeman Hamiltonian then

$$\hat{\mathcal{H}}_1^i(t) = -\gamma_i \hat{\mathbf{I}}^i \cdot \hat{\mathbf{1}} \cdot \mathbf{B}_1(t) = \quad (2.45)$$

$$= -\gamma_i \begin{pmatrix} B_1(t) \\ 0 \\ 0 \end{pmatrix} \cdot \begin{pmatrix} \hat{I}_x^i \\ \hat{I}_y^i \\ \hat{I}_z^i \end{pmatrix} = \quad (2.46)$$

$$= -\gamma_i 2B_1 \cos(\omega_c t + \phi^c) \hat{I}_x^i = \quad (2.47)$$

$$= 2\omega_1 \cos(\omega_c t + \phi^c) \hat{I}_x^i \quad (2.48)$$

As in the vector model, the oscillating $\hat{\mathbf{B}}_1(t)$ field vector can be written as two counter-rotating components. It can be shown that only one of these components has a significant effect on the spin system, allowing the Hamiltonian of Eq. 2.48 to be rewritten as:

$$\hat{\mathcal{H}}_1^i(t) = \omega_1 \exp\left[+i(\omega_c t + \phi^c) \hat{I}_z^i\right] \hat{I}_x^i \exp\left[-i(\omega_c t + \phi^c) \hat{I}_z^i\right] \quad (2.49)$$

It is desirable to transform the external Hamiltonian

$$\hat{\mathcal{H}}_{ext}(t) = \omega_0^i \hat{I}_z^i + \hat{\mathcal{H}}_1^i(t) \quad (2.50)$$

into the Rotating Frame (RF) where $\hat{\mathcal{H}}_{ext}$ is time-independent and the Schrödinger equation can be solved easily, i.e. the nuclear spins and the oscillating *rf* field appears as static. Then, in this frame, rotating around the z-axis at a frequency ω_c , is equivalent to transform the external Hamiltonian into the Zeeman interaction frame. This can be written as follows:

$$\hat{\mathcal{H}}_{ext}^{RF}(t) = \exp\left(-i\omega_c t \hat{I}_z^i\right) \hat{\mathcal{H}}_{ext}(t) \exp\left(i\omega_c t \hat{I}_z^i\right) \quad (2.51)$$

Then the external Hamiltonian expressed in the rotating frame can be expressed as:

$$\hat{\mathcal{H}}_{ext}^{RF}(t) = \Delta_0^i \hat{I}_z^i + \omega_1 \exp\left[+i\phi^c \hat{I}_z^i\right] \hat{I}_x^i \exp\left[-i\phi^c \hat{I}_z^i\right] = \quad (2.52)$$

$$= \Delta_0^i \hat{I}_z^i + \omega_1 \left[\hat{I}_x^i \cos(\phi^c) + \hat{I}_y^i \sin(\phi^c) \right] \quad (2.53)$$

where $\Delta\omega_0^i = (\omega_0^i - \omega_c)$ denotes the offset frequency or the resonance offset with respect to the carrier frequency. For a strong pulse ($|\Delta\omega_0^i| \ll |\omega_1|$) or small offsets ($\Delta\omega_0^i \approx 0$) reduces to:

$$\hat{\mathcal{H}}_{ext}^{RF}(t) \approx \omega_1 \left[\hat{I}_x^i \cos(\phi^c) + \hat{I}_y^i \sin(\phi^c) \right] \quad (2.54)$$

From now on the superscript label “RF” will be dropped for the sake of simplicity.

2.4.3 Chemical Shift Interaction

The interaction of a nuclear spin with the magnetic fields induced in the electronic environment by the main field is called the CS interaction. This can be compared to the principle of the Faraday's law of induction, i.e., electron currents surrounding the nucleus directly originated by the presence of a strong external magnetic field, \mathbf{B}_0 induce the appearance of a local magnetic field \mathbf{B}_{ind} in the sample (several times lower than the Zeeman field), which in turn can have orientations in all the directions with respect to the LAB frame where \mathbf{B}_0 is oriented along the z -axis. Then, the resulting local field \mathbf{B}_{loc} felt by the nucleus can be described by

$$\mathbf{B}_{loc} = \mathbf{B}_0 + \mathbf{B}_{ind}^i \quad (2.55)$$

Eq. 2.55 reflects the local environment of the site and is different for nuclei within different electron cloud orientations.

Unlike the Zeeman and rf interactions, the local magnetic field of the CS interaction does not have only one direction. Since the charge distribution is not spherically symmetric, the CS interaction is anisotropic, i.e. it depends on the orientation of the chemical site with respect to the static magnetic field. Therefore, the induced magnetic field has components along the x -, y - and z -directions and a rank-2 tensor is needed to define the orientation of such induced field. Such tensor is called the CS (or shielding) tensor, $\delta^{ij'}$. The induced magnetic field and the shielding tensor are related as follows:

$$\mathbf{B}_{ind}^i = \delta^{ij'} B_0 \quad (2.56)$$

The shielding tensor is expressed in the same way as the general form of a reducible rank-2 Cartesian tensors shown in Eq. 2.3. Therefore, the CS tensor is composed of three irreducible tensor with $k = 0, 1, 2$ components (i.e. $\delta^{CS,ij'} = \delta_0^{CS} + \delta_1^{CS} + \delta_2^{CS}$) as discussed above (Eq. 2.5). the rank-0 term (δ_0^{CS}) corresponds to the *isotropic* CS. The rank-1 term (δ_1^{CS}) is the *antisymmetric* component which has no effect in the spectrum, under the secular approximation. And the rank-2 term (δ_2^{CS}) refers to the *symmetric*, traceless component which corresponds to the Chemical Shift Anisotropy (CSA). Then, only the isotropic CS and the CSA terms are important. The latter is sensible to molecular orientation, thus determining the line shape of the spectrum. Thus, the Cartesian CS tensor ($\delta^{ij'}$), consists in the sum of the tensors δ_0 plus δ_2 . In its PAS, $\delta^{ij'}$ is diagonal and has the following form:

$$\delta^{PAS} = \begin{pmatrix} \delta_{xx}^{PAS} & 0 & 0 \\ 0 & \delta_{yy}^{PAS} & 0 \\ 0 & 0 & \delta_{zz}^{PAS} \end{pmatrix} \quad (2.57)$$

where the diagonal elements are called the *principal values* of the CS tensor. They can be ordered as follows:

$$|\delta_{zz}^{PAS} - \delta_{iso}^i| \geq |\delta_{xx}^{PAS} - \delta_{iso}^i| \geq |\delta_{yy}^{PAS} - \delta_{iso}^i| \quad (2.58)$$

where the isotropic shift is defined in Eq. 2.35

In terms of spherical tensors, the secular CS Hamiltonian can be written based on Eq. 2.15b and Table 2.2 as follows:

$$\hat{\mathcal{H}}_i^{CS} = C^{CS} \times \left([A_{0,0}^{CS}] [\hat{\mathcal{T}}_{0,0}^{CS,ij'}] + [A_{2,0}^{CS}]^L [\hat{\mathcal{T}}_{2,0}^{CS,ij'}]^L \right) = \quad (2.59)$$

$$= -\delta_{iso}^i \omega_0^i \hat{I}_z^i + \sqrt{\frac{2}{3}} \omega_{CSA}^i \hat{I}_z^i \quad (2.60)$$

where $\omega_{CSA}^i = [A_{2,0}^{CS}]^{LAB}$, which can be calculated from the spherical components of the CSA in the PAS (Eqs. 2.30 or 2.28).

Indeed, the “spin parts” $\hat{\mathcal{T}}_{2,0}^{CS,ij'}$ (spin and spin-field part) of the CS Hamiltonian given in Eq. 2.60 are components of the spin-field tensor $\hat{\mathbf{T}}_2^{CS}$ defined in section 2.2 for a given interaction Λ , which combines spin polarisation and field components. Indeed the CS Hamiltonian *only has an irreducible rank-1 tensor with respect to the spin rank*. However the tensor $\hat{\mathbf{T}}_2^{CS}$ behaves as a rank-2 irreducible tensor under *simultaneous rotation* of the spins and the external magnetic field.

Combining the CS Hamiltonian with the Zeeman Hamiltonian for a spin i in the rotating frame one gets:

$$\hat{\mathcal{H}}_i^{Z,CS} = \left[\omega_0^i (1 - \delta_{iso}^i) - \omega_c + \sqrt{\frac{2}{3}} \omega_{CSA}^i \right] \hat{I}_z^i = \quad (2.61)$$

$$= \left(\omega_{iso}^i + \sqrt{\frac{2}{3}} \omega_{CSA}^i \right) \hat{I}_z^i \quad (2.62)$$

where

$$\omega_{iso}^i = \omega_0^i (1 - \delta_{iso}^i) - \omega_c \quad (2.63)$$

is the isotropic CS frequency in the rotating frame.

2.4.4 Direct Dipole-Dipole Interaction

This group of interactions (homonuclear and heteronuclear dipole-dipole couplings), contrarily to the interactions discussed above (Zeeman, *rf*, and CS interactions), involve the interaction between two spins.

Homonuclear Direct Dipole-Dipole Interaction

It describes a magnetic through-space interaction between neighboring nuclear spins i and j of the same type.

In the irreducible spherical tensor notation, the secular Hamiltonian of the homonuclear dipole-dipole interaction may be written as:

$$\hat{\mathcal{H}}_{ij}^D = C^{Dij} \left([A_{2,0}^D]^{LAB} [\hat{\mathcal{T}}_{2,0}^{D,ij}]^{LAB} \right) = \quad (2.64)$$

$$= \omega_{ij}^D \frac{1}{\sqrt{6}} \left(3\hat{I}_z^i \hat{I}_z^j - \hat{I}^i \cdot \hat{I}^j \right) = \quad (2.65)$$

$$= \omega_{ij}^D \frac{1}{\sqrt{6}} \left(2\hat{I}_z^i \hat{I}_z^j - \frac{1}{2} [\hat{I}_+^i \hat{I}_-^j + \hat{I}_-^i \hat{I}_+^j] \right) \quad (2.66)$$

with $\hat{I}^i \cdot \hat{I}^j = \hat{I}_x^i \hat{I}_x^j + \hat{I}_y^i \hat{I}_y^j + \hat{I}_z^i \hat{I}_z^j$. The expressions for the terms ω_{ij}^D and $[\hat{\mathcal{T}}_{2,0}^{D,ij}]^{LAB}$ are depicted in Table 2.2.

Heteronuclear Direct Dipole-Dipole Interaction

The heteronuclear dipole-dipole interaction between two nuclear spins i and j of different types (I and S), may be written as:

$$\hat{\mathcal{H}}_{IS}^D = C^{DIS} \left([\mathcal{A}_{2,0}^D]^{LAB} [\hat{\mathcal{T}}_{2,0}^{D,IS}]^{LAB} \right) = \quad (2.67)$$

$$= \omega_{IS}^D \sqrt{\frac{2}{3}} \hat{I}_z^i \hat{S}_z^j \quad (2.68)$$

The expressions for the terms ω_{IS}^D and $\hat{\mathcal{T}}_{2,0}^{D,IS}$ are depicted in Table 2.2.

It is possible to determine the spin-spin internuclear distance between nuclei i and j in both homo- and heteronuclear cases by calculating the result of the dipolar coupling constants given in Table 2.2, i.e. by finding the numerical value of $\frac{b_{ij}}{2\pi}$ or $\frac{b_{IS}}{2\pi}$ (in hertz units) for the homonuclear or heteronuclear cases, respectively.

In the heteronuclear dipole-dipole interaction the transversal spin operators \hat{I}_x and \hat{I}_y are not present because the two spins I and S are non-degenerated. This important point is of great importance in homonuclear dipolar couplings where the degeneracy leads to flip-flop transitions affecting drastically the spectrum. This will be discussed next.

The influence of degenerate energy levels in dipolar coupling

The homonuclear dipole-dipole Hamiltonian contains two spin operator terms: (i) a term containing the bilinear operator $\hat{I}_z^i \hat{I}_z^j$, which is responsible for giving a first-order change in energy of all the states; (ii) a term containing raising and lowering operators $\hat{I}_+^i \hat{I}_-^j + \hat{I}_-^i \hat{I}_+^j$ (also known as *flip-flop operator*), which have non-zero elements in its matrix representation between the $\alpha\beta$ and $\beta\alpha$ basis functions, [19]

$$[\hat{I}_+^i \hat{I}_-^j + \hat{I}_-^i \hat{I}_+^j] = \begin{pmatrix} 0 & 0 & 0 & 0 \\ 0 & 0 & 1 & 0 \\ 0 & 1 & 0 & 0 \\ 0 & 0 & 0 & 0 \end{pmatrix} \quad (2.69)$$

Observing this matrix representation one concludes that the eigenfunctions of the operator defined in Eq. 2.69 include two linear combinations of the $|\alpha\beta\rangle$ and $|\beta\alpha\rangle$ functions and not only pure Zeeman functions. The remaining functions $|\alpha\alpha\rangle$ and $|\beta\beta\rangle$ are not mixed by such spin operators.

The term $[\hat{I}_+^i \hat{I}_-^j + \hat{I}_-^i \hat{I}_+^j]$ does not commute with the operator $\hat{I}_z^i \hat{I}_z^j$ because they have no common eigenfunctions and therefore will not commute with the Zeeman operator as well. Since both of these terms can not be represented by the Zeeman basis (in secular approximation) it becomes problematic to find a solution for the homonuclear dipolar Hamiltonian. Only the first spin term of Eq. 2.66 is expected to form the secular part. However, one exception happens when the two coupled spins I and S are degenerate. In this situation the Zeeman states $|\alpha\alpha\rangle$, $|\alpha\beta\rangle$, $|\beta\alpha\rangle$ and $|\beta\beta\rangle$ of the operator $\hat{I}_z^i \hat{I}_z^j$ are not only its own eigenfunctions, because the $|\alpha\beta\rangle$ and $|\beta\alpha\rangle$ are degenerated (the same energy), any linear combination of them is also an eigenfunction of $\hat{I}_z^i \hat{I}_z^j$. Hence, the eigenfunctions $|\alpha\alpha\rangle$ and $|\beta\beta\rangle$ and any

linear combination of $|\alpha\beta\rangle$ and $|\beta\alpha\rangle$ are eigenfunctions of both spin operators, $\left[\hat{I}_+^i \hat{I}_-^j + \hat{I}_-^i \hat{I}_+^j\right]$ and $\hat{I}_z^i \hat{I}_z^j$. This situation corresponds to the homonuclear case where the term $\left[\hat{I}_+^i \hat{I}_-^j + \hat{I}_-^i \hat{I}_+^j\right]$ also contributes to the secular part.

In a multiple spin system the situation becomes much more complex, i.e. a linear combination of degenerate Zeeman functions is needed for every coupled pair of nuclei in the sample. For example, if i =spin 1 and j =spin 2, a linear combinations of degenerate Zeeman states are needed to build an eigenfunction for the term $\left[\hat{I}_+^i \hat{I}_-^j + \hat{I}_-^i \hat{I}_+^j\right]$. Now if i =spin 2 and j =spin 3 a different linear combination is required. In addition, these possible combined states of the spin system change with time under the influence of the dipolar coupling. Strictly speaking, each wavefunction will be a time-dependent combination of degenerated Zeeman states for the spin system. Then a time-dependent wavefunction is required to describe the spin system. As a result, the energy of the spin system under the influence of the time-dependent wavefunction will have different values at each time instant, since different couplings are continuously established over the time. Such effect will lead to an homogeneous line broadening, which strongly hampers the NMR spectra. However, in this thesis I shall show some examples of homonuclear decoupling in ^1H - ^1H couplings by applying pulse sequences that significantly improves the spectral resolution helping in a better characterisation of materials containing high proton concentrations.

In heteronuclear couplings the term $\left[\hat{I}_+^i \hat{I}_-^j + \hat{I}_-^i \hat{I}_+^j\right]$ does not contribute to the secular Hamiltonian since the coupled spin species have different precession frequencies, and then it is not possible the occurrence of state transitions in a conservative way.

2.4.5 Indirect Dipole-Dipole Interaction

The indirect dipole-dipole interaction also known as *J-coupling*, involves the coupling between two nuclear spins through the bonding electrons. Therefore, the *J-coupling* is intimately dependent on the chemical nature of the bonds and the orbitals involved to form the bond. Additionally it is also dependent on the nature of the observing nuclei. In solution NMR, the isotropic value of the *J-coupling* is often directly obtained from the NMR spectrum and it is very helpful in structure elucidation. In SSNMR, the *J-coupling* is general very weak (see typical size in Table 2.1) and is usually overshadowed by the other interactions. If all the strong interactions can be suppressed in solids then the *J-couplings* becomes accessible albeit confined to compounds having long transversal relaxations. Very recently, a *J-coupling* mediated by hydrogen bonding have been reported. [23]

Homonuclear *J-coupling*

In irreducible spherical tensor representation the homonuclear *J-coupling* Hamiltonian can be expressed by its rank-0 (isotropic *J-coupling*) and rank-2 (anisotropic part) terms, as follows:

$$\hat{\mathcal{H}}_{ij}^J = C^\Lambda \left([\mathcal{A}_{0,0}^J] \left[\hat{T}_{0,0}^{J,ij} \right] + [\mathcal{A}_{2,0}^J]^{LAB} \left[\hat{T}_{2,0}^{J,ij} \right]^{LAB} \right) = \quad (2.70)$$

$$= 2\pi J_{iso}^{ij} \hat{I}^i \cdot \hat{I}^j + \omega_{J,aniso}^{ij} \frac{1}{\sqrt{6}} \left(3\hat{I}_z^i \hat{I}_z^j - \hat{I}^i \cdot \hat{I}^j \right) \quad (2.71)$$

where J_{iso}^{ij} is the indirect coupling constant defined in Hertz also called the *scalar coupling*. Note that the second term of Eq. 2.71 (the *J-anisotropy*), has spin terms identical to the homonuclear dipolar interactions discussed above. The spin and spatial parts of Eq. 2.70 can be found in table 2.1.

It is worth noting that for cases in which the coupled spins have very different CSs or in case of heteronuclear J -couplings the flip-flop operator $[\hat{I}_+^i \hat{I}_-^j + \hat{I}_-^i \hat{I}_+^j]$ containing in $\hat{I}^i \cdot \hat{I}^j$ can be removed from the isotropic and anisotropic parts of Eq. 2.71 because it has no effect under the high-field approximation. Thus, the Hamiltonian of Eq. 2.71 can be further simplified.

Heteronuclear J -coupling

To define the heteronuclear indirect dipole-dipole interaction in irreducible spherical tensors, basically, one just have to add the anisotropic part to the heteronuclear dipolar coupling (Eq. 2.68).

$$\hat{\mathcal{H}}_{IS}^J = C^\Lambda \left([A_{0,0}^{J,IS}] [T_{0,0}^{J,IS}] + [A_{2,0}^{J,IS}]^{LAB} [T_{2,0}^{J,IS}]^{LAB} \right) = \quad (2.72)$$

$$= 2\pi J_{iso}^{IS} \hat{I}_z^i \hat{S}_z^j + \omega_{J,aniso}^{IS} \sqrt{\frac{2}{3}} \hat{I}_z^i \hat{S}_z^j \quad (2.73)$$

The values needed to build Eq. 2.73 are given in table 2.2.

In both Eqs. 2.71 and 2.73 the anisotropic terms do not have any effect in solids due to their weakness and can usually be neglected. In addition the heteronuclear J -coupling interaction is not directly discernible from the direct dipole-dipole heteronuclear interaction.

2.4.6 Electric Quadrupole Interaction

For nuclei having spin quantum numbers $I_i > 1/2$, the quadrupolar interaction has to be considered. In spin $> 1/2$ the electrical charge distribution of the nucleus is non-spherical, giving rise to an electric quadrupole moment (eQ), which in turn is able to interact or couple with any Electric Field Gradient (EFG) at the nucleus (i.e. the nuclear electric environment). Such gradients arise naturally in solids for all nuclei which are not in a cubic symmetry, caused by the surrounding of other “nuclei and electrons” in their vicinity.

The basic form of the quadrupole Hamiltonian in Cartesian representation can be retrieved from Table 2.1, where the the EFG tensor \mathbf{V} can be considered purely anisotropic, because its isotropic part has no relevance for NMR. [24] As any rank-2 tensor, the EFG tensor has three principal components. V_{xx} , V_{yy} and V_{zz} which are associated with the PAS. The off-diagonal elements V_{xy} , V_{xz} , and so on, are zero in the PAS. In the following some important parameters will be reviewed. Using the convention,

$$V_{zz} \geq V_{yy} \geq V_{xx} \quad (2.74)$$

for the assignment of the three PAS directions, the z-axis of the EFG defined in the PAS can be defined as,

$$V_{zz} = eq \quad (2.75)$$

and the asymmetry parameter can be written as follows:

$$\eta^Q = \frac{[V_{xx}]^{PAS} - [V_{yy}]^{PAS}}{[V_{zz}]^{PAS}} \quad (2.76)$$

with eq magnitude of the EFG tensor, and e is the elementary charge.

For arbitrary η^Q , Eqs. 2.75 and 2.76 are solved to give,

$$[V_{xx}]^{PAS} = -\frac{1}{2}(1 - \eta^Q) eq \quad (2.77)$$

$$[V_{yy}]^{PAS} = -\frac{1}{2}(1 + \eta^Q) eq \quad (2.78)$$

One should be aware that some authors use other conventions than the one shown in Eq. 2.74 for the assignment of the X and Y axes of the EFG tensor*. Another important parameter is the CQ defined in Eq. 2.37, which can attain several MHz wide.

Two kinds of local symmetry at the site of the nucleus dictate the symmetry of the EFG tensor. [24]

1. Cubic point symmetry (including eightfold cubic, sixfold octahedral, and fourfold tetrahedral coordinations) results in

$$V_{xx} = V_{yy} = V_{zz} = 0 \quad (2.79)$$

which results in a spherical EFG tensor.

2. Axial point symmetry (including structures where the nucleus lies on a threefold, fourfold, fivefold, or sixfold symmetry axis) results in $\eta^Q = 0$

Apart from its first-order perturbation, the quadrupole interaction also has significant second-order effects in the perturbation of the Zeeman states. This is because it is a dominant interaction in SSNMR spectroscopy. Since in quadrupolar nuclei the central transition (mostly used in NMR observation) is highly affected by the second-order quadrupole Hamiltonian I will also derive the second-order effect of the quadrupole interaction. In the next section I shall discuss separately the first- and second-order contribution of the quadrupole interaction.

First-Order Quadrupole Hamiltonian

In the LAB frame, the first-order quadrupole Hamiltonian (the secular Hamiltonian) involving a spin i can be expressed based on the anisotropic part of Eq. 2.15b using the spatial and spin tensors depicted in table 2.2.

$$\hat{\mathcal{H}}_i^{Q,(1)} = \omega'_{Q,i} \frac{1}{\sqrt{6}} \left(3\hat{I}_{z,i}^2 - \hat{I}_i^2 \right) \quad (2.80)$$

where $\omega'_{Q,i} = \omega_{Q,i} \left[A_{2,0}^Q \right]^{LAB}$. And $\omega_{Q,i}$ is defined as:

$$\omega_{Q,i} = \frac{C_Q}{2I(2I-1)} \quad (2.81)$$

The use of the quadrupole frequency, $\omega_{Q,i}$ is often preferred over the CQ because it describes the actual strength of the quadrupole interaction more closely than does the CQ.

Eq. 2.80 may be expressed in terms of the spatial tensor in the PAS $\left[A_{2,q}^Q \right]^{PAS}$ using the Wigner matrix transformation defined in Eq. 2.25.

*An alternative convention uses the principal components $V_{zz} \geq V_{xx} \geq V_{yy}$ and $\eta^Q = \frac{[V_{yy}]^{PAS} - [V_{xx}]^{PAS}}{[V_{zz}]^{PAS}}$. In this case, $\left[A_{2,\pm 2}^Q \right]^{PAS} = -\frac{1}{2}\eta^Q$.

$$\begin{aligned}\hat{\mathcal{H}}_i^{Q,(1)} &= \frac{C_Q}{2I(I-1)} \left[\sqrt{\frac{3}{2}} d_{0,0}^{(2)}(\Omega_{PL}) + \frac{1}{2} \eta^Q \left(d_{2,0}^{(2)}(\Omega_{PL}) \exp(2i\alpha_{PL}) + d_{-2,0}^{(2)}(\Omega_{PL}) \exp(-2i\alpha_{PL}) \right) \right] \times \\ &\times \frac{1}{\sqrt{6}} \left(3\hat{I}_{z,i}^2 - \hat{I}_i^2 \right) =\end{aligned}\quad (2.82)$$

$$= \frac{\omega_Q}{4} \left(3 \cos^2 \beta_{PL} - 1 + \eta^Q \sin^2 \beta_{PL} \cos 2\alpha_{PL} \right) \left(3\hat{I}_{z,i}^2 - \hat{I}_i^2 \right) \quad (2.83)$$

Eq. 2.83 is valid for a *static single crystal*, as referred before. To obtain the first-order quadrupole Hamiltonian under MAS, one has to express $[\mathcal{A}_{2,q}^Q]^L$ as a function of the spatial tensor in the RAS by applying Eq. 2.28. From now on, the indexes i and j will be dropped for the sake of simplicity. However, use of these indexes will be reused whenever it is indispensable.

Now, following Eq. 2.83, the energy correction due to first-order quadrupole interaction is:

$$E_m^{(1)} = \hbar \frac{\omega_Q}{4} \left(3 \cos^2 \beta_{PL} - 1 + \eta^Q \sin^2 \beta_{PL} \cos 2\alpha_{PL} \right) (3m^2 - I(I+1)) \quad (2.84)$$

In order to calculate the evolution of the density matrix and consequently the positions of the spectral lines, the transition frequencies have to be calculated. The first-order transitions frequencies are given by (following Eq. 2.83):

$$\omega_{m \leftrightarrow m'}^{Q,(1)} = \langle m | \hat{\mathcal{H}}^{Q,(1)} | m \rangle - \langle m' | \hat{\mathcal{H}}^{Q,(1)} | m' \rangle = \quad (2.85)$$

$$= \frac{3\omega_Q}{4} \left(3 \cos^2 \beta_{PL} - 1 + \eta^Q \sin^2 \beta_{PL} \cos 2\alpha_{PL} \right) (m^2 - m'^2) \quad (2.86)$$

One can see in Eq. 2.86 that the central transition (CT) $\omega_{-1/2 \leftrightarrow +1/2}^{(1)}$ (i.e. for $m = -1/2$ and $m' = +1/2$) and the symmetric Multiple-Quantum (MQ) transitions, (e.g. $\omega_{-1 \leftrightarrow +1}^{(1)}$, $\omega_{-3/2 \leftrightarrow +3/2}^{(1)}$, ...) are clearly independent from the first-order quadrupole interaction.

Second-Order Quadrupole Hamiltonian

The second-order quadrupole interaction can be calculated from the second-order perturbation series, such as follows [25]:

$$E_u^{(2)} = \sum_{u \neq v} \frac{\langle u | \hat{\mathcal{H}}^Q | v \rangle \langle v | \hat{\mathcal{H}}^Q | u \rangle}{E_v^0 - E_u^0} \quad (2.87)$$

The second-order Hamiltonian for the quadrupolar interaction in the LAB frame, is given by:

$$\hat{\mathcal{H}}^{Q,(2)} = \frac{\omega_Q^2}{\omega_0} \sum_{q=1,2} \frac{\mathcal{A}_{2,-q}^Q \mathcal{A}_{2,q}^Q \left[\hat{\mathcal{T}}_{2,-q}^Q, \hat{\mathcal{T}}_{2,q}^Q \right]}{q} = \quad (2.88)$$

$$= \frac{\omega_Q^2}{\omega_0} \left(\mathcal{A}_{2,-1}^Q \mathcal{A}_{2,1}^Q \left[\hat{\mathcal{T}}_{2,-1}^Q, \hat{\mathcal{T}}_{2,1}^Q \right] + \frac{1}{2} \mathcal{A}_{2,-2}^Q \mathcal{A}_{2,2}^Q \left[\hat{\mathcal{T}}_{2,-2}^Q, \hat{\mathcal{T}}_{2,2}^Q \right] \right) \quad (2.89)$$

The commutators $[\hat{T}_{2,-q}^Q, \hat{T}_{2,q}^Q]$ given in Eq. 2.89 are defined as[†]:

$$[\hat{T}_{2,-1}^Q, \hat{T}_{2,1}^Q] = \frac{1}{2} \hat{I}_z \left(8\hat{I}_z^2 - 4I(I+I) + 1 \right) \quad (2.90)$$

$$[\hat{T}_{2,-2}^Q, \hat{T}_{2,2}^Q] = \hat{I}_z \left(2\hat{I}_z^2 - 2I(I+1) + 1 \right) \quad (2.91)$$

The spatial product $\mathcal{A}_{2,-q}^Q \mathcal{A}_{2,q}^Q$ in Eq. 2.89 is calculated and converted to a coupled representation $\mathcal{B}_{2q}^{(2k)}$ which facilitates considerably the treatment. The commutators defined in Eqs. 2.90 and 2.91 are likely absorbed into the operator $\mathbb{C}^{(2k)}(I, \hat{I}_z)$. Finally, collecting the spin and spatial parts the second-order quadrupole Hamiltonian under MAS can be expressed as:

$$\hat{\mathcal{H}}^{Q,(2)}(t) = \frac{\omega_Q^2}{18\omega_0} \sum_{k=0}^2 \mathbb{C}^{(2k)}(I, \hat{I}_z) \sum_{q=-k}^{+k} \sum_{q'=-k}^{+k} \left(\mathcal{B}_{2q}^{(2k)}(\eta) \exp(-2iq\alpha_{PR}) d_{2q,2q'}^{(2k)}(\beta_{PR}) \times \right. \\ \left. \times d_{2q',0}^{(2k)}(\theta_m) \exp[-2q'i(\gamma_{PR} + \omega_R t)] \right) \quad (2.92)$$

The contribution of the second-order quadrupole interaction to the frequencies is given by:

$$\omega_{m \leftrightarrow m'}^{Q,(2)}(t) = \frac{\omega_Q^2}{18\omega_0} \sum_{k=0}^2 \mathbb{C}^{(2k)}(I, m) \sum_{q=-k}^{+k} \sum_{q'=-k}^{+k} \left(\mathcal{B}_{2q}^{(2k)}(\eta) \exp(-2iq\alpha_{PR}) d_{2q,2q'}^{(2k)}(\beta_{PR}) \times \right. \\ \left. \times d_{2q',0}^{(2k)}(\theta_m) \exp[-2q'i(\gamma_{PR} + \omega_R t)] \right) \quad (2.93)$$

where the coefficient $\mathbb{C}^{(2k)}$ in Eq. 2.93 may be equal either to $C^{(2k)}$ or $\mathcal{C}^{(2k)}$, for the symmetric transition or Satellite Transition (ST) frequencies, respectively (See Appendix D). The relation between both spin coefficients and their respective numerical values is given in Appendix D. The combined spatial tensors $\mathcal{B}_{2q}^{(2k)}$ are depicted in Appendix D as well.

The frequencies of the symmetric transitions are obtained by calculating Eq. 2.93 for $m' = -m$ setting $m = -1/2$, while for the second-order contribution to the SQ STs by substituting $m' = m - 1$ setting $m = -1/2, -3/2, -5/2, \dots$. The values for the quantities $\mathbb{C}^{(2k)}(I, m)$, $\mathcal{B}_{2q}^{(2k)}(\eta)$ are given in Table D.1 for Multiple-Quantum Magic-Angle Spinning (MQMAS) [27] (top of Table D.1) and Satellite-Transition Magic-Angle Spinning (STMAS) (bottom of Table D.1), respectively. Three spin coefficients $\mathbb{C}^{(0)}(I, m)$, $\mathbb{C}^{(2)}(I, m)$ and $\mathbb{C}^{(4)}(I, m)$ are obtained from Eq. 2.93 for tensor ranks 0, 2 and 4 respectively. It is worth mentioning that $\mathbb{C}^{(0)}(I, m)$ is an isotropic shift, called the *quadrupole induced shift* as it will be discussed in section 10.2 in the framework of MQMAS theory. $\mathbb{C}^{(2)}(I, m)$ may be averaged by MAS, however $\mathbb{C}^{(4)}(I, m)$ can not be removed by simple MAS because rank-4 tensors have a complex angular dependence have been the focus of the development of high-resolution spectra in half-integer quadrupolar spins. This issue will be the aim of Part III of this thesis (Chapter 10).

2.4.7 Second-Order Interactions Involving Cross-Terms

By averaging away all magnetic spin anisotropies that transforms rank-2 tensors, sufficiently rapid MAS can, in principle, afford high-resolution powder NMR spectra of spin-1/2 nuclei.

[†]The comutators $[\hat{T}_{2,-q}^Q, \hat{T}_{2,q}^Q]$ are calculated using the Clebsch-Gordon coefficients and the expression given in ref. [26]

An important exception to this total averaging rule arises when a spin-1/2 nucleus under observation (S) is dipole-coupled to a neighboring quadrupole nucleus $I \geq 1$. [28, 29] MAS averaging will then fail by itself to completely remove the dipolar anisotropies, due to the appearance of high-order quadrupole-dipole cross-terms or cross correlation effects which no longer transform as second-order Legendre polynomials. Such terms are called nonsecular effects and were initially observed by the pioneering work of van der Hart *et al.* on static samples by observation of ^1H NMR spectra. [30] Subsequently, an extensive research have been focused on the so-called residual splittings observed in ^{13}C resonances dipolar coupled to ^{14}N nuclei, in ^{13}C MAS NMR spectra. Such phenomenon happens almost exclusively when ^{13}C nuclei are directly bonded to (^{14}N , $I=1$). The reason is that the second-order quadrupolar effects may be transferred to spin-1/2 spectra by dipolar interactions. The phenomenon is sometimes referred to as residual dipolar coupling. An example of this effect will be observed later in section 9.1.

The cross-terms between the dipolar and quadrupole interactions [31,32] may potentially happen whenever the high-field approximation is no longer valid. For example, in the case of ^{14}N nuclei, the Larmor frequency for ^{14}N in a field of 9.4 T is approximately 29 MHz. If CQs of 2-3 MHz are present, it means that the Zeeman frequency is only a factor of 10 higher than the CQ values. Hence, the nonsecular terms become important and have to be considered. Very recently Gan and Bodenhausen developed a new method to obtain ^{13}C - ^{14}N Two-Dimensional (2D) Heteronuclear Correlation (HETCOR) spectra based on the Heteronuclear Multiple-Quantum Coherence (HMQC) experiment, based on such quadrupole-dipole cross-terms. [33,34]

Taking as an example spin pair I-S, where only one of the nuclei is quadrupolar, lets suppose they are strongly coupled. In such case, an appropriate description will demand the inclusion of the second-order cross-terms to the second-order quadrupole Hamiltonian defined in Eq. 2.89.

Therefore, the total second-order Hamiltonian for an heteronuclear system, can be written as:

$$\hat{\mathcal{H}}_{hetero}^{(2)} = \hat{\mathcal{H}}_I^{Q,(2)} + \hat{\mathcal{H}}_{IS}^{Q,D,(2)} \quad (2.94)$$

The second-order dipole-quadrupole Hamiltonian can be calculated from the perturbation series in a similar way as shown in Eq. 2.87 employing the following expression [25]:

$$E_u^{(2)} = \sum_{u \neq v} \frac{\langle u | \hat{H}_{IS}^D | v \rangle \langle v | \hat{H}_I^Q | u \rangle}{E_u^{(0)} - E_v^{(0)}} + \sum_{u \neq v} \frac{\langle u | \hat{H}_I^Q | v \rangle \langle v | \hat{H}_{IS}^D | u \rangle}{E_u^{(0)} - E_v^{(0)}} \quad (2.95)$$

Then second-order dipole-quadrupole Hamiltonian, $\hat{\mathcal{H}}_{CN}^{Q,D,(2)}$ may be derived from equations similar to Eq. 2.88. For the a dipolar-coupled C-N system, one obtains:

$$\hat{\mathcal{H}}_{CN}^{Q,D,(2)} = \frac{\omega_Q^N C^{D,J}}{\omega_0^N} \sum_{q=-1,1} \left(\mathcal{A}_{2,q}^{Q,N} \mathcal{A}_{2,-q}^{D,CN} \right) \times \hat{T}_{2,0}^N \hat{T}_{1,0}^C \quad (2.96)$$

where $C^{D,J}$ includes the dipolar coupling and the J -coupling constants. All the tensors are defined in the LAB frame.

Finally, by adding Eqs. 2.89 and 2.96, the final expression for Eq. 2.94 is obtained:

$$\begin{aligned} \hat{\mathcal{H}}_{CN}^{(2)} &= \frac{(\omega_Q^N)^2}{\omega_0^N} \sum_{q=1,2} \left[\left(\mathcal{A}_{2,q}^{Q,N} \mathcal{A}_{2,-q}^{Q,N} \right) \times \left[\hat{\mathcal{T}}_{2,-q}, \hat{\mathcal{T}}_{2,q} \right] \right] + \\ &+ \frac{\omega_Q^N C^D}{\omega_0^N} \sum_{q=-1,1} \left(\mathcal{A}_{2,q}^{Q,N} \mathcal{A}_{2,-q}^{D,CN} \right) \times \hat{\mathcal{T}}_{2,0}^N \hat{\mathcal{T}}_{1,0}^C \end{aligned} \quad (2.97)$$

All the parameters of Eq. 2.97 can be found above, except the rank-1 spin tensor for C spins which has the value $\hat{\mathcal{T}}_{1,0}^S = \sqrt{\frac{3}{2}} \hat{S}_z$, with $S=C$ in the case of Eq. 2.97.

Eq. 2.97 shows the complexity of the second-order Hamiltonian when adding the cross-terms. However if one consider a coupling between two distinct quadrupole nuclei I-S, having observable second-order dipole-quadrupole effects, Eq. 2.94 gets the following form,

$$\hat{\mathcal{H}}_{hetero}^{(2)} = \hat{\mathcal{H}}_I^{Q,(2)} + \hat{\mathcal{H}}_{IS}^{QI,D,(2)} + \hat{\mathcal{H}}_{IS}^{QS,D,(2)} \quad (2.98)$$

for the heteronuclear case, when spin I is the observed nucleus and

$$\hat{\mathcal{H}}_{homo}^{(2)} = \hat{\mathcal{H}}_i^{Q,(2)} + \hat{\mathcal{H}}_j^{Q,(2)} + \hat{\mathcal{H}}_{ij}^{Qi,D,(2)} + \hat{\mathcal{H}}_{ij}^{Qj,D,(2)} \quad (2.99)$$

for the homonuclear case, where the spin i and j are observed simultaneously. Eq. 2.99 takes into consideration both second-order quadrupole interactions of spins i and j because they are both observed. Additionally the nonsecular part of the dipolar Hamiltonian must be added to the second-order dipole-quadrupole Hamiltonians, $\hat{H}_{ij}^{Qi,D,(2)}$ and $\hat{H}_{ij}^{Qj,D,(2)}$. The complete expressions for Eqs. 2.98 and 2.99 become increasingly complicated and can be found in ref. [31]. In particular, the second-order Hamiltonian for the homonuclear cases (Eq. 2.99) becomes “huge”, mainly restricted to MQMAS and STMAS experiments.

In addition, the existence of second-order quadrupole-CS cross-terms are also very common, [25, 35] but it will not be covered in this thesis.

Chapter 3

Two-Dimensional NMR Concepts: Selection and Detection of the NMR Signal

This chapter describes basic aspects of 2D spectroscopy and gives some notions about signal selection, which will be needed for later discussion of 2D NMR studies shown in parts II and III of this thesis.

2D NMR spectroscopic techniques can be used to overcome specific problems, for instance to:

- (i) Establish correlation between two homo- and/or heteronuclear nuclear spin pairs;
- (ii) Increase spectral resolution;
- (iii) Provide information on nuclear spin proximities.

2D experiments have the advantage of providing a second dimension (indirect dimension), which allows to perform tasks which are not possible via direct observation, such as MQ coherence detection or application of windowless homonuclear decoupling in strongly dipolar coupled ^1H - ^1H spin pairs.

3.1 Basic Principle

In One-Dimensional (1D) spectroscopy, signal intensity is plotted only along one frequency axis. A single pulse is applied to disturb the spin system from its equilibrium. After that the system will evolve under the influence of local interactions giving rise to a free induction decay (FID) signal, $S(t_2)$, during time t_2 . Fourier transformation of $S(t_2)$ converts the time-domain signal into a frequency domain spectrum $S(\omega_2)$. In most of the cases in liquids and specially in solids, resonance assignments becomes difficult and the wished information can not be obtained. To overcome this difficulty a second time domain, t_1 , between preparation and detection periods can be included. During this evolution period, nuclear interactions may be different from those during t_2 , which can influence the signal $S(t_2)$. In a general case, as shown in *Fig. 3.1*, it is possible to distinguish four time periods [5]:

1. Preparation. In the simplest experiments, the preparation period, t_p corresponds to a single pulse. However, in most solids NMR experiments where Cross-Polarisation (CP) is widely use to transfer magnetization, the preparation consists of two pulses (a 90°

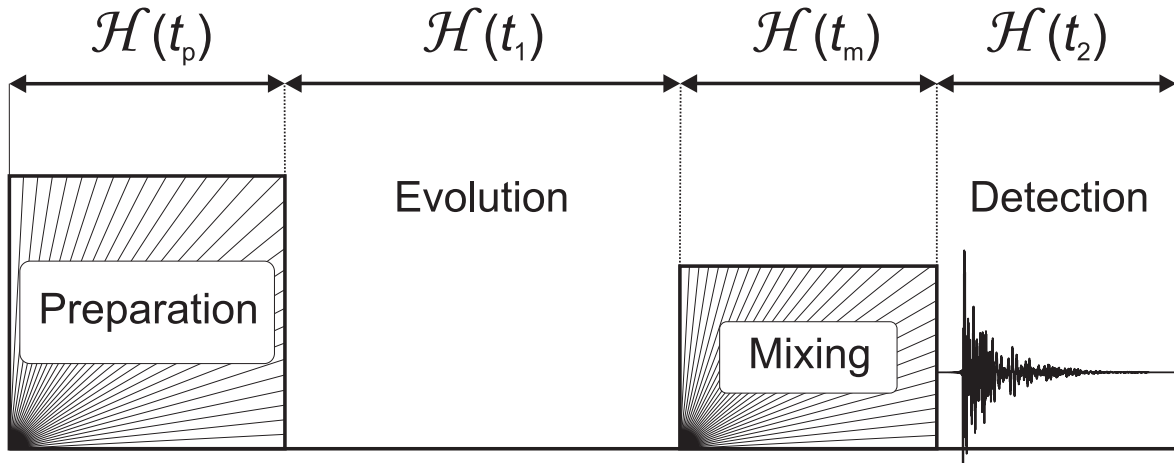


Fig. 3.1: General representation of a 2D time-domain pulse sequence.

pulse followed by the contact time spin lock pulse). Other good examples of more sophisticated preparation periods are the cases of excitation of MQ coherences, such as the Back-to-Back (BABA) and C7 pulse schemes (see chapter 5) where a train of pulses is used to prepare the spin system.

2. Evolution. During the period t_1 the spin system freely evolves under the influence of some internal Hamiltonians, $\hat{\mathcal{H}}(t_1)$. During this period the time interval t_1 is usually incremented according to certain procedures (see section 3.3) until no signal $S(t_1)$ remains.

3. Mixing. As the preparation period, the mixing period, t_m can be made of several pulses as well, which can be separated by variable or fixed time intervals. The mixing block is usually the "heart" of the pulse sequence, in the sense that it transforms any coherence order into observable transverse magnetisation.

4. Detection. This is the last period where the signal is detected for each increment of t_1 separately, thus a 2D time-domain signal is obtained, $S(t_1, t_2)$. A 2D frequency-domain signal $S(\omega_1, \omega_2)$.

3.2 Phase Sensitive Detection in t_2

The influence of the relaxation processes in the time-domain signal usually adds a damping factor or decaying function $\exp(-t/T_2)$, to the FID signal, leading to the broadening of the spectrum lines in the frequency-domain upon Fourier Transform (FT), otherwise it will originate Dirac functions and the absence of dispersive part (imaginary part). Taking into account the damping factor, the time-domain signal $S(t_2)$ can be written as follows:

$$\begin{aligned} S(t_2) &= \exp(-t_2/T_2)a_2\exp(-i\omega_2t_2) = \\ &= \exp(-t_2/T_2)a_2\cos(\omega_2t_2) + \exp(-t_2/T_2)ia_2\sin(\omega_2t_2) \end{aligned} \quad (3.1)$$

where $S(t_2)$ includes the decaying function, $\exp(-t_2/T_2)$ and a_2 represents the complex amplitude of the signal detected during t_2 of a given component including both its intensity $|a_2|$ and phase ζ . In similarity with Eq. 1.6, a_2 may be expressed as:

$$a_2 = |a_2| \exp(i\zeta) \tag{3.2}$$

FT of the damping signal shown in Eq. 3.1 originates the true spectrum which can be written in terms of complex Lorentzian (\mathcal{L}) composed by a absorptive (A) and dispersive (D) components [19]:

$$S(t_2) \xrightarrow{FT} S(\omega_2) = \mathcal{L}(\omega_2, \lambda_2) \tag{3.3}$$

$$= A(\omega_2, \lambda_2) + iD(\omega_2, \lambda_2) \tag{3.4}$$

where, $A(\omega) = \frac{1/T^2}{(1/T^2)^2 + \omega^2}$ and $D(\omega) = \frac{\omega}{(1/T^2)^2 + \omega^2}$. ω_2 is the frequency of a given signal component evolving during t_2 and λ_2 ($\lambda_2 = t_2/T_2$) is the decay rate constant during t_2 . the complex amplitude a_2 is not considered for the sake of simplicity.

Usually, only the absorptive part $A(\omega_2)$ (real part) is important. It is positive definite and its integral does not vanish. The dispersive component, $D(\omega_2)$ (imaginary part) exhibits antisymmetric lineshape having positive and negative intensities which superimpose in a complicated way. Due to its symmetry, the integral over the dispersive lineshape vanishes. Another disadvantage of obtaining a spectrum in dispersive mode is that the signal has broader wings than the absorptive component, thus leading to less resolution. In conclusion, both the absorptive and dispersive components of Eq. 3.4 can be easily separated by quadrature detection in the t_2 period. Only the absorption complement is displayed on the screen.

For 2D experiments the procedure is analogous to 1D FT. A 2D FT can therefore be considered a succession of two 1D FT. 2D spectroscopy needs to use purely absorptive spectrum $A(\omega_1, \lambda_1)A(\omega_2, \lambda_2)$, in order to exclude spectral distortions. However, after applying a "complex" 2D FT the frequency-domain signal $S(\omega_1, \omega_2)^{complex}$, has the general form:

$$\begin{aligned}
 S(t_1, t_2) \xrightarrow{FT} S(\omega_1, \omega_2)^{complex} &= \\
 &= \left[\int_0^\infty S(t_1, t_2) dt_1 dt_2 \right] = \\
 &= \underbrace{(A_1 A_2 - D_1 D_2)}_{Real} + i \underbrace{(D_1 A_2 + A_1 D_2)}_{Imaginary} = \tag{3.5a}
 \end{aligned}$$

$$= S_r(\omega_1, \omega_2) + iS_i(\omega_1, \omega_2) \tag{3.5b}$$

with,

$$S(t_1, t_2) = \exp(-i\omega_1 t_1) \exp(-i\omega_2 t_2) \exp(-t_1/T_2) \exp(-t_2/T_2) \tag{3.6}$$

The arguments of the absorption and dispersive functions were dropped in Eq. 3.5a for the sake of simplicity. The time domain signal $S(t_1, t_2)$ corresponds to a single resonance of a given crystallite. The indexes 1 and 2 in Eq. 3.5a stand for the absorption or dispersive parts centered at frequencies ω_1 and ω_2 , respectively.

The complex signal of 2D spectrum in Eq. 3.5, shows that the real part contains a 2D lineshape containing a mixture of absorption and dispersion components. As a result a phase-twisted lineshape is obtained. There are several strategies to obtain pure-phase spectra, depending on:

- the Coherence Transfer Pathway (CTP) needed for a certain 2D experiment;
- the sensitivity requirements.

Pure absorption 2D spectra can be obtained from a 2D complex data by at least (see ref. [5] for other less common strategies) two different methods:

1. Using **amplitude modulation during t_1** ;
2. Using **phase modulation during t_1** .

The former is the most used in SSNMR 2D experiments and it is extensively used in this thesis. Thus, more details about the obtention of pure phase spectra giving more emphasis on amplitude modulation, will be discussed later in part III of this thesis, in the framework of MQMAS based experiments applied to quadrupolar nuclei.

As it will be discussed later, amplitude modulation during t_1 is very useful to obtain pure phase 2D spectra for experiments where symmetric coherence pathways are needed. In many 2D experiments, simultaneously excited positive and negative coherence orders $\pm p$ evolve during t_1 with frequencies $\omega_1 = \pm\omega_p$ can not be distinguished by a single experiment. Then, mirror images at both sides of $\omega_1 = 0$ will appear in 2D spectra. To overcome this problem, one has to perform two complementary experiments distinct in the phase of the *rf* phase of the excitation pulse. Such phase change will induce a cosine and sine amplitude modulation of the signal during t_1 allowing distinction of $+\omega_p$ and $-\omega_p$ frequencies. FT of these two datasets ($S_{cos}(t_1, t_2)$ and $S_{sin}(t_1, t_2)$), is known as the “hypercomplex” 2D FT (see section 3.3 for further details). This treatment allows to distinguish four data sets instead of only two achieved by the complex 2D FT shown in Eq. 3.5b.

$$S(\omega_1, \omega_2)^{hypercomplex} = S_{rr}(\omega_1, \omega_2) - S_{ii}(\omega_1, \omega_2) + iS_{ri}(\omega_1, \omega_2) + iS_{ir}(\omega_1, \omega_2) \quad (3.7)$$

where the indexes r and i in Eq. 3.7 refers to the combination of the real or imaginary parts of the signal during t_1 or t_2 . For example, the signal $S_{ri}(\omega_1, \omega_2)$ is a signal that combines the real ($S_r(t_1)$) and imaginary ($S_i(t_2)$) parts created during during t_1 and t_2 times, respectively.

The hypercomplex acquisition can combine both real and imaginary parts independently in both t_1 and t_2 dimensions, i.e. the FTs in t_1 and t_2 are independent.

An experimental example of such treatment will be presented in Chapter 10, where a multiplex-hypercomplex acquisition will be demonstrated to select the desired multiple CTPs and obtain pure phase spectra with phase sensitive detection in t_1 . The following section briefly discusses this subject.

3.3 Phase Sensitive Detection in t_1 : States vs TPPI

As referred in section 3.2, to obtain undistorted 2D spectra, phase sensitive detection in t_1 dimension is needed to discriminate the sign of the frequencies evolving during this time-domain. Usually this can be done by four schemes: (i) the Time-Proportional Phase Incrementation (TPPI) [36] and Redfield [37] methods to produce *real* data sets and the States [38] and States-TPPI [39] methods to produce *complex* data sets.

The most used methods are the States and TPPI schemes, thus I shall restrict my discussion to these ones. The former method, also called the States-Haberhorn-Ruben (SHR) or hypercomplex acquisition, involves the acquisition of two experiments separately “each” t_1 increment, a first one with the amplitude of the signal modulated by *cos* and a second

modulated by *sin* (See Table 3.1). To achieve such modulation the *rf* phase ξ^{prep} of the preparation block (typically the excitation pulse) is shifted by $p\Delta\xi$ between each experiment. However, the TPPI method does not need a second experiment but, instead, it has other requirements as I shall discuss. In TPPI, the *rf* phase of the preparation pulse is continuously shifted by $p\Delta\xi$ as long as the evolution period (t_1) is incremented. The *rf* phase shift values for both methods are:

$$\Delta\xi(t_1) = \frac{\pi}{2|p|}k \tag{3.8a}$$

$$k = 0, 1. \quad \text{for States} \tag{3.8b}$$

$$k = 0, 1, 2, 3, \dots \quad \text{for TPPI.} \tag{3.8c}$$

where the k values are integer numbers which represent the counter numbers for the *rf* phase increment of the preparation pulse, which increments t_1 ($t_1 = k\Delta t_1$). Table 3.1 shows a comparison between both methods considering a general expression for the signal intensity $S^p(t_1, t_2 = 0)$ of a certain coherence of order p .

$$S^p(t_1, t_2 = 0) = a_p \cdot \cos[\omega_1 t_1 + p \cdot \Delta\xi] \tag{3.9}$$

where a_p , is the amplitude of the signal represented by the coherence p .

Table 3.1: comparisson between STATES and TPPI acquisition

increment counter(k)	STATES ^[a]		TPPI
0	$a_p \cdot \cos[\omega_1(0)]$	$a_p \cdot \sin[\omega_1(0)]$	$a_p \cdot \cos[\omega_1(0)]$
1	$a_p \cdot \cos[\omega_1(\Delta t_1)]$	$a_p \cdot \sin[\omega_1(\Delta t_1)]$	$a_p \cdot \sin[\omega_1(\Delta t_1)]$
2	$a_p \cdot \cos[\omega_1(2\Delta t_1)]$	$a_p \cdot \sin[\omega_1(2\Delta t_1)]$	$a_p \cdot \{-\cos[\omega_1(2\Delta t_1)]\}$
3	$a_p \cdot \cos[\omega_1(3\Delta t_1)]$	$a_p \cdot \sin[\omega_1(3\Delta t_1)]$	$a_p \cdot \{-\sin[\omega_1(3\Delta t_1)]\}$
⋮	⋮	⋮	⋮
⋮	⋮	⋮	⋮

^[a] The amplitude modulation of the signal (see 3.9) is shown for the two experimental data sets at each Δt_1 increment needed for the States method.

3.3.1 Hypercomplex Acquisition (States)

The states method also called the SHR method was proposed by D. J. States, R. A. Haberkorn and D. J. Ruben. [38] This method can be described by six steps:

1. Signals arising by two data sets shifted by $\frac{\pi}{2|p|}$ (see Eqs. 3.8a and 3.8b);
2. 1D FT with respect to t_2 of both the cosine $S^{\cos}(t_1, t_2)$ and sine $S^{\sin}(t_1, t_2)$ amplitude modulated obtaining the signals $S^{\cos}(t_1, \omega_2)$ and $S^{\sin}(t_1, \omega_2)$, respectively;
3. The real part of the signals $S^{\cos}(t_1, \omega_2)$ and $S^{\sin}(t_1, \omega_2)$ are taken, by discarding the imaginary part resulted from the 1D FT with respect to t_2 ;

4. The two new resulting data sets $Re[S^{\cos}(t_1, \omega_2)]$ and $Re[S^{\sin}(t_1, \omega_2)]$ are combined together into a hybrid complex signal $S^{SHR}(t_1, \omega_2)$;
5. A 1D FT is performed with respect to the indirect dimension, t_1 to form a signal having a complex Lorentzian part;
6. Finally, the imaginary part is discarded and a pure-absorption 2D spectrum, $Re[S^{SHR}(t_1, \omega_2)]$ is obtained with frequency sign discrimination.

Further details can be found in several books. [5, 8, 19]

3.3.2 TPPI Acquisition

The TPPI method consists of a continuous change of the preparation pulse phase and as indicated by Eq. 3.8a with k defined as shown in Eq. 3.8c. Contrarily to the first step of the SHR method discussed in section 3.3.1, the argument of Eq. 3.9 in the TPPI scheme is continuously incremented because of the increasing k values as the 2D experiment progress, i.e. the signal has a frequency shift in t_1 dimension. One can clearly see from the argument of Eq. 3.8a that signals coming from positive and negative coherence orders are shifted to opposite frequencies (see Fig 3.2a). Therefore the Nyquist frequency, i.e. the highest frequency that can fit inside F1 spectral window must be doubled to accommodate the peaks. This means a dwell time in F1 dimension of $\frac{\Delta t_1}{2}$ or a doubling in the sampling rate. Despite the SHR method only needs half the sampling rate, the total experimental time is still the same as TPPI because two data sets are needed to allow frequency sign discrimination along t_1 dimension (see Fig. 3.2b).

From table 3.1 the TPPI acquisition method corresponds to the Redfield one. [37] Thus, it allows to discriminate the sign of the coherences during t_1 evolution even without the imaginary component of t_1 dimension, however such scheme can cause cumbersome mirroring. In contrast, the "hypercomplex" (SHR) acquisition method has the advantage to overcome this problem.

The influence of both schemes in rotor synchronised experiments during the t_1 evolution period is also an important factor to take into consideration in NMR experiments. Rotor synchronisation can contribute significantly to the increase in sensitivity. It is evident that the TPPI method does not allow rotor synchronisation because the resonances are moving continuously as the experiment is running. Therefore, no constructive addition of the spinning sidebands into the central band can be attained. On the other hand, in states acquisition the peaks do not move along t_1 dimension, thus if the spinning speed is synchronized with the sampling rate, aliasing of the lateral bands occur. The SHR method is thus the preferred scheme to gain sensitivity and quality.

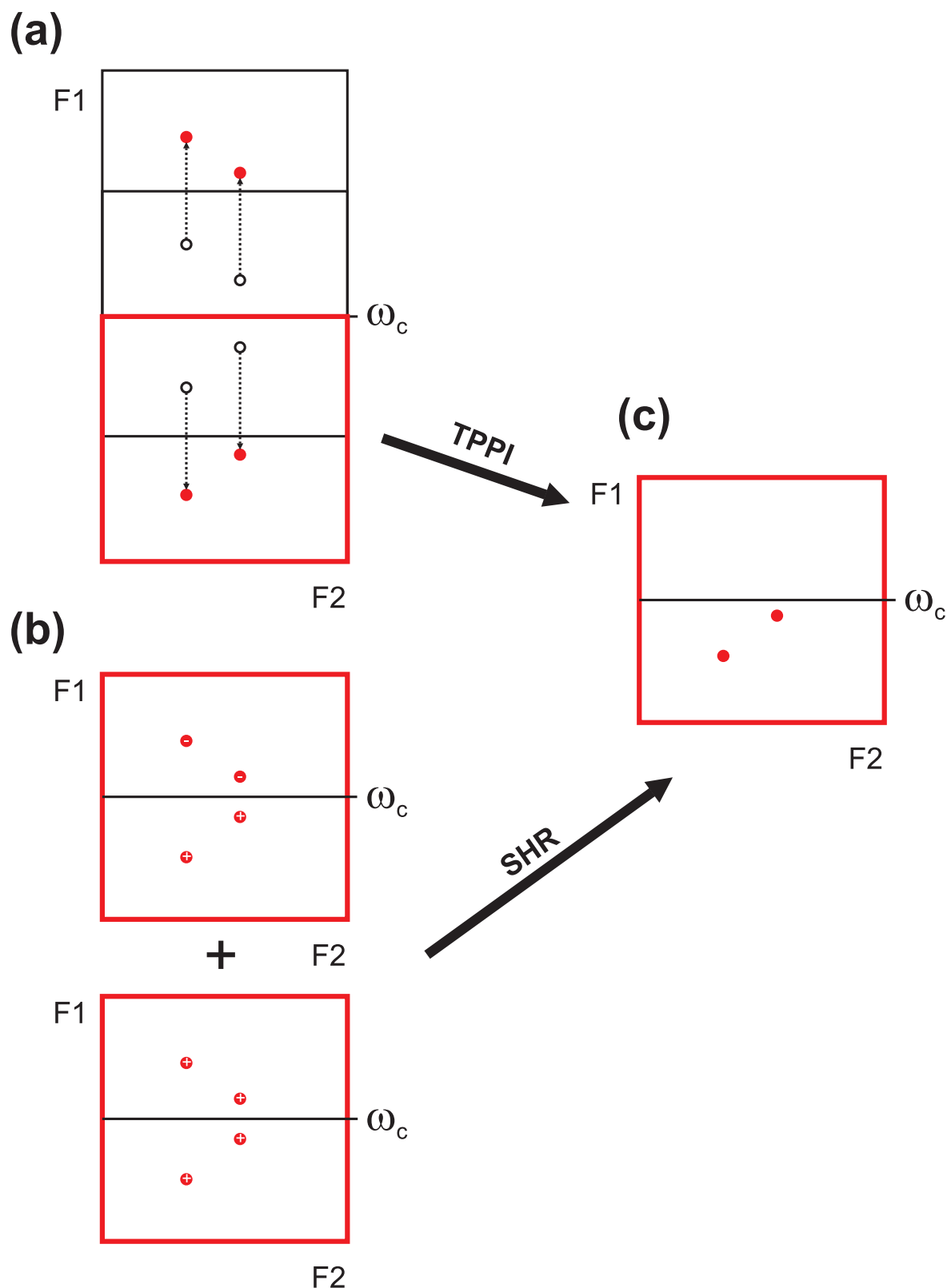


Fig. 3.2: Schematic diagram showing frequency sign discrimination using the (a) TPPI and (b) SHR methods. The final spectrum having the correct frequencies is depicted in (c). ω_c is the carrier frequency, which is always in the middle of the F1 spectral window. The plus and minus signs in (b) refer to positive and negative intensities, respectively. It is worth noting that selection of the correct frequency signs using the TPPI method requires doubling of the Nyquist frequency compared to the SHR scheme.

3.4 Aliasing in NMR

3.4.1 Aliasing in the Frequency Domain

Spectral aliasing, also called “folding”, is directly related with the effect of sampling. When one measures a sinusoidal signal at regular intervals, one may obtain the same sequence of samples that one would get from a sinusoid with lower frequency. The sampling rate required to adequately represent the time-domain signal is determined by the sampling theorem. [5] For a faithful representation of a signal, the critical sampling interval must be obeyed.

$$\Delta t = \frac{1}{2\nu_{\max}} \quad (3.10)$$

where ν_{\max} is the highest frequency that can be found in the true spectrum, also called Nyquist frequency. If the sampling interval Δt , is equal or smaller than this critical interval shown in Eq. 3.10, then the different components of the signal are shown at the true frequency. On the other hand, if the signal is undersampled (see fig. 3.3), i.e., if the sampling interval is $\Delta t > 1/(2\nu_{\max})$, the period $1/(\Delta t)$ of the spectrum $S_T^{\Delta t}(\nu)$ is smaller than the bandwidth $2\nu_{\max}$ (also called Nyquist zone) of the true spectrum $S(\nu)$. Then, the portion of the spectrum with $\nu > 1/(2\Delta t)$ is aliased into the basic period $[-1/(2\Delta t), 1/(2\Delta t)]$ or $[-\nu_{\max}, \nu_{\max}]$ and thus overlaps with the spectral information originally located in this interval. Thereby, a distorted spectrum $S_T^{\Delta t}(\nu)$ is obtained.

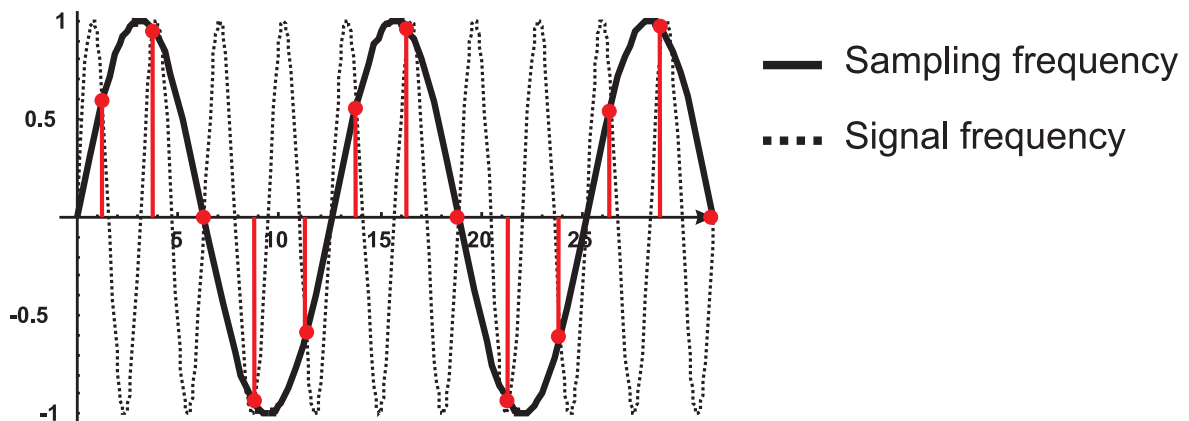


Fig. 3.3: Example of aliasing due to undersampling in time.

3.5 CTP and Phase Cycling Concepts

3.5.1 CTP

The selection of coherence pathways in NMR can be done by propagators \hat{U}_i , which induce coherence transfer between different orders. The propagator may represent a free precession or a in this present case a *rf* pulse (or multiple *rf* pulses). A pulse sequence is usually composed by a series of propagators acting on an initial density operator, $\sigma^p(t_{i-})$ having coherence order p , that after applying the propagators \hat{U}_i originates numerous different orders $\sigma^{p'}(t_{i+})$.

$$\hat{U}_i \sigma^p(t_{i-}) \hat{U}_i^{-1} = \sum_{p'=-2I}^{2I} \sigma^{p'}(t_{i+}) \quad (3.11)$$

where the arguments t_{i-} and t_{i+} refer to the state just before and after the action of \hat{U}_i . I is the nuclear spin number.

A p -quantum coherence has a characteristic transformation behaviour under rotations about the z-axis: [5]

$$\hat{R}_z(\phi) \sigma^p \hat{R}_z(-\phi) = \sigma^p \exp(-ip\phi) \quad (3.12)$$

where $\hat{R}_z(\pm\phi) = \exp(\pm i\phi \hat{I}_z)$.

However, to separate the diverse coherence orders or to select a determined CTP, one must use phase shifted propagators $\hat{U}_i(\phi_i)$, where ϕ_i can be the phase of the i^{th} pulse of a sequence or the i^{th} step of a rf phase shifting on the same pulse to complete a phase cycling. $\hat{U}_i(\phi_i)$ can be written as:

$$\hat{U}_i(\phi_i) = \hat{R}_z(\phi_i) \hat{U}_i(0) \hat{R}_z(-\phi_i) \quad (3.13)$$

Eq. 3.13 comes from an identical relation applied to the Hamiltonians as follows,

$$\hat{H}(\phi) = \hat{R}_z(\phi) \hat{H}(0) \hat{R}_z(-\phi) \quad (3.14)$$

Now, by substitution of the propagator $\hat{U}_i(\phi_i)$ of Eq.3.13 by \hat{U}_i in Eq. 3.11,

$$\hat{U}_i(\phi_i) \sigma^p(t_{i-}) \hat{U}_i^{-1}(\phi_i) = \quad (3.15a)$$

$$= \hat{R}_z(\phi_i) \hat{U}_i(0) \underbrace{\hat{R}_z(-\phi_i) \sigma^p(t_{i-}) \hat{R}_z(\phi_i)}_{\text{employing eq. 3.12}} \hat{U}_i^{-1}(0) \hat{R}_z(-\phi_i) = \quad (3.15b)$$

$$= \hat{R}_z(\phi_i) \hat{U}_i(0) \sigma^p(t_{i-}) \exp(-ip\phi) \hat{U}_i^{-1}(0) \hat{R}_z(-\phi_i) = \quad (3.15c)$$

$$= \exp(-ip\phi) \times \left\{ \hat{R}_z(\phi_i) \underbrace{\left[\hat{U}_i(0) \sigma^p(t_{i-}) \hat{U}_i^{-1}(0) \right]}_{\text{Employing eq. 3.11}} \hat{R}_z(-\phi_i) \right\} = \quad (3.15d)$$

$$= \exp(-ip\phi) \times \left\{ \hat{R}_z(\phi_i) \left[\sum_{p'=-2I}^{2I} \sigma^{p'}(t_{i+}) \right] \hat{R}_z(-\phi_i) \right\} = \quad (3.15e)$$

$$= \exp(-ip\phi) \times \left\{ \sum_{p'=-2I}^{2I} \sigma^{p'}(t_{i+}) \exp(-ip'\phi_i) \right\} = \quad (3.15f)$$

$$= \sum_{p'=-2I}^{2I} \sigma^{p'}(t_{i+}) \exp(-ip'\phi_i - ip\phi) = \quad (3.15g)$$

$$= \sum_{p'=-2I}^{2I} \sigma^{p'}(t_{i+}) \exp(-i\Delta p_i \phi_i) \quad (3.15h)$$

where $\Delta p_i = p'(t_{i+}) - p(t_{i-})$.

Eq. 3.15 can be easily developed making use of Eqs. 3.13 and 3.11. Under a phase shifted propagator, Eq. 3.11 is thus transformed in Eq. 3.15h, which clearly shows the phase shift of a coherence component that has undergone a coherence jump of Δp_i induced by a pulse i .

The corresponding time-domain signal reflects the coherence jump Δp_i induced by $\hat{U}_i(\phi_i)$ and can be expressed as follows:

$$S_{\Delta p_i}(t, \phi_i) = S_{\Delta p_i}(t, 0) \exp(-i\Delta p_i \phi_i) \quad (3.16)$$

Then the total signal from all the coherence transfers in a pulse sequence is

$$S_{\Delta p_{total}}(t, \phi_i) = \sum_{i=1}^n S_{\Delta p_i}(t, \phi_i) = \quad (3.17)$$

$$= \sum_{i=1}^n S_{\Delta p_i}(t, 0) \exp(-i\Delta p_i \phi_i) \quad (3.18)$$

Eq. 3.18 only shows the contribution of the sum of the various coherence order changes, without taking into consideration the N_i phase cycling steps to allow a change, Δp_i in coherence order. I shall discuss afterwards that each coherence transfer, induced by a pulse i , is achieved by summing N_i phase increments ϕ_i ,

$$\phi_i(k_i) = \frac{2\pi k_i}{N_i}, \quad k_i = 0, 1, 2, \dots, N_i - 1 \quad (3.19)$$

Each of the N_i signals, $S_{\Delta p_{total}}(t, \phi_i)$ is accumulated in real time while an experiment is running, for the case of using a nested" or cogwheel" phase cyclings. And it is the way such signals are superposed during the running time of the experiment that will define the selected signal. However, in chapter 10 it will be shown a way of separating all the coherence order in a post processing fashion (after finishing the experiment) allowing to combine the various possible Δp_i coherence transfers by applying a numerical phase shift. This superposition of N_i signals can be unraveled by a Discrete Fourier Transform (DFT) with respect to the phase domain. Then for a desired CTP, $\mathcal{P}^{desired}$, the time-domain signal created during a time t , becomes:

$$S_{\mathcal{P}}(t) = \frac{1}{N_i} \sum_{k_i}^{N_i-1} \left[S(t) \exp\left(\sum_{i=1}^n -i\Delta p_i \phi_i\right) \right] \quad (3.20)$$

where

$$\varphi_{rec} = \sum_{i=1}^n -i\Delta p_i \phi_i \quad (3.21)$$

Eq. 3.20 shows the Fourier relationship between a rf phase ϕ_i and a change in coherence order Δp_i during a pulse. This allows the separation of the signals coming from all the coherence orders p that are created by the i^{th} rf pulses. Examples of applications using this equation will be detailed in section 10.4.

3.5.2 Phase Cycling Principle

The concept of phase cycling: In phase cycling signals from unwanted CTPs are averaged to zero during signal summation by phase shifting the rf pulse phases and then phase shifting the signal before addition into the signal sum. In some cases, a properly designed phase cycling, also suppresses the artifacts arising from instrumental imperfections.

To understand the phase cycling basics, one must enumerate some rules, which have to be taken into consideration.

- **Rule 1** The CTP must start at coherence level $p = 0$, as this corresponds to equilibrium longitudinal magnetization, that is, the magnetization is along the Zeeman z-axis.

- **Rule 2** If the receiver is assumed to be a perfect detector of the observable \hat{I}_+ , it means, by definition, that only the coherence that end on, $p = -1$ will be considered, as only this level contributes to observable magnetization. [5]
- **Rule 3** If a *rf* pulse is changed in phase by ϕ_i , then a coherence undergoing a change in coherence level of Δp_i , experiences a phase shift of $\Delta p_i \phi_i$ (see Eq. 3.21). This is better visualized by considering the effect of a pulse or sequence of pulses on the density operator corresponding to order p , σ^p . The effect of such pulse sequence on the initial density operator can be expressed in terms of unitary transformations or propagators (see section 3.5.1).

Whenever we work with discretely sampled data, we have to deal with the issue of aliasing. In the time domain, a convenient time increment is chosen so that all of the signals lie within the Nyquist zone or spectral width (see section 3.4.1). Similarly, to prevent aliasing in the Δp_i dimension, we need to choose a proper phase increment ϕ_i which is dependent on N_i (see Eq. 3.19).

$$\phi_i < \frac{2\pi}{N_i} \quad (3.22)$$

To understand the concept of aliasing in the coherence domain, Fig. 3.4 shows two schematic examples of possible CTPs for a single spin-1/2 nucleus, where only the coherence orders $p = \pm 1$ are accessible. A two pulse sequence is used, which employs a starting *rf* pulse, δ_1 with phase ϕ_1 and a second final conversion pulse, δ_2 with a phase ϕ_2 . The first example, displayed in Fig 3.4a, shows the case where both the *rf* pulse phases ϕ_1 and ϕ_2 are static, which means that N_i is equal to 1 (or $k_i = 0$ in Eq. 3.19). In these conditions Eq. 3.22 is not obeyed and aliasing of the signal occurs.

In the case illustrated in Fig. 3.4a, both *rf* pulses induce the coherence transfer to all the possible coherence orders, since no phase cycling is used at all. The 2D coherence spectrum shows the presence of all the pairs of coherence order transfers Δp_1 , Δp_2 occurring during δ_1 and δ_2 , respectively, for the six possible CTPs if no quadrature detection is employed, i.e., the receiver detects signal finishing in $p = \pm 1$. In this case all the CTPs are aliased in the coherence domain and thus it becomes impossible to discriminate the various signals. The second example, represented in Fig. 3.4b, considers a quadrature detector, and therefore one can eliminate the three pathways $P = \{\Delta p_1, \Delta p_2\}$, finishing in $p = -1$, having values, $\{+1, 0\}$, $\{0, +1\}$ and $\{-1, +2\}$. Three CTPs are now left and the aim is to select the desired pathway of a simple echo experiment, $\{+1, -2\}$, while separating the other contributing signals, $\{0, -1\}$ and $\{-1, 0\}$. The 2D coherence spectrum of Fig. 3.4b, also shows a yellow box whose size in both Δp_1 and Δp_2 dimensions is related to the number of phase increments N_1 and N_2 , respectively. The 2D coherence spectrum further shows that to select the desired signal, it must be moved along the Δp_1 or/and Δp_2 dimensions until reaching the interior of the yellow box (corresponding to the “discrimination zone”), always by steps of N_1 and N_2 along the Δp_1 and Δp_2 dimensions, respectively. The spectrum of Figs. 3.4a and 3.4b, shows that there is always a way for every CTPs falling inside the yellow box. Then, if all the signals coming from the different CTPs are separately displayed inside that box, in this example along the Δp_2 dimension, an efficient discrimination of the desired CTP from the other pathways is attained. On the other hand, if there is superposition of signals coming from different CTPs with the desired one, the separation fails. In some cases, there is advantage in “forcing” the aliasing between two signals coming from different CTPs as it will be discussed along this thesis. In fact, it is not really necessary to separate the non-desired signals from each other because, only the desired CTP need to be separated from all the remaining ones.

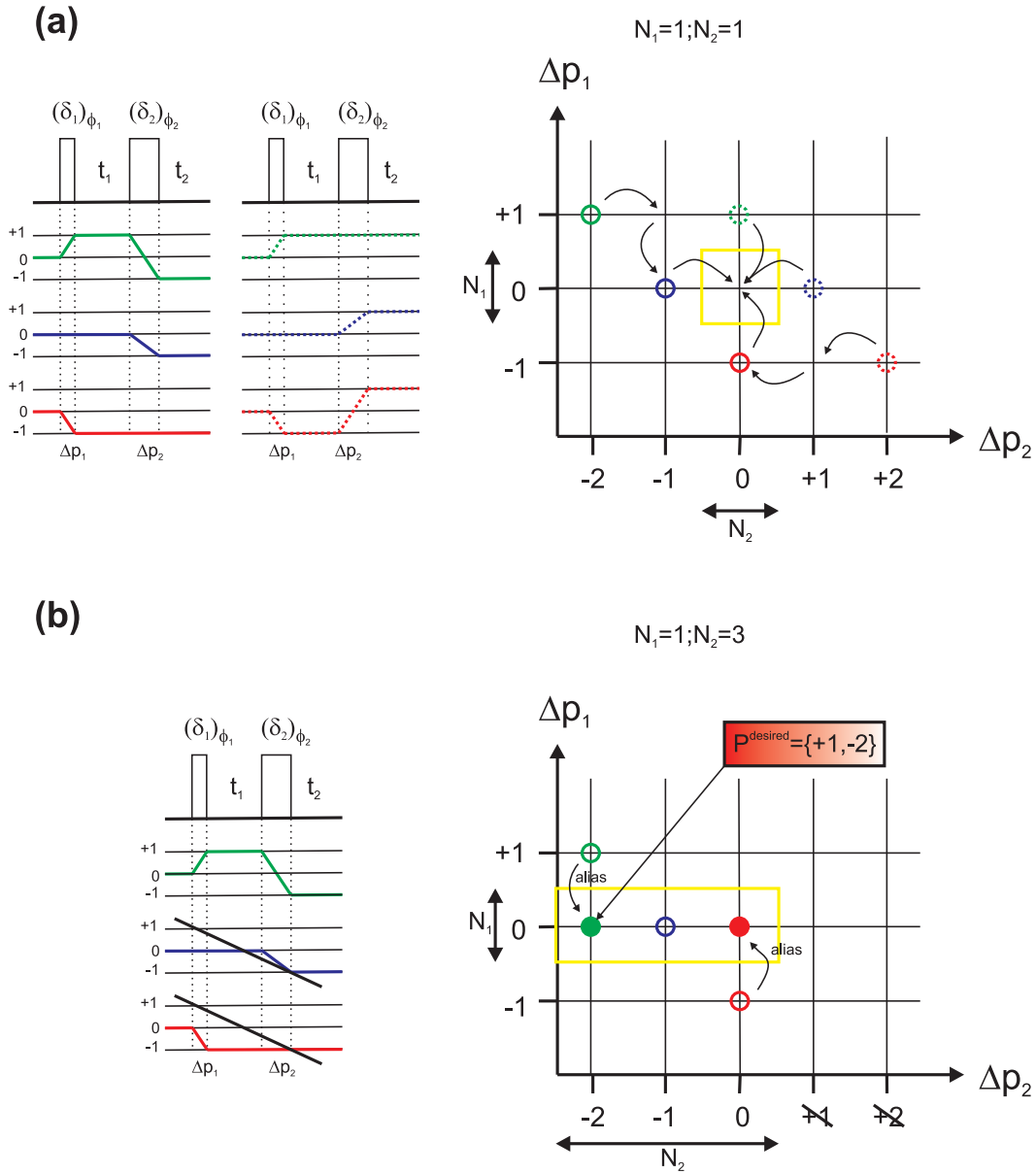


Fig. 3.4: Schematic representation of a two-pulse sequence showing the possible CTPs (left side), where only the coherence orders ± 1 are accessible, and the 2D CTP spectra (right side) having dimensions Δp_1 (vertical) and Δp_2 (horizontal). In (a) a detector without quadrature detection is assumed and six CTP are possible. The respective 2D coherence spectrum is shown for the case where no phase cycling is used, i.e., $N_1 = N_2 = 1$, corresponding to a situation of complete aliasing of every CTPs. (b) illustrates the possible CTPs possible under a well calibrated quadrature detector. This example shows the minimum phase increment steps ($N_1 = 1, N_2 = 3$) necessary to select the desired $\{+1, -2\}$ pathway, being equivalent to the well known echo sequence. The arrows indicate the allowed phase increment steps, N_i , in each dimension. The yellow box contains all the signals that can be separated.

Logically, if more signals are present, shorter phase increment are needed meaning that a bigger yellow box will be required.

In general, the value for N_i needed to avoid aliasing should be:

$$N_i = \Delta p_i^{(\max)} - \Delta p_i^{(\min)} + 1 \quad (3.23)$$

According to that, Eq. 3.22 will be transformed to:

$$\Delta\phi_i = \frac{2\pi}{\Delta p_i^{(\max)} - \Delta p_i^{(\min)} + 1} \quad (3.24)$$

To conclude, the spectrum of Fig. 3.4b shows that a minimum of 3 phase increments ($\frac{2\pi}{3}$, $\frac{4\pi}{3}$ and 2π) are needed to select the desired CTP. The nested phase cycling schemes can be written as follows,

$$\begin{aligned} \phi_1 &= 0^\circ \\ \phi_2 &= 120^\circ, 240^\circ, 0^\circ \\ \varphi_{rec} &= -\phi_1 + 2\phi_2 \end{aligned}$$

where the phase φ_{rec} can be calculated from Eq. 3.21. The type of phase cycling employed refers to the conventional way of doing it (nested phase cycling). A more advanced way of cycling the *rf* pulses is addressed in section 10.4.

Intentional Aliasing in the Coherence Domain

The first and the last points in a DFT are aliased, thus a number of increments $N_2 = 2$ produce phase increments $\Delta\phi_2 = \frac{2\pi}{2}$ and would result in aliasing of our signals from the CPTs, $\{+1, -2\}$ and $\{-1, 0\}$ as shown in Fig. 3.5a. Then the condition necessary to allow coherence aliasing is:

$$\phi_i = \frac{2\pi}{N_i} \quad (3.25)$$

Thus, Figs. 3.5a and 3.5b, depict two cases where two CTPs are intentionally aliased (to allow the SHR [38] acquisition for example, as it will be mentioned later). In both figures, the 2D coherence spectra are very much self-explanatory showing a superposition between the CTPs from the “red” and “green” pathways (See Figs. 3.5a and 3.5b) inside the “yellow boxes”, illustrating that it is impossible to separate the pathways $\{+1, -2\}$, $\{0, -1\}$ (Fig. 3.5a) and $\{+3, -4\}$, $\{-3, +2\}$ (Fig. 3.5b), for the phase increments employed, which follow Eq. 3.25. In short, the “red” and “green” CTPs can not be separated along Δp_2 using the indicated phase increment.

In both Figs. 3.4b and 3.5a-b the minimum phase cycling steps are used. Using higher values of N_1 and/or N_2 will still allow separation of the desired CTP, but it would be a waste of experimental time. The receiver phase corresponding to the CTPs shown in Figs. 3.5a and 3.5b can be easily determined as it was exemplified for Fig. 3.4b. It is worth mentioning that instead of cycling the phase of the pulse δ_2 alone, one could phase cycle both or only the first pulse. In general, a pulse sequence containing n *rf* pulses only needs to phase cycle $n - 1$ *rf* pulse phases.

Such examples of hypothetical pulse sequences with two pulses can be easily represented and analysed in terms of coherence selection by drawing 2D CTP spectra, nevertheless, higher number of pulses would require a n -dimensional representation which becomes more difficult to draw. However by choosing the phase increment needed for a desired Δp_i it is straightforward to calculate the receiver phase that allows the detection of such signal, whatever the number of pulses involved. In sequences, containing several pulses, which must be cycled with respect to each other to select the desired signal, they can be grouped and cycled together to avoid increasing the total phase cycling. This strategy and others are

highly dependent on many factor such as the CTP and the spin couplings involved for a certain experiment. Several examples of such situations are well detailed in the book of James Keeler [40]. Additional explanations can be found in other publications. [41, 42]

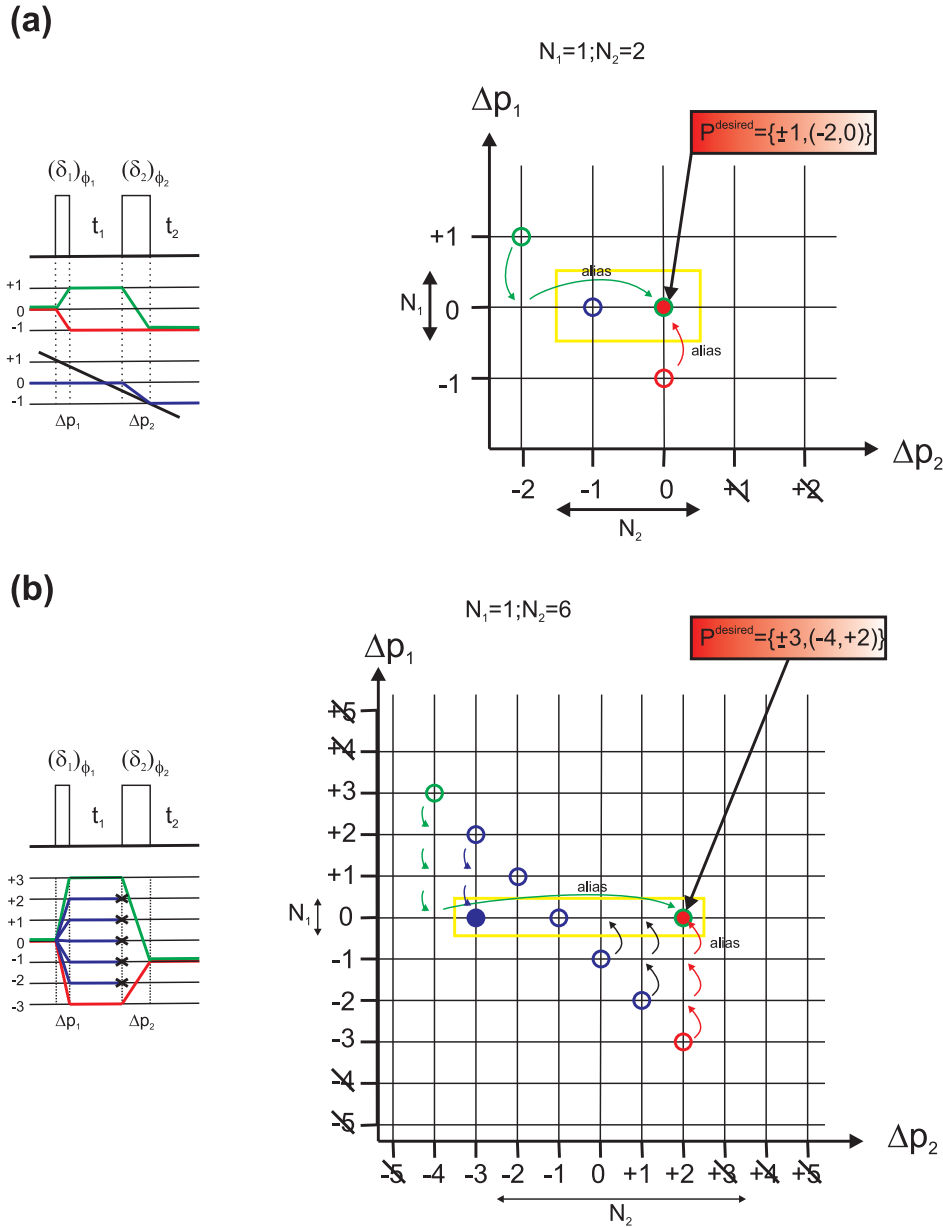


Fig. 3.5: Schematic representation of a two-pulse sequence showing the possible CTPs (left side), where only the coherence orders ± 1 and ± 3 are accessible to (a) and (b), respectively. The 2D CTP spectra (right side) having dimensions Δp_1 (vertical) and Δp_2 (horizontal) are given for both cases. In (a) three CTPs are possible. This example shows the phase increment steps used for each rf pulse ($N_1 = 1, N_2 = 3$) necessary to alias both the $\{+1, -2\}$ and $\{+ - 1, -0\}$ pathways. In (b) six CTPs are possible (this is the case of the two-pulse MQMAS sequence described in Chap. 10), and 2D coherence spectrum shows the aliasing of the CTPs $\{+3, -4\}$ (green) and $\{+ - 3, +2\}$ (red), which are indicated by the green and red arrows, respectively. The yellow box contains all the signals that can be separated.

Chapter 4

^1H - ^1H Homonuclear Dipolar Decoupling

4.1 Introduction

The capacity of removing undesirable interactions and developing new sensitivity enhancement schemes is essential to obtain high-resolution SSNMR spectra recorded in a realistic time. Such improvements, gradually, led to SSNMR applications in fields like material [19,43], polymer [6] and biological sciences [19,44–46]. Resolution and sensitivity enhancement of most commonly observed nuclei in SSNMR (Spin-1/2: ^{13}C , ^{31}P , ^{29}Si and ^{15}N ; Spin>1/2: ^{27}Al , ^{23}Na , ^{11}B and ^{17}O), can be achieved employing the following techniques, either alone or in a combined fashion: MAS [47,48], CP [49–51], heteronuclear dipolar decoupling [52–54], MQ NMR [19,27,55] and STMAS [56].

The most popular spin-1/2 nuclei is ^1H , being widely studied in solution-state NMR. However, the observation of the ^1H nuclei (and ^{19}F) is one of the main challenges encountered in SSNMR because the strong ^1H - ^1H homonuclear dipolar interaction considerably broadens the spectra. This is caused by the high natural abundance (100%) and gyromagnetic ratio of protons. While CSA and heteronuclear dipolar interactions are inhomogeneous in nature, the homonuclear dipolar interactions are homogeneous. [57] Hence, MAS is most effective for averaging rank-2 interactions such as the CSA and heteronuclear dipolar interaction. A narrowing of ^1H spectral lines is possible only if MAS frequencies are larger than the strength of the dipolar interactions, which are usually of tens of kHz. *rf* multiple pulse irradiation schemes must, therefore, be used to overcome the difficulty related with the line-broadening effects originated by ^1H - ^1H dipolar couplings.

Since the pioneering work of Lee and Goldburg [58] and Waugh and Haeberlen, [59] which lead to the introduction of the WHH-4 multiple Lee-Goldburg (LG) pulse schemes, respectively, high-resolution NMR techniques based on homonuclear decoupling have been extensively studied, aiming at making them less sensitive to experimental imperfections and increasing the decoupling performance. Following this pioneering work, several schemes were later developed.

The decisive solution to removing the strong ^1H - ^1H homonuclear couplings, is taking advantage of the symmetry properties of the n^{th} rank of the spin tensor operators (n adopts different values according to the rotational symmetric dependence of the particular interaction), and spatial tensor functions. By applying external perturbations such as sample rotation and/or *rf* pulses, which introduces time-dependence in the spin system, in a controlled fashion, it is possible to cause spin-space averaging. The application of suitable *rf* irradiation schemes produces an effective field B_{eff} , which is tilted by an angle $\xi = \tan^{-1} \frac{B_1}{B_0 - \omega/\gamma}$ with

respect to B_0 can average out the spin part between an homonuclear spin pair, $\hat{\mathcal{T}}_{k,q}^{II}$ (see section 2.2). On the other hand, spinning the sample with the rotation axis tilted by an angle θ with respect to the Zeeman field (B_0), manipulates the spatial tensor function, $\mathcal{A}_{k,q}^{II}$ of the homonuclear dipolar Hamiltonian ($\hat{\mathcal{H}}_{ij}^D$) represented in the spherical tensor notation (section 2.2). The necessity of combining both *rf* and MAS gave rise to the so-called Combined Rotation and Multiple-Pulse Sequences (CRAMPS), developed in the late 1970s by Gerstein *et al.* [60, 61]. Initially, the decoupling sequences were applied to static samples, and therefore they were unable to avoid CSA broadening. CRAMPS techniques were initially used in a "quasi-static" regime, because the cycle time t_c of the pulse schemes were too long and, thus, longer rotor periods were needed to avoid deterioration of spectral resolution, caused by interference of the characteristic frequencies of both *rf* and MAS periodic modulations [62–67]. When the two time scales are similar each modulation should be tuned to avoid interference. Synchronisation argument was proposed in literature [64, 65, 68],

$$n \times \omega_1 = m \times \omega_{MAS} \quad (4.1)$$

where ω_1 stands for the modulation frequency of the multiple pulse sequence and ω_{MAS} for the MAS frequency, n and m are integers.

Some sequences, such as WHH-4, were successfully adapted to perform well under high MAS frequencies, though so far best performance is achieved at slow MAS rates. CRAMPS sequences have always been known for their demanding implementation. This happens because the observation of ^1H is done simultaneously with the ^1H - ^1H homonuclear decoupling, i.e., observation periods, called "windows", during which the free evolution Hamiltonian operates, are strategically inserted in the sequences to allow the signal detection under homonuclear decoupling.

Over the last decade relevant improvements of the ^1H spectra were achieved by the appearance of "windowless" pulse schemes leading to high-resolved ^1H spectra under moderate to fast MAS rates (12–15 kHz). Due to their robustness, such sequences are, nowadays, the most popular ones. The windowless decoupling sequence Frequency-Switched Lee-Goldburg (FS-LG) will be discussed later in section 4.4. The advent of high MAS probeheads with spinning frequencies of up to 70 kHz, has made possible the observation of ^1H spectra employing MAS alone. However, for strongly coupled ^1H systems, such as biomolecules, a combination of both MAS- and *rf*-driven modulation rates is vital for line-narrowing if the lineshape is dominated by homogeneous broadening.

Theoretical tools are necessary to understand mathematically the behavior of the internal Hamiltonian under the influence of external periodic modulation (MAS and *rf* field strength). Any proper explanation of how ^1H homonuclear decoupling in solids work requires the use of Averaged Hamiltonian Theory (AHT) or other approaches, [5] as it will be pointed in section 4.3.2.

In this chapter the following issues will be addressed:

- Overview of homonuclear dipolar decoupling sequences and their classification;
- Revision of some of the theoretical tools available to analyse multiple pulse sequences (AHT, "toogling frame" transformations);
- Case study illustrating the FS-LG principle and the Hamiltonian description under the effect of FS-LG decoupling;
- Optimisation of experiments containing the FS-LG decoupling scheme and examples of the influence of specific experimental parameters in 2D spectra.

- Windowless FS-LG applications and examples of 2D FS-LG spectra.

For more details about the ^1H - ^1H homonuclear decoupling methods excellent books and reviews are recommended, on which some of the following sections will be based. [6, 69, 70]

4.2 Overview of Homonuclear Decoupling Schemes

Many pulse sequences have been developed to decrease or suppress the effects of the ^1H - ^1H dipolar interaction. Prominent examples are WHH-4 [59], MREV-8 [71, 72], Cory-24 [73], BR-24 [74, 75], BLEW-48 and BLEW-12 [76], TREV-8 [77], MSHOT-3 [78], mainly designed for static conditions and, therefore, limited to relatively slow MAS rates. Over the last decades much work concentrated on the development of windowless sequences such as the FS-LG, Phase-Modulated Lee-Goldburg (PM-LG), and the last generation of homonuclear sequences called DUMBO-1. [79, 80] Such windowless sequences works under relatively fast MAS conditions and are adequate to be inserted in 2D experiments during the t_1 evolution periods, or even during CP experiments in the case of FS-LG (TANMA-CP [81]). The employment of such LG based homonuclear decoupling sequences in a windowed fashion, i.e. observing the ^1H spins while decoupling simultaneously, was investigated for some FS-LG variants by Levitt *et al.* [82] and more recently reviewed by Hohwy and Nielsen. [83] However no real application have been so far shown. Then, *windowed* variants of the original PM-LG- n (wPM-LG- n [84, 85]) and DUMBO-1 sequences have been, very recently, adapted to 1D experiments and, specially, to 2D $^{23}\text{Na} \rightarrow ^1\text{H}$ CP-MQMAS-wPMLG-5 [86] and 2D ^1H - ^1H Double-Quantum (DQ) experiments, [87] respectively. Both techniques were performed on relatively simple crystalline materials (sodium citrate dihydrate amino-acids, respectively) and demonstrated good performance. These are examples where the use of a windowed homonuclear decoupling version allows the saving of an additional dimension (if windowless sequences are used for ^1H - ^1H decoupling), thus shortening the experimental time. However windowed sequences are not yet accessible to every NMR users because they are, generally, of difficult implementation due to hardware restraints.

For more details about the performance of the overall sequences, the reading of ref. [69] is recommended, where a clever classification was made. Such classification will be followed here including an additional class and some additional sequences (See Fig. 4.1).

The homonuclear decoupling sequences can be divided in five classes:

CLASS I: These sequences are based on a combination of solid echoes having the following common basic building unit (See Figs. 4.1a-d):

$$\left(\frac{\pi}{2}\right)_x - \tau - \left(\frac{\pi}{2}\right)_y -$$

where τ is the interpulse delay.

The WHH-4 sequence is the most simple sequence of this class composed by only one pair of solid-echoes.

CLASS II: In this case the basic building block consists in a symmetric magic-echo sandwich and as the following form (See Figs. 4.1e-g):

$$\tau - \left(\frac{\pi}{2}\right)_y - \Theta_x - \Theta_{-x} - \left(\frac{\pi}{2}\right)_{-y} - \tau$$

where Θ corresponds to the rf field strength of ν_1 and duration of $\frac{1}{\nu_1}$ and τ a delay of duration $\frac{1}{2\nu_1}$.

CLASS III: This class mainly consists in windowless homonuclear decoupling sequences consisting in a constructive combination of both MAS and *rf* (See Figs.4.2h-j). An attempt to adapt the classic WHH-4 sequence to experiments under high-spinning frequencies is shown in Fig.4.2h. Symmetry arguments have been proposed by the group of Levitt creating two subclasses of symmetry sequences (CN'_n and RN'_n), which have been widely used in NMR applications. [88]

CLASS IV: This class represented in Fig. 4.2k-m, contains the most recently developed homonuclear decoupling dubbed DUMBO-1, a numerically optimised sequence based on a continuous modulation of the phase of the *rf* field, instead of the usual existing multiple-pulse sequences, which consist of a series of discrete pulses. The phase function of the DUMBO-1 sequence shown in Fig. 4.2l is periodic and, thus, can be generated as a Fourier series with six coefficients according to the following formula [79]:

$$\varphi(t) = \sum_{n=0}^6 a_n \cos(n\omega_c t) + b_n \sin(n\omega_c t) \quad (4.2)$$

where $\omega_c = 2\pi/t_c$ is the basic modulation frequency and t_c the time period of the decoupling cycle.

The complex Fourier coefficients $c_n = a_n + ib_n$ provide a set of parameters which can vary continuously and which allow to explore a, potentially infinite, space of functions for decoupling. [79]

For practical reasons some of the BLEW based sequences (BLEW-12 and BHOT-4) were inserted in the same class since DUMBO-1 sequences are based on these ones.

CLASS V: This class refers to the LG based sequences,(Figs. 4.3n-s) which are by far (at least the windowless sequences of Figs. 4.3n-o) the most used sequences for ^1H - ^1H homonuclear decoupling. The last sequences developed in this class, derive from the old LG [58] sequence, taking advantage of the reflection symmetry principle introduced by Mansfield *et al.* [89] (See Fig. 4.5).

During the LG and FS-LG irradiation an off-resonance irradiation is applied, in such a way that the spins rotate in the off-resonance rotating frame (toggling frame) around a direction inclined at an angle $\theta_m = 54.7^\circ$ with respect to the Zeeman field (B_0). A special attention will be paid to the FS-LG sequence since it was the homonuclear decoupling scheme used in the applications part of this thesis (Part II). For this reason, a dedicated discussion is included in sections 4.4-4.10.

Windowed versions of the FS-LG decoupling scheme (Figs. 4.3r-s) were also investigated by researchers and are important to shorten the experimental time. The ^1H spectra can be directly observed through the acquisition windows while decoupling the ^1H spins simultaneously, thus saving an additional dimension. The FS-LG240w sequence introduced by Levitt *et al.* [82] was the first attempt to create a windowed FS-LG sequence. It ensures elimination of the third-order dipolar terms by inserting windows of appropriate timing for every 240° rotation of the interaction frame dipolar Hamiltonian. However, this pulse sequence is not robust. Other attempts were further tested by coupling the windowed FS-LG with the high-order truncating (HOT) sequences producing sequences called HOT-FSLG and HOT-FSLG240W. [83] However, neither of these windowed FS-LG techniques have gained popularity.

An on-resonance version of the FS-LG sequence was recently introduced, [90] called, PM-LG. It consists of a phase modulated version of the FS-LG sequence. A PM-LG

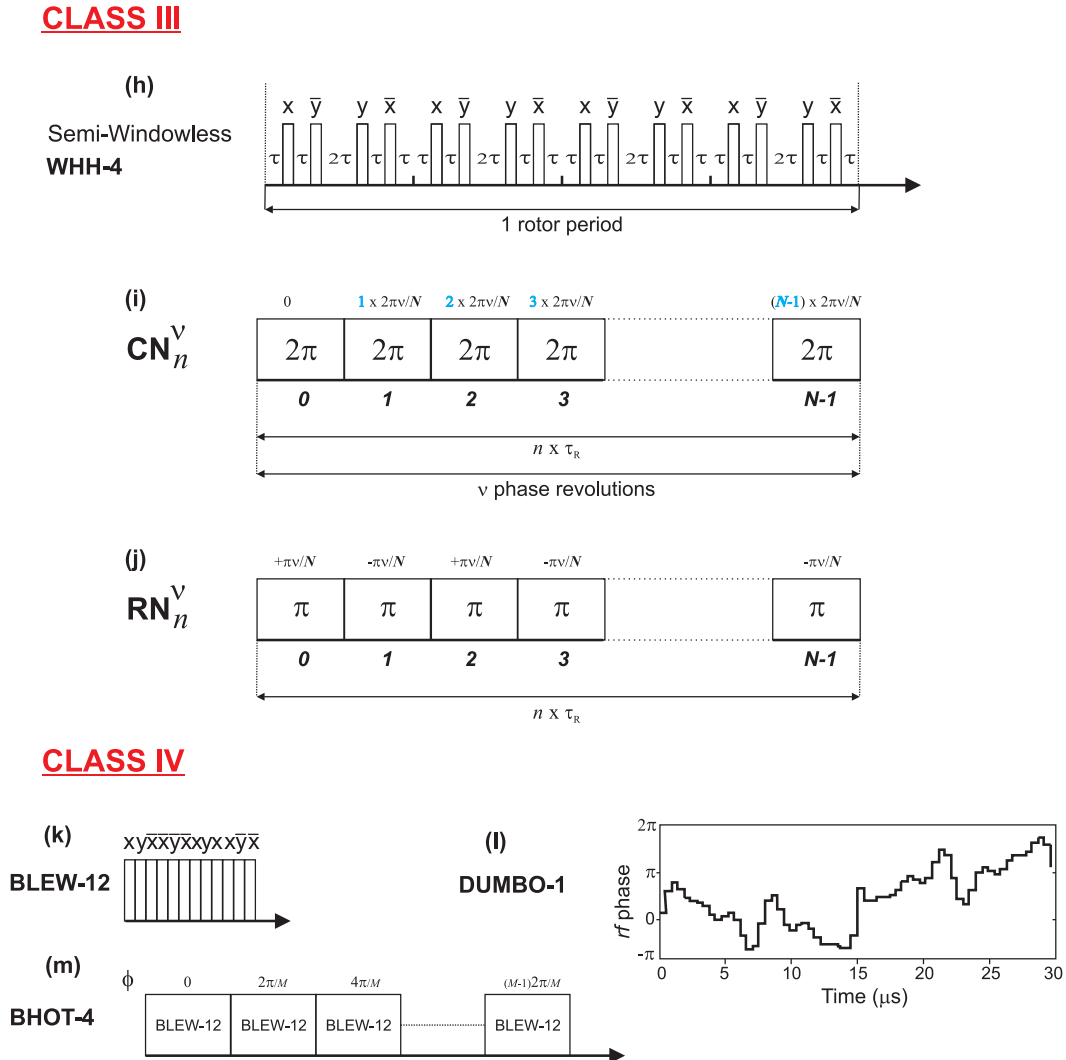


Fig. 4.2: Schematic drawings of rotor-synchronised pulse schemes: (h) synchronised WHH-4 sequence, (i) the CN_n^v consist of N consecutive pulses each performing an effective 360° rotation of the spins and each differing in their overall phase by $2\pi\nu/N$; the N pulses span n rotor periods; (j) the RN_n^v sequence consisting of $N/2$ equal pairs of effective 180° pulses with overall phases flipping between $\pm\pi\nu/N$. A total of $N/2$ pulse pairs span n rotor periods. Schematic drawings of the family of pulse schemes, which gave origin to the DUMBO-1 sequence: (k) BLEW12, (l) phase diagram for the DUMBO-1 sequence (adapted from ref. [79]) and (m) BHOT-4. The diagram was traced using 64 steps per cycle, both in experiments and numerical simulations, by employing eq. 4.2.

4.3 Theoretical Tools

4.3.1 The Average Hamiltonian Theory and the “Toogling Frame”

The averaged Hamiltonian theory was initially introduced by Haeberlen and Waugh [62, 91] to multiple-pulse SSNMR and was further discussed, in more detail by Rhim and coworkers. [71, 74, 92, 93] More recently, the development of the AHT of a class of symmetrical *rf* pulse sequences in the NMR of rotating solids was reported. [94]

AHT has been the method of election to solve Schroedinger’s equation when the Hamiltonian of the spin system $\hat{H}_{tot}(t)$ is periodic, as it is the case in most NMR experiments. Then, the periodic and time-dependent Hamiltonian can be replaced by its average Hamiltonian (in terms of a time independent effective Hamiltonian - H_{eff}), which describes the average motion of the spin system.

In the usual rotating frame, the Hamiltonian describing the nuclear spin system can be split into two terms,

$$\hat{H}_{tot}(t) = \hat{H}_{int} + \hat{H}_{ext}(t) \quad (4.3)$$

where \hat{H}_{int} is the time-independent part and \hat{H}_{ext} the time-dependent part, which can be either due to sample rotation or *rf* irradiation.

To solve the equation of motion for the spin density matrix $\rho(t)$ (Eq. 1.22), the time evolution propagator $\hat{U}(t)$ must be derived,

$$\hat{U}(t) = \hat{T}e^{-i\int_0^t \hat{H}(t')dt'} = \hat{T}e^{-i\int_0^t [\hat{H}_{int} + \hat{H}_{ext}(t')]dt'} \quad (4.4)$$

where \hat{T} is the Dyson time-ordering operator.

Generally, it is not straightforward to establish a direct relation between the total Hamiltonian $\hat{H}_{tot}(t)$ and the corresponding time evolution propagator ($\hat{U}(t)$). To obtain physical insight into the spin evolution of a system subject to multiple pulse *rf* irradiation, it is common practice to transform the spin system Hamiltonian into the interaction frame of the perturbation (in this case $\hat{H}_{ext}(t) = \hat{H}_{rf}(t)$), also called, ”toggling frame”, here denoted by the symbol $\tilde{\cdot}$. This procedure allows to separate the time evolution propagator in two products

$$\hat{U}(t) = \hat{U}_{rf}(t) \hat{U}_{int}(t) \quad (4.5)$$

with

$$\hat{U}_{rf}(t) = \hat{T}e^{-i\int_0^t \hat{H}_{rf}(t')dt'} \quad (4.6)$$

and comparing eqs. 4.4, 4.5 and 4.6,

$$\hat{U}_{int}(t) = \hat{T}e^{-i\int_0^t \tilde{\hat{H}}_{tot}(t')dt'} = \hat{T}e^{-i\int_0^t \tilde{\hat{H}}_{int}(t')dt'} \quad (4.7)$$

where $\tilde{\hat{H}}_{tot}(t)$ is the total Hamiltonian in the time dependent interaction representation (*toggling frame*) with respect to \hat{H}_{rf} .

Once the initial total Hamiltonian is defined in the *toggling frame* ($\tilde{\hat{H}}_{tot}(t)$) the *rf* pulse imposes a time modulation on the internal Hamiltonian generated by the *rf* rotation operator ($\hat{U}_{rf}(t)$). Under such conditions, the time-evolution propagator $\hat{U}_{int}(t)$ becomes easier to handle and only depends on $\tilde{\hat{H}}_{tot}(t)$, which in turn only depends on the time-dependent

internal Hamiltonian. $\hat{U}_{rf}(t)$ is the time evolution propagator determined only by $\hat{H}_{rf}(t)$, and $\hat{U}_{int}(t)$ is the time evolution propagator determined only by $\hat{H}_{int}(t)$.

Finally, the time-dependent toggling frame can be written as follows:

$$\tilde{H}_{int} = \hat{U}_{rf}(t) \hat{H}_{int} \hat{U}_{rf}^{-1}(t) \quad (4.8)$$

Considering that $\hat{U}_{rf}(t)$ is cyclic, as it is the case of the FS-LG sequence widely studied in this thesis, having a characteristic cycle time of nt_c the following condition holds:

$$\hat{U}_{rf}(nt_c) = \hat{U}_{rf}(0) = \mathbf{1}, \quad \forall n \quad (4.9)$$

Then the rotating and toggling frames coincide at times nt_c . Thus, if \hat{H}_{rf} is also **periodic**

$$\hat{H}_{rf}(t + nt_c) = \hat{H}_{rf}(t), \quad \text{with } n = 0, 1, 2, 3, \dots \quad (4.10)$$

By satisfying Eq. 4.9 and 4.10 the periodicity of $\hat{H}_{rf}(t)$ is transferred to $\hat{H}_{int}(t)$ and, thus,

$$\tilde{H}_{int}(t + nt_c) = \tilde{H}_{int}(t), \quad \text{with } n = 0, 1, 2, 3, \dots \quad (4.11)$$

and since the toggling frame internal Hamiltonian ($\tilde{H}_{int}(t)$), is periodic (Eq. 4.10),

$$\hat{U}_{int}(nt_c) = \left[\hat{U}_{int}(t_c) \right]^n, \quad \text{with } n = 0, 1, 2, 3, \dots \quad (4.12)$$

Eq. 4.12 means that the behavior of the spin system during a period nt_c is the same as during a period of duration t_c .

It is worth noting that keeping in mind the unitary condition stated in Eq. 4.9 and substituting in the expression of the general time evolution propagator (Eq. 4.5), considering a cyclic propagator of $t = nt_c$, we obtain:

$$\hat{U}(nt_c) = \hat{U}_{int}(t_c) \quad (4.13)$$

In conclusion, the evolution of the density matrix over any cycle time nt_c , can be totally described by $\hat{U}_{int}(t_c)$, thus Eq. 1.22 can be treated as follows:

$$\hat{\rho}(nt_c) = \hat{U}(nt_c) \hat{\rho}(0) \hat{U}^{-1}(nt_c) \quad (4.14a)$$

Employing the unitary condition of Eq. 4.9 the following expression is obtained:

$$\hat{\rho}(nt_c) = \hat{U}_{int}(nt_c) \hat{\rho}(0) \hat{U}_{int}^{-1}(nt_c) \quad (4.14b)$$

and employing the property of Eq. 4.12

$$\hat{\rho}(nt_c) = \left[\hat{U}_{int}(t_c) \right]^n \hat{\rho}(0) \left[\hat{U}_{int}^{-1}(t_c) \right]^n \quad (4.14c)$$

From Eq. 4.14 the spin system can be easily described just by a single propagator ($\hat{U}_{int}(t_c)$). One can imagine that the spin system evolves under the influence of an effective time-independent Hamiltonian, which has the same effect of the real time-dependent Hamiltonian of the spin system. This effect can be observed in the scheme of Fig. 4.4 and may be written as:

$$\hat{U}_{int}(t_c) = \hat{T} e^{-i \int_0^{t_c} \tilde{H}_{int}(t) dt} \quad (4.15a)$$

$$= e^{-i H_{eff} t_c} \quad \text{time - independent!} \quad (4.15b)$$

where

$$H_{eff}(0, t_c) = \sum_{q=0}^{\infty} \bar{H}_{int}^{(q)}(0, t_c) \quad (4.16)$$

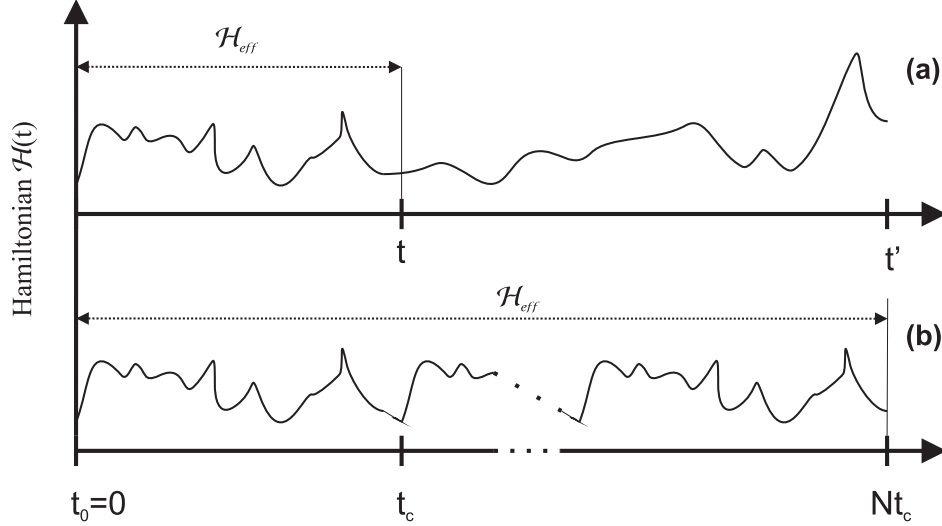


Fig. 4.4: Time dependence of the spin system Hamiltonian. (a) If $\hat{\mathcal{H}}(t)$ is not periodic, \mathcal{H}_{eff} depends on t . Alternatively, (b) if $\hat{\mathcal{H}}(t)$ is periodic, over all multiples of the time interval t_c , then \mathcal{H}_{eff} of the total spin system is the same as the one for a single period t_c . Thus, the spin system evolves under the influence of an average Hamiltonian, which is time independent and has the same effect as the time dependent one.

To find an analytical solution, $\hat{U}_{int}(t_c)$ can be expanded using the Magnus series expansion, and the first orders q components of H_{eff} (Eq. 4.16) can be developed as: [95]

$$\bar{H}_{int}^{(1)} = \frac{1}{t_c} \int_0^{t_c} \tilde{H}_{int}(t) dt \quad \text{Average Hamiltonian} \quad (4.17a)$$

$$\bar{H}_{int}^{(2)} = \frac{-i}{2t_c} \int_0^{t_c} dt_2 \int_0^{t_2} [\tilde{H}_{int}(t_2), \tilde{H}_{int}(t_1)] dt_1 \quad (4.17b)$$

$$\begin{aligned} \bar{H}_{int}^{(3)} = & \frac{-i}{6t_c} \int_0^{t_c} dt_3 \int_0^{t_3} dt_2 \int_0^{t_2} [\tilde{H}_{int}(t_3), [\tilde{H}_{int}(t_2), \tilde{H}_{int}(t_1)]] \\ & + [\tilde{H}_{int}(t_1), [\tilde{H}_{int}(t_2), \tilde{H}_{int}(t_3)]] dt_1 \end{aligned} \quad (4.17c)$$

⋮
⋮

where $t_1, t_2, t_3 \in [t_0, t_c]$

The terms $\bar{H}_{int}^{(q)}$ in Eq. 4.17 can be expressed in contributions from each interaction of

the spin system,

$$\bar{H}_{int}^{(1)} = \bar{H}_{CS}^{(1)} + \bar{H}_D^{(1)} + \sum_{\varepsilon} \tilde{H}_{\varepsilon}^{(1)}; \quad (4.18a)$$

$$\bar{H}_{int}^{(2)} = \bar{H}_{CS}^{(2)} + \bar{H}_D^{(2)} + \bar{H}_{D,CS}^{(2)} + \bar{H}_{\delta,D}^{(2)} + \dots; \quad (4.18b)$$

$$\bar{H}_{int}^{(3)} = \bar{H}_{CS}^{(3)} + \bar{H}_D^{(3)} + \bar{H}_{D,CS}^{(3)} + \dots; \quad (4.18c)$$

$\sum_{\varepsilon} \bar{H}_{\varepsilon}$ account for the sum ε error terms which complete the description of the true experimental situation such as $\varepsilon = \delta$ for pulse length misadjustments.

It is worth noting that the Magnus expansion is only applicable if the series converges quickly. The Magnus expansion of an operator \hat{H} over a time interval $[0, t_c]$ is convergent when $\|\hat{H}_{int}.t_c\| \ll 1$. Additionally if this condition is obeyed the spin system appears to evolve during the time interval t_c under the effect of the first-order average Hamiltonian (Eq. 4.17a). If such condition is not fulfilled, higher-order terms (Eqs. 4.17b and 4.17c) must be taken into account in the development of the average Hamiltonian.

4.3.2 Alternatives to AHT: Other Effective Hamiltonian Theories

Apart from the averaged Hamiltonian theory, other approaches to investigate the Hamiltonian describing the system have been developed. For example, the Floquet theory [96, 97] has been used by some researchers; a combination of both AHT and Floquet theory; [66] synchronisation arguments; [63–65, 68] and numerical methods. [79] Very recently, a new approach called the exact effective Hamiltonian theory, was proposed. [98] The idea behind this treatment is that, given a finite operator basis set, it must be also possible to express the effective Hamiltonian for the system as a finite series of terms with at most the same dimensionality as the basis itself. For more detailed treatment of these theories, the excellent review of ref. [69] is recommended.

4.4 FS-LG Principle

The FS-LG is a phase and frequency-switched technique. Lee and Goldburg showed that the application of an off-resonance irradiation:

$$\Delta\nu_{LG} = \frac{\nu_1}{\sqrt{2}} \quad (4.19)$$

induces an effective field,

$$\nu_{eff} = \sqrt{(\nu_1)^2 + (\Delta\nu_{LG})^2} \quad (4.20)$$

inclined at an angle,

$$\begin{aligned} \theta_m &= \arctan\left(\frac{\nu_1}{\Delta\nu_{LG}}\right) \\ &= \arctan\left(\sqrt{2}\right) \\ &= 54.74^\circ \end{aligned} \quad (4.21)$$

with respect to the static magnetic field, B_0 . This effective field is coincident with the tilted rotating frame- \tilde{z} (or toggling frame), as shown in Fig. 4.6a-b resulting in an efficient ^1H

homonuclear decoupling. By applying LG irradiation (perturbation) the spins precess around the effective field or magic-angle axis of coordinates (1, 1, 1)(Fig. 4.6c), thus canceling the homonuclear dipolar Hamiltonian to first order, over a period

$$\tau_{LG} = \sqrt{\frac{2}{3}} \times \frac{1}{\nu_1} \quad (4.22)$$

i.e., the time to complete a 2π rotation around the tilted field. If applied on-resonance, each of these LG pulses would correspond to a flip angle of $\sim 294^\circ$. By simultaneously switching the *rf* phase and the offset frequency (carrier frequency), between each LG units (Eq. 4.23), the effective field direction is periodically inverted (between each LG unit) by 180° ,

$$\nu_{eff} = \pm \frac{\Delta\nu_{LG}}{\cos\theta_m} \quad (4.23)$$

then producing a LG-type experiment symmetric by reflection (Fig. 4.5). [74, 89] According to this principle all even order terms in the expansion of the effective Hamiltonian (Eq. 4.16) represented in the *rf* interaction frame vanish whenever the perturbation fulfills:

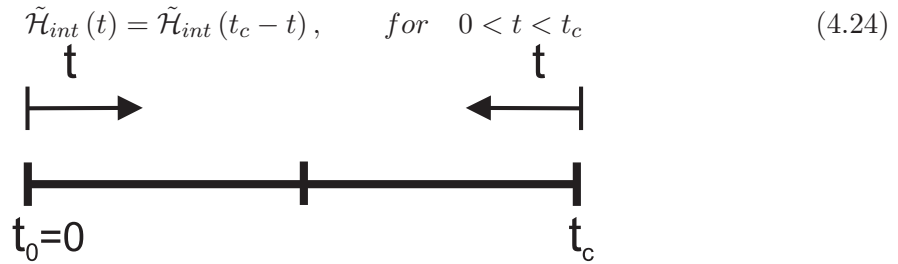
$$\tilde{\mathcal{H}}_{int}(t) = \tilde{\mathcal{H}}_{int}(t_c - t), \quad \text{for } 0 < t < t_c \quad (4.24)$$


Fig. 4.5: Scheme showing the reflection symmetry principle of the toggling frame Hamiltonian described by eq. 4.24.

where t_c is the cycle time defined by the *rf* irradiation.

This experiment improves the dipolar truncation to second-order by eliminating all even-order terms. [71] To first order, the homonuclear dipolar couplings are averaged out, whereas shielding (isotropic and anisotropic parts) is scaled by a theoretical factor of $\frac{1}{\sqrt{3}}$. Higher order error terms (*rf* field inhomogeneity, etc.) can be compensated by such periodic reversing of the phase and the offset of the *rf* field. To eliminate this terms, first one have to make sure that the zero-order dipolar Hamiltonian (average Hamiltonian, Eq. 4.17a) vanishes for the basic cycle (LG block). The higher-order effects left over by the basic cycle are additive and, thus, when generated with the opposite sign in two successive cycles will cancel each other. [93]

To accomplish such reversing of the *rf* phase and offset, FS-LG decoupling requires high switching speed ($< 1\mu s$) of the four-phase modulator (4-PM) and a recent direct digital frequency synthesis to rapidly change the offset frequency between the positive and negative offset frequencies ($\pm\Delta\nu_{LG}$), and guarantee a good phase and *rf* offset initialisation at the beginning of each LG pulse.

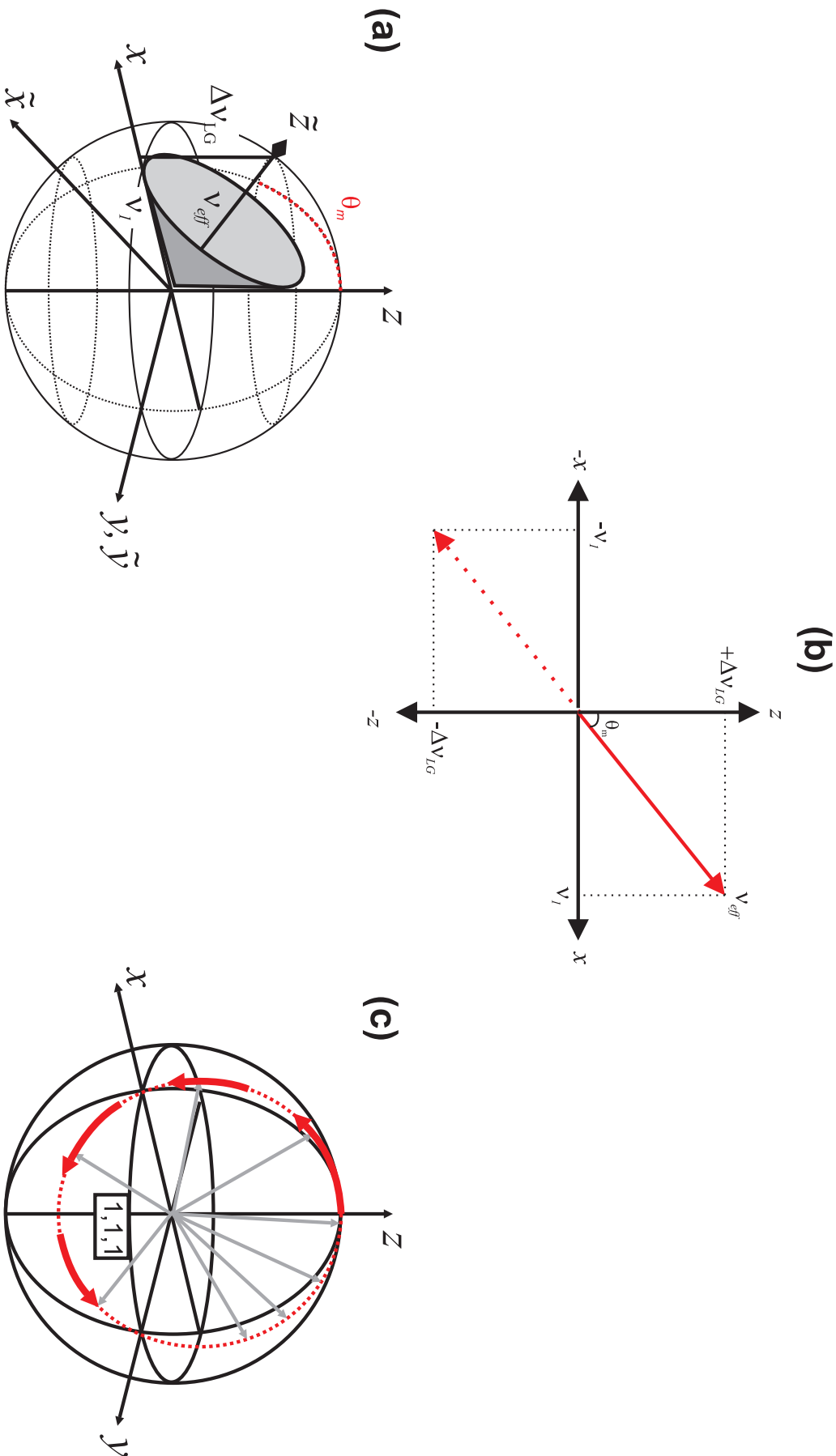


Fig. 4.6: Schematic representation of the FS-LG sequence for homonuclear dipolar decoupling in solids. (a) Representation of the transformation into a tilted frame which is inclined by the angle θ_y with the tilted \tilde{z} -axis along the direction of the effective field $B_{eff} = B_1 \cdot e_x + \left(B_0 - \frac{\omega}{\gamma}\right) \cdot e_z$. (b) Representation of the two components of the total effective field, V_{eff} , evidencing the direction of the LG rf offsets, $\pm \Delta V_{LG}$ and nutation frequencies, ν_I . (c) Trajectory of the rotating frame z -axis in the interaction frame (toggling frame), showing the striking similarity with MAS, which is based on cubic symmetry averaging (direction 1,1,1). Note, however, that the FS-LG decoupling sequence (and others) averages only in the spin space of the spin system Hamiltonian, resulting in the scaling of the CS interaction by a factor ~ 0.58 . This situation of FS-LG decoupling can be thought of as MAS in “spin space”.

4.5 The FS-LG Hamiltonian

Considering only the *rf*, CS and the homonuclear dipole-dipole Hamiltonian, the total Hamiltonian, $\hat{\mathcal{H}}(t)$ of a spin system involving two homonuclear spins i and j can be defined as:

$$\begin{aligned}
\hat{\mathcal{H}}(t) &= \hat{\mathcal{H}}_1(t) + \hat{\mathcal{H}}_i^{CS}(t) + \hat{\mathcal{H}}_{ij}^D(t) \\
\hat{\mathcal{H}}(t) &= \left[(\omega_0^i - \omega_{carrier}) \hat{I}_z^i + \omega_1 \hat{I}_x^i \right] + \hat{\mathcal{H}}_i^{CS}(t) + \hat{\mathcal{H}}_{ij}^D(t) \\
&= \left[\Delta\omega_{LG}^i \hat{I}_z^i + \omega_1 \hat{I}_x^i \right] + \sum_{q'=-2}^{+2} \left[\omega_i^{(q'),CS} e^{iq'\omega_R t} \right] \left[\hat{T}_{1,0}^{CS,i} \right]^{LAB} \\
&\quad + \sum_{q'=-2}^{+2} \left[e^{iq'\omega_R t} \omega_{ij}^{(q'),DD} \right] \left[\hat{T}_{2,0}^{D,ij} \right]^{LAB}
\end{aligned} \tag{4.25}$$

where $\hat{T}_{1,0}^{CS,i} = \hat{I}_z^i$ and $\hat{T}_{2,0}^{D,ij}$ is given in table 2.2. $\omega_{ij}^{(q),D}$ and $\omega_i^{(q'),CS}$ are the homonuclear dipole-dipole and CS frequencies, respectively, enclosing the full transformations from the PAS frame of the interaction to the LAB frame. For rotating samples, their values can be expressed as follows:

$$\omega_{ij}^{(q'),D} = \left[\mathcal{A}_{2,0}^{ij} \right]^{PAS} \sum_{q'=-2}^{+2} d_{0,q'}^{(2)}(\beta_{PR}) \times e^{-iq'\beta_{PR}} d_{q',0}^{(2)}(\theta_m) \tag{4.26}$$

$$\begin{aligned}
\omega_i^{(q'),CS} &= \left[\mathcal{A}_{0,0}^{CS} \right] + \left[\mathcal{A}_{2,0}^{CS} \right]^{LAB} \\
&= \left[\mathcal{A}_{0,0}^{CS} \right] + \left[\mathcal{A}_{2,0}^{CS} \right]^{PAS} \\
&\times \sum_{q'=-2}^{+2} \left\{ d_{q',0}^{(2)}(\theta_m) \left[d_{0,q'}^{(2)}(\beta_{PR}) e^{-iq'\gamma_{PR}} - \frac{\eta^{CS}}{\sqrt{6}} e^{-iq''\alpha_{PR}} d_{q'',0}^{(2)}(\beta_{PR}) \right] \right\}
\end{aligned} \tag{4.27}$$

where the values of the reduced Wigner rotation matrix elements ($d_{q',q}^k(\beta)$) and spatial tensor functions $\left[\mathcal{A}_{2,0}^{ij} \right]^{PAS}$, $\left[\mathcal{A}_{0,0}^{CS} \right]$ and $\left[\mathcal{A}_{2,0}^{CS} \right]^{PAS}$ are listed in Table 2.2.

4.5.1 The *rf* Time Evolution Propagator for FS-LG

The Hamiltonian of the spin system described in eq. 4.25 must be transformed into the *rf* toggling frame in order to obtain a new frame system $(\tilde{x}, \tilde{y}, \tilde{z})$ tilted at θ_m with respect to the LAB frame (x, y, z) , rotating around the effective field or \tilde{z} -axis at angular frequencies of $+\omega_{eff}$ for $0 < t < \frac{t_c}{2}$ and $-\omega_{eff}$ for $\frac{t_c}{2} < t < t_c$ in the case of FS-LG decoupling (see Fig. 4.6a).

To perform such frame transformations one must define the *rf* propagators needed:

- $\hat{\mathcal{H}}(t)$ (Eq. 4.25) can be transformed to a tilted frame, as depicted in Fig. 4.6a, by applying the following propagator:

$$U_y(t) = e^{-i\theta_m \hat{I}_y} \tag{4.28}$$

- Subsequent transformation to the frame rotating with ω_{eff} along the \tilde{z} axis, here denoted as $\tilde{\mathcal{H}}_{eff}^{LG}(t)$, is performed using the propagator:

$$U_{eff}(t) = e^{-i\omega_{eff}t\tilde{I}_z} \quad (4.29)$$

Now, one must apply the propagators of Eqs. 4.28 and 4.29 to the total Hamiltonian of Eq. 4.25 in order to calculate the time-dependent LG interaction frame Hamiltonian,

$$\tilde{\mathcal{H}}_{eff}^{LG}(t) = U_{rf}(t) \hat{\mathcal{H}}(t) U_{rf}^{-1}(t) \quad (4.30)$$

with

$$U_{rf}(t) = U_y(t) U_{eff}(t) \quad (4.31)$$

In the next section the calculus to obtain $\tilde{\mathcal{H}}_{eff}^{LG}(t)$ will be described for the case of FS-LG experiments.

4.5.2 The FS-LG Interaction frame Hamiltonian

In the case of FS-LG, the effective field ω_{eff} is switched between $+\Delta\omega_{LG}/\cos\theta_m$ and $-\Delta\omega_{LG}/\cos\theta_m$ (Eq. 4.23). This leads to the LG time-dependent interaction Hamiltonians

$$\tilde{\mathcal{H}}_{eff}^{+LG}(t) = U_{eff}(t) \tilde{\mathcal{H}}(t) U_{eff}^{-1} \implies +\omega_{eff} \quad \text{if } 0 < t < \frac{t_c}{2} \quad (4.32a)$$

$$\tilde{\mathcal{H}}_{eff}^{-LG}(t) = U_{eff}^{-1}(t) \tilde{\mathcal{H}}(t) U_{eff} \implies -\omega_{eff} \quad \text{if } \frac{t_c}{2} < t < t_c \quad (4.32b)$$

where $\tilde{\mathcal{H}}(t)$ represents the total Hamiltonian $\hat{\mathcal{H}}(t)$ in the tilted frame along the \tilde{z} axis, i.e., under the action of the propagator of Eq. 4.28.

By using Eq. 4.30, the toggling frame representation of the rf interaction, $\tilde{\mathcal{H}}_1$ can be written as:

$$\begin{aligned} \tilde{\mathcal{H}}_{1,eff}^{\pm LG}(t) &= U_{rf}(t) \hat{\mathcal{H}}_1 U_{rf}^{-1}(t) \\ &= U_{rf}(t) \left(\sum_i \left[\Delta\omega_{LG}^i \hat{I}_z^i + \omega_1 \hat{I}_x^i \right] \right) U_{rf}^{-1}(t) \\ &= \omega_{eff}^i \hat{R}_y(\theta_m) \hat{I}_z^i \hat{R}_y^{-1}(\theta_m) \\ &= \pm \omega_{eff}^i \tilde{I}_z^i \end{aligned} \quad (4.33)$$

Similarly, the homonuclear dipole-dipole interaction Hamiltonian is as follows:

$$\tilde{\mathcal{H}}_{ij}^D(t) = U_{rf}(t) \hat{\mathcal{H}}_{ij}^D(t) U_{rf}^{-1}(t) \quad (4.34)$$

By first employing the propagator of Eq. 4.28 one obtain

$$\begin{aligned}
\tilde{\mathcal{H}}^{DD,LG}(t) &= U_y(t) \hat{\mathcal{H}}_{ij}^{DD}(t) U_y^{-1}(t) \\
&= \sum_{q'=-2}^{+2} \left[e^{iq'\omega_R t} \omega_{ij}^{(q'),DD} \right] \times U_y(t) \left[\hat{T}_{2,0}^{ij} \right]^{LAB} U_y^{-1}(t) \\
&= \sum_{q'=-2}^{+2} \left[e^{iq'\omega_R t} \omega_{ij}^{(q'),DD} \right] \times \sum_{\varepsilon=-2}^{+2} \tilde{T}_{2,\varepsilon}^{ij} d_{\varepsilon,0}^{(2)}(\theta_m)
\end{aligned} \tag{4.35}$$

Then, applying the conditions of Eq. 4.32 on eq. 4.35, the final form of the time dependent homonuclear dipole-dipole interaction Hamiltonian has the following form:

$$\begin{aligned}
\tilde{\mathcal{H}}_{eff}^{D,\pm LG}(t) &= \sum_{q'=-2}^{+2} \left[e^{iq'\omega_R t} \omega_{ij}^{(q'),DD} \right] \times U_{eff}(t) \left(\sum_{\varepsilon=-2}^{+2} \tilde{T}_{2,\varepsilon}^{ij} d_{\varepsilon,0}^{(2)}(\theta_m) \right) U_{eff}^{-1}(t) \\
&= \sum_{q'=-2}^{+2} \left[e^{iq'\omega_R t} \omega_{ij}^{(q'),DD} \right] \times \sum_{\varepsilon=-2}^{+2} \tilde{T}_{2,\varepsilon}^{D,ij} d_{\varepsilon,0}^{(2)}(\theta_m) e^{\pm i\varepsilon\omega_{eff} t}
\end{aligned} \tag{4.36}$$

Following the same logic as for the homonuclear dipole-dipole Hamiltonian, the CS interaction frame Hamiltonian can be expressed in the same way. For the sake of simplicity, the anisotropic part of the CS is dropped

$$\begin{aligned}
\tilde{\mathcal{H}}_{eff}^{CS,\pm LG}(t) &= U_{rf}(t) \hat{\mathcal{H}}_i^{CS}(t) U_{rf}^{-1}(t) \\
&= \omega_i^{CS,iso} \times U_{eff}(t) \left[U_y(t) \left[\hat{T}_{1,0}^{CS,i} \right]^{LAB} U_y^{-1}(t) \right] U_{eff}^{-1}(t) \\
&= \omega_i^{CS,iso} \times U_{eff}(t) \left[\cos(\theta_m) \tilde{I}_z^i - \omega_i^{CS,iso} \sin(\theta_m) \tilde{I}_x^i \right] U_{eff}^{-1}(t) \\
&= \omega_i^{CS,iso} \times \left[\cos(\theta_m) \tilde{I}_z^i - \sin(\theta_m) \cos(\omega_{eff} t) \tilde{I}_x^i \mp \sin(\theta_m) \sin(\omega_{eff} t) \tilde{I}_y^i \right] \\
&= \omega_i^{CS,iso} \\
&\quad \times \left[\cos(\theta_m) \tilde{I}_z^i - \sin(\theta_m) \left[\cos(\omega_{eff} t) \tilde{I}_x^i \mp \sin(\omega_{eff} t) \tilde{I}_y^i \right] \right]
\end{aligned} \tag{4.37}$$

Now adding Eqs. 4.33, 4.36 and 4.37, the total FS-LG interaction frame Hamiltonian is:

$$\begin{aligned}
\tilde{\mathcal{H}}_{eff}^{\pm LG}(t) &= \tilde{\mathcal{H}}_{1,eff}^{\pm LG}(t) + \tilde{\mathcal{H}}_{eff}^{CS,\pm LG}(t) + \tilde{\mathcal{H}}_{eff}^{DD,\pm LG}(t) \\
&= \pm \omega_{eff}^i \tilde{I}_z^i \\
&\quad + \omega_i^{CS,iso} \times \left[\cos(\theta_m) \tilde{I}_z^i - \sin(\theta_m) \left[\cos(\omega_{eff} t) \tilde{I}_x^i \mp \sin(\omega_{eff} t) \tilde{I}_y^i \right] \right]
\end{aligned} \tag{4.38}$$

$$+ \sum_{q'=-2}^{+2} \left[e^{iq'\omega_R t} \omega_{ij}^{(q'),DD} \right] \times \sum_{\varepsilon=-2}^{+2} \tilde{T}_{2,\varepsilon}^{ij} d_{\varepsilon,0}^{(2)}(\theta_m) e^{\pm i\varepsilon\omega_{eff} t} \tag{4.39}$$

where $t \in [0, t_c]$.

Eq. 4.38 shows that the secular part (when $\varepsilon = 0$) of the dipole-dipole interaction vanishes because $d_{0,0}^{(2)}(\theta_m) = 0$. The other four non-secular terms, $\tilde{T}_{2,\pm 1}^{D,ij}$ and $\tilde{T}_{2,\pm 2}^{D,ij}$ (when $\varepsilon = \pm 1, \pm 2$),

are therefore responsible for the remaining ^1H - ^1H broadening if all other interactions are suppressed. This means that higher static magnetic fields can help reducing the linewidth. In addition, the evolution under a scaled CS around the \tilde{z} axis can be viewed by the factor $\cos \theta_m = \frac{1}{\sqrt{3}}$ displayed in Eq. 4.38.

4.6 Insertion of FS-LG Blocks in 2D NMR Experiments: Experimental Hints

The windowless FS-LG decoupling sequences can be inserted in many experiments (1D or 2D) to achieve the desired resolution. The most informative and useful experiments in this thesis were the dipolar $^1\text{H}\{\text{FS-LG}\}\text{-X}$ HOMCOR and HETCOR experiments, which have been successfully and mainly applied to biological samples [99–102], and inorganic-organic hybrid materials [103–112].

Other examples of less popular experiments with successful incorporation of the FS-LG homonuclear decoupling scheme are:

- 2D PISEMA pulse sequence; [113,114];
- REDOR [115];
- J -coupling based NMR techniques:
 - J -resolved experiment [116];
 - J -MQ-filter experiment [117];
 - MAS- J -HMQC experiment [118,119];
 - SS-APT experiment [120];
 - J -WISE experiment [121].

In this thesis, homo- and heteronuclear dipolar correlation experiments involving FS-LG decoupling were widely used in part II, concerning applications to inorganic-organic hybrid materials and, thus, I will discuss such sequences in the next section.

4.7 Pulse Scheme Explanation

The description of pulse schemes for 2D homo- and heteronuclear experiments involving through-space correlation is almost equivalent, the latter having just an additional CP step to transfer magnetization from ^1H to X nuclei. Therefore, only the pulse sequence corresponding to 2D ^1H -X HETCOR will be explained in detail. Since, the study of the materials contained in this thesis mainly uses applications involving homo- and heteronuclear dipolar correlation spectroscopy, none of the other pulse sequences employing FS-LG dipolar decoupling will be discussed. However, an example of 2D heteronuclear experiment involving through-bond correlation applied to an inorganic-organic hybrid material is presented in Fig. 4.15.

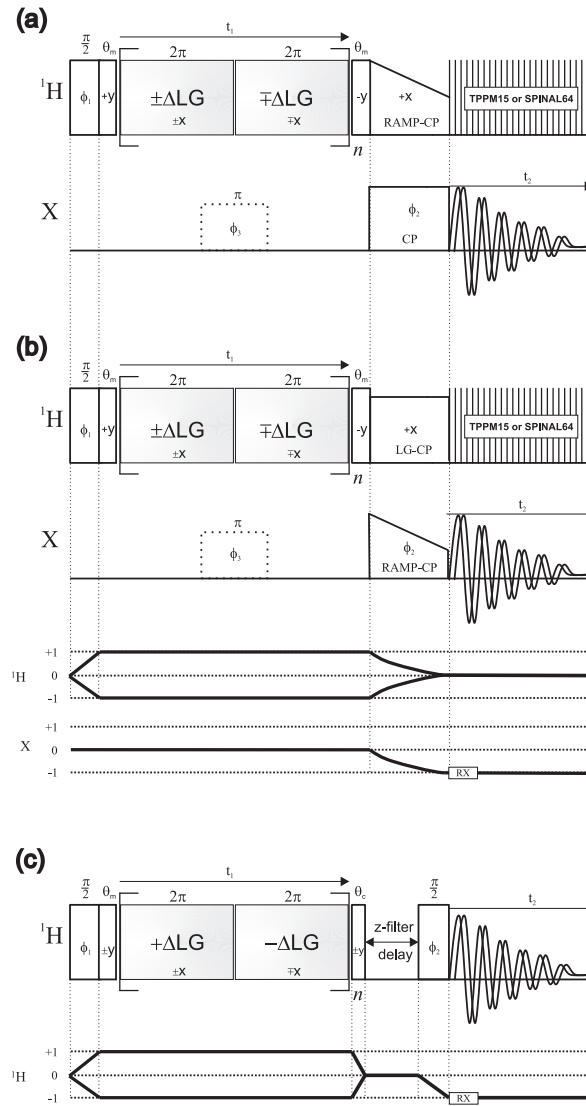


Fig. 4.7: $2D\ ^1H\{FS-LG\}-X$ HETCOR pulse sequences employing (a) CP and (b) LG-CP to polarize the X nuclei from the 1H reservoir. (c) $2D\ ^1H\{FS-LG\}-X$ HOMCOR pulse sequence. X refers to a nucleus other than 1H (e.g. ^{13}C , ^{31}P , ...). θ_m is the magic angle (54.7°) and θ_c is the complementary angle ($90^\circ - \theta_m$).

1. The Preparation Pulses

The pulse sequences start with a preparation step consisting of two pulses, $\frac{\pi}{2} + \theta_m$, which are important for sensitivity reasons. After applying this pair of pulses the proton magnetization is aligned in a plane perpendicular to the \tilde{z} -axis of the toggling frame (interaction frame), thus the 1H magnetisation is ready to be rotated around the effective field (B_{eff}) positioned at the magic angle with respect to the static field (B_0). [122]

In other works [102] just a single 90° pulse, as the preparation step, is applied.

2. The FS-LG Block

As explained before in section 4.4, a ^1H off-resonance frequency-switching irradiation allows the suppression of homonuclear ^1H - ^1H dipolar couplings during the period t_1 , whereas the remaining anisotropic interactions such as the CSA and the heteronuclear dipolar couplings are averaged under fast MAS to their isotropic values, leaving only the scaled heteronuclear J -couplings and the isotropic CSs. The spectra may be improved by introducing a “X” 180° pulse in the center of t_1 evolution (Figs. 4.7a and 4.7b). [118] Such 180° pulse helps removing the net contribution of the heteronuclear couplings. Further details concerning the full optimisation of the FS-LG block are carefully treated in section 4.9.

3. The Conversion Pulses

In HOMCOR experiments, the conversion step can be accomplished by employing a single magic angle (θ_m) pulse to bring ^1H magnetisation to the xy plane or alternatively, by inserting first a 36° pulse ($90^\circ - \theta_m$) with a rf phase perpendicular to the final LG pulse, thus creating a z -filter delay. In a second step, a final 90° pulse is applied to detect the signal. This procedure allows to make spin diffusion studies. During such z -filter delay it is possible to insert homonuclear recoupling schemes, for instance the portion of the radiofrequency-Driven Recoupling (RFDR) sequence where a train of 180° pulses acts as a ZQ recoupling experiment.

In HETCOR experiments the conversion step consists of two steps:

- (a) The return of the ^1H magnetisation to the xy plane caused by a second θ_m pulse with the phase symmetric of the first one, to be ready for a spin-lock needed for a polarization transfer from the high gyromagnetic spin ($\text{I}=\text{H}$) to the diluted or high abundance spin ($\text{X}=\text{C}^{13}, \text{P}^{31}, \text{Al}^{27}, \dots$)
- (b) The ^1H magnetization is spin locked, either in the usual rotating frame if conventional CP is applied, or in the rotating tilted frame if LG-CP is applied. If a CP step is employed, the Hartmann-Hahn (HH) condition must be fulfilled, for a rotating sample:

$$\omega_{1,I} - \omega_{1,S} = n\omega_R \quad \text{with} \quad n = \pm 1, \pm 2 \quad (4.40)$$

For the case of applying a LG-CP step the HH condition is: [123]

$$\frac{\omega_{1,I}}{\sin \theta_m} - \omega_{1,S} = \omega_{eff} - \omega_{1,S} = n\omega_R \quad \text{with} \quad n = \pm 1, \pm 2 \quad (4.41)$$

then the ^1H -X heteronuclear dipolar interaction is scaled by the factor of $\sin \theta_m$. The LG-CP requires that the effective ^1H field strength ($\omega_{eff,H}$) matches the X channel spin-lock field strength, with an applied ^1H rf field strength of $\omega_{eff,H} \times \sin \theta_m$ and a ^1H frequency offset of $\omega_{eff,H} \times \cos \theta_m$.

Some authors use a 36° flip angle pulse immediately before the LG-CP. [102] Such procedure allows to gain more sensitivity because the total magnetisation can be spin-locked directly along the \tilde{z} - axis, instead of just a portion the signal, if the magnetisation is in the xy plane before applying that pulse. instead of a component.

4. Signal Detection in t_2

After the CP step, the carbon magnetization is detected under TPPM [124] or SPINAL64 [125] heteronuclear decoupling schemes. A good review comparing and discussing the heteronuclear decoupling schemes developed until now can be consulted in ref. [126].

4.8 Phase Cycling Schemes

Table 4.1: Example of phase cycling procedure for the three pulse sequences depicted in Figs. 4.7a-c. ϕ_1 and ϕ_2 are the rf phases, which must be cycled to select the desired coherence jump of Δp_1 and Δp_2 , respectively. ϕ_R is the receiver phase for the appropriate coherence pathway. The rf phase ϕ_3 of the ^{13}C π pulse applied in the center of t_1 evolution in the pulses schemes of Figs. 4.7a and 4.7b, does not necessarily need to be cycled.

$\phi_1 \times -\Delta p_1$ ^[a]	$\phi_2 \times -\Delta p_2$ ^[b]	ϕ_R ^[c]	(in spectrometer syntax)
90°	0°	0°	0
270°	0°	180°	2
90°	180°	180°	2
270°	180°	0°	0
90°	90°	90°	1
270°	90°	270°	3
90°	270°	270°	3
270°	270°	90°	1

^[a] The initial $\frac{\pi}{2}$ pulse must be cycled with receiver phase to account for the spin temperature inversion. [127, 128]

^[b] The last pulse, just before the signal detection is cycled for CYCLOPS. [40]

^[c] The receiver phase is calculated according to Eq. 3.21.

Table 4.1, shows one possible phase cycling scheme used to perform the experiments corresponding to the pulse schemes of Figs. 4.7a-c. The θ_m and θ_c pulses flanking the FS-LG decoupling block have their rf phases dependent on the LG irradiation pulse phases.

Details about some phase cycling tricks have to be considered for a better understanding of the way the pulse phases are arranged. The rf phases of such pulses must be always perpendicular with respect to the adjacent LG rf phases. The initial θ_m preparation pulse brings the ^1H magnetisation ready to be spun around the effective rf field, which have the direction of the \tilde{z} - axis (See Fig. 4.6a and 4.6b). On the other hand, just after the FS-LG decoupling block, the θ_m (Fig. 4.7a and 4.7b) and θ_c (Fig. 4.7c) back pulses serve to align the magnetization to the xy plane and the z axis, respectively. These pulses and the LG pulses can be considered as a unique block, which must be cycled depending on the phase acquired by the initial preparation 90° pulse, i.e., if the phase ϕ_1 is set to $+y$ (90°) and $-y$ (270°), as shown in table 4.1, the first θ_m and the $\pm\text{LG}$ pulse phases are $+y$ or $-y^*$ and $\pm x$, respectively. And if the the phase ϕ_1 is set to $+x$ (0°) and $-x$ (180°), the first θ_m and the $\pm\text{LG}$ pulse phases will take the value of $+x$ or $-x$ and $\pm y$, respectively. Apart from this, the phase cycling is performed according to the desired CTP. A detailed explanation of the CTP and the phase cycling procedure needed to select a desired CTP was already given in section 3.5.

*applying $+y$ or $-y$ has the same effect after applying an initial 90° pulse with a phase $+x$ or $-x$ because it will always bring the magnetisation at an angle θ_m with respect to the z -axis

4.9 Calibration of the FS-LG Homonuclear Dipolar Decoupling

The insertion of FS-LG sequence on a pulse program requires special care, because this technique is highly dependent on the good optimization of several parameters and is often limited by the hardware technology.

4.9.1 Typical FS-LG Set-Up

Usually, the FS-LG decoupling is carried out using a moderate ^1H *rf* power corresponding to nutation frequencies of 60-100 kHz. The two off-resonance pulses (LG pulses) with opposite phases (i.e. $+x$, $-x$ or $+y$, $-y$) during the FS-LG decoupling are set to 8.2-12 μs each, and the nutation angle corresponds to a 360° flip angle, which is equivalent to a 294° pulse around the LAB frame. The frequency switching time delay (t_s) between each LG block is typically 0.5-1 μs , depending on the probe quality, and can be optimised by monitoring the *J*-multiplets of the CH and CH_2 groups of adamantane until achieving the best resolution (see Fig. 4.8).

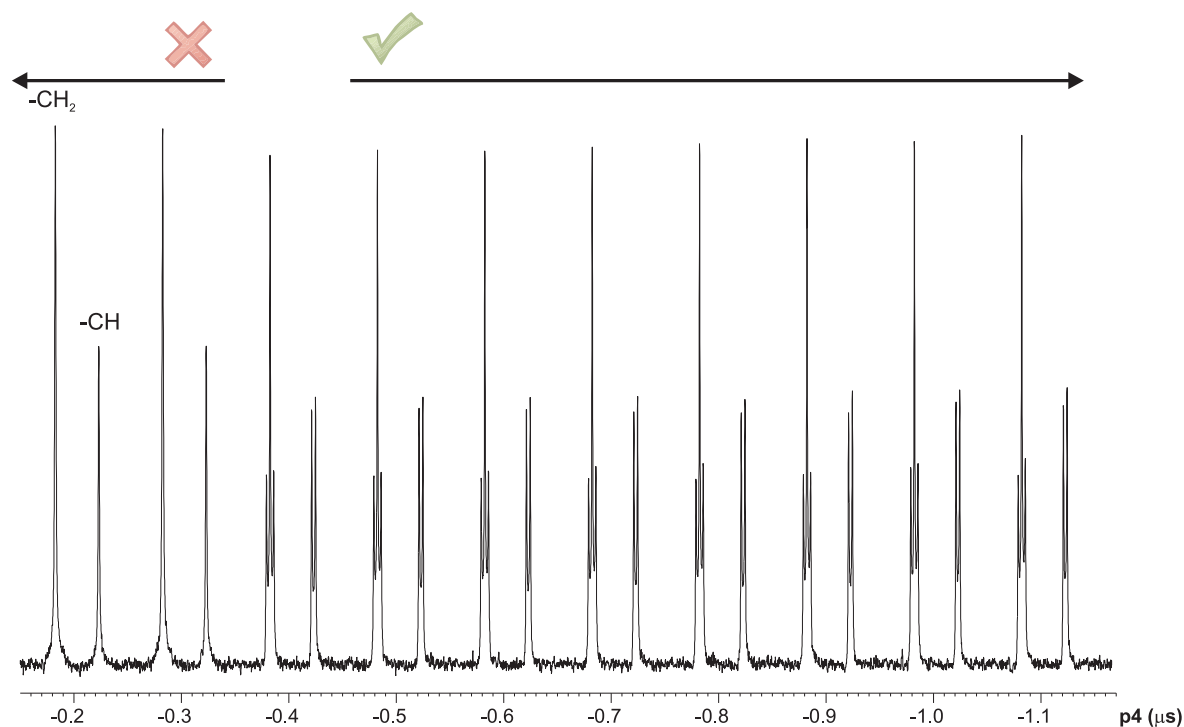


Fig. 4.8: Optimisation of the frequency switching time- t_s (See Fig.4.10) by monitoring the *J*-multiplet of adamantane $-\text{CH}_2$ and $-\text{CH}$ ^{13}C resonances, using the pulse sequence of Fig. 4.9. To guarantee a good inversion of the *rf* phase between consecutive LG pulses, an intermediate delay was introduced in the middle of each LG pulse and optimised in order to allow a fast frequency offset switching at the correct phase in the beginning of each LG pulse. If this pulse length is too short or too long the resolution degrades rapidly

Adamantane or other liquid crystal with high molecular mobility are also suitable to optimise the power level during the τ_{LG} periods. The simple pulse sequence of Fig.4.9 may be used to observe directly the X nuclei (^{13}C in the case of adamantane), while decoupling the

^1H - ^1H dipolar interaction using the FS-LG decoupling, because the adamantane ^{13}C signal is visible after one scan without using CP.

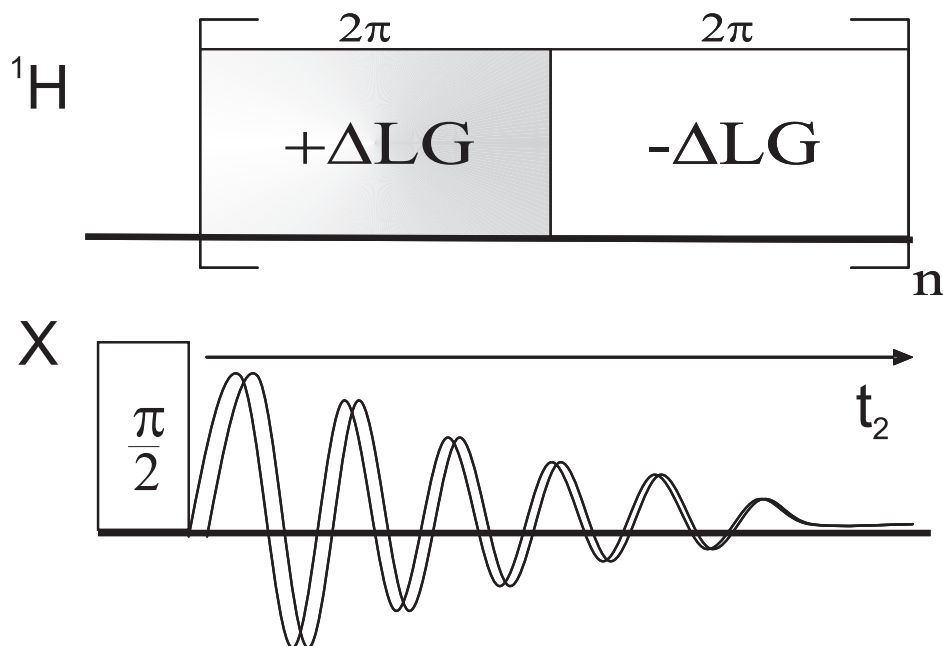
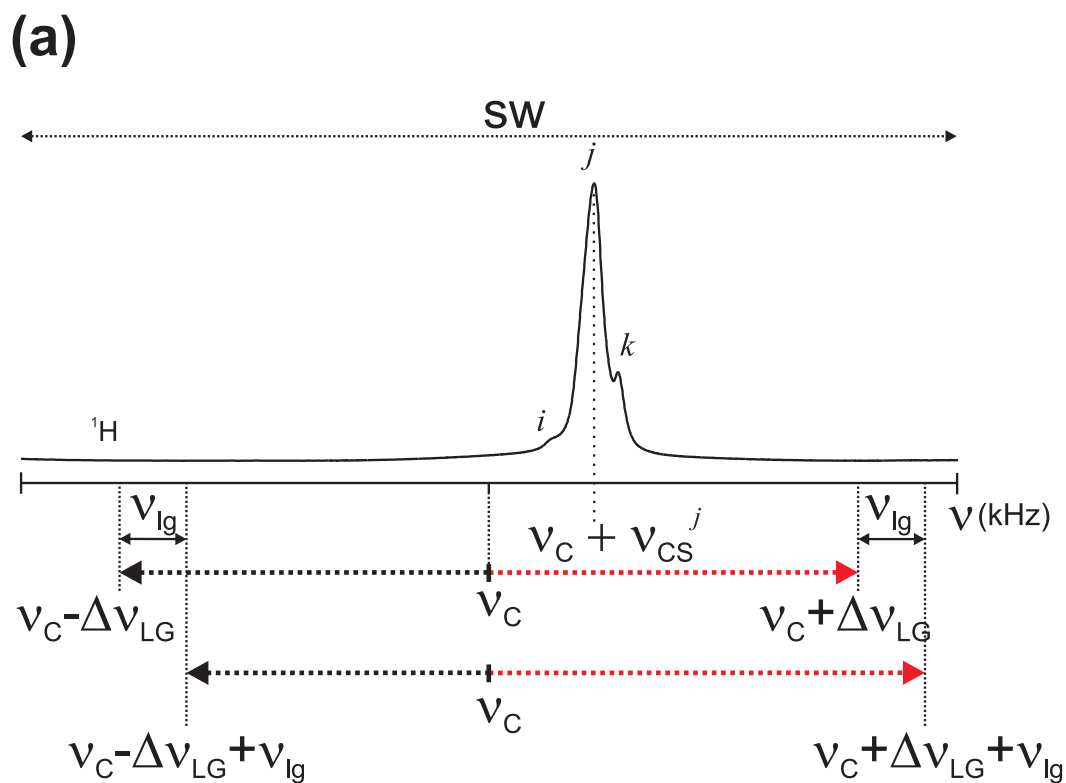


Fig. 4.9: Basic pulse sequence for preliminary optimisation of the FS-LG dipolar decoupling in solids.

The simultaneous frequency and phase shifting were accomplished with a PTS-synthesizer with the help of a 4-phase modulator (4-PM). Ideally the phase modulator should be adjusted as well as possible to a better accuracy in the *rf* pulse phases.

For a better understanding of the offset frequency irradiation switching mechanism during the LG blocks see Fig. 4.10. In addition, the figure also demonstrates the principle of applying asymmetric offset shifts (ν_{lg}) in FS-LG experiments. ν_{lg} values can be preliminary optimised in adamantane as well, however the best way to optimise will be described in section 4.9.2.



ν_C – Carrier frequency

ν_{CS}^j – Chemical shift frequency

$\Delta\nu_{LG}$ – LG offset frequency

ν_{lg} – Asymmetric frequency shift

(b)

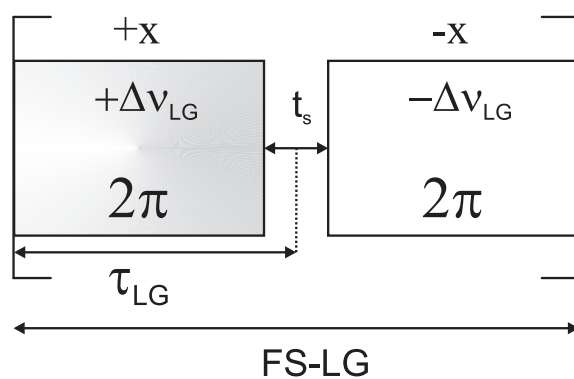


Fig. 4.10: (a) Schematic representation of the role played by the ^1H rf offset values $\Delta\nu_{LG}$ and ν_{lg} . (b) Representation of two back-to-back pulses from the FS-LG decoupling scheme, repeated N times to facilitate the understanding of (a).

4.9.2 FS-LG Optimisation Through 2D Homonuclear Correlation Spectra

The FS-LG rf field strength optimisation

The FS-LG sequence can also be optimised directly through multiple 2D $^1\text{H}\{\text{FS-LG}\}-^1\text{H}$ experiments because they are fast due to the high sensitivity and short longitudinal relaxation of the ^1H nuclei. The most critical parameter to optimise is the power level to be applied during the FS-LG decoupling periods (indeed, this is the unique parameter that needs to be optimised if the theoretical values of rf offsets $\pm\Delta\nu_{LG}$ and pulse lengths (τ_{LG}) are used during the FS-LG decoupling, since these values depend on the FS-LG rf field strength). Although the FS-LG block can be preliminary optimised by acquiring multiple 1D spectra on adamantane (see Fig. 4.11), through ^{13}C observation, the power level obtained rarely corresponds to the best results obtained in a 2D experiment and, therefore, the FS-LG decoupling efficiency must be directly followed through the visualization of the indirect dimension of 2D $^1\text{H}\{\text{FS-LG}\}-^1\text{H}$ HOMO-COR experiments. Then, it is possible to directly monitor the line-shape of the ^1H resonances, most of the times on the sample under study. Fig 4.12 shows the effect of the FS-LG power level for fixed ^1H rf offsets ($\pm\Delta\nu_{LG}$) and LG pulse length (τ_{LG}).

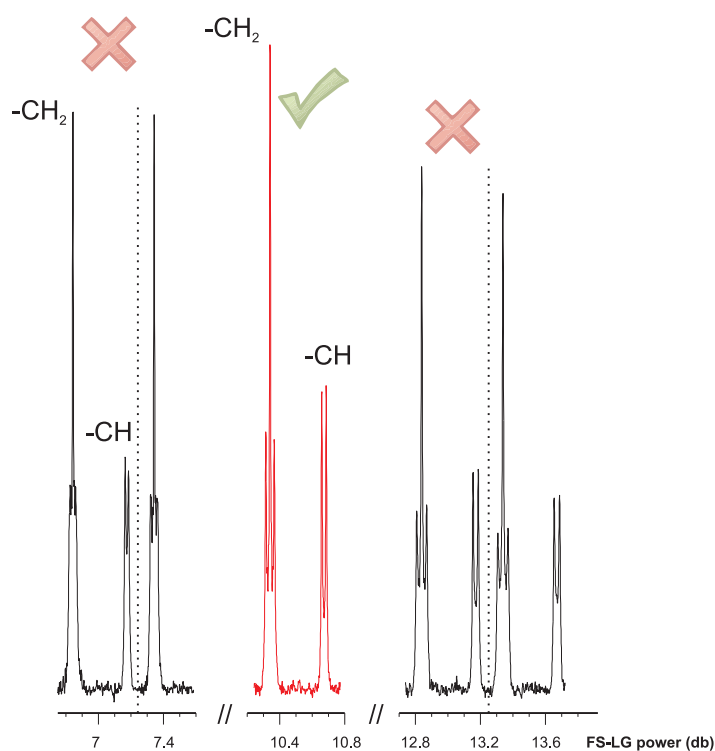


Fig. 4.11: Optimisation of the ^1H rf field strength applied during the FS-LG decoupling in adamantane sample using the pulse sequence of Fig.4.9. To have an idea of how good the shape and resolution of the J -multiplets are, the scaled J -couplings (in the solid) can be compared with the “true” (unscaled) J -coupling values from the liquid-state NMR.

Theoretically, for a value of $\pm\Delta\nu_{LG}=58925$ Hz (as used in spectra of Fig. 4.12), implies a rf field strength of $\nu_1=83.3$ kHz during FS-LG decoupling (Eq. 4.19), which corresponds to an attenuation (p113) of 7.5 db for the probe used. The corresponding spectrum (see Fig. 4.12) is affected by an artifact in the center of F1 dimension when a States-TPPI acquisition method is employed. Contrarily to the direct observation of FS-LG $^1\text{H}-^1\text{H}$ dipolar decoupled 1D spectrum, 2D spectra are perturbed by such artifact that introduces wiggles in the wanted

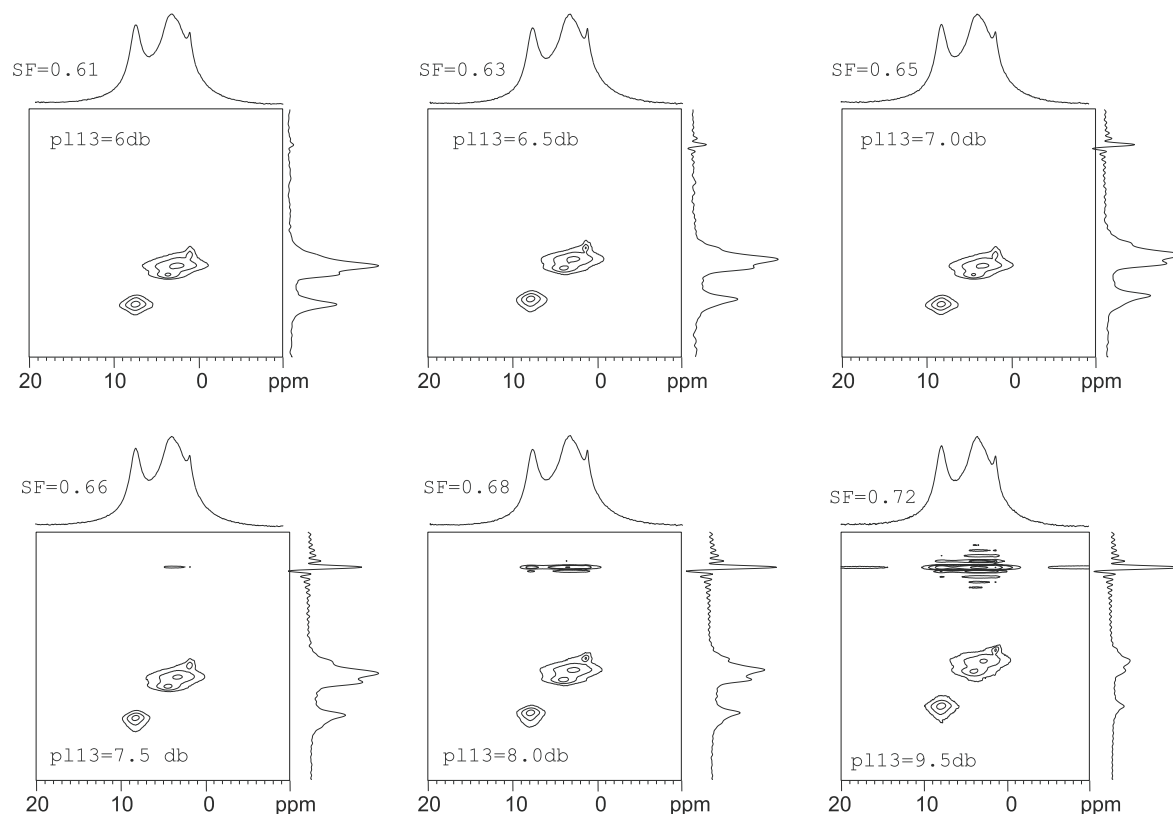


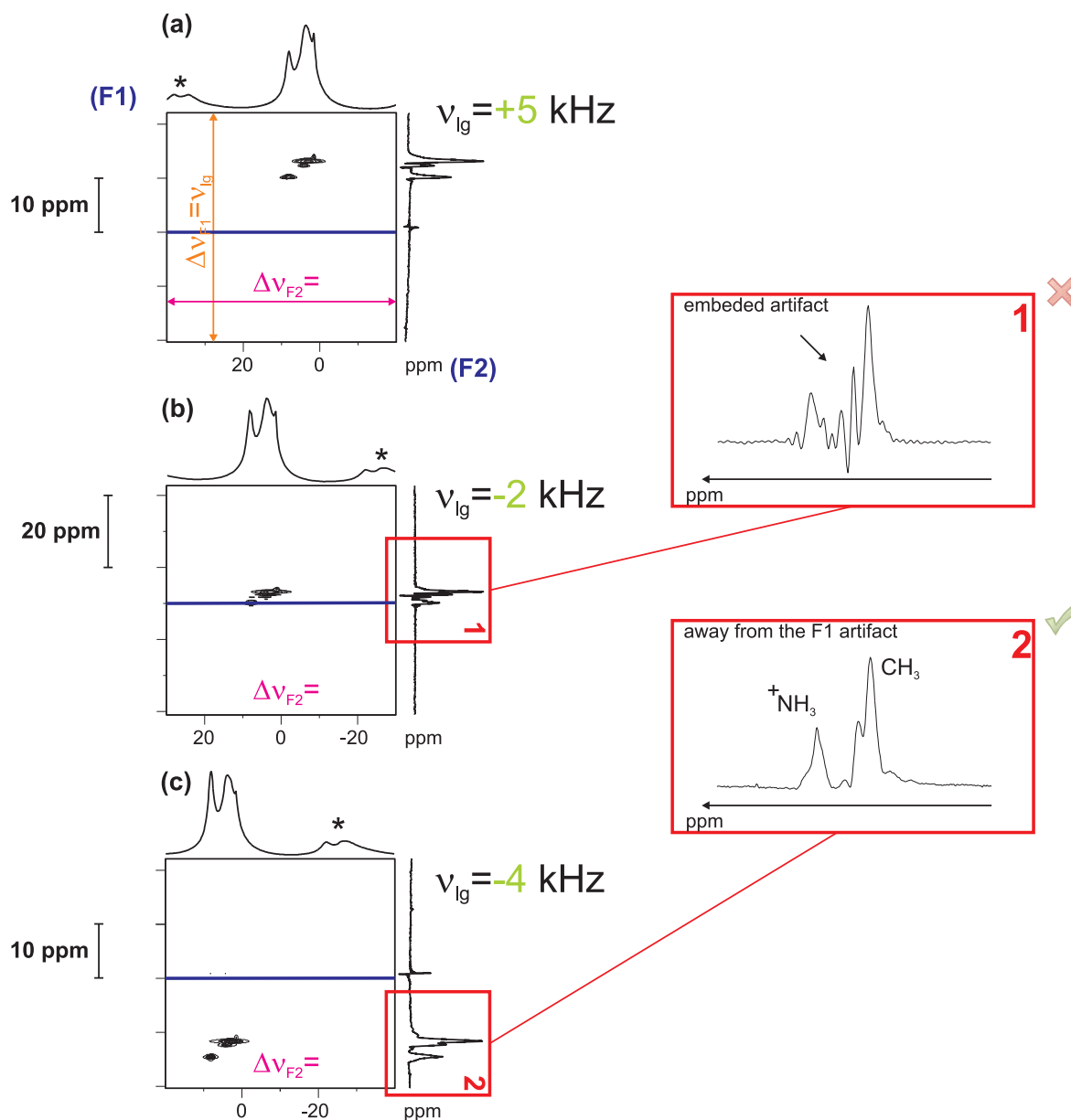
Fig. 4.12: $2\text{D } ^1\text{H}\{\text{FS-LG}\}-^1\text{H}$ HOMICOR spectra of the IST-1 aluminophosphate (See section 9.1), recorded at 12 kHz with different rf field strength during the FS-LG decoupling employed along the t_1 dimension (see Fig. 4.7c). The experimental scaling factors (SF) are indicated for all spectra and were measured considering the isolated NH_3^+ and CH_3 resonances. Recycle delay=300 ms FS-LG conditions: FS-LG rf field strength = 83.3 kHz; $\tau_{\text{LG}}=9.8\mu\text{s}$; $\pm\Delta\nu_{\text{LG}}=\pm 58925$ Hz; $\nu_{\text{lg}}=-4$ kHz.

signal, affecting the quality of the spectral data. This spin lock artifact becomes worse as the FS-LG rf field strength increases (Fig 4.12) and as a consequence it must be minimised. The, experimentally calculated, scaling factor is also slightly affected by the FS-LG power, which means that the resolution changes with the FS-LG rf field strength employed. It is worth mentioning that the scaling factors depicted in Fig. 4.12 were calculated taking into consideration the isolated CH_3 and NH_3^+ ^1H peaks in both F1 and F2 dimensions (See section 9.1 for more details on the peak assignments). The difference, in Hertz, between these peaks were compared in F1 and F2 dimensions allowing to determine the evolution of the scaling factors while changing the delivered FS-LG rf power. The difficulty related with the accurate selection of the peak maxima in both dimensions (this difficulty becomes more severe if superposed peaks contribute to the top of the peaks positions) to calculate such difference, leads to higher scaling factor values than the theoretical 0.577 value for FS-LG ^1H decoupling. However, the relative values obtained, still give an idea of the effects stated above.

In general, the experiments indicate that the best results are only obtained when the artifact appears on the spectra, with intermediate intensity. The total absence of artifact may be reached by reducing the FS-LG rf field strength. However, surprisingly, a simultaneous decrease in spectral resolution is observed (Fig 4.12).

The Optimisation of the ^1H rf offset during FS-LG decoupling

The proximity of the axial artifact with respect to the signal of interest, may be manipulated by changing the ^1H offset during the FS-LG decoupling, i.e., by optimizing the parameter ν_{lg} (See Figs. 4.13a-c). One must displace the artifact away from the NMR signal in order to avoid critical interferences, as depicted in Fig 4.13.



Where the blue line  corresponds to the condition: $\Delta\nu_{F1} = \Delta\nu_{F2} = \text{On-resonance}$

Fig. 4.13: $2\text{D } ^1\text{H}\{\text{FS-LG}\}-^1\text{H}$ HOMCOR spectra of the aluminophosphate IST-1 (see section 9.1 for more details about the material) showing the influence of different ν_{lg} values (a-c). On the right, expanded red boxes of the F_1 projections are depicted.

To avoid such interferences, the ^1H offset frequency selected during the FS-LG decoupling step must be carefully and independently optimised from the rest of the ^1H rf pulses present

in the pulse sequences (See Fig. 4.7). If the ^1H carrier frequency is set on-resonance for the pulses involved in the pulse sequence (including the LG pulses), the spectrum will be displayed like the one shown in Fig. 4.13b exactly in the middle of the F1 and F2 windows, hence in the middle of the F1 central artifact. The best results are obtained when the ^1H resonances are shifted along F1 by an amount $\nu_{lg}=1-7$ kHz.

In addition, the quality of the spectral data is highly dependent on the probe quality and all the mentioned parameters must be optimised individually for each probe.

4.9.3 Difficulties Related With ^1H - ^1H Decoupling Schemes

The optimisation of 2D $^1\text{H}\{\text{FS-LG}\}\text{-X}$ HETCOR experiments is much facilitated by first optimising the 2D $^1\text{H}\{\text{FS-LG}\}\text{-}^1\text{H}$ HOMCOR experiments when possible (See section 4.9.2). Each FS-LG experiment shown in the materials applications studied in this thesis (See part II), was optimised according to the procedure explained above. However, some compounds do not present enough spectral resolution to permit a precise knowledge of the isotropic CS position of the ^1H resonances. In certain cases, as shown in Fig.4.15, the ^1H CS values of the different ^1H resonances of a system are unresolved caused by the homogeneous broadening, thus making difficult the assignment of ^1H resonances. For example, if some ^1H resonances are well resolved in the indirect dimension, but there is insufficient resolution in the direct dimension of a 2D $^1\text{H}\{\text{FS-LG}\}\text{-}^1\text{H}$ HOMCOR spectrum, it becomes impossible to determine the correct ^1H CSs and the scaling factor. In this case, a known compound with well separated peaks may be mixed with the material under study, allowing to calibrate the CSs. This is one of the main drawbacks of the ^1H - ^1H dipolar decoupling schemes. One way to overcome this problem consists in recording a ^1H MAS spectrum as fast as possible, to narrow the linewidth and resolve, at least, two resonances to calculate the scaling factors originated from the FS-LG decoupling. And if, eventually, enough resolution is reached one can establish a comparison with the ^1H resolved indirect dimension of a 2D $^1\text{H}\{\text{FS-LG}\}\text{-}^1\text{H}$ HOMCOR spectrum and correct the ppm scale. Such method usually succeeds in the majority of the cases. Another problem, is concerned with the quantification. Samoson *et al.* discusses this subject in the context of ^1H MAS spectra. [129] Different relative dynamics of the molecular motion may interfere with the cycle time of the pulse narrowing technique precluding the obtention of correct intensities ratios of differently moving molecular units and different convergences of linewidth on increasing rotation speed.

4.10 Some Examples of 2D $^1\text{H}\{\text{FS-LG}\}\text{-X}$ HETCOR Spectra

4.10.1 ^1H - ^{89}Y FS-LG CP HETCOR

Yttrium observation by ^{89}Y SSNMR is usually a difficult task, owing to its long longitudinal relaxation time, low sensitivity due to its long longitudinal relaxation time and low gyromagnetic constant. However ^{89}Y SSNMR spectra can be easily obtained by CP using the pool of ^1H spins. Below, I show an example of a 2D $^1\text{H}\{\text{FS-LG}\}\text{-}^{89}\text{Y}$ HETCOR spectrum where evidence about strong correlations between the aromatic ^1H resonances and the yttrium centres is visible (Fig. 4.14, region A)

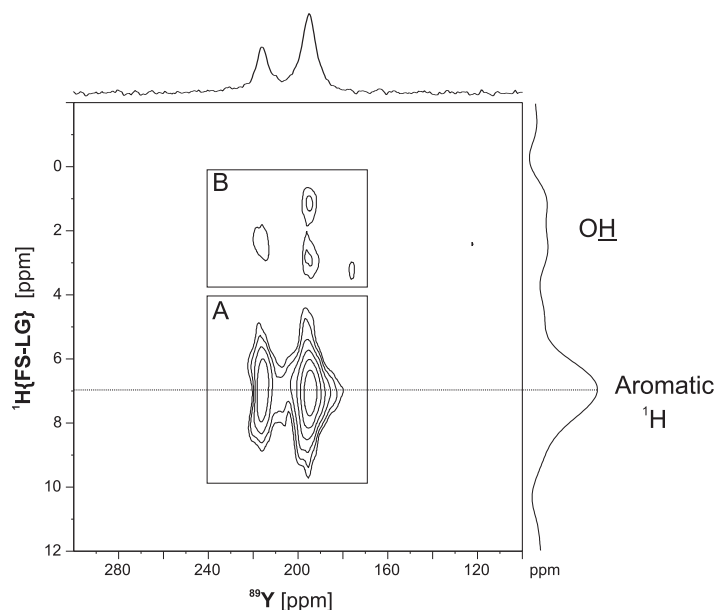


Fig. 4.14: 2D $^1\text{H}\{\text{FS-LG}\}-^{89}\text{Y}$ CP HETCOR NMR spectra of a layered Y_2O_3 intercalated with benzoate residues establishing covalent/ionic bonds, Y-O-C . The spectrum was recorded with 136 t_1 increments each collected with 128 transients. The F_1 increments were synchronized with an integer number of FS-LG units ($n \times 2 \times \tau_{\text{LG}}$) with $n=3$. Short interpretation: ^{89}Y resonances appear at isotropic CS values of ca. 195 and 215 ppm. The two yttrium peaks fall in the range of yttrium compounds containing carbon-based ligands, then indicating that the yttrium atoms are complexed to the organic moieties. The most intense $^1\text{H}-^{89}\text{Y}$ correlation signals correspond to the cross-peaks labeled as “A”, belonging to the strong correlation involving the two ^{89}Y sites and the ^1H resonance centered at ca. 6.9 ppm characteristic of aromatic rings. Region “B” shows faint correlations at CSs between 0 and 4 ppm. These signals may be assigned to adsorbed OH groups or organic impurities. [130]

4.10.2 $^1\text{H}-^{13}\text{C}$ FS-LG HMQC

The majority of the $^1\text{H}-\text{X}$ HETCOR experiments which have been reported so far are based on a direct dipole-dipole coupling driven magnetization transfer instead of using the indirect dipole-dipole (J -coupling) for two main reasons: (i) they have higher sensitivity and (ii) are applicable to a broader range of materials because they do not critically depend on the “true” transversal relaxation time (T_2'). However J -coupling methods may afford higher selectivity since through-bond correlations are formed.

J -coupling based techniques have been emerging in solids over the last few years (see section 4.6). In particular, Emsley and co-workers have been investigating the potential of FS-LG decoupling in liquid-like sequences such as: MQ-J-filters, APT, HSQC and HMQC. The latter is the most used in solids, extensively employed to probe $^1\text{H}-^{13}\text{C}$ systems (almost exclusively applied to crystal plastics and some crystalline organic molecules). A comparison of a 2D $^1\text{H}\{\text{FS-LG}\}-^{13}\text{C}$ CP HETCOR and HMQC spectra of a inorganic-organic hybrid material can be seen in Fig. 4.15.

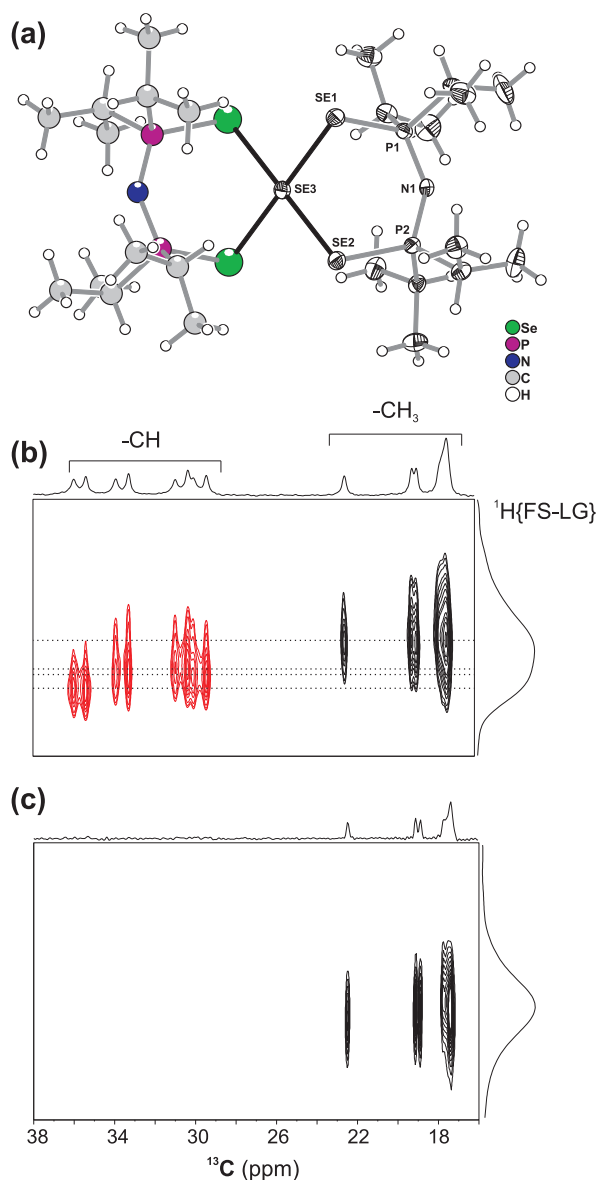


Fig. 4.15: (a) Ball-and-stick representation of a selenium-organic complex, showing the labelling scheme for the atoms belonging to the asymmetric unit. (b) 2D $^1\text{H}\{\text{FS-LG}\}$ - ^{13}C dipolar HETCOR spectrum of the compound shown in (a) employing a Contact time = $50\ \mu\text{s}$. A total of 96 t_1 increments with 144 transients each were collected. The dashed lines represent the number of distinguishable ^1H sites. (c) 2D J-HMQC spectrum with Contact time = 1 ms. A total of 96 t_1 increments with 96 transients each were collected. The evolution period, τ (See pulse sequence in ref. [118] needed to transform the in-phase (C_x) into antiphase ($2H_zC_y$) coherence with respect to the attached proton was set to 4 ms. For all the experiments the F1 increments were synchronized with an integer number of FSLG units ($n \times (2 \times \text{LG})$) with $n=3$ and an lb of 10 Hz was used. The recycle delay was set to 3s. The value of ν_{1g} employed was -2 kHz. The 1D lineshapes at the right represent the F1 projections of the ^1H resonances under FS-LG decoupling.

Chapter 5

2D Homonuclear Dipolar Recoupling Experiments: Spectral Interpretation

5.1 Homonuclear Recoupling Sequences

High spinning speeds and high-power decoupling are in most of the cases prerequisite for obtaining high resolution spectra in solids, because they help in removing the anisotropies of diverse rank-2 interactions. However, the structural information that the anisotropic interactions contain is very informative. Thus, the necessity to reintroduce such interactions led to the creation of the so-called recoupling techniques in SSNMR. A general representation of the recoupling principle can be viewed in Fig. 5.1.

Several recoupling pulse sequences were developed over the last years, for measuring dipole-dipole couplings under MAS. The homonuclear recoupling pulse sequences can be divided in two main categories.

First category. Recoupling pulse sequences dealing with high power *rf* pulses described via δ pulses. Duration of the *rf* pulses t_p has to be, for these pulse sequences, much smaller than the rotational period τ_R . Consequently, with increasing spinning speeds higher *rf* powers and shorter *rf* pulses are required.

Second category. Recoupling pulse sequences based on windowless excitation/conversion sequences. Relatively long *rf* pulses, or spinlock-pulses, are chosen according to the rotor period, i.e. the *rf* field strength which leads to the precession of the spins I in the rotating frame with the angular frequency ω_1 has to be an integer number of the spinning frequency ($\omega_1 = n \times \omega_R$; $n = 1, 2, \dots$). For calculating average Hamiltonians, periods of *rf* pulses where toggling-frame Hamiltonians (interaction frame of the *rf* field) are changing continuously have to be assumed. In general, these pulse sequences are sensitive to the homogeneity of the *rf* field as well as to the sufficiently fast changing of the phases between pulses. The pulse sequences integrated in these category are C7 [131], Permutationally Offset Stabilised C7 (POSTC7) [132] and MELODRAMA [133]. This category of sequences is usually more efficient than the δ pulse sequences of the first category.

Since in this thesis homonuclear recoupling sequences belonging to each of the categories stated above, BABA and POSTC7, were used, the next sections are dedicated to a brief description of both methods, showing experimental examples in the last section.

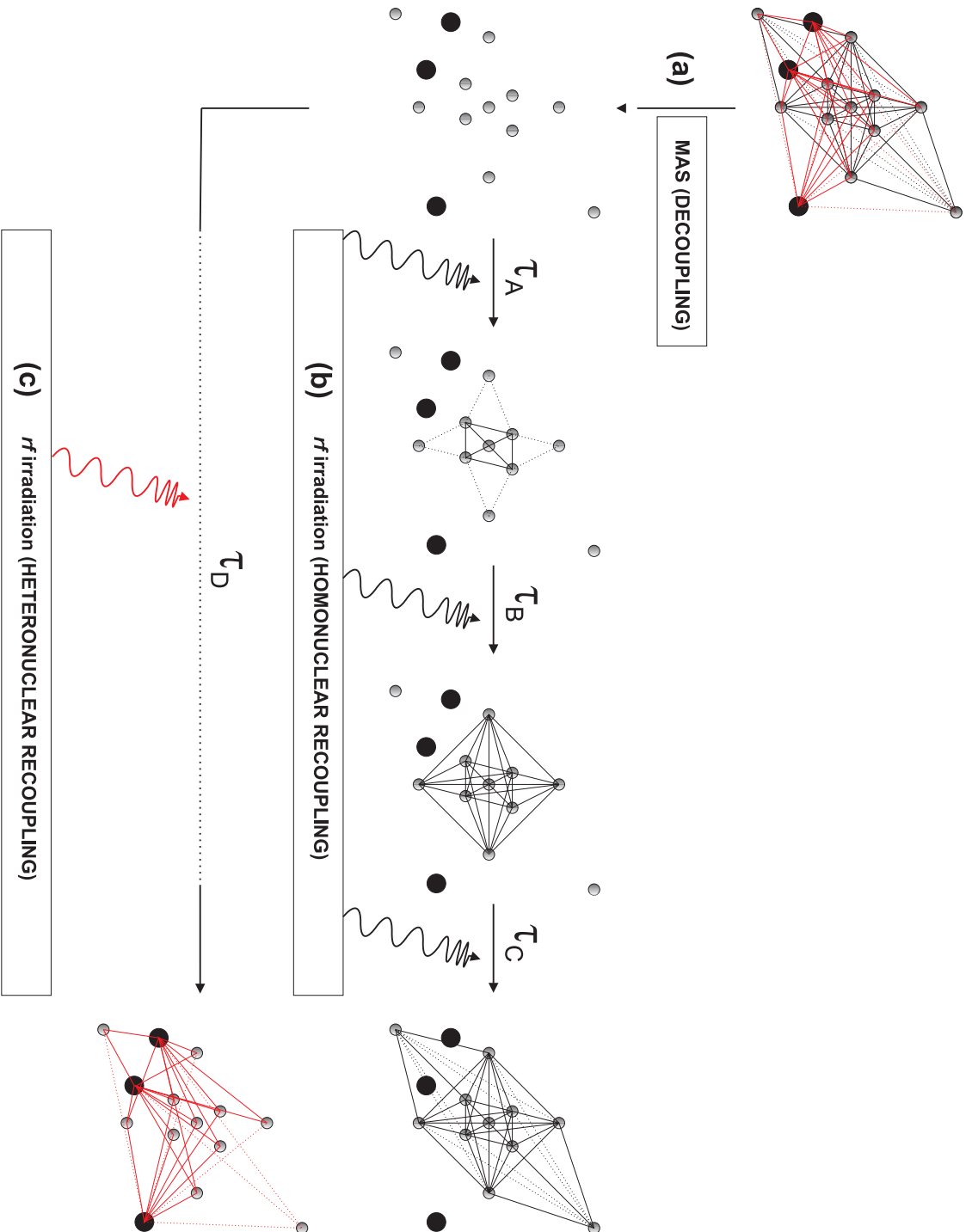


Fig. 5.1: Schematic representation of the recoupling principle. (a) Shows the MAS decoupling, while (b) and (c) depict the homo- and heteronuclear recoupling by spin manipulation through rf irradiation. The grey and black circles represent different nuclei. In (a) the homo- and heteronuclear couplings are removed by spatial averaging (by fast sample spinning). At this stage the system is ready to be recoupled by applying rf pulses to build MQ coherence. In (b) τ_A , τ_B and τ_C are different excitation time instants showing the progressive growth of a cluster size induced by rf irradiation, by formation of homonuclear dipole-dipole couplings (black lines) between the spins (grey circles). In (c) τ_D refers to the excitation time needed to favor the appearance of heteronuclear couplings (red lines) between the spins represented by black and grey circles. The figure shows that the longer the excitation time (τ) the higher the probability for spins to interact

5.1.1 BABA

The BABA [134] pulse scheme has been developed on the basis of Meier-Earl [135] synchronization scheme setting the *rf* pulses *back-to-back*. The BABA sequence can be easily inserted in a 2D experiment as part of the excitation and/or the conversion parts (Fig. 5.2a). Initially, the basic version of the BABA pulse scheme acting in the presence of fast MAS has been conceived by Sommer *et al.* [136] (see Fig. 5.2b). Considering δ -pulses the DQ average Hamiltonian is prepared for this pulse sequence if the synchronization is accomplished as $\tau = \frac{\tau_R}{2}$ and the interpulse delay, $\Delta \rightarrow 0$. This simple basic version of BABA (Fig. 5.2b) acting on one rotor cycle does not remove CSA terms and is also sensitive to the resonance offsets like the DRAMA pulse sequence.

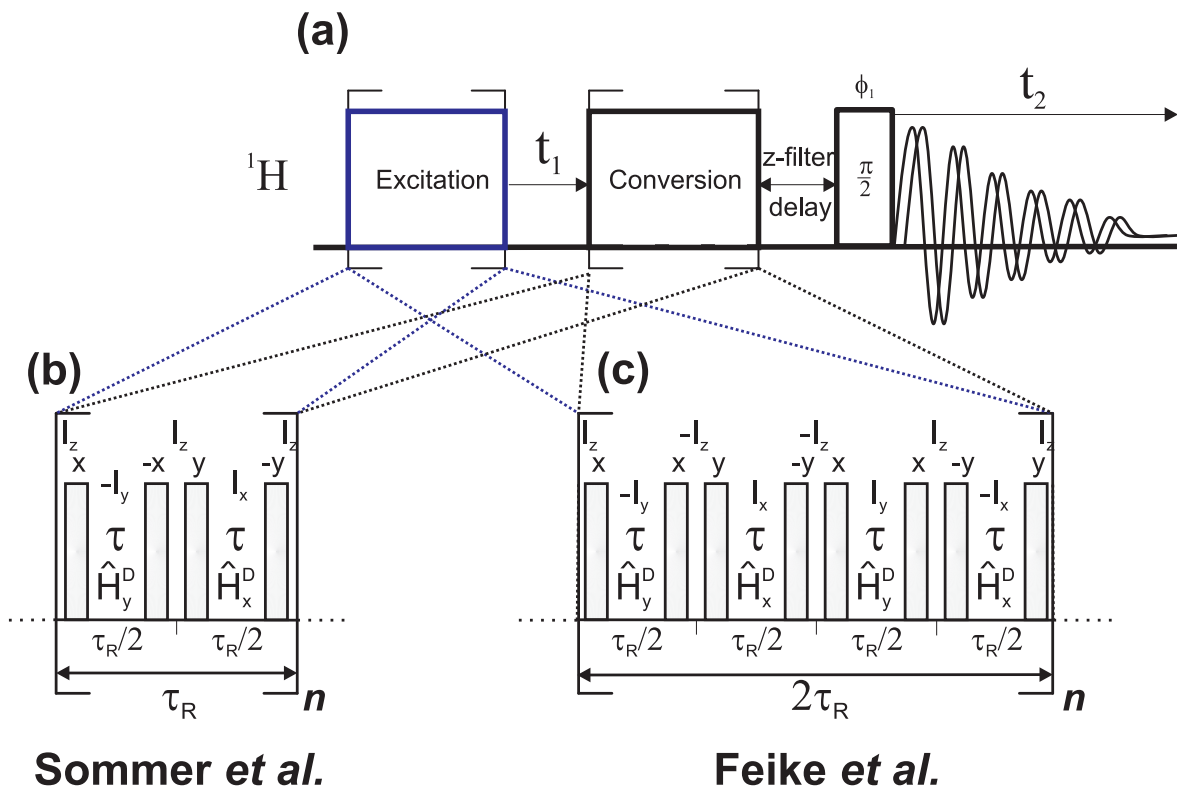


Fig. 5.2: (a) Pulse sequence for the 2D ^1H - ^1H DQ-SQ correlation experiment using as the excitation/conversion steps two different versions of the BABA pulse scheme. One of the versions is the original BABA pulse scheme introduced by Sommer *et al.* having four pulses (b) $\left\{ \frac{\Delta}{2}, \left(\frac{\pi}{2}\right)_x, \tau, \left(\frac{\pi}{2}\right)_{-x}, \Delta, \left(\frac{\pi}{2}\right)_y, \tau, \left(\frac{\pi}{2}\right)_{-y}, \frac{\Delta}{2} \right\}$. (c) Improved version of BABA consisting of eight pulses $\left\{ \frac{\Delta}{2}, \left(\frac{\pi}{2}\right)_x, \tau, \left(\frac{\pi}{2}\right)_x, \Delta, \left(\frac{\pi}{2}\right)_y, \tau, \left(\frac{\pi}{2}\right)_{-y}, \frac{\Delta}{2}, \left(\frac{\pi}{2}\right)_x, \tau, \left(\frac{\pi}{2}\right)_x, \Delta, \left(\frac{\pi}{2}\right)_{-y}, \tau, \left(\frac{\pi}{2}\right)_y, \frac{\Delta}{2} \right\}$. Δ stands for the interpulse delay between two adjacent 90° *rf* pulses. Both sequences must be synchronised with one and two rotor periods, respectively, for (b) and (c).

Thus, the need for an improved version of the BABA scheme led to a new one proposed by Feike *et al.* [137] which is shown in Fig. 5.2c. This sequence is composed by a supercycle of the two original BABA sequences and can solve the problems posed by the original version. An *off-resonance* and *chemical-shift-compensated* pulse sequence can, thus, be generated from the basic BABA four-pulse sequence by considering a supercycle composed of two modified

BABA cycles (eight-pulse sequence). Full compensation can be achieved during two rotor periods as explained in the following.

The linear spin operators \hat{I}_x and \hat{I}_y (describing CS and resonance offset) in Fig. 5.2c differ in sign in the first and the second rotor period, whereas the terms of the dipolar Hamiltonian \hat{H}_x^D and \hat{H}_y^D of an homonuclear spin pair $I - I$ are the same. This evidences the advantage over the sequence of Fig. 5.2b in the elimination of CSA and/or resonance offset effects.

The principle of the recoupling pulse sequences is well established [138,139] and can easily be understood by considering the rotor modulations which are introduced by the sample rotation. The spatial parts of the interaction Hamiltonians are modulated by the MAS frequency according to the Fourier components, defined in Eq. 2.30. In rank-2 spatial tensors as it is the case of the dipole-dipole and CSA interactions, at least four rotor modulation functions are relevant, which correspond to the terms $q' = \pm 1$ and ± 2 in Eq. 2.30, for $|\omega_R|$ and twice the MAS frequency $|2\omega_R|$, respectively. For illustration, the respective oscillations can be found in ref. [137,138]

Recoupling Mechanism

In order to obtain the average Hamiltonians under the conditions of fast MAS, the toggling-frame states of the Hamiltonians created by the pulse sequence must be weighted by the integrals of the rotor-modulation functions. By integrating over a full rotor period, the modulated interactions vanish because positive and negative parts of the oscillations cancel each other. An obvious way to avoid this cancellation is to invert the sign of the spin part by applying strategically *rf* pulses in the sequence, which alternates the sign of the spin part simultaneously to the sign alternation imposed on the spatial part by MAS. Effectively, recoupling is accomplished by inducing a “counter-rotation” in spin space relative to MAS rotation in real space. As there are two modulation frequencies, ω_R and $2\omega_R$, the sign change in the spin part can be performed in intervals of $t_R/2$ or $t_R/4$, respectively. [138] ω_R recoupling is, in general, favorable with respect to the recoupling efficiency, and $2\omega_R$ recoupling is disadvantageous. [138] This is the reason why in BABA a pair of $\pi/2$ -pulses with orthogonal phases is implemented at each time $\tau = \tau_R/2$, in order to invert the sign change of the spatial modulation.

A homonuclear two spin-1/2 system with a dipole-dipole coupling bears analogy to a spin-1 quadrupolar nucleus insofar as the coupled two-spin system can form a DQC. In contrast to the spin-1 nuclei where internal DQ coherences may be created, the dipolar DQ coherence between spin-1/2 nuclei is, in general, not the highest possible coherence order, because further spins can couple to the DQ coherences and, in this way, produce MQ coherences of various orders. [4,140] When the number of spins and couplings increases, the coherent nature of the spin state becomes more and more concealed and is finally lost. In other words, such multi-spin effects bridge the gap between coherent evolutions of spin states and incoherent relaxation phenomena. Therefore, to prevent coherences of order higher than $p = 2$, the sequence is limited to short excitation times (1 or 2 rotor periods, depending on the relaxation effects). It is worth noting that sometimes the four-pulse BABA with a minimal cycle time $\tau_c = \tau_R$ scheme can be advantageous when the excited DQ coherences relax very quickly, however it must be limited to samples with small CS ranges to minimize the negative resonance offset effects.

The Influence of the Δ Delays

It is known that Δ delays are needed for each pulse to account for phase preset delays, i.e. the time needed after setting the phase of the pulse until the phase settles. In the

design of BABA pulse sequences this fact poses a problem because there are pulses which are close together. Error contributions to the zero-order average Hamiltonian arising from pulse imperfections, i.e. finite rf pulses, originates non-zero component in the average Hamiltonian. These imperfections are efficiently eliminated from the $q' = \pm 1$ components of the rotor-modulated function, but not from the $q' = \pm 2$ components (see Eq. 2.30) which contributes to the addition of such errors and can not be eliminated even by shifting the phases of the pulses by 180° . To minimize such effects, the Δ delay must be as short as possible. In old spectrometers, where short times delays are not achievable it is recommended to use the basic sequence of BABA because this error increases proportionally to the number of cycles n . Besides this, in modern spectrometers this error is minimised because fast phase presets are implemented and fast spinning speeds give an additional help to solve the problem since the limit $\Delta \ll \tau_R$ is easily obeyed.

5.1.2 C7 and POSTC7

The C7 pulse sequence belongs to the second category of the recoupling pulse sequences discussed above. It works with relatively long rf pulses with duration fixed to the rotor period despite δ -pulses sequences like DRAMA and BABA. It is a full compensated pulse sequence introduced by Lee *et al.* [131] The name of C7 is derived from the sevenfold-symmetric phase shift scheme acting on the two rotor periods $2\tau_R$. It provides homonuclear dipolar recoupling with better efficiency than previous pulse sequences and is much less sensitive to higher resonance offsets and CSA terms.

The C7 pulse sequence is shown in Fig. 5.3c. Seven elements ($C_{2i\pi/7}$, $i = 0, 1, 2, \dots$) are timed to occupy two rotational periods. Neighbouring elements differ in phase by $\Delta\phi = 2\pi/7$ always rotating in the same sense. In the simplest version [131] each element $C_{2i\pi/7}$ consists of two rf pulses (Fig. 5.3c), both with rf phases differing by π . The strength of the rf field ω_1 has to be adjusted in order to equal seven times the spinning frequency, i.e. $\omega_1 = 7 \times \omega_R$. Then, each element can be described in the conventional notation by $C_{2i\pi/7} = (2\pi)_{2i\pi/7}, (2\pi)_{(2i\pi/7)+\pi}$. The duration of the $C_{2i\pi/7}$ element can be simply estimated as $2\tau_R/7$. C7 compensate for resonance offsets and rf inhomogeneity to *first-order* in the Magnus expansion.

In Fig. 5.3b the second variant of C7 is shown. It was named POSTC7. [132] Theoretical and experimental analysis performed by M. Hohwy *et al.* [132] shows that POST C7 is even less sensitive to the resonance offsets as original version of C7. POSTC7 consists of three pulses in the base element $C_{2i\pi/7} = (\frac{\pi}{2})_{2i\pi/7}, (2\pi)_{(2i\pi/7)+\pi}, (\frac{3\pi}{2})_{(2i\pi/7)}$ (Fig. 5.3b). The zero-order homonuclear dipolar average Hamiltonian of POSTC7 is identical with C7. It is supposed to eliminate isotropic resonance offsets up to *fourth-order* in isotropic resonance offsets/ rf inhomogeneity up to inhomogeneity up to third-order. It also removes the effects of CSA in the zero-order expansion similarly to C7.

5.1.3 2D DQ-SQ Homonuclear Correlation Spectra: Interpretation and Examples

In this section 2D MQ spectroscopy will be briefly explained. As mentioned before, MQ coherences are not detectable directly, thus a 2D experiment is necessary to observe the DQ coherences in the F1 dimension. The coherences are excited during the excitation period (Figs. 5.2a and 5.3a) followed by the evolution period t_1 . In a real system, pure on-resonance excitation is usually impossible, thus resonance offsets caused by linear interactions like e.g. isotropic CSs or CSA will appear p -times shifted from the resonance frequency in the ω_1 dimension for each p -quantum coherence. Broadening caused by CSA will be p -times larger

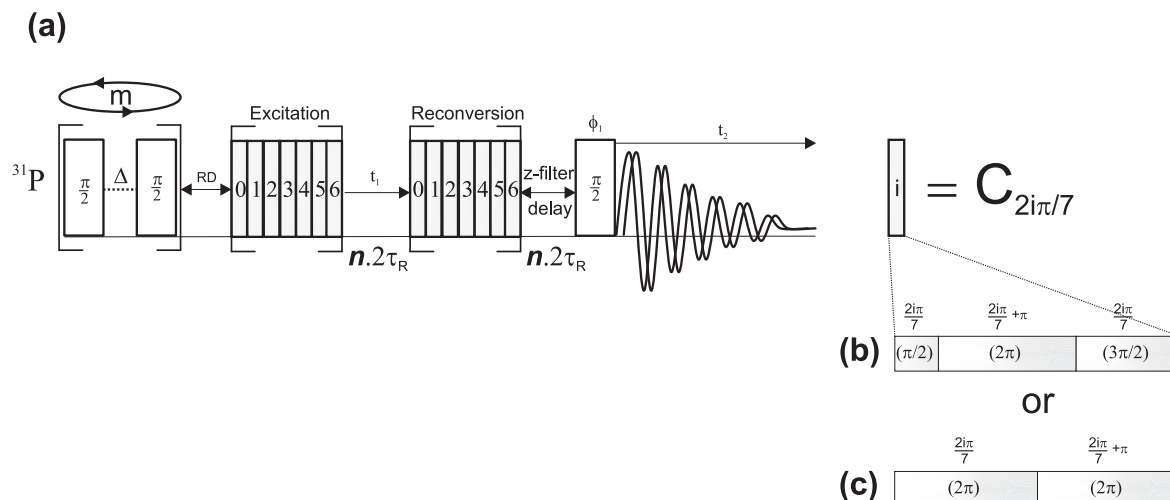


Fig. 5.3: (a) Pulse sequence for 2D DQ-SQ correlation experiments using a (b) C7 or (c) POSTC7 excitation/conversion block. the values of m , n , RD are the saturation pulse loop, the integer number of $2\tau_R$ and the recycle delay, respectively. The 90° detection pulse phase cycling is: $\phi_1 = 0\ 0\ 0\ 0\ 1\ 1\ 1\ 1\ 2\ 2\ 2\ 2\ 3\ 3\ 3\ 3$ and the receiver phase cycling is: $\phi_{rec} = 2\ 0\ 2\ 0\ 3\ 1\ 3\ 1\ 0\ 2\ 0\ 2\ 1\ 3\ 1\ 3$ for the cosine part.

in ω_1 dimension compared to ω_2 dimension. For DQ coherence these frequency shifts (caused by linear interactions) will be twice larger in the DQ dimension than in SQ dimension. In Fig. 5.4 the model system of 3 functional groups represented with three CSs ω_A and ω_B is shown. It serves as an intuitive model for understanding DQ coherence spectra. In Fig. 5.4a system with two molecules intermolecularly close spins is shown. Although the dipolar coupling between nuclei in the two molecules is strong, the coupling between functional groups A and C of each residue is very weak and can be neglected. Only DQ coherence between spins within short distances (either intra- or intermolecular couplings) is excited during the excitation period of a certain DQ pulse sequence and it appears at the sum of the involved CS frequency positions. For example, the coupling pairs A-A or A-B will appear at frequencies $2\omega_A$ and $\omega_A + \omega_B$ in the DQ dimension, respectively. This example shows that both molecules are intermolecularly correlated. In contrast no frequency appears at $\omega_A + \omega_C$ because no coupling exists between the intramolecular pair A-C. In the SQ dimension frequencies for different groups remain unchanged at positions ω_A , ω_B and ω_C . Another schematic example is shown in Fig. 5.4b. Here, two molecules containing also three functional groups are considered. The main difference with respect to the example shown in Fig. 5.4a is that now both molecules do not have all their functional groups in close proximity despite having total intramolecular correlation. For instance, all the sites A, B, C are intramolecularly close and then couplings involving the spin pairs A-B, A-C and B-C will appear at the frequencies, $\omega_A + \omega_B$, $\omega_A + \omega_C$ and $\omega_B + \omega_C$, respectively. However the A-A intermolecular coupling is absent from the spectrum of Fig. 5.4b.

In short, both examples of Figs. 5.4a and 5.4b, the formed couplings evolve during the t_1 evolution time with sum of the CSs involving the two functional groups. After the reconversion period, spins from the different groups carry the (original) frequency at which they appear in the SQ dimension, during the detection period. Drawing a diagonal line between the coherences originated from the same functional groups, A-A, B-B or C-C, DQ coherences representing the connectivities between distinct functional groups appear equally

distributed at the right and left of this line as can be seen from Figs.5.4a and 5.4b.

Care must be taken when analyzing the presence or absence of peaks since it does not exclusively depend on the nuclear distance but also in the mobility of the functional groups.

Examples of 2D spectra using both recoupling techniques (BABA and POSTC7) are shown in Figs. 5.5 and 5.6.

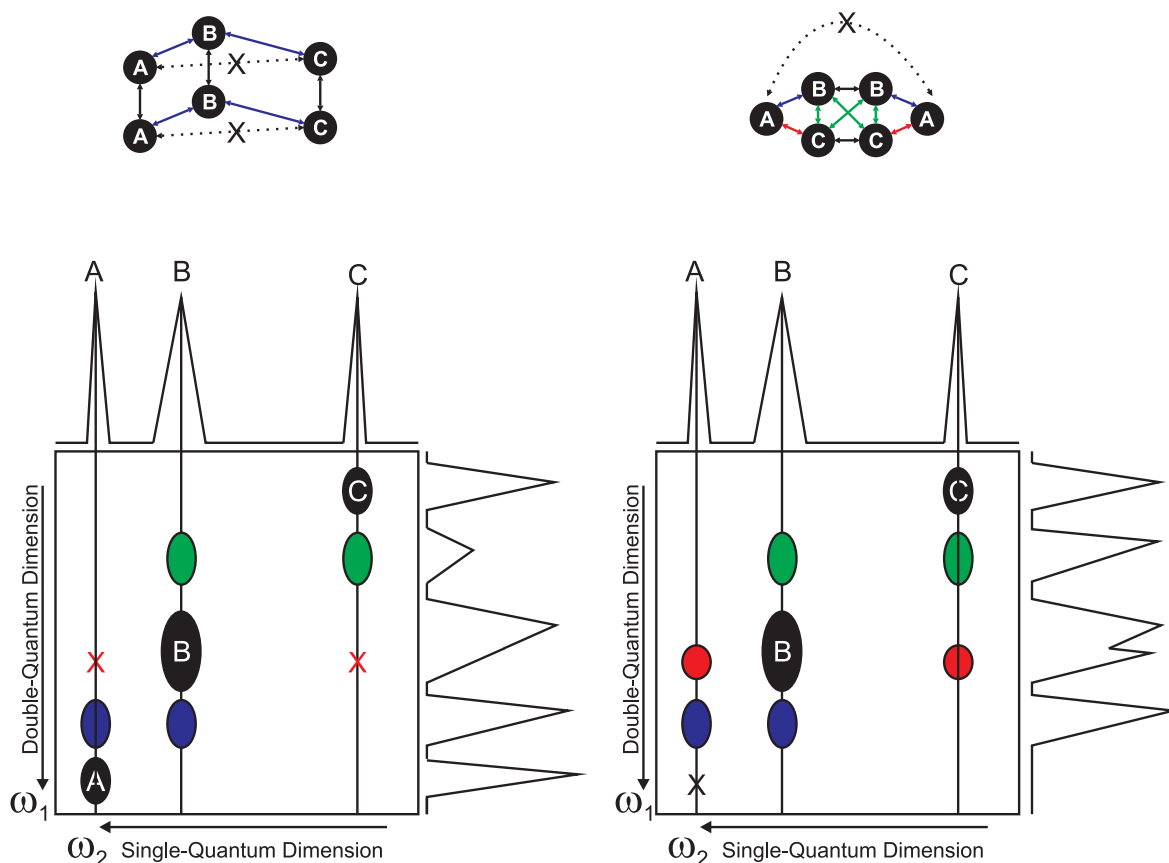


Fig. 5.4: Structure of a 2D DQ-SQ correlation spectrum for a model compound having two spatially close molecules, each one containing three different sites A, B and C. At the right side is located the DQ projection where the coupled nuclei evolve with the sum of the frequencies of the spin pair. At the top one can find the SQ projection. The case (a) shows two molecules where the sites A-C are not coupled due to their distance. Then the off-diagonal corresponding to the DQ frequencies $\omega_A + \omega_C$ is not present. In contrast, in (b) the spin pair A-C is now correlated because the nuclei are spatially close, as it can be seen in the molecular arrangement at the top. Furthermore, this case shows the disappearance of the diagonal peak A-A, due to the long distance between nuclei. Note that in (a) the cross peak B-C having DQ frequency $\omega_B + \omega_C$ is faint with respect to the others because the nuclear distance is relatively high.

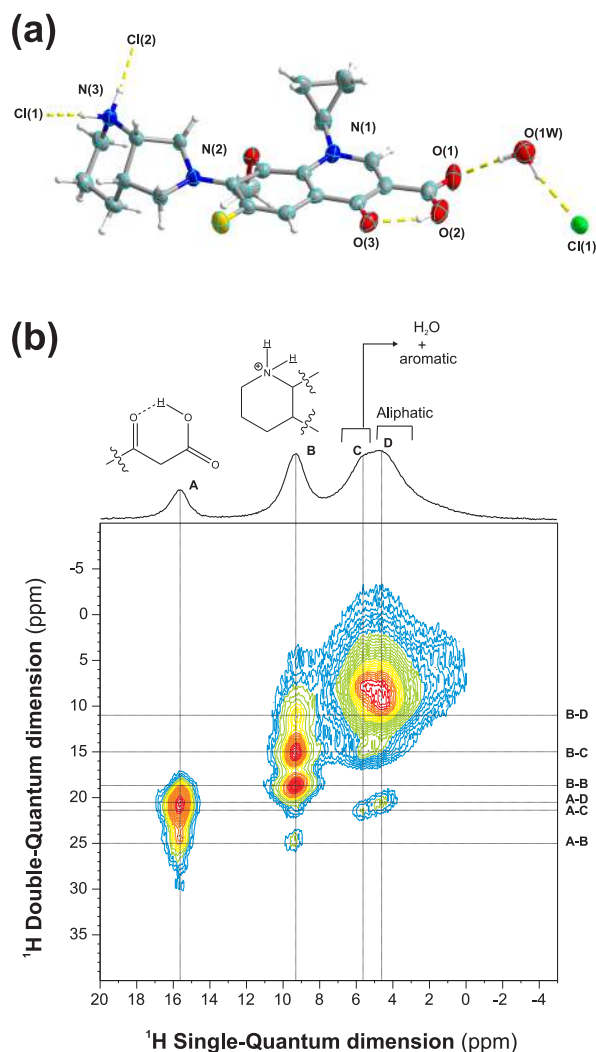


Fig. 5.5: (a) Representation of the chemical structure of hydrated moxifloxacin monochloride molecule hydrogen bonded with HCl residues and its (b) 2D ^1H - ^1H DQ-SQ MAS spectrum recorded using the BABA sequence. The DQ excitation time (τ_{exc}) and reconversion time (τ_{conv}) were set to $66\mu\text{s}$ using the eight pulse version of BABA (Fig. 5.2c). The train of 90° pulses in the BABA sequence was set to $2.5\mu\text{s}$. The spinning speed was 30 kHz. The proximity between carboxylic acid protons (A) of adjacent moxifloxacin molecules are lacking (diagonal peak is not present at $SQ=15.7$, $DQ=31.4$ ppm). However, the A resonances have relatively close (ca. 4.58 \AA) N-H^+ environments (B), despite the low intensity cross peak ($SQ=15.7$, $DQ=25$ ppm), and have further correlation with the aliphatic CH (intermolecular, ca. 2.68 , 3.09 \AA) of the adjacent cyclic amines and rigid H_2O molecules under strong H-bonding ($SQ_{\text{H}_2\text{O}}=5.7$ ppm, ca. 2.8 and 3.4 \AA). The B resonances present a CS typical of protonated amines having an autocorrelation peak since two ^1H atoms are present in each protonated amine (diagonal peak, $SQ=9.3$; $DQ=18.6$ ppm). The presence of a strong cross-peak at $DQ=15$ ppm (B-C) involving the N-H^+ , is a strong indication of proximity between these groups and rigid H_2O molecules under strong H-bonding ($SQ_{\text{H}_2\text{O}}=5.7$ ppm, $d_{\text{H-H}}=2.8\text{ \AA}$ or $d_{\text{N-O}}=4\text{ \AA}$).

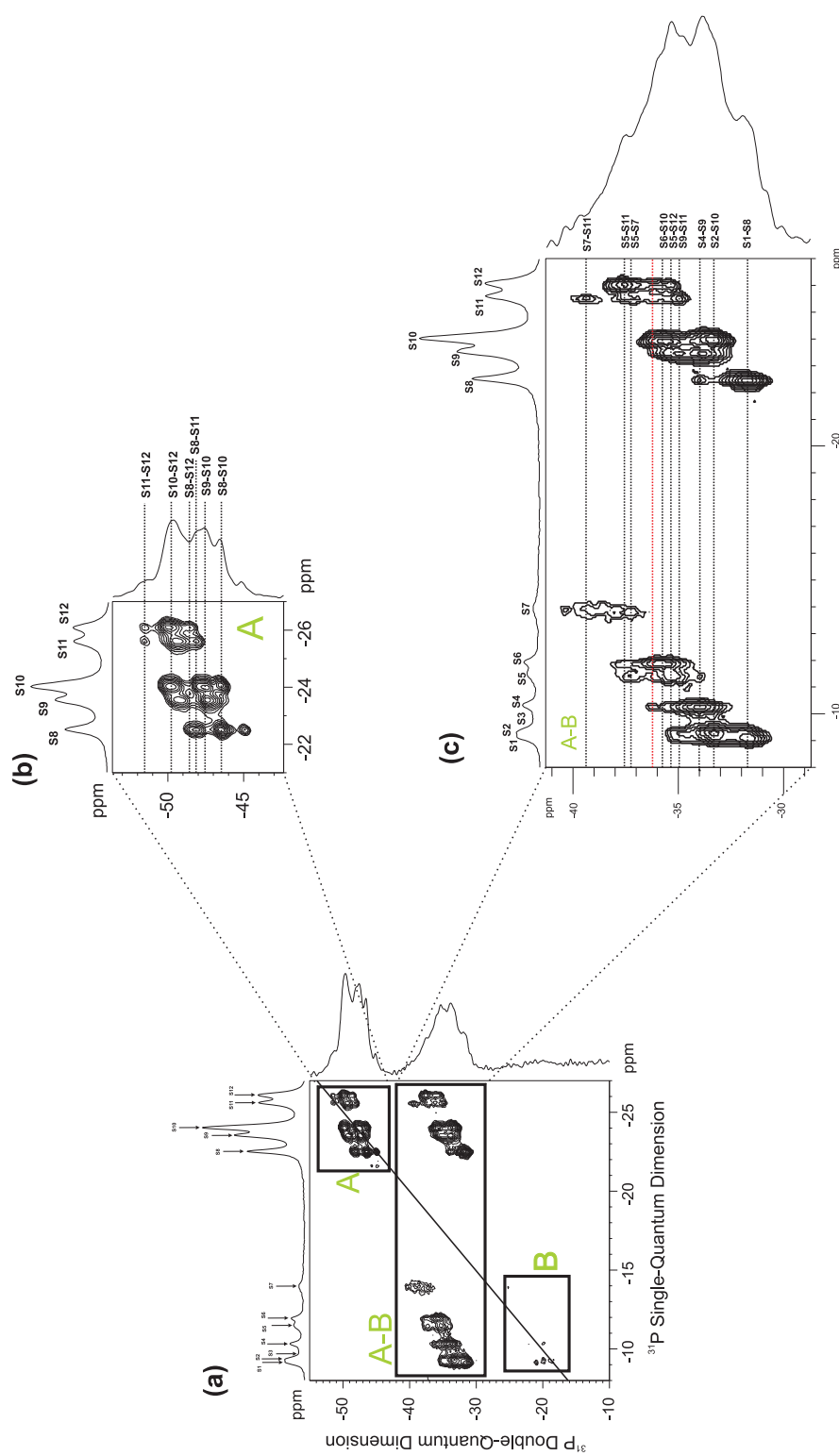


Fig. 5.6: (a) $2D$ ^{31}P - ^{31}P DQ-SQ MAS spectrum of a titanium phosphate layered material having $[\text{Ti}(\text{HPO}_4)(\text{PO}_4)]^-$ anionic sheets, using the POSTC7 sequence (Fig. 5.3c). Prior to the relaxation delay, a saturation comb of 90° pulses with $3.4 \mu\text{s}$ length was applied according to Fig. 5.3a. The 90° pulse employing during the POSTC7 sequence was set to $3.4 \mu\text{s}$ as well, corresponding to a rf field strength of $\omega_1 \approx 70 \text{ kHz}$, obeying the recoupling condition $\omega_1 = 7 \times \omega_R$. Interpretation: the POSTC7 spectrum in (a) shows two main regions **A** and **B** corresponding to the outer and inner ^{31}P sites of the $[\text{Ti}(\text{HPO}_4)(\text{PO}_4)]^-$ anionic sheets. The regions **A** and **B** represent a complex network of crystallographically nonequivalent ^{31}P sites (twelve ^{31}P sites), where correlation can take place between resonances inside the same region (**A-A**) or between different regions (**A-B**). Correlation peaks between ^{31}P sites of region **A** are depicted in the expansion (b), while the cross correlation involving ^{31}P from regions **A** and **B** can be found in expansion (c). The region **B** almost do not show diagonal peaks denoting that the various ^{31}P sites are not close enough to allow the build up of DQ coherences between them.

Part II

Solid-State NMR Applications to Crystalline Inorganic-Organic Hybrid Materials

Chapter 6

General Introduction

Hybrid inorganic-organic hybrid materials have been the subject of considerable world-wide research due to their structural diversity, properties and potential applications in areas such as catalysis, magnetism, optics, photochemistry, electronics, ionics, gas storage, coating films and medicine. [141,142]

The way of combining the organic and inorganic parts, the numerous synthesis procedures (sol-gel, hydrothermal, etc.), and the large variety of properties of hybrids motivated an ever increasing number of specialized areas on these materials. A limitation to a wider application of hybrid materials is the lack of a deeper knowledge on how to predict and control their final structure. Hence, the structural characterization of such materials is very important and necessary to understand structure-property relationships.

The most comprehensive tool for the structural analysis of crystalline solids is X-ray Diffraction (XRD). However, as many authors have shown, [143] not all solids are obtained in the required form of good-quality single crystals. Another important limitation is that in XRD heavy atoms tend to dominate and, hence, low-atomic number atoms, such as ^1H are difficult to probe. [144] Thus, ^1H SSNMR studies play an important role in material chemistry. H-bonds and other acidic functional groups are, generally, easily detected by SSNMR due to their typical high CSs, and because the resonances are usually separated from the more hampered spectral region (in general, ca. 1-8 ppm). Thus, the study of such ^1H environments may be easily studied without the needed of sophisticated techniques. [145,146] The group of H. W. Spiess and coworkers, in particular, has explored the use of homonuclear recoupling techniques, such as Double-Quantum-Filtered (DQF) spectroscopy, to probe H-bonds in organic molecules. [138,145,147–151]

Inorganic-organic materials have also been studied by SSNMR, in particular, organosilica and siloxane-based hybrid materials have been much investigated by routine ^{29}Si and ^{13}C NMR techniques and, sporadically, ^1H NMR, when enough resolution is attainable. [152–167] In addition, inorganic-organic hybrids containing metal phosphates/phophonates have been studied by SSNMR. In particular, ^{27}Al , ^{31}P and ^{19}F studies of open-framework containing amines as directing agents, [168,169] and ^{17}O NMR studies on titania based hybrids. [170]

The use of SSNMR has been more extensively exploited by taking full advantage of sophisticated experiments, such as 2D correlation NMR. However, high-resolution NMR studies of relatively complex ^1H rich hybrid materials are relatively uncommon. ^1H observation suffers, in most cases, from homogeneous broadening, due to strong homonuclear dipolar couplings between neighboring ^1H nuclei. When NMR-active non-proton spins X and Y are present, X-Y dipole-dipole couplings may be probed, taking advantage of their typically large CS ranges (compared to ^1H) to obtain increased resolution for identifying coupled spin pairs. [171] X-Y dipole-dipole interactions, however, are often weak due to low gyromagnetic ratios and,

in many cases, low nuclei natural abundance. These impediments pose serious limitations on the use of X-Y dipole-dipole spin couplings. With the recent hardware developments, the study of the most available nucleus in hybrid materials, ^1H , may be carried out using CRAMPS techniques, as extensively discussed in section 4.2. Thus, ^1H analysis can be employed to overcome the problem of ^1H - ^1H diffusion effects (at least partially), which can be an advantage in particular cases [104] or not [6, 172].

Examples of ^1H CRAMPS-based techniques applied to the study of hybrids are still unusual. [104] And among them ^1H CRAMPS experiments are applied to relatively simple systems.

This chapter illustrates how 2D ^1H FS-LG-based experiments can be used to study four different inorganic-organic hybrid materials. This work is part of a comprehensive study aimed at evaluating the usefulness of high-resolution ^1H NMR techniques to elucidate the structure of such materials. [107, 108]

Chapter 7

Instrumentation

In this section, I give the necessary details on the instrumentation used. Experimental details concerning a particular material (for instance, the synthesis method) and/or experimental techniques will be conveniently indicated in the corresponding section for the sake of clarity.

Vibrational Spectroscopy:

Fourier Transform Infrared (FTIR) spectra were measured from KBr discs (Aldrich, 99%+, FTIR grade) on a Matson 7000 FTIR spectrometer. FT-Raman spectra were measured on a Bruker RFS 100 spectrometer with a Nd:YAG coherent laser ($\lambda=1064$ nm).

Elemental Analysis (EA):

Instrument 1, used in section 8.1, 8.2 and 9.1: EAs for carbon and hydrogen were performed with a FISONs EA1108 instrument.

Instrument 2, used in section 9.2: The phosphorus and titanium contents were determined with a Spectrometer inductively coupled plasma mass spectrometer (ICP-MS) after a weighed amount of the sample was dissolved in aqueous HF. Microanalytical data (C and N) were obtained with a Perkin-Elmer 2400B elemental analyzer.

thermogravimetry (TG)/Differential Scanning Calorimetry (DSC):

Instrument 1, used in sections 8.1, 8.2 and 9.1: TG was carried out using a Shimadzu TGA-50, at a heating rate of $10\text{ }^{\circ}\text{Cmin}^{-1}$, under a nitrogen atmosphere or air, and a flow rate of $20\text{ cm}^3\text{min}^{-1}$. DSC analysis was performed using a Shimadzu DSC-50, at a heating rate of $10\text{ }^{\circ}\text{Cmin}^{-1}$, under nitrogen atmosphere at a flow rate of $20\text{ cm}^3\text{min}^{-1}$.

Instrument 2, used in section 9.2 Thermal analyses were performed under nitrogen atmosphere (heating rate ca. $10\text{ }^{\circ}\text{Cmin}^{-1}$) in a Mettler TA4000 (TG 50 and DSC 30) model. Infrared spectra were recorded with a Perkin-Elmer 1000 FT-IR spectrophotometer using KBr pellets. Micrographs were recorded on a JEOL JSM-6100 electron microscope operating at 20 kV.

Powder XRD:

Instrument 1, used in sections 8.1 and 8.2: Powder XRD patterns were recorded at room temperature using a Philips X'Pert diffractometer, operating with a monochromatic Cu K α radiation source at 40 kV and 50 mA. Simulated powder patterns were based on single-crystal data, and calculated using the STOE Win XPOW software package. [173]

Instrument 2, used in section 9.2: Powder XRD patterns were collected on a conventional powder diffractometer Philips 3040 with graphite monochromatized Cu K α radiation ($\lambda = 1.5418 \text{ \AA}$), operating in the Bragg-Brentano ($\theta/2\theta$) geometry.

Single Crystal X-ray:

Instrument 1, used in section 8.1: Data were collected at 293(2) K on a KUMA4CCD diffractometer with MoK α graphite-monochromated radiation ($\lambda=0.7107 \text{ \AA}$), in the scan mode, and controlled by the CrysAlis CCD software package. [174] Data were corrected for the Lorentz and polarisation effects, and were reduced by using the CrysAlis RED software routines. [175]

Instrument 2, used in section 8.2: Data were collected at 180(2) K on a Nonius Kappa charge coupled device (CCD) area-detector diffractometer (MoK α graphite-monochromated radiation, $\lambda = 0.7107 \text{ \AA}$), equipped with an Oxford Cryosystems cryostream and controlled by the Collect software package. [176] Images were processed using the software packages of Denzo and Scalepack, [177] and intensity data were corrected for Lorentz polarisation and background effects, and also for absorption by using the empirical method employed in Sortav. [178,179]

Solid-State NMR:

The SSNMR measurements concerning the work performed in this chapter were performed at 9.4 T on a Bruker Avance 400 WB spectrometer (DSX model) operating at Larmor frequencies of 400.1, 100.6 and 161.9 MHz for ^1H , ^{13}C and ^{31}P nuclei, respectively. Additional ^{13}C and ^1H data were recorded at 11.4 T on a Bruker Ultrashielded 500 Avance spectrometer operating at Larmor frequencies of 125.7 and 500.1 MHz, respectively. The sample was packed into 4mm and 2mm o.d. ZrO $_2$ rotors, using double-resonance BL CP-MAS VTN probes. In some cases, the sample was restricted to the middle of 4-mm rotors with the help of two plastic inserts (upper and lower insert) in 2D experiments. Such a procedure is necessary because the FS-LG decoupling step is sensitive to rf inhomogeneities, and leads to an improvement of the rf field homogeneity over the whole volume of the sample. Spectra were processed using the Xwin-NMR software package.

Chapter 8

Studies of Phosphonic Acid Based Metal-Organic Hybrid Discrete Units

The concept of secondary building units (SBUs) for predicting topologies of structures is useful to synthesise metal organic frameworks and has been widely used. [180–182] Stimulated by their outstanding properties, [180–184] metal phosphonates, derived from phosphonic acids are becoming increasingly important as SBUs. Phosphonic acids, are gradually replacing carboxylic acids due to their superior complexation properties in acidic solution. [185] Hence, they have been used as organophosphorous ligands in many crystalline complexes and networks such as the extensively used *N*-(phosphonomethyl)iminodiacetic acid (H_4pmida), [186–188] or 1-hydroxyethane-1,1'-diphosphonic acid (H_4hedp), [185, 189, 190] both employed in this work in sections 8.1 and 8.2, respectively.

8.1 A Germanium Binuclear Complex

N-(phosphonomethyl)iminodiacetic acid (Fig. 8.1), H_4pmida , was previously used in the synthesis of some interesting and useful materials. [141, 187, 191–194] In particular, Clearfield and co-workers [141, 187, 193] prepared a series of layered materials by partially deprotonating H_4pmida , leaving a carboxylic acid group which, on the one hand, allows intercalation of amines and, on the other, forms 3D compounds with diamines. Mixed derivatives containing HPO_4^{2-} moieties which led to the isolation of a family of mixed-ligand layers, were also reported by the same authors. [141, 187, 193] More recently, the first 3D mixed-metal frameworks incorporating H_4pmida residues and 4,4'-bipyridine have been isolated. [195] The model hybrid compound studied here is $(C_4H_{12}N_2)[Ge_2(pmida)_2(OH)_2]4H_2O$, which contains the anionic unit $Ge_2(pmida)_2(OH)_2^{2-}$, closely related to the $[V_2O_2(pmida)_2]^{4-}$ unit. The former, is particularly convenient because it is amenable to NMR studies as it contains no paramagnetic centres (such as V^{4+}) and has the spectroscopically useful nuclei 1H , ^{13}C , and ^{31}P available. As with many hybrid compounds, the solid studied here contains protons in the organic and inorganic components and, thus, the attribution of the 1H NMR resonances is not trivial and requires high-resolution spectra. For this purpose, the FS-LG homonuclear decoupling pulse sequence was used, inserted in the 2D HETCOR and HOMCOR experiments as stated in section 4.6. These 2D experiments overcome the difficulties posed by conventional SSNMR techniques, such as MAS and Cross-Polarisation (CP-MAS), which afford poorly resolved spectra, mainly due to the presence of strong 1H - 1H dipolar interactions

which broaden the resonances.

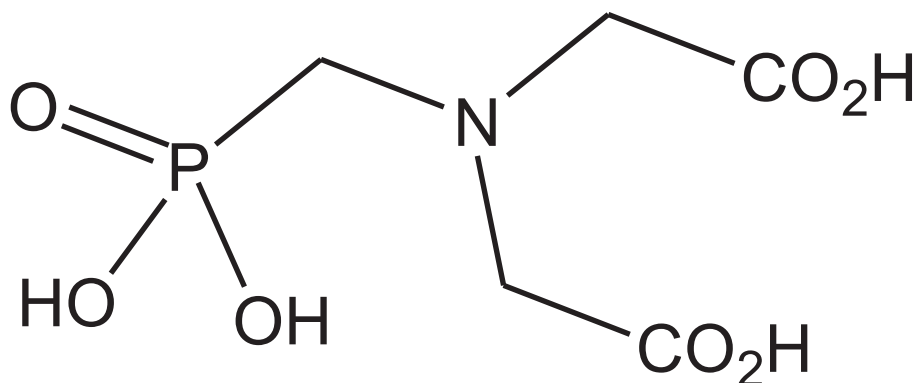


Fig. 8.1: N-(phosphonomethyl)iminodiacetic acid (H_4pmida).

8.1.1 Experimental Section

Synthesis Method

The following synthesis work was performed by Dr. Fa-Nian Shi from the Chemistry Department, University of Aveiro, Portugal.

A suspension containing *N*-(phosphonomethyl)iminodiacetic acid hydrate (0.590 g, H_4pmida , $C_5H_{10}NO_7P$, 97%, Fluka), amorphous germanium(IV) oxide (0.280 g, GeO_2 , 99.99+%, Aldrich), and anhydrous piperazine (0.090 g, $C_4H_{10}N_2$, $\geq 98\%$, Merck-Schuchardt) in distilled water (approximately 4 g) was stirred thoroughly for 30 min at ambient temperature. The resulting homogeneous suspension was transferred to the reaction vessel which was placed inside an oven. The temperature was gradually increased to 140 °C and, after four days, was again increased to 180 °C, where it remained for 24 h. The reaction vessel was allowed to cool slowly to ambient temperature before opening. The resultant colourless solution was carefully transferred to a glass container and allowed to evaporate slowly. After one day, a large quantity of colourless crystals were manually harvested, washed with distilled water, and air dried for single-crystal XRD analysis. An alternative synthesis method is to perform the reaction at a fixed temperature of 100 °C over a period of four days, after which a phase-pure microcrystalline compound can be directly obtained from the autoclave.

Chemicals were readily available from commercial sources and were used as received without further purification. Syntheses were carried out in PTFE-lined stainless-steel reaction vessels (10 mL), under autogeneous pressure and static conditions. The final compound proved to be air- and light-stable, and insoluble in water and common organic solvents.

Routine Measurements

FTIR Assignments: Selected IR data (Raman in italics inside the parentheses): $\nu(O-H, \text{ in lattice water})$ and $\nu(GeO-H)=3509$ (vs) and 3409 (vs) cm^{-1} , $\nu_{asym}(-NH_2^+)=3314$ (vs) cm^{-1} , $\nu_{sym}(-NH_2^+)=3214$ (vs) cm^{-1} , $\nu_{asym}(C-H \text{ in } -CH_2-)=3052$ (s) and 3015 (s); $\nu_{sym}(C-H \text{ in } -CH_2-)=2981$ (s) and 2963 (s) (*2988* and *2965*); $\nu(N^+-H)=2740$ (m), 2600 (m), and 2460(m) (various modes); $\nu(C=O)=1724$ (vs) (*1727*); $\nu_{asym}(-CO_2-)=1675$ (vs) (*1677*); $\delta(-NH_2^+)=1611$ (m); $\tau(-CH_2)=1463$ (m) (*1465*); $\delta(-CH_2-)=1429$ (m) (*1434*) cm^{-1} ; $\nu_{sym}(-CO_2-)=1352$ (vs) (*1351*); $\delta(O-HO)=1333$ (s) (*1335*); $\nu(P=O)=1310$ (m) (*1314*) cm^{-1} ; $\nu(C-O)=1288$ (m) and 1270(m) (*1286* and *1270*); $\delta(C-C-N, \text{ amines})=1177$

(vs) (1181) cm^{-1} ; $\nu(\text{N—C})=1093(\text{m})$ and $1077(\text{s})$ (1092 and 1070); $\nu(\text{P—O})=1046(\text{vs})$ (1044); $\text{g}(\text{O—HO})=916(\text{s})$ (919); $\nu(\text{P—C})=782(\text{vs})$ (788); $\gamma(\text{C=O})=754(\text{s})$ and $747(\text{s})$ (743); $\rho[(\text{C=O})\text{—O}]$ 530(m) and 596(m) (535 and 599); $\delta(\text{C—N—C, amines})=455(\text{m}) \text{cm}^{-1}$.

TG data (weight losses and increases) and **DTG**; in italics inside the parentheses: in air: 50–140 °C -9.6% (77 and 97 °C); 330–420 °C -26.5% (385 and 401 °C); 420–670 °C -10.5% (continuous weight-loss); 670–800 °C -11.2% (690 °C); in nitrogen: 45–123 °C -9.4% (72 and 97 °C); 340–425 °C -28.4% (382 and 407 °C); 425–620 °C -6.7% (continuous weight-loss); 620–700 °C -3.3% (630 °C); 700–800 °C -8.1% (730 °C); **DSC peaks** (endothermic processes): 132, 381, and 393 °C.

EA Based on single-crystal data: EA calc (%) for $\text{C}_{14}\text{H}_{34}\text{Ge}_2\text{N}_4\text{O}_{20}\text{P}_2$ ($M_r=785.57$): C 21.41, N 7.16, H 4.36; found: C 20.61, N 6.98, H 4.40.

X-ray Crystallography Measurements

The following work was carried out in collaboration with Dr. F. Paz from the Chemistry Department, University of Aveiro.

A suitable single-crystal was mounted on a glass fibre with Araldite Rapide, [196] and positioned at approximately 62.25 mm from a KM4CCD/Sapphire charge-coupled device (CCD) area detector. 600 frames at 1.0° intervals were measured with a counting time of 15 s per frame. Two further standard frames for each 150 frames collected were monitored and these showed no significant intensity decrease over the data collection period.*

All non-hydrogen atoms were directly located from difference Fourier maps and refined, when possible, using anisotropic displacement parameters. Hydrogen atoms bound to the nitrogen atom of the crystallographically unique piperazinedium cation were directly located from difference Fourier maps, and refined with a common N–H length restrained to 0.90(1) Å (the H···H distance was further restrained to 1.47(1) Å to ensure a chemically reasonable geometry for this moiety), and an isotropic displacement parameter fixed at 1.5 times U_{eq} of the nitrogen atom to which they are attached. Hydrogen atoms from water molecules were directly located from successive difference Fourier maps, and refined with the O–H length and H···H distance restrained to 0.86(1) Å and 1.40(1) Å, respectively (to ensure a chemically reasonable geometry for these molecules), and using a riding model with an isotropic displacement parameter fixed at 1.5 times U_{eq} of the atom to which they are attached. The hydrogen atom associated with the coordinated –OH group to Ge(1) could also be directly located from successive difference Fourier maps, but instead its position was geometrically restrained by using the HFIX 83 instruction in SHELXL. [198] Hydrogen atoms attached to carbon were located at their idealised positions by using the HFIX 23 instruction in SHELXL, [198] and were included the refinement in the riding-motion approximation with an isotropic thermal displacement parameter fixed at 1.2 times U_{eq} of the carbon atom to which they are attached. It is important to emphasise that the positions for the hydrogen atoms do not reflect the true position of the hydrogen nuclei. The last difference Fourier map synthesis showed the highest peak ($0.490 \text{ e}\text{\AA}^{-3}$) located at 1.37 Å from O(7), and the deepest hole ($-0.455 \text{ e}\text{\AA}^{-3}$) at 0.82 Å from Ge(1). Information concerning crystallographic data collection and structure refinement details are summarised in Table 8.1. Selected bond lengths and angles for the binuclear anionic $[\text{Ge}_2(\text{pmida})_2(\text{OH})_2]^{2-}$ complex are given in ref. [107]. Hydrogen bonding geometry

*The structure was solved by the direct methods of SHELXS-97, [197] and refined by full-matrix least-squares on F^2 using SHELXL-97. [198]

Table 8.1: Crystal data and structure refinement information

formula	$C_{14}H_{34}Ge_2N_4O_{20}P_2$
formula weight	785.57
crystal system	monoclinic
space group	C2/c
a [Å]	12.417(3)
b [Å]	10.091(2)
c [Å]	21.160(4)
β [°]	90.93(3)
volume[Å ³]	2651.0(10)
Z	4
ρ_{calcd} [gcm ⁻³]	1.968
$\mu(MoK\alpha)$ [mm ⁻¹]	2.488
F(000)	1600
crystal size[mm]	0.26x0.21x0.21
crystal type	colourless prisms
θ range	3.78 to 26.02
	$-15 \leq h \leq 15$
index ranges	$-12 \leq h \leq 12$
	$-25 \leq h \leq 26$
reflections collected	12072
independent reflections	2603 ($R_{int} = 0.0360$)
final R indices [$I > 2\sigma(I)$]	$R_1=0.0271$ $wR_2=0.0678$
final R indices (all data)	$R_1=0.0323$ $wR_2=0.0699$
largest diff. peak and hole[eÅ ⁻³]	0.490 and -0.455

is described in Table F.2. CCDC-249364 contains the supplementary crystallographic data[†] (excluding structure factors).

NMR Measurements

General: 2D ¹H{FS-LG}-³¹P HETCOR and ¹H{FS-LG}-¹H HOMCOR experiments were performed using 4mm volume restricted rotors, while 2D ¹H{FS-LG}-¹³C HETCOR were performed on a nonrestricted rotor for reasons of sensitivity.

Efficient heteronuclear decoupling between ¹³C/³¹P and ¹H nuclei was achieved by using the two-pulse phase-modulated (TPPM) [124, 125] decoupling scheme during ¹³C and ³¹P spectral acquisition, with pulse lengths of 4.2 ms (ca. 165° pulses), a phase modulation angle of 15°, and a ¹H rf field strength $\omega_1/2\pi$ (nutating frequency) \approx 100 kHz. Ramped-Amplitude Cross-Polarization (RAMP-CP) [199] was used to transfer magnetisation from ¹H to ¹³C/³¹P. RAMP-CP improves the HH matching condition and the efficiency of the CP step which are known to be very sensitive to rf power instabilities at high MAS rates. With this technique the CP matching profile is less dependent on the MAS rate and, thus, more easily adjustable and maintainable at optimum HH matching for magnetisation transfer. The CSs are quoted

[†]These data can be obtained free of charge from the Cambridge Crystallographic Data Centre via www.ccdc.cam.ac.uk/data_request/cif.

in ppm from TMS or H₃PO₄ (85%) for ¹H, ¹³C, or ³¹P.

¹H MAS NMR spectroscopy: Spectra were collected with a spinning rate of 30 kHz, a 90° pulse length of 1.6 μs and a 2 s recycle delay.

¹³C and ³¹P CP-MAS NMR spectroscopy: A RAMP-CP step with a spinning rate of 12 kHz and 15 kHz for ¹³C and ³¹P respectively, was employed with standard phase cycling, with a 90° pulse length of 3 μs for ¹H. Contact times were varied between 50 μs and 2 ms. Recycle delays employed were 5 s and 6 s for ¹³C and ³¹P, respectively. A ¹³C CP-MAS spectrum was also recorded at a static magnetic field of 500 MHz using a 90° pulse length of 3.75 μs and a ¹H nutation frequency ($\omega_1/2\pi$) of 66 kHz.

2D NMR Spectroscopy: 2D ¹H{FS-LG}-X(³¹P,¹³C) HETCOR and 2D ¹H{FS-LG}-¹H HOMCOR experiments were performed by using the pulse sequence (and phase cycling scheme) described in section 4.8. The former was adapted from the sequence described by van Rossum and co-workers (see Fig. 4.7). [122]

The phase switching time between each LG pulse was previously optimized by monitoring the multiplet- fine structure of adamantane. Before each LG pulse, the frequency offset was alternated between + $\Delta\nu_{LG}$ and - $\Delta\nu_{LG}$ (Table 8.2). Best results were obtained using asymmetric LG offsets, + $\Delta\nu_{LG} + \nu_{lg}$ and - $\Delta\nu_{LG} + \nu_{lg}$, in the FS-LG decoupling blocks. [200] ν_{lg} was added to these frequency jumps, and optimised in order to shift the spectrum out of the axial artifact at the middle of F1 dimension. Each FS-LG block encompasses two successive LG pulses with duration τ_{LG} (Table 8.2).

The phase switching between each LG pulse was optimized by monitoring the multiplet-fine structure of adamantane.

Quadrature detection in t_1 was achieved by using the States-TPPI method. [38] In theory, under FS-LG decoupling, the proton CS is scaled by $1/\sqrt{3}$ (0.57). For the FS-LG HOMCOR/HETCOR schemes, the ¹H CS scale and the scaling factors λ were determined by comparing the 1D ¹H spectrum (See Fig. F.1) recorded under fast MAS (30 kHz) and the ¹H{FS-LG}-¹H HOMCOR spectrum. [201] Scaling factors in the 0.50-0.58 range were obtained for all spectra, which is close to the theoretical value. [202] Further incorporation of a z-filter [203] delay was implemented, which ensures that pure absorption-mode line shapes are obtained (Fig.4.7c). Experimental parameters are summarised in Table 8.2.

8.1.2 Results and Discussion

Structure Description

The reaction between H₄pmida, germanium(iv) oxide and piperazine in aqueous media led to the formation of a highly crystalline product which was formulated as (C₄H₁₂N₂)[Ge₂(pmida)₂(OH)₂]₄H₂O (**I**, where pmida⁴⁻=*N*-(phosphonomethyl) iminodiacetate) on the basis of single-crystal XRD (Table 8.1) and EA. The phase-purity and homogeneity of the bulk sample were further confirmed by direct comparison of the experimental powder XRD pattern and a simulation based on single-crystal data (Fig. F.3). As predicted, the compound contains an anionic binuclear complex, [Ge₂(pmida)₂(OH)₂]²⁻, sharing similarities with the typical anionic [V₂O₂(pmida)₂]⁴⁻ units containing V⁴⁺ centres previously reported (Fig. F.2). [191,195] The pmida⁴⁻ ion appears as a polydentate organic ligand which, in a way very similar to that observed for the V⁴⁺ centres in [V₂O₂(pmida)₂]⁴⁻, completely traps the Ge⁴⁺ inside three distinct five-membered chelate rings formed by the two carboxylate and the phosphonate groups connected in a typical anti-unidentate coordinative fashion. The average bite angle is approximately 84.2° (Table 3), a value significantly higher than those registered for the [V₂O₂(pmida)₂]⁴⁻ units (ca. 76-77°). [191, 195] Such an occurrence can be explained by taking the distorted octahedral coordination environment of the single Ge⁴⁺ centre (GeNO₅) into

Table 8.2: $2D\ ^1H\{FS-LG\}^{-31}P/\ ^{13}C\ HETCOR$ and $^1H\{FS-LG\}^{-1}H\ HOMO\ COR$ experimental parameters for H_4pmida and compound **I**.

Experimental parameters	$^1H\text{-}^{31}P\ HETCOR$		$^1H\text{-}^{13}C\ HETCOR$		$^1H\text{-}^1H\ HETCOR$
	H_4pmida	I	H_4pmida	I	both
number of t_1 points	200	200	128	80	172
dwell times ($t_1 \times t_2$) [μs]	$8t_{LG} \times 24.8$	$8t_{LG} \times 24.8$	$6t_{LG} \times 24.8$	$8t_{LG} \times 24.8$	$8t_{LG} \times 12.4$
recycle delay [s]	4	4	5	5	3
MAS rate [kHz]	12	12	12	12	10
contact time [μs]	50-2000	50-2000	50-2000	50-2000	-
1H offset frequency [kHz]	+2.5	+2.5	+2.5	+2.5	+4
FS-LG decoupling power [kHz]	100	83.3	83.3	83.3	83.3
FS-LG period, t_{LG} [μs]	8.2	9.8	9.8	9.8	9.8
frequency switching time [μs]			0.6		
positive offset frequency ($+\Delta\nu_{LG}$) ^a [Hz]	73710	65925	61925	61925	63925
negative offset frequency ($-\Delta\nu_{LG}$) ^a [Hz]	-67710	-52925	-55925	-55925	-54925

^aThese parameters refer to the frequency jumps of $\pm\nu_i/\sqrt{2}$ ($\pm\Delta\nu_{LG}$) between each LG period (see section 4.7, Fig. 4.9.2, pulse sequences)

account (octahedral angles within the 82.28(7)-100.28(8)° and 167.77(7)-172.61(8)° ranges; Table F.5 and Fig. 8.2).

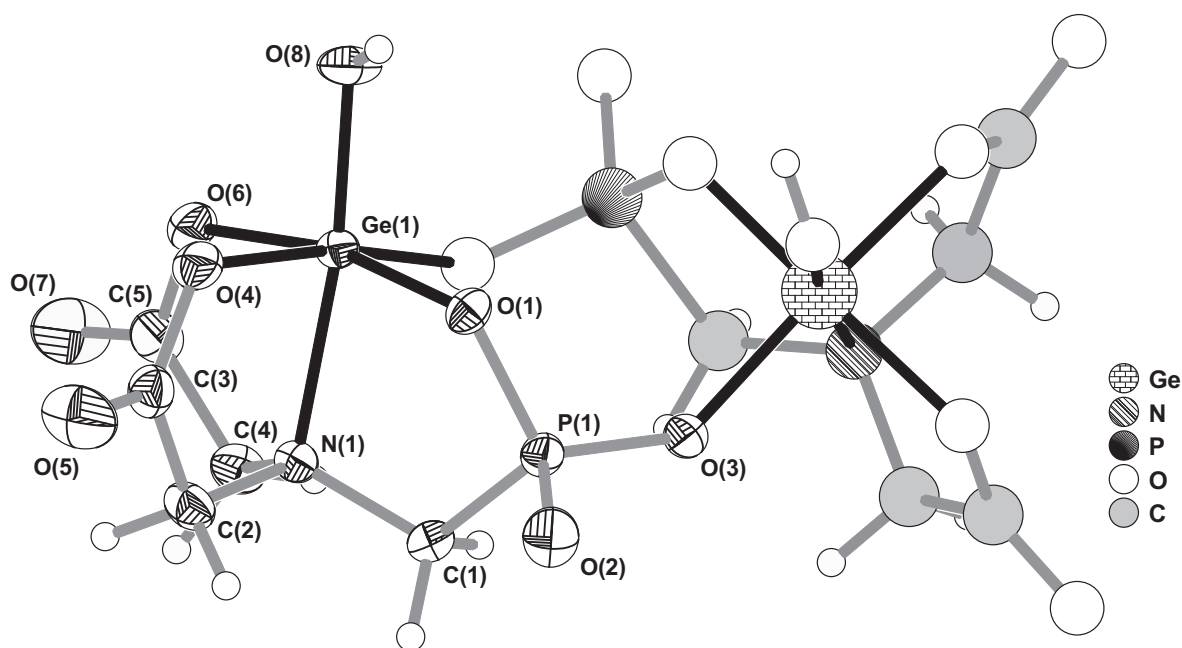


Fig. 8.2: Ball-and-stick representation of the binuclear anionic $[\text{Ge}_2(\text{pmida})_2(\text{OH})_2]^{2-}$ complex showing the labelling scheme for all non-hydrogen atoms belonging to the asymmetric unit. Displacement ellipsoids are drawn at the 50% probability level and hydrogen atoms are shown as small spheres.

In fact, although the V^{4+} and Ge^{4+} centres in the anionic $[\text{V}_2\text{O}_2^-(\text{pmida})_2]^{4-}$ and $[\text{Ge}_2(\text{pmida})_2(\text{OH})_2]^{2-}$ complexes, respectively, are almost identically coordinated to two pmida^{4-} ligands, in the former case the apical position is occupied by an oxo ligand ($\text{V}=\text{O}$), which has a significant *trans* effect in the $\text{V}-\text{N}$ length; [204] in **I**, the Ge^{4+} centre is, instead, coordinated to a hydroxo group ($\text{Ge}-\text{OH}$, 1.767(2) Å; Fig. 8.2) having a smaller *trans* effect than the oxo ligand, leading to a $\text{Ge}-\text{N}$ distance (2.089(2) Å) which is comparable to those observed for the equatorial $\text{Ge}-\text{O}$ bonds (within the 1.868(2)-1.930(2) Å range). Ultimately, the distance-shift of the Ge^{4+} centre from the equatorial plane, ca. 0.18 Å, is smaller than that usually observed for the V^{4+} metal centre, approximately 0.350.39 Å. [191, 195] All $\text{Ge}-\text{O}$, $\text{Ge}-\text{OH}$ and $\text{Ge}-\text{N}$ bond distances are well within the expected ranges found in related compounds. [204–211] As previously mentioned, and in a very similar way to that observed in the $[\text{V}_2\text{O}_2(\text{pmida})_2]^{4-}$ binuclear moieties, the two crystallographically independent carboxylate groups appear coordinated to the Ge^{4+} centre in a typical anti-unidentate coordination fashion but, in this case, the $\text{C}-\text{O}$ bonds do not remain equivalent upon coordination. In fact, there is clear crystallographic evidence for distinct $\text{C}-\text{O}$ bond lengths for the two carboxylate groups ($\text{C}(3)-\text{O}(4)$ 1.309(3), $\text{C}(3)-\text{O}(5)$ 1.214(3), $\text{C}(5)-\text{O}(6)$ 1.317(3), $\text{C}(5)-\text{O}(7)$ 1.202(3) Å). Furthermore, the uncoordinated $\text{C}-\text{O}$ bonds are also significantly affected by thermal disorder as seen in Fig. F.2: for a 50% probability level the elliptical vibration of the oxygen atoms is much larger than that observed for the neighboring atoms. In fact, although the hydrogen bonding network present in compound **I** involves several very strong and highly directional interactions (see below), these are predominantly orientated towards the coordinated $\text{C}-\text{O}$ bond. With one uncoordinated $\text{C}-\text{O}$ bond (belonging to the $\text{C}(3)$ carboxylate group) there is a single homonuclear $\text{O}-\text{H}\cdots\text{O}$ interaction, and the $\text{C}-\text{O}$ bond from the $\text{C}(5)$ carboxylate group is

not engaged in any type of hydrogen bonding interaction.

As observed for the anionic $[\text{V}_2\text{O}_2(\text{pmida})_2]^{4-}$ complexes, the phosphonate group from the crystallographically unique pmida^{4-} ligand establishes physical bridges between adjacent germanium centres (through the O(1) and O(3) atoms), ultimately leading to the formation of the binuclear $[\text{Ge}^{2-}(\text{pmida})_2(\text{OH})_2]^{2-}$ unit and imposing a $\text{Ge}(1)\cdots\text{Ge}(1)^i$ separation of 4.612(2) Å (symmetry code: $i: 2 - x, y, 1/2 - z$). However, there is a striking crystallographic difference between the two complexes concerning local symmetry: while $[\text{V}_2\text{O}_2(\text{pmida})_2]^{4-}$ is generated by a centre-of-inversion positioned at its centre of gravity (Fig. F.2a), $[\text{Ge}_2(\text{pmida})_2(\text{OH})_2]^{2-}$ is formed by a two-fold axis operation symmetry (Fig. F.2b and Fig. 8.2). As a direct consequence, in this complex the two Ge–OH bonds are pointing in the same direction with respect to the plane containing the two neighbouring Ge^{4+} centres (torsion angle of about 68°; F.2a and Fig. 8.2). Furthermore, in the $[\text{Ge}_2(\text{pmida})_2(\text{OH})_2]^{2-}$ complex the two pmida^{4-} anionic ligands are also closer to each other with an $\text{N}(1)\cdots\text{N}(1)^i$ separation of 5.574(4) Å (symmetry code: $i: 2 - x, y, 1/2 - z$) as compared to the smaller values (approximately 5.9 Å) usually observed for the $[\text{V}_2\text{O}_2(\text{pmida})_2]^{4-}$ moiety. [191, 195]

The charge of the anionic complex is compensated by the presence of piperazinedium cations, $\text{C}_4\text{H}_{12}\text{N}_2^{2+}$, which, along with the two water-of-crystallisation molecules, exhibit strong and highly directional hydrogen bonds with the anionic $[\text{Ge}_2(\text{pmida})_2(\text{OH})_2]^{2-}$ complexes (Fig. 8.3 and 8.4, Table F.1). On the one hand, each water molecule acts as a bifurcated donor establishing links between adjacent germanium complexes (Fig. 8.3); on the other hand, while O(1W) accepts the hydrogen atom from the coordinated hydroxo group (Fig. 8.3a), O(2W) is involved in a very strong heteronuclear $\text{N}^+\text{-H}\cdots\text{O}$ interaction with the neighbouring piperazinedium cation (8.3b). It is also interesting to note that the other strong $\text{N}^+\text{-H}\cdots\text{O}$ hydrogen bond is with the $[\text{Ge}_2(\text{pmida})_2(\text{OH})_2]^{2-}$ complex, leading to the formation of a $\text{R}_3^3(8)$ graph set motif (Fig. 8.3b) [212] which further increases the robustness of the crystal structure.

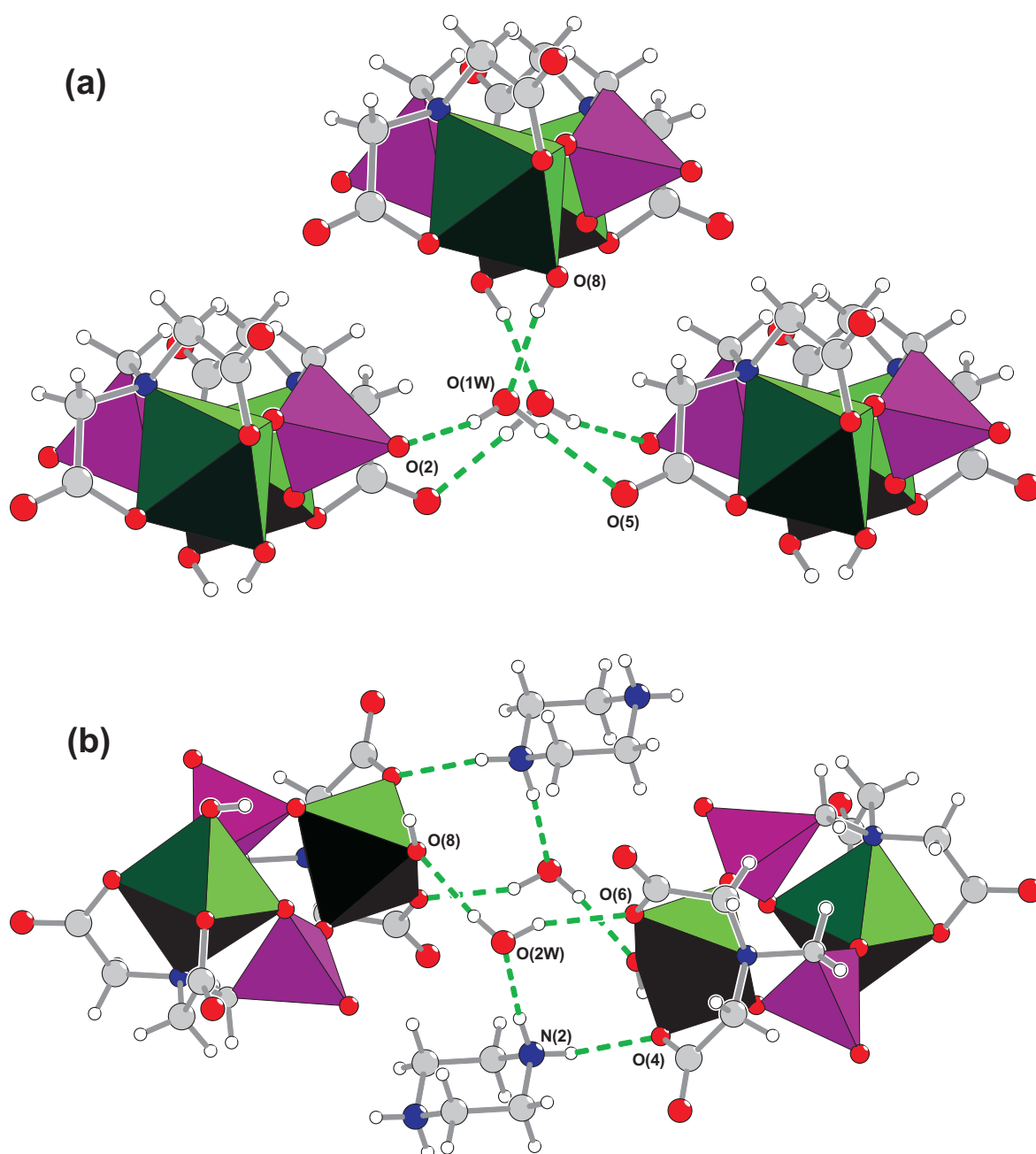


Fig. 8.3: Hydrogen-bonding environment of the crystallisation water molecules: (a) O(1W) and (b) O(2W) (for hydrogen-bonding geometry see Table F.1). Each binuclear anionic $[\text{Ge}_2(\text{pmida})_2(\text{OH})_2]^{2-}$ complex is represented by polyhedra for the germanium and phosphorous centres (octahedron and tetrahedron, respectively). Symmetry transformations used to generate equivalent atoms have been omitted for clarity.

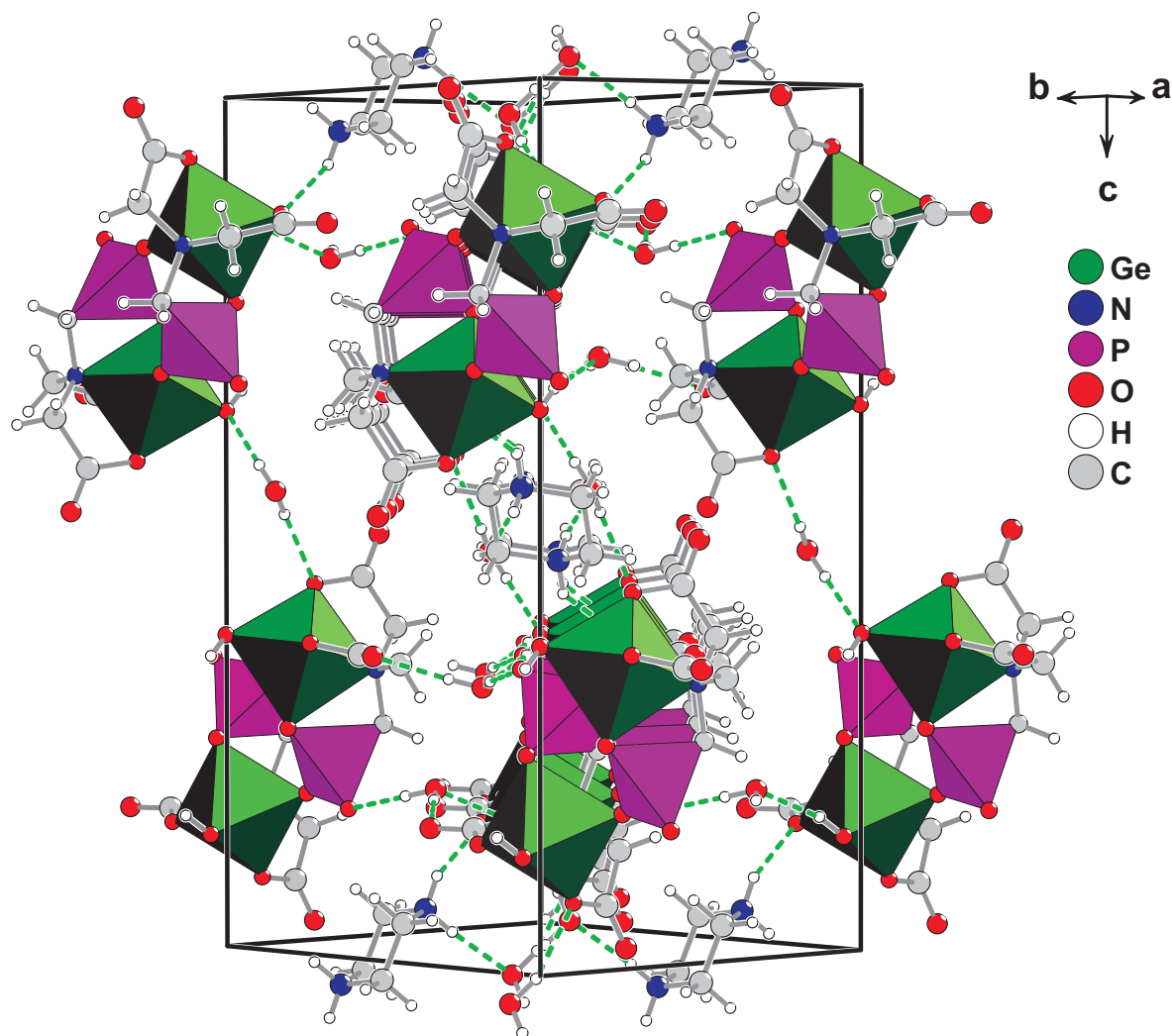


Fig. 8.4: Perspective view of the unit cell contents. Hydrogen bonds are represented as green dashed lines (for hydrogen-bonding geometry see Table F.1).

NMR Analysis

^{13}C CP-MAS NMR: The ^{13}C CP-MAS spectra of H_4pmida and $(\text{C}_4\text{H}_{12}\text{N}_2)[\text{Ge}_2(\text{pmida})_2(\text{OH})_2]4\text{H}_2\text{O}$ (**I**) are shown in Fig. 8.6. The peak centred at ca. 41 ppm is attributed to the piperazinedium cations. The C(1)–C(5) resonances of compound **I** are shifted to high frequency relative to those of the H_4pmida ligand (Fig. 8.6), and this is attributed to the coordination of the H_4pmida ligand to the Ge^{4+} centres, which decreases the electron density of the ^{13}C atoms. The combined effect of Ge^{4+} coordination and hydrogen bonding to the piperazinedium cations and water molecules is reflected in the ^{13}C CSs which result in a larger separation of the $-\text{CH}_2-\text{CO}_2^-$ resonances (Fig. 8.6 and Fig. 8.5): CSs of ca. 0.7 and 0.2 ppm for CH_2 groups (C(2), C(4)) and $-\text{CO}_2^-$ groups (C(3), C(5)) in the free ligand, and ca. 2.9 and 3.2 ppm for the complex (Fig. 8.6). Although the crystal structure of compound **I** calls for a single C(1) site, the ^{13}C CP-MAS spectrum displays two resonances (Fig. 8.6b-d). This splitting (approximately 140 Hz) is attributed to J -coupling interaction, $^1J_{\text{C}(1),\text{P}(1)}$, an assumption supported by: (i) the ^{13}C NMR spectrum of the free ligand in DMSO (not shown),

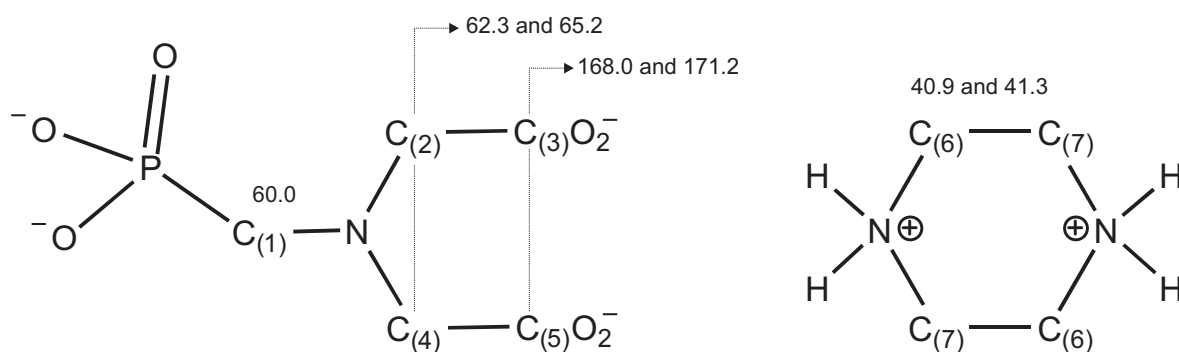


Fig. 8.5: Assignment of the $^{13}\text{C}\{^1\text{H}\}$ CP-MAS resonances of compound **I**. CSs are quoted in ppm (spectra in Fig. 8.6b-c).

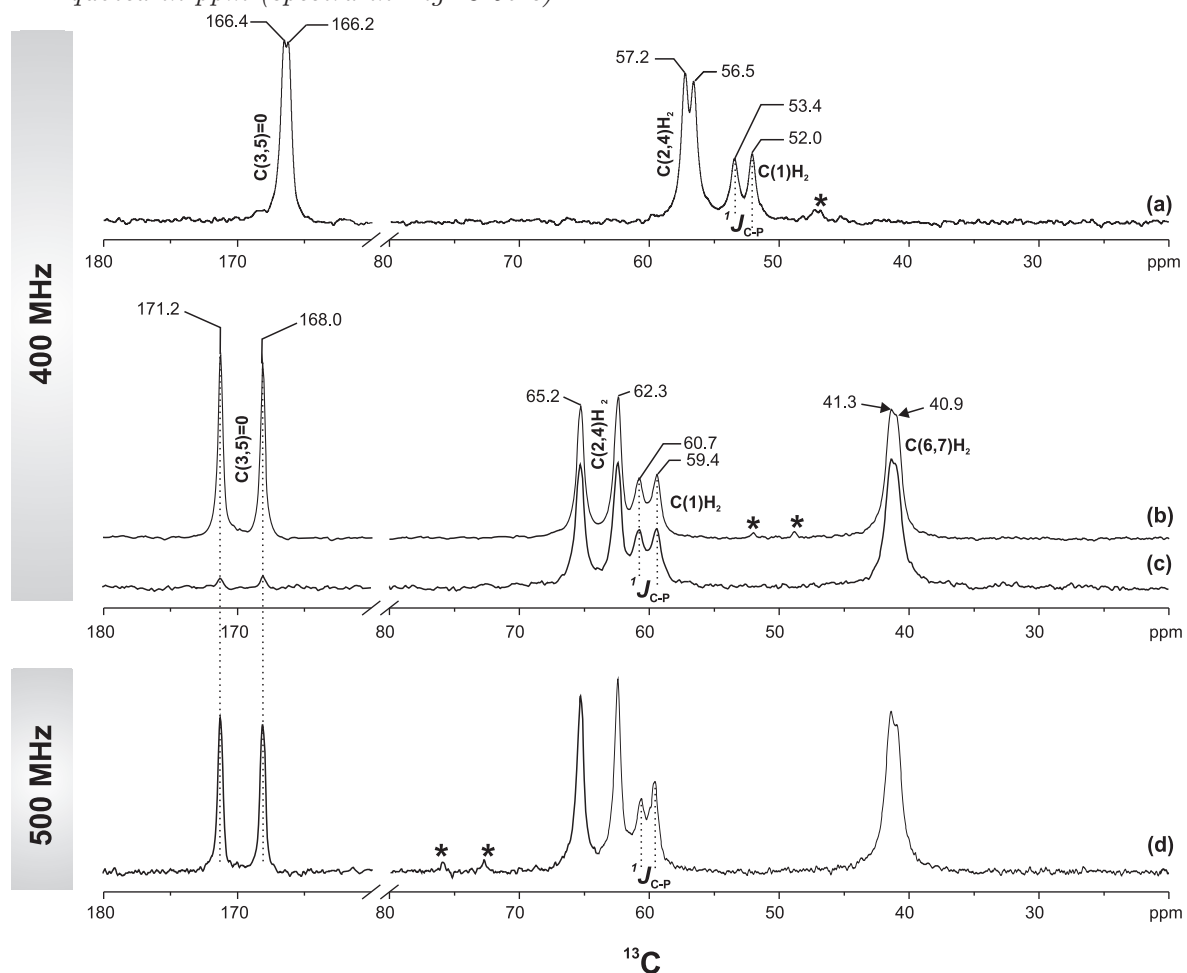


Fig. 8.6: ^{13}C CP-MAS spectra of: (a) H_4pmida ligand with a contact time (τ_{CT}) of $1500 \mu\text{s}$ recorded at 9.4 T ; compound **I** with a τ_{CT} of (b) $2000 \mu\text{s}$ and (c) $100 \mu\text{s}$ recorded at 9.4 T ; (d) compound **I** with a τ_{CT} of $2000 \mu\text{s}$ recorded at 11.4 T . Asterisks depict the spinning sidebands of the isolated $\text{C}=\text{O}$ groups.

which shows a splitting of approximately 150 Hz, and (ii) the ^{13}C CP-MAS spectrum recorded at the higher field of 500 MHz (Fig. 8.6d), which reveals a splitting of about 140 Hz (within experimental error). Typical $^1J_{\text{C,P}}$ couplings are in the 5 to 90 Hz range, [213,214] and spin multiplets are usually not observed in the solid state. A possible reason for observing J -coupling for the H_4pmida ligand and compound **I** is the close proximity of both the electronegative atom N(1) and an electron-withdrawing phosphonate group, leading to a substantial increase of the 1J coupling magnitude.

^{31}P CP-MAS NMR: A comparison of the ^{31}P CP-MAS spectra of H_4pmida and compound **I** shows that upon Ge^{4+} coordination the ^{31}P resonance shifts ca. 6 ppm to lower frequency and broadens (full-width-at-half-maximum, FWHM) from 87 (H_4pmida) to 152 Hz (Fig. 8.7). It was noticeable that the H_4pmida CS measured here (ca. 13.1 ppm) differs from the value ca. 14.8 ppm reported by Khizbullin and coworkers. [215]

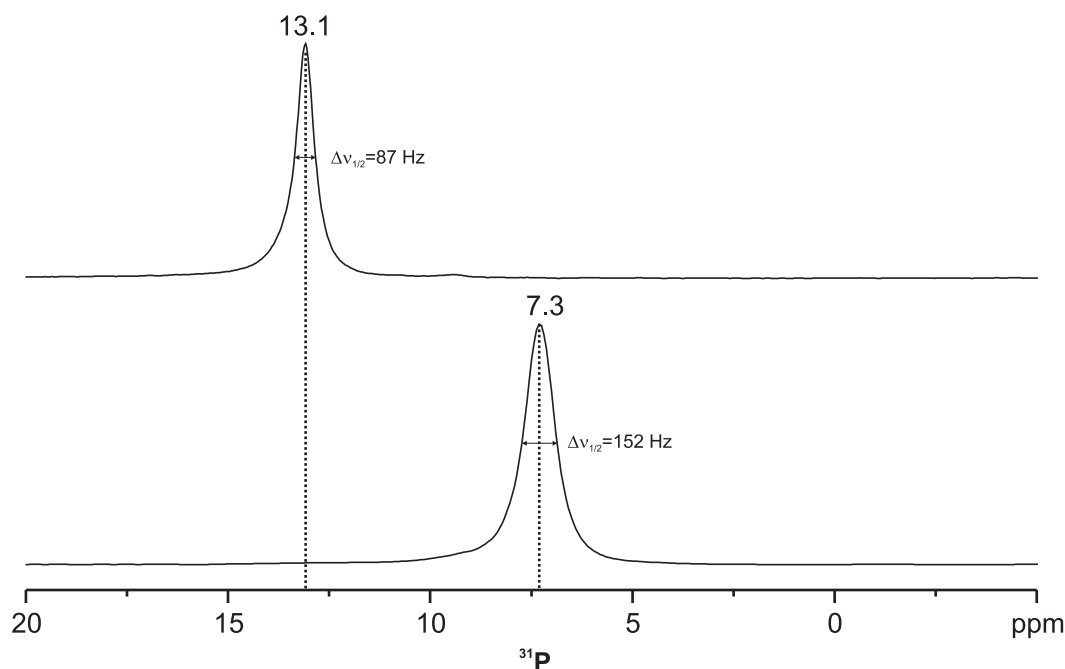


Fig. 8.7: $^{31}\text{P}\{-^1\text{H}\}$ CP-MAS spectra of (top) H_4pmida and (bottom) **I** recorded at 161.97 MHz with a spinning rate of 15 kHz.

2D FS-LG experiments: Strong homonuclear dipolar couplings do not usually allow resolution of different resonances using the conventional MAS technique. To improve ^1H spectral resolution, FS-LG HOMCOR/HETCOR dipolar correlation techniques were used. The $^1\text{H}\{\text{FS-LG}\}^1\text{H}$ HOMCOR spectra of H_4pmida and compound **I** display five and three resolved resonances (Fig. 8.8), respectively. The peak at ca. 8.7 ppm in the spectrum of compound **I** is attributed to the protonated amines of $\text{C}_4\text{H}_{12}\text{N}_2^{2+}$ (Fig. 8.8b). [216]

The 2D $^1\text{H}\{\text{FS-LG}\}^1\text{H}$ HOMCOR spectra of compound **I** and H_4pmida show some similarity in the ca. 3.0-5.5 ppm range (Fig. 8.8), although the intensities of the two resonances (a, b) in this region differ. This is due to the presence of an additional organic molecule in **I** (piperazinedium cations) containing CH_2 groups [$\text{C}=\text{C}(6,7)$], which also contribute to the intensity of the H(6A), H(6B), H(7A), and H(7B) proton resonances in this spectral region. Because H_4pmida and **I** are hydrated, and the ^1H CS of water molecules is usually in the

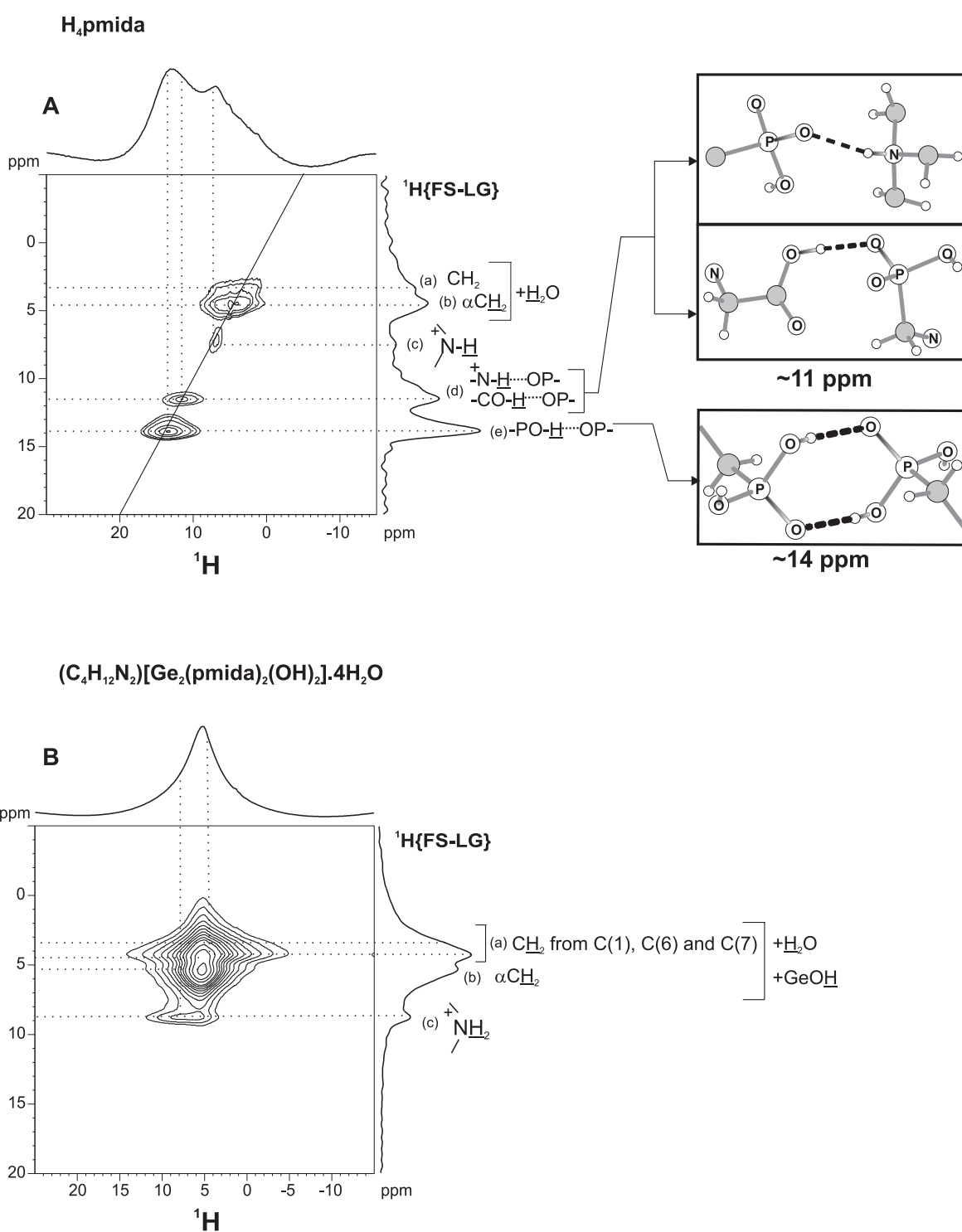


Fig. 8.8: $2D$ $^1\text{H}\{\text{FS-LG}\}\text{-}^1\text{H}$ HOMCOR spectra of (a) H_4pmida and (b) compound **I**

range ca. 4.9-5.2 ppm, the assignment of ^1H resonances in the CH_2 region becomes even more difficult.

For compound **I** the attribution of the $^+\text{N}-\text{H}$ bond resonance was straightforward, whereas this was not the case for H_4pmida , which crystallises in its zwitterionic form, with individual molecular units being involved in several hydrogen bonding patterns ($\text{P}-\text{O}-\text{H}\cdots\text{O}-\text{P}$, $\text{C}-\text{O}-\text{H}\cdots\text{O}-\text{P}$, and $\text{N}^+-\text{H}\cdots\text{O}-\text{P}$, with the latter not represented in Fig. 8.8a). [217] Neighboring molecular units are strongly interconnected by a stable dimer involving two $\text{P}-\text{O}-\text{H}\cdots\text{O}-\text{P}$ interactions (a typical $\text{R}_2^2(8)$ graph set motif). [212] Since hydrogen atoms involved in the $\text{P}-\text{O}-\text{H}\cdots\text{O}$ interactions are generally less shielded than those in $\text{C}-\text{O}-\text{H}\cdots\text{O}$ or $\text{N}^+-\text{H}\cdots\text{O}$ units, the resonances are shifted to higher frequencies. [218] Hence, the peaks at ca. 13.8 and 11 ppm are assigned to $\text{P}-\text{O}-\text{H}$ and $\text{CO}-\text{H}/\text{N}^+-\text{H}$, respectively (Fig. 8.8a). The presence of a resonance at ca. 7.5 ppm (Fig. 8.8a, peak c) supports the assumption that H_4pmida is in the zwitterionic form because it appears in the typical range for protonated amines.

It was difficult to assign the resonances given by the chemically similar CH_2 groups (ca. 3.0-5.5 ppm region) present in compound **I** and H_4pmida . To help solve this problem, $^1\text{H}\{\text{FS-LG}\}-^{13}\text{C}/^{31}\text{P}$ HETCOR spectra were recorded. By manipulating the mixing time and monitoring the intensity of the cross-peaks in a $^1\text{H}\{\text{FS-LG}\}-^{13}\text{C}$ HETCOR experiment it is, in principle, possible to differentiate between ^1H atoms directly bonded to a given ^{13}C atom from those which are at longer distances. Although FS-LG homonuclear decoupling greatly reduces the spin diffusion, during the CP step the homogeneous broadening (flip-flop terms) is partially reintroduced, and degrades the spectral resolution. [43] If relaxation effects are neglected, there are two main ways to minimise spin-diffusion effects during the CP: *(i)* ^1H magnetisation transfer using LG-CP; [219-221] *(ii)* the more classical approach in which very short mixing times are employed. The latter method (mixing times of 50-200 μs) is used here due to its easy implementation.

At long contact times (2000 μs), cross-peaks are observed between all ^1H and ^{13}C resonances in the H_4pmida spectrum (Fig. 8.9). The shoulder at approximately 3.5 ppm F1 (Fig. 8.9, peak a) is assigned to the ^1H atoms bonded to C(1) [H(1A), H(1B)] because they are more shielded than the αCH_2 . By employing τ_{CT} of 100 μs , cross-peaks of ^1H involved in hydrogen bonds disappear. In addition, the cross-peaks with carboxylic ^{13}C (closest protons at approximately 2.5 Å) are also absent. At present, it is not possible to explain why C(1) cross-peaks disappear almost completely. At short contact times it is possible to distinguish the H(2A), H(2B), and the H(4A), H(4B) ^1H resonances, at ca. 4.8 and 5.1 ppm, given by the αCH_2 groups. The same is observed in the $^1\text{H}\{\text{FS-LG}\}-^{31}\text{P}$ HETCOR spectra (Fig. 8.11d-f).

In the ca. 3.0-5.5 ppm region, the F1 projection of the $^1\text{H}\{\text{FS-LG}\}-^{13}\text{C}$ HETCOR of **I** (Fig. 8.10) is slightly less resolved than that of the $^1\text{H}\{\text{FS-LG}\}-^1\text{H}$ HOMCOR spectrum (Fig. 8.8b), probably due to spin-diffusion occurring during CP. For a τ_{CT} of 2000 μs the cross-peaks between C(1) and H(2E) and H(2F) are not very intense. A statistical analysis (Fig. 8.12) based on crystallographic data for the C(15) $\cdots\text{H}$ distances within a 5 Å radius, reveals that C(1): *(i)* is the farthest ^{13}C nucleus from the neighbouring ^1H (median 4.17 Å), and *(ii)* it only has a single ^1H from a piperazinedium cation within this 5 Å radius sphere (H(2E) at 4.11 Å). This analysis can be further used to assign the C(2)-C(5) resonances. As far as the two carboxylic ^{13}C resonances are concerned, the 171.2 ppm cross-peak is stronger and, thus, the nuclei giving this resonance are likely to be closer to the ^1H reservoir. The box plots (Fig. 8.12) and the C $\cdots\text{H}$ distances (Fig. F.6) indicate that the C(3) is closer than C(5) to ^1H (median value of 4.05 Å versus 4.10 Å). Furthermore, since C(3) is also closer than C(5) to H(2E) and/or H(2F), with distances 3.21-3.98 Å and 4.22-4.64 Å, respectively, it is believed that C(3) gives the resonance at 171.2 ppm (Fig. 8.10). The resonance at 62.3 ppm is tentatively assigned to C(4) because this ^{13}C nucleus is closer than C(2) to H(2E)

and H(2F) (Fig. F.6), and also closer to the ^1H reservoir within a 5 Å radius sphere (median 3.91 Å, 75% of distances <4.13 Å, Fig. 8.12). Using the same rationale, the peak at 65.2 ppm is attributed to C(4) (median of 3.95 Å and 75% of distances <4.47 Å).

The $^1\text{H}\{\text{FS-LG}\}\text{-}^{13}\text{C}$ HETCOR spectrum of **I** recorded with a τ_{CT} of 50 μs (Fig. 8.10), reveals that the αCH_2 protons resonate at ca. 5.1 ppm; these are the most acidic protons, expected to be more deshielded than the other CH_2 protons in the structure. Furthermore, spectral analysis shows that the protons of the piperazinedium cations and C(1) are chemically similar, giving overlapping resonances at ca. 4.5 ppm (Fig. 8.6). However, there is a noticeable shoulder at ca. 3.5 ppm in the $^1\text{H}\{\text{FS-LG}\}\text{-}^1\text{H}$ HOMCOR (Fig. 8.8b), also observed in the F1 projection of the $^1\text{H}\{\text{FS-LG}\}\text{-}^{13}\text{C}$ HETCOR spectrum (Fig. 8.10), which contributes to the cross-peak at ca. 41 ppm of F2.

The phosphorus atom, P(1), is structurally positioned in what can be considered as the interface between the organic and the inorganic components of **I**. Because there are no protons directly connected to P(1), ^{31}P is a good nucleus to probe the neighbouring ^1H environments. At short contact times (50 μs), the $^1\text{H}\{\text{FS-LG}\}\text{-}^{31}\text{P}$ HETCOR spectrum of **I** shows the resonance at ca. 3.5 ppm resolved from that at ca. 4.3 ppm (Fig. 8.11d-f). Taking into account the $\text{P}\cdots\text{H}$ distances (Fig. F.4) and the $^1\text{H}\{\text{FS-LG}\}\text{-}^{13}\text{C}$ HETCOR spectra (Figs. 8.10 and 8.9), the former resonance is assigned to protons from C(7), the latter to those from C(1), C(6), and possibly water, in good agreement with the crystallographic nonequivalence of the piperazinedium ^{13}C atoms. Moreover, for a τ_{CT} of 2000 μs the $^1\text{H}\{\text{FS-LG}\}\text{-}^{31}\text{P}$ HETCOR spectrum (Fig. 8.11a-c) exhibits two additional resonances at ca. 5.1 and 8.7 ppm, attributed to αCH_2 and $^+\text{NH}_2$, respectively (Fig. F.4).

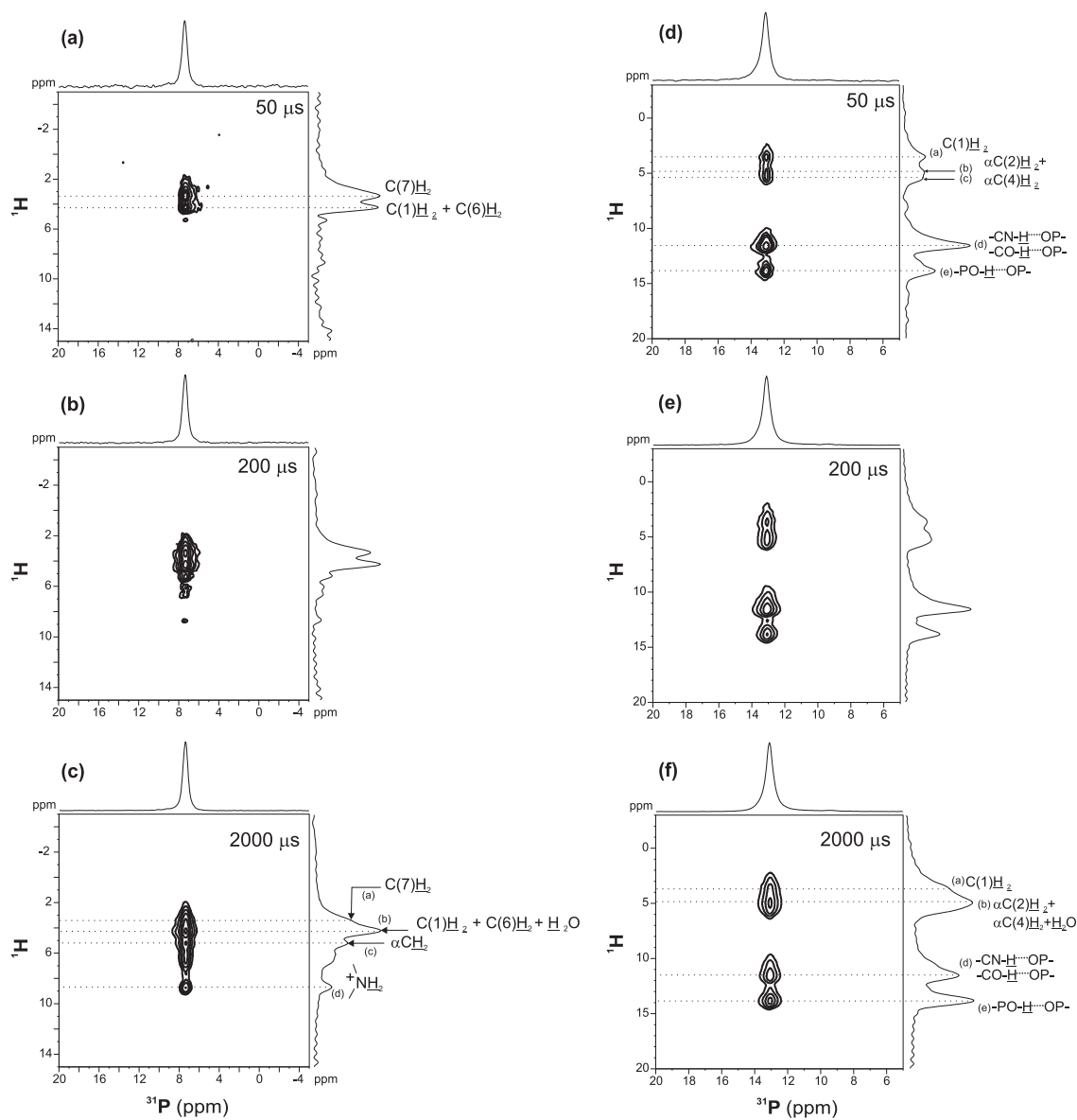


Fig. 8.11: $2\text{D } ^1\text{H}\{FS-LG\}-^{31}\text{P}$ HETCOR spectra of **I** (a, b and c) and H_4pmida (d, e and f) recorded at 12 kHz and contact times depicted.

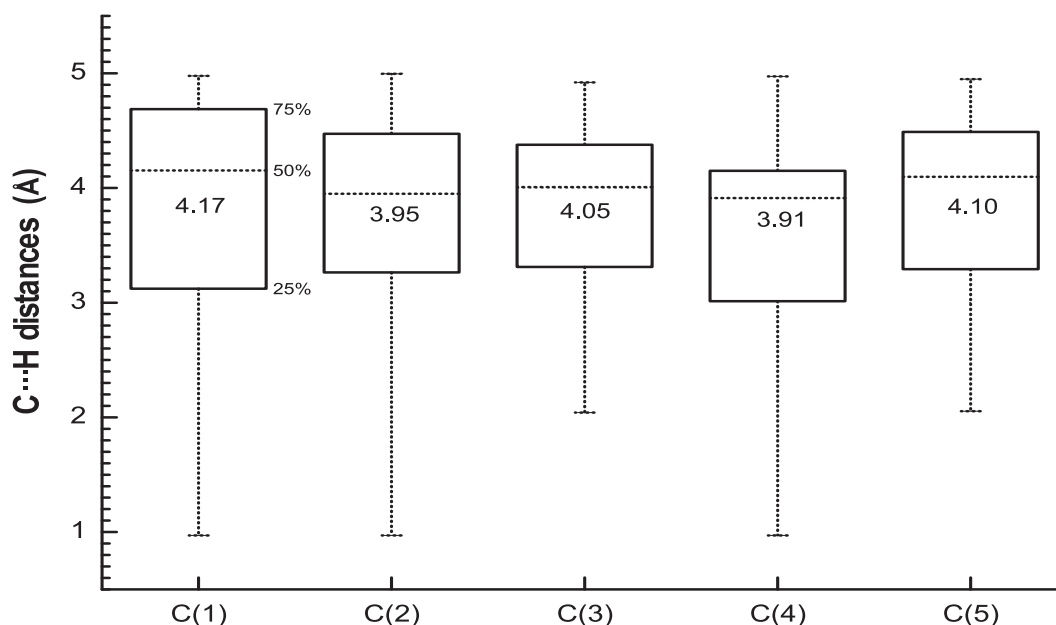


Fig. 8.12: Observed $C \cdots H$ distances (in Å) for $C(1)C(5)$ represented as box plots giving median (also inside the boxes), upper (75%), and lower (25%) quartiles, and maximum and minimum values. Detailed $C \cdots H$ distances are given in Figs. F.5, F.6 and F.7.

Thermal Analysis

Thermal treatment of $(C_4H_{12}N_2)[Ge_2(pmda)_2(OH)_2] \cdot 4H_2O$ in air and nitrogen result in very similar decomposition processes (see section 8.1.1). Below $140^\circ C$ the compound releases all the water-of-crystallisation molecules with registered weight losses of 9.6% and 9.4% (for air and nitrogen atmosphere, respectively) which is in good agreement with the theoretical value for the four molecules (9.2%). The dehydrated material is then thermally stable up to approximately $330^\circ C$, when decomposition starts, involving several consecutive weight losses, indicating a multi-step and complex decomposition. The overlapping decomposition steps led to difficulties in identifying the components that are released at a given temperature. However, between ambient temperature and $800^\circ C$ a combined weight loss of 42.2% and 44.1% (for air and nitrogen atmosphere, respectively) agrees well with the calculated value of 44.7% for the formation of the stoichiometric amount of $Ge_2O(PO_4)_2$.

Vibrational spectroscopy: Interpretation

FT-IR and FT-Raman spectroscopy confirm the presence of the primary building blocks of $(C_4H_{12}N_2)[Ge_2(pmda)_2(OH)_2] \cdot 4H_2O$, through the typical vibrations of phosphonate groups and tertiary/secondary amines, and the vibrational modes for carboxylic acid groups. The spectra (not shown) are also particularly informative concerning the extensive hydrogen-bonding sub-network which involves the water-of-crystallisation molecules ($\nu(O-H)$, $\delta(O-$

H \cdots O) and γ (O–H \cdots O) vibrational modes), the carboxylate, Ge–OH and –NH₂⁺ groups. The measured value of Δ ($[\nu_{asym}(-CO_2^-)] - [\nu_{sym}(-CO_2^-)]$) gives further structural information concerning the coordination mode of the carboxylate groups. [222,223] the calculated value of 323 cm⁻¹ is typical of the unidentate coordination mode, as revealed by the XRD analysis.

8.1.3 Conclusion

The binuclear Ge⁴⁺ complex [Ge₂(pmida)₂(OH)₂]²⁻ was isolated, being closely related to the [V₂O₂(pmida)₂]⁴⁻ unit, previously used to construct 3D coordination frameworks through a hydrothermal approach. By replacing the paramagnetic V⁴⁺ centres by Ge⁴⁺ it was possible to explore the use of high-resolution SSNMR techniques to study a model inorganic-organic compound. This is part of a systematic effort to evaluate the potential use of these tools to elucidate the structure inorganic-organic hybrid materials, including those which are amorphous or disordered. The local ¹³C and ³¹P environments of H₄pmida and (C₄H₁₂N₂)[Ge₂(pmida)₂(OH)₂] \cdot 4H₂O were probed using the ¹³C/³¹P CP-MAS method, showing that the coordination to the Ge⁴⁺ centres shifts all pmida⁴⁻ carbon resonances to high frequency, thus clearly resolving the –CH₂–CO₂⁻ resonances. The resolution of the ¹H spectra was much improved (relative to conventional MAS) by using the FS–LG decoupling scheme in HOMCOR/HETCOR dipolar techniques. Comparison between 2D ¹H{FS-LG}-¹H HOMCOR spectra allowed the systematic study of the hydrogen-bonding interactions in H₄pmida and (C₄H₁₂N₂)[Ge₂(pmida)₂(OH)₂] \cdot 4H₂O, particularly in the region above ca. 5 ppm. As the structures contain several CH₂ groups, which give overlapping resonances in the ca. 3.0–5.5 ppm range, 2D ¹H{FS-LG}-¹³C/³¹P HETCOR experiments with variable mixing times were performed. This work, combined with the analysis of the crystallographic C \cdots H and P \cdots H internuclear distances, allowed the assignment of the CH₂ resonances.

8.2 A Ge⁴⁺/HEDP⁴⁻ Hexanuclear Complex Containing Heteroaromatic Residues

Here, I report the synthesis, single-crystal structure and photoluminescence properties of two germanium-hedp⁴⁻ solids with heteroaromatic amines, 8-hydroxyquinoline (structure **I**) and 1,10-phenanthroline (structure **II**), (HL)₆[Ge₆(OH)₆(hedp)₆] \cdot 2(L) \cdot *n*H₂O, L=hqn or phen, in **I** and **II**, respectively, involved in columnar $\pi - \pi$ stacking and exhibiting a complex hydrogen-bonds networks. The materials have been further characterised by EA, TG, FTIR, Raman and UV-vis spectroscopies. High-resolution SSNMR was used to study the complex hydrogen-bonds network, particularly in compound **I**. The combination of homonuclear recoupling techniques (2D ¹H-¹H DQF, [137, 224] 2D ¹H-¹H RFDR MAS NMR [225, 226]) and CRAMPS techniques [227] (2D ¹H{FS-LG}-¹H, ¹H{FS-LG}-³¹P) provided a powerful means of characterising these materials.

8.2.1 Experimental Section

Synthesis Method

The following syntheses work was performed by Dr. Fa-Nian Shi from the Chemistry Department, University of Aveiro.

Chemicals were readily available from commercial sources and were used as received without further purification. Syntheses were carried out in PTFE-lined stainless steel reaction

vessels (ca. 40 cm³), under autogeneous pressure and static conditions. The reactive mixtures (see compositions below) were transferred to the reaction vessels which were then placed inside the oven. The temperature was gradually increased to 120 °C and kept constant for 3 days, after which the vessels was allowed to cool slowly to ambient temperature before opening. The obtained compounds are air- and light-stable.

Preparation of (Hhq_n)₆[Ge₆(OH)₆(hedp)₆]·2(hqn)·33H₂O (I).

A suspension containing 0.200 g of 1-hydroxyethylidenediphosphonic acid (H₄hedp, C₂H₈O₇P₂, ≥97%, Fluka), 0.100 g of germanium(IV) oxide amorphous (GeO₂, 99.99%, Aldrich), and 0.140 g of 8-hydroxyquinoline (hqn, C₉H₇NO, 99%, Merck) in ca. 12 g of distilled water was stirred thoroughly for 30 minutes at ambient temperature. After reacting, the resulting light-yellow phase was washed with distilled water, filtered and air-dried at ambient temperature. The single-crystalline phase decomposes into a microcrystalline powder during this drying stage. Hence, (Hhq_n)₆[Ge₆(OH)₆(hedp)₆]·2(hqn)·33H₂O samples suitable for single-crystal XRD measurements were isolated still wet directly from the autoclave mother liquor by slow evaporation at ambient temperature for two days.

Preparation of (Hphen)₆[Ge₆(OH)₆(hedp)₆]·2(phen)·20H₂O (II).

A suspension containing 0.200 g of 1-hydroxyethylidenediphosphonic acid (H₄hedp, C₂H₈O₇P₂, ≥97%, Fluka), 0.240 g of germanium(IV) oxide amorphous (GeO₂, 99.99%, Aldrich), and 0.190 g of 1,10-phenanthroline monohydrate (phen, C₁₂H₈N₂·H₂O, ≥99.0%, Fluka) in ca. 16 g of distilled water was stirred thoroughly for 30 minutes at ambient temperature. After reacting, the isolated microcrystalline light-brown phase was washed with distilled water, filtered and air-dried at ambient temperature. Single crystals of (Hphen)₆[Ge₆(OH)₆(hedp)₆]·2(phen)·20H₂O suitable for XRD measurements, were harvested from the autoclave mother liquor by slow evaporation at ambient temperature over one day.

Routine Measurements

FTIR Assignments: Selected IR (KBr pellet, cm⁻¹) and Raman (in italics inside the parenthesis, cm⁻¹) data: Structure **I** - ν(HO-H/GeO-H/CO-H, with evidences of H-bonding) = 3430vs/br, 3254vs/br, 3093vs/br (*3116w*); ν(-aromatic NH⁺) = 2790m,br; ν(C-H, aromatic) = 3093br (3069m); ν_{as}(C-H in -CH₃) = 2969br (*2979w, 2937w*); ν_s(C-H in -CH₃) = (*2875w*); δ_s(CO-H) and δ_{as}(CH₃) = 1421m, 1404m; δ_s(CH₃) = 1384m (*1385s*); ν(NH⁺) = 2580br; δ(-NH⁺) = 1559m; ν(P=O) and ν(C-O) = 1187s and 1169s (*1314*); ν(C-C, skeletal vibrations) = 1603m (*1606m*); δ(O-H, lattice water) = 1635m (*1634w*); ν(C-N, heteroaromatic amines) and δ(O-H, aromatic) = 1312m (*1308w, 1279w*); ν(P-O) = 1010vs (*1064m, 1038w*); γ(C-C) = 488w (*542w, 490m, 474m and 410m*), various modes; γ(O-H, under H-bonding) = 976br,vs; γ(CH, aromatic) = 824m (*716vs*); ω(O-H, under H-bonding) = 583br,m (*578*). Structure **II** - ν(HO-H/GeO-H/CO-H, with evidences of H-bonding), = 3389vs/br, 3237vs/br; ν(-aromatic NH⁺) = 2532s/br; ν(C-H, aromatic) = 3062m (3066m); ν_{as}(C-H in -CH₃) = 2932m (*2990w, 2933w*); ν_s(C-H in -CH₃) = 2807s, 2879s (*2872w*); δ_{as}(CH₃) = 1452m, 1469m (*1452s, 1415vs*); δ_s(CH₃) = 1373w (*1373m*); ν(C-N, heteroaromatic amines) = 1316m (*1316w*); δ(CO-H) = 1289w (*1286w*); ν(NH⁺) = 2532br; δ(-NH⁺) = 1542s; δ(O-H, lattice water) = 1632s/br (*1629w*); ν(C-C, skeletal vibrations) = 1617s, 1596s (*1615m, 1596m*); ν(P=O) and ν(C-O) = 1185vs/br (*1189w*); ν(P-O) = 1053s (*1045m*); γ(C-C) = 487s, 461s (*550w, 508w, 461w*), various modes; γ(O-H, under H-bonding) = 971vs/br, various modes; γ(CH, aromatic) = 847vs, 816s (*848w*); ω(O-H, under H-bonding) = 620vs, 592vs, 568vs, various modes (*598w*).

COMPOUND I:

TG data (mass losses): 20-86 °C -14.2%; 86-155 °C -3.3%; 155-210 °C -2.3%; 210-400 °C -5.5%.
DSC peaks (endothermic processes): 76, 103, 184, 258 and 336 °C.

EA Based on single-crystal data: EA calc (%) for C₈₄H₁₅₈Ge₆N₈O₈₉P₁₂, MW 3511.36; in %): C 28.73, N 3.20, H 4.54. Found (%): C 28.87, N 3.08, H 4.51.

COMPOUND II:

TG data (mass losses): 220-125 °C -10.3%; 125-364 °C -10.0%.

EA Based on single-crystal data: EA calc (%) for C₁₀₈H₁₄₀Ge₆N₁₆O₆₈P₁₂, MW 3557.54; in %): C 36.46, N 6.33, H 3.97. Found (%): C 35.47, N 5.46, H 4.20.

X-ray Crystallography Measurements

The following X-ray work was carried out in collaboration with Dr. F. Paz from the Chemistry Department, University of Aveiro.

Single-crystals of (Hhq_n)₆[Ge₆(OH)₆(hedp)₆]·2(hqn)·33H₂O (**I**) and (Hphen)₆[Ge₆(OH)₆(hedp)₆]·2(phen)·20H₂O (**II**), where Hhq_n stands for 8-hydroxyquinolinium, *hedp* for 1-hydroxyethylidenediphosphonate, hqn for 8-hydroxyquinoline, *Hphen* for 1,10-phenanthroline, and *phen* for 1,10-phenanthroline, were selected from the contents of several vials and mounted on glass fibres using perfluoropolyether oil. [196] Preliminary measurements of several crystals of each sample consistently gave the same primitive triclinic unit cell.

Structures were solved according to the procedure described in section 8.1.1. All non-hydrogen atoms were located in same way as stated in section 8.1.1. For **I**, the four crystallographically unique residues of 8-hydroxyquinoline were anisotropically refined without any geometrical restraints. Hydrogen atoms attached to carbon were located at their idealised positions using the HFIX 43 (for the aromatic carbon atoms) and 137 (for the methyl groups) instructions in SHELXL. [198] Hydrogen atoms associated with the -OH groups from the organic molecules were placed geometrically at their idealised positions using the HFIX 147 instruction to give the best hydrogen bonding fit. All hydrogen atoms were included in subsequent refinement stages in riding-motion approximation with an isotropic thermal displacement parameter fixed at 1.2 (for the aromatic hydrogen atoms) or 1.5 (for the remaining hydrogen atoms) times U_{eq} of the atom to which they are attached. It is important to highlight that the calculated position for each hydrogen atom does not reflect the true position of the hydrogen nuclei.

In compound **II**, the majority of the 1,10-phenanthroline organic residues are severely affected by thermal disorder, even at the low temperature of 180(2) K at which the crystal data was collected. Thus, the four crystallographically unique 1,10-phenanthroline residues had to be refined with geometry heavily restrained to force these moieties to be aromatic (all bond lengths were restrained to be 1.39(1) Å). When refined anisotropically, all the atoms of 1,10-phenanthroline showed large tensors in the two directions which define the plane of the molecule. Thus, as these molecules must be treated as a rigid body, carbon atoms from the same 1,10-phenanthroline were ultimately refined using the instruction *ISOR* to restraint the anisotropic displacement parameters to be approximately isotropic. One of these molecules (residue 4) was successfully refined over two distinct crystallographic positions, with occupancy factors fixed at 50% each.

Structural refinement employing solvent-free reflection data calculated using the SQUEEZE [228] subroutines revealed the existence, in both compounds, of hydrogen atoms attached to the internal μ_2 -bridging oxygen atoms [O(8), O(16) and O(23)] of the anionic [Ge₆(μ_2 -OH)₆(C₂H₄O₇P₂)₆]⁶⁻ moieties Fig. F.11. Moreover, the average Ge-OH bond distance for

compounds **I** and **II** is ca. 1.86 Å, which is longer than the median value (1.78 Å) obtained from a CSD survey of typical Ge-O-Ge bonds in related compounds. [107] Indeed, the Ge-OH bond distances observed in **I** and **II** are near the third quartile boundary of the statistical survey, [107] which is a clear indication of weaker interactions and, thus, the existence of additional hydrogen atoms attached to the internal bridging oxygen atom. A similar structural refinement strategy, closely combined with data extracted from NMR studies, further revealed that three 8-hydroxyquinoline and three 1,10-phenanthroline residues for **I** and **II**, respectively, are indeed protonated, thus balancing the crystal charge. This was further supported by a close inspection of the crystal structures revealing the strong possibility of hydrogen bonds connecting such protonated groups with either the anionic $[\text{Ge}_6(\mu_2\text{-OH})_6(\text{C}_2\text{H}_4\text{O}_7\text{P}_2)_6]^{6-}$ hexamers or water molecules of crystallisation. Calculated positions of these hydrogen atoms, to give the best hydrogen-bonding fit, were then included in successive refinement steps in riding-motion approximation using the original data sets. For **I**, the O-H and N-H distances were restrained to 0.95(1) and 1.00(1) Å, respectively. For **II**, these two types of hydrogen atoms could only produce stable successive least-square refinements when included using the HFIX 43 instruction. All hydrogen atoms were refined using isotropic thermal displacement parameters fixed at 1.5 times U_{eq} of the atom to which they are attached.

Least-squares refinement cycles using the original data sets allowed the direct location from difference Fourier maps of additional [apart from O(1W)] 28 and 17 crystallographically unique but highly disordered and, for the majority, partially-occupied water molecules of crystallisation, which add up to 31 and 18 molecules per anionic $[\text{Ge}_6(\mu_2\text{-OH})_6(\text{C}_2\text{H}_4\text{O}_7\text{P}_2)_6]^{6-}$ hexamer for **I** and **II**, respectively. These oxygen atoms associated with the water molecules of crystallisation were refined with a common isotropic displacement parameter. Even though no attempt was made to either locate from difference Fourier maps or to place in calculated positions the hydrogen atoms associated with the water molecules, these have been included in the empirical formulae of the compounds.

Despite crystal data for the two compounds were collected with resolution up to 0.77 Å, crystals systematically diffracted very weakly at high angle. Applying a cut-off at 0.83 Å resolution results in a good number of reflection observed at the 2 (**I**) level and, thus, good R merging values (Table 8.3). Collection of higher-angle data is only likely to be possible using synchrotron radiation or perhaps a rotating-anode source. Refinements based on the solvent-free reflection data were performed with the full range of collected reflections.

The last difference Fourier map synthesis employing the collected data sets showed, for **I**, the highest peak ($1.133 \text{ e}\text{\AA}^{-3}$) located at 0.15 Å from O(4W), and the deepest hole ($-1.086 \text{ e}\text{\AA}^{-3}$) at 0.05 Å from O(23W) and, for **II**, the highest peak ($0.579 \text{ e}\text{\AA}^{-3}$) located at 1.30 Å from H(8_4), and the deepest hole ($-0.396 \text{ e}\text{\AA}^{-3}$) at 1.41 Å from O(23). [106]

Interestingly, all the mentioned difficulties encountered while solving and refining these two structures were also found when single-crystal data were either collected at different temperatures or from single-crystals from different batches. Thus, the diffuse electron density discussed in the previous sections seem to be an intrinsic property of the compounds and not even when the data sets are mathematically treated to remove the contribution of the disordered solvent, the structural models are better adjusted to the collected data. In fact, for compound **II** the solvent-free reflection data calculated using SQUEEZE produced a model which does not differ much from that calculated using the original data set.

Information concerning crystallographic data[‡] collection and structure refinement details

[‡]Crystallographic data (excluding structure factors) for the structures reported in this paper have been deposited with the Cambridge Crystallographic Data Centre as supplementary publication no. CCDC- 614629 and 614630 for **I** and **II**, respectively. Copies of the data can be obtained free of charge on application to

Table 8.3: Crystal data and structure refinement information for compounds **I** and **II**.^[a]

	I	II
formula	C ₈₄ H ₁₅₈ Ge ₆ N ₈ O ₈₉ P ₁₂	C ₁₀₈ H ₁₄₀ Ge ₆ N ₁₆ O ₆₈ P ₁₂
formula weight	3511.36	3557.54
crystal system	Triclinic	Monoclinic
space group	<i>P</i> ₁	<i>P</i> 2 ₁ / <i>n</i>
<i>a</i> [Å]	16.201(3)	15.432(3)
<i>b</i> [Å]	16.997(3)	27.222(5)
<i>c</i> [Å]	17.321(4)	17.193(3)
α [°]	61.09(3)	—
β [°]	66.08(3)	102.94(3)
γ [°]	74.78(3)	—
volume[Å ³]	3803.4(13)	7039(2)
Z	1	2
<i>D</i> _c [gcm ⁻³]	1.533	1.678
μ (Mo – K α)[mm ⁻¹]	1.402	1.507
F(000)	1802	3632
crystal size[mm]	0.35×0.07×0.05	0.21×0.10×0.07
crystal type	Yellow Blocks	Yellow needles
θ range	3.62 to 24.11 (3.62 to 27.50)	3.52 to 25.35 (3.52 to 25.67)
Data Completeness	99.1% 98.1%	87.4% 87.0%
index ranges	-18 ≤ <i>h</i> ≤ 18 (-20 ≤ <i>h</i> ≤ 21) -19 ≤ <i>k</i> ≤ 19 (-20 ≤ <i>k</i> ≤ 22) -19 ≤ <i>l</i> ≤ 19 (-22 ≤ <i>l</i> ≤ 22)	-18 ≤ <i>h</i> ≤ 18 (-18 ≤ <i>h</i> ≤ 18) -30 ≤ <i>k</i> ≤ 32 (-30 ≤ <i>k</i> ≤ 33) -15 ≤ <i>l</i> ≤ 20 (-15 ≤ <i>l</i> ≤ 20)
reflections collected	30980 (37902)	24076 (24554)
independent reflections	11985 (<i>R</i> _{int} = 0.0594) (17149 (<i>R</i> _{int} = 0.0535)) <i>R</i> ₁ =0.0836 (<i>R</i> ₁ =0.0639)	11271 (<i>R</i> _{int} = 0.0535) (11612 (<i>R</i> _{int} = 0.0495)) <i>R</i> ₁ =0.0930 (<i>R</i> ₁ =0.0952)
final <i>R</i> indices [<i>I</i> > 2σ(<i>I</i>)]	<i>wR</i> ₂ =0.2269 (<i>wR</i> ₂ =0.1602) <i>R</i> ₁ =0.1314 (<i>R</i> ₁ =0.1192)	<i>wR</i> ₂ =0.2192 (<i>wR</i> ₂ =0.2320) <i>R</i> ₁ =0.1724 (<i>R</i> ₁ =0.1554)
final <i>R</i> indices (all data)	<i>wR</i> ₂ =0.2672 (<i>wR</i> ₂ =0.1774)	<i>wR</i> ₂ =0.2661 (<i>wR</i> ₂ =0.2564)
largest diff. peak and hole[eÅ ⁻³]	1.133 and -1.086	0.579 and -0.396

^[a] The structural refinement employing solvent-free reflection data, calculated using the SQUEEZE [228] subroutines are shown in parenthesis.

for the two structures using the collected data sets and also solvent-free data are summarised in Table 8.3. Hydrogen bonding geometry is described in Tables F.2 and F.3 for structures **I** and **II**, respectively. Unless otherwise stated, crystallographic structural drawings were created using the software package Crystal Diamond. [229, 230]

NMR Measurements

CSs are quoted in ppm from TMS (^1H and ^{13}C) and 85% H_3PO_4 (^{31}P). NMR spectra have been recorded using spinning rates between 10 and 30 kHz.

^{13}C CPMAS (4 mm probe) spectra: $\nu_R = 12$ kHz; $\nu_1(^1\text{H}) = 53 \pm 20$ kHz (ramped) and $\nu_1(^{13}\text{C}) = 55$ kHz during CP; NS = 768. During acquisition the ^{13}C spectra were decoupled using the SPINAL-64 scheme, [125] employing a ^1H *rf* field strength of 100 kHz.

2D $^1\text{H}\{\text{FS-LG}\}-^1\text{H}$ or ^{-31}P (4 mm probe) spectra: The FS-LG decoupling power was optimized by recording multiple 2D $^1\text{H}\{\text{FS-LG}\}-^1\text{H}$ experiments on the studied compounds, **I** and **II**, until achieving the best F1 spectral resolution. Quadrature detection in t_1 was achieved using the States-TPPI method. [38] The FS-LG decoupling procedure details were already described in section 8.1.1. A summary of the FS-LG conditions are given in Table. 8.4. The *rf* amplitudes used for the HH matching condition in the $^1\text{H}-^{31}\text{P}$ CP experiments were $\nu_1(^1\text{H}) = 54 \pm 20$ kHz and $\nu_1(^{31}\text{P}) = 55$ kHz. Some $^1\text{H}-^{31}\text{P}$ FS-LG spectra were acquired using LG-CP in order to enhance the ^1H resolution by quenching spin diffusion during CP. [219, 221]

$^1\text{H}-^1\text{H}$ 2D DQF MAS (2.5 mm probe) spectra: For **I**, $R = 30$ kHz; 90° pulse of $2.5 \mu\text{s}$, t_{exc} (excitation time) = t_{conv} (conversion time) = $N \times 2\tau_R$, with $N = 1$; NS (number of scans) = 32. For **II**, $R = 26$ kHz; $t_{exc} = t_{rec} = N \times 2\tau_R$, with $N = 1$; NS = 32. Experiments were performed using the improved version of the Back-to-Back (BABA) sequence. [137] 192 t_1 points with 16 transients each were acquired, and the time increments synchronised with the rotor period. Sign discrimination was achieved in the F1 dimension using TPPI and incrementing the phase of the excitation pulses by $\pi/2p = 45^\circ$ (with $p = 2$ for DQ excitation). The interpulse delay (Δ) was set to $= 1.8 \mu\text{s}$. The pulse sequence can be viewed in Fig. 5.2a.

$^1\text{H}-^1\text{H}$ 2D RFDR MAS (2.5 mm probe) spectra: For **I**, $\nu_R = 30$ kHz; For **II**, $\nu_R = 26$ kHz, 90° *rf* pulse = $2.5 \mu\text{s}$, 180° *rf* pulse = $5 \mu\text{s}$. NS = 16, τ_m (mixing time) = $L1 \times 16 \times \tau_R$, where L1 is multiple of 8 (to complete the XY-8 phase cycling during the train of 180° pulses) and ν_R the rotor period. τ_m values are indicated in the figure captions. The pulse scheme employed can be found in ref. [225] Phase-sensitive detection in t_1 was achieved with States-TPPI.

Photoluminescence Spectroscopy

The photoluminescence work was carried out by Dr. R. Ferreira from the Physics Department, University of Aveiro.

The emission spectra were corrected for detection and optical spectral response of the spectrofluorimeter and the excitation spectra were corrected for the spectral distribution of the lamp intensity using a photodiode reference detector. The time-resolved emission spectra and the lifetime measurements were acquired at 14 K with the setup described for the luminescence spectra using a pulsed Xe-Hg lamp ($6 \mu\text{s}$ pulse at half width and 20-30 μs tail).

Table 8.4: $2D\ ^1\text{H}\{\text{FS-LG}\}\text{-}^1\text{H}\{\text{HOMCOR}\}$ and $^1\text{H}\{\text{FS-LG}\}\text{-}^{31}\text{P}\ \text{HETCOR}$ experimental parameters for **I** and **II**.

Experimental parameters	$^1\text{H}\text{-}^1\text{H}\ \text{HETCOR}$		$^1\text{H}\text{-}^{31}\text{P}\ \text{HETCOR}$	
	I	II	I	II
number of t_1 points	172	150	150	80
dwell time in (t_1) [μs]			$6 \times t_{LG}$	
MAS rate [kHz]			12	
^1H offset frequency shift (ν_{lg}) ^a [kHz]		+5.5		-7.0
FS-LG decoupling power [kHz]			83.3	
FS-LG period, t_{LG} [μs]			9.8	
frequency switching time ^b [μs]			0.6	
positive offset frequency ($+\Delta\nu_{LG} + \nu_{lg}$) ^a [Hz]		+64425		+51925
negative offset frequency ($-\Delta\nu_{LG} + \nu_{lg}$) ^a [Hz]		-53425		-65925

^a The values ν_{lg} correspond to small offset ^1H resonance shifts with respect to the ^1H carrier frequency centered at -9 kHz.

^b The phase switching between each LG pulse was optimised on the multiplet structure of adamantane.

^c These parameters refer to the frequency jumps of $\pm\nu_1/\sqrt{2}$ ($\pm\Delta\nu_{LG}$) between each LG period added by a value, ν_{lg} to facilitate the optimisation of the FS-LG experiment. (see Fig.4.10)

8.2.2 Results and Discussion

Structure Description

The hydrothermal reaction between germanium(IV) oxide, etidronic acid (or 1-hydroxyethylidenediphosphonic acid, H_4hedp , $\text{C}_2\text{H}_8\text{O}_7\text{P}_2$) and 8-hydroxyquinoline (hqn, $\text{C}_9\text{H}_7\text{NO}$) or 1,10-phenanthroline (phen, $\text{C}_{12}\text{H}_8\text{N}_2$), followed by slow evaporation at ambient temperature (Experimental Section), afforded highly crystalline materials, which were formulated as $(\text{Hhqn})_6[\text{Ge}_6(\text{OH})_6(\text{hedp})_6]\cdot 2(\text{hqn})33\text{H}_2\text{O}$ (**I**) and $(\text{Hphen})_6[\text{Ge}_6(\text{OH})_6(\text{hedp})_6]\cdot 2(\text{phen})20\text{H}_2\text{O}$ (**II**) on the basis of single-crystal XRD (Table 8.3) in combination with TG and SSNMR studies. The main structural feature, common to both compounds, is the presence of the centrosymmetric hexameric anionic $[\text{Ge}_6(\mu_2\text{-OH})_6(\text{C}_2\text{H}_4\text{O}_7\text{P}_2)_6]^{6-}$ moiety (Fig. F.11), bearing some similarity with the fragment present in materials recently reported. [231] This anionic moiety is composed of three crystallographically unique Ge^{4+} centres [Ge(1), Ge(2) and Ge(3), Fig. 8.13], each coordinated to two hedp^{4-} residues (via the phosphonate moieties) and two μ_2 -bridging hydroxyl groups, exhibiting GeO_6 slightly distorted octahedral coordination geometries: for both compounds, all the Ge-O bonds are in the range 1.79 to 1.91 Å; however, the cis and trans octahedral angles spun, respectively, from 85.2 to 95.3° and 174.2 to 179.3°. The centrosymmetric hexameric anionic unit described here is different in a fundamental way from that previously reported by Seifullina and collaborators. [231] Indeed, while in compounds **I** and **II** the centre of gravity of this anionic unit is located at an inversion centre (see space group in Table 8.3), which necessarily requires the presence of three crystallographically unique Ge^{4+} centres, for the compounds reported by Seifullina *et al.* inversion arises as a combination of other symmetry elements, namely a two-fold axis and a mirror plane (space group $C2/m$), thus only requiring two single Ge^{4+} centres. [231] Consequently, the $[\text{Ge}_6(\mu_2\text{-OH})_6(\text{C}_2\text{H}_4\text{O}_7\text{P}_2)_6]^{6-}$ moiety present in compounds **I** and **II** is more distorted than its $C2/m$ counterpart. A possible reason for this decrease in symmetry is the significant number of strong hydrogen bonds present in **I** and **II**, involving the phosphonate groups.

In both compounds, the hedp^{4-} organic residues are chelating bridging ligands, linking neighbouring Ge^{4+} centres via the two phosphonate groups, which coordinate the Ge^{4+} centres in cis positions (Fig. F.11a). The $\text{Ge}\cdots\text{Ge}$ internuclear distances range from ca. 3.32 to 3.50 Å (Fig. F.11b), in good accord with the values reported by Seifullina and collaborators [231] (ca. 3.39-3.50 Å). Due to steric hindrance, the six hedp^{4-} ligands forming the anionic $[\text{Ge}_6(\mu_2\text{-OH})_6(\text{C}_2\text{H}_4\text{O}_7\text{P}_2)_6]^{6-}$ moiety are distributed above and below the plane formed by the six Ge^{4+} centres (Figs. F.11a and F.11b). An identical distribution also occurs for the six μ_2 -bridging hydroxyl groups located and pointing towards the inner space of the hexameric moiety (Fig. F.11c F.11d). Each one of the three $\mu_2\text{-OH}$ groups from one side of the $\text{Ge}_6(\text{OH})_6$ hexagonal ring interacts with a neighbouring water molecule of crystallisation (Fig. F.11d) via strong and highly directional $\text{O-H}\cdots\text{O}$ hydrogen bonds (average $\text{O}\cdots\text{O}$ internuclear distance and $\angle(\text{O-H}\cdots\text{O})$ angle of 2.70 Å and 163°, respectively, for both compounds, Tables F.2 and F.3). Within the dihydrated anionic $[\text{Ge}_6(\mu_2\text{-OH})_6(\text{C}_2\text{H}_4\text{O}_7\text{P}_2)_6]^{6-}$ moiety the $\text{O}(1\text{W})\cdots\text{O}(1\text{W})$ distances are ca. 3.18 and 3.31 Å for **I** and **II**, respectively. Interestingly, such arrangement was reported by Seifullina *et al.* only for the material containing $[\text{Mg}(\text{H}_2\text{O})_6]^{2+}$ cations, with a reported equivalent distance of ca. 3.17 Å. [231] The charge of the hexameric anionic $[\text{Ge}_6(\mu_2\text{-OH})_6(\text{C}_2\text{H}_4\text{O}_7\text{P}_2)_6]^{6-}$ moieties is compensated by the presence of protonated 8-hydroxyquinoline (Hhqn^+ , for **I**) or 1,10-phenanthroline (Hphen^+ , for **II**) organic residues, which appear $\pi\text{-}\pi$ stacked, leading to the formation of cationic columnar arrangements (Figs. 8.14 and 8.15): while for **I** the organic residues alternate in a $\text{hqn} / \text{Hhqn}^+ / \text{Hhqn}^+$ fashion, for **II** the rod-like columns are only formed by protonated phen

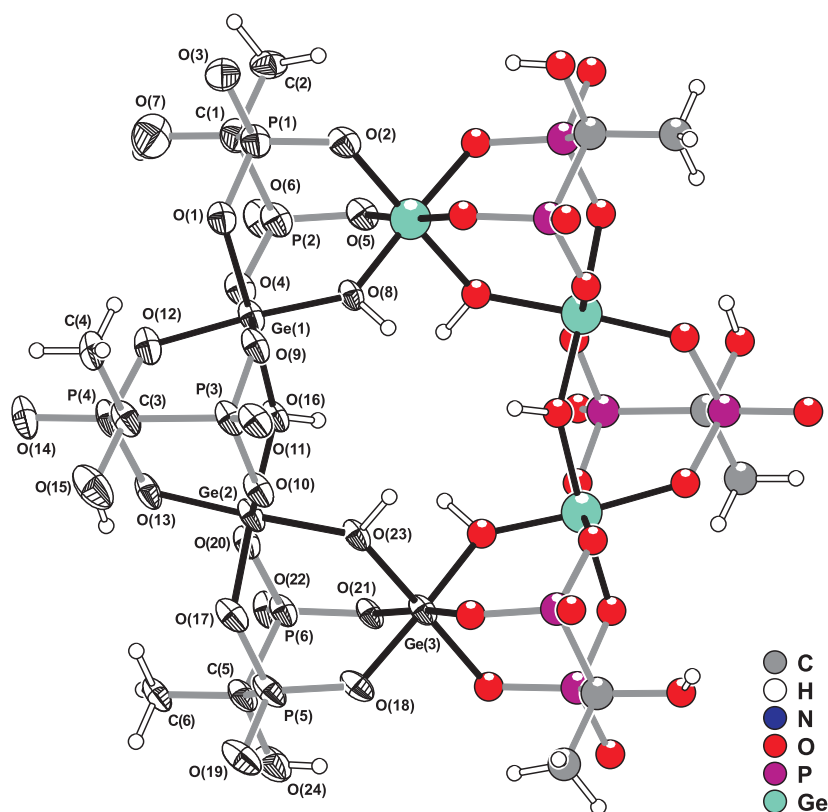


Fig. 8.13: Ball-and-stick representation of the hexameric anionic $[\text{Ge}_6(\mu_2\text{-OH})_6(\text{C}_2\text{H}_4\text{O}_7\text{P}_2)_6]^{6-}$ moiety showing the labelling scheme for all non-hydrogen atoms belonging to the asymmetric unit. Displacement ellipsoids are drawn at the 30% probability level and belong to structure **I**. Hydrogen atoms are represented as small spheres with arbitrary radii.

residues. The location of these charge-balancing H^+ could only be unequivocally confirmed in the crystal structures by SSNMR (see below). This π - π stacking arrangement of organic molecules in both compounds seems to be mainly due to the presence of the relatively large hexameric anionic unit. For example, the crystal structure of pure 1,10-phenanthroline does not contain any π - π interactions, with the stacking of adjacent molecules being instead driven by numerous weak $\text{C-H}\cdots\pi$ interactions. [232] For **I** this particular feature led to significant and interesting photoluminescence properties, as it will be discussed later.

Connections between neighbouring cationic columnar arrangements are mainly assured by weak $\text{C-H}\cdots\pi$ interactions with pairs of π - π -stacked organic molecules. While for compound **I** this distribution generates organic layers (Fig. 8.14), for **II** the packing is much more efficient leading to a 3D supramolecular arrangement of phen / Hphen⁺ residues (Fig. 8.15). Therefore, even though compound **II** has a significantly more available volume per unit cell, the volume accessible to solvent molecules (calculated using Cerius² routines) is approximately half of that for **I**. [107] These supramolecular arrangements of organic residues are closely interacting with the hexameric anionic $[\text{Ge}_6(\mu_2\text{-OH})_6(\text{C}_2\text{H}_4\text{O}_7\text{P}_2)_6]^{6-}$ moieties and water molecules of crystallisation via a series of strong hydrogen bonds (Tables F.2 and F.3), which will be discussed in more detail in the SSNMR section.

As suggested by TG and previous studies on multi-dimensional coordination frameworks exhibiting large channels, [234] it was clear that both compounds would contain a large number of highly disordered water molecules of crystallisation located within the voids, thus re-

sulting in a significant smeared-out electron density visible in XRD data. Peak search routines of SHELXL are not designed to locate maxima in density ridges, thus leading to additional difficulties during refinement and masking important structural features. SQUEEZE [228] subroutines included with the software package PLATON [235, 236] were, hence, employed to eliminate the contribution to the electron density of the water molecules of crystallisation present in the solvent-accessible area (except for the hydrogen-bonded O(1W) molecule, Figs. F.11c and F.11d). Fig. F.12a-b and F.12c-d show the SQUEEZE contour maps for **I** and **II**, respectively, emphasising the diffuse electron density present in some of the regions with solvent-accessible voids. For **I**, PLATON estimated that the unit cell has ca. 1363 Å³ of potential solvent accessible volume (ca. 35.8% of the total volume) in a large cavity centred at (-0.032 0.082 0.439), containing ca. 263 electrons per unit cell. [107] For **II**, the unit cell only has ca. 1144 Å³ of potential solvent accessible area (ca. 16.3% of the total volume) distributed along two identical cavities centred at the special positions (0 0 0) and (1/2 1/2 1/2), and containing ca. 547 electrons per unit cell. [107] In all calculations, O(1W) was assumed to belong to the hybrid hydrogen-bonded frameworks.

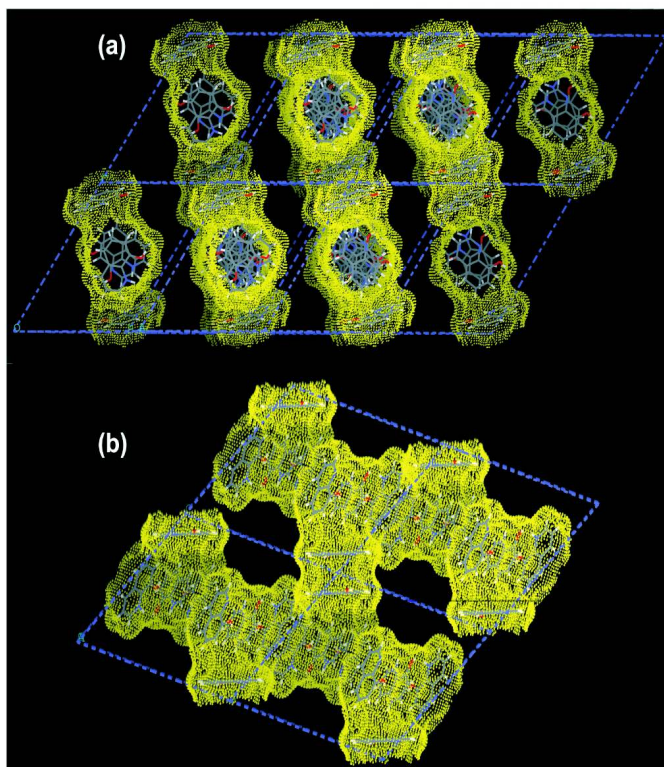


Fig. 8.14: Two different views (a) and (b) of connolly surface (1.4 Å probe radius and 12.0 dot density), generated with the software package Cerius², [233] involving the 8-hydroxyquinoline (hqn) residues in compound **I**: $\pi \cdots \pi$ stacking leads to a columnar arrangement of hqn and Hhqn^+ ; neighbouring columns are interconnected by weak $\text{C-H} \cdots \pi$ interactions with another two π - π -stacked Hhqn^+ residues, leading to a 2D arrangement of organic residues.

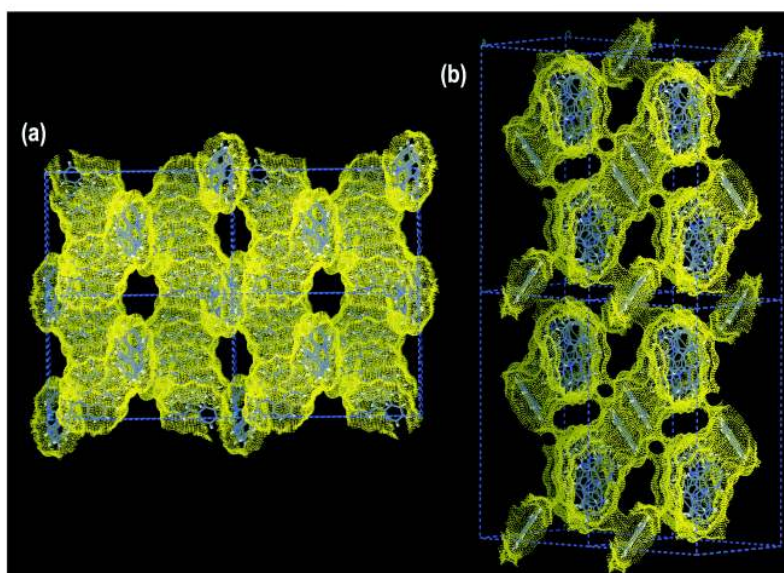


Fig. 8.15: Two different views (a) and (b) of connolly surface (1.4 Å probe radius and 12.0 dot density), generated with the software package Cerius², [233] involving the 1,10-phenanthroline (phen) residues in compound **II**: Hphen^+ π - π stack along the [101] direction of the unit cell, leading to columns which are interconnected into a 3D supramolecular arrangement by a disordered phen residue via a series of weak $\text{C-H} \cdots \pi$ interactions.

NMR Analysis

 ^{13}C RAMP CP-MAS:

The spectra of **I** and **II** exhibit similar features (Fig. 8.16). The hexameric $[\text{Ge}_6(\mu_2\text{-OH})_6(\text{C}_2\text{H}_4\text{O}_7\text{P}_2)_6]^{6-}$ moiety gives the following resonances, for **I** and **II**, respectively: quaternary carbons (C1, C3, C5) - ca. 70.9 and 71.3 ppm; methyl (C2, C4, C6) carbons - ca. 18.6 and 19.9 ppm. This moiety has three crystallographically inequivalent quaternary and methyl carbons, but three resonances are only clearly observed (as shoulders) in the quaternary carbon region of **I**. Above 100 ppm, resonances are assigned to the aromatic carbons involved in the extensive columnar $\pi-\pi$ stacking.

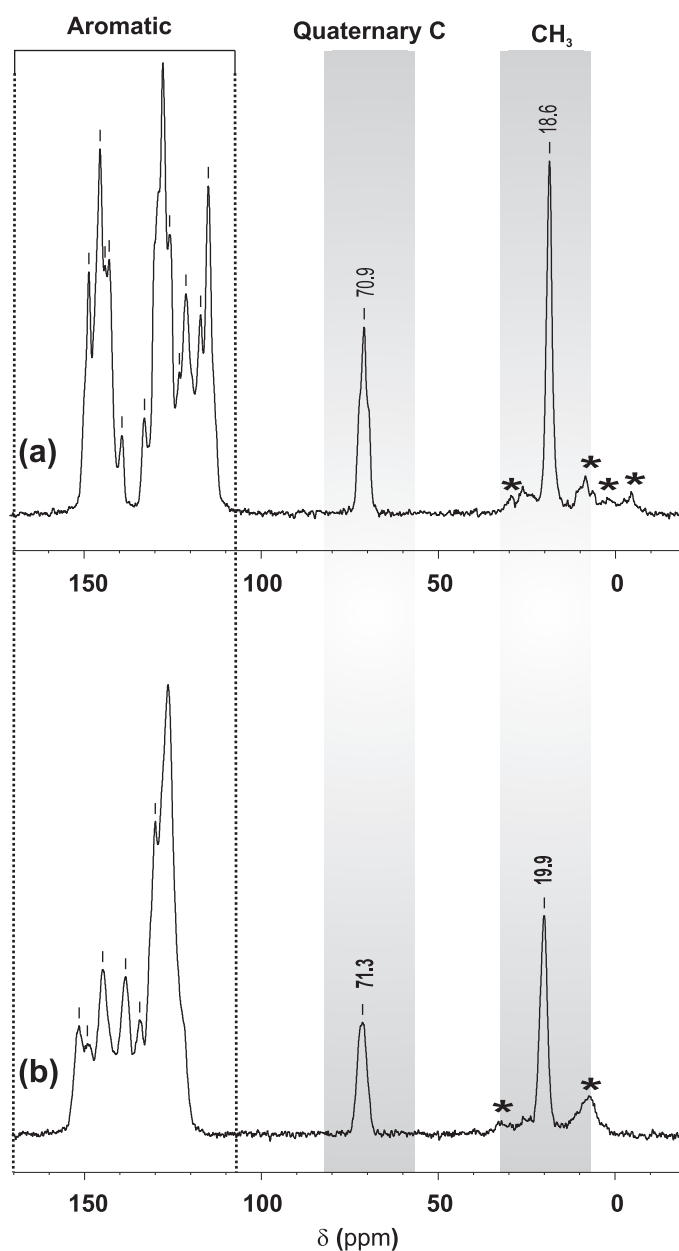


Fig. 8.16: Ramped ^{13}C CP-MAS spectra of (a) **I** and (b) **II**, both with a τ_{CT} of 1800 μs . Asterisks depict the spinning sidebands of the heteroaromatic skeletons.

^1H Spectra: Hydrogen-Bonding Assignment.

2D $^1\text{H}\{\text{FS-LG}\}-^1\text{H}$ HOMCOR: The F1 projection of the $^1\text{H}\{\text{FS-LG}\}-^1\text{H}$ and the ^1H fast (30 kHz) MAS spectra (Fig. 8.17) have similar resolution, showing up to 8 resolved peaks. However, a judicious choice of 2D F2 slices evidences the presence of some 10 resonances. Consider Fig. 8.17c. The resonances (H^a - H^c) in the range 16.6-13.1 ppm are assigned to strong hydrogen bonds, because of their relatively high-frequency shifts (Table 8.5). Hydrogen-bonded systems involving carboxylic ($\text{C}=\text{O}$) and phosphonic ($\text{P}=\text{O}$) acids as electron donors (i.e., proton acceptors) were reported to resonate in the ranges, respectively, 12-20 ppm and 11-17 ppm. [146] In **I**, the $\text{P}=\text{O}$ groups are within hydrogen-bonding distance with the OH groups of the 8-hydroxyquinoline (ArO-H) moieties ($r_{\text{O}\cdots\text{O}} = 2.61 \text{ \AA}$). $\text{P}=\text{O}$ groups involved in hydrogen bonds with OH residues have been reported to resonate at 11-12 ppm. [146, 151] Resonance H^c is tentatively attributed to $\text{ArO-H}\cdots\text{O}=\text{P}$ environments. Such hydrogen bonds ($\text{ArO-H}\cdots\text{O}=\text{P}$) are likely to be stronger than other $\text{CO-H}\cdots\text{O}=\text{P}$ bonds [151] because the base conjugated (ArO-) of the hydrogen donor (ArO-H) is weak, due to aromatic ring stabilisation. When the acidity of a hydrogen-bonded OH group increases its CS also increases and, thus, the resonance H^c appears at a CS larger than 12 ppm.

The crystallographic $\text{N}\cdots\text{O}$ distance range (2.72 - 2.78 \AA) suggests that the protonated nitrogen atom of 8-hydroxyquinoline is hydrogen-bonded to water molecules ($\text{N}^+\text{-H}\cdots\text{OH}_2$). The presence of $\text{N}^+\text{-H}$ groups involved in this type of interactions is likely because the charge of the anionic hexameric unit must be compensated by H^+ . Protonation and hydrogen bonding result in a significant increase of the ^1H CS. Thus, the H^a and H^b resonances at 16.6 and 14.9 ppm are tentatively assigned to $\text{N}^+\text{-H}\cdots\text{OH}_2$ environments (and confirmed below by $^1\text{H}-^1\text{H}$ DQF spectroscopy).

The ^1H resonances H^i and H^j at, respectively, ca. 5.9 and 2.8 ppm are assigned to lattice water and CH_3 . The remaining ^1H peaks between ca. 6 and 11 ppm can not be assigned without the information forthcoming from other 2D techniques (see below). The $^1\text{H}\{\text{FS-LG}\}-^1\text{H}$ spectrum of **II** (Fig. F.8) displays fewer resonances than the spectrum of **I** does. In particular, a peak is observed at ca. 15.1 ppm showing the presence of strong hydrogen bonds between the protonated nitrogen [$\text{N}(21)$] of 1,10-phenantroline and $\text{P}=\text{O}(6)$ groups of the anionic unit ($r[\text{N}(2_1)\cdots\text{O}(14)]=2.68 \text{ \AA}$, table F.3). This supports the assignment of resonances H^a and H^b proposed above for compound **I**.

The presence of signals in $^1\text{H}-^1\text{H}$ DQF spectrum (Fig. 8.18b) reveals dipolar couplings between nuclei and allows the identification of mobile water molecules by comparison with the 30 kHz MAS ^1H NMR spectrum (Fig. 8.18a). The latter is dominated by mobile water located in the channels, resonating at ca. 5.9 and 6.8 ppm for **I** and **II**, respectively (Fig. 8.18a and 8.18c). This peak is suppressed in DQF experiments simplifying the spectra (Figs. 8.18b and 8.18d). In the following discussion, SQ coherences (Table 8.5) identified from $^1\text{H}-^1\text{H}$ FS-LG are taken in consideration in the study of the SQ-DQ correlations.

To facilitate the assignment of the Ar-H resonances (H^e , H^f and H^g , Fig. 8.19) these are classed in three main groups based on their CSs, which are expected in the order (H^e) > (H^f) > (H^g). In solution, pure 8-hydroxyquinoline resonates in the range 7.3 - 9.0 ppm, while for **I**, the CSs range from 7.6 and 9.8 ppm. The identification of the Ar-H resonances was made possible by analysing the DQ frequency of the off-diagonal peaks (Fig. 8.18b), involving the hydrogen-bonded ^1H resonances (H^a , H^b and H^c), which are well resolved.

In the 2D $^1\text{H}-^1\text{H}$ DQF spectrum, H^e resonances exhibit strong off-diagonal correlations with H^a and H^b as they are in ortho positions (adjacent) and, thus, relatively close (2.16 - 2.28 \AA), showing DQ CSs of ca. 26.4 (16.6+9.8) and 24.7 (14.9+9.8) ppm for H^a and H^b , respectively. This evidence allows the assignment of H^a and H^b to $\text{N}^+\text{-H}\cdots\text{OH}_2$ bonds evidenced by XRD data. In a similar way, the resonance at ca. 13.1 ppm (H^c) has a DQ

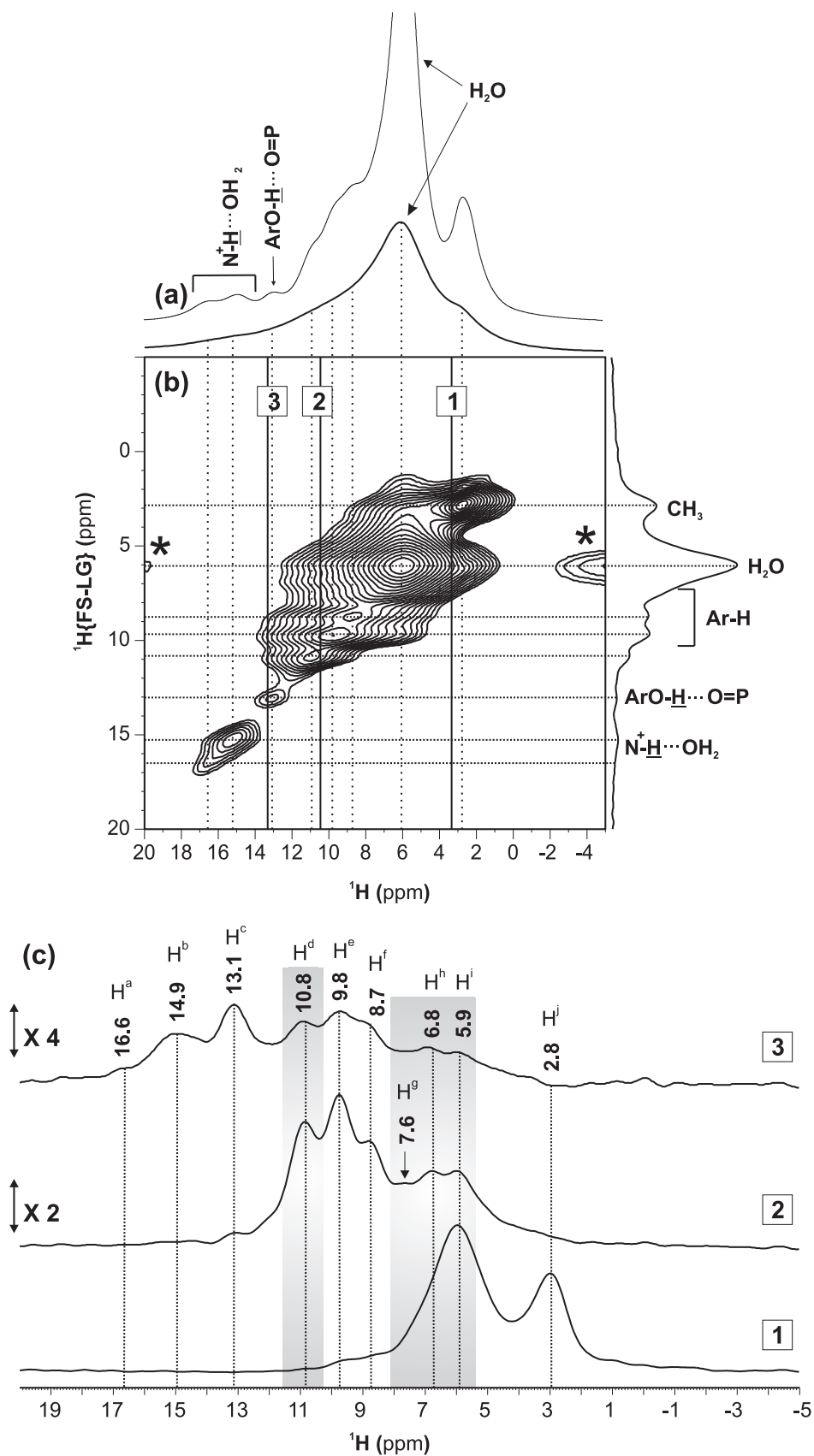


Fig. 8.17: (a) ^1H MAS and (b) $^1\text{H}\{\text{FS-LG}\}$ - ^1H HOMCOR spectra of **I**. (c) F1 cross-sections of the $^1\text{H}\{\text{FS-LG}\}$ - ^1H HOMCOR spectrum of **I**. Asterisks depict spinning sidebands.

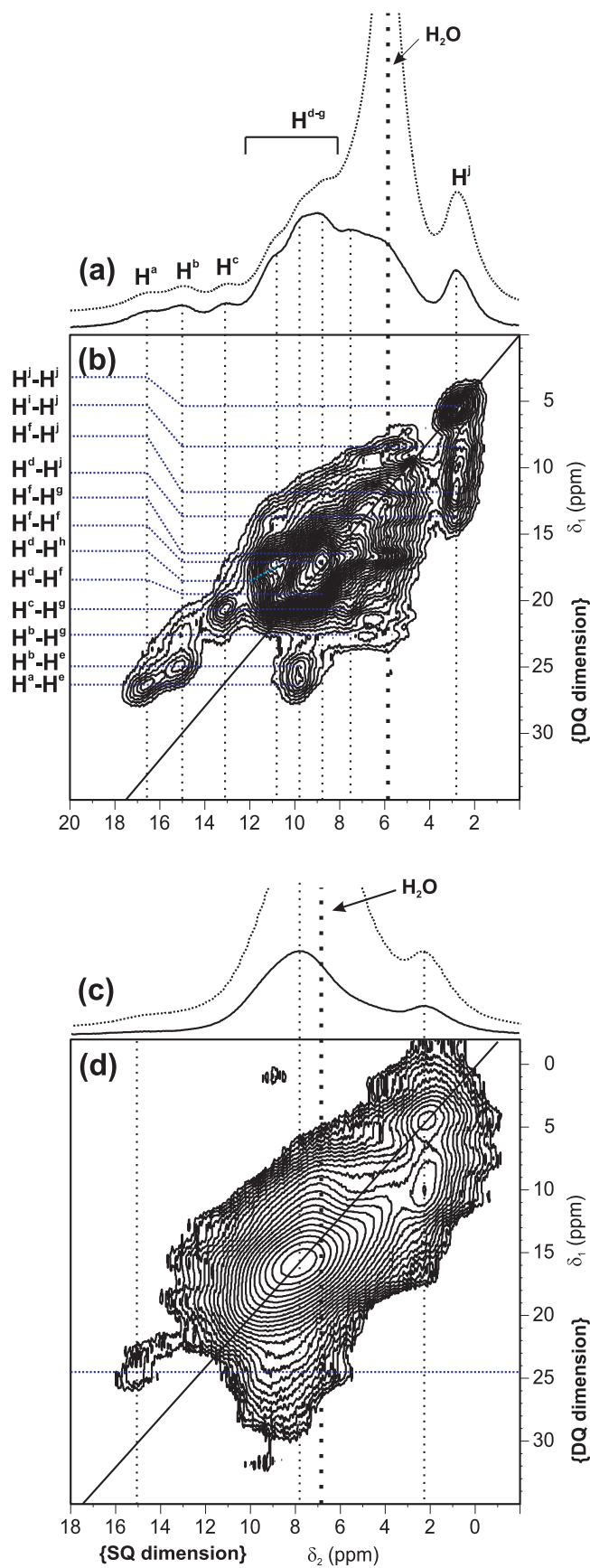


Fig. 8.18: (a) ^1H MAS and (b) ^1H DQ MAS NMR spectra of **I**. (c) ^1H MAS and (d) ^1H DQ MAS NMR spectra of **II**.

Table 8.5: ^1H CS assignment of **I**.

$^1\text{H}^{[a]}$	SQ $\delta_H(\text{ppm})$	DQ $\delta_H(\text{ppm})$	DQ coherences ^[b]
ArN ⁺ - <u>H</u> (H^a)	16.6	26.4	$\text{H}^a \dots \text{H}^e$
ArN ⁺ - <u>H</u> (H^b)	14.9	24.7 22.5	$\text{H}^b \dots \text{H}^e$ $\text{H}^b \dots \text{H}^g$
ArO- <u>H</u> (H^c)	13.1	20.7	$\text{H}^c \dots \text{H}^g$
CO- <u>H</u> (H^d)	10.8	19.5 17.6 13.6	$\text{H}^d \dots \text{H}^f$ $\text{H}^d \dots \text{H}^h$ $\text{H}^d \dots \text{H}^j$
Ar- <u>H</u> (H^e) ^[c]	9.8	26.4 24.7	$\text{H}^e \dots \text{H}^a$ $\text{H}^e \dots \text{H}^b$
Ar- <u>H</u> (H^f)	8.7	16.3 11.5 19.5	$\text{H}^f \dots \text{H}^g$ $\text{H}^f \dots \text{H}^j$ $\text{H}^f \dots \text{H}^d$
Ar- <u>H</u> (H^g) ^[c]	7.6	16.3 20.7 22.5	$\text{H}^g \dots \text{H}^f$ $\text{H}^g \dots \text{H}^c$ $\text{H}^g \dots \text{H}^b$
HO- <u>H</u> (H^h, H^i) ^[d]	5.9, 6.8	8.7 17.6	$\text{H}^i \dots \text{H}^j$ $\text{H}^h \dots \text{H}^d$
CH ₃ (H^j)	2.8	13.6 11.5	$\text{H}^j \dots \text{H}^d$ $\text{H}^j \dots \text{H}^f$

^[a] Resonances observed in the $^1\text{H}\{\text{FS-LG}\}-^1\text{H}$ and $^1\text{H}-^1\text{H}$ DQ spectra are considered.

^[b] DQ coherences are not considered for the self-correlation peaks (diagonal peaks).

^[c] There is evidence of $\text{H}^e \dots \text{H}^j$ and $\text{H}^g \dots \text{H}^j$ correlations, but their observation is difficult (Fig. 8.18).

^[d] These ^1H resonances refer to the two resolved peaks (H^h and H^i) observed in Fig. 8.17, which are tentatively assigned to H_2O protons.

frequency of ca. 20.7 ppm allowing the attribution of the peak at ca. 7.6 ppm to H^g as this resonance is also in ortho position relatively to H^c . Besides, H^c is not correlated with H^e resonances because no DQ frequency appears at ca. 22.9 (13.1+9.8) ppm. Therefore, H^c is not assigned to N^+ -H protons involved in hydrogen bonds with water, because these (H^a and H^b) are always correlated with H^e (Fig. 8.19).

Because the peaks are hidden by neighbour resonances, the correlations involving H^f resonances are harder to ascertain. The remaining peak in the aromatic region at 8.7 ppm is assigned to H^f . This is supported by the DQ self-correlation $\text{H}^f \dots \text{H}^f$ peak at ca. 17.4 ppm in the DQ dimension. The assignment of DQ coherences involving $\text{H}^f \dots \text{H}^g$ and $\text{H}^f \dots \text{H}^e$ was not possible due to the lack of resolution.

Let now consider the tentative attribution of the resonances of **I** at ca. 10.8 (H^d) and 6.8 ppm (H^h). The 2D $^1\text{H}-^1\text{H}$ DQ spectrum suggests that these protons are close in space giving a DQ frequency of ca. 17.6 ppm ($\text{H}^d \dots \text{H}^h$). In accord, XRD data reveals the presence of hydrogen bonds involving the H^d protons of tertiary alcohol groups of HEDP^{4-} and H^h protons of water molecules. Additionally, H^d (10.8 ppm) exhibit another DQ frequency at 13.6 (10.8+2.8) ppm, showing the proximity (< 0.35 nm) between CO-H and CH_3 groups. The spectrum also provides evidence for the proximity between the CH_3 protons (H_j) and 8-hydroxyquinoline because correlations with all the Ar-H (H^e , H^f and H^g) resonances (Table 8.5 and Fig. 8.18b) are observed. As far as compound **II** is concerned, the main conclusion is that the high-frequency resonance (at 15.1 ppm) may be assigned to N^+ -H \dots O=P hydrogen bonds (Fig. F.9b). Indeed, **II** possesses only a single type of very short (1.86 Å) hydrogen

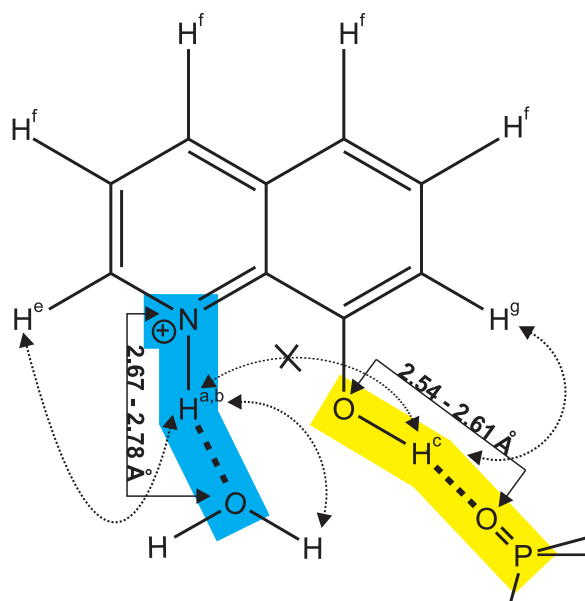


Fig. 8.19: Hydrogen bonds formed by 8-hydroxyquinoline in compound **I**. Dashed arrows show the interactions revealed by XRD.

bond.

The ^1H - ^1H exchange RFDR (Fig. 8.20) and ^1H - ^1H DQ experiments provide complementary information, because the former maps correlations involving both mobile and rigid species, while the latter filters the mobile species.

In **I**, the lattice water resonances (H^i) are correlated with all peaks even at low mixing times, revealing the presence of water molecules dispersed throughout the structure. On the other hand, at the mixing time of 0.53 ms (Fig. 8.20a) the CH_3 (H^j) resonances are not correlated with H^a , H^b and H^c , thus supporting the DQ results and confirming that the H^e protons are only near H^a and H^b (hydrogen bonds involving $\text{N-H}^+-\text{OH}_2$). Moreover, a clear correlation between H^c and H^g , is observed. This pair of resonances $\text{H}^c \cdots \text{H}^g$ is strongly correlated at low mixing times (Fig. 8.20a), supporting the information given by the ^1H - ^1H DQ spectrum (Fig. 8.18b). The ^1H - ^1H RFDR spectrum of structure **II** is far less informative and will not be further discussed (Fig. 8.20d-f).

The ^1H - ^1H DQF spectrum of **I** also reveals important information on the spatial arrangement of the organic residues. Excellent reviews are available on the study of 3D crystal packing based on ring-current effects due to the aromatic π orbitals. [138,237,238] Moreover, the influence of ring currents on neighboring molecules spreads the CSs over a range of 2 to 5 ppm. [239] The Ar-H resonances (H^e , H^f and H^g) of **I** are shifted to high frequency relatively to the resonances of 8-hydroxyquinoline in solution, which may be due to either amine protonation or small ring current effects caused by adjacent molecules. The relative orientation of adjacent 8-hydroxyquinoline molecules may be studied on the basis of the ^1H - ^1H DQ spectrum. The H^b resonance shows an additional off-diagonal correlation at a DQ frequency of 22.5 ppm, clear evidence of spatial proximity between protons H^b and H^g . Because the intra- and inter-molecular distances between these protons are, respectively, 5.3 and 3.2 Å the SQ-DQ correlation is ascribed to the latter proton resonances. Moreover, the absence of diagonal peaks involving the resolved hydrogen bonds indicates that H^a , H^b and H^c are protons belonging to separate molecules (Fig. 8.18b).

The ^1H projection of the $^1\{\text{FS-LG}\}\text{H}-^{31}\text{P}$ spectra of **I** (Fig. F.10) is better resolved than

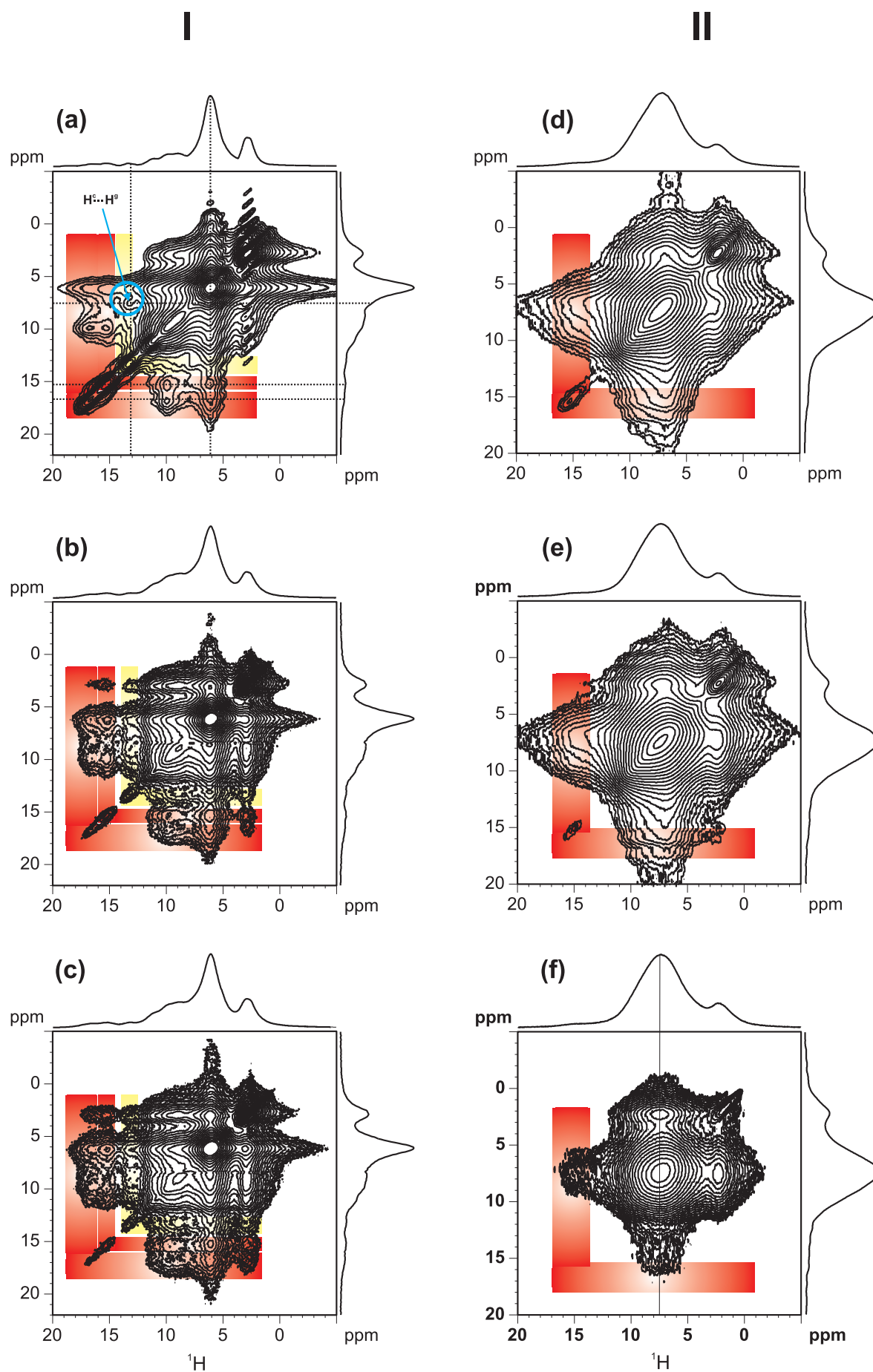


Fig. 8.20: 2D ^1H - ^1H exchange RFDR spectra recorded with mixing times of (a) 0.53, (b) 2.1 and (c) 3.2 ms for compound I and (d) 0.53, (e) 1.0 and (f) 5.3 ms for compound II.

the F1 projection of the $^1\text{H}\{\text{FS-LG}\}-^1\text{H}$ spectra (Fig. 8.17b). Alternatively, the $^1\text{H}\{\text{FS-LG}\}-^{31}\text{P}$ spectra are useful to probe the hydrogen bonds between the HEDP^{4-} phosphonate group and the 8-hydroxyquinoline aromatic residues. At short contact times (0.2 ms) the $^1\text{H}\{\text{FS-LG}\}-^{31}\text{P}$ H^c resonances are slightly more intense than the H^a and H^b , indicating that the H^c protons are hydrogen bonded to $\text{P}=\text{O}$ groups, as mentioned above (Fig. 8.19). It is worth mentioning that the spectrum using LG-CP HETCOR with $\tau_{CT}=3$ ms (Fig. F.10b), did not show any relevant improvement in resolution along the ^1H dimension, with respect to the conventional CP HETCOR (Fig. F.10a).

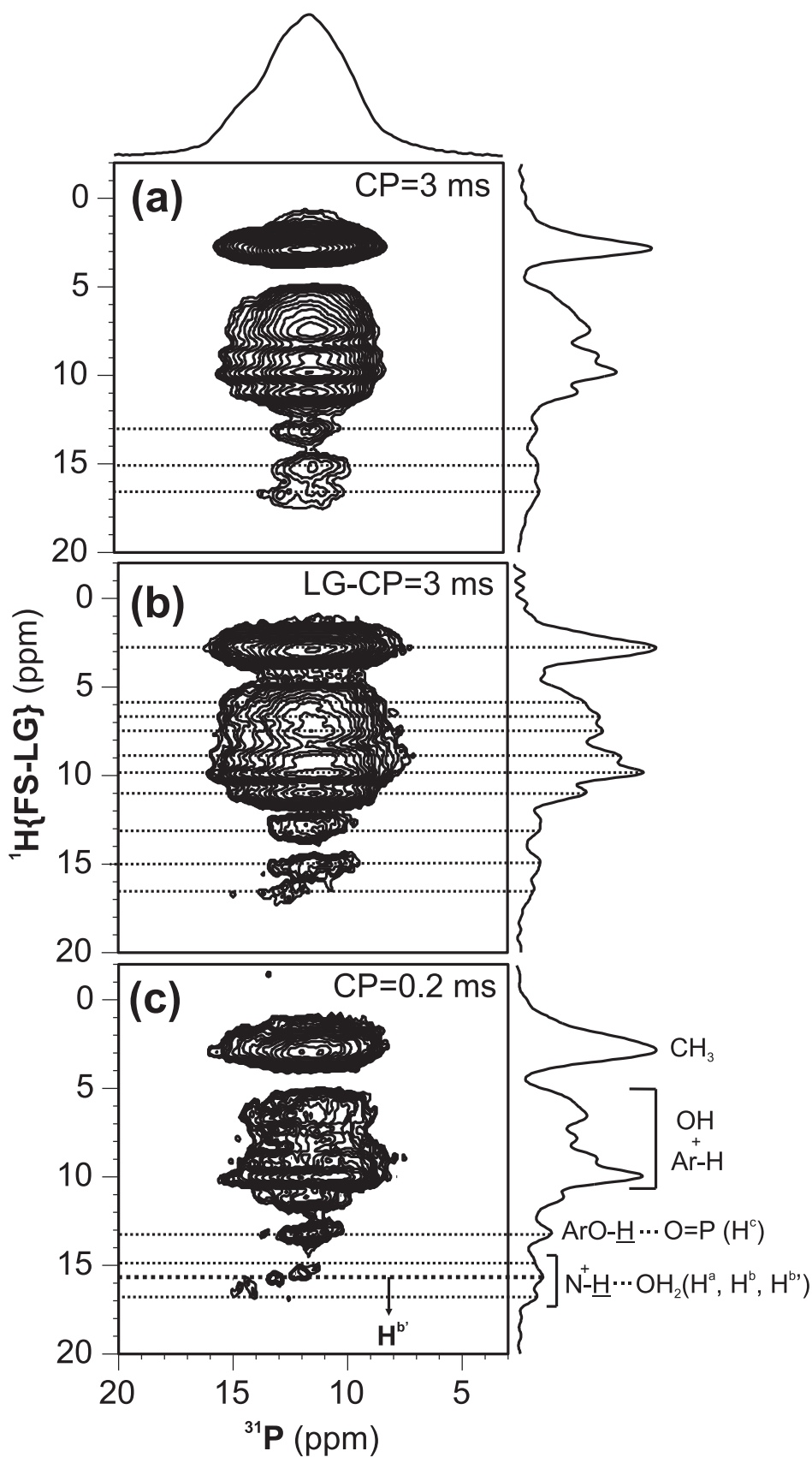


Fig. 8.21: $^1\text{H}\{\text{FS-LG}\}$ - ^{31}P spectra of **I**, recorded at contact times of 3 ms using (a) CP, (b) LG-CP and (c) 0.2 ms using CP.

Photoluminescence Spectroscopy

Fig. 8.22a shows the excitation spectrum of **I** recorded at 14 K. The spectrum consists of a broad band between 270 and 440 nm, assigned to aromatic ring $\pi - \pi^*$ transitions. [240] Exciting **I** within such states, leads to the observation of both a main band in the range 440 to 650 nm, peaking at 530 nm, and another emission component at higher wavelengths (Fig. 8.22a). According to the crystal structures, the aromatic moieties have two distinct packing environments: columnar $\pi - \pi$ stacking and adjacent molecules connected to the columns via weak $\text{C-H} \cdots \pi$ interactions. Hence, the former band may be assigned to the $\pi - \pi^*$ 0-phonon transition of the hydroquinoline adjacent rings, [240] corresponding to a triplet state energy of 18900 cm^{-1} , while the band at higher wavelengths is attributed to the excimer formation via $\pi \cdots \pi$ hydroquinoline interactions. At room-temperature, no efficient emission could be detected, indicating the presence of thermally activated non-radiative channels in **I**.

Fig. 8.22b shows the room-temperature excitation spectra of **II** monitored at 490 nm. The spectrum displays a large broad band between 270 and 400 nm, peaking at 367 nm, ascribed to aromatic ring $\pi - \pi^*$ transitions. [241] The room-temperature reflectance spectrum (not shown) resembles the excitation spectra, displaying an absorption edge at 370 nm. This value is shifted to the red when compared with the singlet energy of the neutral 1,10-phenanthroline ligand (320 nm, 31250 cm^{-1}). [242] This energy difference is induced by the different local environment of the 1,10 phenanthroline, in particular the metal coordination and the packing of the complex in **II**.

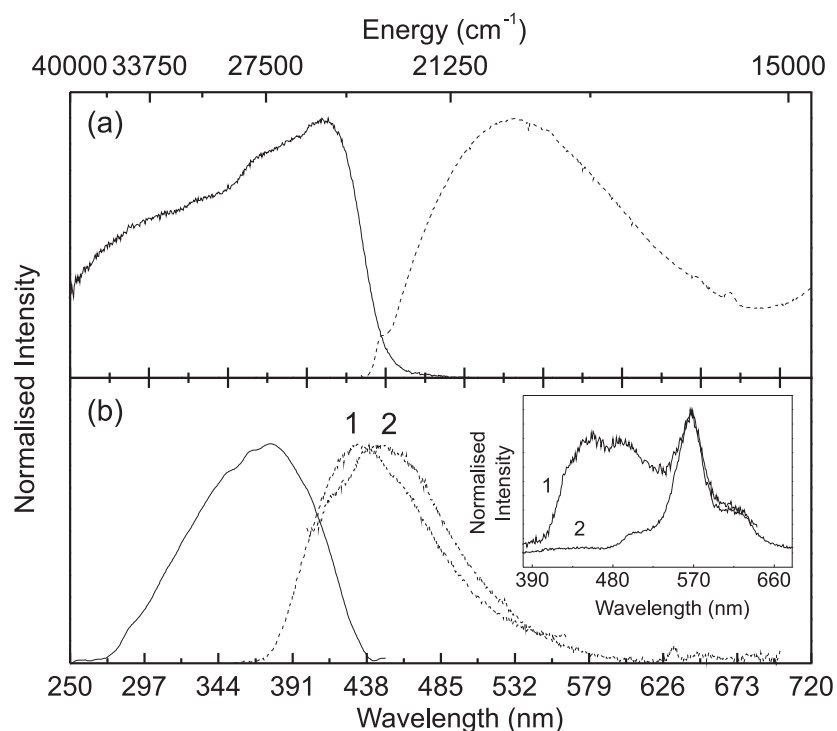


Fig. 8.22: Excitation (solid line) and emission (dashed line) spectra of (a) **I** and (b) **II** complexes recorded at 14 K and room-temperature, respectively. The excitation and emission spectra of **I** were monitored at 535 nm and excited at 408 nm, whereas for **II** the monitoring wavelength was 490 nm and the excitation ones were 330 nm (1) and 365 nm (2). The inset shows the time-resolved emission spectrum (14 K) of **II**, acquired with a starting delay of 0.05 ms and an acquisition window of 10.00 ms.

Under UV excitation (Fig. 8.22b) the emission of **II** consists of a large asymmetrical band between 380 and 550 nm. For excitation wavelengths in the range 270-370 nm, the emission energy peaks at 430 nm and does not depend on the excitation wavelength. For higher excitation wavelengths a broadening and red-shift of the emission spectra are observed. The dependence on the excitation wavelength and the asymmetric shape of the emission suggest the appearance of a new emitting species, preferentially excited at higher wavelengths. As suggested for **I**, the presence of two distinct emission components may be due to the presence of two different packing environments for the 1-10 phenanthroline rings. The spectra acquired for excitation wavelengths between 270-370 nm may correspond to the preferential emission arising from the adjacent 1-10 phenanthroline rings. Like the excitation spectrum (Fig. 8.22a), their emission energy is shifted with respect to that of the free 1-10 phenanthroline chromophore, whose lowest triplet-state energy ($\pi\pi^*$ 0-phonon transition) peaks at 366 nm (27322 cm^{-1}) [243,244] being, however, very similar to that observed for the $\text{Gd}(\text{phen})_2\text{Cl}_3\cdot 2\text{H}_2\text{O}$ [243] compound, with a lowest triplet state energy of 453 nm (22075 cm^{-1}). [245] The emission component at lower energy may be ascribed to the formation of an excimer via the $\pi - \pi$ phenanthroline interactions, as observed in 1,10-phenanthroline compounds with the same crystal packing of **II**. [243,244]

The presence of two distinct emissions in **II** was further established and investigated by time-resolved emission and lifetime measurements. These studies were performed at 14 K, since the room-temperature time-scale of the photoluminescence mechanisms is smaller than the detection limit of our equipment (10^{-5} s). For lower excitation wavelengths, the spectrum consists of a structured broad band (inset in Fig. 8.22a). Changing the excitation wavelength between 363 and 402 nm, there is a decrease in the relative intensity of the lower wavelength side of the spectra, further indicating the presence of two distinct emitting species. Such intensity decrease suggests that the time scale of the emission mechanisms of the emission component at lower wavelengths is smaller than that of the higher energy emission. The short-live emission is consistent with a monomer related component, whereas the longer-live and lower energy emission is compatible with excimer formation. [243,244,246] The excimer emission decay curve was monitored at 568 nm under 330 nm (not shown). The decay curve is well reproduced by a single exponential function, yielding a lifetime of $4.33\pm 0.11\text{ ms}$.

Thermal Analysis

Thermogravimetric studies under a continuous flow of nitrogen further confirmed structural aspects of compounds **I** and **II**, in particular the presence of highly disordered water molecules of crystallisation located inside relatively large cavities. For both compounds, the thermograms clearly reveal significant and relatively constant weight losses starting almost at ambient temperature. After ca. 150°C , and up to ca. 400°C , gradual mass losses were recorded, with no obvious steps or plateaus. For **I**, in the $20\text{--}400^\circ\text{C}$ temperature range it is possible to discern four mass losses (Experimental Section), with a combined total weight loss of ca. 25.5%, which is in good agreement with the liberation of all 33 crystallographic unique water molecules of crystallisation plus two unprotonated 8-hydroxyquinoline residues (calculated mass loss of ca. 25.3%). Although for **I** it was not possible to distinguish the temperature ranges in which the water molecules and the organic components were released, this was not the case for compound **II**. In fact, for the latter material the thermogram clearly shows two regions in which the mass is released in a continuous fashion (Experimental Section): between 20 and 125°C a combined mass loss of ca. 10.3% is in good agreement with the release of all 20 water molecules of crystallisation (calculated ca. 10.1%); after this temperature, and up to ca. 364°C , a total mass loss of ca. 10.0% is attributed to the release of two unprotonated 1,10-phenanthroline organic residues (calculated ca. 10.1%). In summary, TG shows that

the large number of water molecules of crystallisation present in **I** and **II** may be released at a relatively low temperature, which is an indication of the porous nature of these materials. Moreover, it is fair to assume that the two organic molecules which are released after ca. 150 °C are the weakly bounded pairs (Figs. 8.14 and 8.15) which interconnect adjacent $\pi - \pi$ -stacked columns. This would maintain the electroneutrality of the crystal structures and it would not disrupt the energetic cooperative effect of the $\pi - \pi$ stacking of aromatic molecules.

Vibrational Spectroscopy: Interpretation

FT-IR and FT-Raman spectroscopies (spectra not shown) confirm the presence of the primary building blocks of **I** and **II** through the typical vibrations of phosphonate groups and heteroaromatic amines (See section 8.2.1). Hydrogen bonding causes a significant broadening of the FT-IR bands and lowers the mean absorption frequency. Clearly, the OH stretching vibration modes are shifted to lower energy (3300-3400 cm^{-1}). Specifically, the out-of-plane bending $\gamma(\text{O-H})$ and wagging $\omega(\text{O-H})$ vibrational modes show remarkable differences in both structures. The latter are usually of minor importance, showing typical group frequencies in the range 790-520 cm^{-1} . [247] However, in **I** and **II**, these bands are strong and broad (at 583 and 592 cm^{-1} , respectively), indicating the presence of strong hydrogen bonds. The group frequencies at 976 and 971 cm^{-1} for, respectively, **I** and **II**, are also very intense and broad and may be assigned to other type of out-of-plane vibrational modes (γ) of hydrogen-bonded OH groups.

8.2.3 Conclusion

Two germanium-hedp⁴⁻ solids with heteroaromatic amines, 8-hydroxyquinoline (**I**) and 1,10-phenanthroline (**II**) have been prepared and characterised by single-crystal XRD, TG, FTIR and UV-vis spectroscopies. High-resolution SSNMR has been used to study the complex hydrogen-bonded networks, particularly in compound **I**. Certain details of the crystal structure of **I** have been elucidated, mainly concerning the occurrence of $\pi - \pi$ stacking of 8-hydroxyquinoline and the relative orientation of adjacent such molecules. It has been shown that the combination of homonuclear recoupling techniques (2D $^1\text{H}-^1\text{H}$ DQ, 2D $^1\text{H}-^1\text{H}$ RFDR MAS NMR) and CRAMPS techniques (2D $^1\text{H}\{\text{FS-LG}\}-^1\text{H}$, $^1\text{H}\{\text{FS-LG}\}-^{31}\text{P}$) provides a powerful toolbox for the characterisation of organic-inorganic hybrid materials. Compound **II** displays emission from the lowest triplet state energy ($\pi\pi^*$ 0-phonon transition) of the aromatic rings peaking at ca. 320 nm (31250 cm^{-1}) in the range 14 K to room temperature, whereas the triplet emission of complex **I** at ca. 530 nm (18868 cm^{-1}) is detected at low temperature. A long-live and low-energy emission component, resulting from the formation of an excimer state, originated via the $\pi - \pi$ stacking of 1,10-phenanthroline and hydroxyquinoline residues was observed for **I** and **II**, respectively.

Chapter 9

Studies of Amine Guests in Hybrid Materials

9.1 NMR Characterisation of Microporous Aluminophosphate, IST-1

Since the discovery of microporous aluminophosphates by Wilson *et al.* [248], much research has been concentrated on the synthesis of these materials, employing organic templates [249, 250] (generally amines), which play a decisive role as structure-directing agents. In this section, I report NMR studies of a templated aluminophosphate, IST-1 [251], containing two types of methylamine species: [N(1)C(1)] (here denoted MA or NH₂) is linked to six-coordinated Al atom, while [N(2)C(2)] (MA⁺ or NH₃⁺) resides in the channels and is probably protonated and hydrogen-bonded to three framework oxygen atoms [O(1), O(2), and O(12)]. An additional hydroxyl group [O(13)], bridging two Al-atoms [Al(1) and Al(3)], is also present. [251] I have used ¹H NMR resolution-enhancement techniques, such as 2D ¹H{FS-LG}-¹H HOMCOR and ¹H{FS-LG}-X (X = ¹³C, ³¹P, ²⁷Al) correlation HETCOR MAS experiments using FS-LG decoupling, to elucidate the fine details of the IST-1 structure, particularly in what concerns the methyl-ammonium cations, MA⁺, and Al-coordinated methylamine molecules, MA. Moreover, the ³¹P³¹P DQ-SQ experiment was used to confirm the previous assignment of the IST-1 ³¹P resonances. [251]

9.1.1 Experimental Section

The sample was kindly dispensed by Prof. F. Ribeiro from Instituto Superior Técnico, Lisbon. The synthesis method is conveniently described elsewhere. [252] X-ray studies are available in ref. [251].

NMR Measurements

General: 2D FS-LG measurements were performed using a 3 μs ¹H 90° pulse. The ¹H RF field strength was set to ca. 83 and 100 kHz for, respectively, FS-LG and TPPM decoupling. The FS-LG decoupling was optimised according to section 4.9.2.

The phase modulation angle for the TPPM decoupling was set to 15.0°, giving a pulse length of 4.4 μs when optimized directly on the IST-1 sample. RAMP-CP [199] was used in the ¹H channel to transfer magnetization from ¹H to ¹³C/³¹P/²⁷Al. The ¹H *rf* field was ramped from 100 to 50% (from 100 to 50 kHz for ¹³C and ³¹P, and 50-25 kHz for ²⁷Al), while

the X RF field was set to 66, 50, and 12 kHz for ^{13}C , ^{31}P , and ^{27}Al , respectively. CSs are quoted in ppm from TMS (^1H and ^{13}C), $[\text{Al}(\text{H}_2\text{O})_6]^{3+}$ (^{27}Al), and 85% H_3PO_4 (^{31}P).

2D $^1\text{H}\{\text{FS-LG}\}\text{-X}$ ($\text{X} = ^1\text{H}$, ^{13}C , ^{31}P , and ^{27}Al) HOMCOR/HETCOR: The FS-LG optimisation was performed according to the description given in section 8.1.1. Specific experimental conditions of each spectrum are given in the figure captions.

2D $^{31}\text{P}\text{-}^{31}\text{P}$ DQ HOMCOR: The pulse sequence employed for the $^{31}\text{P}\text{-}^{31}\text{P}$ DQ measurements is shown in Fig. 5.3a. Prior to the relaxation delay, a saturation comb of 90° pulses was applied. The POSTC7 sequence was chosen to reintroduce the $^{31}\text{P}\text{-}^{31}\text{P}$ homonuclear dipolar interaction under MAS conditions and to achieve an efficient broad band excitation and reconversion of the DQ coherences. [132] The 90° pulse was set to $3.6 \mu\text{s}$ and the phases were adjusted by using a combination between the digital phase shifter ($n \times 7 \times \frac{2\pi}{7}$ phase increments intercalated by a phase preset of $0.3 \mu\text{s}$) and the four-phase modulator (alternating between $+x$ and $-x$ according to the pulse sequence in Fig. 5.3c). Further details on the experimental conditions are given in the figure captions. After t_1 evolution, the DQ coherences were reconverted using the excitation pulse sequence, with an overall constant phase shift of $\pi/2$ to achieve time reversal. For quadrature detection during t_1 , the States mode was employed. [38] No ^1H decoupling was applied during acquisition.

9.1.2 Results and Discussion

Structure Description

The structure of IST-1 (Fig. 9.1) was refined from high-resolution synchrotron powder XRD data in the non-centrosymmetric space group Pca21, in tandem with SSNMR. [251] Here, I concentrate the attention on the following structural features of IST-1: (i) one methylamine species probably protonated [MA^+ , C(2)N(2)], resides in the channels and is hydrogen-bonded to three framework oxygen atoms; (ii) a second methylamine molecule [MA , C(1)N(1)] bonds directly to a framework Al atom, a relatively uncommon structural feature among aluminophosphates.

NMR Analysis

^1H NMR

The $^1\text{H}\{\text{FS-LG}\}\text{-}^1\text{H}$ HOMCOR spectrum of IST-1 (Fig. 9.2) exhibits four well-resolved resonances at ca. 1.2, 2.4, 3.9 and 7.8 ppm, attributed to the Al-OH, CH_3 , NH_2 (MA) and NH_3^+ (MA^+) species, respectively. Usually, protonated amines resonate at high frequency, typically 7.0-9.0 ppm, depending on the nature of H-bonding network present. [122,253,254] The previous structural study did not provide definitive proof for the presence of MA^+ cations in IST-1. [251] However, the resonance at ca. 7.8 ppm (Fig. 9.2) is clearly attributed to $^+\text{N}\text{-H}\cdots\text{O}^-$ interactions. The large N-Al bond length [$2.10(1) \text{ \AA}$] and, thus, weak chemical bond helps understanding why the NH_2 resonance is much shifted to low frequency relatively to NH_3^+ resonance (3.9 and 7.8 ppm). The spectrum also displays a peak at 1.2 ppm, tentatively assigned to bridging O-H [Al(1)-OH-Al(3)] groups, which resonate at 0.8-1.5 ppm, [253,254] or non-acidic terminal Al-OH groups in AlPOs. [255]

^{13}C NMR

The interpretation of the $^1\text{H}\{\text{FS-LG}\}\text{-X}$ ($\text{X} = ^{13}\text{C}$, ^{31}P , and ^{27}Al) HETCOR spectra is assisted by considering the interatomic separations obtained from the synchrotron powder XRD

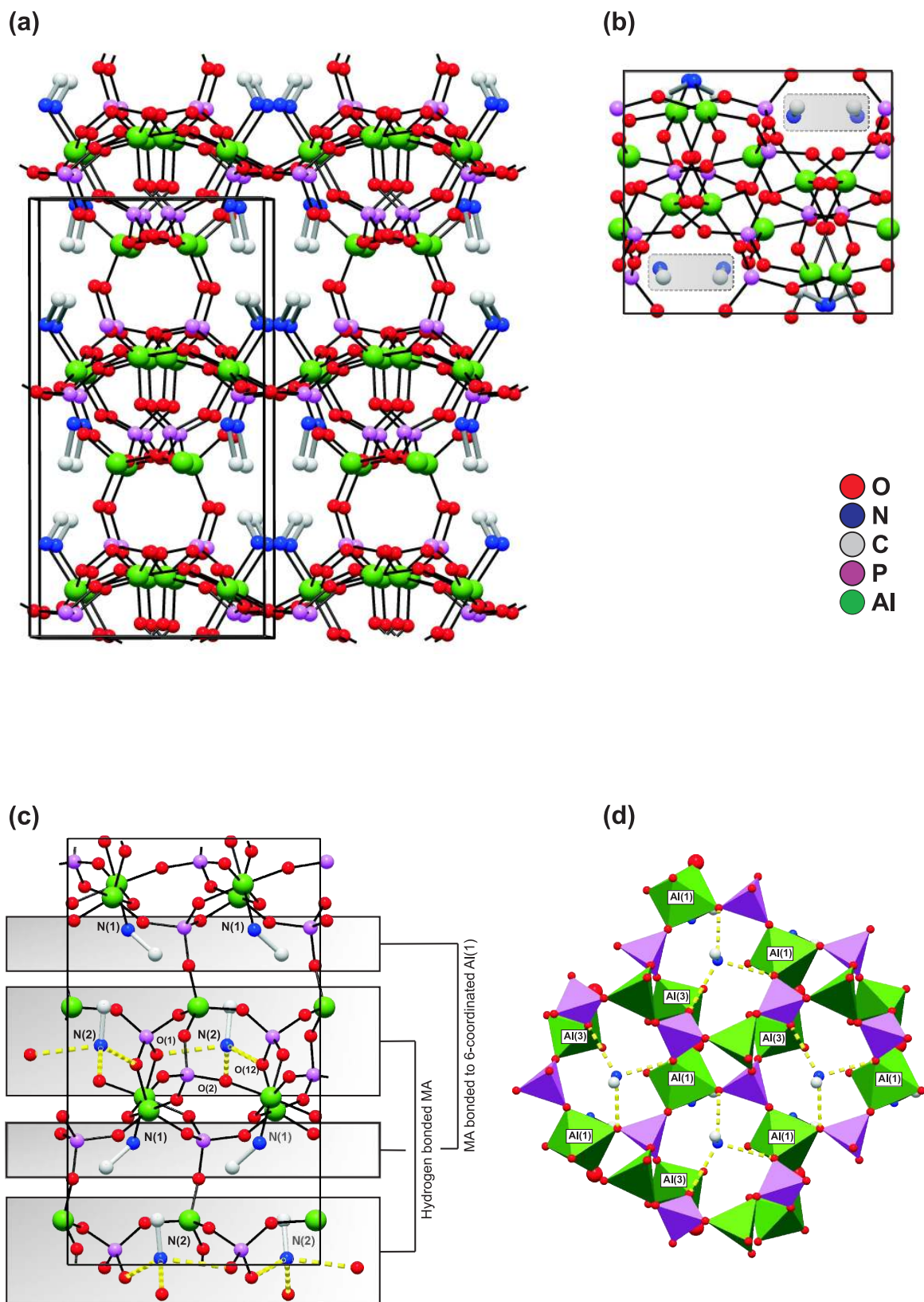


Fig. 9.1: (a) Crystal packing viewed in perspective along the *a*-axis. (b) Unit cell contents viewed along the *c*-axis depicting the location of the extraframework MA [C(2)N(2)] species inside the IST-1 pores. (c) Schematic representation, viewed down the *b*-axis, showing the MA, [N(1)C(1)], species coordinated to Al(1), and the protonated MA⁺ species (residing in the channels, hydrogen-bonded to three framework O-atoms [O(1), O(2) and O(12)]). (d) Polyhedral representation of the structure of IST-1 viewed down the *c*-axis.

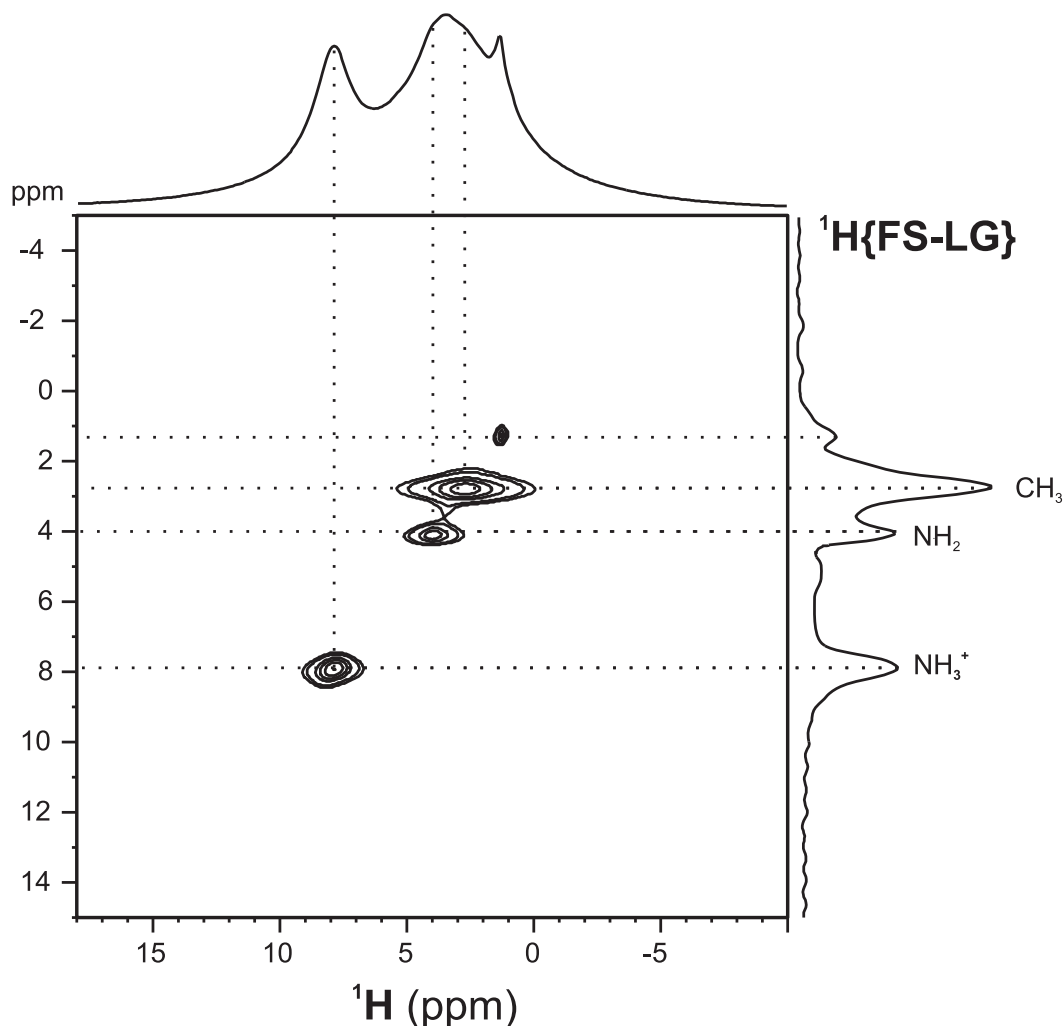


Fig. 9.2: 2D ${}^1\text{H}\{\text{FS-LG}\}{}^1\text{H}$ HOMCOR spectrum of IST-1. A total of 200 t_1 increments with eight transients each were collected. F1 increments were synchronized with an integer number of FS-LG units ($n \times 2 \times \tau_{\text{LG}}$) with $n = 3$. The value of ν_{LG} was ± 3000 Hz and the recycle delay 3 s.

structure. [251] Because no neutron diffraction data were collected, reliable $\text{H} \cdots \text{X}$ distances are not available. Instead, distances between X and the atom to which a given proton is linked will be considered. The 2D ${}^1\text{H}\{\text{FS-LG}\}-{}^{13}\text{C}$ CP HETCOR spectrum recorded with a τ_{CT} of 2000 μs [Fig. 9.3a] is uninformative because all peaks are correlated. However, the spectrum recorded with a $\tau_{\text{CT}} = 200$ μs [Fig. 9.3b] clearly shows that (i) the ${}^1\text{H}$ resonance at ca. 2.4 ppm is attributed to the CH_3 groups, and (ii) the ${}^{13}\text{C}$ resonance at ca. 24.5 ppm is unambiguously assigned to the MA^+ carbon [C(2)], because a unique cross-peak is observed between it and the MA^+ proton peak (ca. 7.8 ppm). The latter conclusion is in contrast with the tentative assignment of the ${}^{13}\text{C}$ resonances based on computational models. [251]

The splitting in ${}^{13}\text{C}$ spectrum: An outstanding feature of the F2 (${}^{13}\text{C}$ axis) projections of the spectra in Fig. 9.3 is the presence of asymmetric doublets centred at ca. 24.5 and 28.2 ppm, which may be attributed to:

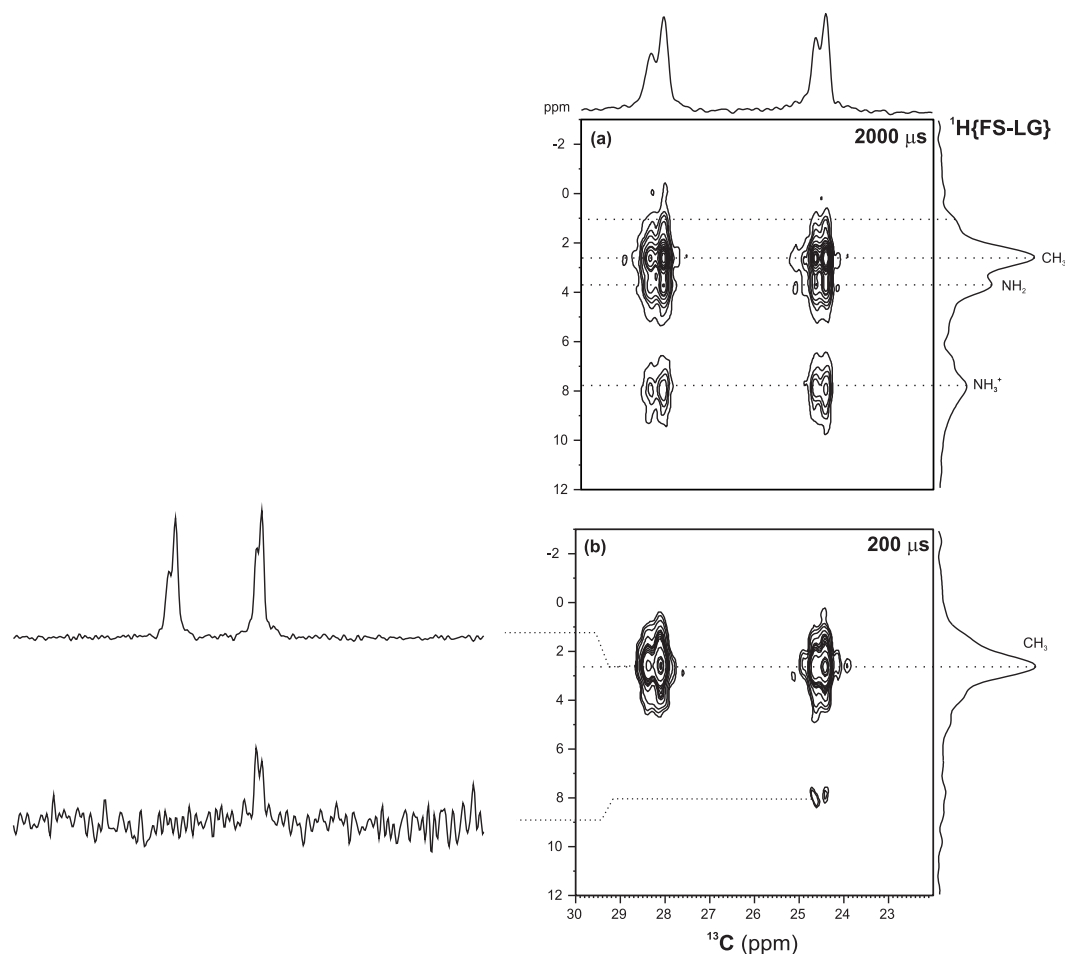


Fig. 9.3: 2D ${}^1\text{H}\{\text{FS-LG}\}{}^{13}\text{C}$ CP HETCOR NMR spectra of IST-1 recorded with (a) $\tau_{\text{CT}}=2000$ and (b) $\tau_{\text{CT}}=200$ μs . 90 t_1 increments with 164 transients each were collected. The F1 increments were synchronized with an integer number of FS-LG units ($n \times 2 \times \tau_{\text{LG}}$) with $n=3$. The recycle delay was 3 s and the value of ν_{LG} was -5000 Hz. The F2 slices of selected cross-peaks are depicted on the left.

- (i) the presence of four non-equivalent MA species, or
- (ii) the unaveraged ${}^{13}\text{C}$ - ${}^{14}\text{N}$ dipolar coupling involving the quadrupolar nucleus ${}^{14}\text{N}$. [256, 257]

The latter usually yields asymmetric doublets with intensities in a 2:1 ratio, which is clearly observed in the ${}^1\text{H}{}^{13}\text{C}$ CP-MAS spectra shown in Fig. 9.4. However, this splitting is usually observed at relatively low B_0 fields and, to the best of our knowledge, has not yet been reported at 9.4 T. The splitting observed in Fig. 9.4 arises because the ${}^{14}\text{N}$ spin states are not purely Zeeman in nature ($|\psi_k\rangle$, with $k = -1, 0, +1$). In a ${}^{13}\text{C}$ - ${}^{14}\text{N}$ coupled spin pair, the quantization axis of ${}^{14}\text{N}$ spin is not strictly along the external magnetic field (B_0) since the quadrupolar interaction of ${}^{14}\text{N}$ has, in many cases, a magnitude comparable to that of the Zeeman interaction. Several systems have been investigated where the first-order perturbation accounts for the effect of residual dipolar coupling to quadrupolar nuclei in SSNMR spectra of spin-1/2 nuclei. [258–264] Olivieri and Harris [29, 263, 264] derived first- and second-order effects on the ${}^{13}\text{C}$ resonance, the latter showing a dependence of the ${}^{13}\text{C}$ splitting, $({}^{(2)}\Delta\nu_k)$ on parameters such as the CN distance, static magnetic field and

quadrupolar constant:

$${}^{(2)}\Delta\nu_k = \frac{D^{IS}C_Q}{\nu_S} \times \frac{3S(S+1) - 9k^2}{20S(2S-1)} \times 3\cos^2(\beta) - 1 + \eta\sin^2\beta\cos 2\alpha \quad (9.1)$$

where β and α are the polar angles specifying the orientation of the IS internuclear vector with respect to the EFG tensor, and ν_S is the S(^{14}N) spins Larmor frequency. Eq. 9.1 is only applicable if certain assumptions hold. [29] Eq. 9.1 shows that the peak positions depend on k^2 and, thus, the $|\psi_{\pm k}\rangle$ state (i.e., $|\psi_{\pm 1}\rangle$ for the ^{14}N nucleus) produces the same shift, since the signal does not influence the eigenstates. The result is the superposition of the $|\psi_{+1}\rangle$ and $|\psi_{-1}\rangle$ states at the same frequency and $|\psi_0\rangle$ at a different frequency, thus yielding the theoretical 2:1 ratio. [29, 263, 264] Eq. 9.1 further shows an inverse dependence of the ^{13}C splitting on the S spins Larmor frequency, in agreement with our results (Fig. 9.4a). Increasing the magnetic field from 9.4 to 11.7 T reduces the splitting, indicating that the ^{14}N second-order quadrupolar effects influence the ^{13}C - ^{14}N dipolar interaction. In principle, the splittings observed for the two resonances, may support the assignment made on the basis of the 2D $^1\text{H}\{\text{FS-LG}\}$ - ^{13}C HETCOR spectra (Fig. 9.3). Olivieri *et al.* [264] reported a nearly linear relationship between the C-N crystallographic distances and the ^{13}C splittings, *i.e.*, the shorter the C-N distance the larger the splitting value. In IST-1, the C-N distances of the MA (resonance at ca. 28.2 ppm) and MA^+ (ca. 24.5 ppm) species are 1.481 and 1.499 Å, respectively. Since the C-N distances are very similar, the CQs of both species probably determine the size of the splittings. However, the CQs of the ^{14}N nuclei are unknown.

^{31}P NMR

The 2D ^{31}P - ^{31}P DQ HOMCOR experiment was performed in order to confirm the previous ^{31}P assignment, based upon ^{27}Al - ^{31}P HETCOR evidence [251] which, because of the complicated spin dynamics involved in the spin locking and polarization transfer between spin-1/2 quadrupolar nuclei, was only tentative. Moreover, ^{27}Al - ^{31}P HETCOR spectroscopy requires a third NMR channel which is not necessary for recording 2D ^{31}P DQ spectra. Consider the F2 (^{31}P) projection in Fig. 9.5. The resonances of the three unique P sites of IST-1 have been labeled according to the internuclear P \cdots P distance depicted in Table 9.1. [251]

The strongest ^{31}P auto-correlation peak (diagonal) is attributed to P(2) because the P(2) \cdots P(2) distance is the shortest one. As expected, the P(3) \cdots P(3) peak is very weak, while the P(1) \cdots P(1) correlation is absent. With this information in hand, the assignment of the cross-peaks is straightforward and it may be confirmed by considering the cross-peak intensities (Fig. 9.5). Clearly, the strongest cross-peaks are P(2) \cdots P(3) and the faintest P(1) \cdots P(3). Consider now the 2D $^1\text{H}\{\text{FS-LG}\}$ - ^{31}P CP HETCOR spectra in Fig. 9.6. In accord with the X-ray structure, the less intense cross-peaks are observed between P and H atoms which are further apart: P(2) \cdots N(1) (5.3 Å) and P(1) \cdots N(2) (3.9 Å). The spectrum in Fig. 9.6 supports the assignment of MA and MA^+ species made previously. The distances depicted in Fig. 9.6b are consistent with the cross-peak intensities observed. For instance, the distance P(2) \cdots N(1) is, by far, the longest (5.3 Å). Accordingly, the faint cross-peak correlating P(2) and the $-\text{NH}_2$ [HN(1)-Al] groups is correctly labeled in Fig. 9.6, allowing the assignment of the C(1)-N(1) group to the MA residues resonating at ca. 3.9 ppm ($-\text{NH}_2$). The ^1H resonances of C(2)-N(2) group may, thus, be assigned to the MA^+ species resonating at ca. 7.8 ppm ($-\text{NH}_3^+$). The P(1) \cdots N(2) cross-peak is much less intense than the P(2), P(3) \cdots N(2) cross-peaks, presumably because the P(1) \cdots N(2) distance is the longest (respectively, 3.9 and 3.7 and 3.4 Å).

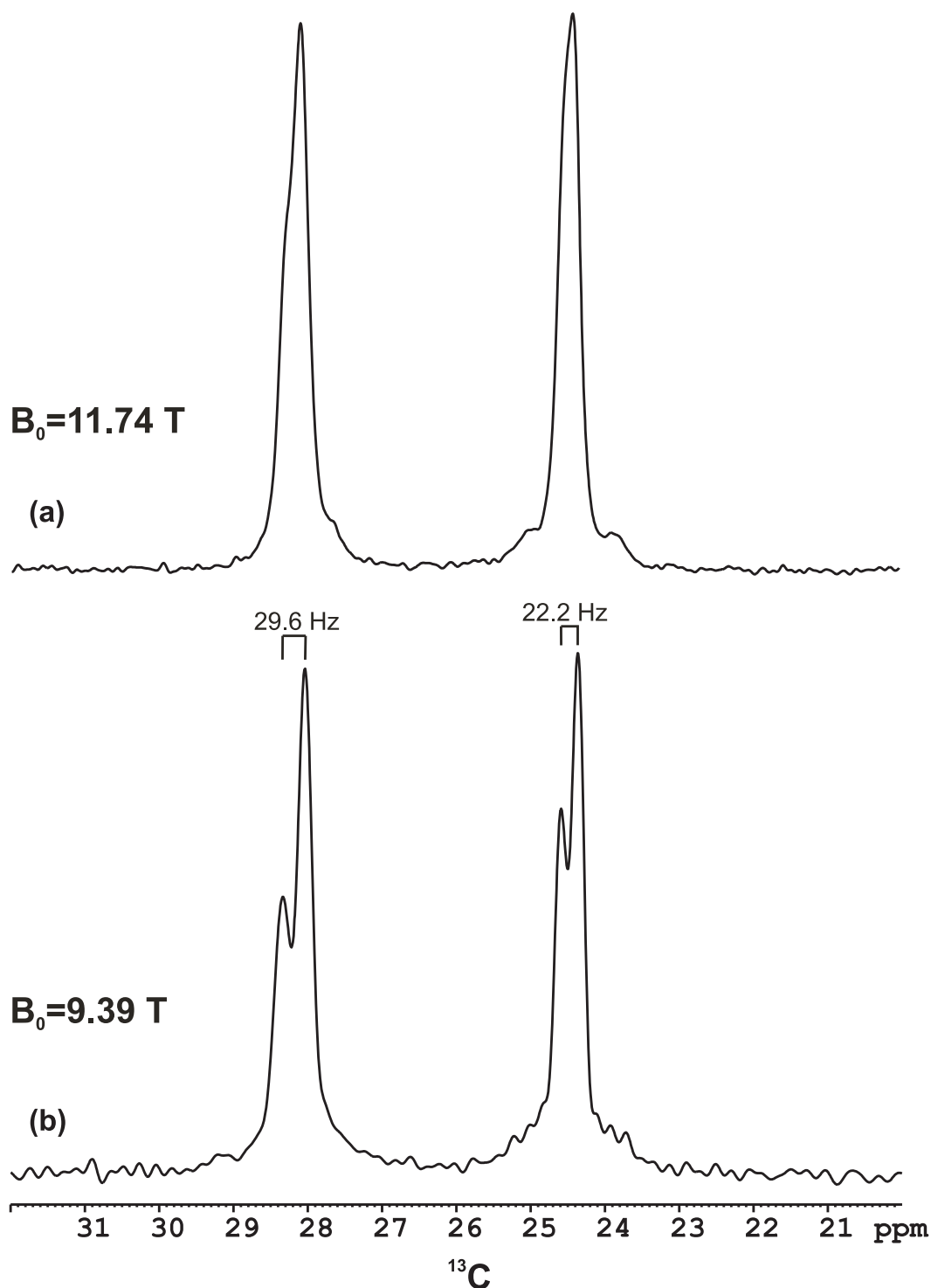


Fig. 9.4: Ramped ^{13}C CP-MAS spectra showing the effect of the Zeeman field (B_0) on the asymmetric doublet pattern. Spectra were acquired at (a) 11.74 T and (b) 9.39 T. The heteronuclear decoupling rf field and the spinning speed used were set to $\nu_1 = 100$ kHz and $\nu_R = 12$ kHz, respectively. TPPM-15 was used as the heteronuclear decoupling scheme. The magic angle was very carefully adjusted to obtain the best resolution.

Table 9.1: $P \cdots P$ crystallographic distances in IST-1 structure (\AA)

P sites ^[a]	P(1)	P(2)	P(3)
P(1)	5.65	-	-
P(2)	4.57	5.03	-
P(3)	4.90	4.23	5.48

^[a] Labeling scheme follows the notation presented in the ^{31}P spectra of Figs. 9.5 and 9.6 is in accord with the X-ray structure. [251]

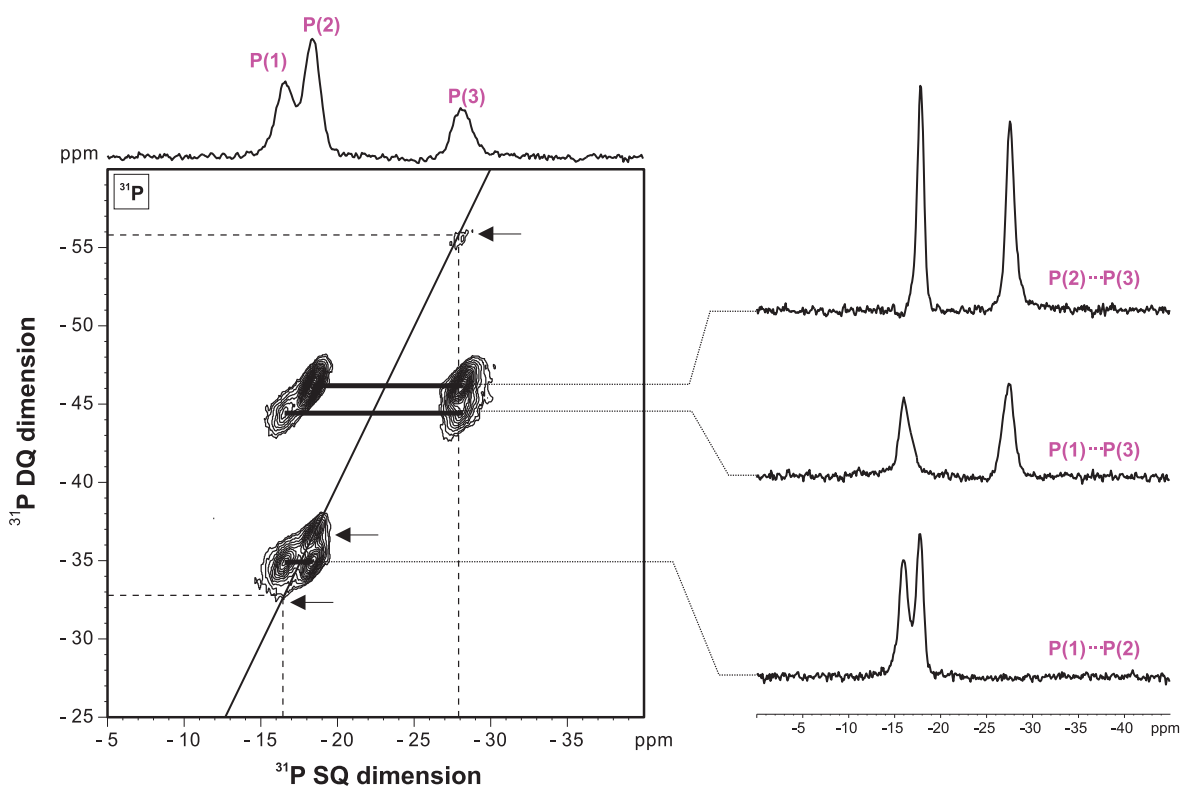


Fig. 9.5: ^{31}P - ^{31}P DQ HOMCOR spectrum of IST-1. A total of 120 t_1 points synchronized with the rotor period $[(1/\nu_R) = 100 \mu\text{s}]$ with 16 transients each were collected. The DQ excitation/reconversion times were 1 ms ($n = 5$, see Fig. 5.3), $m = 10$, $RD = 30$ s and z -filter delay $= 1/\tau_R$. Auto-correlation peaks are depicted with arrows and the DQ coherences between the three different ^{31}P resonances (cross-peaks) are also indicated.

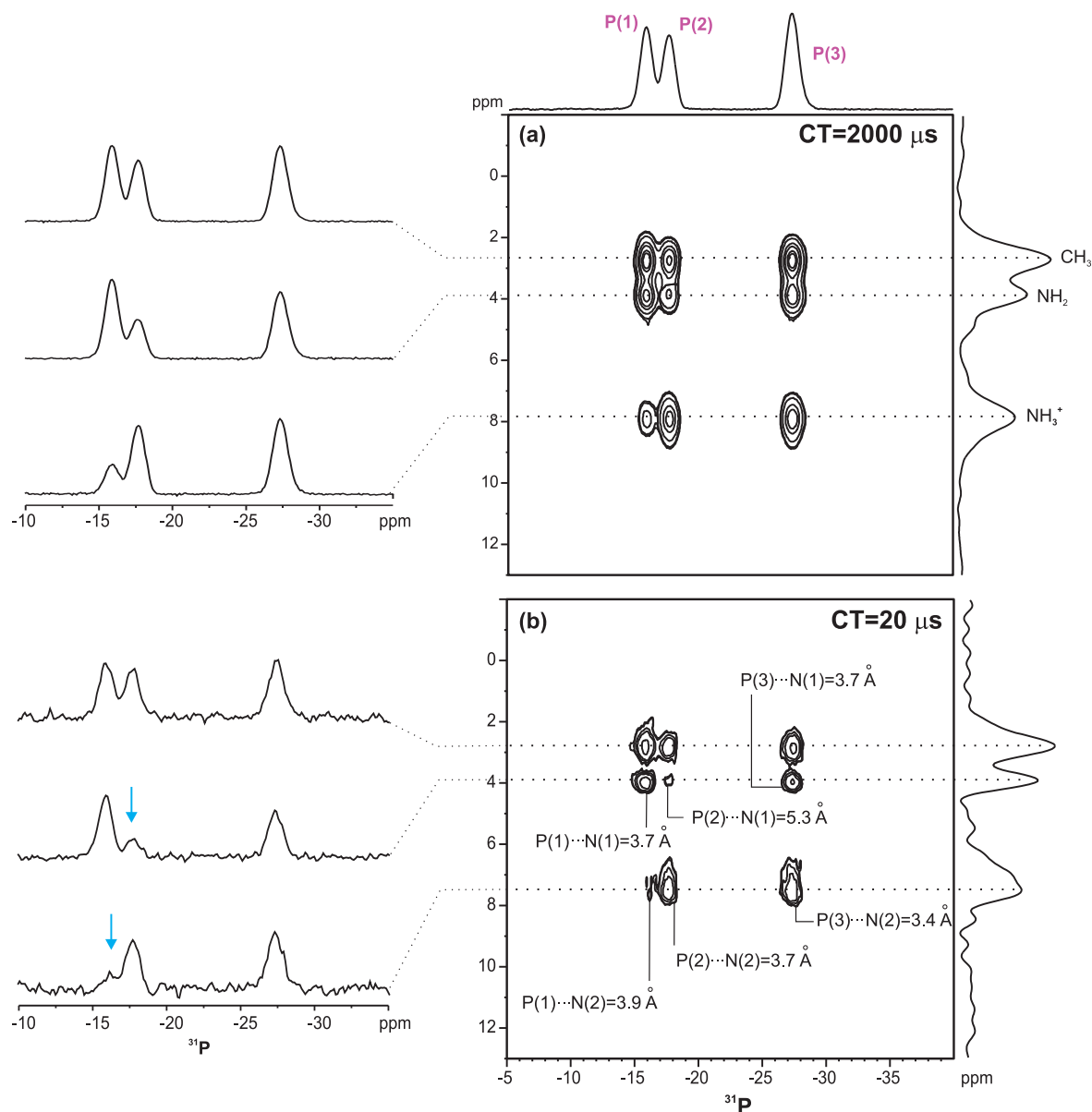


Fig. 9.6: $2D\ ^1H\{FS-LG\}\text{-}^{31}P$ CP HETCOR NMR spectra of IST-1 recorded with (a) $\tau_{CT} = 2000$ and (b) $\tau_{CT} = 20\ \mu s$. 90 t_1 increments with 72 transients each were collected. The $F1$ increments were synchronized with an integer number of FS-LG units ($n \times 2 \times \tau_{LG}$) with $n = 3$. The recycle delay was 3 s and the value of ν_{LG} employed was -5000 Hz.

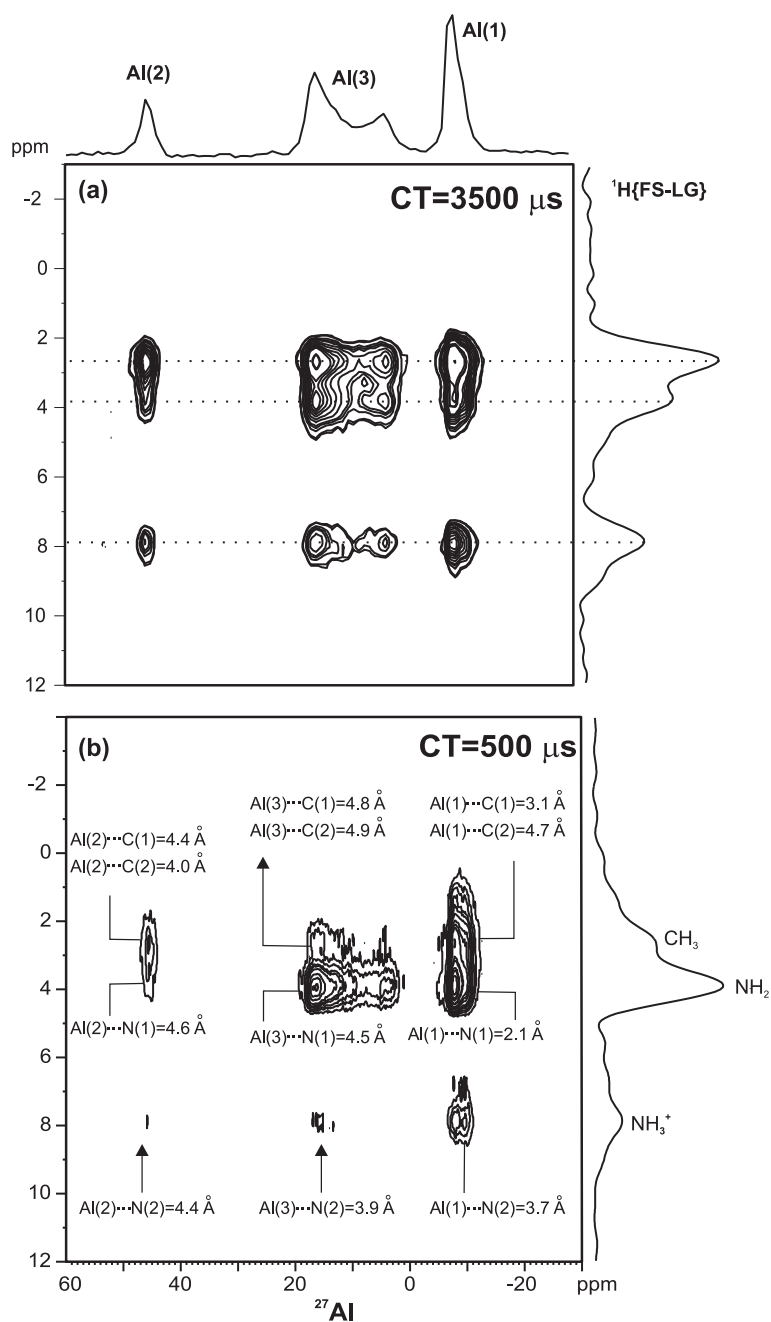
^{27}Al NMR

Fig. 9.7: 2D $^1\text{H}\{\text{FS-LG}\}$ - ^{27}Al CP HETCOR NMR spectra of IST-1 recorded with (a) $\tau_{CT} = 3500$ and (a) $\tau_{CT} = 500 \mu\text{s}$. 128 t_1 increments with 8 transients each were collected for (A) and 128 t_1 increments with 80 transients each were collected for (B). The F1 increments were synchronized with an integer number of FS-LG units ($n \times 2 \times \tau_{LG}$) with $n = 3$. The recycle delay was 3 s and the value of ν_{LG} was -5000 Hz.

The $^1\text{H}\{\text{FS-LG}\}$ - ^{27}Al CP HETCOR spectra of Fig. 9.7, confirm that five-coordinated Al is the furthest from the CH_3 groups [$d_{\text{Al}(3)-\text{C}(1)} = 4.8 \text{ \AA}$, $d_{\text{Al}(3)-\text{C}(2)} = 4.9 \text{ \AA}$]. The six-coordinated Al [$\text{N}(1) \cdots \text{Al}(1)$] still gives the strongest cross-peak at short τ_{CT} value, as

expected. The peak tail at ca. 1.2 ppm in F1 [Fig. 9.7b] may be due to the O(13)-H protons bridging the five- and six-coordinated Al sites. This is further supported by the presence of a strong and narrow O–H stretching FT-IR band at ca. 3512 cm^{-1} . The -NH_2 proton resonance is clearly observed in the $^1\text{H}\{\text{FS-LG}\}\text{-}^{27}\text{Al}$ HETCOR spectra at short τ_{CT} , while the other resonances become faint. This is because five- and six-coordinated Al [Al (3) and Al(1), respectively] are relatively close to the MA residues coordinated to Al(1) (consider the Al \cdots N distances in Fig. 9.7b). The extraction of more information from these spectra is prone to error, due to the complicated spin dynamics involving quadrupolar nuclei during spin locking, [265, 266] which can influence the peak intensity by quadrupolar relaxation effects.

Vibrational spectroscopy: Interpretation

In accord with the NMR evidence, the FT-IR spectrum (not shown) displays group frequencies typical of protonated amines: (i) stretching vibrations, $\nu(\text{NH}_3^+) = 3115\text{ cm}^{-1}$; (ii) asymmetric and symmetric bending vibrations, $\delta_{as}(\text{NH}_3^+) = 1610$ and $\delta_s(\text{NH}_3^+) = 1532\text{ cm}^{-1}$; (iii) wagging vibrations, $\omega(\text{NH}_3^+) = 730$ and 710 cm^{-1} ; and (iv) the typical torsional vibrations of NH_3^+ at 536 and 515 cm^{-1} .

9.1.3 Conclusion

The local ^{13}C , ^{31}P , ^{27}Al and ^1H environments in IST-1 have been studied by 2D high-resolution NMR techniques such as $^1\text{H}\{\text{FS-LG}\}^1\text{H}$ HOMCOR, 2D $^1\text{H}\{\text{FS-LG}\}\text{-X}$ HETCOR and ^{31}P DQ-SQ correlation techniques (X = ^{31}P , ^{13}C , and ^{27}Al). High-resolution ^1H NMR techniques employing FS-LG homonuclear decoupling, used in tandem with X-ray crystallographic evidence, have been shown to be useful tools to investigate the structure of the microporous aluminophosphate IST-1. In this study, I have:

- Proven the existence of protonated amine in the IST-1 pores (MA^+ residues);
- Unambiguously assigned the resonances of methylamine MA species, covalently bonded to a framework Al, and MA^+ residues inside the pores, by combining $^1\text{H}\{\text{FSLG}\}\text{-}^1\text{H}$ HOMCOR and $^1\text{H}\{\text{FS-LG}\}\text{-}^{13}\text{C}/^{31}\text{P}/^{27}\text{Al}$ HETCOR techniques;
- Assigned the ^{31}P crystallographic environments by combining $^{31}\text{P}\text{-}^{31}\text{P}$ DQ-SQ and $^1\text{H}\{\text{FS-LG}\}\text{-}^{31}\text{P}$ HETCOR experiments.

9.2 NMR characterisation Characterization of Layered γ -Titanium Phosphate $(\text{C}_6\text{H}_{13}\text{NH}_3)[\text{Ti}(\text{HPO}_4)(\text{PO}_4)]\cdot\text{H}_2\text{O}$

Crystalline inorganic compounds were initially synthesized by traditional high-temperature methods, such as condensation [267], chemical vapor transport [268], vapor-liquid-solid [269], flux [270], and solution alloy growth. [271] However, there is an increasing interest in synthetic methods, using low or moderate temperatures ($150\text{-}350\text{ }^\circ\text{C}$), that may lead to metastable compounds exhibiting unusual and useful properties. Among such methods, the hydrothermal synthetic approach is now regarded as one of the most effective. [272] Metal salts of phosphoric acid have been known for over a century. However, research on layered metal phosphates, and their relatives, began only in the late 1950s, when some of these salts found applications as cation exchangers for the treatment of radioactive waste streams. [273] Although in an excess of phosphorus, crystalline R-zirconium phosphate may be directly obtained from zirconium(IV) and phosphoric acid solutions [274], due to their low solubility

tetravalent metal phosphates were initially prepared as amorphous gels. In 1964, Clearfield and Stynes [275] obtained the first crystalline compound, α -Zr(HPO₄)₂·H₂O, which allowed a better understanding of their layered structure [276,277] and chemical reactivity. [278,279] Since then, these compounds have been extensively studied due to the possibility of relating their properties and crystalline structure with the many potential applications in the fields of ion exchange, intercalation, catalysis, and ion conduction. [280–284] The preparation of layered zirconium dihydrogenophosphate-phosphate dihydrate, γ -Zr(H₂PO₄)(PO₄)·2H₂O, was first reported in 1968. [285] However, at that time, γ -zirconium phosphate was erroneously believed to be an isomorphous modification of the α -phase; and therefore, it was not possible to give a correct interpretation of the mechanism of formation and the chemical composition and structure of the isolated derivatives. Advances in the knowledge of the γ -layered structure were fundamental for the interpretation of the topochemical mechanism of formation and development of the chemistry of the γ -derivatives. [286,287]

Although only two crystalline forms of layered titanium phosphates are known, α -Ti(HPO₄)₂·H₂O and γ -Ti(H₂PO₄)(PO₄)·2H₂O, many derivatives have been reported, including partially and completely substituted ion-exchanged forms and intercalation compounds. [288–291] Surprisingly, the γ -layered titanium phosphate is less studied than the α -phase, even though the γ -layers are more rigid, thicker, acidic, and amenable to intercalation processes. This is probably due to the fact that the structure of the γ -phase was only theoretically proposed. [292] More than a decade ago, the mechanism of intercalation of *n*-alkylamines in γ -titanium phosphate was reported, showing that 66% of the P-OH groups interact with the amine groups of the guest molecules. [291] Geometrical constraints dictate that compounds with maximum intercalation usually have the empirical formula of γ -Ti(H₂PO₄)(PO₄)·1.3C_{*n*}H_{2*n*+1}NH₂·H₂O (with *n* = 1-6), and crystalline phases with lower amine content can also be isolated.

The hydrothermal synthesis of a γ -titanium phosphate intercalation compound, Ti₂(HPO₄)₂(PO₄)₂·C₂N₂H₁₀, has been recently reported [293], and only one other member of this family is known, Ti₂(H₂PO₄)(HPO₄)(PO₄)₂·0.5C₆N₂H₁₆. [294] Although monoalkylamines are usually employed as templates for the synthesis of titanium phosphate metastable phases, the preparation of a γ -titanium phosphate alkylamine-intercalated compound has not yet been reported. Here, the hydrothermal synthesis and structural characterization of the first member in this family, (C₆H₁₃NH₃)[Ti(HPO₄)(PO₄)]·H₂O, is described. Because of strong preferential orientation effects and thermal disorder of the alkyl chains of the *n*-hexylammonium cations in the interlayer space, solving the structure of this material from only powder XRD evidence proved to be a very difficult task and, thus, a comprehensive SSNMR study has been performed. NMR has been used *ab initio* to inform the XRD and modeling work and, at the final stage, to confirm the obtained crystal structure.

9.2.1 Experimental Section

Synthesis Method

The following synthesis work was performed by Dr. Aránzazu Espina, from the Chemistry Department, University of Oviedo, Spain.

Hydrothermal synthesis of (C₆H₁₃NH₃)[Ti(HPO₄)(PO₄)]·H₂O (yield >90%) was carried out in a stainless steel Teflonlined vessel (designed and manufactured at Oviedo University) under autogenous pressure. *n*-hexylamine (Merck, purity >98%), 85% H₃PO₄ (Merck), and TiCl₄ (Merck, purity >99%) were mixed in the molar ratio 1:10:10 (TiCl₄:H₃PO₄:C₆H₁₃NH₂) in a total volume of ca. 40 cm³. The reaction vessel was sealed and heated to 185 °C for 10 days. The obtained solid was filtered off, washed with an excess of distilled water, and

dried in air at ambient temperature. Intercalation was tested by placing the isolated material in an atmosphere with *n*-hexylamine vapor at ambient temperature for 60 days. The solid obtained was air-dried at 50 °C and stored in a desiccator on top of an aqueous solution of 50% H₂SO₄.

X-ray Measurements

The following work was carried out in collaboration with Dr. S. Khainakov from the Chemistry Department, University of Oviedo.

Table 9.2: Crystal data and structure refinement information

formula	$C_6NH_{19}TiP_2O_9$
formula weight	359.11
crystal system	monoclinic
space group	$P2_1$
a [Å]	5.089(2)
b [Å]	6.335(2)
c [Å]	22.792(5)
β [°]	102.48(2)
Z	2
R_p	0.200
R_{wp}	0.227
R_F	0.210
χ^2	5.8

The sample was gently ground in an agate mortar and side-loaded into a holder to minimize the orientation effects, and data were collected at ambient temperature over the angular range 3-110° 2θ , with a step of 0.02° and a counting time of 10 s/step.

Chemical composition suggested a structure with an inorganic component related to that of the γ -titanium phosphate. As a starting set for the structural model, the coordinates reported for γ -Ti(H₂PO₄)(PO₄)·2H₂O, [292, 295] were used and the refinement was carried out in space group $P2_1$ by use of GSAS [296]. Crystallographic parameters are summarized in Table 9.2, fractional atomic coordinates in Table F.4, selected bond lengths and angles in Table F.5, and short (N,O)···O contacts related to hydrogen bonds in Table F.6.

NMR Measurements

In 2D $^1H\{FS-LG\}-^1H$ HOMCOR experiments the sample was restricted to the center of a 4-mm ZrO₂ rotor. CSs are quoted in ppm from TMS (1H and ^{13}C) and 85% H₃PO₄ (^{31}P).

1H and ^{31}P MAS: Spectra were recorded with spinning rates of 30 and 10 kHz, 60 and 4 s recycle delays, 90° 45° pulses, for 1H and ^{31}P , respectively

1H - ^{13}C and 1H - ^{31}P CP-MAS: Spectra were recorded with, respectively, spinning rates of 4.5 and 10 kHz, a recycle delay of 4 s, a 1H 90° pulse of 3.5 μ s, and contact times in the range 0.1-2 ms.

1H DQ-SQ MAS spectrum: The experiment was performed according to the pulse scheme already stated in Fig 5.2c.

τ_{exc} and τ_{rec} were set to $2 \times \tau_R$, equivalent to a duration of 66 μ s. After the reconversion, a z-filter time of nine rotor periods ($9 \times 33 \mu$ s) was employed to dephase any transversal magnetization. A final 90° was used to create transverse magnetization and for signal detection. A total of 192 t_1 points with 16 transients each were acquired by use of t_1 increments

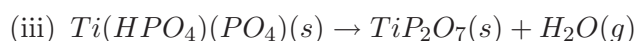
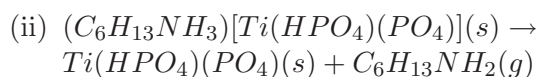
synchronized with the rotor period. Sign discrimination was achieved in the F1 dimension by the TPPI method by incrementing the phase of the excitation pulses by 45°. The train of 90° *rf* pulses in the BABA sequence was set to 2.5 μ s.

$2D^1H\{FS-LG\}^{-1}H$ HOMCOR: In all experiments with FS-LG homonuclear decoupling, the proton *rf* field amplitude was set to ca. 83 kHz. The FS-LG block was optimised according to the procedure detailed in section 4.9.2. Before each LG pulse, the frequency offset was alternated between +58925 + ν_{LG} Hz and -58925 + ν_{LG} Hz, with $\nu_{LG} = 1 - 5kHz$. The LG pulse length (τ_{LG}) was set to 9.8 μ s. Quadrature detection in t_1 was achieved by the States-TPPI method. [38] Specific experimental conditions for each spectrum are given in the figure captions.

9.2.2 Results and Discussion

The Chemical Composition and the Structural Model

The first (and dominant) reflection of the powder XRD pattern of the title compound corresponds to a d-spacing of ca. 22.2 Å (Fig. F.14a). The treatment of this compound with mineral acids (*e.g.*, 0.1 M HNO₃) yields γ -titanium phosphate, Ti(H₂PO₄)(PO₄)·2H₂O (Fig. 9.8a), [292, 297] strongly suggesting that the material possesses an inorganic lattice related to that of the γ -layered structure. According to elemental composition studies and thermal analyses (Table 9.3), the chemical composition of the new titanium phosphate is consistent with the ($C_6H_{13}NH_3$)[Ti(HPO₄)(PO₄)]·H₂O empirical formula. Is it noticeable that when n-hexylamine ($C_6H_{13}NH_2$) inclusion occurs, there is proton transfer from the acidic hydrogenophosphate moieties in the γ -titanium phosphate layers to the amine group, thus leading to the presence of *n*-hexylammonium cations ($C_6H_{13}NH_3^+$) in the interlayer spaces (shown by SSNMR studies, see below). TG gives a total weight loss from ambient temperature to 800 °C of ca. 36.0% (Table 9.3), consistent with a stoichiometric residue of TiP₂O₇ (calculated 38.2%). Differential Thermogravimetry (DTG) and DSC curves show a complex thermal decomposition process, with three partially overlapping steps. The first weight loss, at 50-200 °C, corresponds to the release of a water molecule per formula unit (observed ca. 5.9%, calculated 5.0%). The following two weight losses (at 200-490 and 490-700 °C) correspond to the removal of the n-hexylamine (observed ca. 25.2%, calculated 28.1%) and to the release of structural water from the condensation of hydrogenophosphate groups (observed ca. 4.9%, calculated 5.0%). Heating the sample at ca. 150 °C, followed by stabilization in air, did not change the powder XRD pattern or the EA (Figs. F.14a and 9.8b and Table 9.3). The corresponding decomposition route is as follows:



Intercalates with lower amine content have been isolated by thermal treatment. Heating up the title compound to ca. 350 °C leads to the formation of the ($C_6H_{13}NH_3$)_{0.3}[Ti(H_{1.7}PO₄)(PO₄)] phase (Fig. 9.8c; Table 9.3), characterized by an interlayer spacing of ca. 12 Å, suggesting an arrangement of the ammonium residues nearly parallel to the phosphate layer. When the material is calcined at ca. 400 °C, an amorphous solid is obtained (Fig. 9.8d). The carbon content of this phase indicates that the release of the

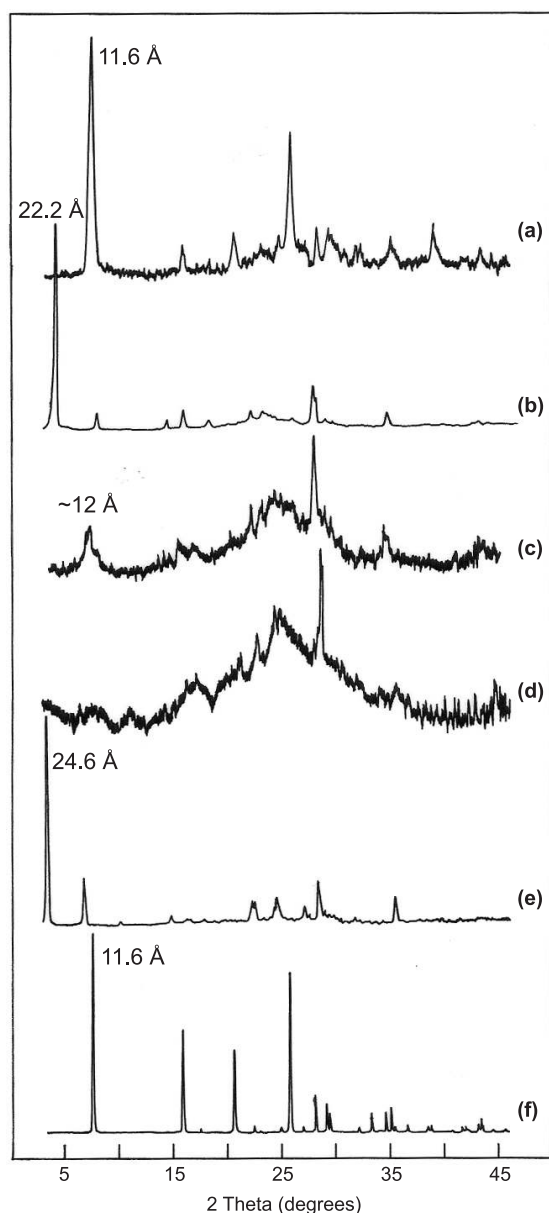


Fig. 9.8: Powder XRD patterns of $(C_6H_{13}NH_3)[Ti(HPO_4)(PO_4)] \cdot H_2O$: (a) treated with 0.1 M HNO_3 , then calcined at (b) 150, (c) 350, and (d) 400 C (and subsequently stabilized in air at room temperature), or (e) stabilized at room temperature in a saturated atmosphere of *n*-hexylamine for 60 days. For comparison, the simulated powder XRD pattern of γ -titanium phosphate, $Ti(H_2PO_4)(PO_4) \cdot 2H_2O$, is also shown (f).

organic residues is not complete (Table 9.3), with the residue having an empirical formula of $(C_6H_{13}NH_3)_{0.2}[Ti(H_{1.8}PO_4)(PO_4)]$. Scanning electron microscopic (SEM) images of $(C_6H_{13}NH_3)[Ti(HPO_4)(PO_4)] \cdot H_2O$ (Fig. F.15) show that the particles are circular plate aggregates with a diameter of ca. 2–8 μm , and the combination with powder XRD further indicates that these plates have an average dimension, perpendicular to the basal plane, of ca. 0.3 μm . SEM inspection of samples treated at high temperature reveals that the particle morphology does not change.

Table 9.3: Analytical data and weight loss at 800 °C for intercalation compounds

formula	exp (%)					calc (%)				
	Ti	P	C	N	weight loss	Ti	P	C	N	weight loss
(C ₆ H ₁₃ NH ₃)[Ti(HPO ₄)(PO ₄)]·H ₂ O ^a	12.7	16.9	19.7	3.8	36.0	13.3	17.3	20.1	3.9	38.2
(C ₆ H ₁₃ NH ₃)[Ti(HPO ₄)(PO ₄)]·H ₂ O ^b	12.8	17.0	19.6	3.8	36.8	13.3	17.3	20.1	3.9	38.2
(C ₆ H ₁₃ NH ₃) _{0.3} [Ti(H _{1.7} PO ₄)(PO ₄)] ^c	17.5	22.3	7.3	1.4	18.1	17.7	23.0	8.0	1.6	17.9
(C ₆ H ₁₃ NH ₃) _{0.2} [Ti(H _{1.8} PO ₄)(PO ₄)] ^d	18.0	23.1	5.2	1.0	14.1	18.7	23.8	5.5	1.1	14.7
(C ₆ H ₁₃ NH ₃) _{0.3} [Ti(H _{1.7} PO ₄)(PO ₄)] ^c	17.5	22.3	7.3	1.4	18.1	17.7	23.0	8.0	1.6	17.9
(C ₆ H ₁₃ NH ₃)[Ti(HPO ₄)(PO ₄)]·0.3C ₆ H ₁₃ NH ₂ ·H ₂ O ^e	11.9	15.5	24.6	4.6	43.7	12.2	15.8	24.4	4.7	43.4

^a Sample obtained by hydrothermal synthesis and stabilization at room temperature.^b Sample thermally treated (1 day) at 150 °C.^c Sample thermally treated (1 day) at 350 °C.^d Sample thermally treated (1 day) at 400 °C.^e Sample obtained by solid-vapor contact of starting sample with *n*-hexylamine (60 days).

When $(\text{C}_6\text{H}_{13}\text{NH}_3)[\text{Ti}(\text{HPO}_4)(\text{PO}_4)]\cdot\text{H}_2\text{O}$ is stored in an atmosphere saturated with *n*-hexylamine, a new crystalline phase with an interlayer distance of ca. 24.6 Å is isolated (Fig. 9.8e). Morphological studies indicate that the intercalation process occurs smoothly without change of the particle morphology (Fig. F.15). This *d*-spacing was previously observed in a material obtained by solidvapor contact of γ -titanium phosphate with *n*-hexylamine, $(\text{C}_6\text{H}_{13}\text{NH}_3)[\text{Ti}(\text{HPO}_4)(\text{PO}_4)]\cdot 0.3(\text{C}_6\text{H}_{13}\text{NH}_2)\cdot\text{H}_2\text{O}$ [291], and elemental composition studies (Table 9.3) confirm the presence of the same phase.

To propose a possible structural model for $(\text{C}_6\text{H}_{13}\text{NH}_3)[\text{Ti}(\text{HPO}_4)(\text{PO}_4)]\cdot\text{H}_2\text{O}$, compatible with the experimental data, modeling studies based on powder XRD data were carried out. From the very beginning, the SSNMR evidence described (for convenience) below was available and was taken into consideration when the model was built up.

- (i) A list of peak positions was obtained from the powder X-ray raw data by use of XFIT [298]. Indexing was performed with TREOR and KOHL, which are included in the CRYSFIRE suite. [299] A monoclinic cell with $a = 5.18$ Å, $b = 6.31$ Å, $c = 22.84$ Å, and $\beta = 104.7^\circ$ ($M_{19} = 20$) was found. The indexed reflections showed systematic absences of the type $0k0$, $k = 2n + 1$, indicating that the space group is either $P2_1$ or $P2_1m$.
- (ii) Since the *a* and *b* parameters were very similar to those of γ -titanium phosphate ($a = 5.181$ Å and $b = 6.347$ Å), [292] it was assumed that the inorganic backbone of the layer is of γ type. When the γ -titanium phosphate *a*, *b*, and β are kept constant (refined in the $P2_1$ space group because the refinement in the $P2_1/m$ group did not progress appropriately, $R_{wp} = 0.340$), and with the known experimental interlayer distance of the intercalation compound, a monoclinic cell ($a = 5.181$ Å, $b = 6.347$ Å, $c = 22.75$ Å, $\beta = 102.59^\circ$) was obtained.
- (iii) After the γ -titanium phosphate inorganic layers were displaced by the interlayer spacing of the intercalation compound, the initial atomic coordinates for the P, Ti, and O atoms were estimated by use of ATOMS. [300]
- (iv) GSAS [296] was used to refine the unit cell parameters (Table 9.2) and the starting structure model by assuming that the C-N bond is perpendicular to the *ab* plane and that the alkyl chains have a trans-trans conformation with bond lengths and angles identical to those of a crystalline *n*-paraffin. [301] Thermal parameters were refined isotropically ($U_{iso} = 0.025$), and a March-Dollase [302, 303] correction along the 00*l* direction was applied for preferred orientations.

Final atomic coordinates and selected bond lengths and angles for the refined model are collected in Tables F.4 and F.5, respectively. This model produces a simulated powder XRD pattern that is in good agreement with the experimental pattern (Fig. F.14). Differences in intensity are most probably due to the preferential orientation of the crystallites and thermal disorder of the alkyl chains of the interlayer *n*-hexylammonium cations. At this point, it is important to stress that, despite the modest figures of merit (Table 9.2), the crystal model is fully supported by all empirical evidence available, particularly the NMR data discussed below. The structures of $(\text{C}_6\text{H}_{13}\text{NH}_3)[\text{Ti}(\text{HPO}_4)(\text{PO}_4)]\cdot\text{H}_2\text{O}$ (Fig. 9.9a) and γ -titanium phosphate [292] are similar. Individual 2D anionic $[\text{Ti}(\text{HPO}_4)(\text{PO}_4)]^-$ sheets are constructed by corner-sharing four-ring chains formed by PO_4 tetrahedra and TiO_6 octahedra (Fig. 9.9b). The Ti-O, P-O, O-Ti-O, and O-P-O bond lengths and angles (Table F.5) are typical and in good agreement with the values reported for other titanium phosphates. [293, 294] The structure contains two kinds of phosphate groups: PO_4^{3-} sharing their oxygen atoms with

titanium centers, and HPO₄²⁻ having two bridging and two terminal oxygen atoms. These terminal HPO₄²⁻ groups are connected to the chains and point toward the interlayer region, directly interacting with the protonated amine groups from neighboring *n*-hexylammonium cations through hydrogen bonds (Table F.6).

SSNMR confirms and further elucidates the details of the proposed crystal structure. The ³¹P MAS NMR spectrum of (C₆H₁₃NH₃)[Ti(HPO₄)(PO₄)]·H₂O exhibits two resonances at ca. -13.5 and -26.5 ppm in a 1:1 intensity (area) ratio (Fig. 9.10b), in accord with the proposed crystal structure, which calls for the presence of two types of ³¹P local environments. The peak at -13.5 ppm is much enhanced upon ¹H-³¹P CP and is, thus, assigned to the HPO₄²⁻ site (Fig. 9.10b). The CP kinetic of both groups was further investigated by variable contact-time experiments (Fig. 9.10c). The CP time constants, T_{IS} depend on the number of protons in a functional group and on the mobility of the group. The shorter the P···H distance, the stronger the P···H dipolar and the faster the CP rate. In terms of T_{IS}, one expects the PO₄³⁻ groups (T_{IS} ≈ 0.3 ms) to present a shorter value with respect to the HPO₄²⁻ groups (T_{IS} ≈ 1 ms). The mobility is also a factor of importance and can influence the choice of the CP model to use. The HPO₄²⁻ groups contain a relatively close ¹H (P-O-H), and in such cases, the I-I*-S model performs better than the classic I-S model. [305] In this work, the classic I-S model (Fig. 9.10c) performs well for the PO₄³⁻ and HPO₄²⁻ groups. For the former, the I-S model is expected to work well, but surprisingly, the same equation also gives good results in fitting the latter, probably because of the mobility or fast exchanging involving the P-O-H groups.

The ¹H-¹³C CP-MAS spectrum (Fig. 9.10a) displays six resonances at ca. 13.4, 22.1, 26.0, 26.7, 31.0, and 39.6 ppm attributed to C-6, C-5, C-3, C-4, C-2, and C-1, respectively, thus fully supporting the proposed crystal structure. In particular, NMR indicates that intercalated *n*-hexylamine is protonated and that there is a single type of *n*-hexylammonium cation in the unit cell. The ¹H MAS (30 kHz spinning rate, Fig. 9.11a) and ¹H{FS-LG}-¹H HOMCOR (Fig. 9.11c) NMR spectra of the title material exhibit five resonances. Deconvolution of the former spectrum requires a total of seven peaks, five of which are attributed to the *n*-hexylammonium ion: 0.8 ppm (relative area 1.5), H-6; 1.3 ppm (3), H-3-5; 1.7 ppm (1), H-2; 3.1 ppm (1), H-1; and 7.6 ppm (1.5), N-H. The remaining resonance has been deconvoluted with two peaks, at 5.7 ppm (0.9), attributed to water molecules, and 5.8 ppm (1), P-OH groups. Indeed, upon sample dehydration (ca. 150 °C, 24 h), the intensity of the former decreases considerably (not shown). The ¹H DQ BABA spectrum (Fig. 9.11d) further confirms the integrity of the *n*-hexylammonium cation in the interlayer space. Importantly, the H₂O and P-OH resonances at ca. 5.7 ppm virtually disappear from the diagonal of the spectrum, which can probably be attributed to fast ¹H exchange involving water molecules or the N-H groups from the *n*-hexylammonium cations and neighboring P-OH groups, and also to some mobile lattice water. Consider now the ¹H-³¹P HETCOR NMR spectrum of the as-prepared sample (Fig. 9.12) and its F1 cross-sections (Fig. 9.13). At relatively short contact times (100 μs) the H₂O, P-OH, and N-H proton resonances dominate the spectrum, while at long contact times (3 ms) the H-1-6 ¹H peaks are considerably enhanced. Again, these observations support the proposed crystal structure because they indicate that H₂O, P-OH, and *n*-hexylammonium residues are closer than the alkyl chain protons to the two phosphorus sites. A second important observation is that, at the short τ_{CT} of 100 μs, the F1 cross-section taken through the ³¹P (HPO₄²⁻) peak at ca. -13.5 ppm reveals a H₂O/P-OH ¹H peak as intense as the N-H resonance. In contrast, the F1 cross-section taken through the ³¹P peak at ca. -26.5 ppm exhibits a much stronger N-H proton resonance. Hence, the ¹H-³¹P HETCOR NMR evidence indicates that the HPO₄²⁻ environment is closer than the PO₄³⁻ site to the water molecules, as expected.

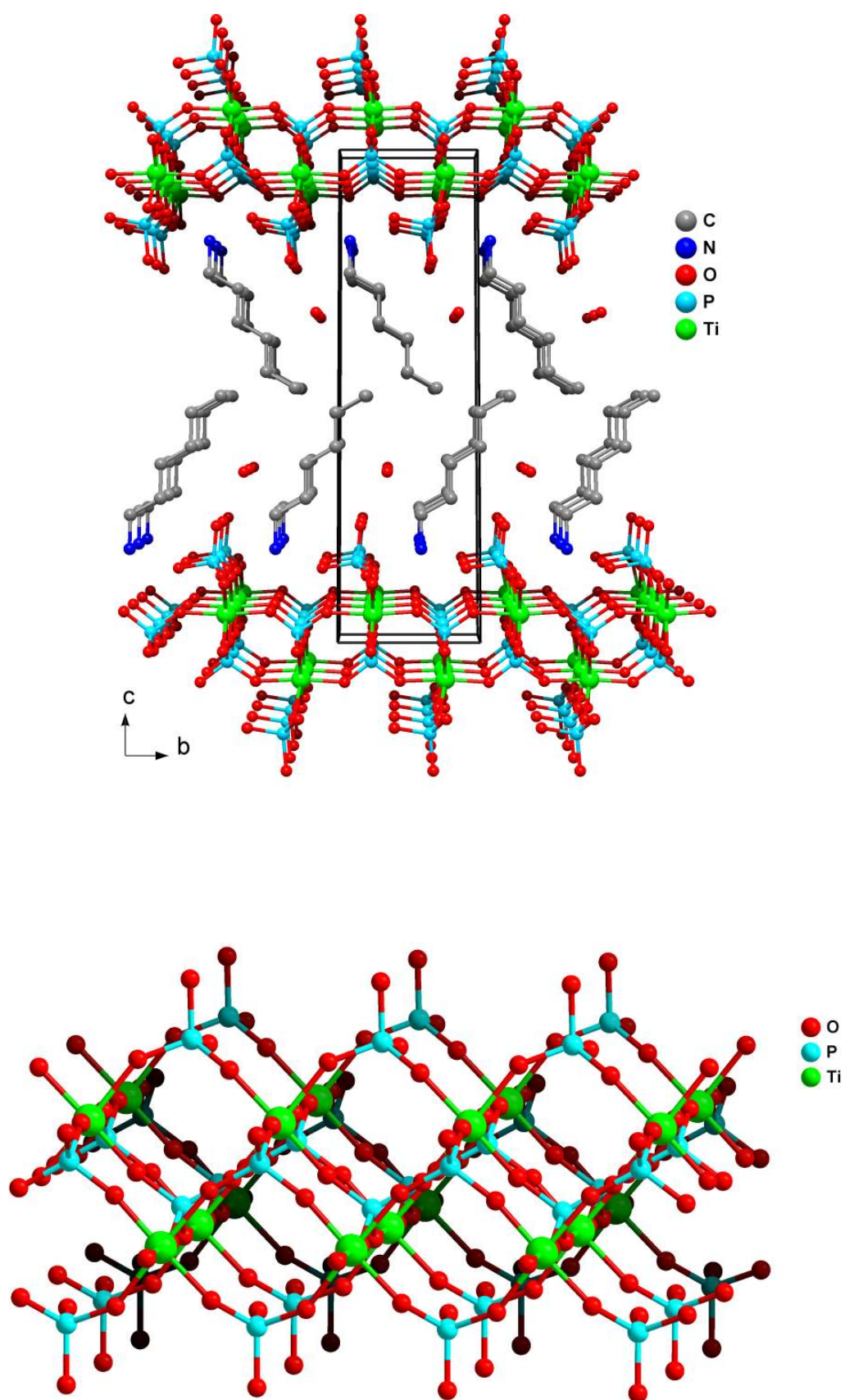


Fig. 9.9: (a) Proposed crystal structure of $(C_6H_{13}NH_3)[Ti(HPO_4)(PO_4)] \cdot H_2O$ viewed along the $[1\ 0\ 0]$ direction. (b) Perspective view of the 2D $[Ti(HPO_4)(PO_4)]^-$ anionic sheet.

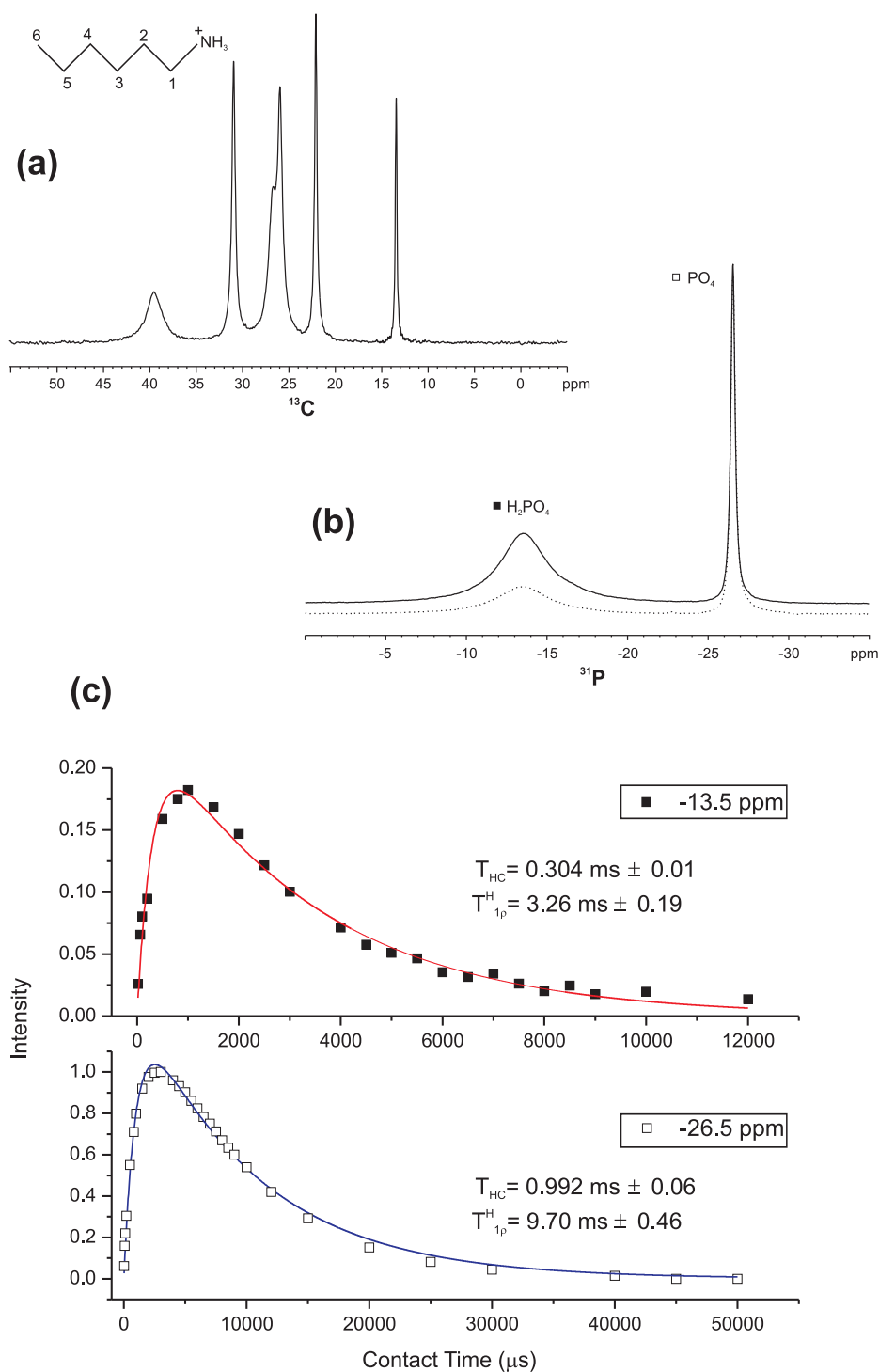


Fig. 9.10: (a) 1H - ^{13}C ($\tau_{CT}=500 \mu s$) and (b) 1H - ^{31}P CP-MAS NMR ($\tau_{CT}=1500 \mu s$) spectra [continuous line], ^{31}P MAS NMR [dotted line], ($\tau_{CT}=1500 \mu s$) of $(C_6H_{13}NH_3)[Ti(HPO_4)(PO_4)] \cdot H_2O$. (c) 1H - ^{31}P CP kinetics ($\nu_R=7$ kHz) for the \blacksquare H_2PO_4 and \square PO_4 groups. The fittings follow the classic I-S model, [304] using the equation:

$$I(t) = I_0 \left(1 - \frac{T_{IS}}{T_{1\rho}^H}\right)^{-1} \left[\exp\left(\frac{-T_{CT}}{T_{1\rho}^H}\right) - \exp\left(\frac{-T_{CT}}{T_{IS}}\right) \right], \quad \text{where } I=^1H, S=^{31}P,$$

T_{CT} =contact time, and the other parameters have their usual meaning.

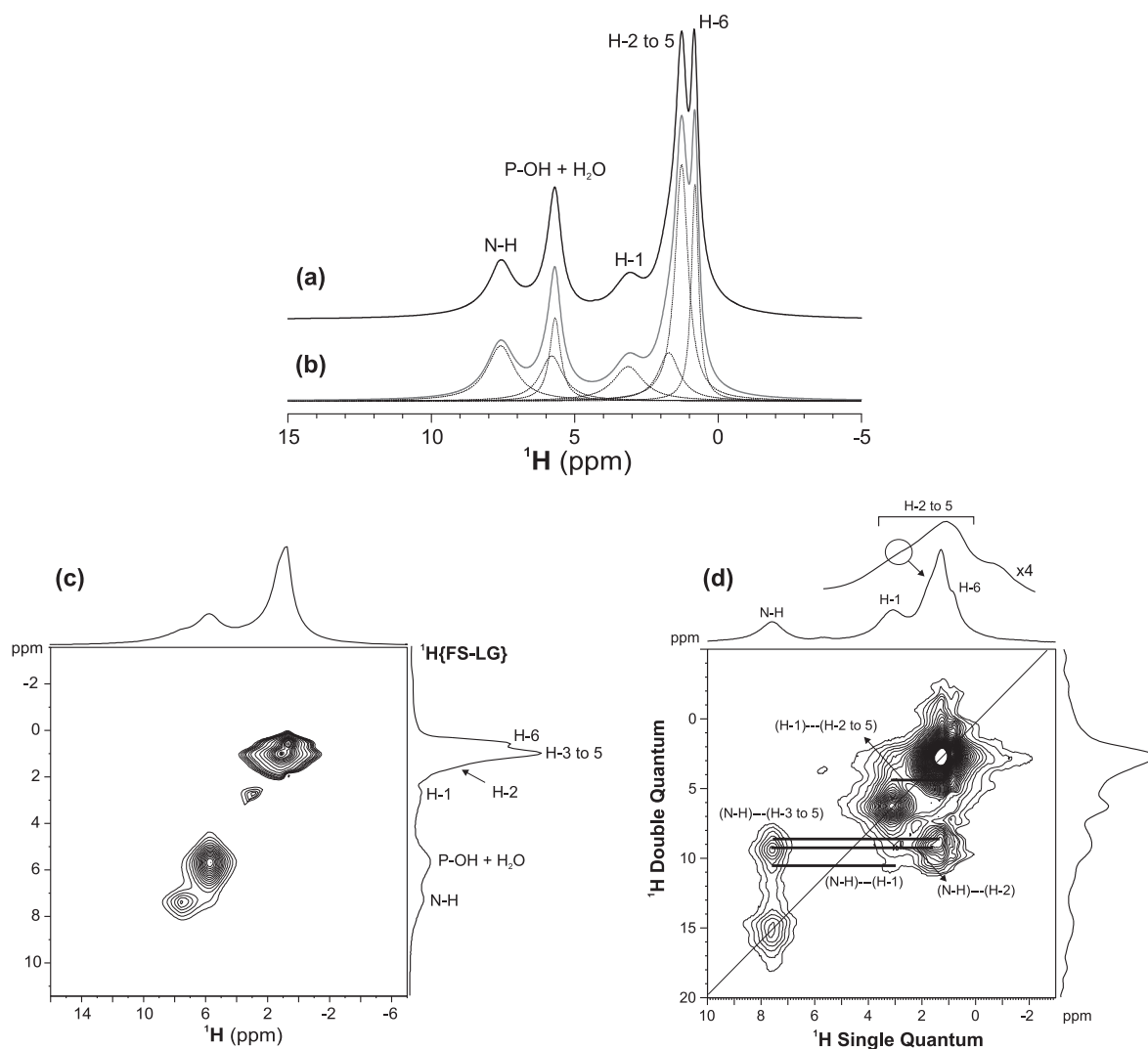


Fig. 9.11: ^1H spectra of $(\text{C}_6\text{H}_{13}\text{NH}_3)[\text{Ti}(\text{HPO}_4)(\text{PO}_4)]\cdot\text{H}_2\text{O}$. ^1H MAS NMR spectrum recorded with a 30 kHz spinning rate. The (a) experimental and (b) simulated and individual simulation peaks are also depicted. (c) $^1\text{H}\{\text{FS-LG}\}$ ^1H HOMICOR spectrum of $(\text{C}_6\text{H}_{13}\text{NH}_3)[\text{Ti}(\text{HPO}_4)(\text{PO}_4)]\cdot\text{H}_2\text{O}$. A total of 350 t_1 increments, with 8 transients each, were collected. F1 increments were synchronized with an integer number of FS-LG units, $n \times 2 \times \tau_{\text{LG}}$, with $n=3$. The value of ν_{LG} used was ± 1000 Hz. The recycle delay was set to 3 s. (d) ^1H DQ MAS spectrum acquired with a spinning rate of 30 kHz. The DQ excitation time (τ_{exc}) and reconversion time (τ_{rec}) was set to 66 μs .

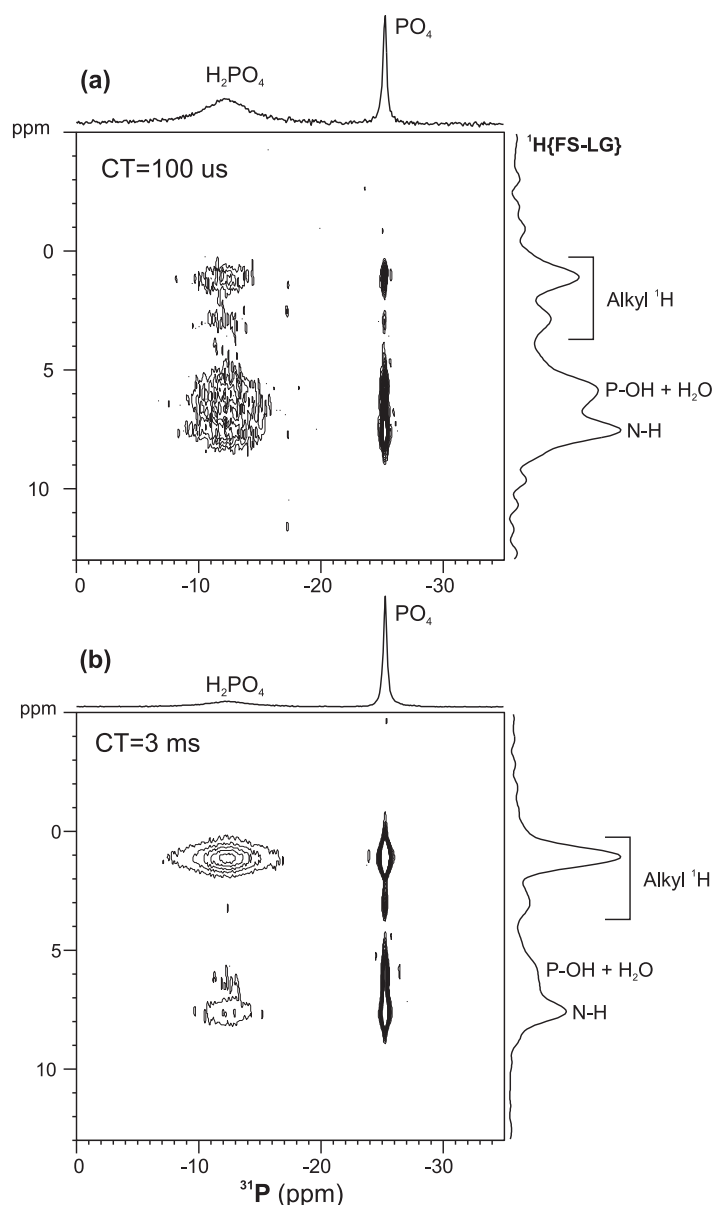


Fig. 9.12: $^1H\{FS-LG\}-^{31}P$ CP HETCOR NMR spectra of $(C_6H_{13}NH_3)[Ti(HPO_4)(PO_4)] \cdot H_2O$ recorded with contact times of (a) 100 μs and (b) 3000 μs . A total of 128 t_1 increments with 16 transients each were collected. In all experiments the F1 increments were synchronized with an integral number of FS-LG units, $n \times 2 \times \tau_{LG}$, with $n = 3$. The recycle delay was set to 3 s. The value of ν_{LG} employed was -5000 Hz.

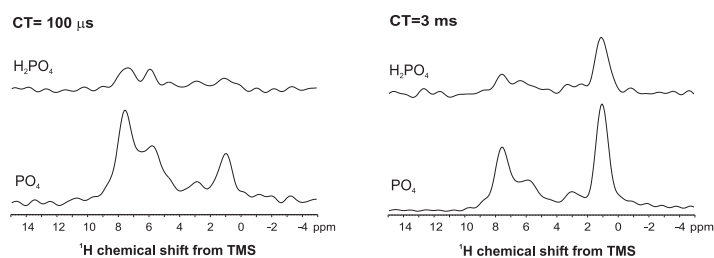


Fig. 9.13: F1 cross-sections of the $^1H\{FS-LG\}-^{31}P$ CP HETCOR NMR spectra of $(C_6H_{13}NH_3)[Ti(HPO_4)(PO_4)] \cdot H_2O$ (see Fig. 9.12).

Vibrational Spectroscopy

The FTIR spectrum (not shown) of the title material (shown in ref. [105]) exhibits a strong band centered at 982 cm^{-1} with shoulders at 1236 and 1155 cm^{-1} , attributed to the various (symmetric and antisymmetric) stretching $\nu(\text{P-O})$ vibrational modes of the phosphate groups together with the presence of C-N stretching vibrations. The presence of the water molecule of crystallization involved in hydrogen bonding with the neighboring moieties is confirmed by the stretching $\nu(\text{O-H})$ (ca. 3414 cm^{-1}) and the in-plane (δ_s) H-O-H deformation (ca. 1622 cm^{-1}) vibrational modes. The *n*-hexylammonium cations give the symmetric (ca. 2859 cm^{-1}) and antisymmetric (ca. $2957, 2930\text{ cm}^{-1}$) stretching (ν) modes from the -CH₂- alkyl chains, and also the bands at ca. 1520 and 2450 cm^{-1} attributed to the N-H in-plane deformation (δ_s) and stretching (ν), respectively, of the protonated amine group. A typical methylene rocking (ρ) vibration, in which all of the methylene groups rock in phase, appears as a medium-intensity band at ca. 700 cm^{-1} . The -CH₂- groups further display a sharp scissoring (δ_s) band near ca. 1400 cm^{-1} .

9.2.3 Conclusion

γ -titanium phosphate compounds intercalated with *n*-alkylamine may be used as precursors in pillaring reactions, because of their water stability, suitable interlayer distance, moderate affinity of the intercalated species toward the host active centers, and an adequate occupied interlayer volume. Despite the many potential applications of these materials, their detailed structural features have remained poorly understood. In this work, the chemical information, spectroscopic and powder XRD data, and modeling studies were combined to propose the first structural model of an organically templated titanium phosphate, $(\text{C}_6\text{H}_{13}\text{NH}_3)[\text{Ti}(\text{HPO}_4)(\text{PO}_4)]\cdot\text{H}_2\text{O}$. In particular, this case study provides an interesting example of how to combine powder XRD, modeling, and SSNMR to elucidate the structure of organic-inorganic hybrid materials.

Part III

New Methods for Observation of Quadrupolar Nuclei

Chapter 10

Application of Multiplex Phase Cycling to MQMAS and STMAS Experiments

10.1 High-Resolution Spectra of Half-Integer Quadrupolar Nuclei

The power of NMR spectroscopy to probe the structure of materials depends strongly on the availability of high-resolution spectra. For nuclei with a spin $I=1/2$ a number of methods are now well established for eliminating the broadening effect of the anisotropic interactions. The resolution and sensitivity gaps between liquid and SSNMR spectroscopies have been decreasing over the years. This tendency started in the 1960s and 1970s with the introduction of MAS, [47,48] *rf* decoupling schemes [52–54] and CP [49–51] methods. In contrast, narrowing the spectral lines of quadrupolar nuclei ($I>1/2$) is a more challenging task and has attracted the efforts of many NMR spectroscopists in the last 15 years or so. The introduction in 1995, by Frydman and Harwood [1] of MQMAS NMR spectroscopy prompted a revolution in this field, making possible to record high-resolution NMR spectra of important half-integer quadrupolar nuclei as ^{23}Na [306–312], ^{27}Al [313–319], ^{87}Rb [320–323], ^{17}O [324–332] and ^{93}Nb [324,333–335].

It is well known that for half-integer quadrupolar spins the orientational dependent first-order quadrupolar interaction acting on the ST ($m - 1 \leftrightarrow m$), with $m \neq 1/2$) is of the order of the quadrupolar frequency ω_Q (Fig. 10.1). Hence, in powdered samples, the spectra can, frequently, be spread over several MHz, which is considerably higher than the range of CSs and the *rf* bandwidth of the spectrometer under pulse excitation. m represent the magnetic quantum numbers of each quantum level $|m\rangle$, (Appendix A). To overcome, such difficulty, the Central Transition (CT) ($-1/2 \leftrightarrow 1/2$) observation is usually more popular for studying materials, because it is not affected by the first-order quadrupolar broadening (Fig. 10.1). However, it is worth mentioning that the CT is still affected by the second-order quadrupolar effect ($\hat{H}^{Q,(2)}$), if other additional line broadenings are neglected, which is typically 10^2 to 10^3 times smaller than ω_Q . In addition, MAS eliminates the first-order broadenings completely and reduces the quadrupolar contribution to the CT line width by a factor of three. Thus observing the CT under MAS brings additional advantages. Usually, the MAS spectrum of half-integer quadrupolar nuclei contains the intense CT with the partial or the entire manifold of spinning sidebands originated by the STs separated by the rotor frequency (ν_R) and broadened only by the second-order quadrupolar effect.

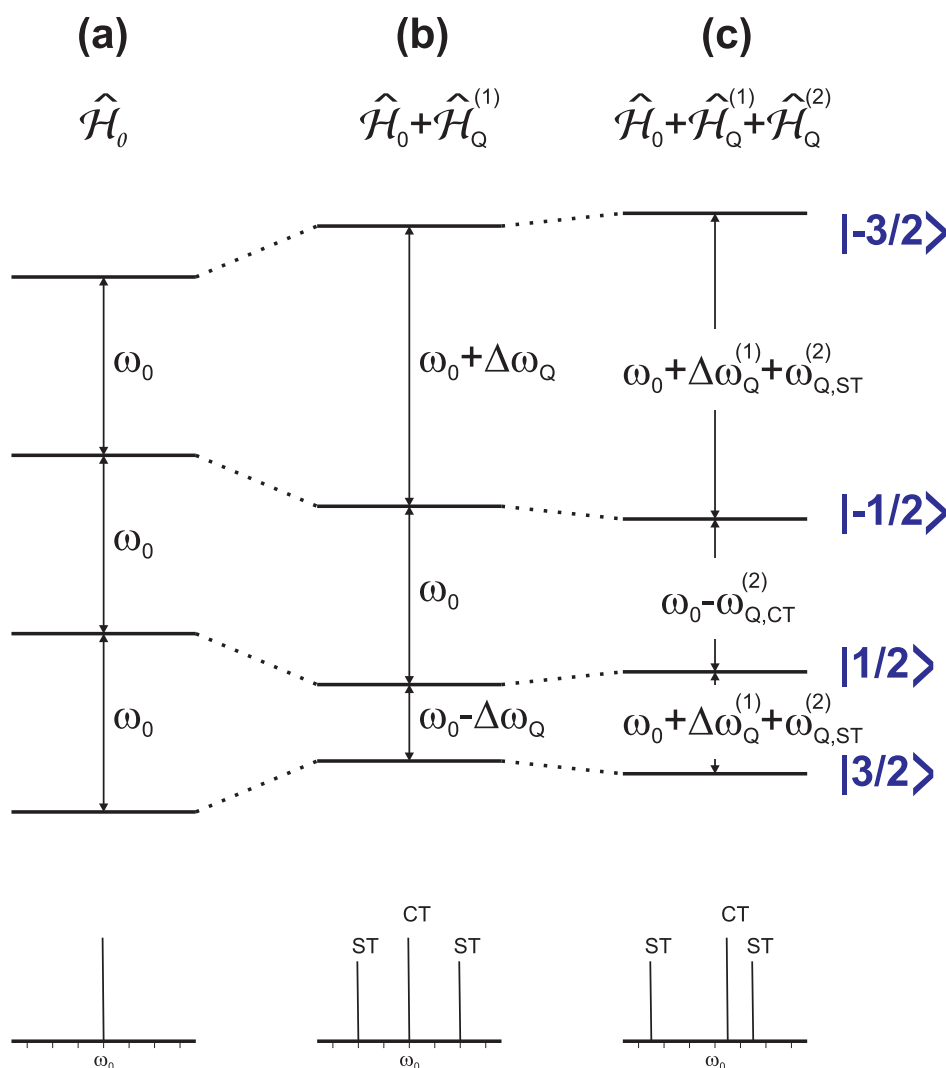


Fig. 10.1: Schematic representation of the energy levels of a quadrupolar spin, $I=3/2$ nucleus showing the effect of (a) the Zeeman interaction, (b) the first-order and (c) second-order quadrupolar interactions on the $2I + 1$ energy levels. In the bottom, the stick spectrum of a single crystal is shown according to each situation. $\omega_{Q,CT}^{(2)}$ and $\omega_{Q,ST}^{(2)}$ are the second-order quadrupolar contribution to the central and ST frequencies.

á

This section will be mainly concentrated in the echo formation and the obtention of pure absorption 2D spectra. Further details about the general theory of half-integer quadrupolar nuclei, pulse schemes and the theoretical description of line narrowing NMR experiments for studying quadrupolar spins and , are very well documented in several reviews and books, [26, 336–340] and are highly recommended.

The High-Resolution Methods

Most research, by far, has been concentrated in obtaining high-resolution spectra of half-integer quadrupolar nuclei by complete averaging of the second order broadening, since the 1980s. The following techniques were developed to obtain informative spectra:

•Based on spatial manipulation:

1. Double Rotation (DOR)
2. Dynamical Angle Spinning (DAS)

•Based on spin manipulation:

1. MQMAS based techniques
2. STMAS based techniques

MAS alone can not eliminate the totality of the anisotropic effects, induced by the second-order quadrupolar interaction. In contrast with the rank-2 tensors, the rank-4 spatial tensor function ($\mathcal{B}_{2q}^{(4)}$) of Eq. 2.92 for $k = 2$, is only partially reduced by the Legendre polynomial, $P_4(\cos \beta)$. Obtaining high-resolution spectra requires the elimination of two terms, $P_2(\cos \beta)^*$ and $P_4(\cos \beta)^*$ (Table 10.1). Such condition is impossible to attain with a unique rotor orientation because there is no common root for both polynomials (Fig. 10.2).

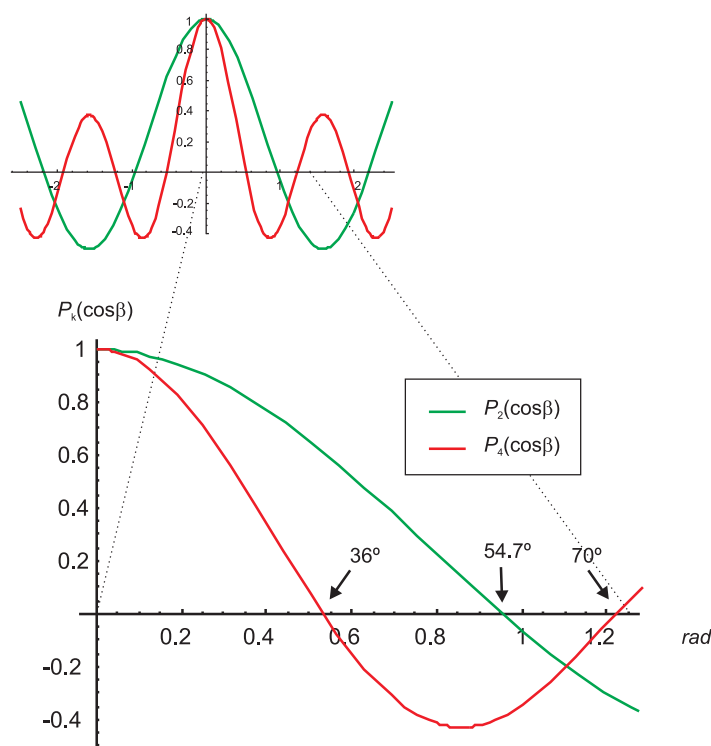


Fig. 10.2: Plot showing the $P_2(\cos \beta)$ and $P_4(\cos \beta)$ Legendre polynomials as a function of the rotor angle (in radians) with respect to B_0 .

*Note that the values of the Legendre Polynomials $P_2(\cos \beta)$ and $P_4(\cos \beta)$ are correspondent to the reduced Wigner matrix elements $d_{0,0}^{(2)}(\beta)$ and $d_{0,0}^{(4)}(\beta)$ (Tables B.2 and B.3), respectively.

Table 10.1: Legendre polynomials up to $k=4$.

k	$P_k(\cos \beta)$
0	1
1	$\cos \beta$
2	$\frac{1}{2} (3 \cos^2 \beta - 1)$
3	$\frac{1}{2} (5 \cos^3 \beta - 3 \cos \beta)$
4	$\frac{1}{8} (35 \cos^4 \beta - 30 \cos^2 \beta + 3)$

High-resolution spectra can be obtained if the observable elements of the density matrix $|\frac{1}{2}\rangle\langle\frac{1}{2}|$ are **free of anisotropies at the same time for all crystallites**. In such case, an echo is formed free of anisotropies and only containing the isotropic terms. By manipulation of Eq. 2.92, the basics of the techniques pointed above can be conveniently explained.

The methods DOR and DAS demonstrated by the groups of Pines and Virlet, [341–343] were the first experiments to give high-resolution quadrupolar spectra, and will be next described briefly as a background knowledge to introduce the MQMAS principle.

The DOR Principle

The DOR experiment, introduced by Samoson *et al* [343], is a 1D technique which consists in rotating the sample at two axes with angles, β_1 and β_2 , simultaneously. The following equality must be obeyed, in order to attain high-resolution spectra:

$$P_2(\cos \beta_2) = P_4(\cos \beta_1) \quad (10.1)$$

This is achieved by spinning the sample in an inner rotor inclined at

$$\beta_1 = \arccos \sqrt{\frac{(6 + \sqrt{96/5})}{14}} \approx 30.56^\circ \quad (10.2)$$

with respect to an outer rotor axis that is inclined at an axis making an angle of $\beta_2 = \arccos \sqrt{1/3} \approx 54.74^\circ$ (the magic-angle) with respect to the external field.

The main disadvantage of this technique is the lack of stability to permit a double rotation during long periods of time. Additionally, the attainable spinning speeds are relatively low and, thus, the spectra become complex with many spinning sidebands.

The DAS Principle

The DAS method [341, 342] appeared almost at the same time as the DOR technique but is more informative. The experiment consists in combining two successive rotations along two different rotor orientations leading to a compensation of the 2nd and 4th rank effects of the Legendre polynomials. In the DAS experiment three pulses are applied. The first, creates SQ coherences, evolving under the quadrupole Hamiltonian with the rotor spinning axis at an angle β_1 with respect to the static magnetic field (B_0). The second *rf* pulse stores the magnetization along the z axis of the LAB frame, allowing time for an angle hop (≈ 30 ms). And finally, the last *rf* pulse creates SQ coherences, which are detected with the rotor spinning axis at an angle β_2 with respect to B_0 , as well. Since the magnetic quantum

number, m remains either $\frac{1}{2}$ or $-\frac{1}{2}$ and since during t_1 evolution the angle is set to β_1 and during t_2 to β_2 , the overall phase accumulated by the $|-1/2\rangle\langle 1/2|$ term of the density matrix is (neglecting the isotropic part, $k=0$):

$$\begin{aligned} \psi^{DAS} \{(\theta_1, t_1); (\theta_2, t_2)\} &= \\ &= \left[C^{(2)} \left(I, -\frac{1}{2} \right) \omega_Q^{(2)} P_2(\cos \beta_1) + C^{(4)} \left(I, -\frac{1}{2} \right) \omega_Q^{(4)} P_4(\cos \beta_1) \right] t_1 \\ &+ \left[C^{(2)} \left(I, -\frac{1}{2} \right) \omega_Q^{(2)} P_2(\cos \beta_2) + C^{(4)} \left(I, -\frac{1}{2} \right) \omega_Q^{(4)} P_4(\cos \beta_2) \right] t_2 \end{aligned} \quad (10.3)$$

where from Eq. 2.92,

$$\omega_Q^{(2k)} = \omega_Q^{(2k)}(\alpha_{PR}, \beta_{PR}, \eta) = \frac{\omega_Q^2}{18\omega_0} \left(\sum_{q=-k}^{+k} B_{2q}^{2k}(\eta) d_{2q,0}^{(2k)}(\beta_{PR}) \exp[-2iq\alpha_{PR}] \right) \quad (10.4)$$

Eq. 10.4 is valid only if the isotropic part, $k=0$ is neglected and considering the limit of fast MAS where the time-dependent terms $q \neq 0$ may be dropped (see Eq.2.92).

The terms $C^{(k)} \left(I, -\frac{1}{2} \right)$ with $k = 2, 4$, are spin operators that incorporate the Clebsch-Gordon coefficients and the irreducible tensor operators ($\hat{T}_{k,q}^Q$).

Then, if the condition, described by the following system of equations,

$$\begin{cases} P_2(\cos \beta_1) t_1 + P_2(\cos \beta_2) t_2 = 0 \\ P_4(\cos \beta_1) t_1 + P_4(\cos \beta_2) t_2 = 0 \end{cases} \quad (10.5)$$

holds for both β_1 and β_2 angles, with $t_1, t_2 \geq 0$, an echo at

$$t_2 = k(\beta_1, \beta_2)t_1, \quad \text{with} \quad k(\beta_1, \beta_2) = -\frac{P_2(\cos \beta_1)}{P_2(\cos \beta_2)} = -\frac{P_4(\cos \beta_1)}{P_4(\cos \beta_2)} \quad (10.6)$$

will be formed refocussing the 2^{nd} and 4^{th} rank anisotropic effects of the second order quadrupolar interaction.

The main disadvantage of the DAS technique is the long time delay needed for hoping the rotor from β_1 to β_2 during the detection. This time is too long (≈ 30 ms) for most common nuclei in NMR (^{27}Al , ^{23}Na , etc), which have short longitudinal relaxation (T_1). Such effect contributes to the broadening of the signal in the isotropic dimension because the homonuclear dipole-dipole interaction act on the longitudinal magnetization retained along the z-axis during the z-filter period, where the rotation axis is shifted from β_1 to β_2 . This method has been mostly used for ^{17}O observation.

As it is understandable, the DOR and DAS are technically demanding techniques and, thus, their application is limited to only a few users, because they need special hardware and meticulous optimisation of several parameters.

Because this chapter mainly involves MQMAS (and STMAS) techniques, I shall explain briefly such techniques in the next section.

10.2 The MQMAS Experiment

10.2.1 The Principle

The MQMAS [27] experiment, was the first technique to study quadrupolar nuclei that utilized *rf* and spin space manipulation, retaining the normal MAS spatial averaging, where the

sample is spun about an unique rotational axis inclined at 57.4° . The MQMAS experiment principle consists in forming an echo by correlating the symmetric MQ transitions corresponding to the density matrix terms, $|-\frac{p}{2}\rangle\langle\frac{p}{2}|$, $p = \{\pm 3, \pm 5, \pm 7 \text{ or } \pm 9\}$, with the observable symmetric SQ CT, corresponding to the terms $|-\frac{1}{2}\rangle\langle\frac{1}{2}|$. Under MAS, the overall phase accumulated by the anti symmetric $| -1/2\rangle\langle 1/2|$ term of the density matrix (neglecting the isotropic part, $k=0$) is:

$$\begin{aligned} \psi^{MQMAS} \left\{ \left(\frac{p}{2}, t_1 \right); \left(-\frac{1}{2}, t_2 \right) \right\} &= \left[C^{(4)} \left(I, \frac{p}{2} \right) \omega_Q^{(4)} (\alpha_{PL}, \beta_{PL}, \eta_Q) P_4 (\cos \theta_m) \right] t_1 + \\ &+ \left[C^{(4)} \left(I, -\frac{1}{2} \right) \omega_Q^{(4)} (\alpha_{PL}, \beta_{PL}, \eta_Q) P_4 (\cos \theta_m) \right] t_2 \end{aligned} \quad (10.7)$$

To obtain an isotropic 2D MQMAS spectrum, the spin part of the quadrupolar second-order Hamiltonian, $\hat{H}^{Q,(2)}$ must be manipulated in order to set the anisotropies to zero. Then the anisotropic part of eq. 10.7 must obey the following equation,

$$C^{(4)}(I, m_1) t_1 + C^{(4)}(I, m_2) t_2 = 0 \quad (10.8)$$

where $m_1 = \frac{p}{2}$ and $m_2 = -\frac{1}{2}$ correspond to the coherence orders p (with $1 < |p| \leq 2I$) and -1 (detectable coherence) evolving during the periods t_1 and t_2 , respectively.

Thus, the second-order quadrupolar broadening is averaged out when an echo is formed at:

$$t_2 = k \left(I, \frac{p}{2}, -\frac{1}{2} \right) t_1, \quad \text{with} \quad k \left(I, \frac{p}{2}, -\frac{1}{2} \right) = -\frac{C^{(4)}(I, \frac{p}{2})}{C^{(4)}(I, -\frac{1}{2})} \quad (10.9)$$

depending on whether $p > 0$ or $p < 0$ for $1 < |p| \leq 2I$ (see the rules below). The terms $k \left(I, \frac{p}{2}, -\frac{1}{2} \right)$ for the echo pathway can be calculated from the $C^{(4)}(I, m)$ values, which are given in Table D.1.

MQMAS can also be performed with values of m_2 different from $-\frac{1}{2}$. An example was demonstrated where 5Q and 3Q coherences were correlated in a spin-5/2 nuclei ($k \left(\frac{5}{2}, \pm\frac{5}{2}, \pm\frac{3}{2} \right) = \frac{25}{19}$), and result in a better resolution than $5Q \rightarrow SQ$ or $3Q \rightarrow SQ$. [344]

A positive k value corresponds to an echo signal having its maximum at $t_2 = kt_1$, and a negative value of k corresponds to an antiecho signal with maximum intensity at $t_2 = -kt_1$, before the conversion pulse. To visualize better the displacement of the echo-antiecho signal, Fig. 10.3 shows the displacement of both echo/antiecho signals for a spin-3/2 nucleus.

It is important to note that the selection of the echo signal depends on the sign of the coherence p evolving during t_1 , which changes according to the nuclear spin, I as follows.

If $|p| = 2I$ is selected:

- The echo corresponds to the pathway with $p < 0$ during t_1 evolution (i.e, $p = -3$ for $I = 3/2$ or $p = -5$ for $I = 5/2$).

If $|p| < 2I$ is selected:

- The echo corresponds to the pathway with $p > 0$ during t_1 evolution (i.e, $p = +3$ for $I = 5/2$ or $p = +5$ for $I = 7/2$).

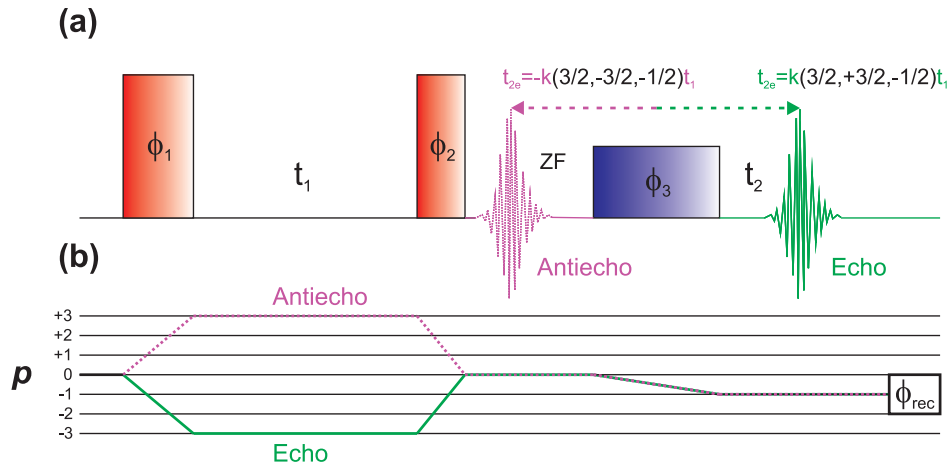


Fig. 10.3: Schematic representation of (a) the pulse sequence, and (b) CTP for the echo and antiecho signals for the z-filtered 3QMAS, $I=3/2$. Here, $p = \pm 3$ and then the condition $p = 2I$ is obeyed meaning that for the selection of the coherence orders $p=+3$ and $p=-3$, will correspond to the antiecho and echo, respectively.

The basic MQMAS Scheme can be viewed in Fig. 10.4a. Generally, as any 2D experiment (Fig. 3.1), the MQMAS scheme consists of:

Excitation period, where the pQ coherences (with $p = \{3, 5, 7, 9\}$), $|\frac{p}{2}\rangle \langle \frac{p}{2}|$, of the density matrix are excited by a strong *rf* pulse. Other ways of excitation are possible for sensitivity enhancement reasons;

t_1 **evolution**, where the excited coherences are created and allowed to evolve and dephase under the influence of the internal Hamiltonians. Many MQMAS schemes contain a split- t_1 evolution procedure, first introduced by Brown and Wimperis [345] to avoid the shearing transformation.

Conversion period, where the pQ coherences are transferred to the observable states $|\frac{1}{2}\rangle \langle \frac{1}{2}|$. Contrarily to the simple two-pulse MQMAS sequence, this step is usually made of more than a single pulse (a hard pulse followed by a soft one), and because of its low efficiency many improvements have been suggested. [26]

Detection period, where the signal is detected during the t_2 evolution as a form of an echo/antiecho or whole echo/antiecho. The QCPMG technique [346] can also be employed during the detection period to increase the S/N ratio if the transversal relaxation allows.

The numerous MQMAS schemes can be classed according to the way of obtaining 2D pure absorption spectra, which depends on the way of collecting and processing the data. This subject will be rapidly described in the next section.

10.2.2 Detection of Pure Absorption 2D Spectra

Displaying 2D spectra in absorption instead of dispersive mode is preferable, because the tails of the absorption lineshape fall off faster in frequency than the dispersion tails. Thus, less peak overlap will occur using pure absorption mode lineshapes.

The problem of obtaining mixed phase spectra was discussed in section 3.2, and can be viewed by considering Eq. 3.5a, where absorption and dispersion modes are present in the real

part of the 2D spectrum. 2D pure phase spectra may be obtained by two methods reported previously, (i) amplitude and (ii) phase modulation in t_1 . In MQMAS (and STMAS in some cases), these two strategies are based on the appearance of the maximum echo signal in the first row of a 2D data set. The former includes amplitude modulated experiments in which $t_{2e} = 0$ for $t_1 = 0$, while the latter involves a delayed formation of the echo signal to $t_{2e} \geq 0$ by applying one selective soft 180° *rf* pulse to induce $\pm 1Q \rightarrow \mp 1Q$ coherence transfers (Hahn echo formation). The important is that in both amplitude or phase-modulated cases, the real part of the resulting 2D spectrum is free of the dispersive terms.

z-Filtered Amplitude-Modulated MQMAS Scheme

This strategy consists in combining linearly the echo (ω_p) and antiecho (ω_{-p}) with the same amplitude to yield an amplitude-modulated signal in t_1 . Thus, after a complex 2D FT a pure-phase 2D spectrum is obtained. The disadvantage of this method is its impossibility to discriminate the sign of the pQ or MQ coherences evolving in t_1 dimension. To solve this problem, strategies such as SHR or TPPI can be used to perform quadrature detection in t_1 , as discussed in section 3.3.

In cases where the coherence pathway is not fully symmetric (for instance, the two-pulse MQMAS scheme in Fig. 10.4a), amplitude modulation in t_1 may pose problems because both echo ($p = -3, I=3/2$ or $p = +3, I=5/2$) and antiecho (where p has the inverse sign of echo signal) pathways are not amplitude modulated with the same amplitude magnitude due to a short living echo, for example, introducing some phase modulation which originates partial phase twisting in 2D spectra. This is a typical case where amplitude and phase modulation in t_1 are both present. Such distortion can be severe depending on the CQ and crystallite orientation.

To combine correctly the echo/antiecho pathways, Amoureux *et al.*, have introduced the *z*-filter concept in solids. [203] A *z*-filtered split- t_1 MQMAS experiment [345] has been reported as well (Fig. 10.4c).

For a better understanding of the amplitude modulation concept, lets consider the CTP of the *z*-filtered MQMAS scheme (Fig. 10.4b). If a suitable phase cycling (see Fig. 10.3) is used to select the desired coherence pathway, $\mathcal{P}^{desired} = \{0 \rightarrow \pm p \rightarrow 0 \rightarrow -1\}$ it becomes easy to derive the time domain signal. Replacing the frequencies ω_1 and ω_2 in Eq. 3.6 by frequencies $\omega_{\pm p}$ and ω_{-1} , active in t_1 and t_2 dimensions, respectively. Then, combining the signals from the $+p$ and $-p$ pathways with amplitudes a_p and a_{-p} , respectively results in the following signals derived from eq. 10.10:

If $a_p = a_{-p}$,

$$S(t_1, t_2) = \underbrace{[a_{(p)} \exp(-i\omega_{(p)}t_1) + a_{(-p)} \exp(-i\omega_{(-p)}t_1)]}_{\text{Combining echo/antiecho pathways}} \times \exp(-i\omega_{(-1)}t_2) \kappa(t_1, t_2) \quad (10.10)$$

$$= [2a_{(p)} \cos(\omega_{(p)})] \exp(-i\omega_{(-1)}t_2) \kappa(t_1, t_2) \quad (10.11a)$$

$$= S^{\cos}(t_1, t_2) \exp(-i\omega_{(-1)}t_2) \quad (10.11b)$$

If $a_p = -a_{-p}$,

$$S(t_1, t_2) = [2a_{(p)}i \sin(\omega_{(p)})] \exp(-i\omega_{(-1)}t_2) \kappa(t_1, t_2) \quad (10.12a)$$

$$= S^{\sin}(t_1, t_2) \exp(-i\omega_{(-1)}t_2) \quad (10.12b)$$

with $\omega_p = -\omega_{-p}$. $\kappa(t_1, t_2)$ accounts for the transversal relaxations during t_1 and t_2 evolutions.

Eqs. 10.11 and 10.12, refer to the cosine and sine amplitude modulated 2D time domain data set, derived from eq. 10.10, using the Euler relation. When a double FT (a complex FT in t_2 followed by real FT in t_1) is applied to either one or other time domain signals, the real part has the form:

$$Re\{FT[S(t_1, t_2)]\} = Re[S(\omega_1, \omega_2)] = \underbrace{[A(\omega_p) + A(\omega_{-p})]}_{\text{no frequency separation in } t_1} A(\omega_{-1}) \quad (10.13)$$

As stated above, although amplitude modulation in t_1 permits obtaining pure absorption 2D lineshapes it does not allow sign discrimination in the indirect dimension, and a hypercomplex acquisition of the data set is needed as it will be treated below.

t_1 sign discrimination by “hypercomplex” 2D FT

The hypercomplex FT procedure, also known as the States method, makes a linear combination of the $S^{\cos}(t_1, t_2)$ [Eq. 10.11b] and $S^{\sin}(t_1, t_2)$ [10.12b] signals to give a pure absorption 2D spectrum without signal ambiguity in t_1 . Such procedure is accomplished by phase shifting the preparation *rf rf* pulse (or pulses for the case of using a to excite the pQ coherences, for instance) as discussed in section 3.3.1. If an additional phase $\Delta\xi$, defined in Eq. 3.8a, is added to the preparation *rf* pulse, the cosine term in Eq. 10.11a becomes a sinus function as follows,

$$\cos(\omega_p) \xrightleftharpoons[k=0]{k=1} \cos(\omega_p + p\Delta\xi) = \sin(\omega_p) \quad (10.14)$$

where the k values are defined in Eq.3.8a. Then for each t_1 increment, two complementary experiments, a cosine ($k = 0$) and a sine ($k = 1$) signal, are recorded successively according to Table. 3.1. And finally, from the two complementary experiments, one obtain four time domain 2D data sets,

$$k = 0 \rightarrow \left\{ \begin{array}{l} S_{rr}(t_1, t_2) \\ S_{ri}(t_1, t_2) \end{array} \right\}, \text{ Experiment 1} \quad \bullet [S^{\cos}(t_1, t_2)] \quad (10.15a)$$

and

$$k = 1 \rightarrow \left\{ \begin{array}{l} S_{ir}(t_1, t_2) \\ S_{ii}(t_1, t_2) \end{array} \right\}, \text{ Experiment 2} \quad \bullet [S^{\sin}(t_1, t_2)] \quad (10.15b)$$

When using such method a new 2D data set is built from the real parts of the two signals $S^{\cos}(t_1, t_2)$ and $S^{\sin}(t_1, t_2)$, and after two successive complex FT in both time dimensions a pure phase 2D spectrum will be obtained:

$$Re[S(\omega_1, \omega_2)]^{\text{hypercomplex}} = A(\omega_p) A(\omega_{-1}) \quad (10.16)$$

More details about such treatment will be discussed later in sections 10.8 and 10.4.4 to process a multiplex “hypercomplex” data set.

Phase Modulated MQMAS Schemes

This strategy is used for MQMAS experiments using whole echo (shifted echo experiments) acquisition. Some examples are depicted in Fig. 10.4e-f, where a last 180° selective pulse is employed just after a delay using a low *rf* field strength ($\nu_1 = 10 - 20\text{kHz}$). Such delay depends on the MQMAS scheme employed as can be seen in Figs. 10.4e and 10.4f. It is worth noting that in the former, the delay will be only equal to τ , while in the latter scheme the delay, $\frac{kt_1}{1+k} + \tau$, just before the 180° pulse can be thought of as being composed by two parts: (i) at the end of the variable delay, $kt_1/1+k$, the MQ coherences are refocused to SQ coherences always at same time position, i.e., it allows to “lock” the appearance of the whole echo in t_2 . This procedure leads to the shearing in the time domain during the experiment rather than applying a shearing transformation at the end of the acquisition in non-split- t_1 experiments. (ii) The constant time delay τ , just delays the formation of the echo signal (or antiecho) in order to allow the formation of a whole-echo during t_2 , which contains a pure absorption mode after FT.

The mathematical description of phase modulation in t_1 will be skipped since this method was not used for obtention of pure phase 2D spectra in this thesis. Further information can be found on refs. [26,347]

Additional Comments

The whole-echo acquisition scheme is referred to be the most efficient in terms of S/N ratio if the samples have long enough transversal relaxation times (T_2). However the z-filtered MQMAS scheme is still the most used technique because of its robustness and easy implementation. The study of the several MQMAS schemes of acquiring the signal to obtain 2D pure absorption spectra, such as z-filter, z-filter+split- t_1 , shifted-echo and shifted-echo split t_1 , can be found in the respective publications [41,203,345] and are summarised in some reviews. [26,347]

Despite the many solutions investigated to enhance the sensitivity of MQMAS experiments, this technique still suffers from low sensitivity, due to the relatively low efficiencies to excite and convert MQ coherences, and this problem becomes worse for higher values of I . Recently, another strategy to improve MQMAS experiments, based on selection of multiple CTPs, was introduced by Gan *et al.*, and for the first time, experimentally demonstrated, in this thesis. Such method is used to acquire the echo and antiecho simultaneously in a z-filtered MQMAS scheme. This will be discussed in section 10.4.

Another method based on the same principle of MQMAS, is STMAS. This clever experiment allows to partially overcome the sensitivity issues observed in MQMAS experiments. The principle will be briefly discussed in the next section.

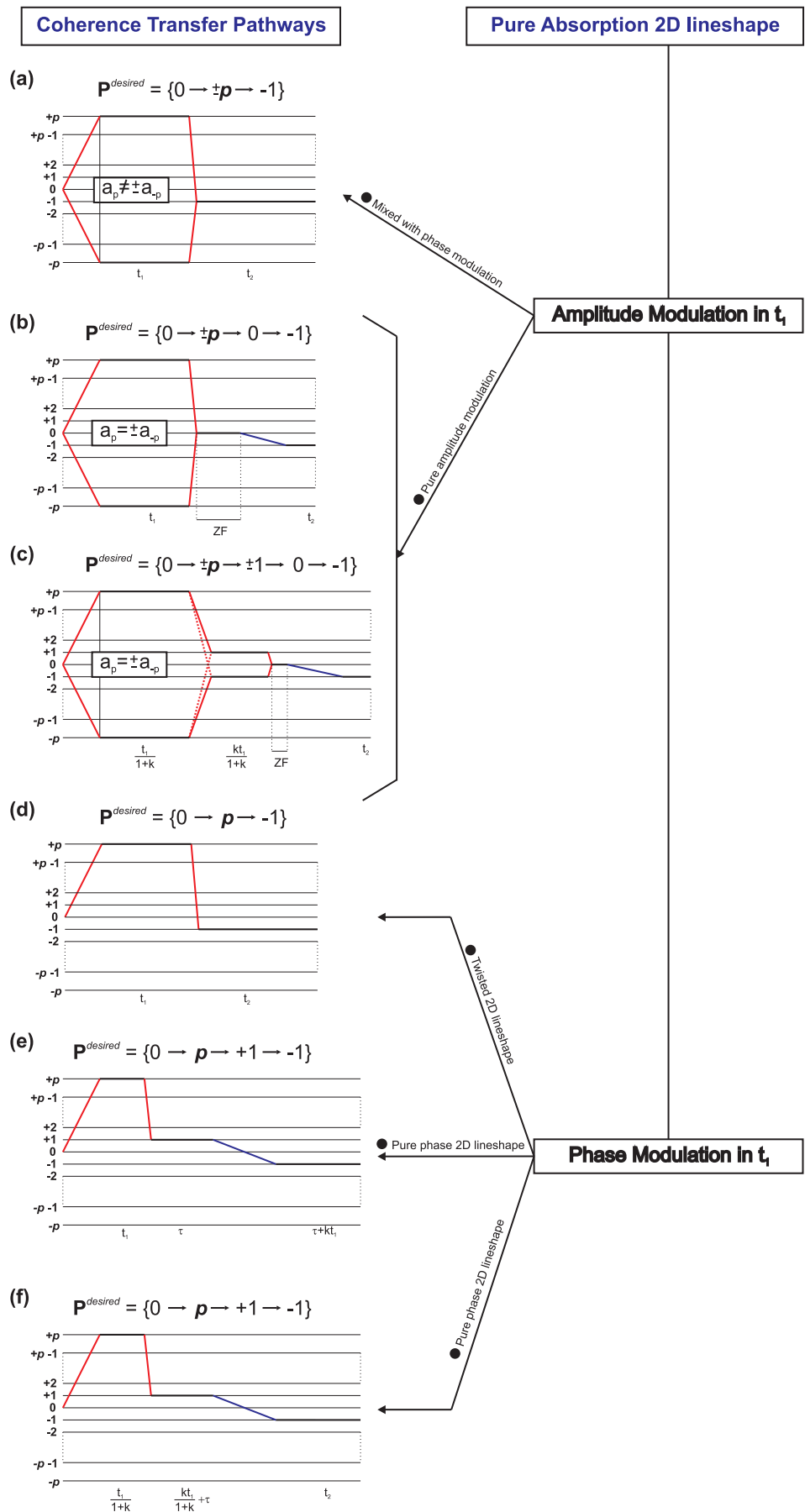


Fig. 10.4: Examples of selected CTPs for MQMAS experiments and their respective classification according to the method of obtaining pure absorption 2D spectra. (a) two pulse scheme, (b) z-filter (c) z-filter with split- t_1 , where the dotted pathway indicates the required coherence transfer for experiments correlating pQ coherence with $5Q$ coherence with $|p| < 2I$ and the solid pathway corresponds to the case $|p| = 2I$; (d) example of a CTP represented by eq. 3.5a, where phase modulation in t_1 with frequency ω_{+p} is employed giving rise to a twisted phase 2D lineshape. (e) shifted-echo (or whole echo), for $|p| < 2I$. For $|p| = 2I$ the CTP would be $P^{desired} = \{0 \rightarrow -p \rightarrow +1 \rightarrow -1\}$, (f) shifted-echo with split- t_1 for $|p| = 2I$. The k values are positive in such schemes. a_p and a_{-p} are the amplitudes of the signals evolving during t_1 with frequencies ω_p and ω_{-p} , respectively (See Eq. 3.2). Red and blue lines in the different CTPs represent, respectively, hard and soft rf pulses that induce coherence transfer. For further information on pulse sequences and phase cycling procedures, ref. [26].

10.3 The STMAS Experiment

10.3.1 The Principle

As stated before, the STMAS experiment, introduced by Z. Gan [56], can be seen as an MQMAS based experiment to respond to the sensitivity problems posed by MQMAS experiments. The STMAS is an alternative to acquire high-resolved NMR spectra of half-integer quadrupolar spins by refocussing the second-order quadrupolar broadening. However, instead of exciting anti symmetric MQ coherences, the asymmetric SQ STs terms of the density matrix, $|n - \frac{1}{2}\rangle \langle n + \frac{1}{2}|$, are now excited. Then after the t_1 evolution, the SQ STs are converted to observable CT $\frac{1}{2} \leftrightarrow -\frac{1}{2}$, and an echo is formed in a similar way as in MQMAS. The expression for the relevant accumulated phase in a 2D STMAS experiment is analogous to the one presented in Eq. 10.7, only the values of the spin coefficients $C^{(4)}$ are different (Appendix D). Such correlation between the satellite and CTs leads to a refocussing echo formed at a time t_2 ,

$$t_2 = k \left(I, n, -\frac{1}{2} \right) t_1, \quad \text{with} \quad k \left(I, n, -\frac{1}{2} \right) = -\frac{C^{(4)}(I, n)}{C^{(4)}(I, -\frac{1}{2})} \quad (10.17)$$

It is important to say that for the conventional STMAS experiments only the SQ transitions are selected. A half-integer quadrupolar nucleus only has $2I - 1$ SQ STs usually labeled “ ST_n ”. For example, a spin-5/2 nucleus will have four ST_n , i.e., $ST_{\pm 1}$ and $ST_{\pm 2}$, for the SQ STs $|\pm \frac{3}{2}\rangle \langle \pm \frac{1}{2}|$ and $|\pm \frac{5}{2}\rangle \langle \pm \frac{3}{2}|$, respectively.

Similarly to MQMAS, the basic STMAS experiment consists on two pulses, where the desired CTPs can be either $P^{desired} = \{0 \rightarrow +1 \rightarrow -1\}$ or $P^{desired} = \{0 \rightarrow -1 \rightarrow -1\}$ for negative and positive values of the ratio $k(I, n, -\frac{1}{2})$, respectively. This asymmetric scheme produces a 2D twisted spectrum like in the MQMAS experiments (Fig. 10.5a). However, the amplitude-modulated z-filtered STMAS scheme (See Fig. 10.5b) where the coherence pathway $P^{desired} = \{0 \rightarrow \pm 1 \rightarrow 0 \rightarrow -1\}$ is followed, gives a pure absorption spectrum. Like MQMAS, after a double FT with respect to t_2 and t_1 of the obtained time domain signal $S(t_1, t_2)$, each $ST_n \rightarrow CT$ narrow resonance ridge appears along the direction $\delta_1 = k(I, n, -\frac{1}{2}) \delta_2$ in the 2D STMAS unshered spectra. The shearing procedure for STMAS experiments is analogous to the MQMAS case, and thus, will be skipped.

Some requirements of the experiment are: (i) a precise setting of the magic-angle (A error inferior to 0.004° is highly recommended [339]) and (ii) a stroboscopic t_1 acquisition on the top of each rotary echo originated from the large first-order quadrupolar broadening. These two factor must be accomplished in order to average out the first-order quadrupolar interaction involving the ST_n levels and are of vital importance for the success of such experiment. Fig. 10.6 shows the influence of the magic-angle misset on the STMAS spectra.

Several modifications of the STMAS experiment have emerged in the SSNMR in the recent years. Some of them are: (i) shifted-echo [339], (ii) split t_1 shifted-echo [339], (iii) iSTMAS [348], (iv) DQ-STMAS and DQF-STMAS [349] and (v) SCAM-STMAS [350]. The latter is a very interesting modification since it compensates for the magic-angle misset applying a “SCAM pulse” in the middle of the t_1 period transferring the coherence between the two STs, ST_{+n} and ST_{-n} . [351] Both these transitions have first-order quadrupolar frequencies, which are equal in magnitude and opposite in sign. The compensation is achieved by correlating both the symmetric STs thus retaining the sign of the second-order quadrupolar frequency of the satellite coherences while inverting that of the first-order quadrupolar frequency. The last development of the STMAS “family”, until now, is the DQF-STMAS experiment introduced by Kwak and Gan. [349] This strategy consists in obtaining a proper 2D spectra free of the

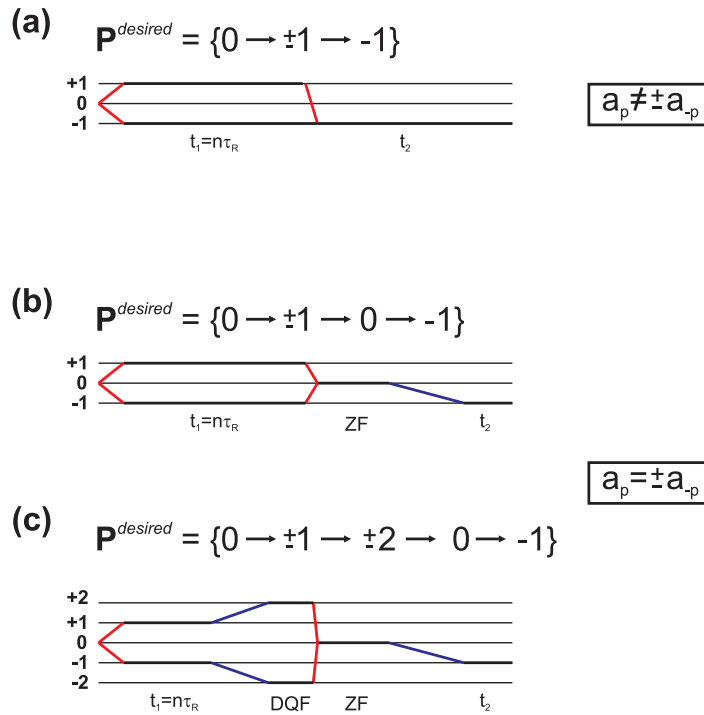


Fig. 10.5: Examples of selected CTPs for STMAS experiments. (a) two pulse scheme, (b) z-filter (c) z-filter with DQF delay. a_p and a_{-p} are the amplitudes of the signals evolving during t_1 with frequencies ω_p and ω_{-p} , respectively, and $p = 1$. Red and blue lines in the different CTPs represent, respectively, hard and soft rf pulses that induce coherence transfer. The t_1 evolution must be synchronised with an integer number of rotor periods $n\tau_R$. Typically, the dwell time during the indirect dimension is set to $\Delta t_1 = \tau_R$. For further information on pulse sequences and phase cycling procedures, ref. [339] contain all the details about the diverse STMAS schemes.

undesirable $CT \rightarrow CT$ correlation, since the CT also evolves during t_1 . This issue will be briefly summarised in the next section.

10.3.2 Suppression of Unwanted CTPs

It was stated that a quadrupolar nucleus only has accessible $2I - 1$ SQ ST energy levels. However, these SQ STs evolve at the same time as the CT, during the t_1 period, having both the same coherence order. Therefore the SQ satellite and CTs become indiscernible, even employing phase cycling. So, in reality, a spin- I nucleus has $2I$ SQ transitions ($CT + ST_n$) all having the same coherence order $p = \pm 1$. Hence, in addition to the desired $ST_{\pm 1} \rightarrow CT$ echo, other parasite transfers can also be present in the spectra, such as: $CT \rightarrow CT$, $ST_n \rightarrow CT$, $CT \rightarrow ST_n$, $ST_n \rightarrow ST_{n'}$. The echo pathways $CT \rightarrow ST_n$ and $ST_n \rightarrow ST_{n'}$ do not generally interfere because they are related with the direct observation of STs during t_2 . The $ST_n \rightarrow CT$ correlation echo will only appear for spin quantum numbers having outer STs, $I > 3/2$. Furthermore the $ST_n \rightarrow CT$ transfer has low efficiency comparing to the desired $ST_{\pm 1} \rightarrow CT$ transfer. Effectively, the main hinderance is the intense $CT \rightarrow CT$ echo pathway, which must be annihilated or at least significantly reduced. It is particularly difficult to suppress $CT \rightarrow CT$ for samples having low CQ values or presenting large distribution of chemical environments, and in both cases the $ST_{\pm 1} \rightarrow CT$ and $CT \rightarrow CT$ signals overlap. There are many varied approaches to the removal of the $CT \rightarrow CT$ signal from STMAS spectra

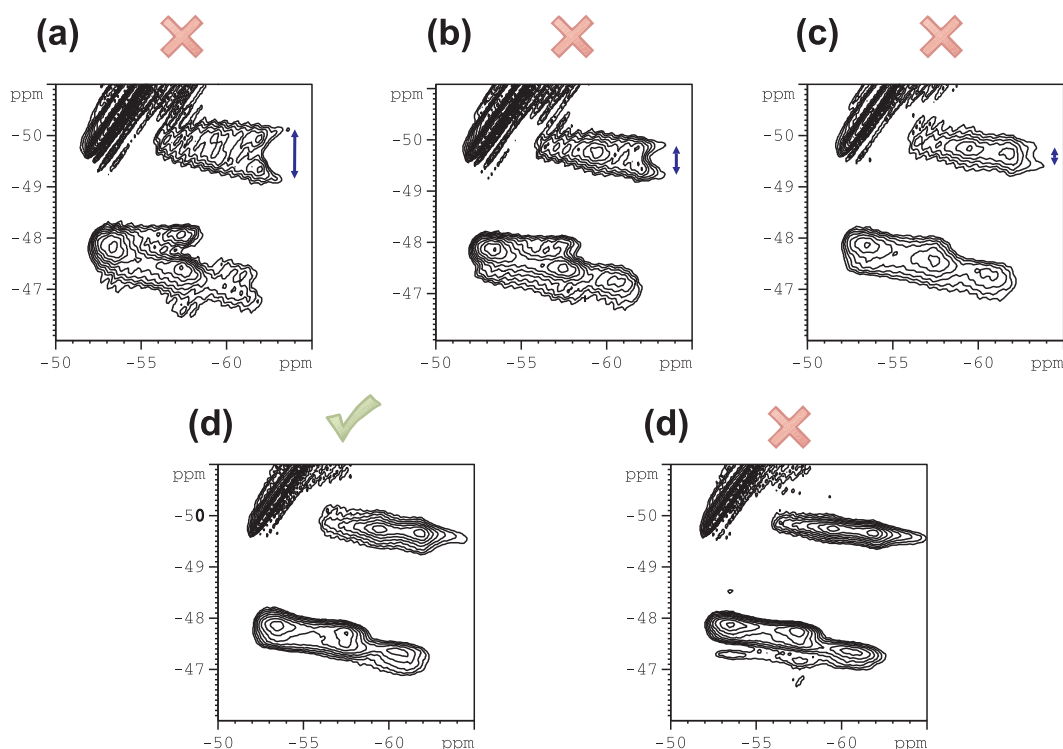


Fig. 10.6: Influence of the magic-angle misset on the ^{89}Rb STMAS spectra of RbNO_3 when changing the rotor angle, with respect to B_0 , from (a) to (e). The magic-angle is well calibrated in (d).

proposed in the literature. Four methods are presented below.

1. Suppression of $CT \rightarrow CT$ involving “presaturation” or rotor synchronisation
 - (a) The CT transition is presaturated by a soft pulse prior to the STMAS sequence. [56] This method becomes difficult to implement when there are many sites with distinct CQ because it is hard to selectively manipulate the CT without exciting at the same time the closer STs. Additionally, this method only works when all species present in the sample have very similar transverse relaxation times;
 - (b) This method consists in subtracting two spectra from each other. One, rotor synchronised during t_1 presenting both the desired and $CT \rightarrow CT$ echoes, and the second, which is not rotor-synchronised, having only the undesired $CT \rightarrow CT$. Such method allows to filter out the $CT \rightarrow CT$ signal at the expense of a S/N ratio loss of $\sqrt{2}$ and twice longer experimental time;
 - (c) The synchronisation of the t_1 evolution with half the rotor period instead of a full rotor period was also employed having the same characteristics of the method discussed in (b).
2. Suppression of $CT \rightarrow CT$ (and $ST_{n \neq \pm 1} \rightarrow CT$) through phase cycling
 - (a) Very recently, the proposed DQF-STMAS experiment, [349] whose CTP is shown in Fig. 10.5 consists in a z-filtered STMAS experiment having an additional 180° soft pulse at the end of t_1 evolution. This selective pulse converts various SQ coherences to different pathways: (i) the CT coherence is inverted $p : \pm 1 \rightarrow \mp 1$,

and (ii) the inner ST coherence, $S_{\pm 1}$ is converted to DQ coherence, $p : \pm 1 \rightarrow \pm 2$ while the outer ST coherence remains unchanged. This separation allows the selection of DQ pathway by phase cycling to filter out undesired $ST_{n \neq \pm 1} \rightarrow CT$ and $CT \rightarrow CT$ signals.

Undoubtedly, the most successful STMAS method developed until now is the DQF-STMAS technique. Its small loss of signal is compensated by having a clean spectra free of the “parasite” transfer pathways and its easy experimental optimization. However, since the CTP passes through DQ coherences before converting the signal, a longer phase cycling scheme is needed, which will be reflected in an additional experimental time for samples with high sensitivity. Like MQMAS experiments, phase cycling length of the DQF-STMAS experiment can be shortened by using a multiplex phase cycling acquisition as it will be discussed in the following sections.

10.4 Signal Selection by Multiplex Phase Cycling

The conventional phase cycling theory was established by Bodenhausen *et al.* [42]. Using this conventional phase cycling method the phases of the rf pulses or pulse trains are incremented consecutively, leading to a “nested” phase cycle. Recently, Levitt and co-workers [352, 353] introduced the cogwheel phase cycling approach, which involves “simultaneous” incrementation of the rf pulse phases, leading, in some experiments to a marked reduction in the total number of phase cycling steps required for selection of a given CTP. The cogwheel strategy have been demonstrated successfully in quadrupolar spin systems [354], where the selection of high coherence orders is usually needed. In cogwheel, the phase increments for each pulse can be written as $\frac{2\pi}{N_i}\nu$, where ν is the winding number. [352] Very recently, another method of phase cycling was proposed by the same author, called multiplex phase cycling. [355] A technique only demonstrated in spin-1/2 systems.

In this section, I will start by explaining the multiplex phase cycling principle. Further explanations will be done, making analogies with the nested phase cycling whenever required. Various experimental demonstrations will be shown for the first time using pulse sequences, normally used for the analysis of quadrupolar nuclei, showing the advantage of its use over the conventional method. Some examples will be shown where a multiplex acquisition of the signal is the only method able to select a desired CTP.

10.4.1 The Principle

In NMR the obtained signal consists of an accumulation of transients, since NMR is an insensitive technique. Then, the number of transients needed, or in other words, the experimental time necessary to get a visible and treatable signal is generally dependent on the concentration of a target nucleus and its sensitivity. However, in some cases, the timespan of the NMR experiment is determined by the need to complete the phase cycling, rather than the necessity of obtaining a sufficiently large S/N ratio.

The multiplex phase cycling consists is a new method that can be used to acquire pure-absorption 2D spectra by the SHR method (section 3.3.1) and eliminate undesired CTPs in a “single” step, i.e., two tasks may be compressed into one, saving experimental time.

The multiplex method first introduced by Ivchenko *et al.* [355] allows to reduce the number of phase increment (or the number of minimal transients) N_i , per Δt_1 by a factor of

$$\frac{4|p|}{2|p|+1} \quad (10.18)$$

where $|p|$ is the excited quantum level, and implies the t_1 evolution of the signal at coherence orders $+p$ and $-p$.

Such factor means a saving in experimental time proportional to an increase of the excited quantum level p , approaching a 50% time saving for large p .

To understand the multiplex idea one must understand the mechanism from which the time saving represented by Eq. 10.18 is gained. Let's consider the excitation block a p -quantum experiment where the desired coherence orders $+p$ and $-p$ are initially selected from the other accessible pathways (Fig. 10.7). To obtain pure-absorption 2D spectra with sign discrimination during t_1 , two classic methods are employed as stated before, the SHR and the TPPI methods. In the former, two experiments must be recorded at each increment Δt_1 , i.e., the cosine- and sine-modulated signals ($S_{\cos}(t_1, t_2)$ [Fig. 10.7a] and $S_{\sin}(t_1, t_2)$ [Fig. 10.7b]). However in TPPI, although the experimental time is equal to the SHR method, only one data set is acquired, as explained before. In the following, only the SHR acquisition method will be considered to establish a comparison between the new "multiplex acquisition method" and the nested phase cycling.

In the SHR method, the cosine- and sine-modulated 2D data set have to be acquired using a minimum number of scans $\mathcal{N} = 2|p|$ each (Fig. 10.7a and 10.7b) to alias simultaneously the $+p$ and $-p$ coherence orders, making a total of $4|p|$ number of scans for the excitation transfer.

For each data set, a complete phase cycling must be completed:

$$\sum_{k_i=0}^{\mathcal{N}_i-1} S_{k_i}^{\cos}(t_1, t_2, \phi_1(k_1), \dots, \phi_n(k_n), \varphi_{rec}(k_1, \dots, k_n)) \quad (10.19)$$

$$\sum_{k_1=0}^{\mathcal{N}_i-1} S_{k_1}^{\sin}(t_1, t_2, \phi_1(k_1), \dots, \phi_n(k_n), \varphi_{rec}(k_1, \dots, k_n)) \quad (10.20)$$

where \mathcal{N}_i is the total number of increments in the phase cycle (or number of transients), and n is the total number of pulses contained in the pulse sequence.

Alternatively, one can select $+p$ and $-p$ coherence orders separately, in two different experiments, and then add them together applying a minimum $2|p| + 1$ -step phase cycling. But, of course, this would originate a longer minimum phase cycling of $\mathcal{N} = 4|p| + 2$, i.e., $2|p| + 1$ transients for each pathways, $0 \rightarrow +p$ and $0 \rightarrow -p$. Therefore such procedure is, obviously, not recommended. Nevertheless, Ivchenko *et al.* showed, in a ^{13}C DQ experiment in organic solids, [355] that it is possible to acquire both cosine- and sine-modulated data set, by just performing a "single" experiment, using the *multiplex* phase cycling principle. Fig. 10.7, shows a comparison between the SHR and multiplex methods, with additional details in the caption. In Fig. 10.7c, one can see that there is no need to perform a second experiment with a phase shifted *rf* pulse with respect to a first experiment. Instead, one set of experimental data set can be used to acquire separately the $+p$ and $-p$ coherence orders (Fig. 10.7c) and afterwards combine them to create the cosine- and sine-modulated signal, by just using a minimum of $2|p| + 1$ -step phase cycling, per t_1 increment, to select the CTPs $\mathcal{P}^{desired} = \mathcal{P}_{+p} + \mathcal{P}_{-p} = \{0 \rightarrow \pm p \rightarrow \dots \rightarrow -1\}$. To make it possible in just a minimum of $2|p| + 1$ -step phase cycle for the excitation pulse, the φ_{rec} must be kept constant in place of changing according to the phase acquired by the *rf* pulses during the duration of an experiment. The individual signals are not combined together, as in nested phase cycling, *but rather stored individually* in the computer hard disk. Then, once completing the experiment a post-acquisition numerical phase, $\varphi_{num}(k_i)$ is applied to calculate $\mathcal{P}^{desired}$. In short, the overall pathway phase of a certain CTP under a multiplex acquisition is:

$$\Phi_{\mathcal{P}} + \varphi_{num}(k_i) = \Delta p_1 \phi_1(k_1) + \dots + \Delta p_n \phi_n(k_n) + \varphi_{rec}(k_1, \dots, k_n) = 0 \quad (10.21)$$

where the only difference with respect to the overall pathway phase of a nested phase cycling is the addition of the term $\varphi_{num}(k_i)$.

In a more generalised form, and taking as an example Fig. 10.7c, the spectrometer phases are selected so that the following equations are satisfied:

1. Multiplex Phase Cycling

$$\frac{1}{N} \sum_{k=0}^{N-1} \exp \left[-i \left\{ \Phi_{\mathcal{P}}(k) + \varphi_{num}^{(+p)}(k) \right\} \right] = \begin{cases} 1 & \text{if } \mathcal{P}_{+p} \in \mathcal{P}^{(desired)} \\ 0 & \text{if } \mathcal{P}_{+p} \notin \mathcal{P}^{(desired)} \end{cases} \quad (10.22)$$

or

$$\frac{1}{N} \sum_{k=0}^{N-1} \exp \left[-i \left\{ \Phi_{\mathcal{P}}(k) + \varphi_{num}^{(-p)}(k) \right\} \right] = \begin{cases} 1 & \text{if } \mathcal{P}_{-p} \in \mathcal{P}^{(desired)} \\ 0 & \text{if } \mathcal{P}_{-p} \notin \mathcal{P}^{(desired)} \end{cases} \quad (10.23)$$

2. Nested Phase Cycling

$$\frac{1}{N} \sum_{k=0}^{N-1} \exp \left[-i \Phi_{\mathcal{P}}(k) \right] = \begin{cases} 1 & \text{if } \mathcal{P} \in \mathcal{P}^{(desired)} \\ 0 & \text{if } \mathcal{P} \notin \mathcal{P}^{(desired)} \end{cases} \quad (10.24)$$

Single experiment

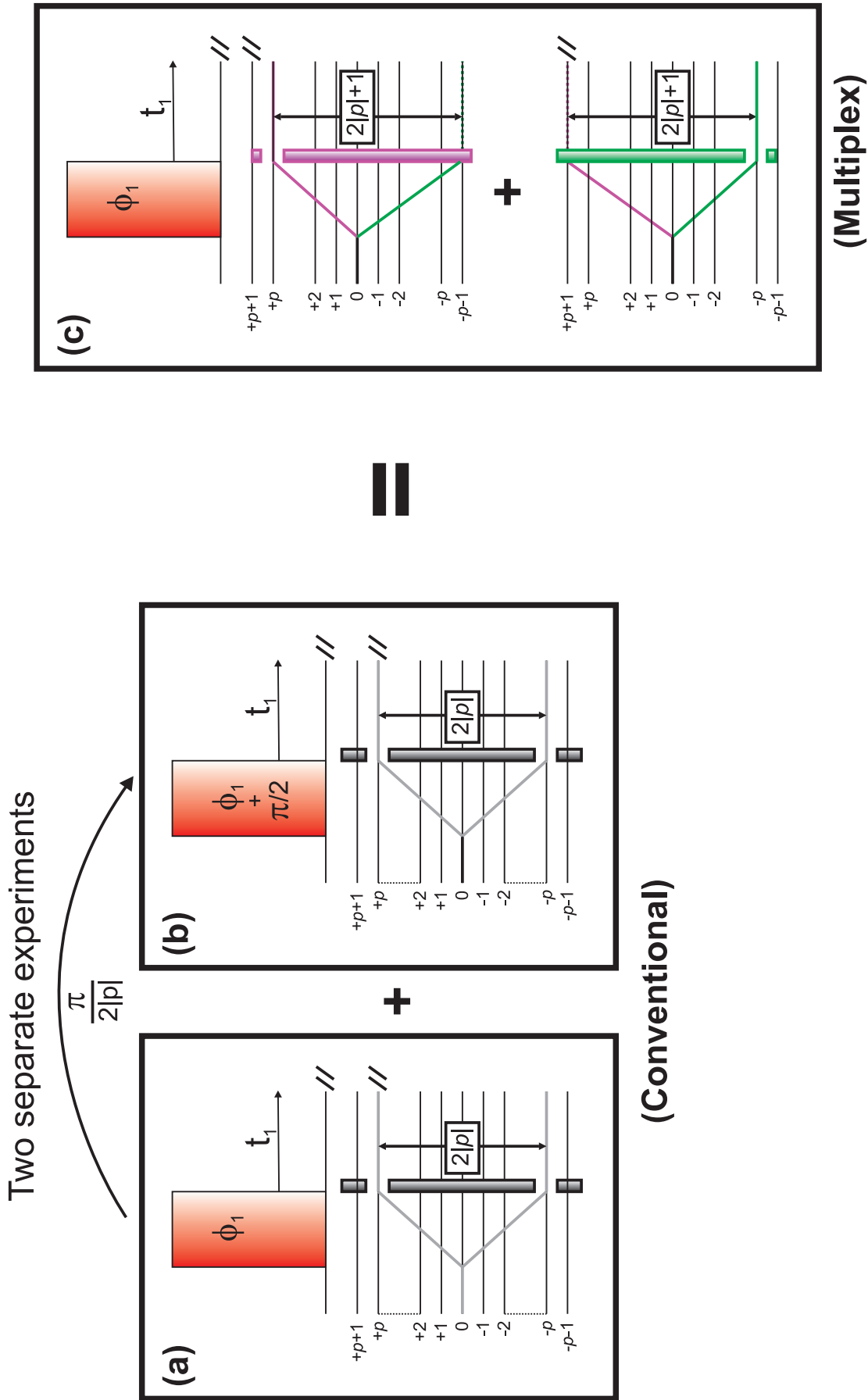


Fig. 10.7: Schematic representation showing a comparison between the SHR and multiplex principles. In the SHR method two separate experiments (a) and (b) are needed for frequency sign discrimination in t_1 , because using a $2 \times |p|$ -step phase cycling both coherence orders $+p$ and $-p$ are aliased. Using the multiplex principle (c), only one data set is needed to achieve sign discrimination because a $2 \times |p| + 1$ -step phase cycle on the preparation rf pulse avoid aliasing the coherences orders $+p$ and $-p$. Such procedure allows to perform a post-acquisition signal selection without wasting experimental time.

Then, when the two signals, $S_{\pm p}(t_1, t_2)$, coming from the two pathways $\mathcal{P}_{\pm p}$ are combined, one can create the cosine- and sine-modulated data sets using the SHR method by just manipulating the post-acquisition numerical phase φ_{num} . This is a very advantageous trick, since it is possible to select different pathways without wasting additional time. Section 10.4.4 describes a prominent example of such manipulation, by constructively adding several pathways, impossible by using a nested phase cycling procedure.

10.4.2 CTP Selection in MQMAS Experiments: Nested vs Multiplex Phase Cyclings

Signal Selection by Nested Phase Cycling

A controlled selection of MQ CTPs is the basis of the acquisition of MQMAS NMR spectra. As shown in the z-filtered MQMAS scheme of Fig. 10.8, for a 3QMAS experiment, two different CTPs have to be selected, for the reasons already mentioned before, i.e., to obtain pure-absorption 2D spectra. Similarly to the example depicted in Figs. 10.7a and 10.7b, the echo and antiecho pathways ($\mathcal{P}_{\pm p,0} = \{0 \rightarrow \pm p \rightarrow 0 \rightarrow -1\}$) in a z-filtered experiment must be recorded to obtain amplitude-modulated signals. Then, in a 3QMAS experiment the two CTPs correspond to $\mathcal{P}_{+3,0}$ (antiecho) and $\mathcal{P}_{-3,0}$ (echo). By applying Eq. 3.21, the general form for the receiver phase, φ_{rec} of a z-filtered p QMAS experiment, is set to fulfil the condition:

$$\varphi_{rec} = -(\Delta p_1 \phi_1 + \Delta p_2 \phi_2 + \Delta p_3 \phi_3) \quad (10.25)$$

All CTPs that do not fulfil the condition of eq. 10.25, will not contribute to the final signal. As a CTP always starts at 0 (equilibrium) and finishes at -1 (observable SQ coherence), the

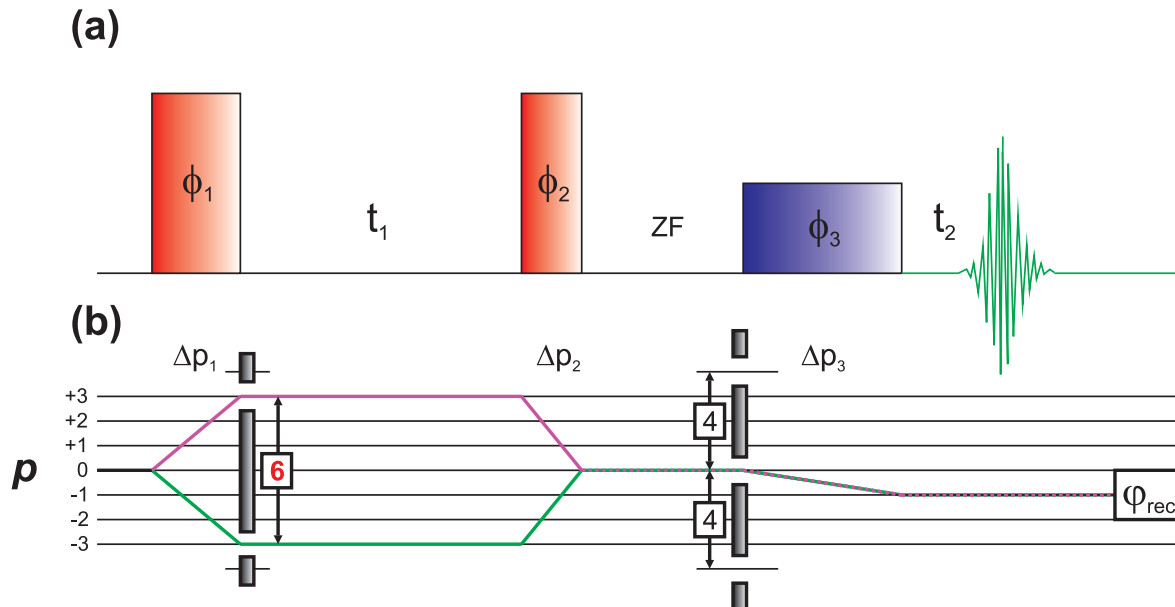


Fig. 10.8: (a) z-filtered MQMAS NMR pulse sequence. The first two pulses are hard while the last one is a soft, selective, 90° pulse on the CT. (b) CTP for the z-filtered 3QMAS experiment. The number of phases is $2|p| = 6$ for the first pulse to select simultaneously (aliasing) the $+p$ and $-p$ coherences. The last pulse is cycled 4 times to retain only the transfer from zero to -1.

Δp_i sum is always -1.

Consequently, only two of the three rf pulses need to be phase cycled, as discussed before. For instance, keeping the phase ϕ_2 of the second rf pulse constant (e.g., $\phi_2 = 0$), eq. 10.25, for a p QMAS experiment can be rewritten as:

$$\varphi_{rec}(k, l) = \pm p\phi_1(k) + \phi_3(l) \quad (10.26)$$

According to the coherence transfers depicted in Fig. 10.8b, the first and last rf pulses with phase ϕ_1 and ϕ_3 are then cycled with $\mathcal{N}_1 = m = |2p|$ and 4 different steps, respectively:

$$\phi_1(k) = \frac{2\pi k}{m}, \quad k = 0, 1, \dots, m-1. \quad (10.27)$$

$$\phi_3(l) = \frac{\pi l}{2}, \quad l = 0, 1, 2, 3. \quad (10.28)$$

The overall number of signal transients to be acquired is thus $\mathcal{N} = 4 \times m$, i.e., $\mathcal{N} = 24$ for 3QMAS and $\mathcal{N} = 40$ for 5QMAS.

In the z -filtered MQMAS technique, for each t_1 increment, the \mathcal{N} acquired signal transients $s_{kl}(t_1, t_2)$ are readily summed up in the acquisition device to generate the final 2D time domain signal.

$$S_{total}(t_1, t_2) = \frac{1}{N} \sum_{l=0}^3 \sum_{k=0}^{m-1} s_{kl}(t_1, t_2) \quad (10.29)$$

Eq. 10.29 is based on Eq. 3.20 where, $s_{kl}(t_1, t_2) = s'_{kl}(t_1, t_2) \exp\left(\sum_{i=1,3} -i\Delta p_i \phi_i\right)$. Eq. 10.29 includes the exponential function for the sake of simplicity.

Applying the SHR method, the number of signal transients \mathcal{N} will be doubled as discussed before, because a second experiment is performed differing by $\frac{\pi}{2|p|}$ in phase with respect to the preparation pulse of the first experiment. Thus, $\mathcal{N}=48$ for 3QMAS and $\mathcal{N}=80$ for 5QMAS. The TPPI acquisition method may also be used as stated before, but in this case, it would not be possible to rotor synchronize along t_1 dimension as stated previously. This procedure becomes advantageous in terms of S/N ratio because the t_1 spinning sidebands are aliased into the main central band.

Signal Selection by Multiplex Phase Cycling

Now, adapting the multiplex principle to the z -filtered MQMAS scheme (Fig. 10.9a), instead of applying a receiver phase shift to fulfil condition of eq. 10.26, it is possible to introduce a numerical phase shift and compute it at the end of the acquisition time, on separated data sets $s_{kl}(t_1, t_2)$.

For example, to select a desired coherence pathway $\mathcal{P}_{\pm p, 0}$ in the z -filtered MQMAS experiment, being $\Delta p_1 = \pm p$ ($p = 3$ in Fig. 10.9b), the change in coherence order for the first pulse, the rf pulse phases have to fulfil the condition of eq. 10.21 and so,

$$\underbrace{\Delta p_1 \phi_1(k) - \phi_3(l) + \varphi_{rec}(k, l)}_{\Phi_{\mathcal{P}}(k, l)} + \varphi_{num}(k, l) = 0 \quad (10.30)$$

The choice of $\varphi_{rec}(k, l)$ and rf pulse phases, can be likewise done by satisfying Eq. 10.23

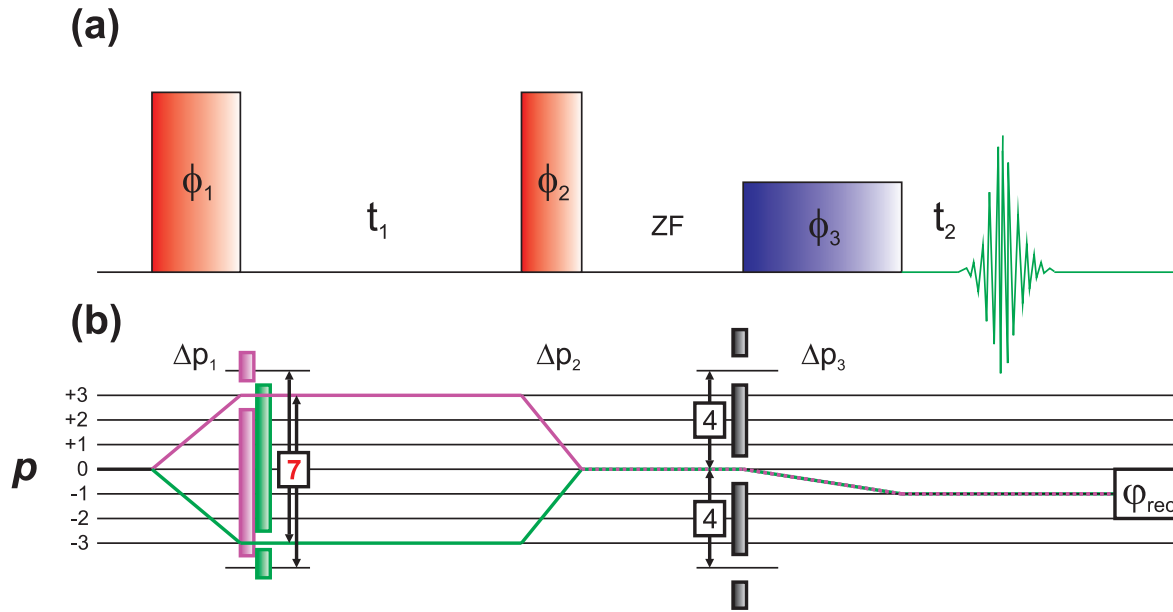


Fig. 10.9: (a) Multiplex z-filtered MQMAS NMR pulse sequence. The first two are hard rf pulses while the last one is a soft, selective, 90° pulse on the CT, exactly as in the conventional z-filtered experiment. (b) CTP for the Multiplex z-filtered 3QMAS experiment. The last pulse is cycled 4 times to retain only the zero to -1 transfer. For the first pulse, the number of phases m is 7, in order to separate all p coherences.

$$\frac{1}{N} \sum_{k=0}^{N-1} \exp \left[-i \left\{ \Phi_{\mathcal{P}}(k, l) + \varphi_{num}^{(\pm p)}(k, l) \right\} \right] = \begin{cases} 1 & \text{if } \mathcal{P}_{\pm p} \in \mathcal{P}^{(desired)} \\ 0 & \text{if } \mathcal{P}_{\pm p} \notin \mathcal{P}^{(desired)} \end{cases} \quad (10.31)$$

It is worth mentioning that, the numerical phase $\varphi_{num}(k, l)$ is a function of p and $\varphi_{rec}(k, l)$ values.

Now, for each t_1 increment, the \mathcal{N} signal transients $s_{kl}(t_1, t_2)$ acquired and stored individually can be summed up to produce the signal $S_{\pm p}(t_1, t_2)$, the final 2D time domain signal corresponding to the coherence pathway $\mathcal{P}_{\pm p, 0}$ will take the form,

$$S_{\pm p}(t_1, t_2) = \frac{1}{\mathcal{N}} \sum_{l=0}^3 \sum_{k=0}^{m-1} s_{kl}(t_1, t_2) \exp \left[-i \varphi_{num}^{\pm p}(k, l) \right] \quad (10.32)$$

which is an equation completely equivalent to Eq. 3.20, however instead of changing $\varphi_{rec}(k, l)$, one must compute $\varphi_{num}^{\pm p}$.

If the receiver phase follows the rf pulse phase $\phi_3(l)$, i.e., $\varphi_{rec}(k, l) = \phi_3(l)$, then the condition of Eq. 10.30 becomes:

$$\varphi_{num}^{\pm p}(k) = -2\pi \Delta p_1 \frac{k}{m} \quad (10.33)$$

and Eq. 10.32 will be transformed to:

$$S_{\pm p}(t_1, t_2) = \frac{1}{m} \sum_{k=0}^{m-1} s_k(t_1, t_2) \exp \left(i 2\pi \Delta p_1 \frac{k}{m} \right) \quad (10.34)$$

where $s_k(t_1, t_2)$ is the sum of the transients acquired for the 4 phase increments of the third rf pulse,

$$s_k(t_1, t_2) = \frac{1}{4} \sum_{l=0}^3 s_{kl}(t_1, t_2) \quad (10.35)$$

The expression of Eq. 10.34 corresponds in the coherence domain (section 3.5) to the DFT of the m $s_k(t_1, t_2)$ data sets acquired in the phase domain. Therefore Eq. 10.34 can be used to unravel and combine the diverse coherence transfers created by the first rf pulse in a post-processing fashion.

Signal Processing

If a $2|p| + 1$ -step phase cycle in the first rf pulse is used, both coherence orders, $+p$ and $-p$, are separated in *one* experimental data set (Fig. 10.7). The next step for the construction of pure-absorption 2D spectra is to combine linearly the 2D time domain signals $S_{+p}(t_1, t_2)$ and $S_{-p}(t_1, t_2)$, which are extracted by the DFT process (Eq. 10.34) and fed these signals into the SHR procedure. The mechanism from which the echo and antiecho signals are provided by the multiplex procedure are different from the conventional way. One can say that the obtention of pure-absorption 2D spectra and signal discrimination of the coherences evolving in t_1 are executed by a *hybrid* “Multiplex-SHR” processing. Explicitly, the p QMAS 2D spectra are constructed according to Figs. 10.10a-f, as follows:

1. In each t_1 increment, m stored s_k transients are generated by applying the numerical phase of eq. 10.33 (Fig. 10.10a).
2. The obtained s_k signals are post-processed in the hard disk according to the desired pathway $\mathcal{P}_{\pm p, 0}$ by applying a DFT (eq. 10.34) in the phase domain (Fig. 10.10b).
3. The cosine- and sine-modulated 2D signals are constructed, according to (Fig. 10.10c).

$$\begin{aligned} S^{\cos}(t_1, t_2) &= \frac{1}{2} [S_{+p}(t_1, t_2) + S_{-p}(t_1, t_2)] = \\ &= \frac{1}{2m} \sum_{k=0}^{m-1} s_k(t_1, t_2) \left(\exp \left[i2\pi \frac{k}{m} p \right] + \exp \left[-i2\pi \frac{k}{m} p \right] \right) = \\ &= \frac{1}{m} \sum_{k=0}^{m-1} s_k(t_1, t_2) \cos \left(2\pi \frac{k}{m} p \right) \end{aligned} \quad (10.36)$$

and

$$\begin{aligned} S^{\sin}(t_1, t_2) &= \frac{1}{2i} [S_{+p}(t_1, t_2) - S_{-p}(t_1, t_2)] = \\ &= \frac{1}{m} \sum_{k=0}^{m-1} s_k(t_1, t_2) \sin \left(2\pi \frac{k}{m} p \right) \end{aligned} \quad (10.37)$$

4. Each signal set Fourier transformed in the t_2 dimension (Fig. 10.10d), as follows,

$$S^{\cos}(t_1, \omega_2) = \int_0^{\infty} [S^{\cos}(t_1, t_2) \exp(-i\omega_2 t_2)] dt_2 \quad (10.38)$$

$$S^{\sin}(t_1, \omega_2) = \int_0^{\infty} [S^{\sin}(t_1, t_2) \exp(-i\omega_2 t_2)] dt_2 \quad (10.39)$$

5. Construction of a new 2D data set from the real parts of $S^{\cos}(t_1, \omega_2)$ and $S^{\sin}(t_1, \omega_2)$, respectively (Fig. 10.10e), according to

$$S^{SHR}(t_1, \omega_2) = \text{Re}[S^{\cos}(t_1, \omega_2)] + i \text{Re}[S^{\sin}(t_1, \omega_2)] \quad (10.40)$$

6. Finally, a FT in the t_1 dimension leads to the pure absorption 2D spectra (Fig. 10.10f).

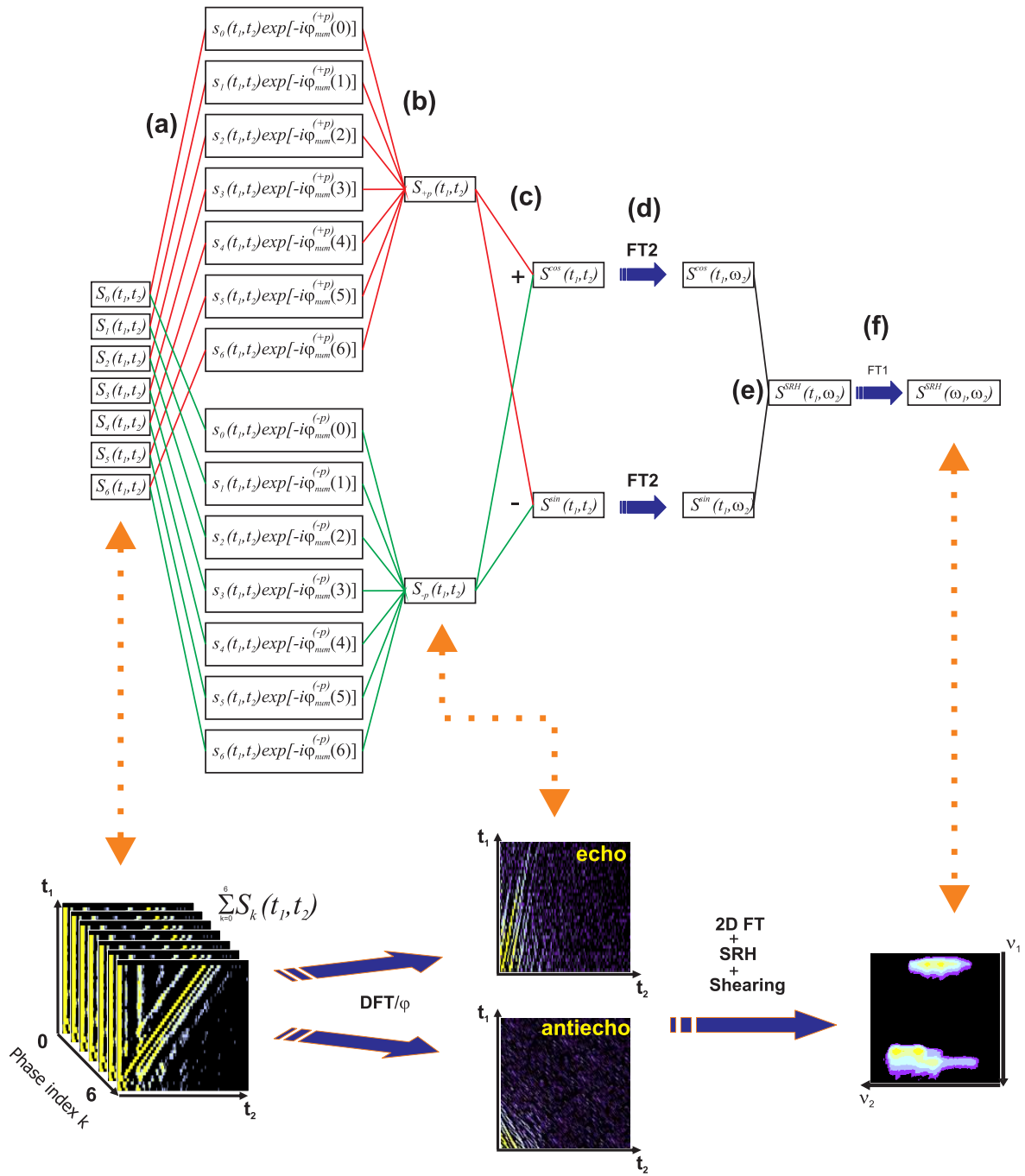


Fig. 10.10: Schematic representation of the Multiplex-SHR signal processing, detailing the different steps needed to obtain pure-absorption 2D 3QMAS spectra employing numerical equations (top) and 2D spectral illustrations (bottom). In step (a) 14 ($2 \times [2|p| + 1]$) data sets are generated in a post-acquisition fashion. 7 $s_k(t_1, t_2)$ signals to select coherence orders $+p$ and $-p$ (in this case $p = 3$). In (b) a DFT is performed on each set of 7 signal transients to select both $+3$ and $+3$ coherence orders after the preparation pulse and then construct the complex conjugated signals $S_{\pm p}(t_1, t_2)$. (c) The echo and antiecho signals are linearly combined as usual to form the cosine- and sine-modulated data sets followed by (d) the first FT applied in the t_2 dimension. (e) The real parts are selected and, finally, (f) a second FT is applied, with respect to t_1 .

Fig. 10.10, clearly shows that the signals $S_{+p}(t_1, t_2)$ and $S_{-p}(t_1, t_2)$ built from 7 data sets each, are constructed independently. Indeed, starting from the 7 $s_k(t_1, t_2)$ signal transients, it is possible to construct 7 additional data sets (Fig. 10.10a). This fact, leads to a considerable experimental time saving, that will be exemplified in the next section.

10.4.3 Experimental Demonstration of the Multiplex Approach

The ^{87}Rb ($I = 3/2$) and ^{27}Al ($I = 5/2$) conventional and multiplex z-filtered 3QMAS NMR spectra are shown in Figs. 10.11 and 10.12, respectively. According to Fig. 10.8, to complete the nested phase cycling, **24** transients per t_1 increment (**6**, $[2|p|]$ and **4** transients for the first and last rf pulses, respectively) were acquired. In addition, the acquisition of a second data set with the same number of transients was necessary in order to apply the SHR method in the 2D FTs. The overall number of acquired transients was thus, **48**.

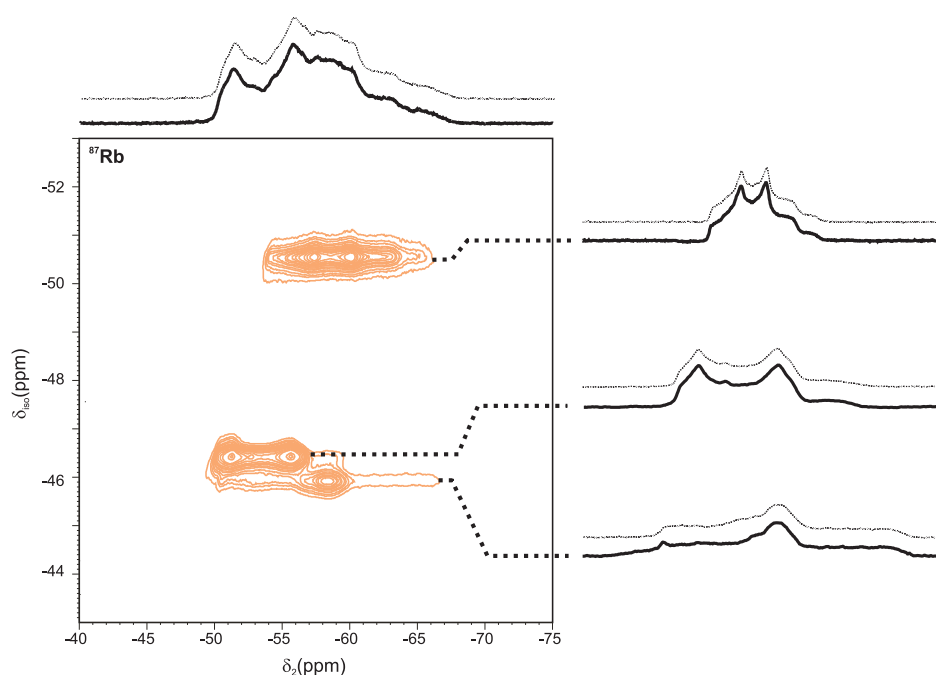


Fig. 10.11: Sheared ^{87}Rb 2D Multiplex 3QMAS spectrum of RbNO_3 . On the right side the cross-sections are represented (bold line) and compared with the corresponding cross-sections of the conventional z-filtered MQMAS spectra (normal line). The Multiplex spectrum was acquired at a spinning rate of $\nu_R = 5$ kHz and a 0.3 s recycle delay. Rotor synchronization was used in the t_1 domain. The initial excitation and conversion hard pulse lengths were 3.3 and 1.2 μs , respectively, using a $(\omega_1/2\pi)$ of ca. 130 kHz. The soft pulse length was 12.5 μs , using a $(\omega_1/2\pi)$ of ca. 10 kHz.

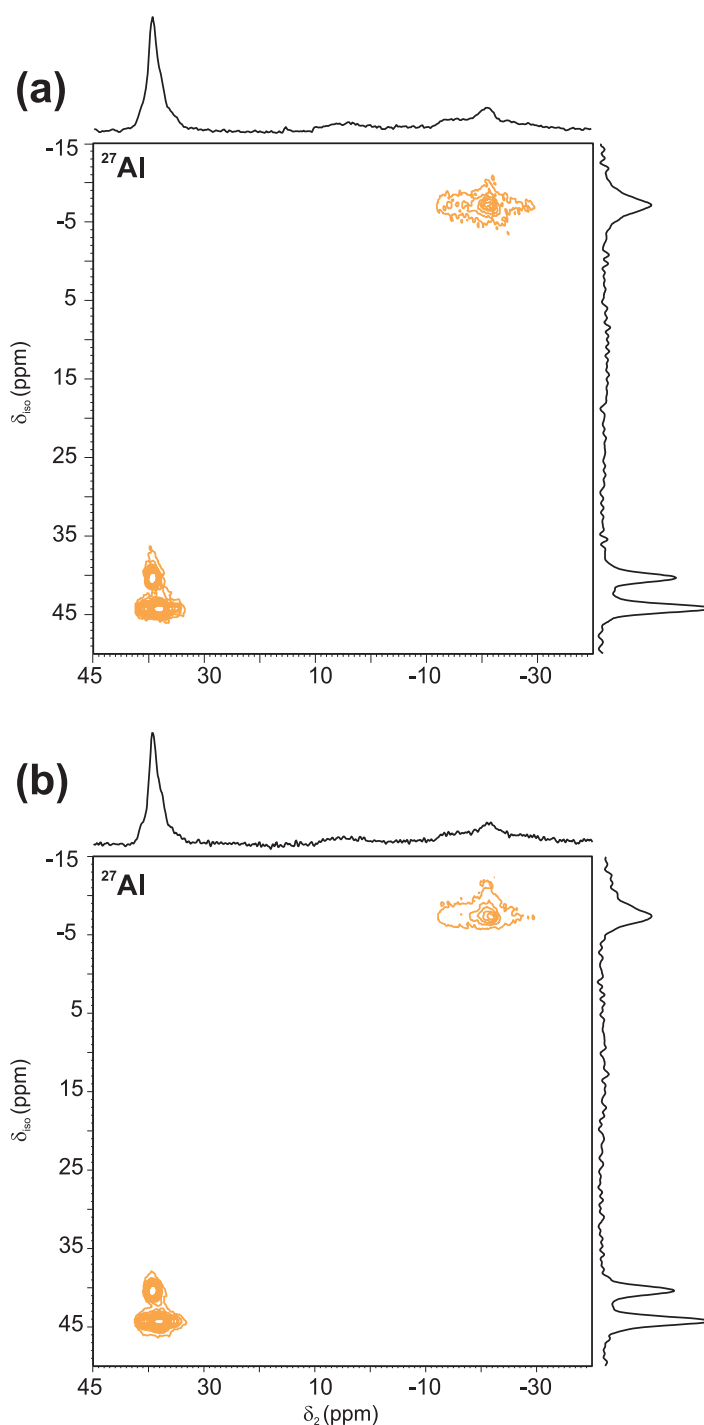


Fig. 10.12: Sheared ^{27}Al 2D (a) z-filtered and (b) multiplex 3QMAS spectrum of the aluminophosphate VPI-5. The conventional z-filtered 3QMAS spectra was recorded with multiples of 48 transients, in this case 96 (including the sine-modulated data), while the multiplex z-filtered 3QMAS was recorded employing twice the minimum number of transients, i.e., $2 \times 44 = 88$. Note that the minimum of transients here must be $4I + 1$ and not $2|p| + 1$ as for a spin-3/2 nucleus, to avoid undesired aliasing. Both spectra were acquired at a spinning rate of $\nu_R = 14$ kHz and a 1 s recycle delay. Rotor synchronization was used in the t_1 domain. The initial excitation and conversion hard pulse lengths were 2.5 and 0.8 μs , respectively, using a $(\omega_1/2\pi)$ of ca. 130 kHz. The soft pulse length was 9 μs , using a $(\omega_1/2\pi)$ of ca. 10 kHz.

The Multiplex z-filtered MQMAS spectrum, in Fig. 10.11 was recorded using the pulse sequence in Fig. 10.9a. The *rf* power and lengths used for the three pulses are exactly the same as in the conventional z-filtered experiment (see figure captions). To perform this experiment, the phase $\phi_1(k)$ of the first *rf* pulse was cycled as follows:

$$\phi_1(k) = k \frac{2\pi}{7}, \quad k = 0, 1, \dots, 6. \quad (10.41)$$

For each phase $\phi_1(k)$, the receiver and the last *rf* pulse phases ($\phi_{rec}(k, l)$ and $\phi_3(l)$) were synchronously cycled 4 times in order to transform $\phi_{num}(k, l)$ uniquely dependent on the first pulse. Then, the resulting 4 transients were added for averaging, following Eq. 10.35. The resulting 7 transients were stored separately for further processing (Fig. 10.10a). Thus, the phase $\phi_{num}(k)$ used to process the data was computed from Eq. 10.33 and can be written as:

$$\phi_{num}^{(\pm 3)}(k) = -\Delta p_1 k \frac{2\pi}{7}, \quad k = 0, 1, \dots, 6 \quad (10.42)$$

Using Eqs. 10.34, 10.36 and 10.36 it is possible, without acquiring any additional data, to obtain the cosine- and sine-modulated 2D signals necessary to perform the SHR procedure. The overall number of acquired transient is, thus, 28.

The cross-sections in Fig. 10.11 show that the conventional and multiplex MQMAS spectra are almost identical. The S/N ratio of both spectra is also very similar. It is interesting to note that the quality of the Multiplex spectrum in the high-resolution dimension (δ_{iso}) is slightly better than in the conventional z-filtered MQMAS spectrum. Indeed, less residual dispersive components were present in the 2D spectrum using the Multiplex method. This seems to indicate that the compensation between the echo and antiecho signals required to get a pure-absorption 2D spectrum is slightly better using this new approach. This may be related to the fact that the cosine- and sine-modulated signals are computed from the same set of data in the Multiplex procedure in a post-acquisition way, instead of being acquired independently in the conventional method during the experimental period, reducing the probabilities of adding experimental phase errors.

The multiplex principle can also be easily applied in the z-filtered STMAS experiments to acquire simultaneously the cosine- and sine-modulated data without the need of a second data set. One should use a 12-step phase cycling to reconstruct a pure-absorption 2D spectrum, i.e., 3 phase increments in the first pulse to avoid the aliasing between the coherence orders ± 1 and the usual 4 phase steps in the third *rf* pulse.

To conclude, the experimental realization of the Multiplex z-filtered MQMAS experiment confirms the validity of the approach. Applying the multiplex procedure to the acquisition of 3QMAS spectra of spin 3/2, reduces the number of acquired transients to $\mathcal{N} = 7 \times 4 = \mathbf{28}$, instead of **48** in the conventional phase cycling. On the other hand, in the acquisition of a multiplex z-filtered MQMAS spectrum in spin-5/2 nuclei the number of phase cycle steps for the first *rf* pulse must be greater than $4I$ (at least $4I + 1$) to avoid undesirable aliased signals coming from coherence orders ± 5 . Then, for a spin-5/2 a minimum of $\mathcal{N} = 11 \times 4 = \mathbf{44}$ transients are needed. The expression for the numerical phase to acquire a 3QMAS spectrum in a spin-5/2 system may be written as:

$$\phi_{num}^{(\pm 3)}(k) = -\Delta p_1 k \frac{2\pi}{11}, \quad k = 0, 1, \dots, 10 \quad (10.43)$$

but a 28-step phase cycle can be used considering that the aliasing of the undesired coherence orders are not important if the excitation of such coherence orders remain inefficient.

As expected and shown experimentally, there are no particular advantages, in terms of signal-to-noise ratio, of using the multiplex procedure to simply acquire the z-filtered

MQMAS. However, the Multiplex method may be very useful when combined with the Soft-Pulse-Added-Mixing (SPAM) approach introduced by Gan and Kwak. [356] This will be discussed in the following section.

10.4.4 Sensitivity Enhancement Through Multiple CTP Selection: The Multiplex-SHR-SPAM Acquisition Scheme

The SPAM Strategy

Recently, Gan and Kwak have shown that the efficiency of the MQMAS experiment can be enhanced by using the signals from multiple-coherence pathways [57]. Indeed, according to the authors, in this experiment the $\mathcal{P}_{\pm p,0} = \{0 \rightarrow \pm p \rightarrow 0 \rightarrow -1\}$ and $\mathcal{P}_{\pm p,\pm 1} = \{0 \rightarrow \pm p \rightarrow \pm 1 \rightarrow -1\}$ coherence pathways yield signals which may be easily added together using a two-step multiplex phase cycling on the third pulse (Fig. 10.13b). Two methods have been proposed to process the data.

Firstly, Gan and Kwak showed that, in principle, multiplex acquisition may be applied using a two-step phase cycle of the third pulse, (Figs. 10.13a and 10.13b) although no actual 2D spectra have been reported in the paper. [356] Secondly, the separation of the echo and antiecho in two different experiments has been proposed. This alternative method, dubbed “SPAM”, has been recently demonstrated experimentally by recording 2D MQMAS of several samples [58]. In short, The SPAM method is focused on the role of the soft mixing pulse and optimal use of signals from three CTPs ($\mathcal{P}_{\pm p,0}$, $\mathcal{P}_{\pm p,+1}$ and $\mathcal{P}_{\pm p,-1}$) instead of optimising the conversion *rf* pulse.

In the following, I demonstrate that it is much simpler to use the multiplex phase cycling procedure to constructively add the three different CTPs, instead of the echo/antiecho SPAM methods. [357] In addition, I shall show that a further decrease in the number of the total transients is possible by applying the multiplex principle to the first and third *rf* pulses of the MQMAS scheme.

Signal Selection With SPAM by Multiplex Phase Cycling

Due to the use of a soft pulse, it is assumed that even-order MQ, $\mathcal{P}_{\pm p,\pm 2}$, and 3Q coherences, $\mathcal{P}_{\pm p,\pm 3}$, do not contribute significantly to the spectrum. The time delay τ between the second and last *rf* pulses is kept as short as possible in order to avoid dephasing of the ± 1 coherence orders (10.13a).

It was said that the objective of the SPAM method is to increase the sensitivity of the experiment by constructively adding multiple CTPs. Now, we must answer the following question: ***How to select the multiple CTPs constructively to allow sensitivity enhancement and employing the minimum phase cycle steps?***

The best way to answer the first part of this question is to analyse Fig. 10.14. First a two-step phase cycle in the third *rf* pulse can not separate the two $\mathcal{P}_{\pm p,+1}$ pathways and the two $\mathcal{P}_{\pm p,-1}$ pathways. However, Figs. 10.14b and 10.14c, which correspond to the echo and antiecho pathways, respectively, show that these CTPs have the same signs, i.e., the pathways $\mathcal{P}_{-3,\pm 1}$ are both positive and $\mathcal{P}_{+3,\pm 1}$ are both negative. Therefore a two-step phase cycle aliases both $\mathcal{P}_{+p,\pm 1}$ and both $\mathcal{P}_{-p,\pm 1}$ pathways adding up their signals constructively. Additionally, The echo pathways $\mathcal{P}_{-3,+1}$, $\mathcal{P}_{-3,0}$ and $\mathcal{P}_{-3,-1}$ all have positive sign (Fig. 10.14b). Thus fixing the *rf* pulse phase $\phi_3 = +x$ aliases constructively the three CTPs. However if the phase ϕ_3 is maintained, the antiecho pathways $\mathcal{P}_{+3,+1}$, $\mathcal{P}_{+3,0}$ and $\mathcal{P}_{+3,-1}$ have no more the same signs ,i.e., $\mathcal{P}_{+3,\pm 1}$ pathways have opposite sign with respect to $\mathcal{P}_{+3,0}$ (Fig. 10.14c). A switch of the third *rf* pulse phase to $-x$ reverses the sign for signal

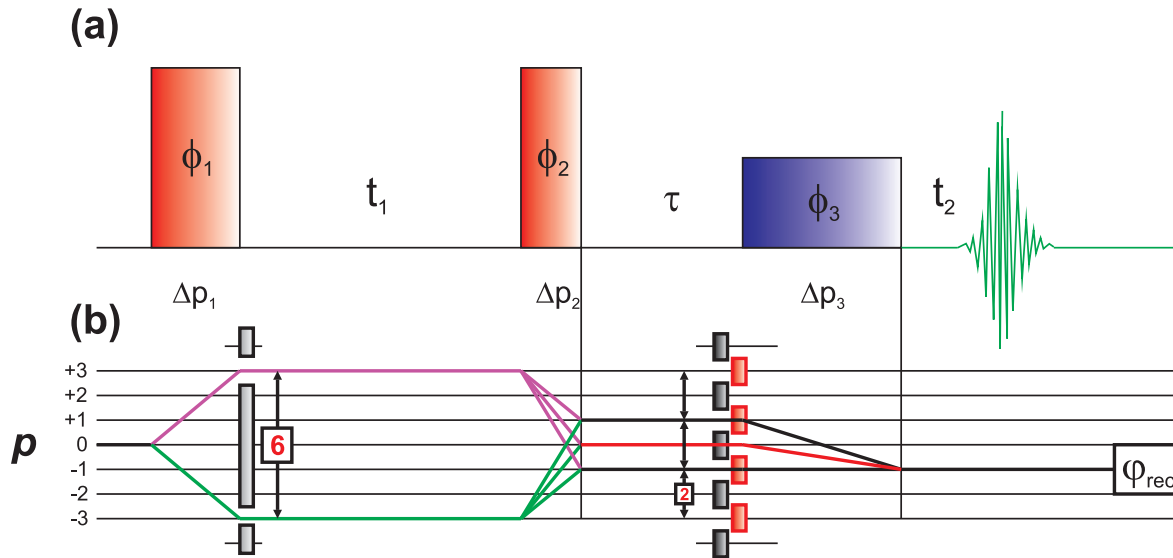


Fig. 10.13: (a) Pulse sequence and (b) CTP theoretically proposed by Gan and Kwak for the Multiplex-SPAM MQMAS NMR sequence. The delay τ between the second and the last pulses must be as short as possible, typically of the order of the phase-shifting time. The coherence orders $\pm p$ can be selected by 6-step nested phase cycling applied to the first rf pulse. While the second pulse has a fixed phase $\phi_2 = +x$, the last pulse is cycled twice between $+x$ and $-x$, to allow the constructive addition between $P_{3,0}$ and $P_{3,\pm 1}$ pathways.

coming from $\mathcal{P}_{+3,0}$ ($\Delta p_3 = -1$) while keeping the other two the same ($\Delta p_3 = 0, -2$) (Fig. 10.14e). Thus, the three antiecho CTPs can be constructively added. In this way, there is no possibility to sum the pathways $\mathcal{P}_{\pm p, \pm 1}$ and $\mathcal{P}_{\pm p, 0}$ in a constructive way, if a conventional z-filtered SPAM MQMAS experiment employing a nested phase cycling is used, for logical reasons. It is here that the role of the multiplex phase cycling becomes a clear advantage.

Therefore, to separate the $\mathcal{P}_{\pm p, \pm 1}$ and $\mathcal{P}_{\pm p, 0}$ coherence pathways, two phases ($\phi_3 = 0, \pi$) are sufficient for the third rf pulse, as discussed above, and must be numerically computed, in a multiplex manner, to manipulate independently the signals from the pathways $\mathcal{P}_{\pm p, \pm 1}$ and $\mathcal{P}_{\pm p, 0}$ in a post-acquisition way. The total number of scans to obtain z-filtered SPAM 3QMAS spectra is $\mathcal{N} = 6 \times 2$. In addition, the acquisition of a second data set (the sine-modulated part) with the same number of \mathcal{N} transients to obtain the pure-absorption 2D spectra will generate a total of **24** signal transients (Fig. 10.13).

However, it is possible to reduce even more the minimum cycle steps to obtain a pure-absorption 2D spectra if the first rf pulse phase is also cycled in a multiplex manner in tandem with the last rf pulse phase (Fig. 10.15). Thus, a “double-multiplex” phase cycling can be performed by putting together the pulse schemes of Figs. 10.9b 10.13b.

Similarly to the preceding case, a new overall pathway phase $\Phi_{\mathcal{P}}(k, l)$ must be defined according to the CTP shown in Fig. 10.15b.

$$\Delta p_1 \phi_1(k) + \Delta p_3 \phi_3(l) + \varphi_{rec}(k, l) + \varphi_{num}(k, l) = 0 \quad (10.44)$$

where $\phi_3(l)$ are defined as follows:

$$\phi_3(l) = l\pi, \quad l = 0, 1. \quad (10.45)$$

and $\phi_1(k)$ having the same form as Eq. 10.41.

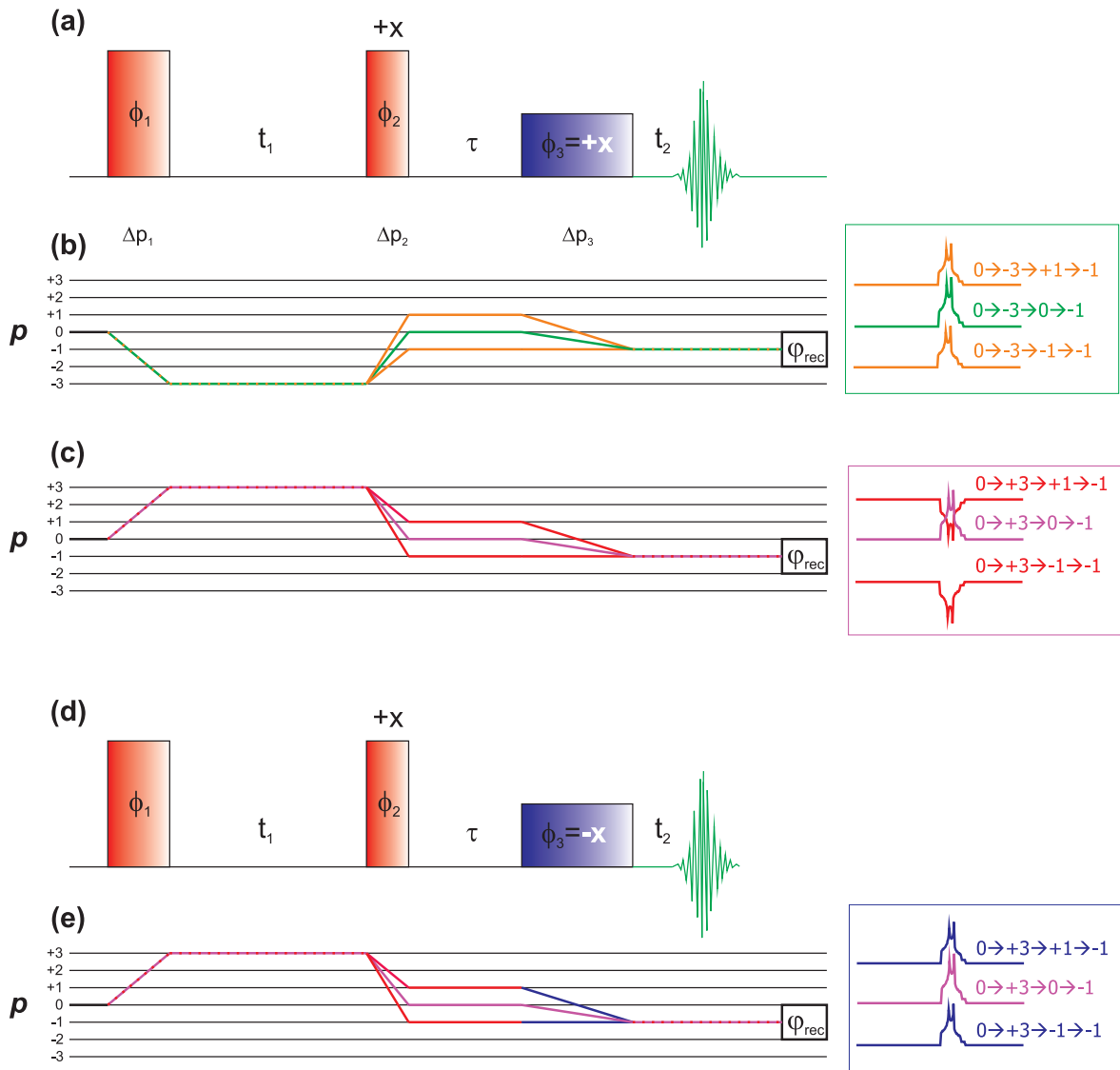


Fig. 10.14: (a) Pulse sequence for Multiplex SPAM MQMAS having $\phi_2 = \phi_3 = +x$. At the right, the signs of the respective CTP signals are depicted. When both phases are the same, the pathways (b) $\mathcal{P}_{-3, \pm 1}$ and (c) $\mathcal{P}_{+3, \pm 1}$ have opposite signs. (d) If the soft pulse is reversed ($\phi_3 = -x$), while keeping $\phi_2 = +x$, the (e) antiecho pathway ($\mathcal{P}_{+3, \pm 1}$) signal becomes positive and thus can be constructively added to the signals resulting from (b). The constructive addition of the complex conjugates with opposite signs, $\mathcal{P}_{-3, \pm 1}$ and $\mathcal{P}_{+3, \pm 1}$, can be accomplished correctly by acquiring these pathways independently in a post-acquisition way computing a numerical phase.

Δp_3 , the change of the coherence order after the third pulse, is equal to -1 and 0 (or -2) for the $P_{\pm p, 0}$ and $P_{\pm p, \pm 1}$ pathways, respectively.

In Eq. 10.44, $\varphi_{rec}(k, l)$ is now set to 0, since the *rf* pulse phases are all numerically cycled. Then, $\varphi_{num}(k, l)$ may be defined as:

$$\varphi_{num}^{(\pm p, \Delta p_3)}(k, l) = -\Delta p_1 k \frac{2\pi}{m} - \Delta p_3 l \pi \quad (10.46)$$

where m represents the number of phase cycle steps used for the excitation pulse ($m=7$ for

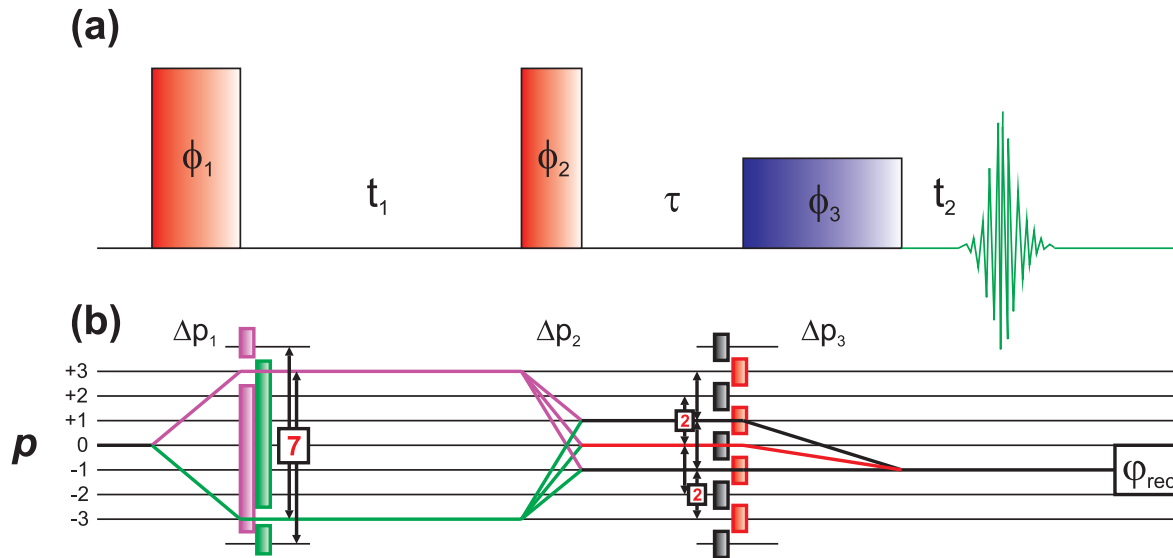


Fig. 10.15: (a) Pulse sequence for the Multiplex-SPAM MQMAS NMR sequence. The first two rf pulses are hard and the last one is a soft, selective, 90° pulse on the CT, exactly like in the conventional z-filtered experiment. The delay between the second and the last pulses must be as short as possible, typically of the order of the phase-shifting time. (b) CTP for the Multiplex z-filtered 3QMAS NMR experiment. In order to separate all p coherences, the number of phases for the first pulse is 7. The last pulse is cycled 2 times to separate the transfers from 0 to -1 and from ± 1 to -1 . The separate selection of the coherence orders $+3$ and -3 are represented by the purple and green vertical rectangles, respectively. On the other hand the individual transfers $\pm 1 \rightarrow -1$ and $0 \rightarrow -1$ are represented by respectively the black and red vertical bars.

3QMAS, and $m=11$ for 5QMAS).

Applying $\varphi_{num}^{(\pm p, \Delta p_3)}(k, l)$ to the different signal transients and adding them together, one obtains the expressions for the three coherence pathways, $S_{\pm p, 0}(t_1, t_2)$ and $S_{\pm p, \pm 1}(t_1, t_2)$, equivalent to the expression defined in Eq. 10.34.

$$S_{\pm p, \Delta p_3}(t_1, t_2) = \frac{1}{2m} \sum_{k=0}^{m-1} \sum_{l=0,1} s_{kl}(t_1, t_2) \exp \left[-i\varphi_{num}^{(\pm p, \Delta p_3)}(k, l) \right] \quad (10.47)$$

Employing the numerical phase defined in Eq. 10.46, the signals $S_{\pm p, 0}(t_1, t_2)$ for $\Delta p_3 = -1$ and $S_{\pm p, \pm 1}(t_1, t_2)$ for $\Delta p_3 = 0, -2$, are processed individually to construct two 2D spectra as usual, $S_0(\omega_1, \omega_2)$ and $S_{\pm 1}(\omega_1, \omega_2)$, respectively, which are added afterwards to originate the final pure-absorption 2D spectrum.

Signal Processing

Next, the various steps to obtain the pure-absorption 2D spectra through the pathways $P_{\pm p, 0}$ and $P_{\pm p, 0}$ are described in the same way as in section 10.4.2.

1. Processing the signal resulting from the pathway $P_{\pm p, 0}$ ($\Delta p_3 = -1$):

- (a) After replacing $\varphi_{num}^{(\pm p, -1)}(k, l)$ (Eq. 10.46) into the expression in Eq. 10.47, $S_{\pm p, 0}(t_1, t_2)$ may be written as follows:

$$\begin{aligned}
S_{\pm p,0}(t_1, t_2) &= \frac{1}{2m} \sum_{k=0}^{m-1} \left(s_{k0}(t_1, t_2) \exp \left[-i\varphi_{num}^{(\pm p, -1)}(k, 0) \right] + \right. \\
&\quad \left. + s_{k1}(t_1, t_2) \exp \left[-i\varphi_{num}^{(\pm p, -1)}(k, 1) \right] \right) = \\
&= \frac{1}{2m} \sum_{k=0}^{m-1} \left(s_{k0}(t_1, t_2) + \right. \\
&\quad \left. + s_{k1}(t_1, t_2) \exp [i\pi\Delta p_3] \right) \exp \left(i2\pi\Delta p_1 \frac{k}{m} \right) = \\
&= \frac{1}{2m} \sum_{k=0}^{m-1} \left(s_{k0}(t_1, t_2) - \right. \\
&\quad \left. - s_{k1}(t_1, t_2) \right) \exp \left(i2\pi\Delta p_1 \frac{k}{m} \right) \quad (10.48)
\end{aligned}$$

- (b) The cosine- and sine-modulated 2D signal is obtained as previously by summing and subtracting the complex conjugate signals from the symmetric $\mathcal{P}_{+p,0}$ and $\mathcal{P}_{-p,0}$ pathways, respectively.

$$\begin{aligned}
S_0^{\cos}(t_1, t_2) &= \frac{1}{2} [S_{+p,0}(t_1, t_2) + S_{-p,0}(t_1, t_2)] = \\
&= \frac{1}{m} \sum_{k=0}^{m-1} \left(s_{k0}(t_1, t_2) - \right. \\
&\quad \left. - s_{k1}(t_1, t_2) \right) \cos \left(2\pi\Delta p_1 \frac{k}{m} \right) \quad (10.49)
\end{aligned}$$

$$\begin{aligned}
S_0^{\sin}(t_1, t_2) &= \frac{1}{2i} [S_{+p,0}(t_1, t_2) - S_{-p,0}(t_1, t_2)] = \\
&= \frac{1}{m} \sum_{k=0}^{m-1} \left(s_{k0}(t_1, t_2) - \right. \\
&\quad \left. - s_{k1}(t_1, t_2) \right) \sin \left(2\pi\Delta p_1 \frac{k}{m} \right) \quad (10.50)
\end{aligned}$$

- (c) Finally the 2D spectrum $S_0(\omega_1, \omega_2)$, equivalent to a normal z-filtered MQMAS spectrum, is obtained by a 2D FT of these signals, following the SHR procedure.

2. Processing the signal resulting from the aliased pathways $P_{\pm p, \pm 1}$ ($\Delta p_3 = 0$ or -2):

- (a) After replacing $\varphi_{num}^{(\pm p, 0)}(k, l)$ (Eq. 10.46) into the expression in Eq. 10.47, $S_{\pm p, \pm 1}(t_1, t_2)$ may be written as follows:

$$\begin{aligned}
S_{\pm p, \pm 1}(t_1, t_2) &= \frac{1}{2m} \sum_{k=0}^{m-1} \left(s_{k0}(t_1, t_2) \exp \left[-i\varphi_{num}^{(\pm p, 0)}(k, 0) \right] + \right. \\
&\quad \left. + s_{k1}(t_1, t_2) \exp \left[-i\varphi_{num}^{(\pm p, 0)}(k, 1) \right] \right) = \\
&= \frac{1}{2m} \sum_{k=0}^{m-1} \left(s_{k0}(t_1, t_2) + \right. \\
&\quad \left. + s_{k1}(t_1, t_2) \right) \exp \left(i2\pi\Delta p_1 \frac{k}{m} \right) \quad (10.51)
\end{aligned}$$

- (b) Because the signal $S_{+p, \pm 1}(t_1, t_2)$ and $S_{-p, \pm 1}(t_1, t_2)$ are complex conjugates with opposite sign [17], the cosine-modulated 2D signal is obtained by subtracting these two signals and the sine-modulated 2D signal obtained by adding them, as follows:

$$\begin{aligned}
S_{\pm 1}^{\cos}(t_1, t_2) &= \frac{1}{2i} [S_{+p, \pm 1}(t_1, t_2) - S_{-p, \pm 1}(t_1, t_2)] = \\
&= \frac{1}{m} \sum_{k=0}^{m-1} \begin{pmatrix} s_{k0}(t_1, t_2) + \\ + s_{k1}(t_1, t_2) \end{pmatrix} \sin \left(2\pi \Delta p_1 \frac{k}{m} \right) \quad (10.52)
\end{aligned}$$

$$\begin{aligned}
S_{\pm 1}^{\sin}(t_1, t_2) &= \frac{1}{2} [S_{+p, \pm 1}(t_1, t_2) + S_{-p, \pm 1}(t_1, t_2)] = \\
&= \frac{1}{m} \sum_{k=0}^{m-1} \begin{pmatrix} s_{k0}(t_1, t_2) + \\ + s_{k1}(t_1, t_2) \end{pmatrix} \cos \left(2\pi \Delta p_1 \frac{k}{m} \right) \quad (10.53)
\end{aligned}$$

(c) A 2D FT using the SHR procedure yields a second MQMAS spectrum: $S_{\pm 1}(\omega_1, \omega_2)$

Both $S_0(\omega_1, \omega_2)$ and $S_{\pm 1}(\omega_1, \omega_2)$ spectra can now be added to produce the final Multiplex SPAM MQMAS NMR spectrum. A schematic representation of the various processing steps can be viewed in Fig. 10.16.

One remark can be made at this stage: indeed, following the Gan and Kwak statement, in the above demonstration it has been assumed that using a soft pulse only signals coming from $\mathcal{P}_{\pm p, 0}$ and $\mathcal{P}_{\pm p, \pm 1}$ are retained. However, it is worth noting that in a more general situation, where the third pulse is not entirely selective, some signal will also come from the $\mathcal{P}_{\pm p, \pm 2}$ and $\mathcal{P}_{\pm p, \pm 3}$ additional pathways, as only two phases are used for the third *rf* pulse. This is not a problem because these signals will also be aliased constructively to the signal coming from the $\mathcal{P}_{\pm p, 0}$ and $\mathcal{P}_{\pm p, \pm 1}$ pathways, respectively. The choice of the power of the last pulse is, thus, a compromise between the efficiency of the SPAM experiment and the need for a good excitation of the full MAS spectrum. This may depend on the spread of CSs.

In conclusion, using a “double-multiplex” phase cycling coupled to the SPAM strategy, it is possible to reduce the minimum total number of transients per t_1 increment by a factor,

$$\frac{2|p| + 1}{8|p|} \quad (10.54)$$

which leads to a more substantial time saving comparing to the application of single multiplex phase cycling (Eq. 10.18) in only one pulse as seen in section 10.4.2.

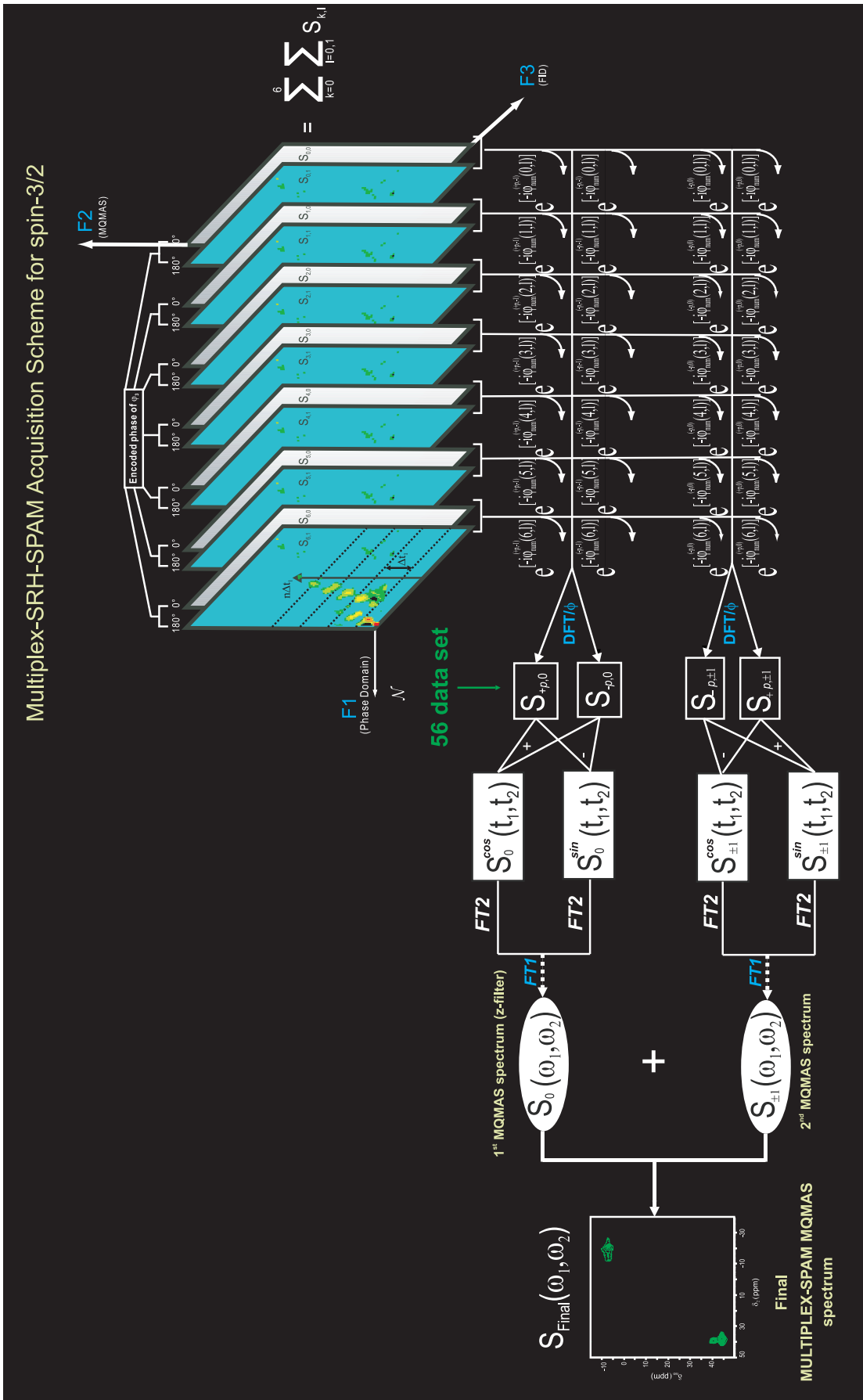


Fig. 10.16: Schematic representation of the Multiplex-SRH-SPAM signal processing of a 3QMAS experiment, detailing the different steps needed to obtain a pure-absorption 2D 3QMAS spectra. On the top, 14 “primitive” coherence maps are acquired during the experiment. The three axes represent the three variables important to obtain the 14 $s_{k,l}(t_1, t_2)$ t_1 signals. Here, $F2$ represent the t_1 evolution dimension, $F3$ represent the t_2 evolution dimension and $F1$ refers to the product between the phase increment of the rf pulses involved in the multiplex phase cycling. In this case $(2|p| + 1) \times 2 = 7 \times 2 = 14$. After a DFT, four data sets are processed independently, $S_{+p,0}$, $S_{-p,0}$, $S_{+p,\pm 1}$ and $S_{-p,\pm 1}$ and $S_{\pm p,0}$ and $S_{\pm p,\pm 1}$ are then processed separately employing the hypercomplex method to form two 3QMAS spectra. Finally they are constructively added together to obtain a sensitivity enhanced 3QMAS spectrum owing to the SPAM method.

10.4.5 Experimental Demonstrations of the Multiplex-SPAM Approach

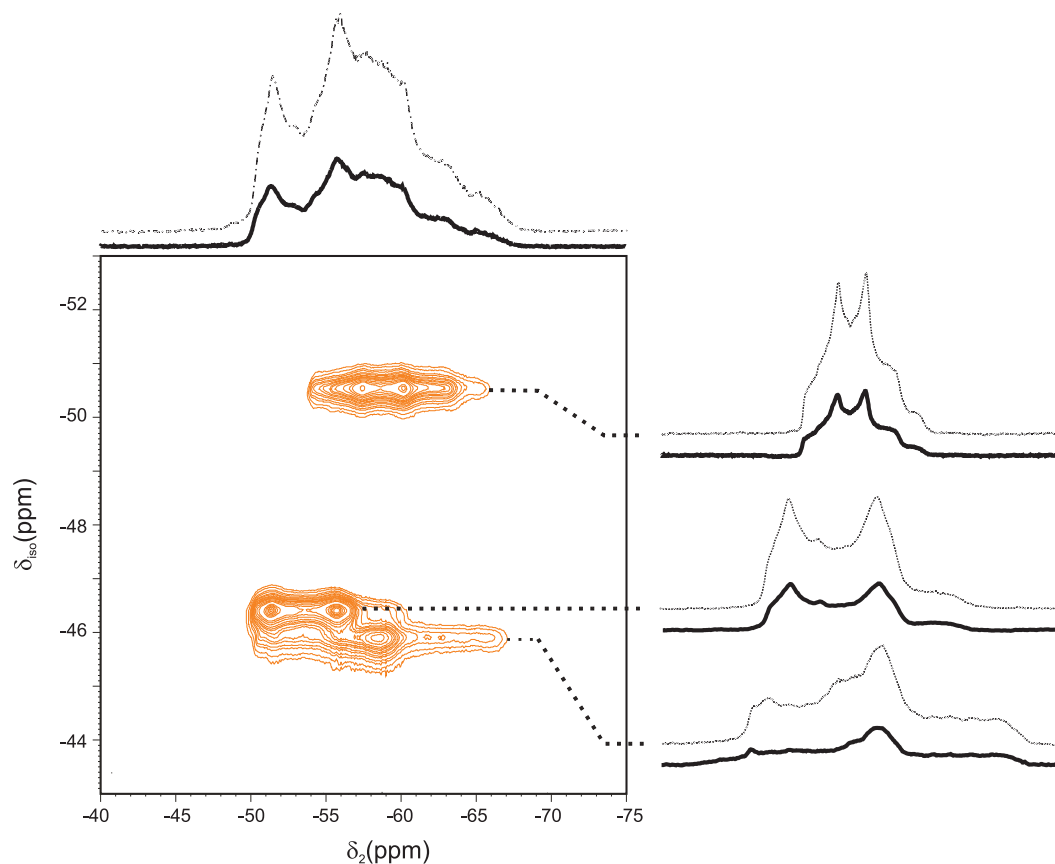


Fig. 10.17: Sheared ^{87}Rb 2D Multiplex SPAM 3QMAS spectrum of RbNO_3 . On the right side, the cross-sections are represented (dotted line) and compared with the corresponding cross-sections of the conventional z-filtered MQMAS spectrum (continuous line). The same number of scans and acquisition time was used in both techniques for a correct comparison of the efficiencies. On the top, the anisotropic projections of both multiplex SPAM (dotted line) and the conventional (continuous line) z-filtered MQMAS experiment, are compared. The amplitudes and lengths of the pulses are the same as in Fig. 10.11.

Fig. 10.17 shows the ^{87}Rb Multiplex SPAM MQMAS spectrum of RbNO_3 acquired using the sequence depicted in Fig. 10.15. The optimisation of the rf pulses in this sequence is straightforward because the settings are exactly the same as in the conventional (or multiplex) z-filtered MQMAS sequence. The first pulse was phase cycled using 7 steps as previously. Only 2 phases were used for the last pulse and the receiver was not cycled as discussed before. This gives a total number of transients $\mathcal{N} = 14$ as shown in Fig. 10.16. The resulting 14 transients were all stored separately and processed using Eq. 10.47 or Eqs. 10.48 and 10.51. The comparison of this spectrum and the conventional z-filtered MQMAS NMR spectrum shows an increase of the S/N ratio by a factor of ca. 1.7 for all sites.

Using the Multiplex and SPAM strategies in an integrated fashion, it is demonstrated, for the first time, that using only 14 transients, a pure-adsorption 2D spectrum for a spin-3/2 nucleus with enhanced intensity may be obtained.

A second example concerns the application of the Multiplex SPAM MQMAS NMR experiment to spin-5/2 nucleus. 3Q and 5QMAS spectra of an AlPO_4 -14 aluminophosphate sample

have been recorded, and display several Al sites with very different quadrupolar coupling constants. [315]

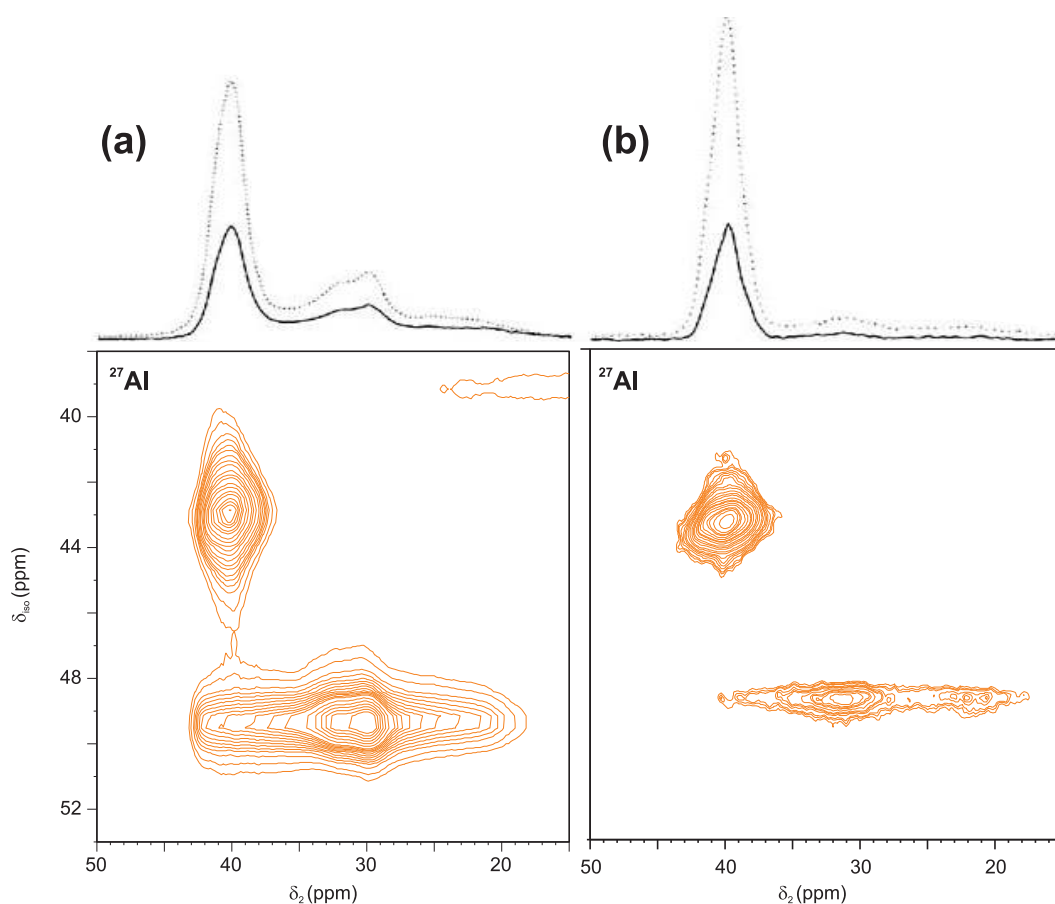


Fig. 10.18: Sheared ^{27}Al 2D Multiplex SPAM (a) 3QMAS and (b) 5QMAS NMR spectra of microporous aluminophosphate $\text{AlPO}_4\text{-14}$ in the tetrahedral-Al region. On the top, the projections are represented for both SPAM (dotted line) and the conventional z-filtered MQMAS spectra (continuous line). The Multiplex spectrum was acquired at a spinning rate of $\nu_R = 14$ kHz and a 0.5 s recycle delay. Rotor synchronization was used in the t_1 domain. For the 3QMAS/5QMAS spectra, the initial excitation and conversion rf hard pulse lengths were 2.4/4.0 and 0.8/2.0 μs , respectively, using a rf field strength ($\omega_1/2\pi$) of ca. 130 kHz. The soft pulse length was 8.3 μs , using a rf field strength ($\omega_1/2\pi$) of ca. 10 kHz.

The conventional z-filtered 3QMAS was obtained using 6 phases for the first pulse (in order to alias simultaneously the +3 and -3 coherence orders in t_1). Similarly, the conventional z-filtered 5QMAS was obtained using 10 phases for the first pulse (in order to alias simultaneously the +5 and -5 coherence orders in t_1). As in 3QMAS, the last pulse was also cycled 4 times.

Figs. 10.18a and 10.18b show the corresponding Multiplex SPAM 3QMAS and 5QMAS spectra, obtained using 11 phases for the first pulse and 2 for the third. It is worth noting that 11 phases are necessary for spin-5/2 nuclei to avoid any undesired aliasing of the MQ coherence, as discussed before.

The signal-to-noise ratio improves by a factor of **1.7** and **2.7** for the Multiplex SPAM 3Q and 5QMAS spectra, respectively.

10.4.6 Simultaneous Acquisition of Multiple Experiments

It was explained before that by computing a numerical phase φ_{num} , one can select as many CTPs as desired, since the spectra is constructed in a post-acquisition fashion, by entering the desired coherence orders into the numerical phase expression. In this way, multiple CTPs can be added and/or selected independently during the timespan of a single experiment, provided the number of phase increments are sufficient to select the desired CTPs.

Thus, taking advantage of this feature, one can imagine acquiring multiple experiments having (or not) a common *rf* pulse sequence but not necessarily sharing the same CTPs. Indeed, it is possible to reconstruct the ^{27}Al 3Q and 5QMAS spectra shown in Fig. 10.18, using the multiplex principle from a single experimental data set, because it is not necessary to change the numerical phase φ_{num} expression in Eq. 10.46. One just has to input the desired coherence order in Eq. 10.46 and build the 56 time domain 2D signals for the 3QMAS and 5QMAS experiments (See Fig. 10.16). A schematic representation of simultaneous selection of 3Q and 5Q coherences can be viewed in Fig. 10.19.

Fig. 10.19 shows that the 12 coherence pathways, $\mathcal{P}_{\pm 3,0}$, $\mathcal{P}_{\pm 3,\pm 1}$, $\mathcal{P}_{\pm 5,0}$ and $\mathcal{P}_{\pm 5,\pm 1}$, are selected simultaneously. Although the experiments works in practice, unfortunately a good S/N ratio can not be obtained for 3Q and 5QMAS simultaneous acquisition. The reason is because the efficiency of the excitation of 3Q and 5Q coherences is very distinct. Indeed, the pulse lengths needed to excite both 3Q and 5Q coherences are quite different (See Fig. 10.18). Best results are obtained if the sequence is optimised close to the 5QMAS conditions, but several transients are needed to obtain a reasonable spectrum and so there is no great interest in coupling these experiments in a simultaneous way.

Alternatively, the MQMAS experiment may be coupled with the STMAS experiment more efficiently than 3QMAS/5QMAS experiments. On one hand the pulse lengths are more similar than in the case of 3QMAS/5QMAS experiments (see experimental conditions in Fig. 10.18). On the other hand, the excitation of both 3Q and SQ coherences are efficient enough to allow the simultaneous recording of the two data sets. The MQMAS and STMAS pulse sequences have the same architecture, which facilitates the simultaneous acquisition. To acquire simultaneously 3QMAS and STMAS spectra one just needs to cycle the first *rf* pulse sufficiently enough to select independently the signal pathways involving the coherence orders changes $0 \rightarrow \pm 1$ and $0 \rightarrow \pm 3$. The classic z-filtered STMAS experiment typically uses a two-step nested phase cycle on the first *rf* pulse, which aliases the coherence orders ± 1 , corresponding to the echo and antiecho signals. The classic z-filtered MQMAS also aliases the coherence orders ± 3 . Then, it becomes impossible to acquire the 4 pathway signals independently if a conventional phase cycling is used. To solve this problem, one just has to apply a 7-step multiplex phase cycle in the first *rf* pulse to guarantee that these 4 coherence pathways are separated (Fig. 10.20a). The procedure is exactly the same as the multiplex 3QMAS experiment discussed before, which also employs 7 phase increment for the excitation *rf* pulse. The only difference is that the t_1 evolution must be synchronised with an integer number of the rotor periods to average out the first-order quadrupolar interaction affecting the satellite transitions. The numerical phase $\varphi_{num}(k)$ has the same form as Eq. 10.33. To construct the 3QMAS or the STMAS spectra seen in Figs. 10.20c and 10.20d, one just need to introduce the coherence order changes corresponding to the excitation *rf* pulse in Eq. 10.33 to produce 7 signals for each pathways $\mathcal{P}_{\pm 3}$ and $\mathcal{P}_{\pm 1}$ originating 28 $s_k(t_1, t_2)$ signals. Finally, by using Eq. 10.34 it is possible to select the desired CTP. The numerical phases needed to acquire simultaneously the 3QMAS/STMAS experiments can be viewed in Fig. 10.20.

Another example of simultaneous selection of multiple CTP through multiplex phase cycling can be applied between different *rf* pulse sequences. For example: The DQF-STMAS

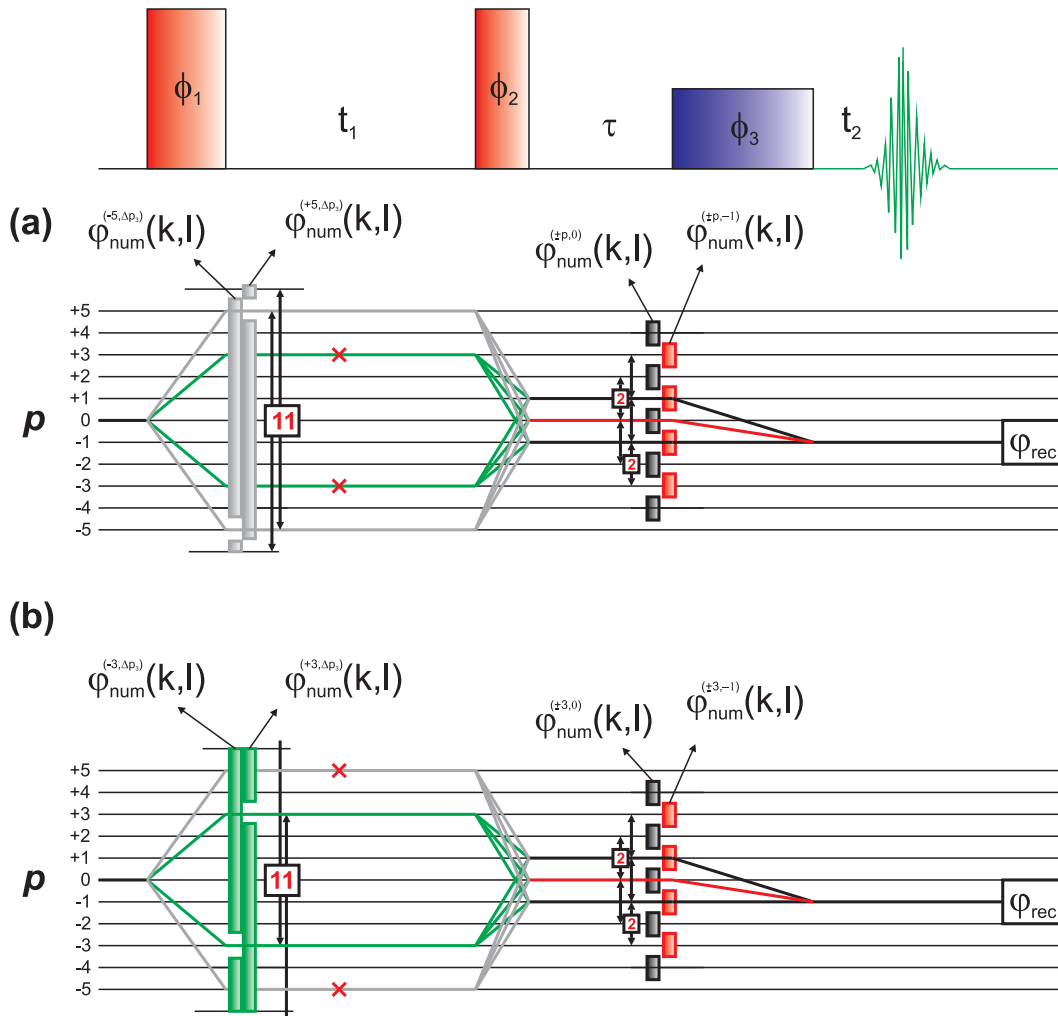


Fig. 10.19: Schematic drawings showing the mechanism of simultaneous acquisition corresponding to the CTPs signals of a multiplex SPAM 3Q and 5QMAS experiment. (a) Shows the the selection of 5Q coherences needed for the 5QMAS experiment, while blocking the +3 and -3 coherence orders. This is accomplish by using a $m=11$ -step multiplex phase cycle on the first rf pulse and by selecting a coherence change of ± 5 into Eq. 10.46. (b) Shows the selection of 3Q coherences needed for the 3QMAS experiment, while blocking the ± 5 coherence orders. Such selection is achieved using the same $m=11$ -step multiplex phase cycling employed in (a), but this time one must input the $\Delta p_1 = \pm 3$ into Eq. 10.46. In (a) and (b) the third rf pulse uses a 2-step multiplex cycling to allows sensitivity enhancement employing the SPAM strategy, as discussed before. The numerical phases needed to construct the signals $S_{\pm p, 0}(t_1, t_2)$, $S_{\pm p, \pm 1}(t_1, t_2)$ for (a) and (b) are depicted in the figure (with $p=3$ or 5 for 3QMAS or 5QMAS, respectively).

and the 3QMAS experiments do not have a the same pulse scheme. The former is composed by 4 rf pulses and the latter only 3 rf pulses (Fig. 10.21a). However this is not a problem since the additional second pulse present after the t_1 evolution in the DQF-STMAS experiment (Fig. 10.21b), is a selective 180° rf pulse which only affects the CT. Thus, if the coherence orders ± 3 are selected this 180° soft rf pulse of the DQF-STMAS sequence will not induce any effect on 3Q coherences. Therefore, since this soft pulse does not affect the CTPs of

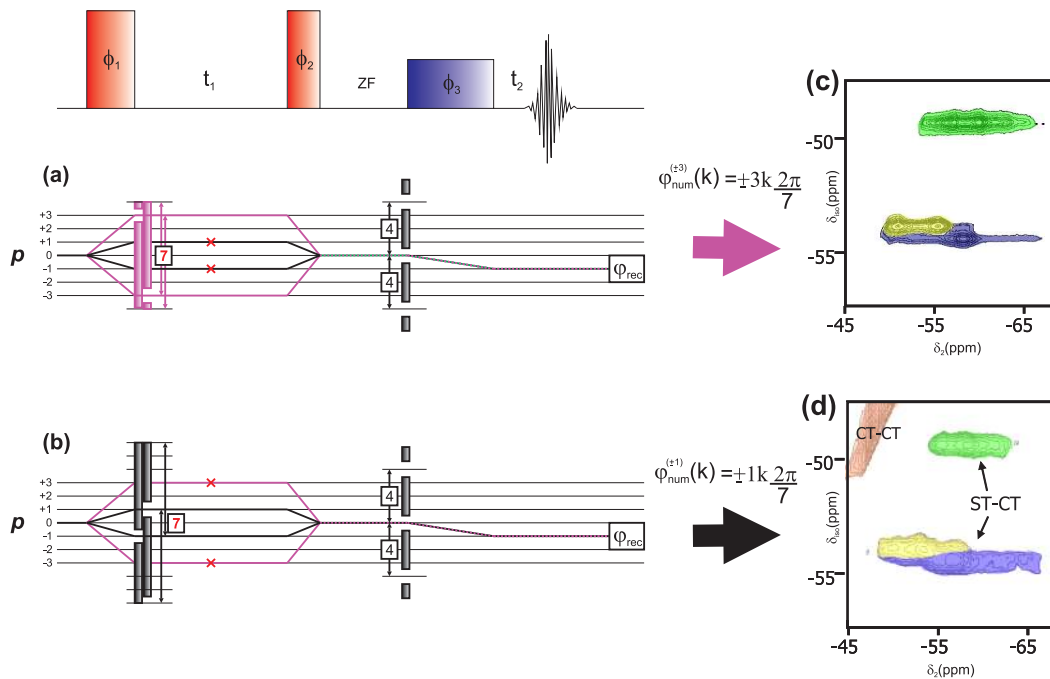


Fig. 10.20: Schematic drawings showing the mechanism of simultaneous acquisition of a multiplex 3QMAS and STMAS experiment for a spin-3/2 nucleus. (a) Shows the CTP for selection of coherence orders $p = \pm 3$, needed for the 3QMAS experiment, while the undesired CTPs are blocked. This is accomplished by using a 7-step multiplex phase cycle on the first rf pulse. (b) Shows the selection of coherences orders $p = \pm 1$ separately needed for a multiplex acquisition of STMAS experiment, while blocking the undesired coherence orders. Such selection is achieved using the same 7-step multiplex phase cycling. A 7-step phase cycle allows to select the desired CPTs \mathcal{P}_{+3} , \mathcal{P}_{-3} , \mathcal{P}_{+1} and \mathcal{P}_{-1} separately. employed in (a), but this time one must input the $\Delta p_1 = \pm 3$ into Eq. 10.46. The numerical phases needed to construct the signals $S_{\pm p,0}(t_1, t_2)$ is depicted (with $p = \pm 3$ and $p = \pm 1$ for 3QMAS or STMAS, respectively). On the right, the resulting ^{87}Rb spectra (c) and (d) correspond, respectively, to the CTPs depicted in (a) and (b).

3QMAS, one can think that both rf pulse sequences are equivalent in terms of number of rf pulses. In MQMAS the multiplex procedure can be employed either on the excitation or conversion rf pulses.

Let's now see which rf pulse phase of the DQF-STMAS pulse scheme can be multiplexed in order to take full advantage of using it. There are three ways of inserting the multiplex acquisition in the DQF-STMAS sequence, since 3 rf pulses are present before the z-filter delay. Multiplexing any of these rf pulses (Fig. 10.21) will save time with respect to the conventional DQF-STMAS experiment, because frequency sign discrimination can be done in a single experiment as discussed previously. However, from Eq. 10.18, it is clear that more time is saved if the multiplex strategy is employed on the rf pulse phase having the highest coherence order change. Therefore, the third rf pulse is the most suitable to apply the multiplex phase cycling because it induces coherence jumps of ± 2 . Then applying a $2|p| + 1$ -step multiplex phase cycle on the third pulse will need 5 phase increments giving a total number of transients $\mathcal{N} = 2 \times 2 \times 5 = 20$ instead of the 32 transients in the conventional DQF-STMAS (including both cosine- and sine-modulated data sets). Indeed, a 5-step phase

cycle is not sufficient to avoid the selection of undesired coherences. Fig. 10.21c illustrates the problem. The pathways $0 \rightarrow \pm 3 \rightarrow 0 \rightarrow -1$ can not be filtered by a 5-step phase cycle on the third *rf* pulse. Then, at least, a 6-step phase cycle will solve the problem with a cost of 4 more transients (Fig. 10.21d) per t_1 increment. It is worth mentioning that performing the multiplex phase cycling shown in Fig. 10.21d is, in this particular case, equivalent to a 3-step phase cycle on the first, 2-phase cycle on the second and 4-phase cycle on the third *rf* pulses, respectively (CTP not shown). Another alternative would correspond to a CTP where the first, second and third *rf* pulses are phase cycled in a 2-, 3- and 4-steps, respectively (CTP not shown). Both alternatives will give the same $\mathcal{N} = 24$ transients.

Let consider now the simultaneous acquisition of 3QMAS and DQF-STMAS experiments. The pathways in Figs. 10.21e and 10.21f, shows two possible ways of performing the experiment. Comparing both CTPs one can see that the multiplex phase cycling has better performance if applied on the third *rf* pulse (Fig. 10.21f), yielding a total of $\mathcal{N} = 28$ transients. Both 3QMAS and DQF-STMAS spectra may then be obtained simultaneously using the following numerical phase:

$$\varphi_{num}^{(\Delta p_3)}(k) = -\Delta p_3 k \frac{2\pi}{7}, \quad k = 0, 1, \dots, 6 \quad (10.55)$$

where Δp_3 is the coherence change in the third *rf* pulse. It is worth mentioning that the receiver must follow the *rf* pulse phases ϕ_1 and ϕ_2 in a nested phase cycling way, because these phases are not multiplexed.

Following Eq. 10.55 one must reconstruct the four CTPs ($\mathcal{P}_{\pm 3}, \mathcal{P}_{\pm 1}$), originating 28 $s_k(t_1, t_2)$ time-domain signals, from the calculated numerical phases, $\varphi_{num}^{(+3)}(k)$, $\varphi_{num}^{(-3)}(k)$, $\varphi_{num}^{(+1)}(k)$ and $\varphi_{num}^{(-1)}(k)$.

Finally, the two 2D spectra $S^{3QMAS}(\omega_1, \omega_2)$ and $S^{DQF-STMAS}(\omega_1, \omega_2)$ can be viewed in Figs. 10.21h and 10.21i, after processing the signal according to the shortest multiplex phase cycling possible to select the 3QMAS and STMAS CTPs depicted in Fig. 10.21f.

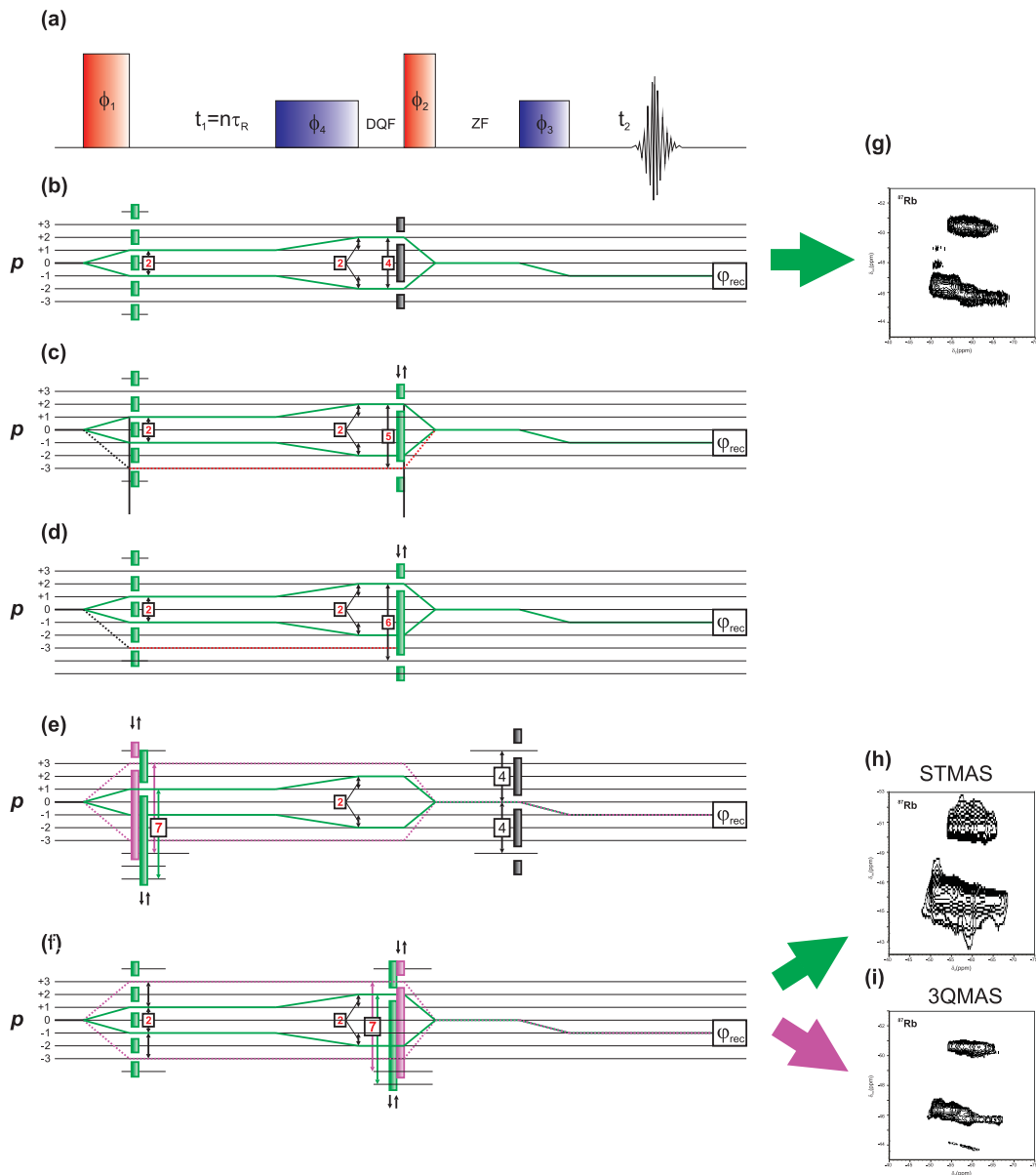


Fig. 10.21: (a) Pulse sequence of a DQF-STMAS experiment. Blue and red colored squares represent soft and hard pulses respectively. Representation of the different possible CTPs: (b) conventional CTP employing a nested phase cycling ($N=32$); (c) 5-step multiplex phase cycle CTP on the third rf pulse ($N=20$); despite the illustrated multiplex phase cycling employed corresponds to a $2 \times |p| + 1$ in this example such rule is not applicable due to the pathway observed in red dashed lines (see text); (d) 6-step multiplex phase cycle CTP on the third rf pulse ($N=24$) to perform a correct multiplex DQF-STMAS experiment; (e) possible simultaneous acquisition of 3QMAS/DQF-STMAS experiment using a 7-step multiplex phase cycle on the first rf pulse, and 2- and 4-step nested phase cycle on the second and third pulses; (f) simultaneous acquisition of 3QMAS/DQF-STMAS experiment used to acquire the experimental data obtained in (h) and (i) to obtain a DQF-STMAS or 3QMAS spectrum, respectively. 28 transients are sufficient to obtain both spectra.

10.4.7 Concluding Remarks: Advantages and Disadvantages of Multiplex Phase Cycling

It has been shown that MQMAS and SPAM MQMAS spectra are easily recorded using the multiplex concept introduced by Ivchenko *et al.* The reduction of the phase cycling is significant but probably not crucial in the conventional z-filtered experiment. However, combination with SPAM allows performing the experiment using only 14 scans for 3Q and 22 for 5QMAS.

The multiplex phase cycling procedure has both advantages and disadvantages compared to the nested phase cycling.

1. Advantages

- (a) In NMR spectroscopy it is very important to reduce the experimental time. The multiplex phase cycling offers a way to reduce the minimum number of scans required to complete an experiment. Table 10.2 shows the time saving allowed for the various experiments studied for model compounds. For experiments using the multiplex principle one obtains a factor of $1 - \frac{2|p|+1}{4|p|}$ in time saving, corresponding to ca. 40-50%. However if a multiplex coupled with SPAM strategy is performed one obtains an outstanding time saving factor of $1 - \frac{2|p|+1}{8|p|}$, approaching the 75% for high coherence orders. This time saving becomes more important for experiments requiring excitation of high order coherences and are specially valuable for NMR experiments with long pulse delays that may take days to record.
- (b) Multiplex allows the separation of CTPs which are impossible or that would take much longer by using the conventional phase cycling method. Additionally, multiplex phase cycling can select several CTPs in a single experiment. This property allows the acquisition of multiple experiments simultaneously. The possibility of simultaneously recording 3Q/5QMAS, 3QMAS/STMAS experiments using a single set of experimental data has been discussed and demonstrated.
- (c) Less dispersive contributions have been observed in the Multiplex or Multiplex SPAM 2D MQMAS spectra than in the conventional z-filtered MQMAS, which uses a nested phase cycling procedure. Hence, it is convenient to use this method to get pure-absorption MQMAS NMR spectra.
- (d) The receiver phase shifts are generally only changed in steps of 90° phase shifts, which imposes several limitations. For example, in a 3QMAS experiment one needs at least a 7-step phase cycle to separate the coherence orders ± 3 , which means incrementing the receiver by $p \times 51.43^\circ$. This is difficult to implement. The only way is using a 12-step phase cycle on the first *rf* pulse, which induces a receiver phase shift of $p \times 30^\circ = 90^\circ$. However by applying a numerical phase shift one can shift it without worrying about the receiver phase increment, thus shortening the experimental duration.

2. Disadvantages

- (a) In the case of using an old computer there may be some problems of disk space or low memory. Multiplex phase cycling requires additional memory and a sufficiently robust computer is needed. This is due to the fact that the signals are stored individually, while incrementing the *rf* pulse phase or phases.

Table 10.2: Phase cycling table for the various techniques studied, comparing them with the conventional phase cycling.

Experiment	Number of phase cycle steps, \mathcal{N}	Phases ϕ_i , ($\frac{2\pi}{\mathcal{N}}$)				φ_{rec}	φ_{num}
		ϕ_1	ϕ_2	ϕ_3	ϕ_4		
Conventional							
3QMAS	24 (48)	$\frac{2\pi}{6}$	0	$\frac{2\pi}{4}$	-	$\mp 3\phi_1 + \phi_3$	-
5QMAS	40 (80)	$\frac{2\pi}{10}$	0	$\frac{2\pi}{4}$	-	$\mp 5\phi_1 + \phi_3$	-
STMAS	8 (16)	$\frac{2\pi}{2}$	0	$\frac{2\pi}{4}$	-	$\mp \phi_1 + \phi_3$	-
DQF-STMAS	16 (32)	$\frac{2\pi}{2}$	$\frac{2\pi}{4}$	0	$\frac{2\pi}{2}$	$\mp \phi_1 \mp \phi_4 \pm 2\phi_2$	-
Multiplex							
3QMAS	28	$\frac{2\pi}{7}$	0	$\frac{2\pi}{4}$	-	$+\phi_3$	$\mp 3\phi_1$
5QMAS	44	$\frac{2\pi}{11}$	0	$\frac{2\pi}{4}$	-	$+\phi_3$	$\mp 5\phi_1$
STMAS	12	$\frac{2\pi}{3}$	0	$\frac{2\pi}{4}$	-	$+\phi_3$	$\mp 3\phi_1$
DQF-STMAS	24	$\frac{2\pi}{2}$	$\frac{2\pi}{6}$	0	$\frac{2\pi}{2}$	$+\phi_3 \pm \phi_4$	$\mp 3\phi_1$
Multiplex SPAM							
3QMAS	14	$\frac{2\pi}{7}$	0	π	-	0	$\mp 3\phi_1 + \phi_3; \mp 3\phi_1$
5QMAS	22	$\frac{2\pi}{11}$	0	π	-	0	$\mp 5\phi_1 + \phi_3; \mp 5\phi_1$
Simultaneous Acquisition							
Multiplex 3QMAS/5QMAS	44	$\frac{2\pi}{11}$	0	$\frac{2\pi}{4}$	-	$+\phi_3$	$\mp 3\phi_1; \mp 5\phi_1$
Multiplex 3QMAS/STMAS	28	$\frac{2\pi}{7}$	0	$\frac{2\pi}{4}$	-	$+\phi_3$	$\mp 3\phi_1$ (3QMAS); $\mp \phi_1$ (STMAS)
Multiplex 3QMAS/DQF-STMAS	28	$\frac{2\pi}{2}$	$\frac{2\pi}{6}$	0	$\frac{2\pi}{2}$	$+\phi_3 \pm \phi_4$	$\mp 3\phi_1$ (3QMAS); $\mp \phi_1$ (DQF-STMAS)
Multiplex SPAM 3QMAS/5QMAS	22	$\frac{2\pi}{11}$	0	2π	-	0	$\mp 5\phi_1 + \phi_3; \mp 5\phi_1$ (5QMAS) $\mp 3\phi_1 + \phi_3; \mp 3\phi_1$ (3QMAS)

It is worth noting that the time savings, shown in table 10.2, achieved by multiplex phase cycling are valuable if the signal comes out within the minimum number of scans required to complete a full phase cycle. For samples lacking sensitivity, there will be no gain in the acquisition time of course.

10.4.8 Instrumentation and Processing Program

All NMR spectra have been recorded at 9.4 T on a Bruker Avance 400 spectrometer using a 4 mm double bearing probe. Larmor frequencies are 130.9 and 104.3MHz for ^{87}Rb and ^{27}Al , respectively. The acquisition of the 2D MQMAS data sets has been performed in a rotor-synchronized fashion by advancing the evolution time t_1 in increments equal to the rotor period. [358] The shearing procedure was systematically applied to each 2D spectra and the scaling of the spectra was done following conventions of ref. [359] Specific experimental conditions are given in the figure captions. The model compounds rubidium nitrate (RbNO_3 , Aldrich) and the aluminophosphates $\text{AlPO}_4\text{-14}$ and VPI-5 were used to carry out the various MQMAS NMR experiments. The pulse sequences used in this work and the processing programs (adapted to the Bruker XWinNMR software) will be available on the Internet as separate resources*.

*<http://www-lcs.ensicaen.fr> or on demand

Chapter 11

Conclusions and Outlook

At the end of each thesis chapter I have produce a number of (partial) conclusions. In this section, I shall briefly describe the main results and conclusions of this thesis, detailing some important aspects. I shall also discuss some possible future research work, particularly in the field of hybrid materials applications and methodology developments in SSNMR.

11.1 Main Conclusions

The thesis reports:

- Detailed discussion of the optimization of FS-LG based experiments. I have tried to discuss the effect of some decisive parameters of FS-LG decoupling in a didactic way, providing solutions to practical problems. For example, I introduce a simple way to optimize FS-LG decoupling directly on 2D $^1\text{H}\{\text{HOMCOR}\}-^1\text{H}$ spectra.
- Structural elucidation of the four complex crystalline inorganic-organic hybrids structures.
 - **Ge-phosphate binuclear complex** (section 8.1) - This material consists of discrete Ge-phosphonate units surrounded by piperazinedium cations. I have presented a study combining SSNMR and single crystal X-ray diffraction evidence. $^1\text{H}\{\text{FS-LG}\}-\text{X}$ ($\text{X} = ^1\text{H}, ^{13}\text{C}, ^{31}\text{P}$) correlation experiments were carried out to test the robustness of FSLG decoupling. The $^1\text{H}\{\text{FS-LG}\}-^1\text{H}$ HOMCOR spectrum was particularly useful to probe the protonation of the piperazine residues, an almost impossible task if this technique was not applied. In the $\delta=3.0\text{-}5.5$ ppm region, the F1 projection of the $^1\text{H}\{\text{FS-LG}\}-^{13}\text{C}$ HETCOR spectrum of I was difficult to analyse. To assist the assignment of the resonances, I resorted, with much success, to a statistical analysis of the crystallographic $\text{C}(1-5)\cdots\text{H}$ distances, considering a 5 Å radius sphere centred on these C atoms.
 - **Ge-phosphonate hexanuclear complex** (section 8.2) - This material is also built up of discrete Ge-phosphonate units surrounded by - stacked heteroaromatic amines. Again, the NMR characterisation of this material was done in tandem with single-crystal X-ray diffraction. In this case study I have concentrated the attention on the complex hydrogen-bonding networks. Outstanding spectral resolution was achieved employing the $^1\text{H}\{\text{FS-LG}\}-^1\text{H}$ HOMCOR and $^1\text{H}\{\text{FS-LG}\}-^{31}\text{P}$ HETCOR techniques on material I, allowing the assignment of the ^1H resonances. ^1H DQ-SQ HOMCOR was further used to complement this assignment.

- **Templated microporous aluminophosphate, IST-1** (section 9.1) - SSNMR was able to solve a question not answered in past studies: the nature of the two methylamine (MA and MA⁺) species present in the structure. ¹H{FS-LG}-¹³C HETCOR and ¹H{FS-LG}-¹H HOMCOR techniques were able to assign specific resonances to both MA residues. ³¹P SQ-DQ HOMCOR and ¹H{FS-LG}-³¹P HETCOR assisted the attribution of the three framework ³¹P resonances. ¹HFS-LG-²⁷Al HETCOR was used to try to assign the ¹H resonances of the bridging (Al)-OH (-Al) groups, however no correlation involving this resonance was observed.
- **Templated layered γ -titanium phosphate** (section 9.2) - This case study provides an interesting example of how to combine powder XRD, modeling, and solid-state NMR to elucidate the structure of organic-inorganic hybrid materials. Simulation of ¹H MAS NMR spectrum indicates that intercalated *n*-hexylamine is protonated and that there is a single type of *n*-hexylammonium cation in the unit cell. The H₂O and P-OH groups are filtered out of the ¹H DQ-SQ spectrum due to dynamic effects. ¹H-³¹P HETCOR studies further indicated that HPO₄²⁻ is closer than PO₄³⁻ to the water molecules, helping rationalising the orientation of the *n*-hexylammonium relatively to the titanium phosphate layers.
- Development of a straightforward procedure to process 2D data using the multiplex phase cycling principle. This method was used to record 2D MQMAS and STMAS spectra. I have shown the possibility of recording simultaneously multiple CTPs in the timespan of a single experiment. Moreover, the combination of the multiplex approach and SPAM method considerably increases the signal-to-noise ratio of the conventional MQMAS experiment; I present a simple way of acquiring echo/antiecho pathways taking advantage of the multiplex procedure. Model compounds, RbNO₃, ALPO₄-14 and VPI-5, were used to illustrate the methods.

The application work of this thesis is part of a comprehensive study aimed at evaluating the usefulness of high-resolution ¹H NMR techniques to elucidate the structure of inorganic-organic hybrid materials, both crystalline and amorphous or disordered. I have shown how useful it is to use CRAMPS in conjugation with homonuclear ¹H recoupling techniques to assign and correlate ¹H NMR resonances. Using this strategy, CRAMPS allows the labeling of ¹H resonances while recoupling techniques establish nuclear correlations on the basis of crystallographic distances, and group nobilities. One of the limitations of this thesis is the fact that dynamic studies are absent, which could provide important information on the stability and rigidity of hydrogen-bond networks. For instance, relaxation measurements at different temperatures could provide information on the activation energy of reorientation processes. High-resolution ¹H studies using CRAMPS NMR are still technically demanding. Many parameters have to be optimized, and problems posed by off-resonance effects on the scaling factor further complicate the application of such technique. Moreover, in most cases, CRAMPS techniques still do not afford the ultimate spectral resolution. The homogeneous broadening caused by strong ¹H-¹H dipolar couplings is an intrinsic problem, which can only be partially solved by applying *rf* pulses in tandem with MAS. Recently, very fast MAS (40-60 kHz) has been shown to afford outstanding ¹H resolution. However, the cycle time of ¹H homonuclear decoupling multiple pulses sequences become too long at these large MAS rates and, thus, there is no advantage in using CRAMPS. Therefore in the near future, I expect to see routine ¹H studies performed under 50-70 kHz MAS, without suffering from considerable lack of sensitivity, even using small rotors (1.2mm o.d.), specially if cryo-MAS probes are used. Nevertheless, fast mechanical rotation may be deleterious for systems highly sensitive to temperature, mechanical or acoustic effects. Another disadvantage is related

with 2D heteronuclear studies using CP: fast MAS considerably reduces the CP transfer, compromising the sensitivity. In such cases, intermediate spinning speeds are still needed and, thus, there will always be an interest in acquiring high-resolution ^1H spectra using moderate MAS rates. I must stress that employing relatively high power *rf* irradiation to decouple ^1H (typically 80-100 kHz in CRAMPS) may also pose problems related with heating and sample stability, as well instrumental artifacts. Methods have been developed to overcome this problem, particularly important in the study of biomolecules such as peptides and proteins. Spinning samples very fast can also be a considerable advantage when low power is required. One of the main advantage of using very high spinning speeds (>50 kHz) is the fact that heteronuclear decoupling can be done at very low *rf* field strengths. ^1H decoupled ^{13}C spectra were reported using *rf* irradiation below 15 kHz. [360] Unfortunately CRAMPS can not profit from high MAS rates at the moment.

Apart from manipulating the internal Hamiltonian, other well-known possibilities may be used if further insight on the structure is wanted. Isotopic labeling with ^2H is an example. Recently, a decrease in the ^1H spins density, obtained by employing 90% D_2O in the crystallization buffer, resulted in a 4-fold reduction in the ^1H linewidth (compared to a sample recrystallised from pure H_2O), [361] and an increase in resolution by a factor of 10-15 compared to standard heteronuclear correlation experiments using PM-LG decoupling in the indirect dimension. [362] Alternatively, the direct observation of natural abundance ^2H is also possible, as reported by Mizuno *et al.* [363]. The authors use ^1H - ^2H CPMAS and stroboscopic acquisition to observe ^2H . This method is restricted to high magnetic fields.

11.2 Future NMR Studies on Hybrid Materials

In addition to ^1H studies, observation of other nuclei is essential to retrieve as much information as possible on a given material. One of the main problems is the attribution of the ^1H resonances of OH groups or water molecules because they are usually broad. In particular, the role of water in hybrid materials is very important because it this molecule has a considerable influence on the structural stability of the materials, which in turn determines their chemical properties. Therefore, the uptake and desorption of water may change the spectra of other nuclei easier to probe than ^1H nuclei. As an example, in Fig. 11.1 I show how the release of water from the structure of a certain hybrid material changes the ^{31}P spectra, taking advantage of $^2J_{\text{P-P}}$ through P-C-P bonds (unpublished work).

Clearly, upon sample rotation some water is released from the structure, remaining inside the rotor. ^{31}P or ^{13}C (not shown) NMR is highly sensitivity to the changes taking place in this process. Probing the ^1H environment would be difficult due to the high water content, which gives rise to broad bands. The ^{31}P DQ-SQ through-bond spectrum of Fig. 11.1 suggests that the crystal center of inversion is being progressively lost along with the water release. This example also illustrates how useful experiments taking advantage of *J*-coupling are. They complement the techniques based on dipolar couplings. Usually single X-ray diffraction measurements are done at very low temperature to minimize thermal disorder while MAS NMR are recorded at much higher temperature. Therefore, care must be taken when studying hybrid materials by X-ray and NMR techniques, because water clusters are usually present and have an important role. A comprehensive study requires recording spectra and collecting diffraction data at similar and several temperatures. Although this thesis deals with crystalline materials with known structure, in the near future I will extend the work to coordination polymers and amorphous or disordered inorganic-organic hybrids.

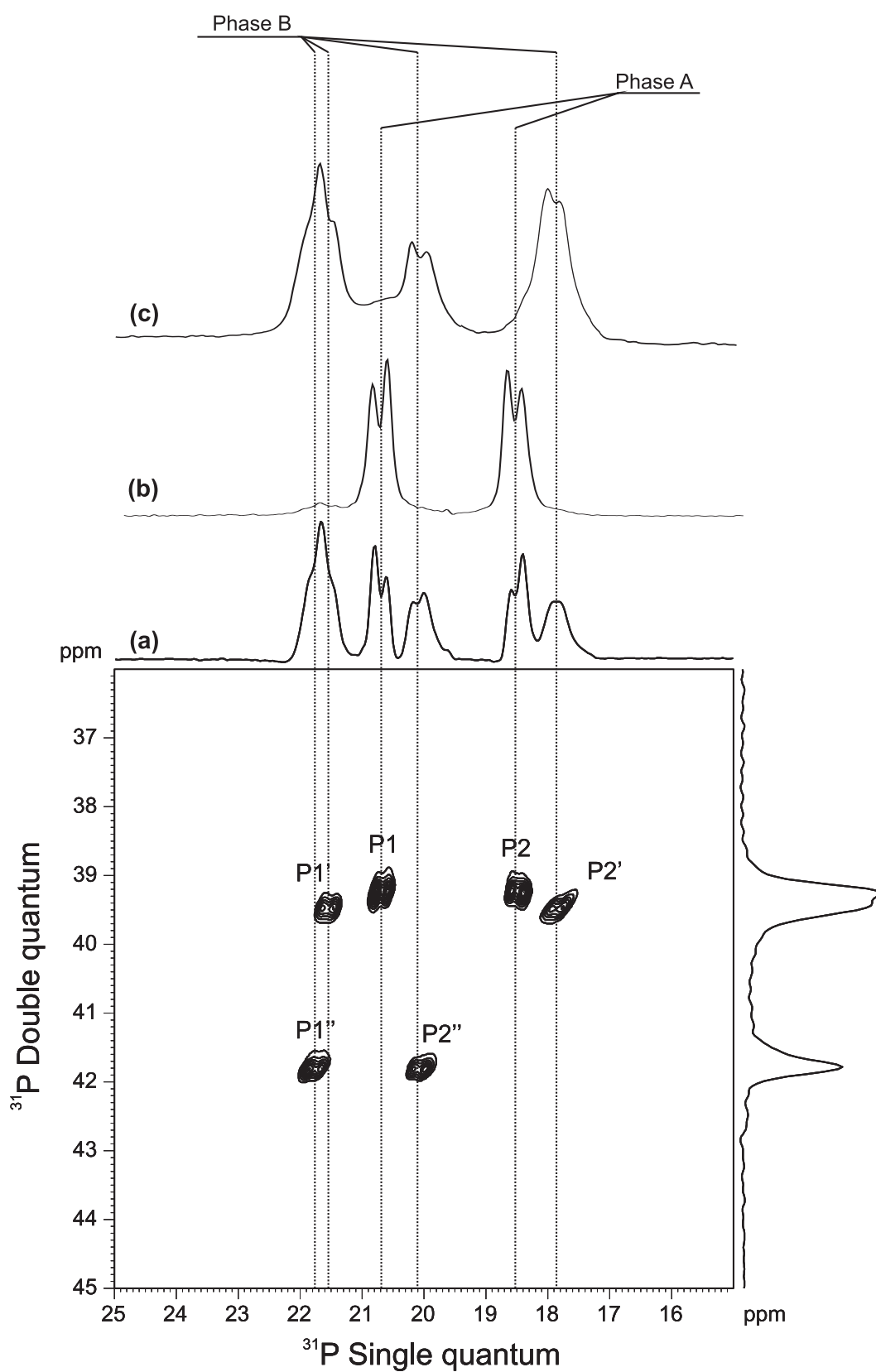


Fig. 11.1: ^{31}P - ^{31}P refocused inadequate spectrum of a metalphosphonate guest included in a complex 3D water framework, after 8 h of sample spinning (a). ^{31}P CP-MAS spectra recorded immediately after packing the rotor (initial phase) (b), and after being in the desiccator for 4 days (c).

11.3 Future Methodology Developments in Quadrupolar Nuclei

The multiplex approach can be conveniently used to gain experimental time bypassing the requirements of conventional phase cycling. As shown in this thesis, the main advantage of multiplex is the ability to acquire multiple CTPs in a single experiment. This approach is particularly useful for techniques involving excitation of high-coherence orders, such as high-resolution 2Q6Q homonuclear correlation experiments where a minimum of 384 scans are needed using a nested phase cycling scheme. Unfortunately, due to the enormous lack of sensitivity of such technique, a large number of transients must be recorded and, hence, there is no gain in applying multiplex phase cycling. Examples of recording simultaneous experiments, such as MQMAS/STMAS, were reported in this thesis. Such experiments become very difficult or fail when both techniques require different *rf* pulse optimizations (e.g. 3QMAS/5QMAS). This idea could be extended to spin-1/2 nuclei, for which 90° pulses are generally used for 1Q, 2Q or 3Q excitation. For instance, the experiments involving MQ dipolar or *J*-coupling filters it should be possible to acquire simultaneously 1Q, 2Q and 3Q data in a single experiment through multiplex phase cycling. However, although the pulse length required to excite the three coherence orders are the same, the time evolution periods needed to excite the various coherence orders are different. I must say that I believe that the future concerning the progress of multidimensional NMR consists in better ways to acquire and process the signal. This may be the main source of improvements in the near future, since the research on new pulse sequence is reaching a plateau and original suggestions are becoming scarce. I think that the idea of employing, for example, non-Cartesian signal sampling schemes may lead to a considerable reduction in the experimental time. Sampling of the data violating the Fourier periodicity may also be very useful to accelerate the experiments. Recently, harmonic inversion noise reduction (HINR) [364,365] has been proposed for detection of weak NMR signals which are unobservable by conventional FT techniques. This method was successfully applied to observe ¹³C-¹³C couplings and record ¹⁵N and ¹⁷O spectra without enrichment. In NMR, the most informative techniques are often long in experimental time, sometimes even impossible to perform due to poor sensitivity (e.g. *J*-coupling and DQ based techniques). In the last years, much attention has been dedicated to the observation of ¹⁴N, either indirectly or directly due to the relevance of this nucleus in biological problems. Very recently, although with significant spectral distortions, ¹³C-¹⁴N HMQC spectra have been reported for the first time, using the quadrupole-dipole cross-terms to transfer magnetization from ¹³C to ¹⁴N. However, such experiment requires considerable signal accumulation and strongly depends on the CQ and heteronuclear dipolar coupling. Towards the end of my Ph.D. studies, I started working on a way to observe the evolution of antiphase signals during the evolution of a ¹³C-¹⁴N coupled spin pair. I have found that, indeed, it is possible to observe the formation of this antiphase operator, even without observing the usual dipolar splitting in the ¹³C spectra. This can assist the preliminary optimization of the ¹³C-¹⁴N HMQC experiment (data not shown). I have also approached this problem by direct observation, through stroboscopic acquisition of the ¹⁴N signal, profiting from the aliasing of the first-order quadrupole spinning sidebands into the centreband to enhance the signal (Fig. 11.2). The main disadvantage of this technique is evident: the noise included in the bandwidth excitation also folds back into the observable spectral window. In addition, since the techniques lies on the direct observation of ST, the resonance lineshapes depend on many parameters (such as *rf* bandwidth, magic-angle misset, Q factor, preamplifier impedance, cable lengths, third-order effects, etc), which makes this nucleus difficult to observe directly. The actual hardware does not allow the efficient direct observation of MHz-wide signals and,

thus, the indirect observation through 2D NMR is still the best option.

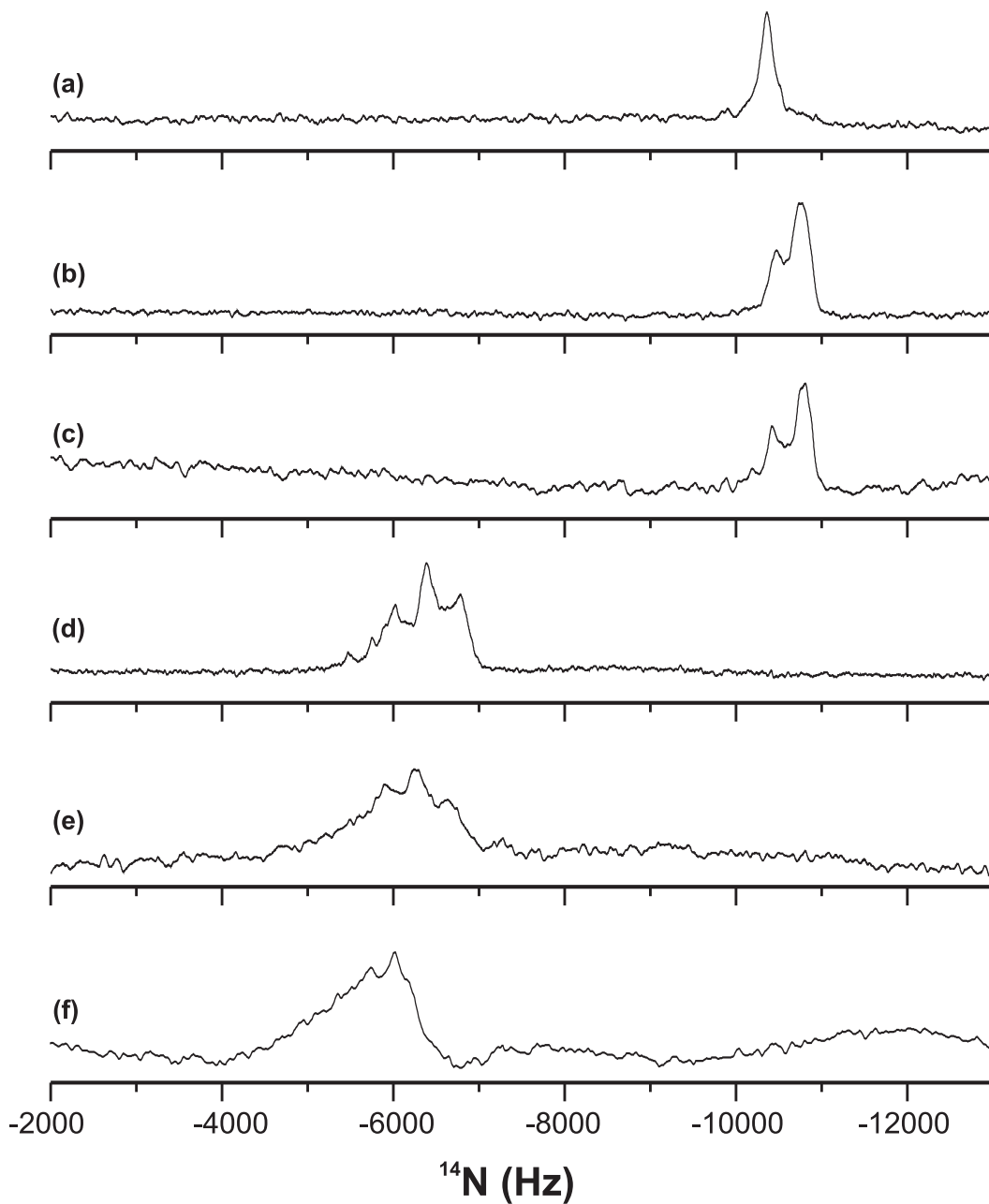


Fig. 11.2: ^{14}N spectra of zeolite NH_4Y (a), RbNO_3 (b), NaNO_3 (c), serine (d), leucine (e), and glycine (f), recorded at 28.9 MHz (9.4 T) on a Bruker Avance 400 (DSX model), using a standard 4 mm triple-resonance probe and a 1 kW amplifier. The spinning rate used was 12 kHz 3 Hz, excitation pulse 2–3 μs ($\omega_1/2\pi=83.3$ kHz - 90° pulse of 3 μs) and recycle delay 2 s. Number of scans: 3000 for (a–c), 6400 for (d–f).

Appendix A

Nuclear Spin Operators

Spin-1/2 angular momentum operators are proportional to Pauli matrices and are important in quantum physics. Indeed, they constitute the basis for the matrix representation of the wavefunctions and Hamiltonians in NMR. [13] The matrix representations for the single spin-1/2 operators in the Zeeman basis $|m\rangle$ with $m = \{\frac{1}{2}, -\frac{1}{2}\}$ or $\{\alpha, \beta\}$ are listed below:

$$\hat{I}^2 = \frac{3}{4} \begin{pmatrix} 1 & 0 \\ 0 & 1 \end{pmatrix} = \frac{3}{4} (|\alpha\rangle \langle\alpha| + |\beta\rangle \langle\beta|) \quad (\text{A.1})$$

$$\hat{I}_x = \frac{1}{2} \begin{pmatrix} 0 & 1 \\ 1 & 0 \end{pmatrix} = \frac{1}{2} (|\alpha\rangle \langle\beta| + |\beta\rangle \langle\alpha|) \quad (\text{A.2})$$

$$\hat{I}_y = \frac{1}{2i} \begin{pmatrix} 0 & 1 \\ -1 & 0 \end{pmatrix} = \frac{1}{2i} (|\alpha\rangle \langle\beta| - |\beta\rangle \langle\alpha|) \quad (\text{A.3})$$

$$\hat{I}_z = \frac{1}{2} \begin{pmatrix} 1 & 0 \\ 0 & -1 \end{pmatrix} = \frac{1}{2} (|\alpha\rangle \langle\alpha| - |\beta\rangle \langle\beta|) \quad (\text{A.4})$$

$$\hat{I}_+ = \begin{pmatrix} 0 & 1 \\ 0 & 0 \end{pmatrix} = |\alpha\rangle \langle\beta| \quad (\text{A.5})$$

$$\hat{I}_- = \begin{pmatrix} 0 & 1 \\ 0 & 0 \end{pmatrix} = |\beta\rangle \langle\alpha| \quad (\text{A.6})$$

Table A.1 is list the action of some of the operators defined above under the influence of an eigenfunction $|m\rangle$

Table A.1: Nuclear Spin Operators for a spin- I .

Operator	^[a] Operator $ I, m\rangle =$
$\hat{\mathbf{I}}$	$\sqrt{I(I+1)}\hbar I, m\rangle$
$\hat{\mathbf{I}}^2 = \hat{I}_x^2 + \hat{I}_y^2 + \hat{I}_z^2$	$I(I+1)\hbar^2 I, m\rangle$
\hat{I}_z	$m\hbar I, m\rangle$
$\hat{I}_\pm = \hat{I}_x \pm i\hat{I}_y$	$\sqrt{I(I+1) - m(m \pm 1)}\hbar I, m \pm 1\rangle$

^[a] In NMR, the factor \hbar of these eigenvalues is commonly ignored and included instead in the operator. In this thesis I adopted this convention. I and m are the spin quantum number and the magnetic quantum number m takes the values $I, I-1, \dots, -I$.

It is immediately apparent from table A.1 that $|I, m\rangle$ is an eigenfunction of both $\hat{\mathbf{I}}^2$ and \hat{I}_z so that $|I, m\rangle$ is unchanged. In this case it is said that both operators $\hat{\mathbf{I}}^2$ and \hat{I}_z commute. In contrast the raising and lowering operators, \hat{I}_+ and \hat{I}_- , change the spin function so that $|I, m\rangle$ is not an eigenfunction of \hat{I}_+ or \hat{I}_- operators. The raising and lowering operators describe changes in z -component of the spin state corresponding to a transition of a spin between energy levels. Indeed, a *rf* pulse contain these operators and so *rf* pulses generates off diagonal matrix elements.

Appendix B

Wigner Matrices

The following tables are needed to calculate the Wigner matrices of Eq. 2.20 of rank- k .

Table B.1: The values of the reduced Wigner matrix elements $d_{q',q}^{(1)}(\beta)$.

$d_{q',q}^{(k)}(\beta)$	$q = 1$	0	-1
$q' = 1$	$\frac{1}{2}(1 + c\beta)$	$-\frac{1}{\sqrt{2}}s\beta$	$\frac{1}{2}(1 - c\beta)$
0	$-d_{1,0}^{(1)}(\beta)$	$c\beta$	$d_{1,0}^{(1)}(\beta)$
-1	$\frac{1}{2}(1 - c\beta)$	$-d_{1,0}^{(1)}(\beta)$	$\frac{1}{2}(1 + c\beta)$

Table B.2: The values of the reduced Wigner matrix elements $d_{q',q}^{(2)}(\beta)$.

$d_{q',q}^{(k)}(\beta)$	$q = 2$	1	0	-1	-2
$q' = 2$	$c^4 \left(\frac{\beta}{2}\right)$	$-\frac{1}{2}(1 + c\beta) s\beta$	$\sqrt{\frac{3}{8}}s^2\beta$	$\frac{1}{2}(1 - c\beta) s\beta$	$s^4 \left(\frac{\beta}{2}\right)$
1	$-d_{2,1}^{(2)}(\beta)$	$(c\beta - \frac{1}{2})(c\beta + 1)$	$-\sqrt{\frac{3}{8}}s^2\beta$	$(c\beta + \frac{1}{2})(c\beta - 1)$	$d_{2,-1}^{(2)}(\beta)$
0	$d_{2,0}^{(2)}(\beta)$	$-d_{1,0}^{(2)}(\beta)$	$\frac{1}{3}(3c^2\beta - 1)$	$d_{1,0}^{(2)}(\beta)$	$d_{2,0}^{(2)}(\beta)$
-1	$-d_{2,-1}^{(2)}(\beta)$	$d_{1,-1}^{(2)}(\beta)$	$-d_{1,0}^{(2)}(\beta)$	$d_{1,1}^{(2)}(\beta)$	$d_{2,1}^{(2)}(\beta)$
-2	$d_{2,-2}^{(2)}(\beta)$	$-d_{2,-1}^{(2)}(\beta)$	$d_{2,0}^{(2)}(\beta)$	$-d_{2,1}^{(2)}(\beta)$	$d_{2,2}^{(2)}(\beta)$

Table B.3: The values of the reduced Wigner matrix elements $d_{q',q}^{(4)}(\beta)$ (only minimal set).

$d_{0,0}^{(4)}(\beta) = \frac{1}{8}(35c^4\beta - 30c^2\beta + 3)$	$d_{2,4}^{(4)}(\beta) = \frac{\sqrt{7}}{8}(c\beta + 1)^2 s^2\beta$
$d_{1,0}^{(4)}(\beta) = \frac{\sqrt{5}}{4}(7c^3\beta - 3c\beta) s\beta$	$d_{3,0}^{(4)}(\beta) = -\frac{\sqrt{35}}{4}c\beta s^3\beta$
$d_{2,0}^{(4)}(\beta) = \frac{\sqrt{10}}{8}(7c^2\beta - 1) s^2\beta$	$d_{4,0}^{(4)}(\beta) = \frac{\sqrt{70}}{16}s^4\beta$
$d_{2,1}^{(4)}(\beta) = \frac{\sqrt{2}}{8}(16c^3\beta + 10c^2\beta - 10c\beta - 3) s\beta$	$d_{4,1}^{(4)}(\beta) = -\frac{\sqrt{14}}{8}(c\beta + 1) s^3\beta$
$d_{2,2}^{(4)}(\beta) = \frac{1}{4}(c\beta + 1)(7c^3\beta - 6c\beta + 1)$	$d_{4,3}^{(4)}(\beta) = -\frac{\sqrt{2}}{8}(c\beta + 1)^3 s\beta$
$d_{2,3}^{(4)}(\beta) = \frac{\sqrt{14}}{8}(c\beta + 1)^2(2c\beta - 1) s\beta$	$d_{4,4}^{(4)}(\beta) = \frac{1}{16}(c\beta + 1)^4$

where c and s notation in Tables B.1, B.2 and B.3 indicate cosine and sine functions.

Appendix C

Interpretation of MQMAS Spectra

The aim of the MQMAS experiment is to obtain a high-resolution dimension “free” of anisotropies. As stated above, the 2D MQMAS experiment makes use of invisible MQ transitions combined with MAS to remove the anisotropy of the quadrupolar interaction. Once the 2D spectra are devoided from the anisotropic part, the isotropic CS information remains difficult to get, since the isotropic part of the spectra is the sum of the isotropic parts of the chemical and quadrupolar shifts. Therefore, just after a 2D FT, a scaled isotropic CS is obtained, which is reflected, by the appearance of a broad F1 projection because the anisotropic(A) axis, is not parallel to F2 axis. Thus, to overcome such inconvenient, a shearing transformation is performed to obtain the A axis parallel to F2, resulting in a peak projected in F1 without anisotropic broadening.

For a better understanding let's write the isotropic part of a MQMAS experiment as the sum of the isotropic CS described in Eq. 2.60 and quadrupolar induced shift in angular frequency units (*before shearing*),

$$\begin{aligned}\omega_{MQMAS}^{iso} &= \omega_{CS}^{iso}(I, p) + \omega_Q^{iso}(I, p) = \\ &= p\omega_0\sigma_{iso} + \frac{3p[4I(I+1) - 3p^2]}{10[4I(2I-1)]^2\omega_0} P_Q^2\end{aligned}\quad (C.1)$$

where the coherence p in the first part of eq. C.1, is the MQ coherence evolving during t_1 . ω_Q^{iso} can be easily derived from Eq. 2.93 by taking only the isotropic term, i.e., the terms with $k = 0$. In eq. C.1, the resonance offset is not considered for the sake of simplicity.

Now, transforming Eq. C.1 into relative units (ppm), multiplying by the apparent Larmor frequency ($10^6/(-p\omega_0)$), the CS in F1 can be written as:

$$\delta_1 = \delta_{CS}^{iso} - \underbrace{\frac{3[4I(I+1) - 3p^2]}{10[4I(2I-1)]^2\omega_0^2} P_Q^2}_{\delta_Q^{iso}(I,p)} \times 10^6 \quad (C.2)$$

and to obtain the CS in F2 dimension, one must set $p = -1$ (detection coherence) in Eq. C.2 and multiply by the Larmor frequency ($10^6/\omega_0$),

$$\delta_2 = \delta_{CS}^{iso} - \frac{12I(I+1) - 9}{10[4I(2I-1)\omega_0]^2} P_Q^2 \times 10^6 \quad (C.3)$$

with the second-order quadrupolar effect $P_Q(SOQE) = C_Q\sqrt{1 + \frac{\eta_Q^2}{3}}$.

Eq. C.3 is equivalent to the centre of gravity in the MAS spectra of a spin>I quadrupolar nuclei and is not influenced by the shearing because there is no dependence on p .

Finally, by multiplying eq. C.1 by a scaling factor of $\kappa = \frac{[1+k(I, \frac{p}{2}, -\frac{1}{2})] \times 10^6}{[k(I, \frac{p}{2}, -\frac{1}{2}) - |p|]\omega_0}$, given by Amoureux *et al.*, a sheared spectra is obtained in ppm units, [347]:

$$\begin{aligned}\delta_{iso} &= \delta_{CS}^{iso} + \kappa \times [\omega_Q^{iso}(I, p)] = \\ &= \delta_{CS}^{iso} + \frac{[1 + k(I, \frac{p}{2}, -\frac{1}{2})] \omega_Q^{iso}(I, p)}{[k(I, \frac{p}{2}, -\frac{1}{2}) - p]\omega_0} \times 10^6 = \\ &= \delta_{CS}^{iso} - \frac{10}{17} \delta_Q^{iso}(I, -1)\end{aligned}\quad (C.4)$$

The second part of eq. C.4 shows that after the shearing the quadrupolar shift is independent of p . Furthermore, eq. C.4 gives the slope of two special axis in a sheared 2D MQMAS spectrum: (i) the CS axis with slope 1 and (ii) the quadrupolar shift (Q) with slope $-\frac{10}{17}$. The former, describes the variable isotropic CS in the case of total absence of quadrupolar shift, i.e., the isotropic CS lies along the CS axis (Fig. C.1). On the other hand, the latter, describes variable quadrupolar shifts at one value of δ_{CS}^{iso} , which is given by the intersection between the CS and the Q axes. The shift difference between the intersection point and the center of gravity of a signal gives the quadrupolar shift depicted in eq. C.4.

In short, a sheared spectrum allows to have a high-resolution dimension, δ_{iso} , referred to $[k(I, \frac{p}{2}, -\frac{1}{2}) - |p|]$, allowing at the same time to retrieve relevant information about the distribution of CS and quadrupole parameters through the distribution of the signal along the CS and Q axes, respectively. The study of the distribution of these parameters becomes more informative in materials having distribution of bond angles and bond lengths, which are present in amorphous or disordered materials. Such intrinsic properties of the materials (for example, glasses) limit considerably the spectral resolution, that could be obtained along the δ_{iso} axis of MQMAS spectra. Further information about scaling and labeling of δ_{iso} axis (the δ_1 after shearing) is well covered by P. P. Man [366] and Goldbourn *et al.* [26].

In most applications the distributions of the δ_{CS}^{iso} and of P_Q are encountered simultaneously, which complicates the spectral analysis. However, these distributions can be easily separated because the directions of the CS and Q axis differ by approximately 75° . [347] It is important to note that sample rotation, makes the quadrupole interaction time-dependent, thus requiring sophisticated routines to simulate the MQMAS spectra. Many researchers have created specialised software able to provide the determination of such parameters. Prominent examples are:

- REGULAR [367]
- MQSIM [368];
- PULSAR [359];
- SIMPSON [11];
- GAMMA [369].

Despite the many solutions investigated to enhance the sensitivity of MQMAS experiments, this technique still suffers from low sensitivity, due to the relatively low efficiencies to excite and convert MQ coherences, and this problem becomes worse for higher values of I . Recently, another strategy to improve MQMAS experiments, based on selection of multiple CTPs, was introduced by Gan *et al.*, and for the first time, experimentally demonstrated, in this thesis. Such method is used to acquire the echo and antiecho simultaneously in a z-filtered MQMAS scheme. This will be discussed in section 10.4.

Another method based on the same principle of MQMAS, is STMAS. This clever experiment allows to partially overcome the sensitivity issues observed in MQMAS experiments. The principle will be briefly discussed in the next section.

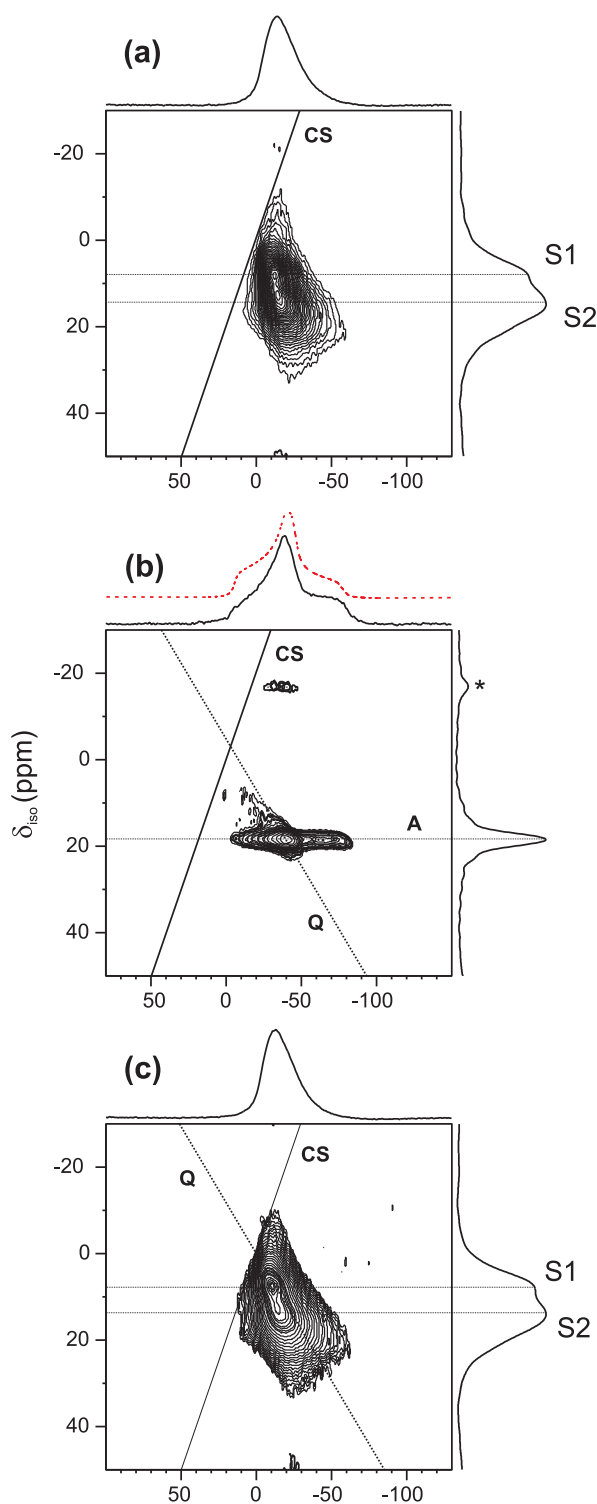


Fig. C.1: Sheared ^{23}Na 3QMAS NMR spectra of (a) as-synthesised, (b) dehydrated at 300°C and (c) re-hydrated porous hybrid La-hedp sample containing Na nuclei in the pores and La atoms in the framework (hedp is a phosphonic acid). The CS and Q axes are plotted, and correspond to the CS and quadrupolar induced shift axes, respectively. The dashed line in (b) represents the simulated quadrupolar pattern from the ^{23}Na MAS single pulse experiment showing a CQ of ca. 3.6 MHz and an asymmetry parameter (η_Q) of ca. 0.88. Asterisk denotes a spinning sideband.

Appendix D

Spin Coefficients $\mathbb{C}^k(\hat{I}_z, m)$ for MQMAS and STMAS

Table D.1: The values of $C^{(k)}(I, m)$ for:

MQMAS					
k	$C^{(k)}(3/2, 1/2)$	$C^{(k)}(3/2, 3/2)$			
0	-3	9			
2	-24	0			
4	-54	42			
k	$C^{(k)}(5/2, 1/2)$	$C^{(k)}(5/2, 3/2)$	$C^{(k)}(5/2, 5/2)$		
0	-8	-6	50		
2	-64	-120	40		
4	-144	-228	300		
k	$C^{(k)}(7/2, 1/2)$	$C^{(k)}(7/2, 3/2)$	$C^{(k)}(7/2, 5/2)$	$C^{(k)}(7/2, 7/2)$	
0	-15	-27	15	147	
2	-120	-288	-240	168	
4	-270	-606	-330	966	
k	$C^{(k)}(9/2, 1/2)$	$C^{(k)}(9/2, 3/2)$	$C^{(k)}(9/2, 5/2)$	$C^{(k)}(9/2, 7/2)$	$C^{(k)}(9/2, 9/2)$
0	-24	-54	-30	84	324
2	-192	-504	-600	-336	432
4	-432	-1092	-11440	-168	2232
STMAS					
k	$C^{(k)}(3/2, 3/2)$				
0	-6				
2	-12				
4	-48				
k	$C^{(k)}(5/2, 3/2)$	$C^{(k)}(5/2, 5/2)$			
0	-1	-28			
2	28	-80			
4	42	-264			
k	$C^{(k)}(7/2, 3/2)$	$C^{(k)}(7/2, 5/2)$	$C^{(k)}(7/2, 7/2)$		
0	6	-21	-66		
2	84	-24	-204		
4	168	-138	-648		
k	$C^{(k)}(9/2, 3/2)$	$C^{(k)}(9/2, 5/2)$	$C^{(k)}(9/2, 7/2)$	$C^{(k)}(9/2, 9/2)$	
0	15	-12	-57	-120	
2	156	48	-132	-384	
4	330	24	-486	-1200	

where the spin coefficients values $C^{(k)}(I, m)$ for MQMAS in Table D.1 are calculated based on the following expressions:

$$C^{(0)}(I, m) = -\frac{2}{\sqrt{5}} (2m [3m^2 - I(I+1)]) \quad (\text{D.1})$$

$$C^{(2)}(I, m) = \frac{1}{\sqrt{14}} (2m [12m^2 - 8I(I+1) + 3]) \quad (\text{D.2})$$

$$C^{(4)}(I, m) = \frac{1}{\sqrt{70}} (2m [34m^2 - 18I(I+1) + 5]) \quad (\text{D.3})$$

which are derived from the combination between the Clebsch-Gordon coefficients given in ref. [26] and the irreducible spin tensors $\hat{T}_{k,q}$.

In contrast the spin coefficients for STMAS, $\mathcal{C}^{(k)}(I, m)$ calculated in Table D.1, are obtained from $C^{(k)}(I, m)$ by:

$$\mathcal{C}^{(k)}(I, m) = \frac{1}{2} \left[C^{(k)}(I, m-1) - C^{(k)}(I, m) \right] \quad (\text{D.4})$$

and their values for $k = 0, 2, 4$ are given by the following three equations:

$$\mathcal{C}^{(0)}(I, m) = -\frac{2}{\sqrt{5}} \left[-9m^2 - 9m - 3 + I(I+1) \right] \quad (\text{D.5})$$

$$\mathcal{C}^{(2)}(I, m) = \frac{1}{\sqrt{14}} \left[-36m^2 + 36m - 15 + 8I(I+1) \right] \quad (\text{D.6})$$

$$\mathcal{C}^{(4)}(I, m) = \frac{1}{\sqrt{70}} \left[-102m^2 + 102m - 39 + 18I(I+1) \right] \quad (\text{D.7})$$

The combined spatial tensors $\mathcal{B}_{2q}^{(2k)}$ are described below:

$$B_0^{(0)} = \frac{3 + \eta^2}{2\sqrt{5}} \quad (\text{D.8})$$

$$B_0^{(2)} = \frac{\eta^2 - 3}{2\sqrt{7}} \quad B_{\pm 2}^{(2)} = \eta^2 \sqrt{\frac{3}{7}} \quad (\text{D.9})$$

$$B_0^{(4)} = \frac{\eta^2 + 18}{2\sqrt{70}} \quad B_{\pm 2}^{(4)} = \frac{3\eta}{\sqrt{28}} \quad B_{\pm 4}^{(4)} = \frac{\eta^2}{4} \quad (\text{D.10})$$

Appendix E

Math Reminder

E.1 Complex Numbers

A complex number

$$z = x + iy \quad (\text{E.1})$$

can be graphically represented as in Fig. E.2.

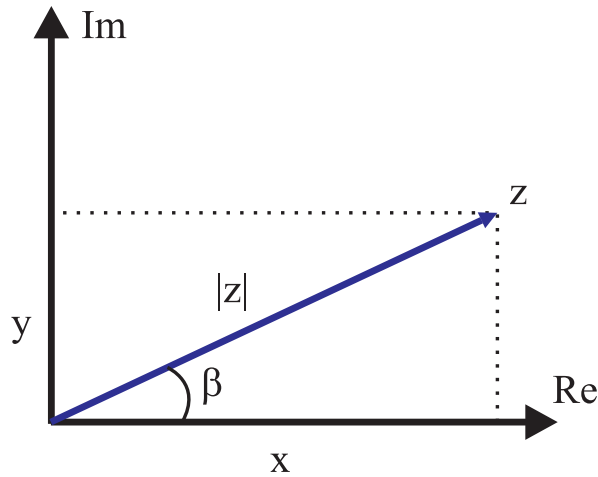


Fig. E.1: Graphic representation of a complex number $z = x + iy$, where $i = \sqrt{-1}$ is the imaginary unit, **Im** is the imaginary axis, **Re** is the real axis, **x** is the real part of **z**, **y** is the coefficient of the imaginary part of **z**, $|z|$ is the modulus (absolute value) of **z** and β is the argument of **z**.

The number z is fully determined when either x and y or $|z|$ and β are known. The relations between these two pairs of variables are:

$$x = |z| \cos \beta \quad (\text{E.2})$$

$$y = |z| \sin \beta \quad (\text{E.3})$$

According to Eq. E.1,

$$z = |z| \cos \beta + i |z| \sin \beta = |z| (\cos \beta + i \sin \beta) \quad (\text{E.4})$$

Using Euler's relation, one obtains:

$$z = |z| e^{i\beta} \quad (\text{E.5})$$

The complex number,

$$z^* = x - iy = \quad (\text{E.6})$$

$$= |z| e^{-i\beta} \quad (\text{E.7})$$

is called the “complex conjugate” of z .

E.2 Series Expansions of e^x , $\sin x$, $\cos x$ and e^{ix}

The exponential functions describes most of everything happening in nature. The e^x series is

$$e^x = 1 + x + \frac{x^2}{2!} + \frac{x^3}{3!} + \dots \quad (\text{E.8})$$

The sine and cosine series are:

$$\sin x = x - \frac{x^3}{3!} + \frac{x^5}{5!} - \frac{x^7}{7!} + \dots \quad (\text{E.9})$$

$$\cos x = x - \frac{x^2}{2!} + \frac{x^4}{4!} - \frac{x^6}{6!} + \dots \quad (\text{E.10})$$

The e^{ix} series is:

$$e^{ix} = 1 + ix - \frac{x^2}{2!} - \frac{ix^3}{3!} + \frac{x^4}{4!} + \frac{ix^5}{5!} \dots \quad (\text{E.11})$$

Separation of the real and imaginary terms gives

$$e^{ix} = \underbrace{1 - \frac{x^2}{2!} + \frac{x^4}{4!} - \frac{x^6}{6!} + \dots}_{\cos x} + i \underbrace{\left(x - \frac{x^3}{3!} + \frac{x^5}{5!} - \dots \right)}_{\sin x} \quad (\text{E.12})$$

Recognising the sine and cosine series one obtains the Euler formula $e^{ix} = \cos x + i \sin x$.

E.3 Elementary Rotation Operator

Considering a complex number r which as a modulus $|r|$ and with argument α :

$$r = e^{(i\alpha)} = \cos \alpha + i \sin \alpha \quad (\text{E.13})$$

Multiplying a complex number such as Eq. E.5 by r leaves the modulus of z unchanged and increases the argument by α such as follows:

$$z \times r = |z| e^{(i\beta)} e^{(i\alpha)} = |z| e^{i(\beta+\alpha)} \quad (\text{E.14})$$

Eq. E.14 describes the rotation of the vector Oz by an angle α (see Fig. E.2). The complex number r is called an “*elementary rotation operator*”. As most of the NMR* monographs use the notation $\hat{R}(\alpha)$ for rotation operators to describe a rotation of α degrees, such notation is also used in this thesis. Thus, in this example

$$r = \hat{R}(\alpha) \quad (\text{E.15})$$

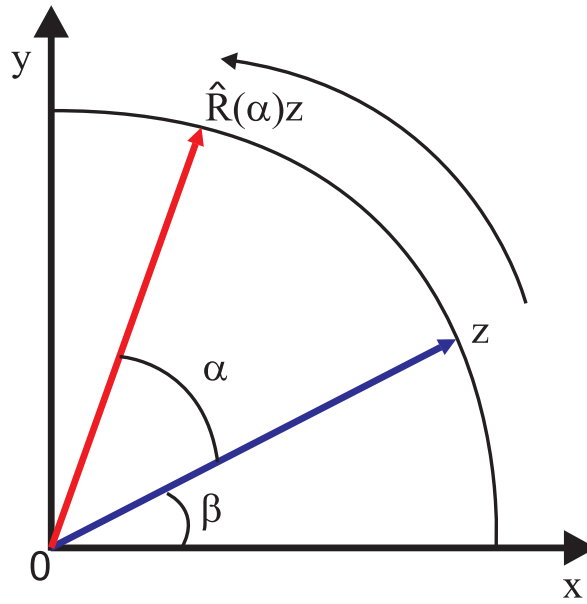


Fig. E.2: Effect of the rotation operator $\hat{R}(\alpha) = e^{(i\alpha)}$ on the complex number $z = |z|e^{(i\beta)}$.

In NMR, in order to get an explicit matrix expression for $R(\alpha)$ for a rf pulse along the x -axis, one have to calculate,

$$\hat{R}_x(\alpha) = e^{(i\alpha\hat{I}_x)} \quad (\text{E.16})$$

using a series expansion of the exponential (see Eq. E.8) expression of Eq. E.16 can be rewritten as:

$$\hat{R}_x(\alpha) = 1 + i\alpha\hat{I}_x + \frac{(i\alpha)^2\hat{I}_x^2}{2!} + \frac{(i\alpha)^3\hat{I}_x^3}{3!} + \dots \quad (\text{E.17})$$

where the powers of \hat{I}_x present in Eq. E.17 can be easily deduced from Eq. A.2.

In general for $n = \text{even}$, \hat{I}_x^n has the form,

$$\hat{I}_x^n = \frac{1}{2^n} \begin{pmatrix} 1 & 0 \\ 0 & 1 \end{pmatrix} = \left(\frac{1}{2^n}\right) \cdot \hat{1} \quad (\text{E.18})$$

and for $n = \text{odd}$ the expression for \hat{I}_x^n becomes:

$$\hat{I}_x^n = \frac{1}{2^n} \begin{pmatrix} 0 & 1 \\ 1 & 0 \end{pmatrix} = \left(\frac{1}{2^n}\right) \cdot 2\hat{I}_x \quad (\text{E.19})$$

Thus, introducing Eqs. E.18 and E.19 in Eq. E.17 and separating the even and odd terms gives:

*Although more complicated, the rotation operators in the density matrix treatment of multipulse NMR are of the same form as the elementary operator. In NMR the rotation operators are usually expressed as a matrix (see Eqs. E.23 and E.24)

$$\begin{aligned}\hat{R}_x(\alpha) &= \left[1 - \frac{(\alpha/2)^2}{2!} + \frac{(\alpha/2)^4}{4!} - \dots \right] \times \begin{pmatrix} 1 & 0 \\ 0 & 1 \end{pmatrix} + \\ &+ i \left[\alpha/2 - \frac{(\alpha/2)^3}{3!} + \frac{(\alpha/2)^5}{5!} - \dots \right] \times \begin{pmatrix} 0 & 1 \\ 1 & 0 \end{pmatrix}\end{aligned}\quad (\text{E.20})$$

By applying the sine and cosine series of Eqs. E.9 and E.10 one can express Eq. E.20 in the following way:

$$\hat{R}_x(\alpha) = \cos \frac{\alpha}{2} \cdot \hat{1} + i \sin \frac{\alpha}{2} \cdot 2\hat{I}_x = \quad (\text{E.21})$$

$$= \begin{pmatrix} \cos \frac{\alpha}{2} & 0 \\ 0 & \cos \frac{\alpha}{2} \end{pmatrix} + \begin{pmatrix} 0 & i \sin \frac{\alpha}{2} \\ i \sin \frac{\alpha}{2} & 0 \end{pmatrix} = \begin{pmatrix} \cos \frac{\alpha}{2} & i \sin \frac{\alpha}{2} \\ i \sin \frac{\alpha}{2} & \cos \frac{\alpha}{2} \end{pmatrix} \quad (\text{E.22})$$

From Eq. E.22 that substituting $\alpha = 90^\circ$ or 180° pulse, one can obtain the matrix representation for a rotation induced by a 90° or 180° *rf* pulse along *x*. Thus according to Eq. E.22, the matrix form of these rotation operators will be

$$\hat{R}_x(90) = \frac{1}{\sqrt{2}} \begin{pmatrix} 1 & i \\ i & 1 \end{pmatrix} \quad (\text{E.23})$$

$$\hat{R}_x(180) = \begin{pmatrix} 0 & i \\ i & 0 \end{pmatrix} \quad (\text{E.24})$$

For rotation along the *y* axis the logic is the same and $\hat{R}(\alpha)$ must be calculated taking into consideration the spin angular momentum operator \hat{I}_y .

E.4 Some Trigonometric Relations

► Expressing sine and cosine in terms of exponentials:

$$\cos \alpha = \frac{e^{i\alpha} + e^{-i\alpha}}{2} \quad (\text{E.25})$$

$$\sin \alpha = \frac{e^{i\alpha} - e^{-i\alpha}}{2i} \quad (\text{E.26})$$

► Sum and difference of two angles:

$$\sin(\alpha \pm \beta) = \sin \alpha \cos \beta \pm \cos \alpha \sin \beta \quad (\text{E.27})$$

$$\cos(\alpha \pm \beta) = \cos \alpha \cos \beta \mp \sin \alpha \sin \beta \quad (\text{E.28})$$

► Angle 2α :

$$\sin 2\alpha = 2 \sin \alpha \cos \alpha \quad (\text{E.29})$$

$$\cos 2\alpha = \cos^2 \alpha - \sin^2 \alpha = 2 \cos^2 \alpha - 1 \quad (\text{E.30})$$

► Angle 3α :

$$\sin 3\alpha = 3 \sin \alpha - 4 \sin^3 \alpha \quad (\text{E.31})$$

$$\cos 3\alpha = 4 \cos^3 \alpha - 3 \cos \alpha \quad (\text{E.32})$$

$$(\text{E.33})$$

► Other relations:

$$\cos^2 \alpha = \frac{1 + \cos 2\alpha}{2} = \frac{e^{2i\alpha} + 2 + e^{-2i\alpha}}{4} \quad (\text{E.34})$$

$$\cos \alpha \sin \alpha = \frac{\sin 2\alpha}{2} = \frac{e^{2i\alpha} - e^{-2i\alpha}}{4i} \quad (\text{E.35})$$

$$\cos^3 \alpha = \frac{\cos 3\alpha + 3 \cos \alpha}{4} = \frac{e^{3i\alpha} + 3e^{i\alpha} + 3e^{-i\alpha} + e^{-3i\alpha}}{8} \quad (\text{E.36})$$

$$\cos^2 \alpha \sin \alpha = \frac{\sin 3\alpha + 3 \sin \alpha}{4} = \frac{e^{3i\alpha} + e^{i\alpha} - e^{-i\alpha} - e^{-3i\alpha}}{8} \quad (\text{E.37})$$

$$\cos \alpha \cos \beta = \frac{\cos(\alpha - \beta) + \cos(\alpha + \beta)}{2} \quad (\text{E.38})$$

$$\sin \alpha \sin \beta = \frac{\cos(\alpha - \beta) - \cos(\alpha + \beta)}{2} \quad (\text{E.39})$$

$$\sin \alpha \cos \beta = \frac{\sin(\alpha - \beta) + \sin(\alpha + \beta)}{2} \quad (\text{E.40})$$

Appendix F

Additional Data for the Study of Hybrid Materials

F.1 Ge Binuclear Complex

F.1.1 Additional Spectra and Figures: ^1H MAS NMR, Powder XRD

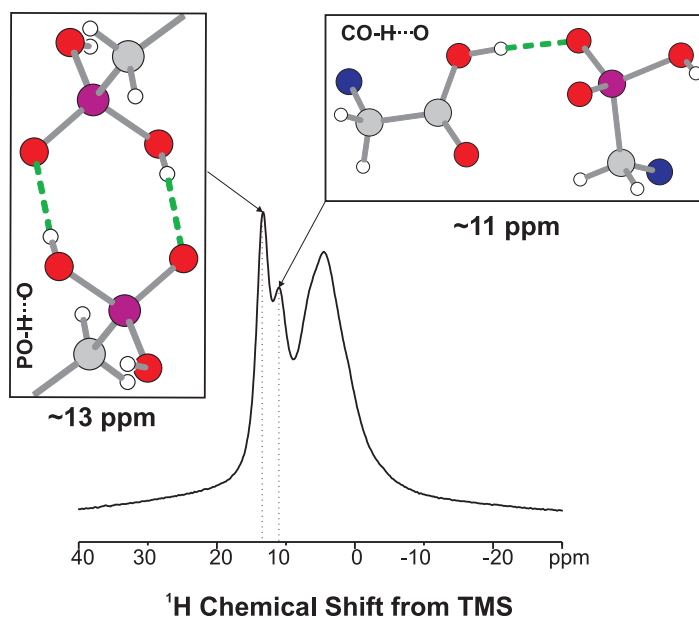


Fig. F.1: ^1H MAS spectrum of the H_4pmida ligand recorded at 30 kHz.

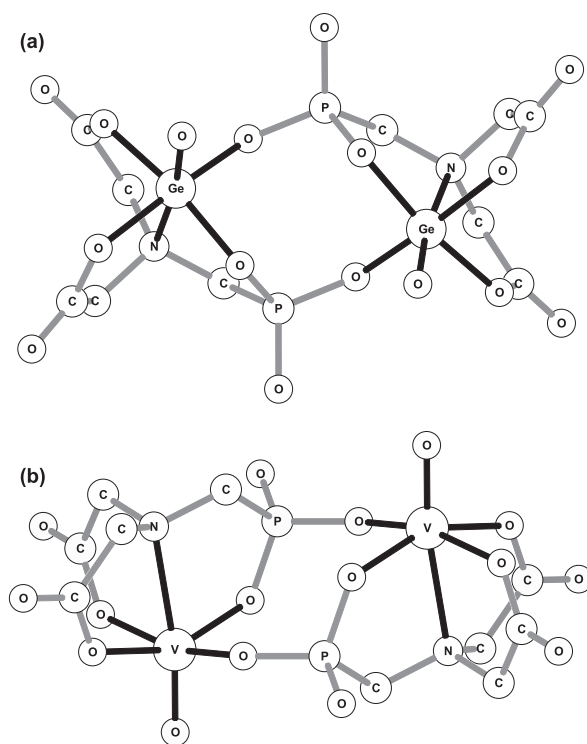


Fig. F.2: Schematic representations of the binuclear anionic: (a) $[\text{Ge}_2(\text{pmida})_2(\text{OH})_2]^{2-}$; (b) $[\text{V}_2\text{O}_2(\text{pmida})_2]^{4-}$ complexes.

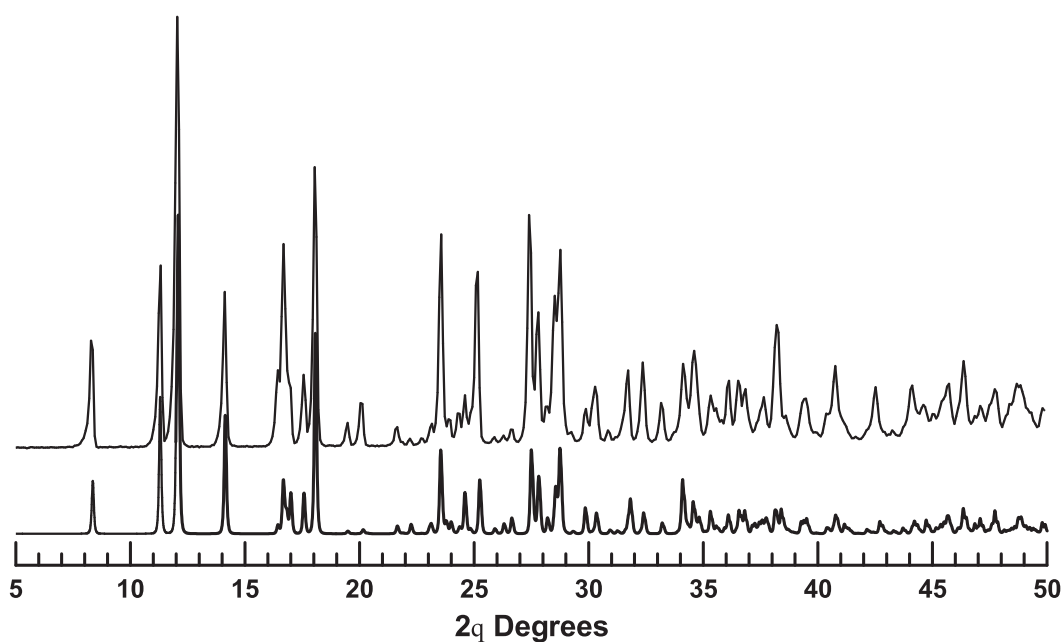


Fig. F.3: Comparison between the simulated (bottom) and the experimental (top) powder X-ray diffraction patterns.

F.1.2 Table of Hydrogen Bond Lengths

Table F.1: Hydrogen-bonding geometry: distances \AA and angles $[\circ]$.^[a,b]

D-H...A	d(D-H)	d(H...A)	d(D...A)	<(DHA)
O(8)-H(8)...O(1W) ⁱⁱ	0.82	1.88	2.685(3)	164.8
O(1W)-H(1C)...O(2)	0.86(3)	1.83(3)	2.679(3)	169(3)
O(1W)-H(1D)...O(5) ⁱⁱⁱ	0.86(3)	1.96(3)	2.816(3)	177(4)
O(2W)-H(2C)...O(8) ^{iv}	0.86(3)	1.89(3)	2.742(3)	173(3)
O(2W)-H(2D)...O(6) ^v	0.85(3)	2.06(3)	2.872(3)	159(3)
N(2)-H(2E)...O(4) ^{vi}	0.87(4)	2.16(4)	2.870(3)	138(3)
N(2)-H(2F)...O(2W) ^{vii}	0.87(4)	1.89(4)	2.761(3)	172(4)

^a The O-H and N-H distances were restrained to 0.86(1) and 0.90(1) \AA , respectively.

ⁱⁱ : $1.5-x, -\frac{1}{2}+y, \frac{1}{2}-z$; ⁱⁱⁱ : $1-x, y, \frac{1}{2}-z$; ^{iv} : $x-1, 1+y, z$; ^v : $1-x, 1-y, 1-z$; ^{vi} : $x, 1+y, z$; ^{vii} : $1-x, 2-y, 1-z$.

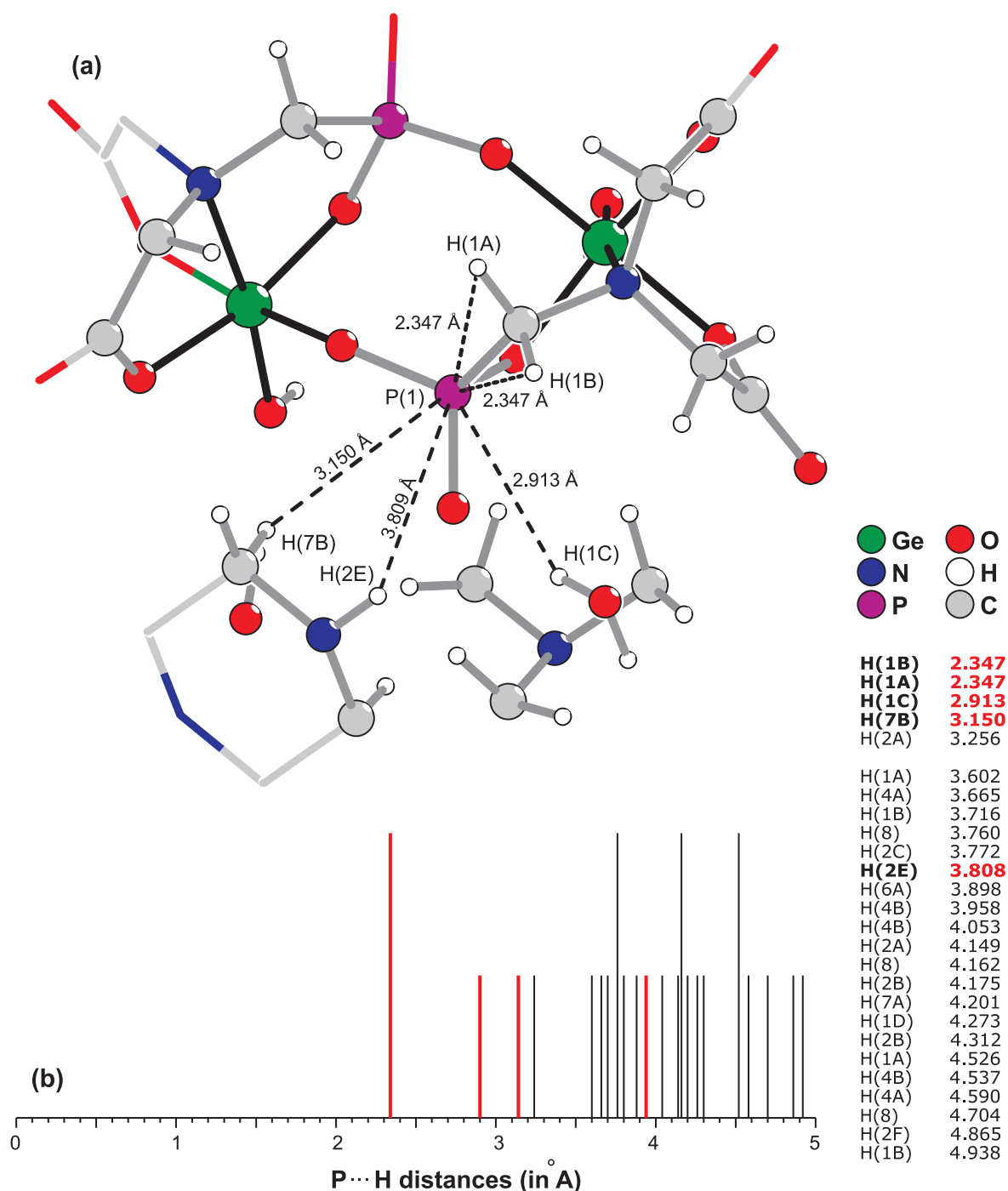
F.1.3 Histogram of the P \cdots H and C \cdots H Distances

Fig. F.4: Spherical environment with a 5 radius around the central P(1) atom. (b) Histogram of the P \cdots H distances (in Å) in the 0-5 Å range and respective distances (in the right). Standard uncertainties for the distances are in 2-3 units range at the last decimal place.

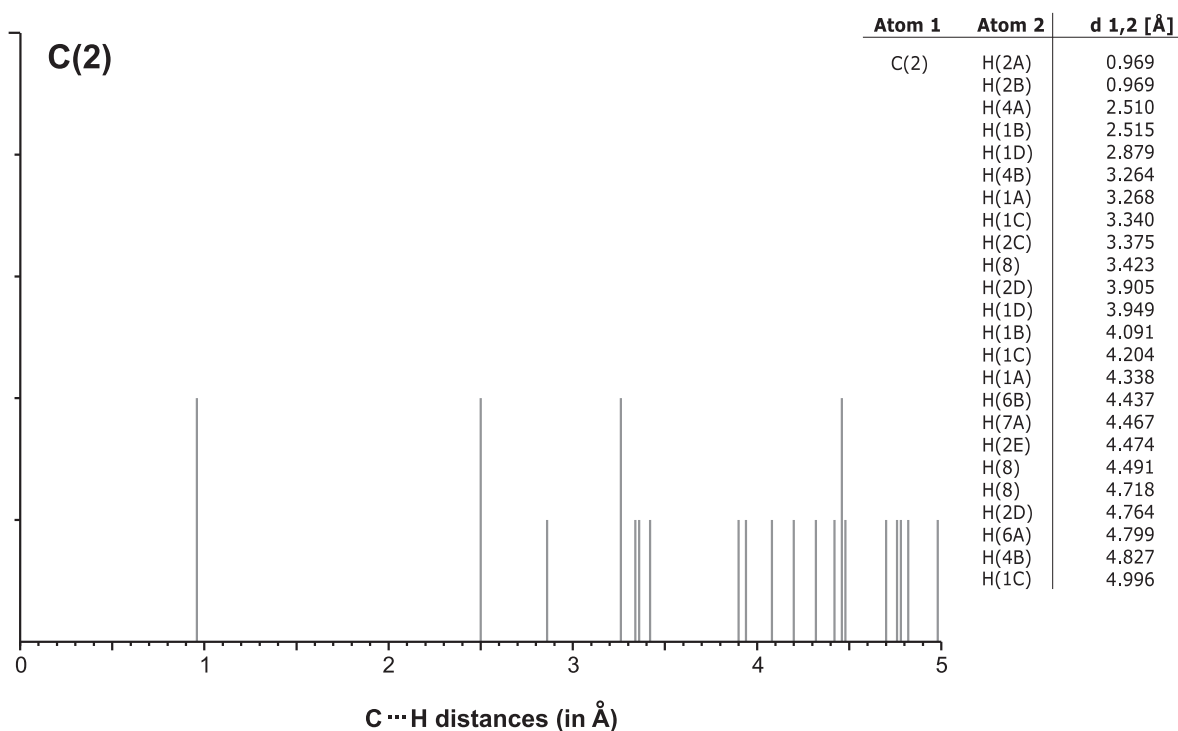
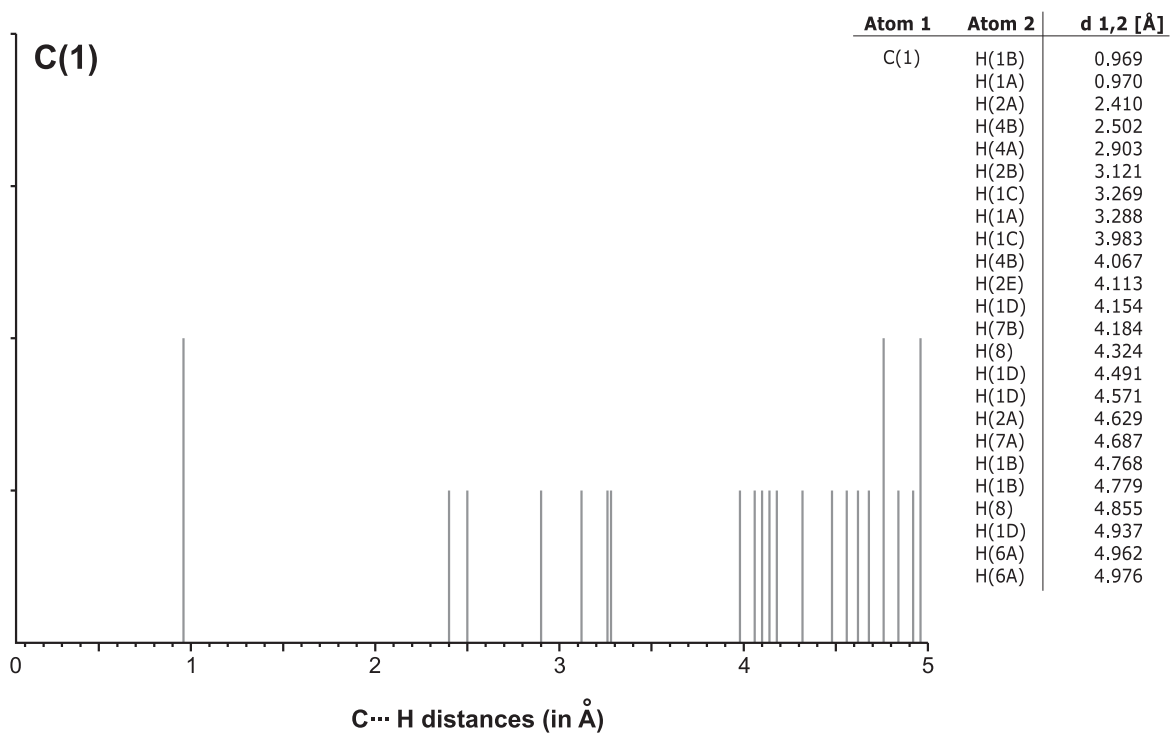


Fig. F.5: Histogram of the C(1)···H and C(2)···H distances in the 0-5 Å range and respective distances (on the right). Standard uncertainties for the distances are in 2-3 units range at the last decimal place.

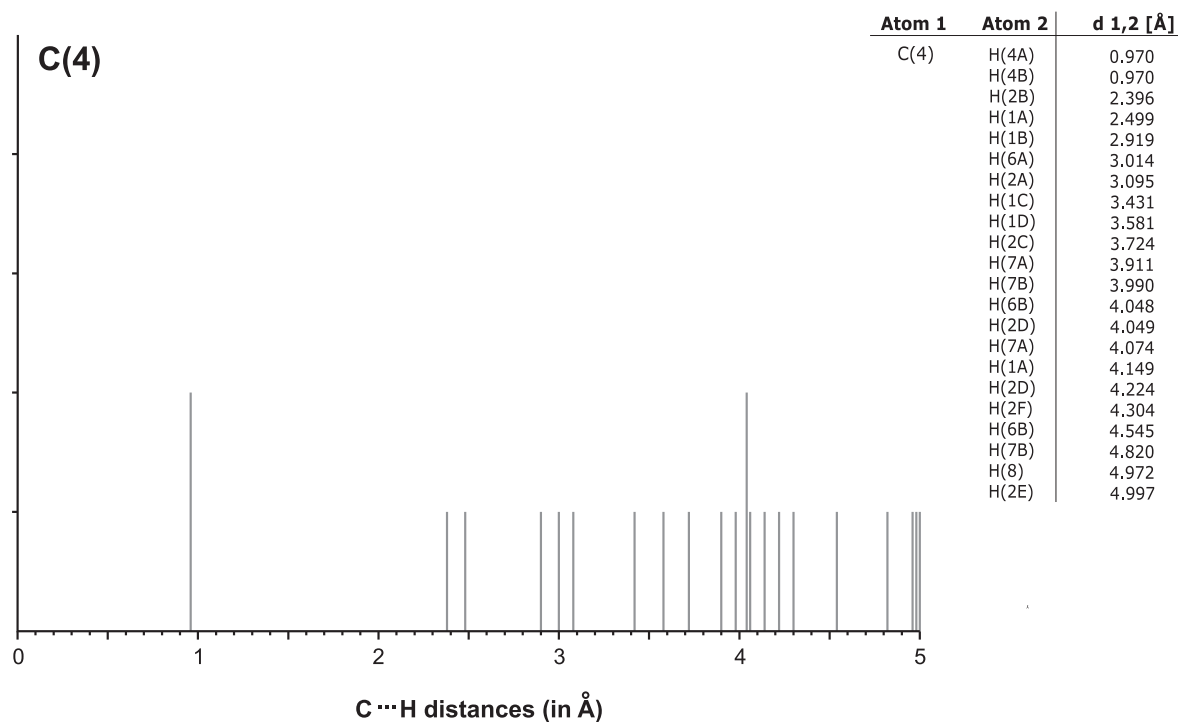
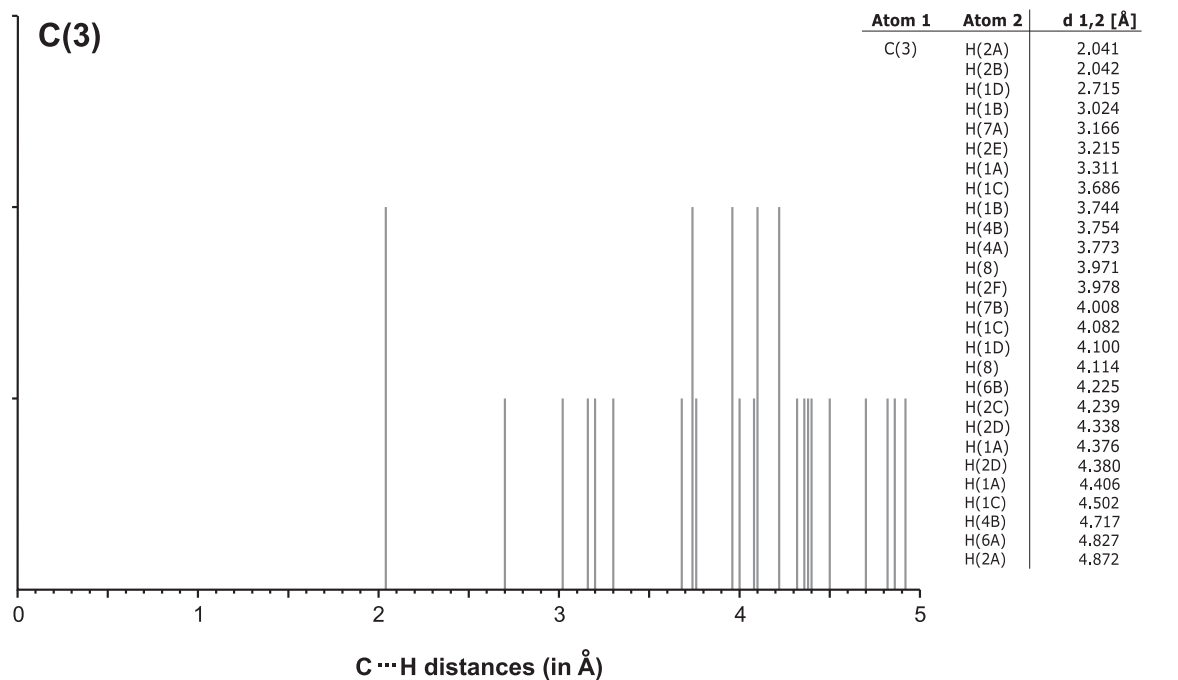


Fig. F.6: Histogram of the $C(3)\cdots H$ and $C(4)\cdots H$ distances in the 0-5 Å range and respective distances (on the right). Standard uncertainties for the distances are in 2-3 units range at the last decimal place.

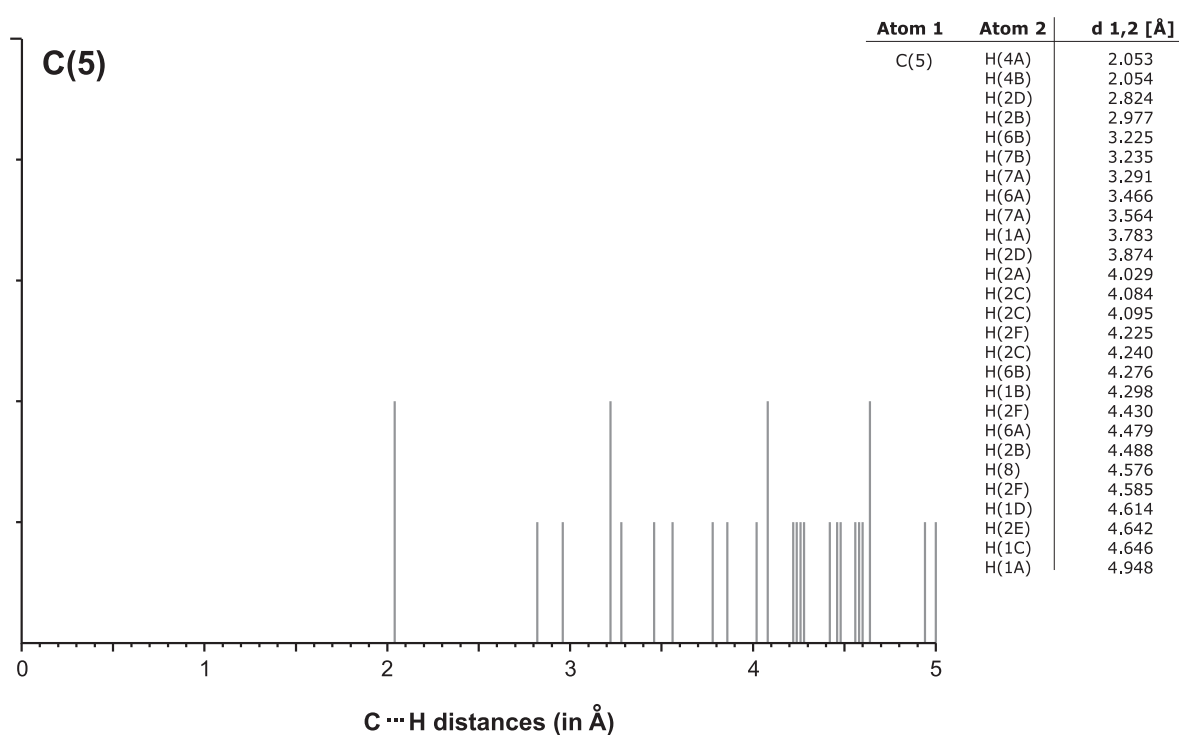


Fig. F.7: Histogram of the $C(5)\cdots H$ distances in the 0-5 Å range and respective distances (on the right). Standard uncertainties for the distances are in 2-3 units range at the last decimal place.

F.2 A Germanium/HEDP⁴⁻ Hexanuclear Complex Containing Heteroaromatic Residues

F.2.1 Additional Spectra and Tables: NMR Spectra, powder XRD, Hydrogen Bond Lengths for Structures I and II

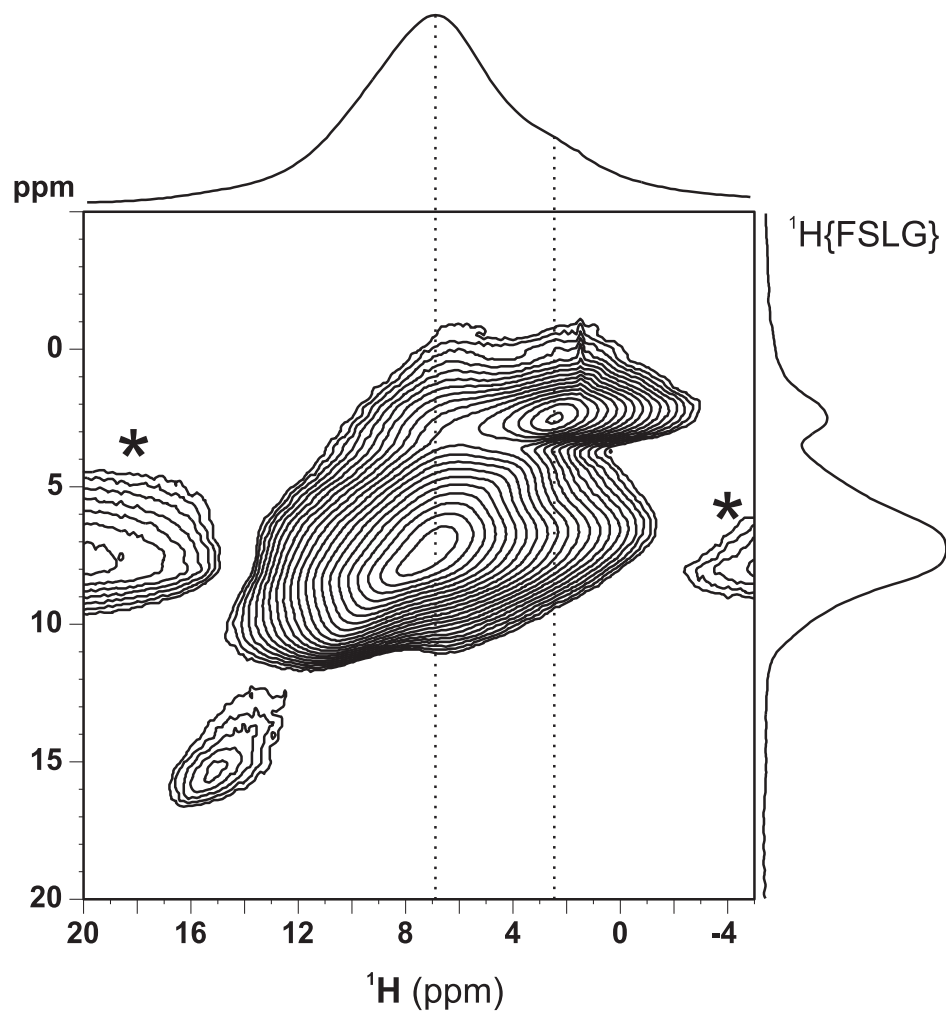


Fig. F.8: $^1\text{H}\{\text{FS-LG}\}-^1\text{H}$ spectrum of **II**.

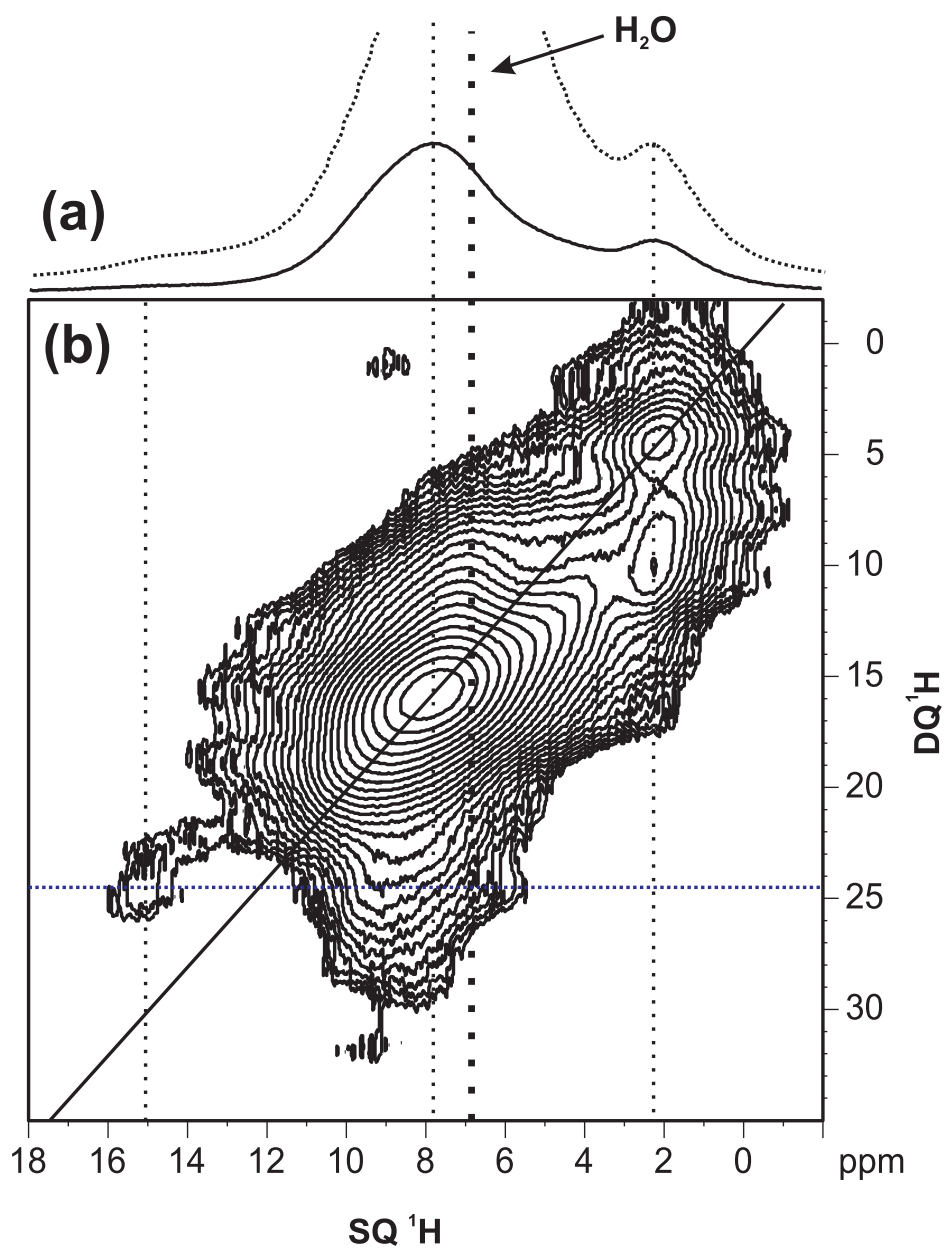


Fig. F.9: (a) ¹H MAS and (b) ¹H DQ MAS NMR spectra of II.

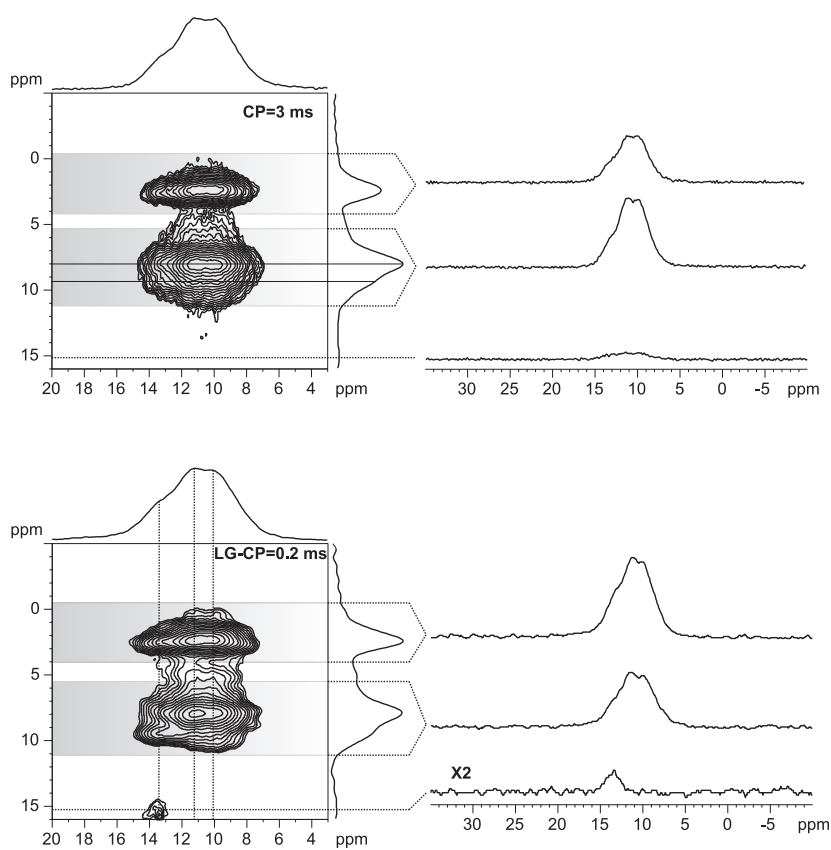


Fig. F.10: $^1\text{H}\{\text{FS-LG}\}-^{31}\text{P}$ spectra of **II**, recorded at (a) $CT=3$ ms and (b) $CT=0.2$ ms (using LG-CP). The F2 cross-sections summed over the shaded area are shown at the right side. For $CT=0.2$ ms the resonance at ca. 15.1 ppm becomes more visible employing LG-CP comparing with comparison to a conventional CP.

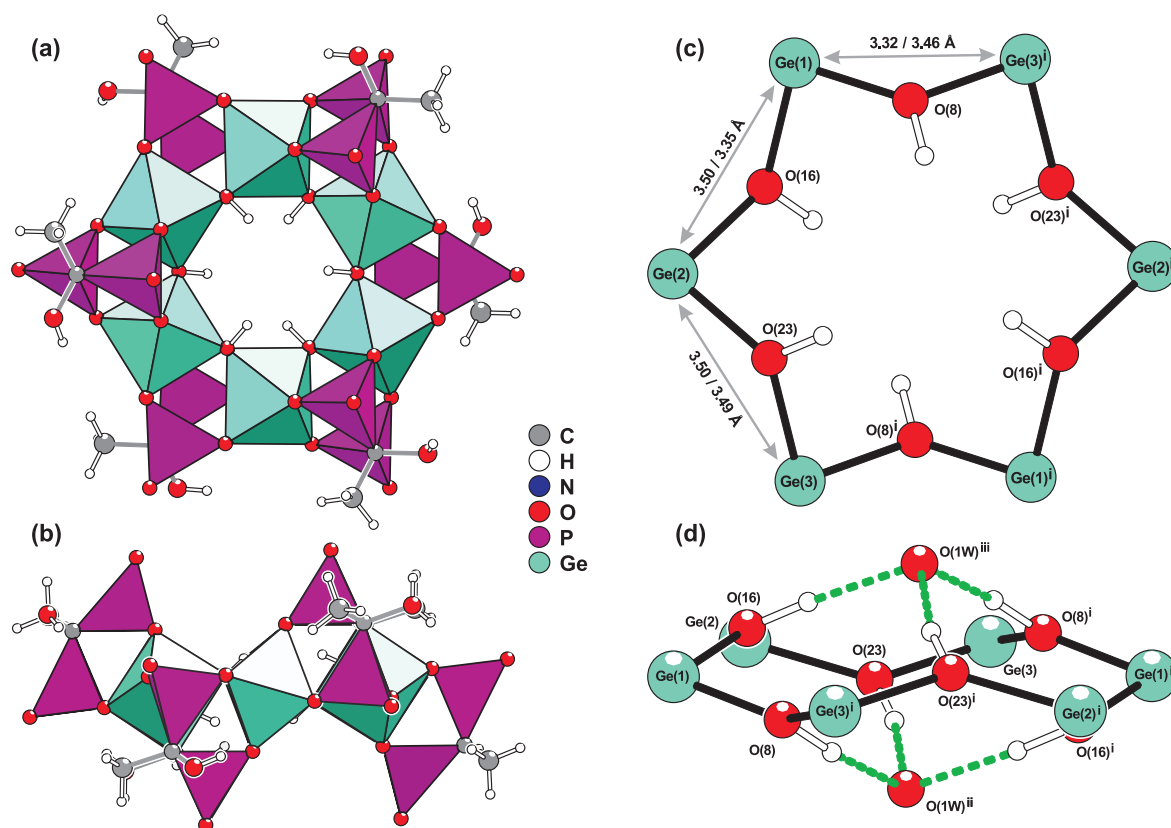


Fig. F.11: (a, b) Polyhedral representation of the hexameric anionic $[Ge_6(\mu_2-OH)_6(C_2H_4O_7P_2)_6]^{6-}$ moiety viewed from the top and from a lateral perspective. (c, d) Ball-and-stick representation of the $[Ge_6(OH)_6(C_2H_4O_7P_2)_6]^{6-}$ moieties. Hydrogen bonds with neighbouring $O(1W)$ water molecules are represented as dashed green lines. Selected bond lengths and angles are given in Tables S2 and S3 and hydrogen bonding geometry in Tables S4 and S5 (ESI). Symmetry codes to generate equivalent atoms, **I**: (i) $1-x, 2-y, 2-z$; (ii) $x, y, 1+z$; (iii) $1-x, 2-y, 1-z$; **II**: (i) $1-x, 1-y, 2-z$; (ii) $x, -1+y, z$; (iii) $1-x, 1-y, 2-z$.

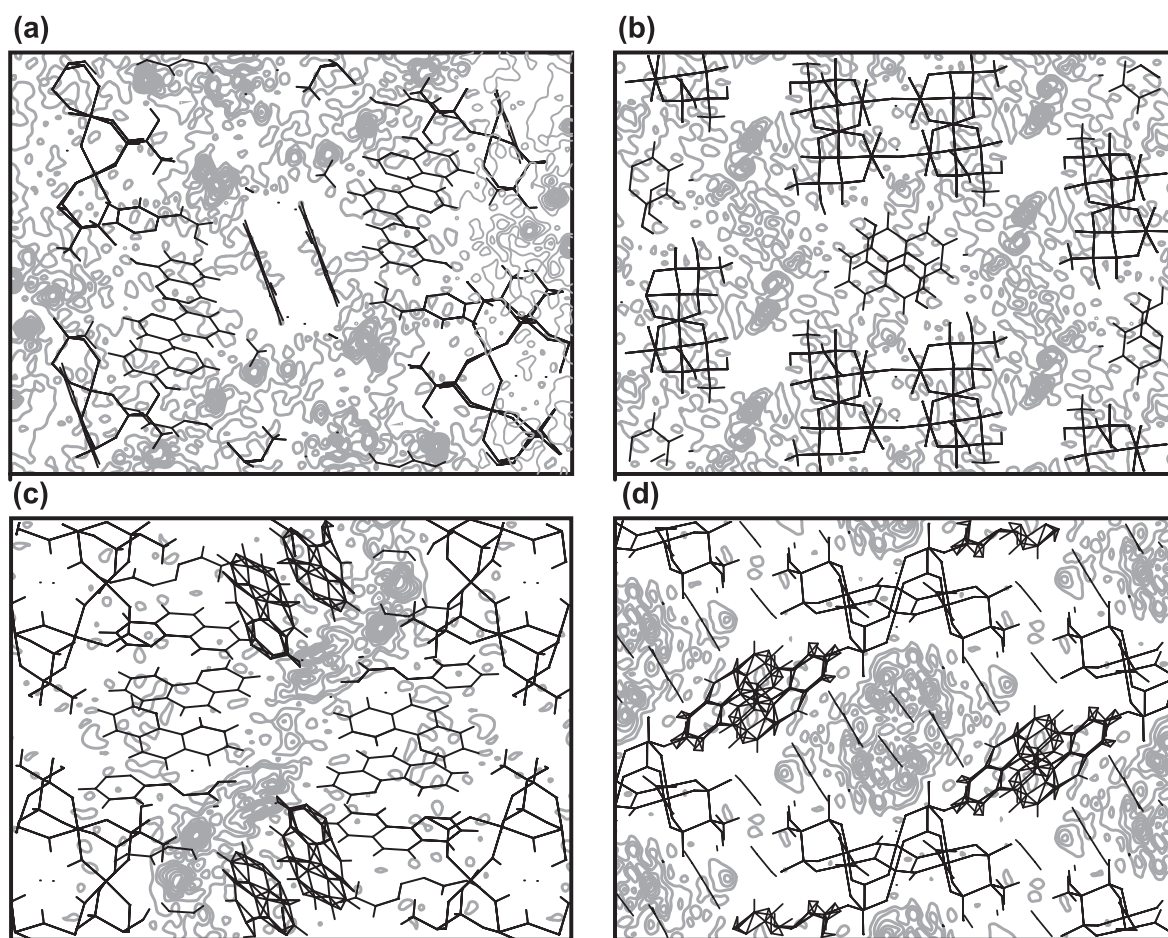


Fig. F.12: (Contouring of difference Fourier SQUEEZE maps (grey) of compound I viewed parallel to the (a) YZ and (b) XY planes and compound II viewed along the same directions (c) and (d), respectively.

Table F.2: Hydrogen bonding geometry (distances in Å and angles in degrees) for compound **I**.^[a,b]

D-H...A	d(D...A)	<(DHA)
O(7) H(7)...O(28W)	2.91(5)	130(1)
O(8) H(8)...O(1W) ⁱ	2.679(10)	160(9)
O(15) H(15)...O(10W) ⁱ	2.71(3)	139(1)
O(16) H(16)...O(1W) ⁱⁱ	2.696(8)	171(1)
O(23) H(23)...O(1W) ⁱ	2.687(8)	167(1)
O(24) H(24)...O(8W)	2.569(18)	154(1)
O(1_1) H(1_1)...O(11) ⁱⁱⁱ	2.606(8)	166(1)
O(1_2) H(1_2)...O(3) ^{iv}	2.612(10)	165(1)
O(1_3) H(1_3)...O(6) ⁱⁱ	2.590(10)	178(1)
O(1_4) H(1_4)...O(14) ^v	2.537(10)	150(1)
N(1_1) H(1_A1)...O(6W)	2.779(13)	163(9)
N(1_2) H(1_A2)...O(4W)	2.666(16)	161(2)
N(1_3) H(1_A3)...O(3W) ^{vi}	2.718(14)	170(2)
C(1_1) H(1_1)...O(22)	3.439(12)	154(1)
C(2_1) H(2_1)...O(21)	3.174(11)	133(2)
C(3_1) H(3_1)...O(9) ^{iv}	3.207(10)	126(2)
C(1_3) H(1_3)...O(20W) ⁱⁱ	3.36(3)	145(2)
C(3_3) H(3_3)...O(4) ^{vii}	3.261(14)	136(1)
C(9_3) H(9_3)...O(20) ^{vii}	3.474(16)	174(1)
C(2) H(2B)...O(2)	3.073(13)	113(1)
C(2) H(2B)...O(22W) ⁱⁱ	2.79(3)	125(1)
C(4) H(4B)...O(14W) ^{viii}	3.01(3)	138(1)

^[a] Symmetry transformations used to generate equivalent atoms: (i) $x, y, 1 + z$; (ii) $1 - x, 2 - y, 1 - z$; (iii) $x, y, -1 + z$; (iv) $1 - x, 2 - y, 2 - z$; (v) $-x, 1 - y, 2 - z$; (vi) $x, 1 + y, z$; (vii) $1 + x, y, -1 + z$; (viii) $x, 1 + y, 1 + z$.

^[b] The numbers after the underscore indicate the residue number to which the atoms belong.

Table F.3: Hydrogen bonding geometry (distances in Å and angles in degrees) for compound **II**.^[a,b]

D-H...A	d(D...A)	<(DHA)
O(7)-H(7)...O(11W)	2.50(2)	147(1)
O(8)-H(8)...O(1W) ⁱ	2.684(9)	162(2)
O(15)-H(15)...O(3W)	2.717(9)	121(1)
O(16)-H(16)...O(1W) ⁱⁱ	2.716(9)	163(1)
O(23)-H(23)...O(1W) ⁱ	2.713(8)	155(2)
O(24)-H(24)...O(13)	3.197(9)	162(2)
N(2_1)-H(2_A1)...O(14)	2.678(9)	155(2)
N(1_2)-H(1_2)...O(19) ⁱⁱⁱ	2.819(11)	153(1)
N(1_3)-H(1_3)...O(11) ^{iv}	2.948(12)	153(2)

^[a] Symmetry transformations used to generate equivalent atoms: (i) $1 - x, 1 - y, 2 - z$; (ii) $x, 1 - y, 2 - z$; (iii) $1/2 + x, 1/2 - y, -1/2 + z$; (iv) $x, y, -1 + z$.

^[b] The numbers after the underscore indicate the residue number to which the atoms belong.

F.3 Layered γ -Titanium Phosphate $(C_6H_{13}NH_3)[Ti(HPO_4)(PO_4)] \cdot H_2O$

F.3.1 Additional Tables: Atomic Coordinates, Bond Lengths and Angles

Table F.4: Fractional Atomic Coordinates of $(C_6H_{13}NH_3)[Ti(HPO_4)(PO_4)] \cdot H_2O$

	<i>x</i>	<i>y</i>	<i>z</i>
Ti(1)	0.802(1)	0.250(1)	0.068(1)
P(1)	0.221(1)	0.238(1)	-0.033(1)
P(2)	0.378(1)	0.140(1)	0.163(1)
O(1)	0.989(1)	0.238(1)	0.000(1)
O(2)	0.791(1)	0.552(1)	0.073(1)
O(3)	0.791(1)	-0.064(1)	0.071(1)
O(4)	0.498(1)	0.239(1)	0.007(1)
O(5)	0.126(1)	0.248(1)	0.130(1)
O(6)	0.626(1)	0.206(1)	0.140(1)
O(7)	0.325(1)	0.897(1)	0.151(1)
O(8)	0.451(1)	0.162(1)	0.235(1)
O(W)	0.421(1)	0.347(1)	0.341(1)
N(1)	0.749(1)	0.581(1)	0.193(1)
C(1)	0.749(1)	0.581(1)	0.258(1)
C(2)	0.749(1)	0.786(1)	0.291(1)
C(3)	0.749(1)	0.786(1)	0.358(1)
C(4)	0.749(1)	0.991(1)	0.392(1)
C(5)	0.749(1)	0.991(1)	0.459(1)
C(6)	0.749(1)	0.195(1)	0.492(1)

Table F.5: Selected Bond Lengths and Angles of $(C_6H_{13}NH_3)[Ti(HPO_4)(PO_4)] \cdot H_2O^a$

Ti(1)-O(1)	1.99(2)	O(1)-Ti(1)-O(2)	96.3(2)
Ti(1)-O(2)	1.92(1)	O(1)-Ti(1)-O(3)	90.6(2)
Ti(1)-O(3)	1.99(2)	O(1)-Ti(1)-O(4)	82.9(1)
Ti(1)-O(4)	1.84(1)	O(1)-Ti(1)-O(5) ^b	95.4(2)
Ti(1)-O(5) ^b	1.93(1)	O(1)-Ti(1)-O(6)	169.7(3)
Ti(1)-O(6)	2.06(3)	O(2)-Ti(1)-O(3)	173.1(2)
P(1)-O(1) ^c	1.53(1)	O(2)-Ti(1)-O(4)	93.0(1)
P(1)-O(2) ^d	1.48(2)	O(2)-Ti(1)-O(5) ^b	89.7(1)
P(1)-O(3) ^e	1.52(1)	O(2)-Ti(1)-O(6)	93.7(1)
P(1)-O(4)	1.50(1)	O(3)-Ti(1)-O(4)	87.9(1)
P(2)-O(5)	1.50(1)	O(3)-Ti(1)-O(5) ^b	89.7(1)
P(2)-O(6)	1.53(1)	O(3)-Ti(1)-O(6)	79.4(2)
P(2)-O(7)	1.58(3)	O(4)-Ti(1)-O(5) ^b	177.0(1)
P(2)-O(8)	1.61(4)	O(4)-Ti(1)-O(6)	99.1(2)
N(1)-C(1)	1.50(1)	O(6)-Ti(1)-O(5) ^b	82.2(2)
C(1)-C(2)	1.50(1)	P(1)-O(4)-Ti(1)	168.7(1)
C(2)-C(3)	1.53(1)	P(2)-O(6)-Ti(1)	148.1(1)
C(3)-C(4)	1.51(1)	O(1) _c -P(1)-O(2) ^d	111.6(1)
C(4)-C(5)	1.53(1)	O(1) _c -P(1)-O(3) ^e	109.9(1)
C(5)-C(6)	1.50(1)	O(1) _c -P(1)-O(4)	115.1(1)
		O(2) _d -P(1)-O(3) ^e	108.3(2)
N(1)-C(1)-C(2)	119.3(2)	O(2) _d -P(1)-O(4)	106.5(1)
C(1)-C(2)-C(3)	119.3(2)	O(3) _e -P(1)-O(4)	105.0(1)
C(2)-C(3)-C(4)	120.8(1)	O(5)-P(2)-O(6)	112.5(1)
C(3)-C(4)-C(5)	120.8(1)	O(5)-P(2)-O(7)	105.2(2)
C(4)-C(5)-C(6)	120.2(1)	O(5)-P(2)-O(8)	117.1(3)
		O(6)-P(2)-O(7)	109.3(2)
		O(6)-P(2)-O(8)	107.5(2)
		O(7)-P(2)-O(8)	104.8(4)

^a Bond lengths are given in angstroms; bond angles are given in degrees.^b Symmetry code used to generate equivalent atoms: $(1+x, y, z)$. ^c $(-1+x, y, z)$. ^d $(1-x, -1/2+y, -z)$.^e $(1-x, 1/2+y, -z)$.**Table F.6:** Short $(N, O) \cdots O$ Contacts in $(C_6H_{13}NH_3)[Ti(HPO_4)(PO_4)] \cdot H_2O^a$

N(1) \cdots O(2)	2.80(1)	O(7) \cdots O(3) ^b	2.94(2)
N(1) \cdots O(6)	2.68(3)	O(1W) \cdots O(8)	2.72(3)
N(1) \cdots O(7) ^c	2.95(2)		

^a Contacts are given in angstroms.^b Symmetry code used to generate equivalent atoms: $(-1+x, 1+y, z)$. ^c $(x, 1+y, z)$.

F.3.2 Thermogravimetric Data

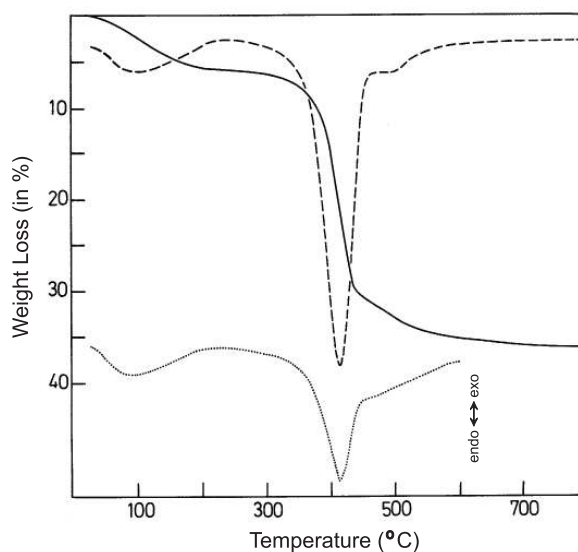


Fig. F.13: - TG (—), DTG (---) and DSC (···) curves for $(C_6H_{13}NH_3)[Ti(HPO_4)(PO_4)] \cdot H_2O$

F.3.3 X-ray Data

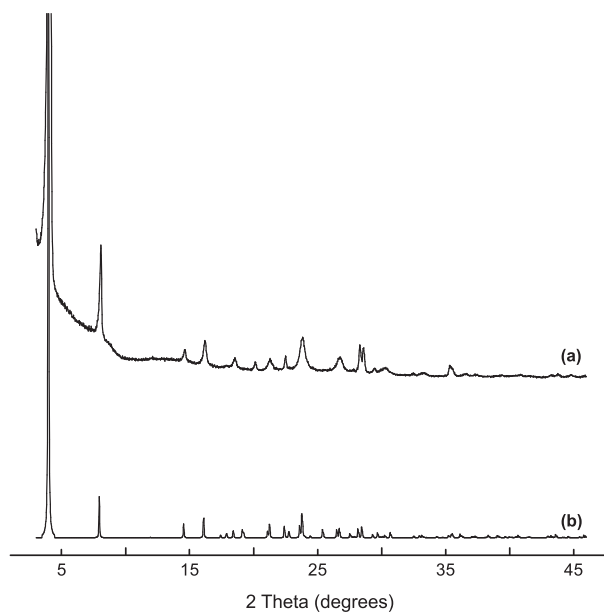


Fig. F.14: (a) Experimental and (b) simulated powder XRD patterns of $(C_6H_{13}NH_3)[Ti(HPO_4)(PO_4)] \cdot H_2O$

F.3.4 SEM Images

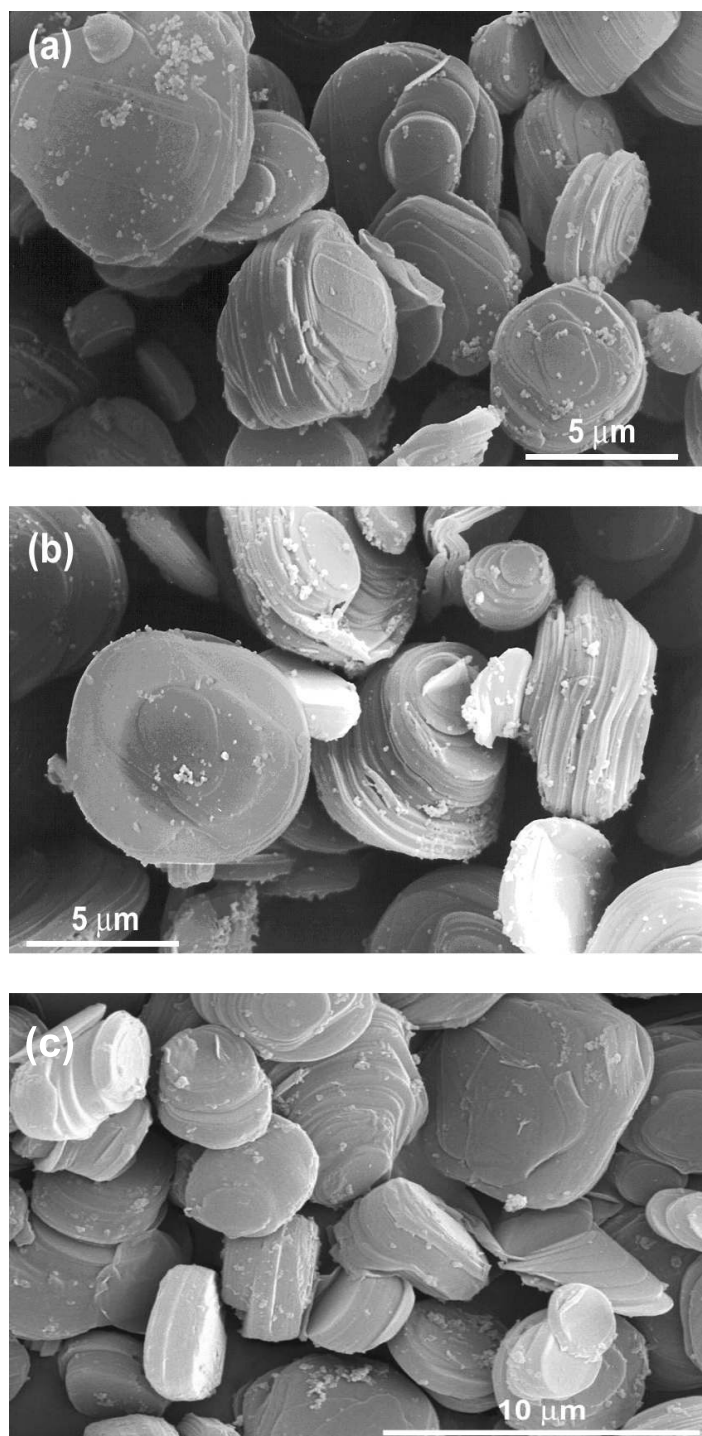


Fig. F.15: SEM images of $(C_6H_{13}NH_3)[Ti(HPO_4)(PO_4)] \cdot H_2O$: (a) stabilized in air at ambient temperature; (b) treated at $400^\circ\text{Cmin}^{-1}$, and (c) stabilized at ambient temperature in a saturated atmosphere of *n*-hexylamine (60 days).

Bibliography

- [1] G. D. Mateescu and A. Valeriu. *2D NMR: Density Matrix and Product Operator Treatment*. Solomon Press Book, 1993.
- [2] A. Blaquière. *Calcul Matriciel Tome II: Application à la Mécanique Quantique*. Classique Hachette, 1960.
- [3] M. Edén. Computer Simulations in Solid-State NMR.I. Spin Dynamics Theory. *Concepts in Magnetic Resonance Part A*, 17A:117–154, 2003.
- [4] M. Munowitz. *Coherence and NMR*. New York: Wiley, 1988.
- [5] R. R. Ernst, G. Bodenhausen, and A. Wokaun. *Principles of Nuclear Magnetic Resonance in One and Two Dimensions*. Oxford, UK: Clarendon, 1987.
- [6] K. Schmidt-Rohr and H. W. Spiess. *Multidimensional Solid-State NMR and Polymers*. Academic Press, London, 1994.
- [7] M. Mehring and Weberuss V. A. *Object-Oriented Magnetic Resonance. Classes and Objects, Calculations and Computations*. London: Academic, 2001.
- [8] M. H. Levitt. *Spin Dynamics. Basics of Nuclear Magnetic Resonance*. Chichester, UK: Wiley, 2001.
- [9] T. C. Farrar. Density Matrices in NMR Spectroscopy. II. *Concepts in Magnetic Resonance*, 2:55–61, 1990.
- [10] J. J. Sakurai. *Modern Quantum Mechanics*. Addison-Wesley, 2nd edition, 1994.
- [11] M. Bak, J. T. Rasmussen, and N. C. Nielsen. Simpson: A General Simulation Program for Solid-State NMR Spectroscopy. *Journal of Magnetic Resonance*, 147:296–330, 2000.
- [12] W. H. Press, B. P. Flannery, S. A. Teukolsky, and W. T. Wetterling. *Numerical Recipes*. Cambridge Univ. Press, Cambridge, 1986.
- [13] M. E. Rose. *Elementary Theory of Angular Momentum*. John Wiley & Sons, Inc, 1957.
- [14] M. Bak. *Magnitudes and Relative Orientation of Dipolar and Chemical Shielding Tensors Determined Using Homonuclear Rotary Resonance MAS NMR and A Novel Method for Efficient Powder Averaging*. PhD thesis, University of Aarhus, 1996.
- [15] M. Mehring. *Principles of High Resolution NMR in Solids*. Springer-Verlag, Berlin, 1983.
- [16] P. Hodgkinson and L. Emsley. Numerical Simulation of Solid-State NMR Experiments. *Progress in Nuclear Magnetic Resonance Spectroscopy*, 36:201–239, 2000.

- [17] O. N. Antzutkin. Sideband Manipulation in Magic-Angle-Spinning Nuclear Magnetic Resonance. *Progress in Nuclear Magnetic Resonance Spectroscopy*, 35:203-266, 1999.
- [18] D. A. Varshalovich, A. N. Moskalev, and V. K. Khersonskii. *Quantum Theory of Angular Momentum*. World Scientific, Singapore, 1988.
- [19] M. J. Duer. *Solid-State NMR Spectroscopy: Principles and Applications*. Blackwell Science Ltd, 2002.
- [20] C. P. Slichter. *Principles of Magnetic Resonance*. Springer-Verlag, Berlin, 1992.
- [21] M. H. Levitt. The Signs of Frequencies and Phases in NMR. *Journal of Magnetic Resonance*, 126:164-182, 1997.
- [22] M. H. Levitt and O. G. Johannessen. The Signs of Frequencies and Phases in NMR: The Role of Radio-Frequency Mixing. *Journal of Magnetic Resonance*, 142:190-194, 2000.
- [23] S. P. Brown, M. Perez-Torralla, D. Sanz, R. M. Claramunt, and L. Emsley. The Direct Detection of a Hydrogen Bond in the Solid State by NMR through the Observation of a Hydrogen-Bond Mediated ^{15}N - ^{15}N J -Coupling. *Journal of the American Chemical Society*, 124:1152-1153, 2002.
- [24] A. J. Vega. *Encyclopedia of Nuclear Magnetic Resonance*, chapter Quadrupolar Nuclei in Solids, pages 3869-3888. J. Wiley, Chichester, 1996.
- [25] A. Jerschow. From Nuclear Structure to the Quadrupolar NMR interaction and High-Resolution Spectroscopy. *Progress in Nuclear Magnetic Resonance Spectroscopy*, 46:63-78, 2005.
- [26] A. Goldbourt and P. K. Madhu. Multiple-Quantum Magic-Angle Spinning: High-Resolution Solid-State NMR of Half-Integer Spin Quadrupolar Nuclei. *Annual Reports on NMR Spectroscopy*, 54:81-153, 2005.
- [27] L. Frydman and J. S. Harwood. Isotropic Spectra of Half-Integer Quadrupolar Spins from Bidimensional Magic-Angle-Spinning NMR. *Journal of the American Chemical Society*, 117:5367-5368, 1995.
- [28] R. K. Harris. *Encyclopedia of Nuclear Magnetic Resonance*. Wiley, New York, 1995.
- [29] R. K. Harris and A. C. Olivieri. Quadrupolar Effects Transferred to Spin-1/2 Magic-Angle Spinning Spectra of Solids. *Progress in NMR Spectroscopy*, 24:435-456, 1992.
- [30] D. L. VanderHart, H. S. Gutowsky, and T. C. Farrar. Dipole-dipole interactions of a spin-1/2 nucleus with a quadrupole-coupled nucleus. *Journal of the American Chemical Society*, 89:5056-5057, 1967.
- [31] S. Wi and L. Frydman. Residual Dipolar Couplings Between Quadrupolar Nuclei in High Resolution Solid State NMR: Description and Observations in the High-field Limit. *Journal of Chemical Physics*, 112:3248-3260, 2000.
- [32] M. Goldman, P. J. Grandinetti, A. Llor, Z. Olejniczak, and J. R. Sachleben. Theoretical Aspects of Higher-Order Truncations in Solid-State Nuclear Magnetic Resonance. *Journal of Chemical Physics*, 97:8947-8959, 1992.

- [33] Z. Gan. Measuring Amide Nitrogen Quadrupolar Coupling by High-Resolution $^{14}\text{N}/^{13}\text{C}$ NMR Correlation under Magic-Angle Spinning. *Journal of the American Chemical Society*, 128:6040–6041, 2006.
- [34] S. Cavadini, A. Lupulescu, S. Antonijevic, and G. Bodenhausen. Nitrogen-14 nmr spectroscopy using residual dipolar splittings in solids. *Journal of the American Chemical Society*, 128:7706–7707, 2006.
- [35] T. Giavani, H. Bildsøe, J. Skibsted, and H. J. Jakobsen. Determination of Nitrogen Chemical Shift Anisotropy From the Second-Order Cross-Term in ^{14}N MAS NMR Spectroscopy. *Chemical Physics Letters*, 377:426–432, 2003.
- [36] D. Marion and K. Wüthrich. Application of Phase Sensitive Two-dimensional Correlation Spectroscopy (COSY) for Measurements of ^1H - ^1H Spin-Spin Coupling Constants in Proteins. *Biochemical and Biophysical Research Communications*, 113:967–974, 1983.
- [37] A. G. Redfield and R. K. Gupta. Fourier-Transform NMR Spectrometer For Use With H_2O Solutions. *Journal of Chemical Physics*, 54:1418–1419, 1971.
- [38] D. J. States, R. A. Haberkorn, and D. J. Ruben. A Two-Dimensional Nuclear Overhauser Experiment With Pure Absorption Phase in Four Quadrants. *Journal of Magnetic Resonance*, 48:286–292, 1982.
- [39] D. Marion, M. Ikura, R. Tschudin, and A. Bax. Improved Solvent Suppression in One-Dimensional and Two-Dimensional NMR Spectra by Convolution of Time-Domain Data. *Journal of Magnetic Resonance*, 85:393–399, 1989.
- [40] J. Keeler. *Understanding NMR Spectroscopy*. University of Cambridge, UK, 2005.
- [41] D. Massiot, B. Touzo, J. P. Coutures, J. Virlet, P. Florian, and P. J. Grandinetti. Two-Dimensional Magic-Angle Spinning Isotropic Reconstruction Sequences for Quadrupolar Nuclei. *Solid State Nuclear Magnetic Resonance*, 6:73–83, 1996.
- [42] G. Bodenhausen, H. Kogler, and R. R. Ernst. Selection of Coherence-Transfer Pathways in NMR Pulse Experiments. *Journal of Magnetic Resonance*, 58:370–388, 1984.
- [43] K. J. D. Mackenzie and M. E. Smith. *Multinuclear Solid-State Nuclear Magnetic Resonance of Inorganic Materials*. Pergamon Press Inc (Elsevier Science), 2002.
- [44] J. D. van Beek, L. Beaulieu, H. Schäfer, M. Demura, T. Asakura, and B. H. Meier. Solid-State NMR Determination of the Secondary Structure of *Samia cynthia ricini* silk. *Nature*, 405:1077–1079, 2000.
- [45] F. Castellani, B. van Rossum, A. Diehl, M. Schubert, K. Rehbein, and H. Oschkinat. Structure of a Protein Determined by Solid-State Magic-Angle-Spinning NMR Spectroscopy. *Nature*, 420:98–102, 2002.
- [46] R. Tycko. Applications of Solid State NMR to the Structural Characterization of Amyloid Fibrils: Methods and Results. *Progress in Nuclear Magnetic Resonance Spectroscopy*, 42:53–68, 2003.
- [47] E. R. Andrew, A. Bradbury, and R. G. Eades. Nuclear Magnetic Resonance Spectra From a Crystal Rotated at High Speed. *Nature*, 182:1659–1659, 1958.

- [48] I. J. Lowe. Free Induction Decays of Rotating Solids. *Physical Review Letters*, 2:285–287, 1959.
- [49] S. R. Hartmann and E. L. Hahn. Nuclear Double Resonance in the Rotating Frame. *Physical Reviews*, 128:2042–2053, 1962.
- [50] F. M. Lurie and C. P. Slichter. Spin Temperature in Nuclear Double Resonance. *Physical Reviews A*, 133:1108–1122, 1964.
- [51] A. Pines, M. G. Gibby, and J. S. Waugh. Proton-Enhanced NMR of Dilute Spins in Solids. *Journal of Chemical Physics*, 59:569–590, 1973.
- [52] V. Royden. Measurement of the Spin and Gyromagnetic Ratio of C-13 by the Collapse of Spin-Spin Splittings. *Physical Review*, 96:543–544, 1954.
- [53] A. L. Bloom and J. N. Shoolery. Effects of Perturbing Radiofrequency Fields on Nuclear Spin Coupling. *Physical Review*, 97:1261–1265, 1955.
- [54] M. Mehring, A. Pines, W-K. Rhim, and J. S. Waugh. Spin-Decoupling in the Resolution of Chemical Shifts in Solids by Pulsed NMR. *Journal of Chemical Physics*, 54:3239–3240, 1971.
- [55] M. Mehring. *High Resolution NMR Spectroscopy in Solids*. Springer-Verlag, Berlin, 1976.
- [56] Z. Gan. Isotropic NMR Spectra of Half-Integer Quadrupolar Nuclei Using Satellite Transitions and Magic-Angle Spinning. *Journal of the American Chemical Society*, 122:3242–3243, 2000.
- [57] M. M. Maricq and J. S. Waugh. NMR in Rotating Solids. *Journal of Chemical Physics*, 70:3300–331, 1979.
- [58] M. Lee and W. I. Goldberg. Nuclear-Magnetic-Resonance Line Narrowing by a Rotating *rf* Field. *Physical Review*, 140:1261, 1965.
- [59] J. S. Waugh, L. M. Huber, and U. Haeberlen. Approach to High-Resolution NMR in Solids. *Physical Reviews Letters*, 20:180–182, 1968.
- [60] B. C. Gerstein, C. Chow, R. G. Pembleton, and R. C. Wilson. Utility of Pulse Nuclear Magnetic Resonance in Studying Protons in Coals. *Journal of Chemical Physics*, 81:565–570, 1977.
- [61] L. M. Ryan, R. E. Taylor, A. J. Paff, and B. C. Gerstein. An Experimental Study of Resolution of Proton Chemical Shifts in Solids: Combined Multiple Pulse NMR and Magic-Angle Spinning. *Journal of Chemical Physics*, 72:508–515, 1980.
- [62] U. Haeberlen and J.S. Waugh. Coherent Averaging Effects in Magnetic Resonance. *Physical Reviews*, 175:453–467, 1968.
- [63] S. Hafner and D. E. Demco. Solid-State NMR Spectroscopy Under Periodic Modulation by Fast Magic-Angle Sample Spinning and Pulses: A Review. *Solid State Nuclear Magnetic Resonance*, 22:247–274, 2002.
- [64] D. E. Demco, S. Hafner, and H. W. Spiess. Rotation-Synchronized Homonuclear Dipolar Decoupling. *Journal of Magnetic Resonance, Series A*, 116:36–45, 1995.

- [65] S. Hafner and H. W. Spiess. Multiple-Pulse Line Narrowing under Fast Magic-Angle Spinning. *Journal of Magnetic Resonance, Series A*, 121:160–166, 1996.
- [66] C. Filip and S. Hafner. Analysis of Multiple-Pulse Techniques Under Fast MAS Conditions. *Journal of Magnetic Resonance*, 147:250–260, 2000.
- [67] D. P. Burum. Combined Rotation and Multiple Pulse Spectroscopy (CRAMPS). *Concepts in Magnetic Resonance*, 2:213–227, 1990.
- [68] S. Hafner and H. W. Spiess. Multiple-Pulse Assisted Line-Narrowing by Fast Magic-Angle Spinning. *Solid State Nuclear Magnetic Resonance*, 8:17–24, 1997.
- [69] E. Vinogradov, P. K. Madhu, and S. Vega. *Topics in Current Chemistry: New Techniques in Solid-State NMR*, chapter Strategies for High-Resolution Proton Spectroscopy in Solid-State NMR, pages Vol. 246, 33–88. Springer, 2005.
- [70] S. P. Brown and H. W. Spiess. Advanced Solid-State NMR Methods for the Elucidation of Structure and Dynamics of Molecular, Macromolecular, and Supramolecular Systems. *Chemical Reviews*, 101:4125–4155, 2001.
- [71] W. K. Rhim and D. D. Elleman. Analysis of Multiple Pulse NMR in Solids. *Journal of the American Chemical Physics*, 59:3740–3749, 1973.
- [72] P. Mansfield. Symmetrized Pulse Sequences in High Resolution NMR in Solids. *Journal of Physics Chemistry: Solid State Physics*, 4:1444–1452, 1971.
- [73] D. G. Cory. A New Multiple-Pulse Cycle for Homonuclear Dipolar Decoupling. *Journal of Magnetic Resonance*, 94:526–534, 1991.
- [74] D. P. Burum and W. K. Rhim. Analysis of Multiple Pulse NMR in Solids. *Journal of Chemical Physics*, 71:944–956, 1979.
- [75] D. P. Burum and W. K. Rhim. An Improved NMR Technique for Homonuclear Dipolar Decoupling in Solids: Application to Polycrystalline Ice. *Journal of Chemical Physics*, 70:3553–3554, 1979.
- [76] D. P. Burum, M. Linder, and R. R. Ernst. Low-Power Multipulse Line Narrowing in Solid-State NMR. *Journal Magnetic Resonance*, 44:173–188, 1981.
- [77] K. Takegoshi and C. A. McDowell. A “Magic Echo” Pulse Sequence for the High-Resolution NMR Spectra of Abundant Spins in Solids. *Journal Chemical Physics*, 116:100–104, 1985.
- [78] M. Hohwy, P. V. Bower, H. J. Jackobsen, and N. C. Nielsen. A High-Order and Broadband CRAMPS Experiment Using z-Rotational Decoupling. *Journal Chemical Physics*, 97:297–303, 1997.
- [79] D. Sakellariou, A. Lesage, P. Hodgkinson, and L. Emsley. Homonuclear Dipolar Decoupling in Solid-State NMR Using Continuous Phase Modulation. *Chemical Physics Letters*, 319:253–260, 2000.
- [80] A. Lesage, D. Sakellariou, S. Hediger, B. Eléna, P. Charmont, S. Steuernagel, and L. Emsley. Experimental Aspects of Proton NMR Spectroscopy in Solids Using Phase-Modulated Homonuclear Dipolar Decoupling. *Journal of Magnetic Resonance*, 163:105–113, 2003.

- [81] K. Nishimura and A. Naito. Reduction of *rf* Power of Observed Nuclei for H-1-Homonuclear Decoupled Cross-Polarization in Solid-State NMR spectroscopy. *Chemical Physics Letters*, 380:569–576, 2003.
- [82] M. H. Levitt, A. C. Kolbert, A. Bielecki, and D. J. Rubben. High-Resolution ^1H NMR in Solids With Frequency-Switched Multiple-Pulse Sequences. *Solid State Nuclear Magnetic Resonance*, 2:151–163, 1993.
- [83] M. Hohwy and N. C. Nielsen. Systematic Design and Evaluation of Multiple-Pulse Experiments in Nuclear Magnetic Resonance Spectroscopy Using a Semi-Continuous Baker-Campbell-Hausdorff Expansion. *Journal of Chemical Physics*, 109:3780–3791, 1998.
- [84] E. Vinogradov, P. K. Madhu, and S. Vega. Proton Spectroscopy in Solid State Nuclear Magnetic Resonance With Windowed Phase Modulated Lee-Goldburg Decoupling Sequences. *Chemical Physics Letters*, 354:193–202, 2002.
- [85] L. Bosman, P. K. Madhu, S. Vega, and E. Vinogradov. Radio frequency Imperfections in Windowed Phase Modulated LeeGoldburg Decoupliong Experiments. *Journal of Magnetic Resonance*, 169:39–48, 2000.
- [86] A. Goldbourt, E. Vinogradov, G. Goobes, and S. Vega. High Resolution Heteronuclear Correlation NMR Spectroscopy Between Quadrupolar Nuclei and Protons in the Solid State. *Journal of Magnetic Resonance*, 169:342–350, 2004.
- [87] S. P. Brown, A. Lesage, B. Elena, and L. Emsley. Probing Proton-Proton Proximities in the Solid State: High-Resolution Two-Dimensional ^1H - ^1H Double-Quantum CRAMPS NMR Spectroscopy. *Journal of the American Society*, 126:13230–13231, 2004.
- [88] M. H. Levitt. *Encyclopedia of Nuclear Magnetic Resonance*, chapter Symmetry-Based Pulse Sequences in Magic-Angle Spinning Solid-State NMR, pages Vol. 9, 165196. John Wiley & Sons, Ltd, Chichester, 1996.
- [89] P. Mansfield, M. J. Orchard, D. C. Stalker, and K. H. B. Richards. Symmetrized Multipulse Nuclear-Magnetic-Resonance Experiments in Solids: Measurement of the Chemical-Shift Shielding Tensor in Some Compounds. *Physical Review B*, 7:90–105, 1973.
- [90] E. Vinogradov, P. K. Madhu, and S. Vega. High-resolution proton solid-state nmr spectroscopy by phase-modulated lee-goldburg experiment. *Chemical Physics Letters*, 314:443–450, 1999.
- [91] U. Haeberlen. *High Resolution NMR in Solids: Selective Averaging*. Academic Press, New York, 1976.
- [92] W. K. Rhim, D. D. Elleman, and R. W. Vaughan. Enhanced Resolution for Solid State NMR. *Journal Chemical Physics*, 59:3740–3749, 1973.
- [93] W. K. Rhim, D. D. Elleman, L. B. Schreiber, and R. W. Vaughan. Analysis of Multiple Pulse NMR in Solids. II. *Journal of Chemical Physics*, 60:4595–4604, 1974.
- [94] M. Edén and M. H. Levitt. Pulse Sequence Symmetries in the Nuclear Magnetic Resonance of Spinning Solids: Application to Heteronuclear Decoupling. *The Journal of Chemical Physics*, 111:1511–1519, 1999.

- [95] J. S. Waugh. *Encyclopedia of Nuclear Magnetic Resonance*, chapter Average Hamiltonian Theory. John Wiley & Sons, Ltd, Chichester, 1996.
- [96] A. D. Bain and R. S. Dumont. Introduction to Floquet theory: The Calculation of Spinning Sideband Intensities in Magic-Angle Spinning NMR. *Concepts in Magnetic Resonance*, 13:159–170, 2001.
- [97] E. Vinogradov, P. K. Madhu, and S. Vega. Phase Modulated Lee-Goldburg Magic Angle Spinning Proton Nuclear Magnetic Resonance Experiments in the Solid State: A Bimodal Floquet Theoretical Treatment. *Journal of Chemical Physics*, 115:8983–9000, 2001.
- [98] T. S. Untidt and N. Chr. Nielsen. Closed Solution to the Baker-Campbell-Hausdorff Problem: Exact Effective Hamiltonian Theory For Analysis of Nuclear-Magnetic-Resonance Experiments. *Physical Review E*, 65:021108 1–17, 2002.
- [99] B. J. van Rossum, G. J. Boender, F. M. Mulder, J. Raap, T. S. Balaban, A. Holzwarth, K. Schaffner, S. Prytulla, H. Oschkinat, and H. J. M. de Groot. Multidimensional CP-MAS ^{13}C NMR of Uniformly Enriched Chlorophyll. *Spectrochimica Acta Part A*, 54:11671176, 1998.
- [100] B. J. van Rossum, D. B. Steensgaard, F. M. Mulder, G. J. Boender, K. Schaffner, A. R. Holzwarth, and H. J. M. Groot. A Refined Model of the Chlorosomal Antennae of the Green bacterium chlorobium tepidum From Proton Chemical Shift Constraints Obtained With High-Field 2-D and 3-D MAS NMR Dipolar Correlation Spectroscopy. *Biochemistry*, 40:1587–1595, 2001.
- [101] B. J. van Rossum, Schulten, E. A. M., Raap, J., Oschkinat, H., and H. J. M. de Groot. A 3-D Structural Model of Solid Self-Assembled Chlorophyll a/H₂O From Multispin Labeling and MAS NMR 2-D Dipolar Correlation Spectroscopy in High Magnetic Field. *Journal of Magnetic Resonance*, 155:1–14, 2002.
- [102] B. J. van Rossum, F. Castellani, K. Rehbein, J. Pauli, and H. Oschkinat. Assignment of the nonexchanging protons of the alpha-spectrin sh3 domain by two- and three-dimensional h-1-c-13 solid-state magic-angle spinning nmr and comparison of solution and solid-state proton chemical shifts. *ChemBioChem*, 2:906–914, 2001.
- [103] J. Trebosc, J. W. Wiench, S. Huh, V. S.-Y. Lin, and M. Pruski. Studies of Organically Functionalized Mesoporous Silicas Using Heteronuclear Solid-State Correlation NMR Spectroscopy under Fast Magic Angle Spinning. *Journal of the American Chemical Society*, 127:7587–7593, 2005.
- [104] D. Massiot, B. Alonso, F. Fayon, F. Fredoueil, and B. Bujoli. New NMR Developments For Structural Investigation of Proton-Bearing Materials at Different Length Scales. *Solid State Sciences*, 3:11–16, 2001.
- [105] L. Mafra, F. A. A. Paz, J. Rocha, A. Espina, S. A. Khainakov, J. R. Garcia, and C. Fernandez. Structural Characterization of Layered γ -Titanium Phosphate (C₆H₁₃NH₃)[Ti(HPO₄)(PO₄)] · H₂O. *Chemistry of Materials*, 17:6287–6294, 2005.
- [106] L. Mafra, F. A. A. Paz, F. N. Shi, R. A. Ferreira, L. D. Carlos, T. Trindade, C. Fernandez, J. Klinowski, and J. Rocha. Crystal structure, Solid-State NMR and Photoluminescence studies of Organic-Inorganic Hybrid Materials

- (HL)₆[Ge₆(OH)₆(hedp)₆]·2(L)·nH₂O, L=hqn or phen. *European Journal of Inorganic Chemistry*, Submitted, 2006.
- [107] L. Mafra, F. A. A. Paz, F. N. Shi, J. Rocha, T. Trindade, C. Fernandez, A. Makal, K. Wozniak, and J. Klinowski. X-ray Diffraction and Solid-State NMR Studies of a Germanium Binuclear Complex. *Chemistry-A European Journal*, 12:363–375, 2006.
- [108] L. Mafra, J. Rocha, C. Fernandez, and F. A. A. Paz. Characterization of Microporous Aluminophosphate IST-1 Using H-1 Lee-Goldburg Techniques. *Journal of Magnetic Resonance*, 180:236–244, 2006.
- [109] D. Massiot, F. Fayon, M. Capron, I. King, S. Le Calve, B. Alonso, J. O. Durand, B. Bujoli, Z. H. Gan, and G. Hoatson. Modelling One- and Two-Dimensional Solid-State NMR Spectra. *Magnetic Resonance in Chemistry*, 40:70–76, 2002.
- [110] R. Frantz, J.-O. Durand, F. Carré, G. F. Lanneau, J. Le Bideau, B. Alonso, and D. Massiot. Synthesis and Solid-State NMR Studies of p-Vinylbenzylphosphonic Acid. *Chemistry: A European Journal*, 9:770–775, 2003.
- [111] K. Murata, H. Kono, E. Katoh, S. Kuroki, and I. Ando. A Study of Conformational Stability of Polypeptide Blends by Solid State Two-Dimensional C-13-H-1 Heteronuclear Correlation NMR Spectroscopy. *Polymer*, 44:4021–4027, 2003.
- [112] J. Brus and J. Dybal. Hydrogen-Bond Interactions in Organically-Modified Polysiloxane Networks Studied by 1D and 2D CRAMPS and Double-Quantum H-1 MAS NMR. *Macromolecules*, 35:10038–10047, 2002.
- [113] R. Q. Fu, C. L. Tian, and T. A. Cross. NMR Spin Locking of Proton Magnetization Under a Frequency-Switched Lee-Goldburg Pulse Sequence. *Journal of Magnetic Resonance*, 154:130–135, 2002.
- [114] S. V. Dvinskikh, Z. Luz, H. Zimmermann, A. Maliniak, and D. Sandstrom. Molecular Characterization of Hexaoctyloxy-Rufigallol in the Solid and Columnar Phases: A Local Field NMR Study. *Journal of Physical Chemistry B*, 107:1969–1976, 2003.
- [115] R. Q. Fu. Measurement of N-15-H-1 Bond Lengths by Rotational-Echo Double-Resonance NMR Spectroscopy. *Chemical Physics Letters*, 376:62–67, 2003.
- [116] A. Lesage, L. Emsley, M. Chabanas, C. Copret, and J.-M. Basset. Observation of a H-Agostic Bond in a Highly Active Rhenium-Alkylidene Olefin Metathesis Heterogeneous Catalyst by Two-Dimensional Solid-State NMR Spectroscopy. *Angewandte Chemie International Edition*, 41:4535–4538, 2002.
- [117] D. Sakellariou, A. Lesage, and L. Emsley. Spectral Editing in Solid-State NMR Using Scalar Multiple Quantum Filters. *Journal of Magnetic Resonance*, 151:40–47, 2001.
- [118] A. Lesage and L. Emsley. Through-Bound Heteronuclear Single-Quantum Correlation Spectroscopy in Solid-State NMR, and Comparison to Other Through-Bound and Through-Space Experiments. *Journal of Magnetic Resonance*, 148:449–454, 2001.
- [119] H. Kono, T. Erata, and M. Takai. Determination of the Through-Bond Carbon-Carbon and Carbon-Proton Connectivities of the Native Celluloses in the Solid State. *Macromolecules*, 36:5131–5138, 2003.

- [120] A. Lesage, S. Steuernagel, , and L. Emsley. Carbon-13 Spectral Editing in Solid-State NMR Using Heteronuclear Scalar Couplings. *Journal of the American Society*, 120:7095–7100, 1998.
- [121] S. Hediger, A. Lesage, and L. Emsley. A New NMR Method for the Study of Local Mobility in Solids and Application to Hydration of Biopolymers in Plant Cell Walls. *Macromolecules*, 35:5078–5084, 2002.
- [122] B. J. van Rossum, H. Forster, and H. J. M. de Groot. High-Field and High-Speed CP-MAS C-13 NMR Heteronuclear Dipolar-Correlation Spectroscopy of Solids with Frequency- Switched Lee-Goldburg Homonuclear Decoupling. *Journal Magnetic Resonance*, 124:516–519, 1997.
- [123] D. Huster, X. Yao, and M. Hong. Membrane Protein Topology Probed by ^1H Spin Diffusion from Lipids Using Solid-State NMR Spectroscopy. *Journal of the American Chemical Society*, 124:874–883, 2002.
- [124] A. E. Bennett, C. M. Rienstra, M. Auger, and K. V. Lakshmi. Heteronuclear Decoupling in Rotating Solids. *Journal of Chemical Physics*, 103:6951–6958, 1995.
- [125] B. M. Fung, A. K. Khitrin, and K. Ermolaev. An Improved Broadband Decoupling Sequence For Liquid Crystals and Solids. *Journal of Magnetic Resonance*, 142:97–101, 2000.
- [126] P. Hodgkinson. Heteronuclear Decoupling in the NMR of Solids. *Progress in Nuclear Magnetic Resonance Spectroscopy*, 46:197–222, 2005.
- [127] M. Goldman. *Spin Temperature and Nuclear Magnetic Resonance in Solids*. Oxford Univ. Press, London, 1970.
- [128] J. Schaefer and E. O. Stejskal. Carbon-13 Nuclear Magnetic Resonance of Polymers Spinning at the Magic Angle. *Journal of the American Chemical Society*, 98:1031–1032, 1976.
- [129] A. Samoson, T. Tuherm, J. Past, A. Reinhold, T. Anup old, and I. Heinmaa. *Topics in Current Chemistry: New Horizons for Magic-Angle Spinning NMR*. Springer-Verlag Berlin Heidelberg, 246: 1531, 2004.
- [130] M. Karmaoui, L. Mafra, R. A. S. Ferreira, J. Rocha, L. D. Carlos, and N. Pinna. Photoluminescent Rare-Earth Based Biphenolate Lamellar Nanostructures. *Journal of Physical Chemistry C*, Submitted, 2006.
- [131] Y. K. Lee, N. D. Kurur, M. Helmle, O. G. Johannessen, Nielsen N. C., and Levitt M. H. Efficient Dipolar Recoupling in the NMR of Rotating Solids - a Sevenfold Symmetrical Radiofrequency Pulse Sequence. *Chemical Physics Letters*, 242:304–309, 1995.
- [132] M. Hohwy, H. J. Jakobsen, M. Edén, M. H. Levitt, and N. C. Nielsen. Broadband Dipolar Recoupling in the Nuclear Magnetic Resonance of Rotating Solids: A Compensated C7 Pulse Sequence. *Journal of Chemical Physics*, 108:2686, 1998.
- [133] B.-Q. Sun, P. R. Costa, D. Kocisko, Jr. P. T. Lansbury, and R. G. Griffin. Internuclear Distance Measurements in Solid State Nuclear Magnetic Resonance: Dipolar Recoupling Via Rotor Synchronized Spin Locking. *The Journal of Chemical Physics*, 102:702–707, 1995.

- [134] M. Feike, R. Graf, I. Schnell, C. Jager, and H. W. Spiess. Structure of Crystalline Phosphates From P-31 Double-Quantum NMR Spectroscopy. *Journal of the American Chemical Society*, 118:9631–9634, 1996.
- [135] B. H. Meier and William L. Earl. Excitation of Multiple Quantum Transitions Under Magic Angle Spinning Conditions: Adamantane. *The Journal of Chemical Physics*, 85:4905–4911, 1986.
- [136] W. Sommer, J. Gottwald, D. E. Demco, and H. W. Spiess. Dipolar Heteronuclear Multiple-Quantum NMR Spectroscopy in Rotating Solids. *Journal of Magnetic Resonance Series A*, 113:131–134, 1995.
- [137] M. Feike, D. E. Demco, R. Graf, J. Gottwald, S. Hafner, and H. W. Spiess. Broadband Multiple-Quantum NMR Spectroscopy. *Journal of Magnetic Resonance, Series A*, 122:214–221, 1996.
- [138] I. Schnell. Dipolar Recoupling in Fast-MAS Solid-State NMR Spectroscopy. *Progress in Nuclear Magnetic Resonance Spectroscopy*, 45:145–207, 2004.
- [139] I. Schnell and H. W. Spiess. High-Resolution H-1 NMR Spectroscopy in the Solid State: Very fast Sample Rotation and Multiple-Quantum Coherences. *Journal of Magnetic Resonance*, 151:153–227, 2001.
- [140] J. Baum, M. Munowitz, A. N. Garroway, and A. Pines. Multiple-quantum dynamics in solid state nmr. *The Journal of Chemical Physics*, 83:2015–2025, 1985.
- [141] A. Clearfield, C. V. K. Sharma, and B. P. Zhang. Crystal Engineered Supramolecular Metal Phosphonates: Crown Ethers and Iminodiacetates. *Chemistry of Materials*, 13:3099–3112, 2001.
- [142] P. J. Hagrman, D. Hagrman, and J. Zubietta. Organic-Inorganic Hybrid Materials: From "Simple" Coordination Polymers to Organodiamine-Templated Molybdenum Oxides. *Angewandte Chemie-International Edition*, 38:2639–2684, 1999.
- [143] D. M. Poojary and A. Clearfield. Application of X-ray Powder Diffraction Techniques to the Solution of Unknown Crystal Structures. *Accounts of Chemical Research*, 30:414–422, 1997.
- [144] R. K. Harris. NMR Crystallography: The Use of Chemical Shifts. *Solid State Sciences*, 6:1025–1037, 2004.
- [145] E. Brunner and U. Sternberg. Solid-State NMR Investigations on the Nature of Hydrogen Bonds. *Progress in Nuclear Magnetic Resonance Spectroscopy*, 32:21–57, 1998.
- [146] R. K. Harris, P. Jackson, L. H. Merwin, B. J. Say, and G. Hagele. Perspectives in High-Resolution Solid-State Nuclear Magnetic-Resonance, with Emphasis on Combined Rotation and Multiple-Pulse Spectroscopy. *Journal of the Chemical Society-Faraday Transactions I*, 84:3649–3672, 1988.
- [147] S. P. Brown, I. Schnell, J. D. Brand, K. Mullen, and H. W. Spiess. The Competing Effects of π - π Packing and Hydrogen Bonding in a Hexabenzocoronene Carboxylic Acid Derivative: A H-1 Solid-State MAS NMR Investigation. *Physical Chemistry Chemical Physics*, 2:1735–1745, 2000.

- [148] G. R. Goward, M. F. H. Schuster, D. Sebastiani, I. Schnell, and H. W. Spiess. High-Resolution Solid-State NMR Studies of Imidazole-Based Proton Conductors: Structure Motifs and Chemical Exchange From H-1 NMR. *Journal of Physical Chemistry B*, 106:9322–9334, 2002.
- [149] I. Schnell, S. P. Brown, H. Y. Low, H. Ishida, and H. W. Spiess. An Investigation of Hydrogen Bonding in Benzoxazine Dimers by Fast Magic-angle Spinning and Double-Quantum H-1 NMR Spectroscopy. *Journal of the American Chemical Society*, 120:11784–11795, 1998.
- [150] A. E. Aliev and K. D. M. Harris. *Probing Hydrogen Bonding in Solids Using Solid State NMR Spectroscopy*. Springer-Verlag Berlin, 2004.
- [151] S. Pawsey, M. McCormick, S. De Paul, R. Graf, Y. S. Lee, L. Reven, and H. W. Spiess. H-1 Fast MAS NMR Studies of Hydrogen-Bonding Interactions in Self-Assembled Monolayers. *Journal of the American Chemical Society*, 125:4174–4184, 2003.
- [152] H. Z. Liu, S. X. Zheng, and K. M. Nie. Morphology and Thermomechanical Properties of Organic-Inorganic Hybrid Composites Involving Epoxy Resin and an Incompletely Condensed Polyhedral Oligomeric Silsesquioxane. *Macromolecules*, 38:5088–5097, 2005.
- [153] Y. S. Chiu, K. H. Wu, and T. C. Chang. Miscibility and Dynamics of the Poly(Vinylimidazole-co-Methyl Methacrylate)-Silica Hybrids Studied by Solid-State NMR. *European Polymer Journal*, 39:2253–2259, 2003.
- [154] Y. K. Seo, S. B. Park, and D. H. Park. Mesoporous Hybrid Organosilica Containing Urethane Moieties. *Journal of Solid State Chemistry*, 179:1285–1288, 2006.
- [155] J. J. E. Moreau, L. Vellutini, M. W. C. Man, C. Bied, P. Dieudonne, J. L. Bantignies, and J. L. Sauvajol. Lamellar Bridged Silsesquioxanes: Self-Assembly Through a Combination of Hydrogen Bonding and Hydrophobic-Interactions. *Chemistry-A European Journal*, 11:1527–1537, 2005.
- [156] E. Lindner, S. Brugger, S. Steinbrecher, E. Plies, and H. A. Mayer. Investigations on the Mobility of Novel Sol-Gel Processed Inorganic-Organic Hybrid Materials. *Journal of Materials Chemistry*, 11:1393–1401, 2001.
- [157] C. S. Wu and H. T. Liao. Polyethylene-Octene Elastomer/Silica Hybrids Prepared by a Sol-Gel process Using Tetraethoxysilane. *Designed Monomers and Polymers*, 6:369–381, 2003.
- [158] S. Vitry, A. Mezzino, C. Gauthier, J. Y. Cavaille, F. Lefebvre, and E. Bourgeat-Lami. Hybrid copolymer latexes cross-linked with methacryloxy propyl trimethoxy silane. Film formation and mechanical properties. *Comptes Rendues Chimie*, 6:1285–1293, 2003.
- [159] F. Belva, S. Bourbigot, S. Duquesne, C. Jama, M. Le Bras, C. Pelegris, and M. Rivenet. Heat and Fire Resistance of Polyurethane-Polydimethylsiloxane Hybrid Materials. *Polymers For Advanced Technologies*, 17:304–311, 2006.
- [160] K. F. Ni, G. R. Shan, Z. X. Weng, N. Sheibat-Othman, G. Fevotte, F. Lefebvre, and E. Bourgeat-Lami. Synthesis of Hybrid Core-Shell Nanoparticles by Emulsion (co)Polymerization of Styrene and γ -Methacryloxypropyltrimethoxysilane. *Macromolecules*, 38:7321–7329, 2005.

- [161] T. M. Lee, C. C. M. Ma, C. W. Hsu, and H. L. Wu. Effect of Molecular Structures and Mobility on the Thermal and Dynamical Mechanical Properties of Thermally Cured Epoxy-Bridged Polyorganosiloxanes. *Polymer*, 46:8286–8296, 2005.
- [162] P. Innocenzi, G. Brusatin, S. Licocchia, M. L. Di Vona, F. Babonneau, and B. Alonso. Controlling the Thermal Polymerization Process of Hybrid Organic Anorganic Films Synthesized From 3-Methacryloxypropyltrimethoxysilane and 3-Aminopropyltriethoxysilane. *Chemistry of Materials*, 15:4790–4797, 2003.
- [163] J. S. Chung, D. J. Kim, W. S. Ahn, J. H. Ko, and W. J. Cheong. Synthesis, characterization, and applications of organic-inorganic hybrid mesoporous silica. *Korean Journal of Chemical Engineering*, 21:132–139, 2004.
- [164] S. R. Davis, A. R. Brough, and A. Atkinson. Formation of Silica/Epoxy Hybrid Network Polymers. *Journal of Non-Crystalline Solids*, 315:197–205, 2003.
- [165] W. J. Liang, H. M. Kao, and P. L. Kuo. Solid Polymer Electrolytes, Morphology and Ionic Conductivity Studies of Hybrid Electrolytes Based on Epoxide-Crosslinked Polysiloxane/Polyether Networks. *Macromolecular Chemistry and Physics*, 205:600–610, 2004.
- [166] C. Lesaint, F. Frebault, C. Delacote, B. Lebeau, C. Marichal, A. Walcarius, and J. Patarin. Synthesis and Characterization of Mesoporous Silicas Functionalized by Thiol Groups, and Application as Sorbents for Mercury (II). *Nanoporous Materials IV*, 156:925–932, 2005.
- [167] A. Jimenez-Morales, P. Aranda, and J. C. Galvan. Nanocomposite Materials Based on Organopolysiloxane/Macrocycle Systems for Electrochemical Sensors. *Journal of Materials Processing Technology*, 143:5–10, 2003.
- [168] T. Loiseau, G. Ferey, M. Haouas, and F. Taulelle. Structural Analysis of F/OH Distribution in a Hybrid Open-Framework Fluorinated Gallium Oxalate-Phosphate Templated by 1,3-Diaminopropane (MIL-90). *Chemistry of Materials*, 16:5318–5326, 2004.
- [169] G. Mali, N. Rajic, N. Z. Logar, and V. Kaucic. Solid-State NMR Study of an Open-Framework Aluminophosphate-Oxalate Hybrid. *Journal of Physical Chemistry B*, 107:1286–1292, 2003.
- [170] V. Lafond, C. Gervais, J. Maquet, D. Prochnow, F. Babonneau, and P. H. Mutin. O-17 MAS NMR Study of the Bonding Mode of Phosphonate Coupling Molecules in a Titanium Oxo-Alkoxo-Phosphonate and in Titania-Based Hybrid Materials. *Chemistry of Materials*, 15:4098–4103, 2003.
- [171] S. C. Christiansen, N. Hedin, J. D. Epping, M. T. Janicke, Y. del Amo, M. Demarest, M. Brzezinski, and B. F. Chmelka. Sensitivity Considerations in Polarization Transfer and Filtering Using Dipole-Dipole Couplings: Implications For Biomineral Systems. *Solid State Nuclear Magnetic Resonance*, 29:170–182, 2006.
- [172] M. Wilhelm, H. Feng, U. Tracht, and H. W. Spiess. 2D CP/MAS C-13 Isotropic Chemical Shift Correlation Established by H-1 Spin Diffusion. *Journal of Magnetic Resonance*, 134:255–260, 1998.
- [173] Stoe. *Win XPOW THEO Version 1.15*. STOE & Cie GmbH, 1999.

- [174] Kuma. *CRYNALIS CCD, Kuma Diffraction, Wroclaw, Poland*. 1999.
- [175] Kuma. *CRYNALIS RED, Kuma Diffraction, Wroclaw, Poland*. 1999.
- [176] R. Hoofst. Collect: Data collection software, 1998.
- [177] Z. Otwinowski and W. Minor. Methods in Enzymology. In C.W. Carter Jr. and R.M. Sweet, editors, *Methods in Enzymology*, volume 276 of *Macromolecular Crystallography, Part A*, page 307. Academic Press, New York, 1997.
- [178] R. H. Blessing. Outlier Treatment in Data Merging. *Journal of Applied Crystallography*, 30:421–426, 1997.
- [179] R. H. Blessing. An Empirical Correction for Absorption Anisotropy. *acta crystallographica A*, 51:33–38, 1995.
- [180] M. Eddaoudi, D. B. Moler, H. L. Li, B. L. Chen, T. M. Reineke, M. O’Keeffe, and O. M. Yaghi. Modular Chemistry: Secondary Building Units as a Basis For the Design of Highly Porous and Robust Metal-Organic Carboxylate frameworks. *Accounts of Chemical Research*, 34:319–330, 2001.
- [181] M. Eddaoudi, H. L. Li, and O. M. Yaghi. Highly Porous and Stable Metal-Organic Frameworks: Structure Design and Sorption Properties. *Journal of the American Chemical Society*, 122:1391–1397, 2000.
- [182] R. Murugavel, M. G. Walawalkar, M. Dan, H. W. Roesky, and C. N. R. Rao. Transformations of Molecules and Secondary Building Units to Materials: A Bottom-Up Approach. *Accounts of Chemical Research*, 37:763–774, 2004.
- [183] P. Ayyappan, O. R. Evans, B. M. Foxman, K. A. Wheeler, T. H. Warren, and W. B. Lin. New Open Frameworks Based on Metal Pyridylphosphonates. *Inorganic Chemistry*, 40:5954–5961, 2001.
- [184] B. L. Zhang, D. M. Poojary, and A. Clearfield. Synthesis and Crystal Structure of the Linear Chain Zirconium Organophosphonate $(\text{NH}_4)\text{Zr}[\text{F}_2][\text{H}_3\{\text{O}_3\text{PCH}_2\text{NH}(\text{CH}_2\text{CO}_2)_2\}_2]\cdot 3\text{H}_2\text{O}\cdot\text{NH}_4\text{Cl}$. *Inorganic Chemistry*, 37:249–254, 1998.
- [185] M. P. Jensen, J. V. Beitz, R. D. Rogers, and K. L. Nash. Thermodynamics and Hydration of the Europium Complexes of a Nitrogen Heterocycle Methane-1,1-Diphosphonic Acid. *Journal of the Chemical Society-Dalton Transactions*, pages 3058–3064, 2000.
- [186] D. M. Poojary, B. L. Zhang, and A. Clearfield. Structure of a Mixed Phosphate Phosphonate Layered Zirconium Compound from Synchrotron X-Ray-Powder Diffraction Data. *Angewandte Chemie-International Edition in English*, 33:2324–2326, 1994.
- [187] J. G. Mao, Z. Wang, and A. Clearfield. New Lead Inorganic-Organic Hybrid Microporous and Layered Materials: Synthesis, Properties, and Crystal Structures. *Inorganic Chemistry*, 41:6106–6111, 2002.
- [188] Z. Wu, Z. Liu, P. Tian, Y. Yang, L. Xu, H. Song, X. Bao, X. Liu, and X. Liu. Syntheses and Structures of sodium Aluminodiphosphonates With Different Morphologies (Diphosphonate=1-Hydroxyethylidenediphosphonate). *Journal of Crystal Growth*, 264:400–408, 2004.

- [189] K. L. Nash, R. D. Rogers, J. Ferraro, and J. Zhang. Lanthanide Complexes With 1-Hydroxyethane-1,1-Diphosphonic Acid: Solvent Organization and Coordination Geometry in Crystalline and Amorphous Solids. *Inorganica Chimica Acta*, 269:211–223, 1998.
- [190] V. Deluchat, S. Lacour, B. Serpaud, and J-C. Bollinger. Washing Powders and the Environment: Has TAED Any Influence On the Complexing Behaviour of Phosphonic Acids? *Water Research*, 36:4301–4306, 2002.
- [191] D. C. Crans, F. L. Jiang, O. P. Anderson, and S. M. Miller. Dinuclear Oxovanadium(IV) *N*-(Phosphonomethyl)iminodiacetate Complexes: $Na_4[V_2O_2\{(O)_2P(O)CH_2N(CH_2COO)_2\}_2] \cdot 10H_2O$ and $Na_8V_2O_2\{(O)_2P(O)CH_2N(CH_2COO)_2\}_2 \cdot 16H_2O$. *Inorganic Chemistry*, 37:6645–6655, 1998.
- [192] S. O. H. Gutschke, D. J. Price, A. K. Powell, and P. T. Wood. Solvothermal Synthesis of the Canted Antiferromagnet $K_2[Co(O_3PCH_2N(CH_2CO_2)_2)_6 \cdot xH_2O]$. *Angewandte Chemie-Internation Edition*, 38:1088–1090, 1999.
- [193] J. G. Mao and A. Clearfield. Metal Carboxylate-Phosphonate Hybrid Layered Compounds: Synthesis and Single Crystal Structures of Novel Divalent Metal Complexes With *N*-(Phosphonomethyl)iminodiacetic Acid. *Inorganic Chemistry*, 41:2319–2324, 2002.
- [194] H. X. Pei, S. M. Lu, Y. X. Ke, J. M. Li, S. B. Qin, S. X. Zhou, X. T. Wu, and W. X. Du. Synthesis and Crystal Structure of a New Copper-PMIDA Compound ($H_4PMIDA=H_2O_3PCH_2N(CH_2CO_2H)_2$). *Structural Chemistry*, 15:207–210, 2004.
- [195] F. A. A. Paz, F. N. Shi, J. Klinowski, J. Rocha, and T. Trindade. Synthesis and Characterisation of the First Three-Dimensional Mixed-Metal-Center Inorganic-Organic Hybrid Framework With *N*-(Phosphonomethyl)iminodiacetate. *European Journal of Inorganic Chemistry*, 13:2759–2768, 2004.
- [196] T. Kottke and D. Stalke. Crystal Handling at Low-Temperatures. *Journal of Applied Crystallography*, 26:615–619, 1993.
- [197] G. M. Sheldrick. *SHELXS-97, Program for Crystal Structure Solution*, University of Göttingen. University of Göttingen, 1997.
- [198] G. M. Sheldrick. *SHELXL-97, Program for Crystal Structure Refinement*, University of Göttingen. University of Göttingen, 1997.
- [199] G. Metz, X. L. Wu, and S. O. Smith. Ramped-Amplitude Cross-Polarization in Magic-Angle-Spinning NMR. *Journal of Magnetic Resonance Series A*, 110:219–227, 1994.
- [200] C. Foces-Foces, A. Echevarria, N. Jagerovic, I. Alkorta, J. Elguero, U. Langer, O. Klein, M. Minguet-Bonvehi, and H. H. Limbach. A Solid-State NMR, X-ray Diffraction, and *ab initio* Computational Study of Hydrogen-Bond Structure and Dynamics of Pyrazole-4-Carboxylic Acid Chains. *Journal of the American Chemical Society*, 123:7898–7906, 2001.
- [201] A. Lesage, L. Duma, D. Sakellariou, and L. Emsley. Improved Resolution in Proton NMR Spectroscopy of Powdered Solids. *Journal of the American Chemical Society*, 123:5747–5752, 2001.

- [202] C. E. Hughes, R. Pratima, T. Karlsson, and M. H. Levitt. Double-Quantum Solid-State NMR of C-13 Spin Pairs Coupled to N-14. *Journal of Magnetic Resonance*, 159:25–35, 2002.
- [203] J-P. Amoureux, C. Fernandez, and S. Steuernagel. Z-filtering in MQMAS NMR. *Journal of Magnetic Resonance, Series A*, 123:116–118, 1996.
- [204] S. R. Batten and R. Robson. Interpenetrating Nets: Ordered, Periodic Entanglement. *Angewandte Chemie-International Edition*, 37:1461–1494, 1998.
- [205] C. Bibal, S. Mazieres, H. Gornitzka, and C. Couret. From Chlorogermynes to Stable Hydroxy- and Siloxy-Germylene- Tungsten Complexes. *Organometallics*, 21:2940–2943, 2002.
- [206] H. C. Chiang, S. M. Lin, and C. H. Ueng. Synthesis and Structure of Dihydroxo(Eta-3-2,2'- Iminodiethoxo)Germanium(IV). *Acta Crystallographica C*, 48:991–993, 1992.
- [207] C. Glidewell, M. B. Hursthouse, D. Lloyd, K. W. Lumbard, and R. L. Short. The Crystal and Molecular-Structure of Di[Bis(Trimethylsilyl)Amino]Dihydroxygermane. *Journal of Chemical Research, Synopses*, pages 400–401, 1986.
- [208] R. R. Holmes, R. O. Day, A. C. Sau, C. A. Poutasse, and J. M. Holmes. Stereochemically Nonrigid 5-Coordinated Germanates - Synthesis and Structure of Hydroxy-Containing and Halo-Containing Spirocyclic Germanium(IV) Complexes. *Inorganic Chemistry*, 24:193–199, 1985.
- [209] A. B. Ilyukhin, L. M. Shkolnikova, I. I. Seifullina, T. P. Batalova, and N. M. Dyatlova. Synthesis, Structure and Properties of Germanium(IV) Complex with Genta(H₂O)(OH)-2H₂O Nitriloacetic Acid. *Koord. Khimiya*, 17:795–800, 1991.
- [210] S. J. Lin, Y. J. Chen, J. H. Chen, F. L. Liao, S. L. Wang, and S. S. Wang. Crystal Structures of Chloro(Meso-Tetraphenylporphyrinato)Germanium(IV), Ge(tpp)Cl₂, and Dihydroxo(Meso-Tetraphenylporphyrinato)Germanium(IV), Ge(tpp)(OH)₂, and Two-Stage Hydrolysis of its Homologue Dimethoxo(Meso-Tetraphenylporphyrinato)Germanium(IV), Ge(tpp)(OMe)₂. *Polyhedron*, 16:2843–2850, 1997.
- [211] T. Mizuta, T. Yoshida, and K. Miyoshi. A Novel Structure of Spontaneously Resolved Germanium(IV) Complex with Ethylenediaminetriacetatemonoacetic Acid (Hedta). *Inorganica Chimica Acta*, 165:65–71, 1989.
- [212] J. Bernstein, R. E. Davis, L. Shimoni, and N. L. Chang. Patterns in Hydrogen Bonding - Functionality and Graph Set Analysis in Crystals. *Angew. Chem. Int. Edit.*, 34:1555–1573, 1995.
- [213] A. Ben Akacha, S. Barkallah, and H. Zantour. C-13 NMR and P-31 NMR Spectral Assignment of New β -Phosphonylated hydrazones. *Magnetic Resonance in Chemistry*, 37:916–920, 1999.
- [214] E. Gacs-Baitz, L. A. Wozniak, and M. Kajtar-Peredy. Conformational Properties of Diastereomeric 5'-O-DMT-2' Deoxythymidine 3'-O-(S-Methylmethanephosphonothiolate)s and - (se-Methyl-Methanephosphonoselenolate)s in Solution as Studied by NMR Methods. *Chirality*, 12:675–680, 2000.

- [215] F. F. Khizbullin, B. P. Strunin, E. I. Maslennikov, Y. B. Yasman, and V. D. Simonov. Investigation of Some Aminophosphonates by High-Resolution NMR in the Solid. *Journal of Structural Chemistry*, 27:394–398, 1986.
- [216] J. Z. Hu, F. Zhou, F. Deng, F. Hanqiao, N. Yang, L. Li, and C. Ye. High Resolution ^1H Spectra of Powdered Solids Observed by Hahn Echo Pulse Sequence With Magic-Angle Spinning. *Solid State NMR*, 6:85–94, 1996.
- [217] L. M. Shkolnikova, M. A. Poraikoshits, N. M. Dyatlova, G. F. Yaroshenko, M. V. Rudomino, and E. K. Kolova. X-Ray Structural Study of Organic-Ligands of the Complexone Type .3. Crystal and Molecular-Structure of Phosphonomethylglycine and Iminodiacetic-Monomethylphosphonic Acid. *Journal of Structural Chemistry*, 23:737–746, 1982.
- [218] R. M. Silverstein and F. X Webster. *Spectroscopic Identification of Organic Compounds*. John Wiley & Sons, Inc., New York, 6th edition, 1998.
- [219] J. Brus and A. Jegorov. Through-Bonds and Through-Space Solid-State NMR Correlations at Natural Isotopic Abundance: Signal Assignment and Structural Study of Simvastatin. *Journal of Physical Chemistry A*, 108:3955–3964, 2004.
- [220] M. Hong, X. L. Yao, K. Jakes, and D. Huster. Investigation of Molecular Motions by Lee-Goldburg Cross-Polarization NMR Spectroscopy. *Journal of Physical Chemistry B*, 106:7355–7364, 2002.
- [221] V. Ladizhansky and S. Vega. Polarization Transfer Dynamics in Lee-Goldburg Cross Polarization Nuclear Magnetic Resonance Experiments on Rotating Solids. *Journal of Chemical Physics*, 112:7158–7168, 2000.
- [222] G.B. Deacon and R.J. Phillips. Relationships Between the Carbon-Oxygen Stretching Frequencies of Carboxylate Complexes and the Type of Carboxylate Coordination. *Coordination Chemical Reviews*, 33:227–250, 1980.
- [223] C. Oldham. Carboxylates, squarates and related species. In Sir Geoffrey Wilkinson, editor, *Comprehensive Coordination Chemistry*, volume 2, pages 435–459. Pergamon Press, 1st edition, 1987.
- [224] A. Banerjee, S. K. Maji, M. G. B. Drew, D. Halder, and A. Banerjee. An Amyloid-Like Fibril Forming Antiparallel Supramolecular β -Sheet From a Synthetic Tripeptide: a Crystallographic Signature. *Tetrahedron Letters*, 44:6741–6744, 2003.
- [225] A. E. Bennett, J. H. Ok, R. G. Griffin, and S. Vega. Chemical-Shift Correlation Spectroscopy in Rotating Solids - Radio Frequency-Driven Dipolar Recoupling and Longitudinal Exchange. *Journal of Chemical Physics*, 96:8624–8627, 1992.
- [226] A. E. Bennett, C. M. Rienstra, J. M. Griffiths, W. Zhen, P. T. Lansbury, Jr., and R. G. Griffin. Homonuclear Radio Frequency-Driven Recoupling in Rotating Solids. *Journal of Chemical Physics*, 108:9463–9479, 1998.
- [227] A. Bielecki, A.C. Kolbert, and M.H. Levitt. Frequency-Switched Pulse Sequences: Homonuclear Decoupling and Dilute Spin NMR in Solids. *Chemical Physics Letters*, 155:341–346, 1989.

- [228] P. van der Sluis and A. L. Spek. BYPASS: An Effective Method For the Refinement of Crystal Structures Containing Disordered Solvent Regions. *Acta Crystallographica A*, 46:194–201, 1990.
- [229] W. T. Pennington. DIAMOND - Visual Crystal Structure Information System. *Journal Applied Crystallography*, 32:1028–1029, 1999.
- [230] <http://www.crystalimpact.com>.
- [231] I. I. Seifullina, E. E. Martsinko, G. G. Aleksandrov, and V. S. Sergienko. Synthesis, Properties, and Structure of Polynuclear Hydroxyethylidene-1,1-Diphosphonatogermanates: Crystal and Molecular Structure of Two Complexes On the Basis of These Compounds. *Russian Journal of Inorganic Chemistry*, 49:844–852, 2004.
- [232] S. Nishigaki, H. Yoshioka, and K. Nakatsu. Crystal and Molecular-Structure of Ortho-Phenanthroline. *Acta Crystallographica B*, 34:875–879, 1978.
- [233] Cerius², Version, and 4.2. *Molecular Simulations Inc.*, 2000.
- [234] F. A. A. Paz and J. Klinowski. Novel cadmium-organic frameworks with nitrilotriacetate. *Journal Physical Organic Chemistry*, 16:772–782, 2003.
- [235] A. L. Spek. Platon. *Acta Crystallographica A*, 46:C34, 1990.
- [236] A. L. Spek. Single-crystal structure validation with the program platon. *Journal Applied Crystallography*, 36:7–13, 2003.
- [237] M. Umetsu, J. G. Hollander, J. Matysik, Z. Y. Wang, T. Adschiri, T. Nozawa, and H. J. M. de Groot. Magic-Angle Spinning Nuclear Magnetic Resonance Under Ultrahigh Field Reveals Two Forms of Intermolecular Interaction Within CH₂Cl₂-Treated (3¹R)-Type bacteriochlorophyll *c* Solid Aggregate. *Journal of Physical Chemistry B*, 108:2726–2734, 2004.
- [238] J. S. Waugh and R. W. Fessenden. Nuclear Resonance Spectra of Hydrocarbons: The Free Electron Model. *Journal of the American Chemical Society*, 79:846–849, 1957.
- [239] A. Hoffmann, D. Sebastiani, E. Sugiono, S. Yun, K. S. Kim, H.W. Spiess, and I. Schnell. Solvent Molecules Trapped in Supramolecular Organic Nanotubes: A Combined Solid-State NMR and DFT Study. *Chemical Physics Letters*, 388:164–169, 2004.
- [240] D. Imbert, S. Comby, A-S. Chauvin, and J-C. G. Bünzli. Lanthanide 8-Hydroxyquinoline-Based Podates With Efficient Emission in the NIR Range. *Chemical Communications*, 11:1432–1434, 2005.
- [241] C-J. Xua, F. Xiea, X-Z. Guoa, and H. Yang. Synthesis and Cofluorescence of Eu(Y) Complexes With Salicylic Acid and o-Phenanthroline. *Spectrochimica Acta Part A*, 61:2005–2008, 2005.
- [242] H. Xin, M. Shi, X. C. Gao, Y. Y. Huang, Z. L. Gong, D. B. Nie, H. Cao, Z. Q. Bian, F. Y. Li, and C. H. Huang. The Effect of Different Neutral Ligands on Photoluminescence and Electroluminescence Properties of Ternary Terbium Complexes. *Journal Physical Chemistry B*, 108:10796–10800, 2004.

- [243] R. Caballo, B. Covelo, C. Lodeiro, and Ezequiel M. Vazquez-L. One-Dimensional Fluorescent Stacking Structure Based on Zinc Mixed-Complex Salt Encapsulated Within an Ice-Like Three-Dimensional Hydrogen-Bonded Water Network. *Crystal Engineering Communication*, 48:294–296, 2005.
- [244] K. Hayashi, H. Akutsu, H. Ozaki, and H. Sawai. Bis(phenanthroline)-Ethylenediamine Conjugate Displays Excimer Fluorescence Upon Binding With DNA. *Chemical Communications*, 12:1386–1387, 2004.
- [245] B. Yan, H. Zhang, S. Wang, and J. Ni. Intramolecular Energy Transfer Mechanism Between Ligands in Ternary Rare Earth Complexes With Aromatic Carboxylic Acids and 1,10-Phenanthroline. *Journal of Photochemistry and Photobiology A: Chemistry*, 116:209–214, 1998.
- [246] N. J. Turro. *Modern Molecular Photochemistry*. Benjamin/Cummings, Menlo Park, 1978.
- [247] J. Coates. Interpretation of Infrared Spectra, A Practical Approach. In R. A. Meyers, editor, *Encyclopedia of Analytical Chemistry*, pages 10815 – 10837. John Wiley & Sons, Chichester, 2000.
- [248] S. T. Wilson, B. M. Lok, C. A. Messina, T. R. Cannan, and E. M. Flanigen. Aluminophosphate Molecular Sieves: a New Class of Microporous Crystalline Inorganic Solids. *Journal of the American Chemical Society*, 104:1146–1147, 1982.
- [249] W. T. A. Harrison. Templated Inorganic Networks: Recent Developments. *Current Opinion in Solid State and Materials Science*, 6:407–413, 2002.
- [250] K. Wang, J. Yu, P. Miao, Y. Song, J. Li, Z. Shi, and R. Xu. A New Layered Aluminophosphate $[C_4H_{12}N_2][Al_2P_2O_8(OH)_2]$ Templated by Piperazine. *Journal of Materials Chemistry*, 11:1898–1902, 2001.
- [251] J. L. Jordá, L. B. McCusker, C. Baerlocher, C. M. Morais, J. Rocha, C. Fernandez, C. Borges, J. P. Lourenço, M. F. Ribeiro, and Z. Gabelica. Structure Analysis of the Novel Microporous Aluminophosphate IST-1 Using Synchrotron Powder Diffraction Data and HETCOR MAS NMR. *Microporous and Mesoporous Materials*, 65:43–57, 2003.
- [252] A. C. G. R. Borges de Azevedo. *Incorporação de Cobre e Cobalto em Aluminofosfatos Microporosos. Síntese e Caracterização de Novas Estruturas*. PhD thesis, Universidade Técnica de Lisboa. Instituto Superior Técnico, 2003.
- [253] M. Hunger, S. Ernst, S. Steuernagel, and J. Weitkamp. High-Field 1H MAS NMR Investigations of Acidic and Non-Acidic Hydroxyl Groups in Zeolites H-Beta, H-ZSM-5, H-ZSM-58 and H-MCM-22. *Microporous Materials*, 6:349–353, 1996.
- [254] K. Maeda, A. Tuel, and C. Baerlocher. Synthesis and Characterization of a New Layered Aluminophosphate Templated With 1,3-Diaminopropane: $[H_3N(CH_2)_3NH_3]_{0.5}[AlPO_4(OH)(OH_2)] \cdot H_2O$. *J. Chemical Society, Dalton Transactions*, pages 2457–2462, 2000.
- [255] M. H. Zahedi-Niaki, S. M. J. Zaidi, and S. Kaliaguine. Acid Properties of Titanium Aluminophosphate Molecular Sieves. *Microporous and Mesoporous Materials*, 32:251–255, 1999.

- [256] S. J. Opella and M. H. Frey. Detection of Individual Carbon Resonances in Solid Proteins. *Journal of the American Chemical Society*, 101:5856–5857, 1979.
- [257] C. A. McDowell. *Encyclopedia of Nuclear Magnetic Resonance*, chapter Magic Angle Spinning Carbon-13 Lineshapes: Effect of Nitrogen-14, pages Vol.5, 2901–2908. John Wiley & Sons, Ltd, Chichester, 1996.
- [258] K. Eichele, D. Lumsden, and R. E. Wasylshen. Nitrogen-14 Coupled Dipolar-Chemical Shift ^{13}C NMR Spectra of the Amide Fragment of Peptides in the Solid State. *Journal of Physical Chemistry*, 97:8909–8916, 1993.
- [259] Z. Gan and D. M. Grant. Molecular and Structural Information From Variable-Angle Spinning NMR Dipolar Spectra of ^{13}C - ^{14}N Systems. *Journal of Magnetic Resonance*, 90:522–534, 1990.
- [260] J. G. Hexem, M. H. Frey, and S. J. Opella. Influence of ^{14}N on ^{13}C NMR Spectra of Solids. *Journal of American Chemical Society*, 103:224–226, 1981.
- [261] C. E. Hughes, R. Pratima, T. Karlsson, and M. H. Levitt. Double-Quantum Solid-State NMR of ^{13}C Spin Pairs Coupled to ^{14}N . *Journal of Magnetic Resonance*, 159:25–35, 2002.
- [262] A. Naito, S. Ganapathy, and C.A. McDowell. ^{14}N Quadrupole Effects in CP-MAS ^{13}C NMR Spectra of Organic Compounds in the Solid State. *Journal of Magnetic Resonance*, 48:367–381, 1982.
- [263] A. C. Olivieri. Quadrupolar Effects in the CP-MAS NMR Spectra of Spin-1/2 Nuclei. *Journal of Magnetic Resonance*, 81:201–205, 1989.
- [264] A. C. Olivieri, L. Frydman, and L. E. Diaz. A Simple Approach for Relating Molecular and Structural Information to the Dipolar Coupling ^{13}C - ^{14}N in CPMAS NMR. *Journal of Magnetic Resonance*, 75:50–62, 1987.
- [265] S. E. Ashbrook and S. Wimperis. Spin-Locking of Half-Integer Quadrupolar Nuclei in Nuclear Magnetic Resonance of Solids: Creation and Evolution of Coherences. *Journal of Chemical Physics*, 120:2719–2731, 2004.
- [266] A. J. Vega. MAS NMR Spin Locking of Half-Integer Quadrupolar Nuclei. *Journal of Magnetic Resonance*, 96:50–68, 1992.
- [267] S. S. Brenner. *The Art and Science of Growing Crystals*. Wiley, 1963.
- [268] F. Rosemberg. *Preparation and Characterization of Materials*. Oxford University Press, Oxford, 1st edition, 1987.
- [269] R. S. Wagner, W. C. Ellis, S. M. Arnold, and K. A. Jackson. Study of Filamentary Growth of Silicon Crystals from Vapor. *Journal of Applied Physics*, 35:2993–3000, 1964.
- [270] H. J. Scheel. *Crystal Growth from High-Temperature Solutions*. Academic Press, London, 1st edition, 1975.
- [271] M. R. Lorenz. Preparation of CdTe Crystals from Near Stoichiometric and Cd Rich Melt Compositions Under Constant Cd Pressure. *Journal Applied Physics*, 33:3304, 1962.

- [272] A. Rabenau. The Role of Hydrothermal Synthesis in Preparative Chemistry. *Angew. Chem. Int. Edit. Engl.*, 24:1026–1040, 1985.
- [273] K. A. Kraus and H. O. Phillips. Adsorption on Inorganic Materials .1. Cation Exchange Properties of Zirconium Phosphate. *Journal of the American Chemical Society*, 78:694–694, 1956.
- [274] C. Trobajo, S. A. Khainakov, A. Espina, and J. R. Garcia. On the Synthesis of α -Zirconium Phosphate. *Chemistry of Materials*, 12:1787–1790, 2000.
- [275] A. Clearfield and J. A. Stynes. The Preparation of Crystalline Zirconium Phosphate and Some Observations on Its Ion Exchange Behaviour. *Journal of Inorganic and Nuclear Chemistry*, 26:117–129, 1964.
- [276] A. Clearfield and G. D. Smith. Crystallography and Structure of α -Zirconium Bis(Monohydrogen Orthophosphate) Monohydrate. *Inorganic Chemistry*, 8:431–436, 1969.
- [277] J. M. Troup and A. Clearfield. Mechanism of Ion-Exchange in Zirconium-Phosphates .20. Refinement of Crystal-Structure of α -Zirconium Phosphate. *Inorganic Chemistry*, 16:3311–3314, 1977.
- [278] L. Kullberg and A. Clearfield. Mechanism of Ion-Exchange in Zirconium-Phosphates .32. Thermodynamics of Alkali-Metal Ion-Exchange on Crystalline α -Zrp. *J. Phys. Chem.*, 85:1585–1589, 1981.
- [279] L. Kullberg and A. Clearfield. Mechanism of Ion-Exchange in Zirconium-Phosphates .31. Thermodynamics of Alkali-Metal Ion-Exchange on Amorphous Zrp. *J. Phys. Chem.*, 85:1578–1584, 1981.
- [280] A. Clearfield. *Inorganic Ion Exchange Materials*. Ed., CRC Press:, Boca Raton, FL, 1st edition, 1982.
- [281] G. Alberti. *Recent Developments in Ion Exchange*. Elsevier Applied Science, London, 1st edition, 1987.
- [282] G. Alberti and U. Costantino. *Inclusion Compounds. Inorganic and Physical Aspects of Inclusion*, volume 5. Oxford University Press, Oxford, 1991.
- [283] G. Alberti and U. Costantino. *Intercalation Chemistry*. Academic Press, New York, NY, 1st edition, 1982.
- [284] A. Clearfield. *Design of New Materials*. Plenum Press, New York, NY, 1st edition, 1987.
- [285] A. Clearfield, R. H. Blessing, and J. A. Stynes. New Crystalline Phases of Zirconium Phosphate Possessing Ion-Exchange Properties. *Journal of Inorganic and Nuclear Chemistry*, 30:2249–2258, 1968.
- [286] G. Alberti. *Comprehensive Supramolecular Chemistry*. Pergamon Press, Oxford, 1996.
- [287] D. M. Poojary, B. Shpeizer, and A. Clearfield. X-Ray-Powder Structure and Rietveld Refinement of γ -Zirconium Phosphate, $\text{Zr}(\text{PO}_4)(\text{H}_2\text{PO}_4)\cdot 2\text{H}_2\text{O}$. *Journal of the Chemical Society, Dalton Transactions*, 1:111–113, 1995.

- [288] A. Espina, J. R. Garcia, J. M. Guil, E. Jaimez, J. B. Parra, and J. Rodriguez. Calorimetric Study of Amine Adsorption on α - and γ -Titanium Phosphate. *Journal Physical Chemistry B*, 102:1713–1716, 1998.
- [289] A. Espina, E. Jaimez, S. A. Khainakov, C. Trobajo, J. R. Garcia, and J. Rodriguez. Synthesis of New *n*-Alkylamines Intercalation Compounds With α -Titanium Phosphate. Process Selectivity and Structural and Morphological Characterization. *Chemistry of Materials*, 10:2490–2496, 1998.
- [290] R. Llavona, M. Suarez, J. R. Garcia, and J. Rodriguez. Lamellar Inorganic-Ion Exchangers - Alkali-Metal Ion-Exchange on Alpha-Titanium and Gamma-Titanium Phosphate. *Inorganic Chemistry*, 28:2863–2868, 1989.
- [291] A. Menendez, M. Barcena, E. Jaimez, J. R. Garcia, and J. Rodriguez. Intercalation of N-Alkylamines by γ -Titanium Phosphate - Synthesis of New Materials by Thermal-Treatment of the Intercalation Compounds. *Chemistry of Materials*, 5:1078–1084, 1993.
- [292] A. N. Christensen, E. K. Andersen, I. G. K. Andersen, G. Alberti, M. Nielsen, and M. S. Lehmann. X-Ray-Powder Diffraction Study of Layer Compounds - the Crystal-Structure of α -Ti(HPO₄)₂·H₂O and a Proposed Structure for γ -Ti(H₂PO₄)(PO₄)·2H₂O. *Acta Chem. Scand.*, 44:865–872, 1990.
- [293] C. Serre, F. Taulelle, and G. Ferey. Synthesis and Characterisation of MIL-43 and MIL-44, two New Layered Templated Tetravalent Phosphates: Zr(PO₄)₂·N₂C₂H₁₀ and Ti-2(PO₄)₂(HPO₄)₂·N₂C₂H₁₀. *Solid State Sci.*, 3:623–632, 2001.
- [294] C. Chen, Y. L. Yang, K. L. Huang, Z. H. Sun, W. Wang, Z. Yi, Y. L. Liu, and W. Q. Pang. Hydrothermal Synthesis and Intercalation Behavior of a Layered Titanium Phosphate Ti₂(H₂PO₄)(HPO₄)(PO₄)₂·0.5C₆N₂H₁₆, With an Extended γ -Phase Intercalated Into Organic Amine. *Polyhedron*, 23:3033–3042, 2004.
- [295] M. A. Salvado. PhD thesis, University of Oviedo, 1999.
- [296] A. C. Larson and R. B. Von Dreele. *General Structure Analysis System (GSAS)*. Los Alamos National Laboratory Report LAUR 86-748, 2000.
- [297] E. Gonzalez, R. Llavona, J. R. Garcia, and J. Rodriguez. Lamellar Inorganic-Ion Exchangers - H⁺/Cs⁺ Ion-Exchange In γ -Titanium Phosphate. *Journal of the Chemical Society, Dalton Trans.*, pages 1825–1829, 1989.
- [298] R. W. Cheary and A. A. Coelho. *XFIT, Deposited in CCP14 Powder Diffraction Library*. Engineering and Physical Sciences Research Council, Daresbury Laboratory, Warrington, England, 1997.
- [299] R. Shirley. *The CRYSFIRE System for Automatic Powder Indexing: User's Manual*. Lattice Press, Guildford, Surrey, England, 2000.
- [300] www.shapesoftware.com.
- [301] J. Fabry, V. Petricek, J. Kroupa, and I. Cisarova. Ferroelastic Structures of *n*-Pentyl-, *n*-Hexyl- and *n*-Nonylammonium Dihydrogenphosphate Crystals. *Acta Crystallographica B*, 56:906–914, 2000.
- [302] A. March. Mathematische Theorie der Regelung nach der Korngestalt bei Affiner Deformation. *Z. Kristallogr.*, 81:285–297, 1932.

- [303] W. A. Dollase. Correction of Intensities for Preferred Orientation in Powder Diffraction - Application of the March Model. *Journal of Applied Crystallography*, 19:267–272, 1986.
- [304] W. Kolodziejcki and J. Klinowski. Kinetics of Cross-Polarization in Solid-State NMR: A Guide for Chemists. *Chemical Reviews*, 102:613–628, 2002.
- [305] A. Kaflak-Hachulska, A. Slosarczyk, and W. Kolodziejcki. Kinetics of NMR Cross-Polarization from Protons to Phosphorus-31 in Natural Brushite. *Solid State Nuclear Magnetic Resonance*, 15:237238, 2000.
- [306] R.J. Accardi, R.F. Lobo, and M. Kalwei. Paramagnetic Effect of Oxygen in the Na-23 MAS NMR and Na-23 MQMAS NMR Spectroscopy of Zeolite LiNaX. *Journal of Physical Chemistry B*, 105:5883–5886, 2001.
- [307] S. Antonijevic, S. E. Ashbrook, R. I. Walton, and S. Wimperis. A Multiple-Quantum Na-23 MAS NMR Study of Amorphous Sodium Gallium Silicate Zeolite Precursors. *Journal of Materials Chemistry*, 12:1469–1474, 2002.
- [308] S. Caldarelli, A. Buchholz, and M. Hunger. Investigation of Sodium Cations in Dehydrated Zeolites LSX, X, and Y by Na-23 Off-Resonance RIACT Triple-Quantum and High-Speed MAS NMR Spectroscopy. *Journal of the American Chemical Society*, 123:7118–7123, 2001.
- [309] L. Delevoye, J. L. Robert, and J. Grandjean. Na-23 2D 3QMAS NMR and Si-29, Al-27 MAS NMR Investigation of Laponite and Synthetic Saponites of Variable Interlayer Charge. *Clay Minerals*, 38:63–69, 2003.
- [310] S. W. Ding and C. A. McDowell. Na-23 Solid-State NMR Studies of Hydrated Disodium Adenosine Triphosphate. *Chemical Physics Letters*, 320:316–322, 2000.
- [311] C. A. Fyfe, H. M. Z. Altenschildesche, and J. Skibsted. Characterization of Na₅P₃O₁₀ polymorphs by Na-23 MAS, Na-23 MQMAS, and P-31 MAS NMR spectroscopy. *Inorganic Chemistry*, 38:84–92, 1999.
- [312] A. Wong and G. Wu. Experimental Solid-State Na-23 NMR and Computational Studies of Sodium Ethylenediaminetetraacetates: Site Resolution and Spectral Assignment. *Canadian Journal of Analytical Sciences and Spectroscopy*, 46:188–197, 2001.
- [313] S. E. Ashbrook, J. McManus, K. J. D. MacKenzie, and S. Wimperis. Multiple-Quantum and Cross-Polarized Al-27 MAS NMR of Mechanically Treated Mixtures of Kaolinite and Gibbsite. *Journal of Physical Chemistry B*, 104:6408–6416, 2000.
- [314] K. Damodaran, P. R. Rajamohanam, D. Chakrabarty, U. S. Racherla, V. Manohar, C. Fernandez, J. P. Amoureux, and S. Ganapathy. Triple-Quantum Magic Angle Spinning Al-27 NMR of Aluminum Hydroxides. *Journal of the American Chemical Society*, 124:3200–3201, 2002.
- [315] C. Fernandez, J. P. Amoureux, J. M. Chezeau, L. Delmotte, and H. Kessler. Al-27 MAS NMR Characterization of AlPO₄-14 Enhanced Resolution and Information by MQMAS. *Microporous Materials*, 6:331–340, 1996.
- [316] A. Goldbourn, M. V. Landau, and S. Vega. Characterization of Aluminum Species in Alumina Multilayer Grafted MCM-41 Using Al-27 FAM(II)-MQMAS NMR. *Journal of Physical Chemistry B*, 107:724–731, 2003.

- [317] S. R. Jansen, H. T. Hintzen, R. Metselaar, J. W. de Haan, L. J. M. van de Ven, A. P. M. Kentgens, and G. H. Nachtegaal. Multiple Quantum Al-27 Magic-Angle-Spinning Nuclear Magnetic Resonance Spectroscopic Study of SrAl₁₂O₁₉: Identification of a Al-27 Resonance from a Well-Defined AlO₅ Site. *Journal of Physical Chemistry B*, 102:5969–5976, 1998.
- [318] K. Kanehashi and K. Saito. Investigation on Chemical Structure of Minerals in Coal Using Al-27 MQMAS NMR. *Fuel Processing Technology*, 85:873–885, 2004.
- [319] J. McManus, S. E. Ashbrook, K. J. D. MacKenzie, and S. Wimperis. Al-27 Multiple-Quantum MAS and Al-27H-1 CPMAS NMR Study of Amorphous Aluminosilicates. *Journal of Non-Crystalline Solids*, 282:278–290, 2001.
- [320] F. H. Larsen and N. C. Nielsen. Effects of Finite *rf* Pulses and Sample Spinning Speed in Multiple-Quantum Magic-Angle Spinning (MQ-MAS) and Multiple-Quantum Quadrupolar Carr-Purcell-Meiboom-Gill Magic-Angle Spinning (MQ-QCPMG-MAS) Nuclear Magnetic Resonance of Half-Integer Quadrupolar Nuclei. *Journal of Physical Chemistry A*, 103:10825–10832, 1999.
- [321] P. K. Madhu, A. Goldbourn, L. Frydman, and S. Vega. Sensitivity Enhancement of the MQMAS NMR Experiment by Fast Amplitude Modulation of the Pulses. *Chemical Physics Letters*, 307:41–47, 1999.
- [322] R. Siegel, T. T. Nakashima, and R. E. Wasylshen. Signal Enhancement of NMR Spectra of Half-Integer Quadrupolar Nuclei in Solids Using Hyperbolic Secant Pulses. *Chemical Physics Letters*, 388:441–445, 2004.
- [323] T. Vosegaard, P. Florian, P. J. Grandinetti, and D. Massiot. Pure Absorption-Mode Spectra Using a Modulated RF Mixing Period in MQMAS Experiments. *Journal of Magnetic Resonance*, 143:217–222, 2000.
- [324] S. E. Ashbrook and S. Wimperis. Satellite-Transition MAS NMR of Spin $I=3/2$, $5/2$, $7/2$, and $9/2$ Nuclei: Sensitivity, Resolution, and Practical Implementation. *Journal of Magnetic Resonance*, 156:269–281, 2002.
- [325] L. M. Bull, B. Bussemer, T. Anupold, A. Reinhold, A. Samoson, J. Sauer, A. K. Cheetham, and R. Dupree. A High-Resolution O-17 and Si-29 NMR Study of Zeolite Siliceous Ferrierite and *ab initio* Calculations of NMR Parameters. *Journal of the American Chemical Society*, 122:4948–4958, 2000.
- [326] D. Freude, T. Loeser, D. Michel, U. Pingel, and D. Prochnow. O-17 NMR Studies of Low Silicate Zeolites. *Solid State Nuclear Magnetic Resonance*, 20:46–60, 2001.
- [327] K. J. Pike, V. Lemaitre, A. Kukol, T. Anupold, A. Samoson, A. P. Howes, A. Watts, M. E. Smith, and R. Dupree. Solid-State O-17 NMR of Amino Acids. *Journal of Physical Chemistry B*, 108:9256–9263, 2004.
- [328] J. E. Readman, N. Kim, M. Ziliox, and C. P. Grey. O-17 MQMAS NMR Studies of Na-A and Ca-A. *Chemical Communications*, pages 2808–2809, 2002.
- [329] S. H. Wang and J. F. Stebbins. Multiple-Quantum Magic-Angle Spinning O-17 NMR Studies of Borate, Borosilicate, and Boroaluminate Classes. *Journal of the American Ceramic Society*, 82:1519–1528, 1999.

- [330] G. Wu and S. Dong. Two-Dimensional O-17 Multiple Quantum Magic-Angle Spinning NMR of Organic Solids. *Journal of the American Chemical Society*, 123:9119–9125, 2001.
- [331] M. Zeyer, L. Montagne, V. Kostoj, G. Palavit, D. Prochnow, and C. Jaeger. O-17 Nuclear Magnetic Resonance Study of Na₂O-P₂O₅ glasses. *Journal of Non-Crystalline Solids*, 311:223–232, 2002.
- [332] P. Zhao, P. S. Neuhoff, and J. F. Stebbins. Comparison of FAM Mixing to Single-Pulse Mixing in O-17 3Q- and 5Q-MAS NMR of Oxygen Sites in Zeolites. *Chemical Physics Letters*, 344:325–332, 2001.
- [333] C. M. Morais, M. Lopes, C. Fernandez, and J. Rocha. Assessing the Potential of Fast Amplitude Modulation Pulses for Improving Triple-Quantum Magic Angle Spinning NMR Spectra of Half-Integer quadrupolar nuclei. *Magnetic Resonance in Chemistry*, 41:679–688, 2003.
- [334] S. Prasad, P. Zhao, J. Huang, J. J. Fitzgerald, and J. S. Shore. Niobium-93 MQMAS NMR Spectroscopic Study of Alkali and Lead Niobates. *Solid State Nuclear Magnetic Resonance*, 19:45–62, 2001.
- [335] D. H. Zhou, G. L. Hoatson, and R. L. Vold. Local Structure in Perovskite Relaxor Ferroelectrics: High-Resolution Nb-93 3QMAS NMR. *Journal of Magnetic Resonance*, 167:242–252, 2004.
- [336] D. Freude. *Encyclopedia of Analytical Chemistry*, chapter Quadrupolar Nuclei in Solid-State Nuclear Magnetic Resonance, pages 12188–12224. John Wiley & Sons Ltd, 2000.
- [337] M. E. Smitha and E. R. H. van Eck. Recent Advances in Experimental Solid State NMR Methodology for Half-Integer Spin Quadrupolar Nuclei. *Progress in Nuclear Magnetic Resonance Spectroscopy*, 34:159201, 1999.
- [338] A. Medek and L. Frydman. Multiple - Quantum Magic - Angle Spinning NMR: A New Technique for Probing Quadrupolar Nuclei in Solids. *Journal of the Brazilian Chemical Society*, 10:263–277, 1999.
- [339] S. E. Ashbrook and S. Wimperis. High-Resolution NMR of Quadrupolar Nuclei in Solids: the Satellite-Transition Magic Angle Spinning (STMAS) Experiment. *Progress in Nuclear Magnetic Resonance Spectroscopy*, 45:53–108, 2004.
- [340] J. Rocha, C. M. Morais, and C. Fernandez. *Topics in Current Chemistry: Progress in Multiple-Quantum Magic-Angle Spinning NMR Spectroscopy*. Springer-Verlag Berlin Heidelberg, 246: 141194, 2004.
- [341] A. Llor and J. Virlet. Towards High-Resolution NMR of More Nuclei in Solids - Sample Spinning With Time-Dependent Spinner Axis Angle. *Chemical Physics Letters*, 152:248–253, 1988.
- [342] B. F. Chmelka, K. T. Mueller, A. Pines, J. Stebbins, Y. Wu, and J. W. Zwanziger. O-17 NMR in Solids by Dynamic-Angle Spinning and Double Rotation. *Nature*, 339:42–43, 1989.
- [343] A. Samoson, E. Lippmaa, and A. Pines. High-Resolution Solid-State NMR Averaging of 2nd-Order Effects by Means of a Double-Rotor. *Molecular Physics*, 65:1013–1018, 1988.

- [344] A. Jerschow, J. W. Logan, and A. Pines. High-Resolution NMR of Quadrupolar Nuclei Using Mixed Multiple-Quantum Coherences. *Journal of Magnetic Resonance*, 149:268–270, 2001.
- [345] S. P. Brown, S. J. Heyes, and S. Wimperis. Two-Dimensional MAS Multiple-Quantum NMR of Quadrupolar Nuclei, Removal of Inhomogeneous Second-Order Broadening. *Journal of Magnetic Resonance, Series A*, 119:280–284, 1996.
- [346] T. Vosegaard, F. H. Larsen, H. J. Jakobsen, P. D. Ellis, and N. C. Nielsen. Sensitivity-Enhanced Multiple-Quantum MAS NMR of Half-Integer Quadrupolar Nuclei. *Journal of the American Chemical Society*, 117:9055–9056, 1997.
- [347] J-P. Amoureux and M. Pruski. *Encyclopedia of Nuclear Magnetic Resonance*, chapter Advances in NMR. J. Wiley, Chichester, 2002.
- [348] J-P. Amoureux, C. Morais, J. Trebosc, J. Rocha, and C. Fernandez. I-STMAS, a New High-Resolution Solid-State NMR Method for Half-Integer Quadrupolar Nuclei. *Solid State Nuclear Magnetic Resonance*, 23:213–223, 2003.
- [349] H-T. Kwak and Z. Gan. Double-Quantum Filtered STMAS. *Journal of Magnetic Resonance*, 164:369372, 2003.
- [350] S. E. Ashbrook and S. Wimperis. High-Resolution NMR Spectroscopy of Quadrupolar Nuclei in Solids: Satellite-Transition MAS with Self-Compensation for Magic-Angle Misset. *Journal of the American Chemical Society*, 124:11602–11603, 2002.
- [351] S. E. Ashbrook and S. Wimperis. SCAM-STMAS: Satellite-Transition MAS NMR of Quadrupolar Nuclei With Self-Compensation for Magic-Angle Misset. *Journal of Magnetic Resonance*, 162:402–416, 2003.
- [352] M. H. Levitt, P. K. Maduh, and C. E. Hughes. Cogwheel Phase Cycling. *Journal of Magnetic Resonance*, 155:300–306, 2002.
- [353] N. Ivchenko, C. E. Hughes, and M. H. Levitt. Application of Cogwheel Phase Cycling to Sideband Manipulation Experiments in Solid-State NMR. *Journal of Magnetic Resonance*, 164:286–293, 2003.
- [354] T. Brauniger, K. J. Pike, R. K. Harris, and P. K. Madhu. Efficient 5QMAS NMR of Spin-5/2 Nuclei: Use of Fast Amplitude-Modulated Radio-Frequency Pulses and Cogwheel Phase Cycling. *Journal of Magnetic Resonance*, 163:64–72, 2003.
- [355] N. Ivchenko, C. E. Hughes, and M. L. Levitt. Multiplex Phase Cycling. *Journal of Magnetic Resonance*, 160:52–58, 2003.
- [356] Z. H. Gan and H-T. Kwak. Enhancing MQMAS Sensitivity Using Signals from Multiple Coherence Transfer Pathways. *Journal of Magnetic Resonance*, 168:346–351, 2004.
- [357] J-P. Amoureux, L. Delevoye, S. Steuernagel, Z. Gan, S. Ganapathy, and L. Montagne. Increasing the Sensitivity of 2D High-Resolution NMR Methods Applied to Quadrupolar Nuclei. *Journal of Magnetic Resonance*, 172:268–278, 2005.
- [358] D. Massiot. Sensitivity and Lineshape Improvements of MQ-MAS by Rotor-Synchronized Data Acquisition. *Journal of Magnetic Resonance*, 122:240–244, 1996.

- [359] J-P. Amoureux and C. Fernandez. Triple, Quintuple and Higher Order Multiple Quantum MAS NMR of Quadrupolar Nuclei. *Solid State Nuclear Magnetic Resonance*, 10:211–223, 1998.
- [360] M. Ernst, M. A. Meier, T. Tüherm, A. Samoson, and B. H. Meier. Low-Power High-Resolution Solid-State NMR of Peptides and Proteins. *Journal of the American Chemical Society*, 126:4764–4765, 2004.
- [361] V. Chevelkov, K. Rehbein, A. Diehl, and B. Reif. Ultra-High Resolution in Solid-State NMR at High Levels of Deuteration. *Angewandte Chemie-International Edition*, 45:3878–3881, 2006.
- [362] V. Agarwal, A. Diehl, N. Skrynnikov, and B. Reif. Solid-State NMR using Deuterated Proteins with Selective ^1H , ^2H Isotopic Labeling of Methyl Groups. *Journal of the American Chemical Society*, 128:12620–12621, 2006.
- [363] T. Mizuno, T. Nemoto, M. Tansho, T. Shimizu, H. Ishii, and K. Takegoshi. ^2H Natural-Abundance MAS NMR Spectroscopy: An Alternative Approach to Obtain ^1H Chemical Shifts in Solids. *Journal of the American Chemical Society*, 128:9683–9686, 2006.
- [364] S. D. Kunikeev and H. S. Taylor. Saving Measurement Time in ^{13}C NMR Spectroscopy. *Journal of Physical Chemistry A*, 108:743–753, 2004.
- [365] S. D. Kunikeev, H. S. Taylor, T. Schroer, R. Haiges, C. J. B. Jones, and K. O. Christie*. New Signal Processing Method for the Faster Observation of Natural-Abundance ^{15}N NMR Spectra and Its Application to N_5^+ . *Inorganic Chemistry*, 45:437–442, 2006.
- [366] P. P. Man. Scaling and Labeling the High-Resolution Isotropic Axis of Two-Dimensional Multiple-Quantum Magic-Angle Spinning Spectra of Half-Integer Quadrupole Spins. *Physical Reviews B*, 58:2764–2782, 1998.
- [367] L. Delevoye. *Quatification des Spectres MQMAS et Application a l'Etude des Materiaux Microporeux*. PhD thesis, Université de Lille, 1998.
- [368] T. Charpentier. *Resonance Magnetique Nucleaire Haute-Resolution sur les Noyaux Quadrupolaires Dans les Solides*. PhD thesis, University of Paris XI Orsay, France, 1998.
- [369] S. A. Smith, T. O. Levante, B.H. Meier, and R. R. Ernst. Computer-Simulations in Magnetic-Resonance - An Object-Oriented Programming Approach. *Journal of Magnetic Resonance, Series A*, 106:75–105, 1994.